Late-glacial and Holocene variations in the Si cycle in the Nile Basin: Multi-isotope evidence from modern waters and lake sediments.

Cockerton, Helen Elizabeth

Swansea University
Prifysgol Abertawe

Late-glacial and Holocene variations in the Si cycle in the Nile Basin: multi-isotope evidence from modern waters and lake sediments

Helen Elizabeth Cockerton

Submitted to Swansea University in fulfilment of the requirements for the Degree of Doctor of Philosophy

Department of Geography

2012

Abstract

Until recently the continental Si cycle at Quaternary (decadal to million-year) time scales has been largely neglected. Emphasis was placed on silicate-rock weathering and resulting CO_2 drawdown on geological time scales, rather than on shorter-term biogenic processes occurring along the land-ocean continuum. The ability of some terrestrial plants (e.g. tropical rainforest trees, savanna and wetland grasses, *Papyrus*) and aquatic organisms (e.g. diatoms in lakes, rivers and swamps) to take up, store and recycle significant amounts of Si is increasingly being recognised, although their impact on the continental Si cycle and Si export to the oceans under different climatic regimes remains unquantified. The main aim of this thesis was to reconstruct spatial and temporal patterns of Si cycling in the Nile Basin during the last 15ka BP.

Seasonal variations in hydrology and Si cycling in the Nile Basin were investigated using stable isotope (H, O, and Si) compositions of surface waters, as a basis for interpreting lacustrine diatom sequences. During the dry season, both $\delta^{18}O$ and $\delta^{30}Si$ increased, due to enhanced evapotranspiration and to decreased Si supply relative to biological demand, respectively. Both $\delta^{18}O$ and $\delta^{30}Si$ showed progressive enrichment downstream, reflecting cumulative evaporation losses from swamps and open water, and preferential uptake of ^{28}Si by Si-accumulating aquatic organisms. This research has increased the measured upper limit of $\delta^{30}Si$ for dissolved Si (DSi) in the world's rivers by >1‰.

Si- and O-isotope analysis of diatom silica in cores from Lakes Victoria and Edward, in the headwaters of the White Nile, were employed to reconstruct changes in biotic Si cycling and palaeohydrology, respectively. The relative abundances of lipid biomarkers (hydrocarbon-fraction) permitted major changes in terrestrial and aquatic ecosystems to be tracked. During drier conditions (e.g. the last glacial and late Holocene) (high $\delta^{18}O_{diatom}$), Si cycling was greatly reduced. Diminished biomass, reduced biotic weathering, a declining soil stock of amorphous silica (ASi) and decreased run-off in the catchment resulted in biological demand for Si (high $\delta^{30}Si_{diatom}$). In contrast, enhanced monsoon rainfall (low $\delta^{18}O_{diatom}$) during the early to mid-Holocene enabled the proliferation of vegetation in the catchment, which in turn accelerated silicate-rock weathering and the mobilisation of DSi in surface runoff, providing a plentiful supply of Si (low $\delta^{30}Si_{diatom}$). Both the modern waters and palaeo-records indicate that the riverine flux of Si to the oceans on glacial \ interglacial time scales was not constant; resulting in important implications for the marine Si budget and consequently the global C cycle.

Declaration

This work has not previously been accepted in substance for any degree and is not being concurrently submitted in candidature for any degree.

Signed .. .. (candidate)

Date ..... 14.02.13 .....

STATEMENT 1

This thesis is the result of my own investigations, except where otherwise stated. Where correction services have been used, the extent and nature of the correction is clearly marked in a footnote(s).

Other sources are acknowledged by footnotes giving explicit references. A bibliography is appended.

Signed ... . (candidate)

Date ..... 14.02.13 .....

STATEMENT 2

I hereby give consent for my thesis, if accepted, to be available for photocopying and for inter-library loan, and for the title and summary to be made available to outside organisations.

Signed .. .. (candidate)

Date ..... 14.02.13 .....

NB: *Candidates on whose behalf a bar on access has been approved by the University (see Note 7), should use the following version of Statement 2:*

I hereby give consent for my thesis, if accepted, to be available for photocopying and for inter-library loans **after expiry of a bar on access approved by the Swansea University.**

Signed . ..... (candidate)

Date ..... 14.02.13 .....

There is no bar on this thesis Student & supervisor have confirmed that this statement was included in error.
SG 8/3/13.

Table of contents

Acknowledgements

Most importantly I would like to thank my family and friends for continuous support and encouragement during a busy four years. I would especially like to thank my fiancé, Mark, for the amazing support he has given me, particularly during the last few months when I would come home to delicious homemade meals and all the housework done!

I would like to express my gratitude to my supervisors Professor Alayne Street-Perrott and Dr Kath Ficken. To Alayne for introducing me to the exciting world of silicon isotopes and the global biogeochemical cycle of Si, and for the constructive criticism and guidance through my PhD. To Kath, for sharing her expertise in organic geochemistry and being there to give good advice. I also thank Professors Melanie Leng at the NIGL and Phil Barker at Lancaster University for their involvement in the project, particularly for advice on methodologies, diatom identifications and for hosting me at the respective labs.

There are so many people at Swansea University that I would like to thank for being so cooperative and helpful: The ladies in stores (Cath, Diane and Jean) for being so accommodating with fieldwork and conference reservations, obtaining laboratory equipment and generally looking after finances. Even shipping a new pH meter to Uganda when my other one broke; Jonathan Woodman-Ralph for obtaining lab equipment and providing safety advice when required; Phil Bevan for organizing fieldwork equipment; Anna Ratcliffe and Nicola Jones for drawing fantastic maps and helping me to understand Adobe Illustrator; and Dr Thierry Maffeis and Rich Brown in the Engineering Department for training me to use the SEM.

Those externally, I would like to thank: Professor Jim Russell, at Brown University in Rhode Island, USA for providing data and in-depth information on age-models for Lake Edward, providing material from Lake Mahoma, and giving advice on sampling Lake Victoria cores; Professor Tom Johnson at the University of Minnesota, USA for sharing information and data on Lake Victoria cores; the LacCore staff at the University of Minnesota for their cooperation and swift delivery of lake sediments; Dr Roger Flower at UCL for conversations on the sedimentology of Lake Qarun and for providing sediment and water samples from the Faiyum; Dr Henry Lamb and Dr Sarah Davies at Aberystwyth University for providing sediments from Lake Tana and assisting me with sampling strategy; Hilary Sloane at NIGL for analysing cleaned diatoms frustules for O- and Si-isotopes; Carol Arrowsmith at NIGL for carrying out O- and H-isotope analysis on the water samples; Dr Simon Chenery and Thomas Barlow at the BGS for the analysis of major ion concentrations in the water samples; Dr Matt Horstwood, Dr Steve Noble and Vanessa Pashley for their patience and persistence on cracking the measurement of Si-isotopes on waters by HR-MC-ICP-MS at NIGL; and Laetitia Pichevin at the University of Edinburgh for showing me the ropes for preparing waters for Si-isotope analysis using column chemistry.

Without them I would not have been able to achieve the fieldwork that I did, thank you to my friends and family, Charlotte Bristol, Alexandra Goldsack, Sarah Cockerton and Mark Fox for being superb field assistants. I would also like to thank: NERC for the financial support in proving a DTG; the NERC Isotope Geosciences Laboratory for a grant in kind for analysing all the water and diatom samples in this thesis for O-, H- and Si-isotope analysis; the National Geographic Society for the Research and Exploration Grant which enabled three extensive field seasons; and the Department of Geography at Swansea University for proving office space and quality lab facilities to undertake this research.

List of figures

Chapter 2 Research background

Chapter 3 Study region: the Nile Basin

Chapter 4 Methods development: Si-isotope analysis of waters

Chapter 5 Research design and methodology

Chapter 6 Modern surface water results

Chapter 7 Lake Victoria, East Africa

Chapter 8 Lake Edward, East Africa

Chapter 9 Discussion

List of tables

Chapter 2 Research background

Chapter 4 Methods development: Si-isotope analysis of waters

Chapter 5 Research design and methodology

Chapter 6 Modern surface water results

Chapter 7 Lake Victoria, East Africa

Chapter 8 Lake Edward, East Africa

Notations and abbreviations used in this thesis

Ka BP	Kiloannum calendar years Before Present (A.D. 1950)
GMWL	Global Meteoric Water Line
AMWL	African Meteoric Water Line
LELs	Local evaporative lines
ppm	parts per million
ppb	parts per billion
mg/L	milligrams per litre
µmol	micromolar; amount of substance concentration
‰	per mil; isotopic ratios are reported in parts per thousand (‰)
BSi%	Percentage biogenic silica
TOC	Total organic carbon
TON	Total organic nitrogen
C/N	Carbon/nitrogen ratios
HI	Hydrogen Index
HCl	Hydrochloric acid
H_2O_2	Hydrogen peroxide
HNO_3	Nitric acid
VSMOW	Vienna Standard Mean Ocean Water; standard for oxygen isotope analysis
NBS-28	Quartz sand reference material used as a standard for silicon and oxygen isotope analysis
BFC	Diatomite reference material for Shastra County, California, USA, used as a standard for silicon and oxygen isotope analysis
$\delta^{18}O$	Stable oxygen isotope composition; the ratio of ^{18}O to ^{16}O in a sample relative to a standard
$\delta^{18}O_{calcite}$	Oxygen isotope composition of calcite
$\delta^{18}O_{diatom}$	Oxygen isotope composition of diatom silica
$\delta^{2}H$	Stable hydrogen isotope composition; the ratio of ^{2}H to ^{1}H in a sample relative to a standard
$\delta^{30}Si$	Stable silicon isotope composition; the ratio of ^{30}Si to ^{28}Si in a sample relative to a standard
$\delta^{30}Si_{diatom}$	Silicon isotope composition of diatom silica
$\delta^{13}C$	Stable carbon isotopes; the ratio of ^{13}C to ^{12}C in a sample relative to a standard
P_{wax}	An *n*-alkane proxy for terrestrial plant and aquatic emergent plant input
P_{aq}	An *n*-alkane proxy for submerged and floating aquatic macrophytes input
P_{alg}	An *n*-alkane proxy for algal input
P/E	Precipitation/evaporation ratio
LGM	Last Glacial Maximum
EAHP	East African Humid Period
AHP	African Humid Period (~15-5 ka BP)
ASi	Amorphous silica; biogenic and non-biogenic amorphous silica
BSi	Biogenic silica. e.g phytoliths, diatoms
DSi	Dissolved silicon; silicic acid; $Si(OH)_4$
TSi	ASi + DSi; biologically reactive Si

Chapter 1: Introduction

The Quaternary period was characterised by cyclic variations in climate and ice-sheet extent, creating "glacials", characterized by the existence of large ice sheets in the polar regions and "interglacials", associated with warm conditions. Natural variations in global atmospheric CO_2 concentrations have occurred in phase with these cycles, so that CO_2 concentrations rose from ~190-200 ppmv (parts per million by volume) at the Last Glacial Maximum (LGM, ~21,000 yrs ago) to ~270-280 ppmv prior to the Industrial Revolution (Petit et al., 1999). One group of explanations for these variations in CO_2 involves changes in the nutrient inventory of the ocean, notably in the supply of iron (Fe), phosphorus (P), nitrogen (N) and silicon (Si) for marine plankton (Alverson et al., 2003). Of these elements, Fe, P and Si are derived mainly from rock weathering and transported to the ocean by rivers and aeolian processes. This thesis focuses on past variations in the fluvial transport of dissolved Si, which are poorly known. Most research on the global Si cycle has focussed exclusively on weathering (Berner et al., 1983; Berner, 1995; Hilley and Porder, 2008) on the oceanic Si cycle (De La Rocha et al., 1998; Dugdale and Wilkerson, 2001; Ragueneau et al., 2006) and has not explored the role of continental biota in controlling the flux of Si to the oceans (see Street-Perrott and Barker (2008) and Struyf et al. (2009) for reviews).

The global biogeochemical cycles of carbon and silicon are closely linked by two main groups of processes (i.e. geological and biological) that act on different time scales: (1) long-term silicate rock weathering, whereby CO_2 is consumed and silicic acid ($Si(OH)_4$), otherwise known as dissolved Si (DSi), is released, making Si readily available for biological uptake; and (2) the faster transfer of CO_2 from the atmosphere to the deep ocean by siliceous marine organisms (primarily diatoms: unicellular phytoplankton), which is commonly referred to as the biological Si pump (Ragueneau et al., 2006). Diatoms require Si in the form of $Si(OH)_4$ to build their shells (frustules). Therefore, the supply of Si reaching the oceans may ultimately affect the regulation of CO_2 in the atmosphere, and hence global climate on glacial / interglacial time scales. Although both mechanisms result in a net drawdown of CO_2, it is the relatively unknown biotic control on Si export from the continents to the oceans *via* rivers that most needs to be explored.

1: Introduction

Some terrestrial plants (e.g. tropical rainforest trees, savanna and wetland grasses, *Papyrus*) and freshwater organisms (e.g. diatoms and sponges in lakes, rivers and swamps) have the ability to take up, store and recycle significant amounts of Si. Si is taken up in dissolved form (DSi) and converted to amorphous silica (ASi), during which these organisms preferentially incorporate the lighter isotopes (^{28}Si and ^{29}Si), leaving the residual fluid enriched in the heavier isotope (^{30}Si) (Leng et al., 2009). An increasing number of studies is showing that ASi contents of plants differ greatly, generally ranging from 1 to 10% dry weight, with some species exceeding 20%, in particular bamboo (Epstein, 1994; Ma and Yamaji, 2006; Struyf and Conley, 2009). Even the ASi contents of plants that are not classified as Si accumulators (accumulator plants being defined as those in which Si is taken up to a greater extent, proportionally, than water) may be comparable to those of essential macronutrients such as P, S, Ca and Mg (Epstein, 1994). Although there has so far been no attempt to quantify the potential storage of Si by siliceous freshwater aquatic organisms such as diatoms, it is estimated that global annual terrestrial ASi production (terrestrial and aquatic) is of the same order of magnitude as the global oceanic ASi production by diatoms (~240 Tmol yr^{-1}) (Conley, 2002; Laruelle et al., 2009). Continental biotic Si cycling, therefore, should have a significant impact on Si fluxes to the ocean, the productivity of siliceous marine organisms and the rate of CO_2 drawdown by the marine biological pump. Although the ability of terrestrial and freshwater organisms to store significant amounts of Si is increasingly being recognised, their impact on the continental Si cycle and Si export to the oceans under different climatic regimes remains to be established.

1.1 Main Aim

The main aim of this thesis was to reconstruct temporal and spatial changes in Si biocycling in the Nile Basin since the last major arid episode (desiccation event) at ~15 ka BP (calendar years), using sediment cores from lakes along the course of the river. Diatoms preserved in the sediments allowed silicon- and oxygen-isotope analyses to be carried out, enabling glacial / interglacial changes in Si cycling and hydrology, respectively, to be reconstructed. The relative abundances of higher-plant leaf waxes and algal biomarkers permitted major changes in terrestrial and aquatic ecosystems to be tracked and used to interpret the isotope data.

1.2 Objectives

Specific objectives were:

- To collect and analyse modern waters from the Nile river system for $\delta^{2}H$, $\delta^{18}O$ and $\delta^{30}Si$ and to investigate the downstream evolution of these parameters in response to seasonal changes in moisture balance and Si cycling, in order to provide a firm foundation for interpreting the sediment record.
- To reconstruct millennial-scale variations in Si cycling in the White Nile headwater basins of Lakes Victoria and Edward during the last 15 ka BP from $\delta^{30}Si$ in diatom silica preserved in lake sediments.
- To reconstruct past changes in monsoon rainfall and hydrology in the White Nile headwaters from $\delta^{18}O_{diatom}$, in parallel with the $\delta^{30}Si_{diatom}$ measurements.
- To link these results to past changes in terrestrial and aquatic ecosystems using abundance ratios of lipid biomarkers (*n*-alkanes, *n*-alkenes and botryococcenes).

1.3 Research Hypothesis

This thesis aims to test the hypothesis that riverine fluxes of dissolved Si to the oceans varied as a result of Late Quaternary climatic and ecosystem changes driven by orbital forcing. At the LGM, under cooler and drier conditions, plant biomass, biotic weathering and Si cycling should have been greatly reduced, while large amounts of stored biogenic silica should have been released to drainage waters through vegetation degradation and increased erosion of soils and sediments. In turn, this would reduce Si-isotope fractionation (low $\delta^{30}Si_{diatom}$). In contrast, enhanced monsoon rainfall and expansion of forest, savannas, lakes and swamps during the East African Humid Period (EAHP, ~15-5 ka BP) should have resulted in increased biological demand for Si and greater isotopic fractionation (high $\delta^{30}Si_{diatom}$).

1.4 Rationale for selection of the study region

The Nile Basin was selected as a suitable study area to test the above hypothesis due to the availability of riverine lakes and swamps to investigate past changes in Si cycling. Previous coring expeditions, such as the International Decade of East African Lakes (IDEAL) project, provided a source of (palaeo)lake sediments for this research as it was not feasible, during the timeframe of the PhD and the budget available, to core the lakes myself. In addition, Late Quaternary palaeoclimate and palaeoenvironmental records and established chronologies were available to assist with interpretation of the data obtained in this thesis. Due to its geographical positioning, with its flow south to north across distinct latitudinal climates (equatorial to hyper-arid conditions) and the corresponding large-scale vegetation gradient, seasonal climate variability and differing geology in the two main tributaries, which join to form the Main Nile at Khartoum, the Nile Basin give rise to variables that are thought to be important in the global Si cycle.

1.5 Thesis structure

The thesis consists of a further nine chapters. Chapter 2 contains information about the global biogeochemical cycle of Si and its coupling to the global biogeochemical C cycle. Emphasis is placed on the role of continental biota and their ability to take up, store and recycle Si, and on the techniques and applications used to track the continental Si cycle. I also describe the principles of stable-isotope hydrology and the use of lipid biomarkers to infer past changes in terrestrial and aquatic ecosystems. Chapter 3 presents an overview of the Nile Basin study region, including the long-term controls on climate variability and previous palaeoclimate and palaeoenvironmental studies undertaken in the Basin. Chapter 4 includes information about how the NERC Isotope Geosciences Laboratory (NIGL) team and I developed a methodology and capacity for analysing Si isotopes on waters using a Neptune high-resolution Multi-Collector Inductively-Coupled-Plasma Mass-Spectrometer (MC-ICP-MS). In chapter 5 I describe the sampling strategy and the methods used to analyse the modern waters for H-, O- and Si-isotopes. I also go into detail about extracting pure diatom silica from lake sediments for Si- and O-isotope analysis and the methods used to determine abundance ratios of lipid biomarkers. Chapter 6 presents results of the physical, chemical and isotopic characteristics of the modern water samples and their seasonal variability in the Nile Basin. Chapter 7 is dedicated to Lake Victoria, a lake in the headwaters of the White Nile. This chapter includes a site description; a summary of previous palaeo-studies and their findings, the sample material available for the thesis and related existing data; an account of the site-specific methods used to prepare diatoms for isotope analysis; and finally the results of the stable- isotope and lipid-biomarker analyses. Chapter 8 covers Lake Edward, another lake in the headwaters of the White Nile, and is structured similarly to Chapter 7. The first part of Chapter 9 is the interpretation of the modern water data for the Nile Basin, which are then used to help explain the palaeo-records of Lakes Victoria and Edward. This chapter is rounded off by discussing the implications of this study for past changes in the Si flux from the River Nile to the Mediterranean Sea during the Late Quaternary. Chapter 10 draws together the major conclusions of this thesis including the implications for the global Si cycle and for future research directions.

Chapter 2 Research background

2.1 Introduction

This chapter provides the reader with background information about the key components of the thesis in order to set the scene for the following chapters. An explanation of the global biogeochemical cycle of Si and its connections with the global C cycle is presented. Emphasis is placed on the role of continental biota on the global Si cycle which forms the basis of this thesis. Following that, information on the tools used to trace the Si cycle and examples of their applications, with particular emphasis on using the isotopic composition of diatom silica are discussed. The principles of stable isotope hydrology are outlined and their application to natural waters and diatom silica are discussed. The chapter draws to a close on the principles of lipid analysis in lake sediments with particular focus on using hydrocarbons for reconstructing past vegetation variations.

2.2 The global biogeochemical cycle of Si

Silicon is the second most abundant element in the Earth's crust, comprising 28.8 wt% of the total crust (Wedepohl, 1995). Through the consumption of CO_2 during silicate-rock weathering and by the sequestration of CO_2 to the deep ocean by siliceous marine organisms (also known as the biological pump), the global biogeochemical cycles of Si and C are intrinsically linked (Figure 2.1). These processes operate on different timescales (Tréguer et al., 1995), with silicate-rock weathering being important over geological timescales (10^2 to 10^8 years) and the biological pump on glacial / interglacial time scales (10 to 10^4 years). In addition, vascular plants themselves accelerate silicate rock weathering by increasing soil CO_2 and moisture content, producing organic acids and generating chelating ligands (Lovering, 1959; Berner, 1992; Drever, 1994; Cochran and Berner, 1996; Berner, 1997; Kelly et al., 1998; Moulton et al., 2000; Hinsinger et al., 2001; Lucas, 2001; Brantley et al., 2011), and thereby introduce another coupling between the global C and Si cycles through the consumption of CO_2 by photosynthesis (Figure 2.1).

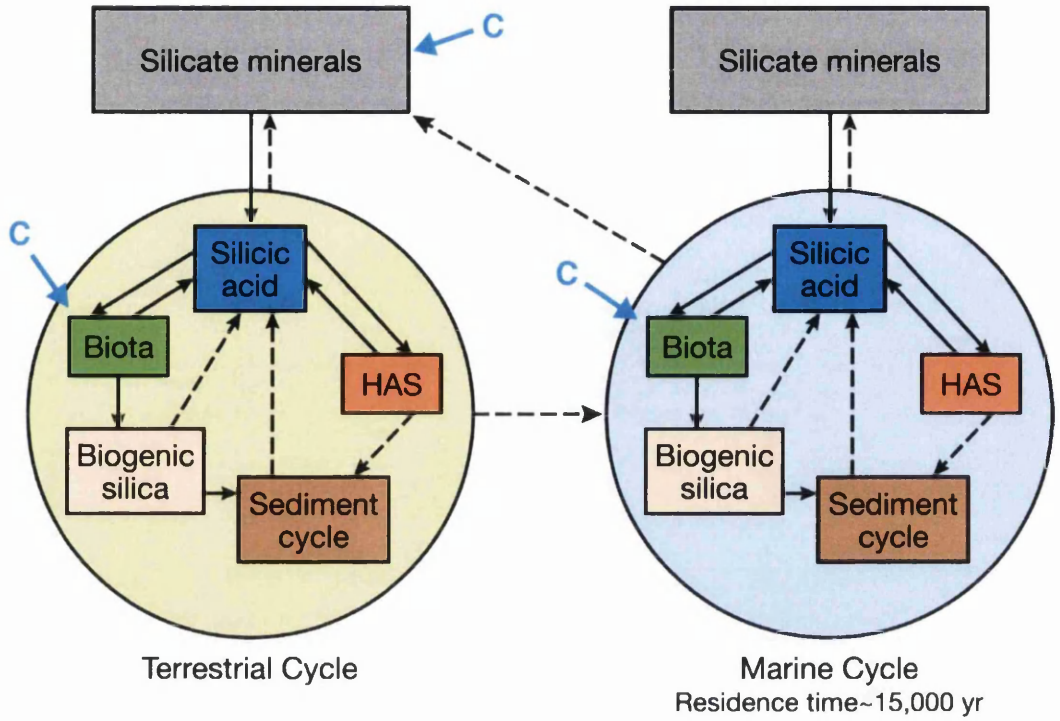

Figure 2.1: The coupling of terrestrial and marine biogeochemical cycles of silicon with the carbon cycle (modified after Exley (1998)). Broken arrows represent slower rates of exchange between compartments; C = interface with the carbon cycle; HAS = hydroxyalumino-silicates.

Silicate-rock weathering plays an important role in regulating climate through the control of CO_2 in the atmosphere and the oceans (Berner et al., 1983; Berner, 1995; Kump et al., 2000). Weathering of silicate minerals (Ca- and Mg-silicates) on the continents by carbonic acid can be represented by the idealised reaction (Berner et al., 1983; Berner, 1995):

$$2CO_2 + 3H_2O + CaSiO_3 \rightarrow Ca^{2+} + 2HCO_3^- + Si(OH)_4 \qquad \textbf{(Equation 1),}$$

where Ca^{2+} can be substituted by Mg^{2+}.

Carbonic acid is either derived directly from the atmosphere, or from oxidation of soil organic matter during the degradation of plant biomass (Berner, 1992, 1995; Berner and Berner, 2012), which ultimately draws down carbon from the atmosphere via photosynthesis, resulting in the net consumption of atmospheric CO_2 in the weathering process.

The idealised reaction of Equation 1 suggests that simple congruent dissolution occurs during silicate weathering. However, congruent dissolution of silicate minerals is rare (Berner and Berner, 2012). More commonly, the minerals involved dissolve to varying extents as a result of their chemical stability and solubility (Goudie, 2004). Therefore, silicate weathering is usually associated with the reprecipitation of insoluble elements and the production of secondary weathering products in the form of secondary clay minerals, or Fe and Al oxides and hydroxides, as the more soluble elements dissolve and new products form (Loughnan, 1969; Berner and Berner, 2012). For instance, the example used by Street-Perrott and Barker (2008) shows the complexity of the silicate weathering reaction of Ca-plagioclase feldspar to kaolinite:

$$CaAl_2Si_2O_8 + 2H_2CO_3 + H_2O \rightarrow Al_2Si_2O_5(OH)_4 + 2HCO_3^- + Ca^{2+} \quad \textbf{(Equation 2),}$$

further weathering allows dissolved silicon ($Si(OH)_4$) to be leached from the kaolinite lattice, forming gibbsite:

$$Al_2Si_2O_5(OH)_4 + H_2O \rightarrow 2Al(OH)_3 + 2Si(OH)_4 \quad \textbf{(Equation 3).}$$

The rate of silicate rock weathering is not only affected by atmospheric CO_2 content but also by temperature and hydrological controls, which are strongly influenced by the concentration of CO_2; enhanced atmospheric CO_2 tends to warm the land and intensify the hydrological cycle. In turn, this increases the amount of silicate minerals in contact with water, accelerating silicate weathering and the drawdown of CO_2 (Berner et al., 1983; Berner and Caldeira, 2002). Other factors affecting the extent and rate of silicate rock weathering on various temporal scales include: changes in the continental surface area as a result of uplift rate; sea-level change; runoff; lithology; and vegetation type, extent and biomass (Knoll and James, 1987; Berner, 1992; Bluth and Kump, 1994; White and Blum, 1995; Moulton et al., 2000; Dessert et al., 2003; Fulweiler and Nixon, 2005).

In addition to CO_2 being consumed during silicate-rock weathering, dissolved Si (DSi) is released as orthosilicic acid (e.g. $Si(OH)_4$) (see Equations 1 and 3). Although previously, the global Si cycle was considered to be predominantly a geochemical cycle, it is becoming increasingly recognised that continental biota play an important role in the global Si cycle both by enhancing silicate-rock weathering

and by modifying the flux of Si from the continents through the uptake, storage and recycling of DSi before it is exported via rivers to the oceans (Figure 2.2) (Conley, 2002; Street-Perrott and Barker, 2008; Struyf et al., 2009; Cornelis et al., 2011; Struyf and Conley, 2012). The supply of DSi is essential for the productivity of marine diatoms, which are the main phytoplankton in today's oceans (Tréguer et al., 1995; Tréguer and Pondaven, 2000; Dugdale and Wilkerson, 2001; Yool and Tyrrell, 2003), accounting for ~54% of the total primary production (Nelson et al., 1995), and are estimated to utilise ~240 Tmol yr^{-1} of Si (Tréguer et al., 1995). Diatoms draw down CO_2 to the deep ocean via the biological pump. A proportion of the diatomaceous opal may become permanently buried in sediments until it is recycled through tectonics (Sigman and Boyle, 2000; Ragueneau et al., 2006). Tréguer et al. (1995) estimated that currently 80% of DSi is derived from runoff from the continents with the remainder being derived from wind-blown material and sea-floor (hydrothermal) weathering. Therefore, variations in the fluvial supply of DSi from the continents are likely to have considerable implications for the carbon export to the deep sea on glacial / interglacial time scales, due to the resulting changes in phytoplankton productivity and/or species composition (Archer et al., 2000; Tréguer and Pondaven, 2000). Based on Germanium/Silicon (Ge/Si) ratios of marine diatom silica, **Froelich et al. (1992) suggested that Si fluxes from rivers to the oceans during the last glacial were even higher than they are at present, encouraging even more drawdown of CO_2 by diatoms.**

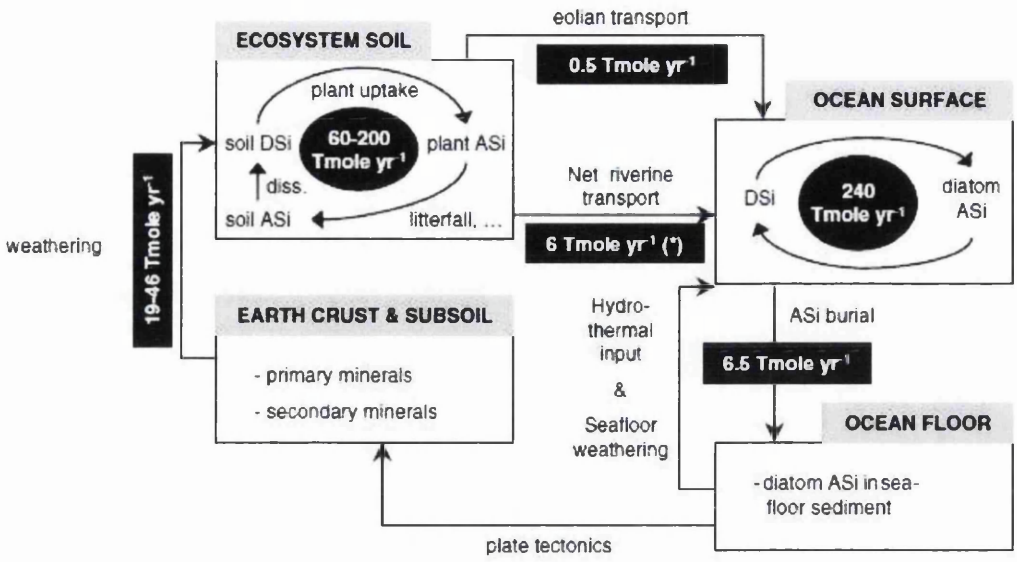

Figure 2.2: The global biogeochemical cycle of Si. Rectangular black boxes represent Si fluxes between the primary Si pools. Circular black boxes represent Si fluxes within the primary Si pools. (*) The 6 Tmole yr^{-1} flux is partitioned between the net riverine transport (excluding ASi retained in estuaries) and the flux resulting from hydrothermal activity and sea-floor weathering. DSi: dissolved silicon ($Si(OH)_4$). ASi: amorphous silica. From Struyf et al. (2009).

2.3 The terrestrial Si cycle and the role of biota

Growing interest in the role of continental biota in the global Si cycle reflects the close coupling between the global biogeochemical cycles of Si and C (see Street-Perrott and Barker (2008) and Struyf et al. (2009) for reviews). Previously, the main focus was on long-term geological processes of silicate-rock weathering and the drawdown of CO_2 in the marine realm (Berner et al., 1983; Berner, 1994; Berner, 1995; Smetacek, 1998; Dugdale and Wilkerson, 2001; Yool and Tyrrell, 2003; Ragueneau et al., 2006; Hilley and Porder, 2008). However, growing evidence shows that certain plants and aquatic organisms have the ability to modify the Si cycle by taking up, recycling and storing significant amounts of Si in their cells before it reaches the ocean (Figure 2.3) (Conley, 1997, 2002; Street-Perrott and Barker, 2008; Struyf and Conley, 2009; Struyf and Conley, 2012). Although Si is not classified as an essential nutrient for plants, amongst other benefits, it can enhance structural rigidity and growth, and reduce abiotic and biotic stresses (Jones and Handreck, 1967; Raven, 1983; Epstein, 1999; Ma et al., 2001). Certain plants that

contain >1% dry weight of silica are known as Si accumulators (Jones and Handreck, 1967; Marschner, 1995; Ma et al., 2001; Hodson et al., 2005). These are abundant in a variety of terrestrial and aquatic ecosystems (e.g. grasslands, tropical rainforests, temperate deciduous forests and wetlands). They have the potential to retain large amounts of Si (Table 2.1) (Bartoli, 1983; Alexandre et al., 1997; Struyf et al., 2005; Blecker et al., 2006; Struyf et al., 2007; Ding et al., 2008b; Gérard et al., 2008; Street-Perrott and Barker, 2008; Struyf and Conley, 2009; Cornelis et al., 2010a; Schoelynck et al., 2010; Alexandre et al., 2011).

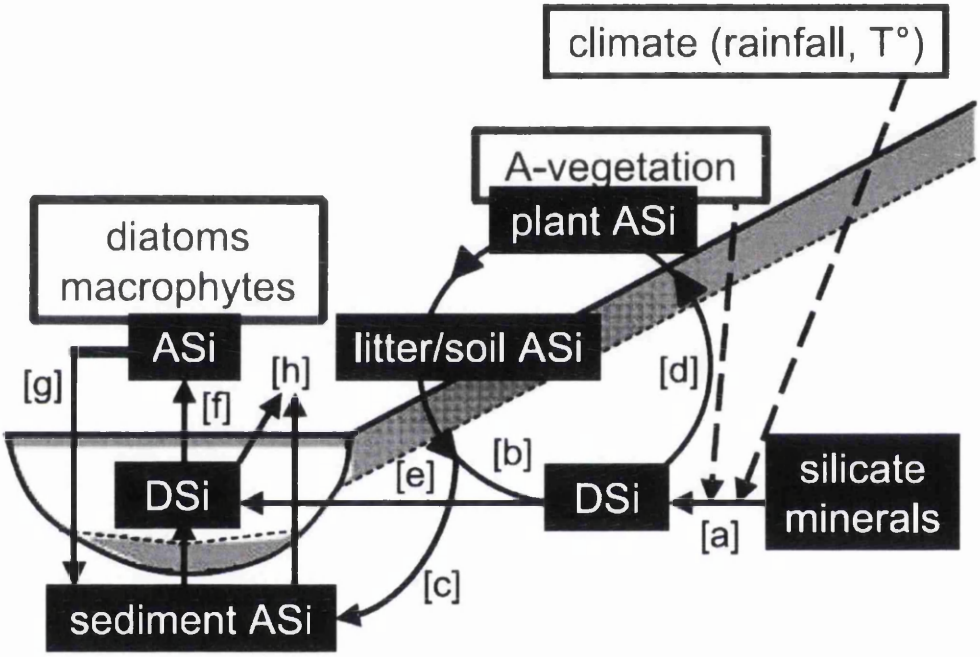

Figure 2.3: Schematic representation of the terrestrial biogeochemical cycle of Si in a general ecosystem (from Struyf et al. (2009)). Black boxes represent the major Si pools. White boxes represent factors which influence terrestrial Si cycling. Solid arrows indicate Si fluxes; [a] weathering of primary and secondary silicates, [b] dissolution of litter/soil ASi to DSi, [c] ASi transport to rivers through topsoil erosion, [d] plant uptake of DSi, [e] DSi flux towards rivers through the flux of groundwater, [f] uptake of DSi by diatoms and macrophytes in the riverine environment, [g] burial of death diatom and macrophytes biomass, [h] export of DSi and ASi with the downstream river flux. Dashed arrows indicate influences on the weathering of silicates exerted by climate and vegetation. T°: temperature. DSi: dissolved silicon ($Si(OH)_4$). ASi: amorphous silica.

Table 2.1: Estimated storage, recycling and export of Si fluxes in forest and grassland ecosystems (from Cornelis et al. (2011)). Reference: 1. Lucas et al. (1993), 2. Alexandre et al. (1997), 3. Bartoli (1983), 4. Cornelis et al. (2010a), 5. Markewitz and Richter (1998), 6. Gérard et al. (2008), 7. Blecker et al. (2006).

	Si ($kg\,ha^{-1}\,yr^{-1}$)			
	Vegetation uptake	Restitution by litterfall	Export by drainage	Reference
Equatorial forest (Ferralsols)		41	11	1
Equatorial forest (Ferralsols)	58–76	58–76	16	2
Temperate deciduous forest (Cambisols)	23	22	3	3
Temperate deciduous forest (Cambisols)	18–23	18–19	6–7	4
Temperate coniferous forest (Cambisols)	30–43	29–42	0.7–1	4
Temperate coniferous forest (Cambisols)	44	36	5	6
Temperate pine forest (Cambisols)	2.3	2.1	9.4	4
Temperate pine forest (Podzols)	6	5	28	3
Temperate pine forest	16	14	17	5
Dry grasslands (Aridisols)	–	26	0.2	7
Humid grasslands (Mollisols		59	11	7

Si is ultimately derived from silicate-rock weathering and is released in dissolved form as orthosilicic acid ($Si(OH)_4$). Dissolved Si (DSi) present in soil solution may be taken up by terrestrial vegetation and precipitated as hydrated amorphous silica bodies (phytoliths), or transported into rivers and lakes, where Si-accumulating aquatic organisms, such as diatoms, sponges and aquatic macrophytes, progressively extract DSi (Figure 2.3). The residual DSi is transported via rivers, eventually reaching the oceans where it is an essential nutrient for the siliceous phytoplankton that dominate the marine biological pump (Harrison, 2000; Tréguer and Pondaven, 2000). On glacial to interglacial time scales, the Si flux to the oceans can therefore be expected to vary as a result of changes in climate, vegetation type and distribution, hydrology and limnology (Georg et al., 2006a; Street-Perrott and Barker, 2008; Engström et al., 2010; Cornelis et al., 2011).

2.4 Tracers of the Si cycle

2.4.1 Silicon isotopes

Silicon has three stable isotopes: ^{28}Si (92.23%), ^{29}Si (4.67%) and ^{30}Si (3.10%). The Si isotope composition of a sample is expressed as $\delta^{29}Si$ or $\delta^{30}Si$ in per mille (‰), relative to the reference material, NBS-28:

$$\delta^{29}Si = \left[\frac{\left({}^{29}Si / {}^{28}Si \right)_{sample}}{\left({}^{29}Si / {}^{28}Si \right)_{NBS-28}} - 1 \right] \times 1000 \qquad \textbf{(Equation 4)}$$

$$\delta^{30}Si = \left[\frac{\left({}^{30}Si / {}^{28}Si \right)_{sample}}{\left({}^{30}Si / {}^{28}Si \right)_{NBS-28}} - 1 \right] \times 1000 \qquad \textbf{(Equation 5).}$$

The fractionation of stable Si isotopes can be used to trace biogeochemical processes, as they are fractionated during neoformation of secondary minerals (e.g. clays) and by biological processes. Measurements of Si isotopes in natural samples are still relatively scarce: previously reported $\delta^{30}Si$ values for fresh waters range from –0.17 to +3.4‰ (De La Rocha et al., 2000; Ding et al., 2004; Alleman et al., 2005; Gao et al., 2006; Georg et al., 2006a; Reynolds et al., 2006a; Georg et al., 2007; Georg et al., 2009; Cardinal et al., 2010; Engström et al., 2010; Ding et al., 2011; Opfergelt et al., 2011; Hughes et al., 2012), showing that DSi in rivers and lakes is isotopically enriched in ^{30}Si compared with primary minerals (felsic magmatic rocks: $\delta^{30}Si$ = –0.07 ± 0.05‰; gneisses, granulites and migmatites: $\delta^{30}Si$ = –0.10 ± 0.15‰ (André et al., 2006); and mafic magmatic rocks: $\delta^{30}Si$ = –0.29 ± 0.08‰ (Savage et al., 2011)). During formation of secondary products (e.g. phytoliths, diatoms and clays), the light isotope of Si (^{28}Si) is preferentially incorporated into the product (De La Rocha et al., 2000), thereby enriching the residual aqueous solution in the heavier isotopes ^{29}Si and ^{30}Si. Hence, Si isotopes offer great potential as tracers of the continental Si cycle (Street-Perrott and Barker, 2008).

Diatom silica is formed of biogenic opal ($SiO_2 \cdot nH_2O$) containing oxygen (see section 2.5) and silicon isotopes that can be used in palaeoenvironmental studies (Leng and Barker, 2006; Leng and Swann, 2010). Si is an essential nutrient for the survival of diatoms and during biomineralization is incorporated into their frustules in dissolved

form as silicic acid ($Si(OH)_4$) (Round et al., 1990; Smol and Stoermer, 2010). The isotopic composition of the frustules reflects the aqueous environment in which they formed. As a result of biological fractionation, the lighter isotope (^{28}Si) is preferentially incorporated in the diatom frustule. Progressive utilization of DSi results in an enrichment of both diatom and the residual water, making $\delta^{30}Si_{diatom}$ a suitable tracer of the Si cycle (Leng et al., 2009). The Si-isotope composition of lacustrine diatoms ($\delta^{30}Si_{diatom}$) is related to the availability of this nutrient, which in turn is connected to local factors such as catchment geology and vegetation, chemical weathering, river and groundwater inputs, water-residence time and the occurrence of seasonal diatom blooms (Leng et al., 2009; Leng and Swann, 2010). Experiments have demonstrated that the Si isotope enrichment factor in diatoms of -1.1 to -1.9‰ (closed system) has no dependence on temperature, pCO_2, pH or species effects during Si isotope fractionation, making $\delta^{30}Si_{diatom}$ a valid proxy for nutrient utilisation (De La Rocha et al., 1997; De La Rocha et al., 2000; Milligan et al., 2004; Varela et al., 2004; Alleman et al., 2005).

Very few studies have used $\delta^{30}Si_{diatom}$ in lake sediments so far (Street-Perrott et al., 2008; Swann et al., 2010; Chen et al., 2012). Most studies of $\delta^{30}Si_{diatom}$ have been made on marine diatoms, investigating and reconstructing DSi utilisation in the oceans (De La Rocha et al., 1998; Varela et al., 2004; De La Rocha and Bickle, 2005; Pichevin et al., 2009; Egan et al., 2012). Until now, measurements of $\delta^{30}Si_{diatom}$ in continental environments have been restricted to relatively small catchment-lake ecosystems. Street-Perrott et al. (2008) attempted to reconstruct Si cycling on Mount Kenya over orbital time scales during the last 38 ka BP using a multi-proxy approach including $\delta^{30}Si_{diatom}$. Unfortunately, it was not possible to purify diatoms for Si-isotope analysis from sediments younger than ~14 ka BP. The study suggested that Si was available for diatom production during the last glacial, whereas during the late glacial and early Holocene, as the catchment stabilised, limited mobilisation of Si caused a reduction in diatom productivity in the lake. The study showed how changes in catchment vegetation can have an impact on ASi and DSi outputs. In a lake-catchment ecosystem in north-east Siberia, the first combined O- and Si-isotope analysis of diatom silica was presented for the last 23 ka BP (Figure 2.4) (Swann et al., 2010). The authors interpreted $\delta^{30}Si_{diatom}$ as reflecting changes in nutrient availability due to climate-induced variations in chemical weathering in the catchment and water-column mixing within the lake. High $\delta^{30}Si_{diatom}$ values during the last glacial and the mid- to late Holocene reflected

decreased weathering and nutrient delivery from the catchment, resulting in increased utilisation of DSi. In contrast, the early Holocene thermal maximum exhibited low $\delta^{30}Si_{diatom}$ due to greater mobilisation of Si from the catchment and recycling of nutrients within the lake from enhanced mixing. A study in a small tropical lake in South China used $\delta^{30}Si_{diatom}$ as a palaeotemperature proxy for the last 2000 years (Chen et al., 2012). However, it is difficult to imagine that temperature variations in the tropics would have been great enough to cause large changes in diatom productivity and hence DSi utilisation.

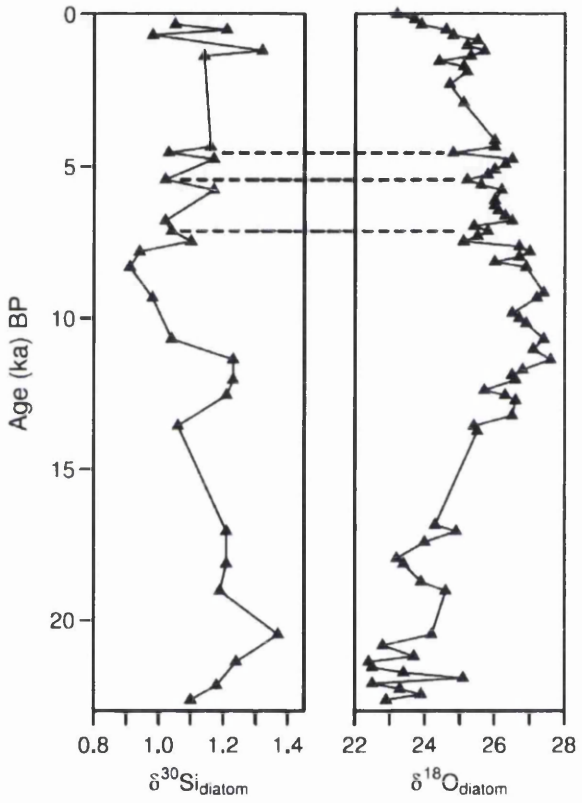

Figure 2.4: Changes in $\delta^{30}Si_{diatom}$ and $\delta^{18}O_{diatom}$ in Lake El'gygytgyn, northeast Siberia. From Swann et al. (2010).

In the context of the large, relatively shallow tropical lakes in the headwaters of the River Nile, long-term (millennial-scale) changes in $\delta^{30}Si_{diatom}$ are likely to reflect changes in the Si supply from the catchment rather than changes in nutrient cycling within the lake in response to stratification or overturning. Several authors have shown that over long time scales, riverine inputs of biologically available Si (DSi and ASi) to Lakes Malawi, Victoria and Edward were most important, as the internal

(lake) Si cycle cannot sustain itself beyond several decades (Johnson et al., 1998; Johnson et al., 2001; Johnson et al., 2002; Bootsma, 2003; Russell and Johnson, 2005; Johnson et al., 2011).

2.4.2 Ge/Si ratios

A relatively new technique has been developed to aid the determination of the source of dissolved Si, i.e. whether it originated within the soil-plant cycle or through purely geochemical processes. Germanium/silicon (Ge/Si) ratios reflect these two naturally occurring pathways (Kurtz and Derry, 2004; Derry et al., 2005). Germanium behaves like a pseudo-isotope of silicon; hence Ge/Si ratios can be used as a tracer of Si cycling, particularly in tropical environments (Kurtz and Derry, 2004). Solutions with high Ge/Si ratios are thought to reflect dissolution of secondary aluminosilicates such as allophone or kaolinite, as the latter are enriched in Ge (Murnane and Stallard, 1990; Filippelli et al., 2000; Kurtz et al., 2002; Kurtz and Derry, 2004), whereas low Ge/Si ratios may reflect dissolution of BSi (e.g. phytoliths) or weathering of primary rock minerals (Kurtz and Derry, 2004; Derry et al., 2005; Delvigne et al., 2009; Lugolobi et al., 2010). Combining Ge/Si measurements with other techniques such as Si-isotope analysis will provide a powerful tool for deciphering Si cycling in a catchment (Derry et al., 2006; Street-Perrott and Barker, 2008; Cornelis et al., 2010b).

2.5 Stable isotope hydrology

Hydrogen has two stable isotopes: ^{1}H (99.985%) and ^{2}H (0.015%). Oxygen has three stable isotopes: ^{16}O (99.76%), ^{17}O (0.04%) and ^{18}O (0.20%). The H- and O-isotope composition of a sample is expressed as $\delta^{2}H$ and $\delta^{18}O$ respectively, in per mille (‰), relative to the reference material, VSMOW (Vienna Standard Mean Ocean Water), where:

$$\delta^{2}H = \left[\frac{\left({}^{2}H/{}^{1}H \right)_{sample}}{\left({}^{2}H/{}^{1}H \right)_{VSMOW}} - 1 \right] \times 1000$$

(Equation 6)

$$\delta^{18}O = \left[\frac{\left({}^{18}O/{}^{16}O \right)_{sample}}{\left({}^{18}O/{}^{16}O \right)_{VSMOW}} - 1 \right] \times 1000$$

(Equation 7).

Surface waters can be valuable indicators of the average isotopic composition of rainfall, especially in situations in which limited evaporative enrichment has occurred since precipitation (Fritz, 1981; Stern and Blisniuk, 2002). Craig (1961) was the first to establish the linear relationship between δ^2H and $\delta^{18}O$ in meteoric waters, defining it as $\delta^2H = 8 \cdot \delta^{18}O + 10‰$, which is known as the Global Meteoric Water Line (GMWL). This represents the average of many local and regional meteoric water lines that vary due to differing climatic and geographical factors (Clark and Fritz, 1997). Hence, in regional or site-specific studies, a Local Meteoric Water Line (MWL) may be preferred. Globally, variations in the δ^2H and $\delta^{18}O$ ratios of precipitation are controlled by climatic (temperature, rainfall amount, humidity, evaporation, wind regime) and geographical parameters (latitude, altitude, distance from moisture source) as described by Dansgaard (1964). At low latitudes, the spatial distribution of isotopes in precipitation is primarily controlled by the source of the water, subsequently modified by continental, altitude and amount effects that are explained by the Rayleigh distillation process (Figure 2.4). Along the trajectory of an air mass, isotopically heavy water molecules preferentially fall from a diminishing vapour mass, leaving the residual vapour to become progressively depleted (leading to lower δ^2H and $\delta^{18}O$). Subsequent rainfall becomes increasingly lower in isotopic composition (Figure 2.4) (Dansgaard, 1964; Gat, 1996; Clark and Fritz, 1997; Gat, 2000). This rain-out effect occurs during the transport of an air mass from an oceanic moisture source to the interior of a landmass (continental effect), during orographic uplift (altitude effect) and during heavy convective rainstorms such as those associated with the passage of the ITCZ (amount effect).

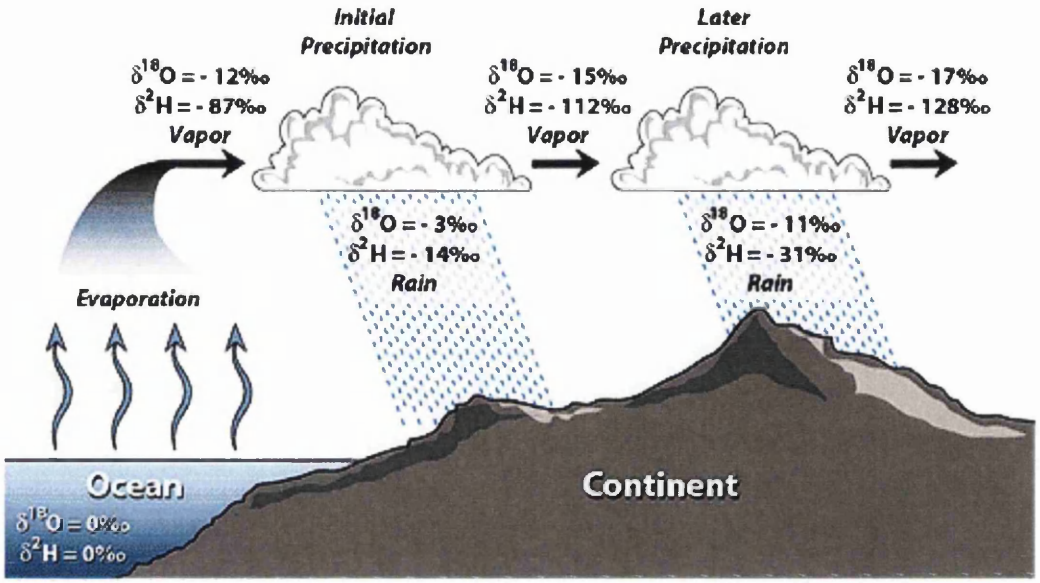

Figure 2.5: Impact of the Rayleigh distillation process on δ^2H and $\delta^{18}O$ values during atmospheric transport. From SAHRA (2005).

Deviation from the GMWL/MWL indicates that kinetic effects have modified the original isotopic composition of the precipitation since it was formed. Several processes can cause this effect. Surface water or rainfall that has undergone evaporation will typically plot below the MWL on independent Local Evaporation Lines (LELs) (Figure 2.5) (Craig, 1961; Gat et al., 1994). Slopes between 2 and 5 are common; the exact slope depending on the humidity. Low humidity leads to slopes very different from the MWL as water-vapour exchange is minimized, and evaporation becomes an increasingly non-equilibrium (kinetic) process, leaving the residual water enriched in the heavier isotopes ^{18}O and ^{2}H (Craig and Gordon, 1965). Rain condensed from this evaporated vapour will plot above the MWL (i.e. with a greater y-intercept, or deuterium excess). The concept of deuterium excess (or d-excess), defined as $d\ (‰) = \delta^2H - 8 \cdot \delta^{18}O$, was introduced by Dansgaard (1964) to describe the relationship between the hydrogen and oxygen isotope compositions of water. It measures the degree of evaporation at the moisture source or the amount of evaporative enrichment in ^{18}O after the water has condensed. The most important control on d-excess is thought to be humidity (Merlivat and Jouzel, 1979). Information about the fractionating processes in convective systems can be obtained from d-excess values, which may have been modified from their original source composition during their transportation to the

precipitation site (Figure 2.6) (Fröhlich et al., 2002). Values lower than +10‰ may indicate secondary evaporation processes, such as the evaporation of falling raindrops in a warm, dry atmosphere (Stewart, 1975; Araguás-Araguás et al., 2000). Recycling of water vapour in continental basins may be responsible for large d-excess values, as identified in the Amazon Basin (Gat and Matsui, 1991) and the Great Lakes region of North America (Gat et al., 1994).

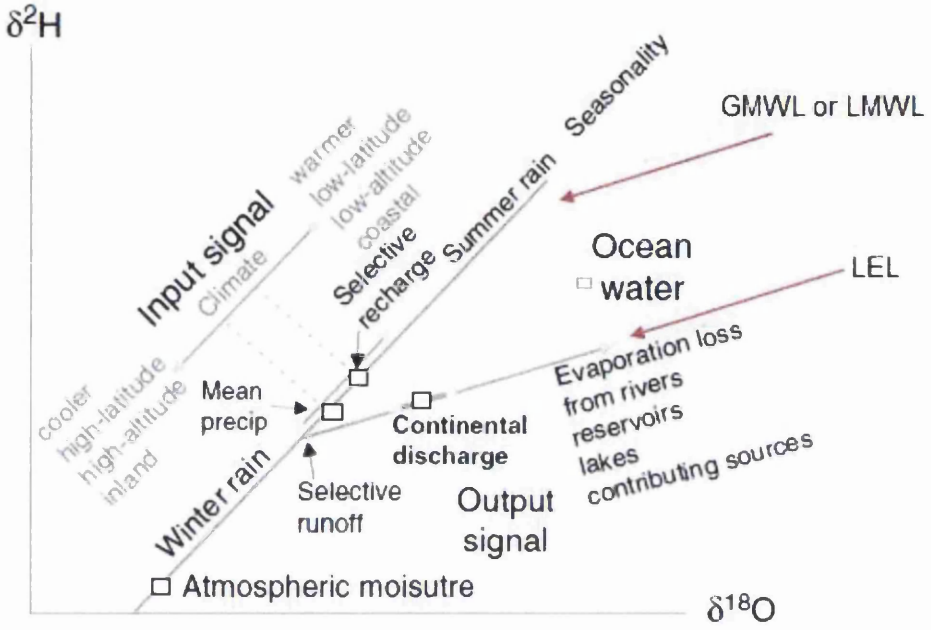

Figure 2.6: Conceptual model of δ^2H versus $\delta^{18}O$ for the hydrological cycle. GMWL (Global Meteoric Water Line) / LMWL (Local Meteoric Water Line) represent values of global or local precipitation values from which LEL's (Local Evaporation Line) can form from. Modified after Gibson et al. (2010).

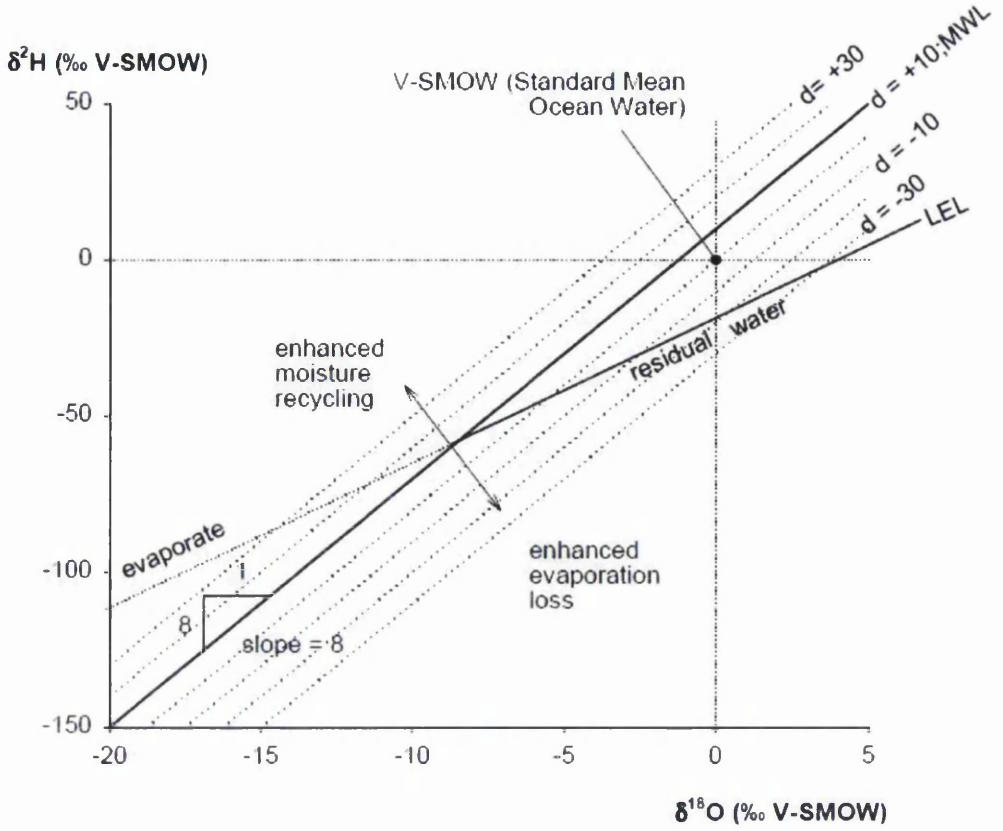

Figure 2.7: Schematic plot of δ^2H versus $\delta^{18}O$ showing the global meteoric water line (MWL; d = 10, slope = 8) of Craig (1961), local evaporation line (LEL; slope <8), ocean water (SMOW) and relative changes in the d-excess (d). D-excess in precipitation increases in response to enhanced moisture recycling as a result of increased evaporate content. d-excess is reduced in the case where water is lost by evaporation. From Fröhlich et al. (2002).

As identified in section 2.4.1, the isotopic composition of diatom silica reflects the isotopic composition of the aqueous environment in which it formed. The oxygen-isotope composition of diatoms ($\delta^{18}O_{diatom}$) is controlled primarily by water temperature and/or by the isotope composition of the lake water (Leng and Marshall, 2004; Leng and Barker, 2006). In the tropics, seasonal temperature changes are small (Rozanski et al., 1993; Rozanski et al., 1996). Instead the isotopic composition of the lake water is likely to be the main control on $\delta^{18}O_{diatom}$ which is influenced by a combination of factors including the amount of precipitation, the $\delta^{18}O$ of the vapour over the source region and surface processes (i.e. evaporative enrichment) (Barker et al., 2001; Leng and Barker, 2006; Polissar et al., 2006; Barker et al., 2007; Hernández et al., 2010; Barker et al., 2011; Hernández et al., 2011).

Similarly to silicon isotopes on diatom silica, it is important to understand the processes which influenced the $\delta^{18}O_{diatom}$ composition. Due to the difficulty of separating individual diatom species as a result of their small size, isotopic analysis is usually performed on mixed assemblages. However, there is limited evidence at present to suggest species effects or any that are measurable beyond analytical error (Shemesh et al., 1995; Brandriss et al., 1998; Moschen et al., 2005; Schiff et al., 2009). Indeed, the different size fractions measured in this thesis, and on occasion species-specific samples, did not indicate significant offsets in $\delta^{18}O_{diatom}$ composition. Dissolution is a process that may lead to isotope fractionation, although experiments have been unable to determine the effect on $\delta^{18}O_{diatom}$ (Swann and Leng, 2009; Leng and Swann, 2010). Again, this is unlikely to have had a significant impact on $\delta^{18}O_{diatom}$ values measured in this thesis as the diatoms analysed showed no signs of dissolution or diagenesis. The effect of maturation (the amount of isotopic exchange between the inner and outer hydroxyl layer of diatom silica) on $\delta^{18}O_{diatom}$ is still unknown and requires further investigation (Swann and Leng, 2009; Leng and Swann, 2010). However, it has been suggested that these effects are small and therefore $\delta^{18}O_{diatom}$ for the time being is at least useful for qualitative interpretations (Swann and Leng, 2009; Leng and Swann, 2010; Swann et al., 2010).

2.6 Lipid biomarkers

Organic matter forms part of lake sediments and consists of a mixture of lipids, carbohydrates, proteins and other biochemicals from living organisms which lived within the lake (autochthonous), such as phytoplankton, bacteria and submerged/floating macrophytes, and in the lake catchment (allochthonous), for example, vascular land plants (Meyers and Ishiwatari, 1993). Such "chemical fossils" can provide important information about terrestrial and aquatic palaeoenvironments (Meyers, 1997): more diagnostic than bulk geochemical properties (Castañeda and Schouten, 2011). Individual compounds or compound classes that can be traced to a particular source organism or group of organisms (e.g. terrestrial plants, aquatic macrophytes, algae and bacteria) are called "biomarkers" (Peters et al., 2007; Castañeda and Schouten, 2011). Lipids are a fraction of organic matter which are insoluble in water but can be extracted by organic solvents (Meyers and Ishiwatari, 1993; Killops and Killops, 2005). Within the lipid fraction are hydrocarbons (organic compounds consisting exclusively of

hydrogen and carbon, the simplest of which are the straight-chain *n*-alkanes and *n*-alkenes), *n*-alkanols and *n*-alkanoic acids, all of which are abundant and have relatively well known biological origins (Meyers and Ishiwatari, 1993; Meyers, 1997; Killops and Killops, 2005; Castañeda and Schouten, 2011). *n*-Alkanes (saturated hydrocarbons) are least susceptible to degradation and therefore are most commonly used in palaeoenvironmental reconstructions (Meyers and Ishiwatari, 1993).

n-Alkanes are biosynthetically derived from decarboxylation of fatty acids: as a result, they have a strong odd-over-even carbon number predominance (Killops and Killops, 2005). *n*-Alkanes generally have chain lengths ranging from C_{15} to C_{35} (Barnes and Barnes, 1978). An assessment of the preservation of n-alkanes can be undertaken using the relative abundance of odd versus even carbon-numbered *n*-alkanes, the carbon preference index (CPI) (Bray and Evans, 1961):

$$\mathbf{CPI} = \frac{1}{2}\left(\frac{(C_{25}+C_{27}+C_{29}+C_{31}+C_{33})}{(C_{24}+C_{26}+C_{28}+C_{30}+C_{32})} + \frac{(C_{25}+C_{27}+C_{29}+C_{31}+C_{33})}{(C_{26}+C_{28}+C_{30}+C_{32}+C_{34})}\right) \quad \textbf{(Equation 8).}$$

This equation can be adjusted to include the range of carbon numbers encountered in a specific study, for example (Ficken et al., 1998):

$$\mathbf{CPI} = \frac{1}{2}\left(\frac{(C_{23}+C_{25}+C_{27}+C_{29}+C_{31})}{(C_{22}+C_{24}+C_{26}+C_{28}+C_{30})} + \frac{(C_{23}+C_{25}+C_{27}+C_{29}+C_{31})}{(C_{24}+C_{26}+C_{28}+C_{30}+C_{32})}\right) \quad \textbf{(Equation 9).}$$

CPI values close to 1 indicate that a smooth distribution of *n*-alkanes (almost equal odd-to-even predominance), which may suggest degradation by oxidation, microbial activity or erosion during transport (Meyers and Ishiwatari, 1993).

Suites of *n*-alkane compounds have been identified as characteristic of certain plant groups can be used to investigate contributions from specific sources (i.e. terrestrial or aquatic). Long-chain homologues (C_{27}-C_{35}) are generally characteristic of terrestrial higher plants (Eglinton and Hamilton, 1967), whereas short-chain homologues (C_{17}-C_{21}) are characteristics of aquatic algae (Cranwell et al., 1987). Ficken et al. (2000) demonstrated that C_{23}-C_{25} *n*-alkanes (mid-chain lengths) were the main component of submerged and floating (non-emergent) aquatic macrophytes. Specific homologues may be characteristic of certain plant types. For

example, the C_{31} *n*-alkane is dominant in grasses and, while the C_{27} and C_{29} *n*-alkanes are common in deciduous trees (Cranwell, 1973).

Biomarker proxies, based on ratios of these key groups of source contributors (long-chain, mid-chain, and short-chain compounds) have been developed to assess the relative contributions of each group for palaeoenvironmental interpretations. For example, the P_{wax} ratio is given by the abundance of long-chain *n*-alkanes over the sum of mid- and long-chain *n*-alkanes ($P_{wax} = (C_{27} + C_{29} + C_{31})/(C_{23} + C_{25} + C_{27} + C_{29} + C_{31})$), and reflects the proportions of contributions from terrestrial plants and emergent aquatic macrophytes such as reeds, relative to submerged/floating aquatic macrophytes (Zheng et al., 2007). Ficken et al. (2000) proposed the *n*-alkane P_{aq} proxy ($P_{aq} = (C_{23} + C_{25})/(C_{23} + C_{25} + C_{29} + C_{31})$) to distinguish the relative contribution of submerged/floating aquatic macrophytes from that of emergent aquatic and terrestrial plants. A P_{aq} value of >0.4 signifies that an important fraction of the *n*-alkanes originated from submerged/floating plants (Ficken et al., 2000).

Alkenes are unsaturated hydrocarbons (those which have double bonds between adjacent carbon atoms). Several studies of lacustrine and riverine sediments have reported high abundances of mid- to long-chain *n*-alkenes and suggested that they are algal indicators (Matsumoto et al., 1990; Zhang et al., 2004; Theissen et al., 2005; de Mesmay et al., 2007; Xu and Jaffé, 2009). With this in mind, Zhang et al. (2004) formulated a proxy for algal (mixed) inputs based upon the proportion of *n*-alkenes and a hydrocarbon compound produced by the green alga *Botryococcus* (cyclobotryococcatriene) relative to terrestrial plant input. This index was termed $P_{alg} = (C_{23:1} + C_{25:1} + C_{27:1} + \text{cyclobotryococcatriene})/(C_{23:1} + C_{25:1} + C_{27:1} + \text{cyclobotryococcatriene} + C_{29} + C_{31} + C_{33})$.

Care must be taken when allocating these broad classifications of *n*-alkanes (long-, mid-, and short-chain compounds) to specific sources, as a few studies have identified exceptions to the general pattern (Castañeda and Schouten, 2011). For example, *Betula*, a deciduous tree, was found to contain a large proportion of C_{23} *n*-alkanes (Sachse et al., 2006), which would incorporate it into the submerged and floating aquatic macrophyte classification, based on the *n*-alkane-based proxies above.

2.7 Summary

This chapter summarises the general scientific background to this study. An account of the global biogeochemical Si cycle and its coupling with the global C cycle highlights the importance of the relatively neglected and poorly understood role of continental biota in the global Si cycle. Emphasis is placed on the principles underlying the analytical techniques used in this thesis, particularly the relatively new application of Si isotopes to diatom silica as a tracer of the Si cycle. The principles of stable isotope hydrology are outlined, followed by consideration of the processes that may affect the isotopic composition of diatom silica. Background information on lipid biomarker analysis and biomarker-based proxies that can be used to determine the palaeoenvironment in and around lakes is also presented.

Chapter 3 Study region: the Nile Basin

3.1 Introduction

This chapter introduces the physical environment of the broader study area, the Nile Basin, including information about its geography, geology, climatology, hydrology and vegetation. The second half describes the controlling mechanisms for long-term climate change across north-east Africa and the evidence for past changes in hydrology and vegetation.

3.2 Geography

The River Nile is located in northeast Africa, and drains from the tropics northwards into the Mediterranean Sea (Figure 3.1). The Nile Basin covers an area of over 3 million km^2 across ten countries; Burundi, Rwanda, Democratic Republic of Congo, Tanzania, Kenya, Uganda, South Sudan, Republic of the Sudan, Ethiopia, Eritrea and Egypt. The length of the river is about 6700 km, making the Nile the longest river in the world. The catchment extends from 4°S to 32°N, spanning a wide variety of altitudinal, geological, geomorphological, climatic and vegetation zones (Figures 3.1-3.7). The main tributaries are the White Nile, originating from the headwaters of the equatorial great lakes in East Africa, and the Blue Nile and Atbara which descend from the Ethiopian Highlands. The two Niles converge at Khartoum, Sudan, and flow northwards to the Mediterranean Sea. Climate and vegetation are closely correlated with precipitation amount and the number of dry months, which are primarily governed by the northward migration of the Intertropical Convergence Zone (ITCZ) in boreal summer and by orography (Nicholson, 1996).

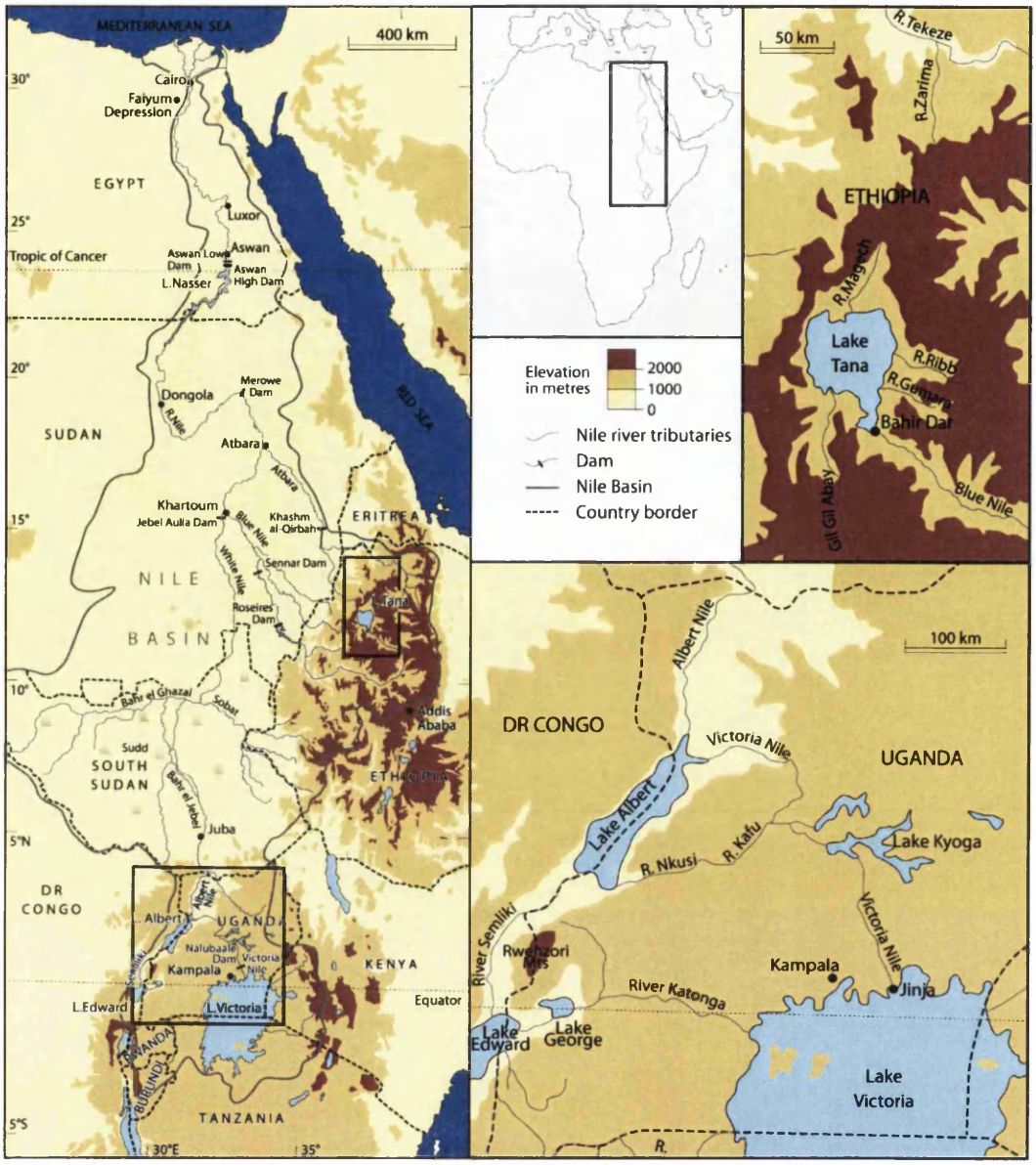

Figure 3.1: Location of the River Nile and its tributaries.

3.3 Geology

The White Nile and Blue Nile catchments are geologically distinct (Figure 3.2). A large portion of the Nile Basin is underlain by Precambrian granitic and metamorphic rocks. Volcanic rocks are more extensively developed in Ethiopia than anywhere else along the East African Rift system (Williams et al., 2006; Schlüter, 2008). Although the Blue Nile Basin is underlain by Precambrian crystalline basement, more than two-thirds of the Upper Blue Nile Basin is covered by a thick stack of weathered trap basalts (Kebede et al., 2005). The Atbara passes through a similar succession of rock types. In the headwaters of the White Nile, small pockets of volcanics occur along the Western Rift (e.g. Virunga Mountains) and east of Lake Victoria. However, more than two-thirds of Uganda are underlain by Precambrian granites, granulites and gneissic sequences that continue further downstream into the western part of the Sudd and the Bahr el Ghazal. From Juba northwards along the main channel and in the plains in the east, unconsolidated sediments are widespread. In northern Sudan and southern Egypt, the Main Nile flows over continental clastic sequences and crystalline basement rocks. The remainder of its passage to the Delta crosses unconsolidated marine sediments.

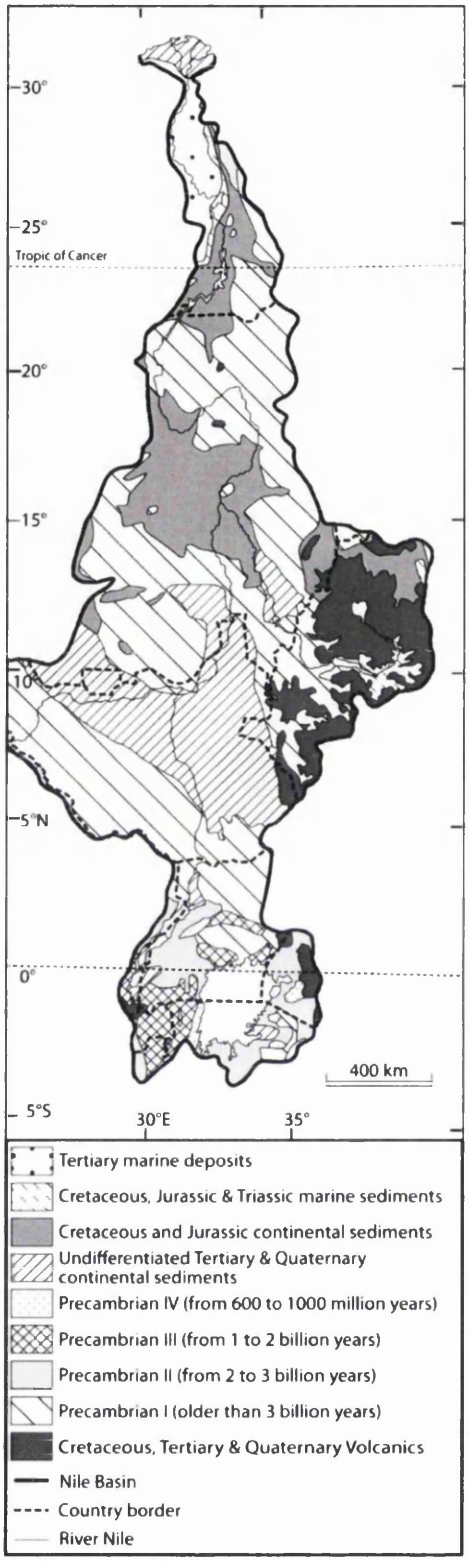

Figure 3.2: Simplified geology of the Nile basin (modified after Furon (1958)).

3.4 Climate

Annual variations in the hydrological budget of the River Nile are largely governed by the seasonal migration of the Intertropical Convergence Zone (ITCZ), which separates the relatively stable, dry northeast monsoon from the southeasterly monsoon airflow from the Indian Ocean, and moves north and south across the Equator following the overhead sun (Figure 3.3). The Congo Air Boundary (CAB) defines the convergence of unstable, moist westerly flow from the Atlantic Ocean, also known as the Congo Air Stream, and easterly flow from the Indian Ocean (Nicholson, 1996). The passage of the ITCZ usually coincides with maximum rainfall due to intensified convective activity; as a result, the equatorial regions of the White Nile catchment exhibit a bimodal rainfall pattern (Figure 3.4). Two rainy seasons occur during the months of March, April, May (MAM) ("long rains") and October, November, December (OND) ("shorter rains"), with the north-western tip of Uganda experiencing a third rainy season during August (Ogallo, 1988). During this time East Africa is under the influence of prevailing easterly winds (Griffiths, 1972; Nicholson, 1996), bring moisture from the equatorial and northwest Indian Ocean during OND and from the south-western Indian Ocean during MAM. In contrast, the Blue Nile headwaters in the north-western Ethiopian Highlands are characterised by a single rainy season between the months of June and September, when the ITCZ reaches its most northerly position (~18°N) (Kebede et al., 2006). In both regions, mean annual rainfall exceeds 1000 mm/year, with additional factors such as topography and continental water bodies (notably the equatorial great lakes and Lake Tana) having an influence on regional and local climates through the distribution of orographic precipitation, rain shadows and land-lake circulations (Nicholson, 1996). In contrast, northern Sudan (from ~18°N) and Egypt, which lie well beyond the maximum northward limit of the ITCZ (Figure 3.4), experience negligible rainfall (<50 mm annually) (Camberlin, 2009).

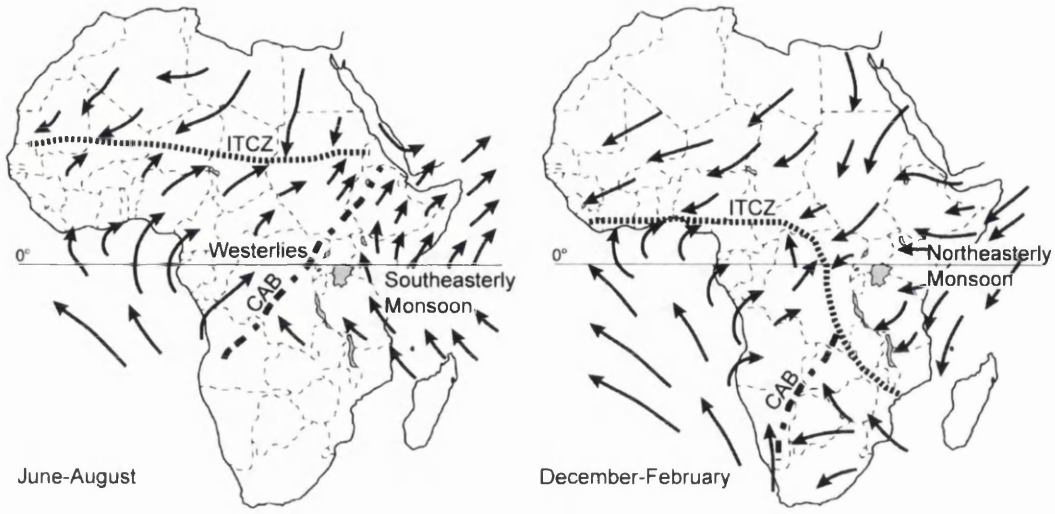

Figure 3.3: Schematic of the low-level mean flow over tropical Africa in boreal (June–August) and austral summer (December–February) based on NCEP reanalysis 925 hPa mean winds and Nicholson (1996). The approximate positions of the Intertropical Convergence Zone (ITCZ) and the Congo Air Boundary (CAB) are shown (modified after Levin et al. (2009)).

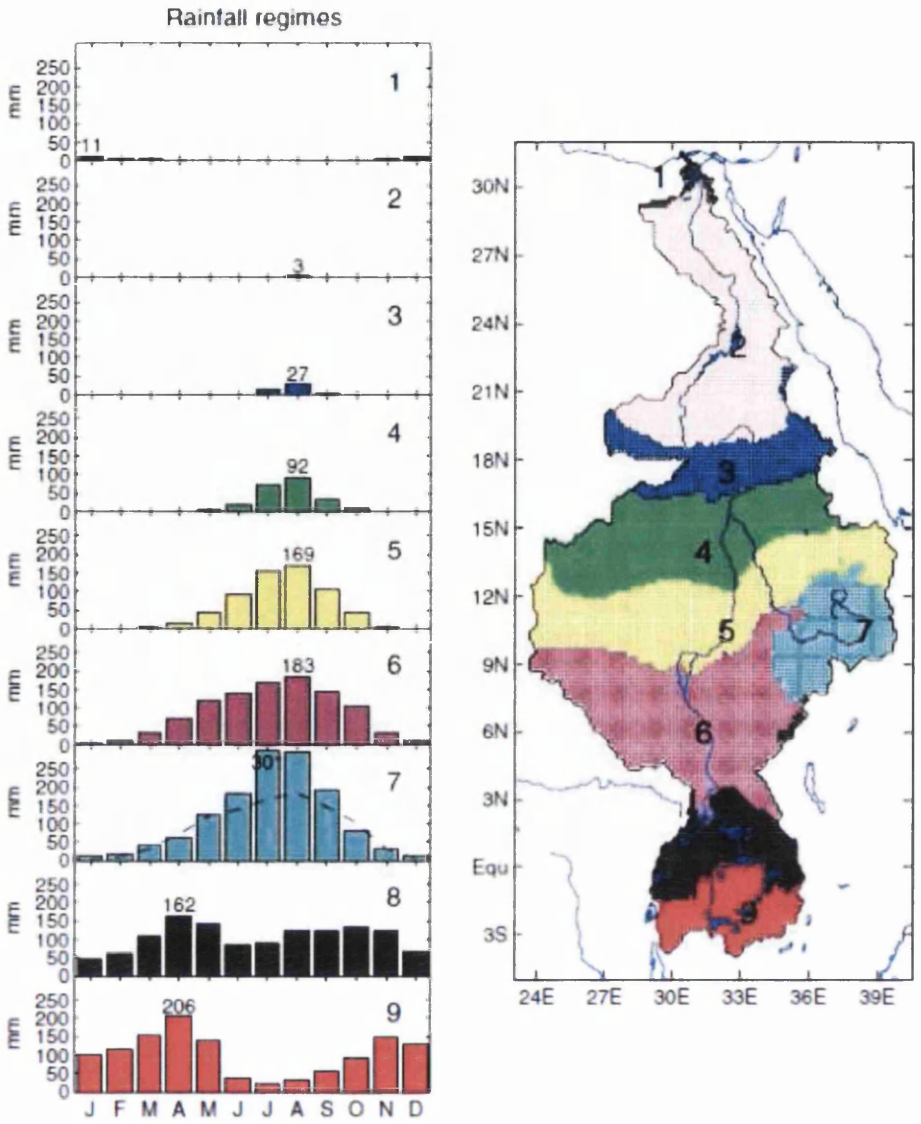

Figure 3.4: Annual rainfall regimes for the Nile basin based on an hierarchical cluster analysis of mean monthly rainfall for 1961–1990 (CRU CL 2.0 data). Data in the bar charts to the left represent maximum monthly rainfall. For type 7, type 6 is shown as a dashed line for comparison (from Camberlin (2009)).

As noted above, other factors such as topography and large continental water bodies play an important role in influencing regional and local climates in additional to large-scale processes. The Ethiopian Highlands block moist, unstable Congo air from reaching coastal areas in Ethiopia and Somalia (Nicholson, 1996). Likewise, the low-level Somali Jet, an integral part of the southeast monsoon, is deflected to the northeast towards Somalia and the Arabian Sea by the highlands of Kenya and Ethiopia during northern summer, whilst the Ethiopian Highlands deflect flow from the northeast monsoon during winter along the Somalian Coast, both enhancing

aridity as a result of frictionally induced subsidence (Nicholson, 1996; Sepulchre et al., 2006; Levin et al., 2009). Orographic uplift plays an important role in local climates. Generally the highest rainfall occurs in mountainous regions (e.g. the Rwenzori Mountains and the Ethiopian Highlands; >2000 mm/yr) (Nicholson, 1996). Also, land-lake circulation, in the form of lake breezes, enhances local convection. For example, areas north and west of Lake Victoria receive rainfall nearly all year round (Nicholson, 1996), and isotope data from the IAEA-WMO station at Entebbe, on the northern shores of the lake, indicate that significant rainfall occurs from evaporated waters from Lake Victoria (Rozanski et al., 1996). In summary, a very pronounced south-to-north gradient of decreasing rainfall (equatorial, tropical and arid) and increasing total number of dry months characterizes the Nile Basin.

3.5 Hydrology

The White Nile flows northwards from the equatorial lakes plateau (Lakes Victoria, Edward, George and Albert) through a series of lakes and swamps. The western (Rwenzori Mountains, Lake Edward, River Semliki and Lake Albert) and eastern (Lake Victoria, Lake Kyoga and Victoria Nile) branches of the White Nile meet at the northern end of Lake Albert to form the Albert Nile (Figure 3.1). The most distant tributary of the White Nile is the Kagera (fed by an upper branch from Burundi: the Ruvyironza River), which flows into Lake Victoria (the largest lake in Africa: 68,000 km^2) from the mountains of Burundi and Rwanda in the west. This is the largest inflow to the lake. The only outflow is via the Victoria Nile near Jinja, which is controlled today by the Nalubaale Dam (Figure 3.5).

From Uganda, the White Nile flows into South Sudan as the Bahr el Jebel and enters vast wetlands (30,000-40,000 km^2) known as the Sudd, where the river spills over from the main channel into swamps and seasonal grasslands; only about half the inflow is returned to the main channel as a result of evaporative losses (Sutcliffe and Parks, 1999; Mohamed et al., 2005). Beyond the Sudd, the Bahr el Ghazal enters from the west, although its contribution to the Nile is negligible due to evaporation and overspill. The Sobat, which drains the south-western Ethiopian Highlands and the South Sudan Plains, is the final tributary to enter the White Nile, contributing about half the total flow (Sutcliffe and Parks, 1999).

The White Nile, fed by more consistent year-round rainfall in the equatorial lakes region, contributes a smaller proportion (~30%) of the total Nile flow but a more constant discharge throughout the year than the Blue Nile (Figure 3.6) (Hurst, 1952; Foucault and Stanley, 1989). Its seasonal variations in flow are also dampened by storage in major lakes, reservoirs and wetlands (Green and El-Moghraby, 2009). In contrast, the Blue Nile descends from Lake Tana (3156 km^2, 1,800 m a.s.l.) in the western Ethiopian Highlands (average ~2000-3000 m a.s.l., rising to >4000 m) and contributes about 56% of the Main Nile flow (Figure 3.6) (Foucault and Stanley, 1989). Lake Tana alone supplies ~8% of the main river flow, the remainder coming from tributaries draining the central and southwestern Blue Nile basin (Shahin, 1985; Conway, 2000). Near Roseires, at the Ethiopian-Sudan border, the river drops steeply down to the plains of Sudan (<700 m) before flowing northwestwards towards Khartoum (Shahin, 1985; Sutcliffe and Parks, 1999). The highly seasonal flow of the Blue Nile (Figure 3.6a) reflects the unimodal rainfall regime at this latitude (Figure 3.4). Its sediment load is also very high (72% of total Nile sediment load) (Figure 3.6), due to the steep slopes and relatively sparse vegetation of the Ethiopian Highlands (Foucault and Stanley, 1989; Sutcliffe and Parks, 1999). Downstream from the confluence of the White and Blue Niles, the Main Nile flows northwards through ~3000 km of desert, with its final tributary, the Atbara, joining 300 km north of Khartoum (Figure 3.1). The Atbara drains the northern Ethiopian Highlands and parts of Eritrea. It exhibits an even more flashy flow regime than the Blue Nile, due to its proximity to the northern summer limit of the ITCZ, though it still provides ~14% of the total Nile flow (Figure 3.6) (Foucault and Stanley, 1989). Below the confluence with the Atbara, several major dams, including the new Merowe Dam and the older High and Low Dams at Aswan, regulate the flow and store summer flood waters for hydroelectric power and irrigation (Figure 3.5), thereby enhancing evaporative losses (Abu-Zied and El-Shibini, 1997). Lake Qarun, near Cairo, is a closed lake fed by a major irrigation canal from the Main Nile (Flower et al., 2006; El-Shabrawy and Dumont, 2009).

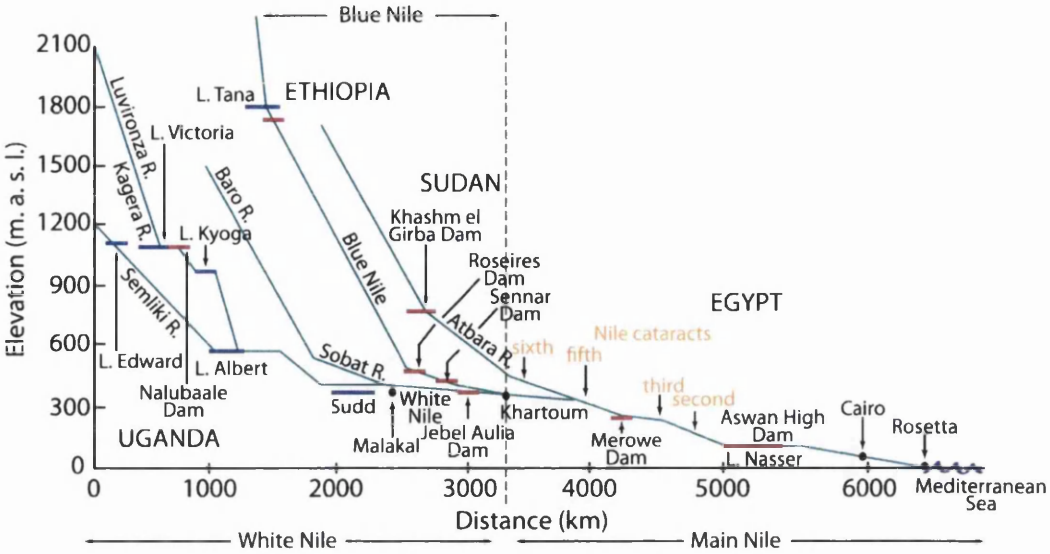

Figure 3.5: A long profile of the River Nile and its major tributaries showing the main river management controls (modified after Church et al. (2011)).

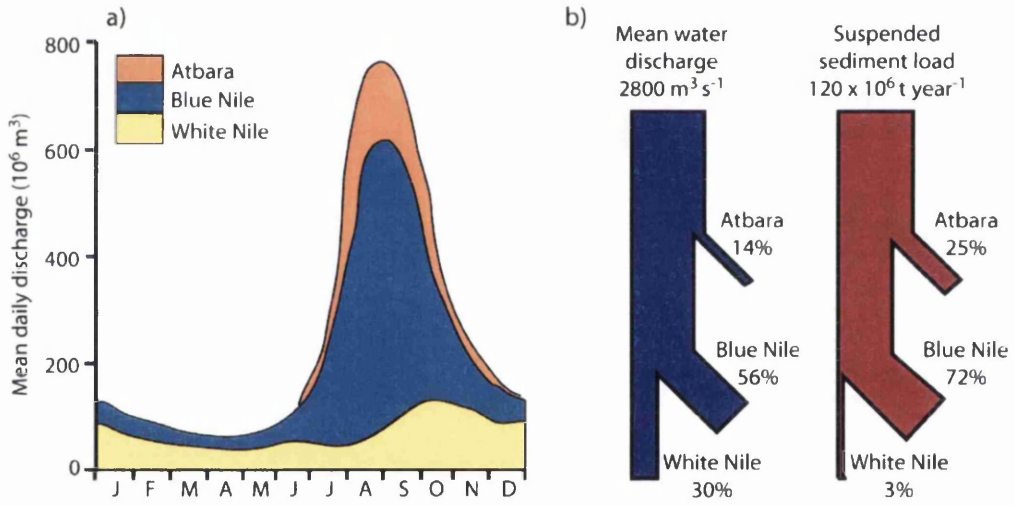

Figure 3.6: Typical annual flow regime of the Nile prior to dam formation at Aswan (1912–1936 averages) (a) and the discharge and suspended sediment budget of the Nile's major tributaries (b) (redrawn from Woodward et al. (2007) after (Hurst, 1952)).

3.6 Vegetation

The large-scale pattern of natural vegetation and plant biomass in the Nile drainage reflects the northward decrease in mean annual rainfall, topography and the distribution of surface water bodies (Figures 3.7 and 3.8). Biomass decreases northwards in the Nile Basin following the rainfall gradient (Figure 3.4).

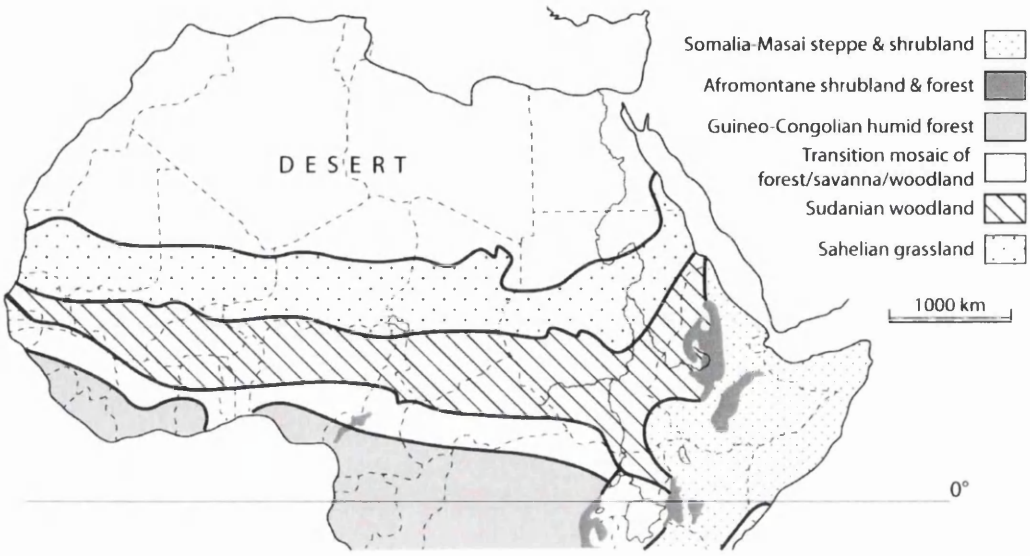

Figure 3.7: Simplified vegetation map of northern Africa including the River Nile, showing the distribution of the major floristic regions (redrawn from White (1983)).

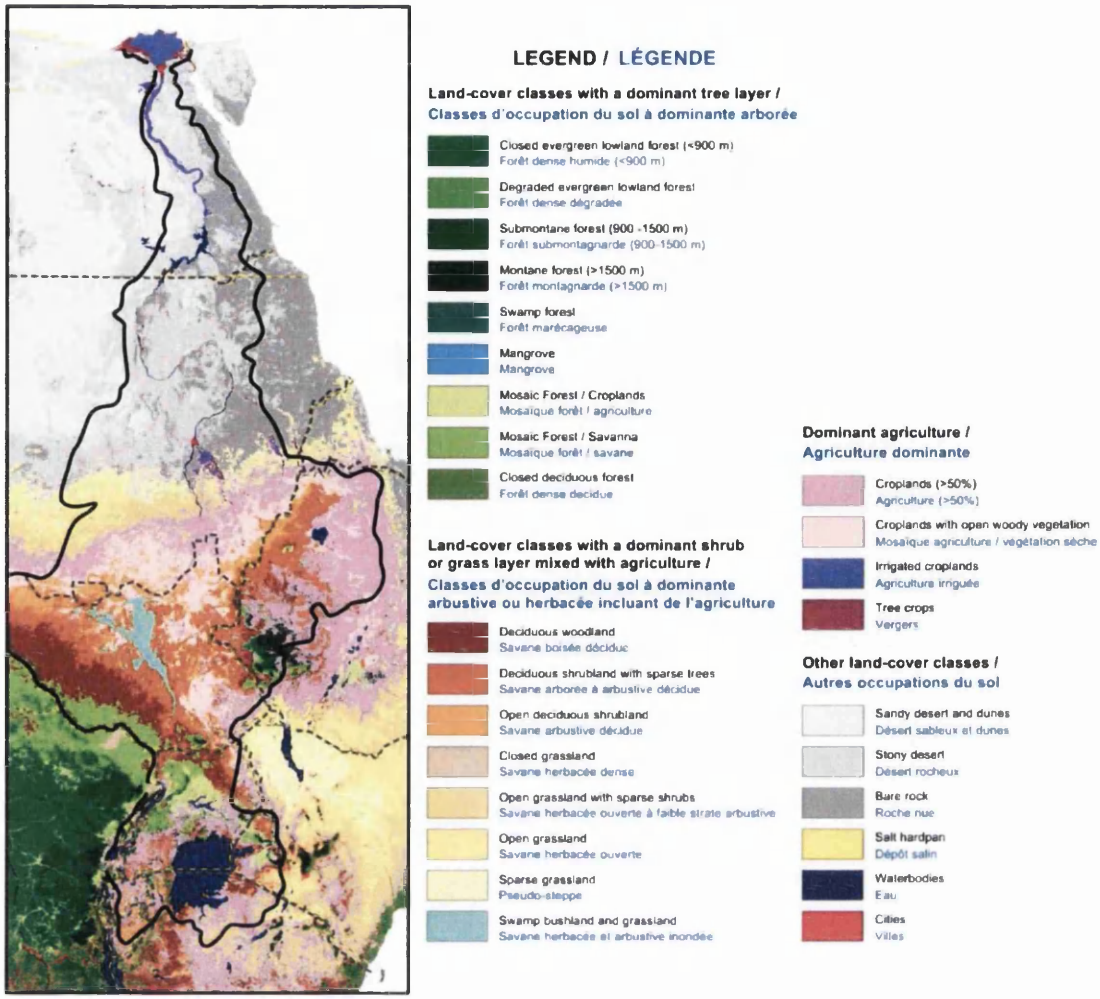

Figure 3.8: Detailed land cover map of the Nile Basin from satellite data. Detailed land cover map of the Nile Basin from satellite data. Clearly visible are the vegetation belts that transverse the north African continent, controlled largely by rainfall amount. Modified after Mayaux et al. (2003).

Terrestrial vegetation in the headwaters of the White Nile is dominated by a mosaic of savanna, woodland and semi-evergreen rainforest at low-, mid- and high-elevations, respectively, and montane forest in the highlands in the south-western part of the basin (Langdale-Brown et al., 1964; White, 1983). Further downstream, the swamps of the Sudd and Bahr el Ghazal cover a vast area (>40,000km^2), dominated by *Cyperus papyrus*, *Vossia* sp., *Typha domingensis* and floating macrophytes (*Eichhornia crassipes* and *Pistia stratiotes*) in the permanently flooded channels and swamps (Green and El-Moghraby, 2009). Seasonally flooded grasslands back the main swamps and grade into open woodland (with *Acacia seyal* and *Balanites aegyptiaca*). In the east, the Sobat drains a large area of wetland known as the Machar Marshes, characterised by papyrus swamp and

wooded grassland. The Upper Blue Nile and Atbara Basins in the Ethiopian highlands consist of grassy uplands (formerly forested but now only remnants due to agriculture) with occasional scattered trees (of acacia and doum palm) and seasonal wetlands around Lake Tana (*Cyperus papyrus*, *Echinochloa pyramidalis* and *Echinochloa stagnina*), with some of the more humid south-western tributaries containing papyrus swamps (e.g. Dabus swamp; 900 km^2) (Conway, 1997). Acacia woodland and scrubland characterise the Sudan plains from which tributaries of the Blue Nile drain (Sutcliffe and Parks, 1999). Vegetation along the Main Nile from about 18°N is very sparse (Figures 3.7 and 3.8), co nsisting mainly of acacia bush and doum palms, although the banks of the Nile are fringed by riparian swamps and irrigated fields.

Surrounding the equatorial lakes (e.g. Victoria, Kyoga, George, Edward and Albert) and Lake Tana are extensive wetlands composed of aquatic grasses (*Phragmites australis, Vossia cuspidata,* Echinochloa sp.), large sedges (*Cyperus papyrus*), herbaceous reeds (*Typha domingensis*), and floating and submerged macrophytes (*Eichhornia crassipes, Pistia stratiotes, Ceratophyllum demersum*) (Figure 3.9) (Langdale-Brown et al., 1964; Kendall, 1969; Conway, 1997; Sutcliffe and Parks, 1999; Green, 2009; Green and El-Moghraby, 2009). In addition, the main river channels and many of their tributaries are lined with swamps and small ponds, including the vast areas of the Sudd and Bahr el Ghazal swamps (the area of the latter is uncertain but smaller than the Sudd) (Sutcliffe and Parks, 1999).

Figure 3.9: Common macrophyte species found around the equatorial lakes and Lake Tana, in the Sudd and along the banks of the River Nile tributaries. a) *Phragmites australis*, b) *Eichhornia crassipes*; c) *Cyperus papyrus*; d) *Typha domingensis*; e) *Vossia cuspidata*.

3.7 Causes of long-term climate variability in north-east Africa

During the Quaternary period, variations in the Earth's orbital parameters (eccentricity, obliquity and precession) are thought to be the main drivers of glacial / interglacial cycles (Figure 3.10) (Hays et al., 1976; Imbrie and Imbrie, 1979). Small variations in these parameters can lead to significant changes in the Earth's receipt of solar radiation, resulting in seasonal and latitudinal changes in insolation, and ultimately consequences for the general atmospheric circulation. Milankovitch in 1941 theorised that through a combination of orbital configurations, lower summer radiation receipts in the northern high latitudes would result in a stronger temperature gradient between the equator and the poles, causing intensified general circulation and enabling the transport of enhanced moisture polewards, which together with warmer winters would favour the expansion of the ice sheets.

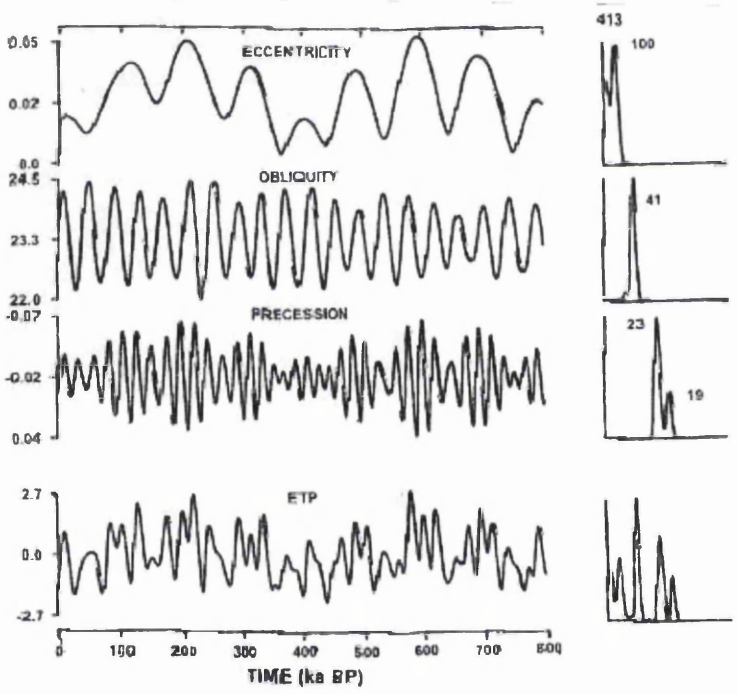

Figure 3.10: Variations of eccentricity, obliquity, precession, and the combination of all three parameters (ETP) during the last 800,000 years with their period characteristics indicated by the power spectrum to the right of the time series (from Bradley (1999)).

3: Study region

During the Late Quaternary, changes in the precession of the equinoxes resulted in increased insolation during the summer months across northern Africa. Between ~15000 and 6000 years ago, the northern hemisphere in summer was tilted towards the sun at perihelion (Earth closest to the Sun), resulting in ~8% more insolation during the summer than today (Figure 3.11) (Street-Perrott and Kutzbach, 1985; Kutzbach and Guetter, 1986; Prell and Kutzbach, 1987; COHMAP, 1988). A large land-sea temperature gradient caused a strengthening and intensification of the summer monsoon which brought about wetter conditions in North Africa during the early Holocene, often referred to as the African Humid Period (AHP) (deMenocal et al., 2000a). Inland penetration of the enhanced summer monsoon enabled a shift in vegetation belts northwards by ~5° (Street-Perrott et al., 1990; Kutzbach et al., 1996), transforming parts of the now arid Sahel and Sahara into vegetated landscapes with expanded waterbodies, including that of palaeolake MegaChad (>400,000 km^2; Drake and Bristow (2006)). The beginning of the so called AHP was not a smooth transition as expected from orbital forcing alone, but an abrupt transition when insolation reached 470 Wm^{-2} (~4.2% more insolation than present day) at ~15ka BP (Figure 3.11), as recorded in many palaeoclimate archives (Street-Perrott and Kutzbach, 1985; Gasse, 2000; Barker et al., 2004; Kiage and Liu, 2006; Gasse et al., 2008). Positive feedbacks from associated changes in surface boundary conditions (expanded vegetation and waterbodies, increased soil moisture) and sea-surface temperatures further amplified the climate response to orbital forcing (Street-Perrott et al., 1990; Kutzbach et al., 1996; Kutzbach and Liu, 1997).

Across Africa a wide range of proxies from various archives support long term forcing by orbital variations as the controlling factor of climatic changes on a multi-millennial time scale (for reviews see Gasse (2000) and Barker et al. (2004)). The geological and palaeoecological evidence suggests that during the Last Glacial Maximum (LGM: ~18ka) North Africa was generally dry; humid conditions prevailed during the early to middle Holocene and drier conditions resumed during the late Holocene (Gasse, 2000). Superimposed on these long-term trends were millennial-scale climatic events registered in archives quasi-globally. The release of freshwater inputs into the North Atlantic Ocean associated with the melting of the Laurentide Ice Sheet caused intervals of weakened Atlantic Meridional Overturning Circulation (AMOC) during the last 20,000 years, resulting in changes to global climates (Bard, 2002; McManus et al., 2004). Input of meltwater slowed the AMOC due to decreases in salinity and temperature and thereby reduced the cross-equatorial

heat transport and shifted the ITCZ southwards, resulting in decreased rainfall over tropical Africa (Street-Perrott and Perrott, 1990; deMenocal et al., 2000b; Tjallingii et al., 2008). During deglaciation of the northern hemisphere ice sheets, catastrophic iceberg release into the North Atlantic, known as the Heinrich 1 event (Bond et al., 1992; Hemming, 2004), resulted in a freshening of the North Atlantic Ocean and is considered to be the cause of Late Pleistocene desiccation of so many East African lakes (e.g. Lakes Victoria, Albert, Tana) (Stager et al., 2002; Stager et al., 2011). Another severe cold period, the Younger Dryas, occurred at the very end of the Late Pleistocene period (~12.5-11.5ka BP), hypothesised to be from a sudden pulse of meltwater into the northern North Atlantic Ocean from the Laurentide ice sheet (Teller et al., 2002; Teller et al., 2005), and was recorded in many African climate archives (Roberts et al., 1993; Gasse, 2000; Stager et al., 2002; Barker et al., 2004; Kiage and Liu, 2006; Garcin et al., 2007; Gasse et al., 2008). Several other abrupt climatic events occurred during the Holocene (e.g. 8.2 and 4.2 ka) but were short lived (decades to centuries), again these were associated with disruption of the AMOC and its associated heat transport (Alley et al., 1997; deMenocal et al., 2000b; Bond et al., 2001). An injection of glacial meltwater from breached ice-dammed Lake Agassiz into the Labrador Sea caused the centennial-scale cooling event centred around 8500-8250 years BP (Barber et al., 1999; Clarke et al., 2004; Daley et al., 2011), and is recognised in many climate archives around the globe including Africa (Alley et al., 1997). A combination of interactions between orbital forcing, atmospheric circulation, oceanic parameters and land surface conditions have occurred during the Late Quaternary, resulting in different scales of hydrological fluctuations (deMenocal et al., 2000a; Gasse, 2000).

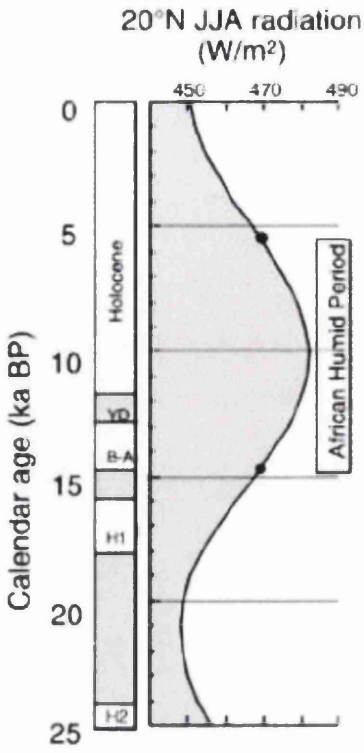

Figure 3.11: Northern hemisphere summer (JJA) radiation receipt computed for 20°N during the last 25 ka BP. By about 10-11 k a BP, summer insolation in the Northern Hemisphere had peaked to about 8% greater than today due to changes in the earth's orbital parameters (Berger and Loutre, 1991). Early climate models found that an 8% increase in summer insolation would cause a 40% increased in African monsoonal precipitation (Kutzbach and Street-Perrott, 1985; Prell and Kutzbach, 1987). From deMenocal et al. (2000a).

3.8 Late Quaternary palaeoenvironments of the Nile Basin

During the Middle to Late Quaternary, tropical Africa was strongly affected by quasi-periodic variations in the Earth's orbital parameters (see section 3.7). During boreal-summer insolation maxima, monsoon rains penetrated deep into the Sahara, causing a northward migration of the major vegetation belts, increases in river discharge, and an expansion of lakes and wetlands (Kutzbach and Street-Perrott, 1985; Street-Perrott et al., 1990; Kutzbach et al., 1996; Kutzbach and Liu, 1997; Jolly et al., 1998; Joussaume et al., 1999; Prentice et al., 2000). Changes to the hydrology and terrestrial and aquatic ecosystems in the Nile Basin during this period are becoming increasingly well documented from the sediment record (dune sands, river deposits, lake sediments, lake shorelines, archaeological remains and Mediterranean sapropels) (Pachur and Kröpelin, 1987; Williams et al., 2006;

Williams et al., 2010). During and after the Last Glacial Maximum (LGM, ~21ka), tropical Africa was generally drier and colder, resulting in eventual desiccation of several of the headwater lakes (Victoria, Albert and Tana) and their isolation from the Nile (Talbot and Livingstone, 1989; Johnson et al., 1996; Beuning et al., 1997c; Talbot and Lærdal, 2000; Lamb et al., 2007; Stager and Johnson, 2008). White Nile discharge was low and extremely seasonal, while the Blue Nile flood was even more flashy than today (Adamson et al., 1980; Said, 1993; Johnson, 1996; Williams et al., 2000). Refilling and overflow of the White Nile headwater lakes and Lake Tana occurred around 14.5 ka BP, marking the abrupt onset of the enhanced summer monsoon and the so-called "Wild Nile" (Adamson et al., 1980; Rossignol-Strick et al., 1982; Talbot et al., 2000; Williams et al., 2006; Lamb et al., 2007; Revel et al., 2010). During the interval ~15 ka to 5 ka BP, a general increase in rainfall across the entire Nile Basin, apart from the northernmost Sahara, resulted in enhanced vegetation cover and river discharge; perennial flow into the Nile from large Saharan wadi systems (Pachur and Kröpelin, 1987; Williams et al., 2010); and widespread proliferation of lakes and swamps. A 450 km^2 palaeolake west of the Main Nile in northern Sudan (Williams et al., 2010) and a greatly enlarged Lake Qarun near Cairo (≤ 2100 km^3: Hassan (1986)) were fed by increased overspill of Nile floodwaters. From mid-Holocene to present, the climate of the Nile Basin has become much drier due to the southward retreat of the enhanced monsoon, and the modern discharge regime of the Nile has been established. The collapse of the Old Kingdom in the Nile valley is thought to have been associated with a decline in White Nile flow linked to widespread aridity across tropical Africa at ~4.2ka BP (Hassan, 1997; Stanley et al., 2003).

3.9 Chapter Summary

Flowing from south to north, from tropical headwaters through desert lowlands to the Mediterranean Sea, the Nile Basin is diverse. Spanning a wide variety of altitudinal, geological, geomorphological, climatic and vegetation zones, the River Nile is the longest in the world. Precipitation and vegetation distributions are controlled largely by the passage of the ITCZ, resulting in a very marked south to north climatic and vegetation gradient, but also greatly influenced by orography and large continental waterbodies.

3: Study region

Large-scale climatic changes affected the Nile Basin and northern Africa as a whole during the Late Quaternary, controlled primarily by orbital forcing which bought about enhanced summer monsoons between ~15 and 5 ka BP resulting in proliferation of rivers, lakes and wetlands and a shift of the main zonal vegetation belts to more northerly positions. Superimposed on the long-term trend were centennial- to millennial-scale events which appear to be linked with deep water formation in the North Atlantic. An increasing number of palaeoclimate and palaeoenvironment archives are available for the Nile Basin to document these changes.

Chapter 4 Methods development: Si-isotope analysis of waters

4.1 Introduction

Measurement of Si-isotope compositions of waters collected from lakes and rivers in the Nile Basin was a key element of this project. Using High Resolution Multi Collector-Inductively Coupled Plasma Mass Spectrometry (MC-ICP-MS) at the NERC Isotope Geosciences Laboratory, UK, a new method was devised to analyse Si isotopes in waters. Currently there is no agreed protocol for analysing Si isotopes in natural materials by MC-ICP-MS due to its recent development. Through extensive investigation and exhaustive experimentation, the most suitable analytical set-up for obtaining accurate and precise data on a Neptune Plus MC-ICP-MS at NIGL has been achieved. This chapter describes the advancement of MC-ICP-MS for Si-isotope analysis, the various methodologies developed for varying instruments and the problems that need to be overcome to obtain data of the high precision and a accuracy required for Si-isotope analysis.

4.2 Sample storage

Although methods for storing waters for Si isotope analysis and maximising their longevity was not widely described in the literature, Georg et al. (2006b) provided enough detail, together with various other authors, to collect, store and preserve waters for Si-isotope analysis effectively. All samples were filtered through 0.45 µm Millipore cellulose nitrate filters (47mm diameter) in the field to remove colloidal and particulate Si (including biogenic silica), together with suspended organic matter, and acidified with ultra-pure HCl to a pH of between 2-3 to prevent any further biological activity and polymerization. Water samples were collected and stored in clean high density polyethylene bottles and kept in the dark until it was possible to store them at 4°C on return to the UK, where they remained until further analysis. All additional preparation for Si isotope analysis was carried out in August-September 2011 at the NERC Isotope Geosciences Laboratory in a class 100 clean suite using sub-samples of the bulk sample. Further details of sample preparation can be found in Chapter 5, section 5.3.4.

4.3 Current methods for determining Si concentrations and other major elements

It is useful to determine the Si concentration (and composition of other elements) of waters for both additional data about environmental conditions but also so that an appropriate dilution can be made prior to isotope analysis (Chapter 5, section 5.3.4.1). The most widely used method to determine dissolved Si (DSi) concentrations is the colorimetric technique (molybdenum blue method) using spectrophotometry (De La Rocha et al., 2000; Georg et al., 2006b, a; Georg et al., 2009; Cardinal et al., 2010; Opfergelt et al., 2011; Hughes et al., 2012) or by ICP-MS/ICP-AES (van den Boorn et al., 2006; Engström et al., 2010; Ding et al., 2011; Hughes et al., 2012). The colorimetric procedure measures dissolved silica (SiO_2) rather than Si so a correction for the oxygen atoms is required. However, it is not always clear in the literature whether authors have made this correction. The benefit of using inductively coupled plasma spectrometry is that other elements can be measured at the same time. In contrast, colorimetric methods use smaller sample sizes and are thought to be more sensitive, especially when concentrations are low, and their instrument costs are lower.

For a batch of 23 Nile water samples, I measured DSi both colorimetrically using a Hach Lange colorimeter (at the Earth Science Department, University of Edinburgh) and by ICP-MS (measurements carried out by Dr Simon Chenery and Thomas Barlow at the British Geological Survey, Keyworth). The two methods produced significantly different Si concentrations (paired t-test, p = 0.002) (Figure 4.1). Si concentrations determined by ICP-MS were generally greater than colorimetrically measured Si, particularly at high concentrations (Figure 4.2). The reasons for the differences are not fully understood, but it may be that the high temperatures associated with the plasma resulted in the measurement of colloidal material that was not measured colorimetrically. Also, human error cannot be discounted, through the preparation of standards, calculation errors, and dilutions, which may have influenced the results. It is possible that the water samples were measured within the Low Range (0-1.600mg/L (ppm)) silica function of the spectrophotometer and therefore the high Si concentrations would not have been accurately calculated. Both procedures remain valid techniques. Due to the availability of suitable equipment and requirement to measure other elements within the water samples, ICP-MS was chosen in this instance. Precision was typically ±2% for colorimetric methods and ±3-15% for ICP.

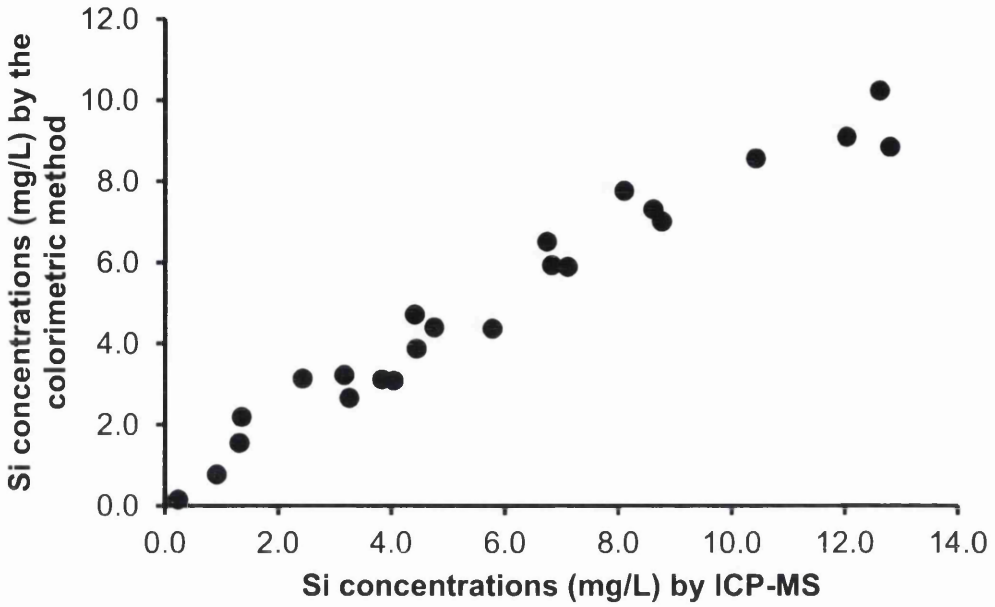

Figure 4.1: The relationship between dissolved Si measured colorimetrically and by ICP-MS on River Nile waters. A paired t-test clearly shows a significant difference between the Si concentrations obtained through the two methods (p = 0.002).

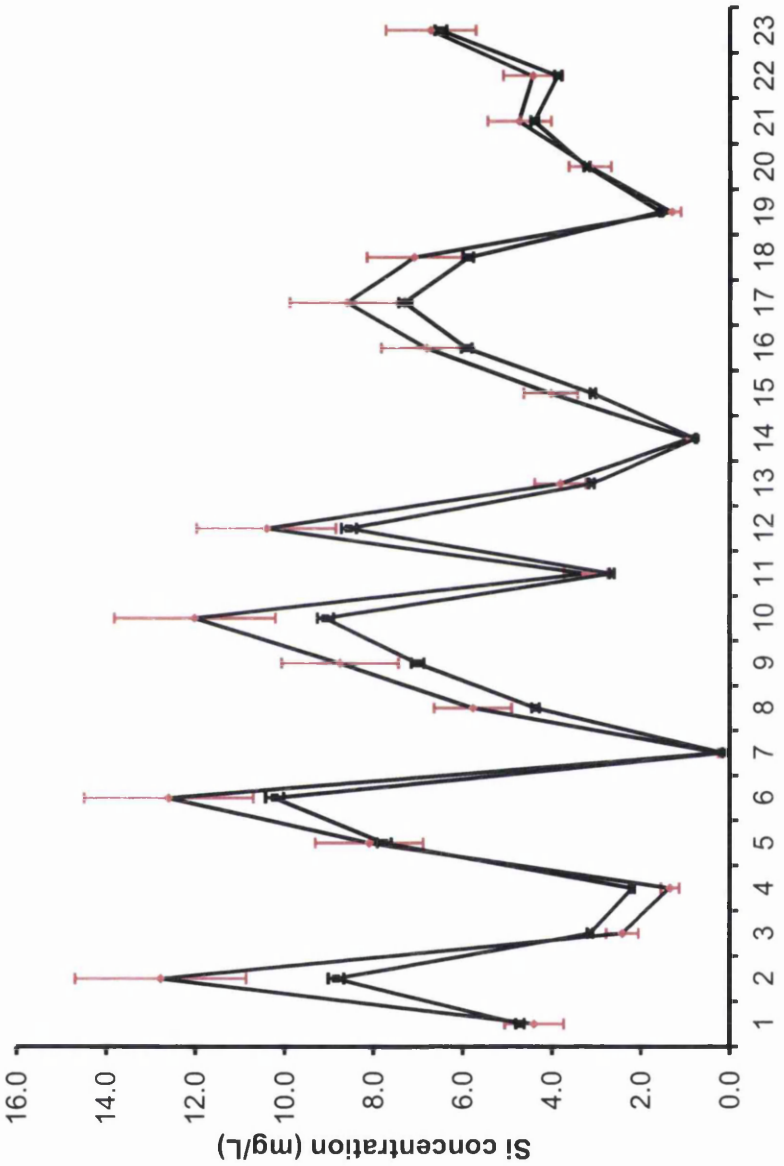

Figure 4.2: Si concentrations by colorimetric methods (black) and by ICP-MS (red) for individual River Nile samples. Error bars represent ±2% (2σ) and ±15% (3σ) precision, respectiveiy.

4.4 Advancement in the methods used for Si isotope measurements

Traditional methods for determining Si isotope compositions of natural samples (natural waters, biogenic silica, primary and secondary minerals, meteorites/lunar rocks) use gas source Isotope Ratio Mass Spectrometry (IRMS) and require fluorination of precipitated SiO_2 in the preparation stages (Reynolds and Verhoogen, 1953; Douthitt, 1982; De La Rocha et al., 1996; Ding et al., 1996; De La Rocha et al., 2000; Ding et al., 2004; Ding et al., 2008a; Ding et al., 2008b; Leng and Sloane, 2008; Ding et al., 2011), which is associated with the potential release of hazardous fluorinating gases, such as bromine pentafluoride (BrF_5) or fluorine (F_2) (De La Rocha et al., 1996; Ding et al., 1996; De La Rocha, 2002; Ding et al., 2004). Since the introduction of MC-ICP-MS for Si isotope measurement during the last decade (De La Rocha, 2002; Cardinal et al., 2003), a renewed interest in the opportunity to study the biogeochemical cycle of Si has arisen as a result of less complicated preparation procedures and safer analytical conditions.

During the last decade progress has been made to improve the way in which Si isotope analysis of natural samples is carried out both in the preparatory stages (De La Rocha et al., 1996; Engström et al., 2006; Georg et al., 2006b; van den Boorn et al., 2006) and in the determination of their Si isotope composition (De La Rocha et al., 1996; De La Rocha, 2002; Cardinal et al., 2003; Engström et al., 2006; Georg et al., 2006b). Even though determining Si isotope compositions by MC-ICP-MS has its associated difficulties (time consuming, mass bias, matrix effects etc; will be discussed later), it is still deemed much safer than the fluorination of silicon (De La Rocha, 2002), and has been received well by the scientific community. However, there is still no agreed protocol for analyzing Si isotope compositions in natural samples by MC-ICP-MS, presumably because it is still in its infancy and users are running samples on varying instruments.

4.5 Development in the preparation and purification of Si prior to Si isotope analysis

In 1996, over forty years after the first measurements of Si isotope abundances in natural samples were carried out (Reynolds and Verhoogen, 1953), De La Rocha and colleagues reignited interest in the determination of Si isotope compositions in

natural samples with their attempt to improve methodologies for quantitatively recovering and purifying Si from biogenic silica and water samples. They devised a procedure, modified after Defreitas et al. (1991), which included using 2.5 M HF to dissolve biogenic silica, followed by the precipitation of dissolved silicon with the addition of cleaned TEA-moly reagent and subsequent fluorination of the precipitated product with F_2 to form silicon tetrafluoride (SiF_4) gas for analysis by IRMS. At the same time Ding et al. (1996) were making improvements to their fluorination line after the methodology created by Clayton and Mayeda (1963) using bromine pentafluoride (BrF_5) as the fluorinating reagent. Both procedures allowed good recovery of Si, however, safety considerations when using HF and the potential release of dangerous fluorinating gases during analysis meant that the methodology was not completely satisfactory.

With the advent of MC-ICP-MS for stable isotope analysis, allowing more timely and safer measurements of Si isotopes to be carried out, new preparation techniques were necessary prior to isotope analysis. Samples needed to be introduced to the mass spectrometer as a solution rather than a gas as is required for gas source IRMS, and to be free from other components that could potentially cause matrix interference with the measurement of the isotopic abundances of Si (see section 4.6). Initially, samples (biogenic silica, minerals and standards) were prepared by dissolving them in HF and HCl, and those containing organic matter underwent an acid digestion (hot H_2O_2 or HNO_3) before dissolution in HF/HCl (De La Rocha, 2002; Cardinal et al., 2003). A few years later, a new wave of purification and recovery protocols for Si isotope analysis were developed (Engström et al., 2006; Georg et al., 2006b; van den Boorn et al., 2006). These workers took advantage of ion exchange resin to purify Si by chromatographic separation, first demonstrated by Wickbold (1959) for other purposes.

Engstrom et al. (2006) applied the use of anion-exchange resin to purify and pre-concentrate Si in water samples for isotope analysis. Several elution and wash stages through the column were used to remove major inorganic constituents and to recover Si in the final phase. Si recovery was satisfactory (>97%); however, the use of HF to pretreat some of the samples prior to being loaded on to the column and also as part of the elution stages in the chromatograph purification, resulted in final solutions containing significant quantities of HF. Georg et al. (2006b) took the principle of ion exchange a step further, and removed the need to use HF almost

entirely, making it a much safer procedure. They used cation-exchange resin to separate Si (Si is neutrally (H_4SiO_4) or negatively ($H_3SiO_4^-$) charged in solutions with pH 2-8) from positively charged ions (anions) using purely Milli-Q water to elute. In addition, Georg et al. (2006b) found that sensitivity increased (higher beam intensity) and higher mass bias stability was obtained as a result of avoiding the use of HF which ultimately improved the precision of the Si isotope measurements. The use of HF in Si isotope measurements by MC-ICP-MS should be avoided as Si can be easily lost by volatilization, and corrosion of the glass parts of the internal apparatus by HF are likely to cause significant background noise (Georg et al., 2006b; van den Boorn et al., 2006). Chromatographic recovery and purification of Si for MC-ICP-MS, without the use of HF, is more reliable, faster, simpler and safer, improves accuracy and precision through the removal of most matrix interferences, prevents Si isotope fractionation, enables high recovery of Si (>98%) and allows the use of small sample sizes (Georg et al., 2006b).

4.6 Development of MC-ICP-MS for the analysis of Si isotope compositions in natural samples

Increasingly being used for the determination of Si isotopes abundances is MC-ICP-MS, favoured over the use of gas source IRMS due to faster preparation procedures and analytical time, less complicated and safer methodologies owing to the avoidance of HF and fluorinating gases, and the utilization of much smaller sample sizes. However, associated with the use of MC-ICP-MS are some important analytical difficulties (such as matrix interferences, sensitivity and background issues, mass bias effects) which must be overcome to enable accurate and precise measurement of Si isotope abundances, comparable to IRMS (De La Rocha, 2002). During the last few years, various analytical and instrumental (e.g. Nu Plasma, Nu 1700 and Neptune) setups have been developed/tested to try and overcome these problems (De La Rocha, 2002; Cardinal et al., 2003; Engström et al., 2006; Georg et al., 2006b; van den Boorn et al., 2006; Abraham et al., 2008; van den Boorn et al., 2009; Hughes et al., 2011; Zambardi and Poitrasson, 2011).

One of the main problems associated with MC-ICP-MS, but not with IRMS, as most major mass interference problems are eliminated by measuring Si as SiF_4^+ ions (Cardinal et al., 2003), is the effect of isobaric and polyatomic matrix interferences that can occur with species that have similar masses to Si. A list of all the potential

isobaric interferences on the Si isotope peaks are presented in Table 4.1. The doubly charged ions (e.g. $^{56}Fe^{2+}$, $^{58}Fe^{2+}$, $^{58}Ni^{2+}$, $^{60}Ni^{2+}$) can be removed and eliminated during ion-exchange resin purification (van den Boorn et al., 2006). However, several interferences from N-, O- and C-containing species are impossible to remove chemically or by ion-exchange purification since they are entrained from the atmosphere (Engström et al., 2006). Although, the use of a Cetac Aridus desolvating nebulizer, allowing the mass spectrometer to operate in dry-plasma mode, is thought to reduce the introduction of interfering atmospherically derived species substantially (Cardinal et al., 2003; van den Boorn et al., 2006). In particular, major interferences with the ^{28}Si and ^{30}Si peaks are caused by $^{14}N_2$ and $^{14}N^{16}O$, respectively.

Table 4.1: Potential matrix interferences with Si isotope peaks (from Engström et al. (2006) and van den Boorn et al. (van den Boorn et al., 2006)).

		Type of interferent			
Isotope	**Importance**	**Hydrides**	**Nitrogen based**	**Carbon based**	**Doubly charged**
^{28}Si	Major		$^{14}N^{14}N^+$	$^{12}C^{16}O^+$	
	Minor				$^{56}Fe^{2+}$
^{29}Si	Major		$^{14}N^{14}N^1H^+$	$^{12}C^{16}O^1H^+$	
	Minor	$^{28}Si^1H^+$	$^{15}N^{14}N^+$	$^{12}C^{17}O^+$	$^{58}Fe^{2+}$
				$^{13}C^{16}O^+$	$^{58}Ni^{2+}$
^{30}Si	Major		$^{14}N^{16}O^+$		
	Minor	$^{29}Si^1H^+$	$^{14}N^{15}N^1H^+$	$^{13}C^{17}O^+$	$^{60}Ni^{2+}$
			$^{14}N^{14}N^2H^+$		

In the very early stages of developing the use of MC-ICP-MS for Si isotope analysis, it was not possible to overcome interferences with the ^{30}Si peak, and so emphasis was placed on the two lighter isotopes of Si (De La Rocha, 2002; Cardinal et al., 2003). $\delta^{30}Si$ was determined using the empirically derived relationship $\delta^{30}Si = 1.93\delta^{29}Si$ (De La Rocha, 2002). However, this was not entirely satisfactory as the assumption was that the samples had been subjected only to mass-dependent isotope fractionation. Changes to instrumental setup and analytical settings have allowed progress to be made in resolving interferences with all three Si peaks. High-resolution capabilities of both the Neptune and NuPlasma 1700 MC-ICP-MS are sufficient to accurately and precisely measure the Si isotopes on the interference free plateaus (Engström et al., 2006; Georg et al., 2006b; Reynolds et al., 2006b; Zambardi and Poitrasson, 2011). van den Boorn et al. (2006) also managed to

measure all three peaks interference-free using a Neptune MC-ICP-MS at medium resolution, and suggested that using an Cetac Aridus desolvating nebulizer prevented tailing on the ^{30}Si peak by $^{14}N^{16}O$ interference as experienced by Engström et al. (2006) using wet-plasma mode. Further measures that have been considered to improve sensitivity include the type of solution in which the samples and standards are introduced into the mass spectrometer, in order to prevent competition for ionization energy in the plasma (van den Boorn et al., 2006). Georg et al. (2006b) found that running samples in HF-free solutions improved sensitivity by 30-40% as a result of eliminating fluoride ions in the plasma and van den Boorn et al. (2006) suggested that higher sensitivities are obtained in HNO_3 matrix, although the use of HCl may be more suitable to avoid further interference from NO^+ ions (Engström et al., 2006).

As highlighted earlier, when using the commonly adopted use of cation-exchange resin to prepare samples, it is not possible to separate Si from other anionic species or from other species that are not positively charged. Originally, it was thought that these species (e.g. sulphates, nitrates and dissolved organic carbon) did not interfere with Si isotope abundance measurements (George et al. 2006). However, it has been shown subsequently that high concentrations of these species can have significant impact on Si isotope measurements (van den Boorn et al., 2009; Hughes et al., 2011). van den Boorn et al. (2009) were the first to show that sulphur present in samples could cause a shift of up to +1.3‰ in $\delta^{30}Si$ values, and suggested that significant offsets could occur in SO_4/Si ratios above 0.02 wt.%. The reason for these offsets is uncertain. However, as sulphur isotopes have much higher masses than Si isotopes, which therefore excludes isobaric matrix effects, it is thought instead that instrumental mass bias is the cause of the offset (van den Boorn et al., 2009). Later, Hughes et al. (2011) showed that dissolved organic matter, nitrates and chloride ions, which are not removed by the cation-exchange purification procedure, may also contribute to Si isotope offsets. To overcome these potential problems Hughes et al. (2011) suggested that doping of both samples and bracketing standards (matrix-match) at the same level with quartz distilled sulphuric acid (for sulphate), nitric acid (for nitrate) and hydrochloric acid (for chloride) in sufficient quantities to exceed the natural concentrations, would prevent isotopic bias (van den Boorn et al., 2009; Hughes et al., 2011). Due to the complexity of organic matrices it is not possible to balance the contaminant with doping solutions, instead various methods are suggested for decomposing organic matter prior to

column chemistry (Hughes et al., 2011). It must be noted that their results were only based on two samples, both with high DOC/Si ratios, and may not be representative of typical river samples. Even so, these problems should be given serious consideration when planning Si isotope analysis, in particular for natural water and altered rocks as they may contain elevated concentrations of these species.

To correct for these mass bias effects, standard-sample bracketing techniques (matrix-matched) and doping samples and standards with Mg of a known isotopic composition ($^{25}Mg/^{24}Mg$), allow the data to be corrected. Any measured deviation from the known Mg isotope composition is attributed to mass bias drift and the Si isotope data are corrected accordingly. Mg, with its three isotopes (24, 25, 26) being close to the mass of Si, is the most suitable external standard for silicon (Cardinal et al., 2003). However, De La Rocha (2002) suggested that the mass fractionation of Mg would be unlikely to reflect that of Si due to the superior transmission of Mg through the MC-ICP-MS. In addition, Georg et al. (2006b) suggested that doping with Mg would add to the problem of matrix effects, causing further instability. Several authors have recently shown that Mg doping is a reliable mass bias drift correction of Si ratios (Cardinal et al., 2003; Engström et al., 2006; Hughes et al., 2011; Zambardi and Poitrasson, 2011). Zambardi and Poitrasson (2011) encouraged the use of Mg spiking and suggested that there was no evidence that significant bias in the fractionation factors between Si and Mg was induced by MC-ICP-MS. Although Mg doping does not improve the accuracy of silicon isotope measurements, it does allow for the correction of mass bias drift, leading to more precise Si measurements. Accuracy is achieved through the standard-sample bracketing approach by normalising to the reference material.

4.7 Chapter Summary

Currently there is no consensus on a standard procedure for preparing and measuring Si isotopes by MC-ICP-MS. Presumably this is because it is a new technique, researchers are using varying instruments and there is limited information available on the problems that have arisen when developing the methodologies. Extensive research and experimentation by Dr Matt Horstwood and Vanessa Pashley at the NERC Isotope Geosciences Laboratory (NIGL) led to the analytical set-up chosen for analysis of Si-isotopes in solutions on a Neptune Plus MC-ICP-MS, which will be presented in the following chapter.

Chapter 5 Research design and methodology

5.1 Introduction

This chapter describes the rationale underlying the sampling strategy for both the modern system and the sediment core analysis. Details of the methodologies used for analysing water samples for isotope analysis (H, O and Si), in particular, the new methodology developed for this thesis at the NIGL for Si isotopes in waters, and the final analytical set-up that was decided on to overcome the problems effecting Si-isotope analysis by MC-ICP-MS (covered in Chapter 4) are presented. The procedures used for isolating diatoms from lake sediments are described and the newly developed system for simultaneously measuring O and Si isotopes of diatom silica at the NIGL using a fluorination technique and Gas Chromatography-Isotope Ratio Mass Spectrometry (GC-IRMS) are explained. The methodology used for extracting, quantifying and identifying biomarkers from lake sediments are described in detail.

5.2 Sampling scheme

Transects of surface waters along the length of the River Nile were sampled for hydrogen (H), oxygen (O) and silicon (Si) isotopes during both wet and dry seasons in order to investigate the downstream evolution of their stable-isotope compositions in response to seasonal changes in moisture balance and Si cycling. Understanding the isotope systematics of the modern Nile Basin should help to interpret the Late Quaternary lacustrine diatom palaeo-record. Diatom silica is formed of biogenic opal ($SiO_2 \cdot nH_2O$) containing oxygen and silicon isotopes that can be used in palaeoenvironmental studies (Leng and Barker, 2006; Leng and Swann, 2010). The isotopic composition of the frustules reflects the aqueous environment in which they formed. Utilising available sediment cores and sections from along the River Nile, coupled measurements of stable Si and O isotopes on preserved lacustrine diatoms were employed to reconstruct downstream changes in biotic Si cycling and palaeohydrology, respectively. Abundance ratios of lipid biomarkers (*n*-alkanes) were used to track corresponding vegetation changes in terrestrial and aquatic ecosystems.

5.3 Surface water sampling

5.3.1 Sampling strategy

A total of 79 surface water samples was collected from the White, Blue and Main Nile drainages, including major tributaries and lakes, during both low-flow ("dry season": May-June 2009 and April-May 2011 (n = 34)) and high-flow conditions ("wet season": October-December 2010 (n = 45)), in order to represent seasonal variations (Figure 5.1; Table 5.1). The aim was to obtain a representative coverage of the Nile Basin catchments in order to understand the processes operating within the Basin. Selected rivers and lakes were identified prior to fieldwork from maps and research articles covering individual sub-basins. Sampling locations were largely defined by ease of access to the River Nile tributaries, often by the presence of bridges crossing rivers and proximity to roadways, allowing access to rivers banks. Occasionally samples were collected from aboard boats whilst traversing the river. Generally samples were collected from tributaries or Nile-fed lakes just prior to them merging with the main Nile branches (e.g. White, Blue and Main Niles) or with other tributaries which eventually flow into the Nile. The number of samples collected during different seasons was dependent on budgetary constraints and therefore the ability to access remote sites. For example, during the first expedition in May-June 2009 to the headwaters of the Blue and White Niles, resources were limited and reliance was placed on the use of public transport, which meant that remote areas were not easily accessible. For the second (2010) and third (2011) field expeditions, a National Geographic grant allowed private hire of local vehicles and enabled isolated sites to be sampled.

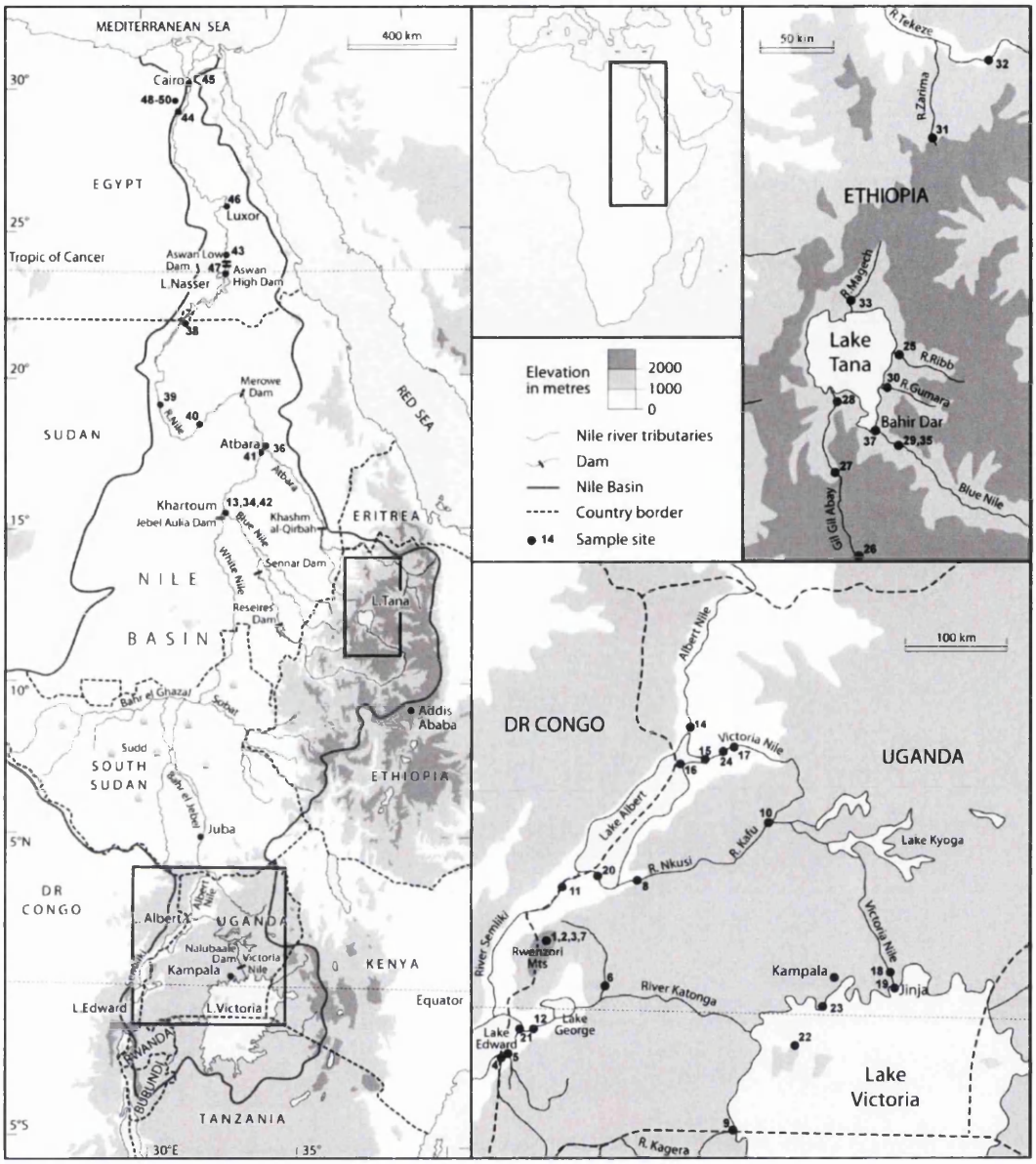

Figure 5.1: Sampling site locations of collected water samples from the Nile Basin. Numbered sites correspond to those in Table 5.1.

Table 5.1: Water sample locations. Site number corresponds to those in Figure 5.1.

			Wet season				*Dry season*			
	Site No.	Sample site name	Date (month-year)	Lat. (dec. deg.)	Long. (dec. deg.)	Alt. (m.a.s.l.)	Date (month-year)	Lat. (dec. deg.)	Long. (dec. deg.)	Alt. (m.a.s.l.)
White Nile	1	Bujuku River, Rwenzori Mts., Uganda	Oct-10	0.3581	29.9718	2552	-	-	-	-
	2	River Mubuku, Rwenzori Mts., Uganda	Oct-10	0.3581	29.9718	2552	-	-	-	-
	3	River Mubuku, Rwenzori Mts., Uganda	Oct-10	0.3436	30.0399	1608	-	-	-	-
	4	River Ishasha, Uganda	Oct-10	-0.6157	29.6578	934	-	-	-	-
	5	River Ntungwe, Uganda	Oct-10	-0.5667	29.7235	938	-	-	-	-
	6	Mpanga River, Uganda	Oct-10	0.0832	30.3224	1201	-	-	-	-
	7	Lake Mahoma, Rwenzori Mts., Uganda	Oct-10	0.3455	29.9684	2880	-	-	-	-
	8	River Nkusi, Uganda	Nov-10	1.1301	30.9946	1029	-	-	-	-
	9	River Kagera, Uganda	Oct-10	-0.9393	31.7632	1139	-	-	-	-
	10	River Kafu, Uganda	Nov-10	1.5454	32.0389	1045	-	-	-	-
	11	River Semliki, Uganda-Congo	Oct-10	1.0287	30.5283	653	Jun-09	1.0630	30.2269	636
	12	Kazinga Channel, Uganda	Oct-10	-0.1883	29.9073	918	Jun-09	-0.1849	29.9055	917
	13	White Nile, Khartoum, Sudan	Dec-10	15.6141	32.4937	391	May-11	15.6141	32.4937	391
	14	Albert Nile, Uganda	Nov-10	2.2859	31.3727	633	May-09	2.3913	31.4769	614
	15	Victoria Nile Delta, Uganda	Nov-10	2.2509	31.3834	628	May-09	2.2449	31.3913	618
	16	Lake Albert (north), Uganda-Congo	Nov-10	2.2208	31.3316	631	May-09	2.2601	31.3486	614
	17	Murchison Falls, Victoria Nile, Uganda	Nov-10	2.2749	31.6752	635	May-09	2.2735	31.6693	623
	18	Victoria Nile, Bujagali Falls, Uganda	Nov-10	0.4831	33.1630	1112	Jun-09	0.4610	33.1755	1126
	19	Outflow from Lake Victoria, Uganda	Nov-10	0.4208	33.1964	1135	Jun-09	0.4208	33.1963	1137
	20	Lake Albert (south), Uganda-Congo	Oct-10	1.0440	30.5294	618	Jun-09	1.0309	30.5076	620
	21	Lake Edward, Uganda	-	-	-	-	Jun-09	-0.2093	29.8856	911
	22	Ssese Islands, Lake Victoria, Uganda	-	-	-	-	Jun-09	-0.2554	32.0386	1133
	23	Lake Victoria, Entebbe, Uganda	-	-	-	-	Jun-09	0.0560	32.4814	1134
	24	Paraa, Victoria Nile, Uganda	-	-	-	-	May-09	2.2864	31.5747	622
Blue Nile and Atbara River	25	Ribb River, east Lake Tana, Ethiopia	Oct-10	11.9937	37.7109	1799	May-09	11.9943	37.7130	1794
	26	Gish Abay, Ethiopia	Oct-10	10.9716	37.1991	2721	-	-	-	-
	27	Gilgel Abay, Ethiopia	Oct-10	11.3648	37.0341	1875	-	-	-	-
	28	Chimba, Gilgel Abay, Ethiopia	Oct-10	11.7060	37.1673	1809	May-09	11.7081	37.1680	1808
	29	Alata River, Ethiopia	Oct-10	11.4963	37.5909	1617	May-09	11.4929	37.5902	1647
	30	Gumara River, E. Lake Tana, Ethiopia	Oct-10	11.8393	37.6354	1795	May-09	11.8379	37.6359	1795
	31	River Zarima, Ethiopia	Oct-10	13.3419	37.8788	1220	-	-	-	-
	32	River Tekezé, Ethiopia	Oct-10	13.7337	38.1878	900	-	-	-	-
	33	River Magech, N. Lake Tana, Ethiopia	Oct-10	12.4872	37.4475	1882	-	-	-	-
	34	Blue Nile, Khartoum, Sudan	Dec-10	15.6139	32.5325	409	May-11	15.6139	32.5325	409
	35	Tis Issat Falls, Blue Nile, Ethiopia	Oct-10	11.4904	37.5855	1642	May-09	11.4904	37.5855	1642
	36	River Atbara, Atbara, Sudan	Dec-10	17.6778	33.9762	353	Apr-11	17.6778	33.9762	353
	37	Blue Nile, Bahir Dar, Ethiopia	Oct-10	11.6059	37.4074	1804	May-09	11.6050	37.4079	1788
Main Nile	38	Main Nile (L. Nasser), Sudan	Dec-10	21.8079	31.3156	170	Apr-11	22.0218	31.3393	178
	39	Main Nile, Dongola, Sudan	Dec-10	19.1811	30.4874	223	Apr-11	19.1811	30.4874	223
	40	Main Nile, Karima, Sudan	Dec-10	18.4957	31.8091	258	Apr-11	18.4957	31.8091	258
	41	Main Nile, Atbara, Sudan	Dec-10	17.6620	33.9745	357	Apr-11	17.6620	33.9745	357
	42	Main Nile, Khartoum, Sudan	Dec-10	15.6473	32.5086	409	May-11	15.6569	32.5103	377
	43	Main Nile, Aswan, Egypt	Dec-10	24.0829	32.8869	77	Apr-11	24.0888	32.8922	81
	44	Bahr Yusuf, Faiyum, Egypt	Nov-10	29.3084	30.8450	8	Apr-11	29.3084	30.8451	20
	45	Main Nile, Cairo, Egypt	Nov-10	30.0430	31.2276	4	Apr-11	30.0420	31.2269	8
	46	Main Nile, Luxor, Egypt	Dec-10	25.7032	32.3847	82	Apr-11	25.7028	32.6370	67
	47	Main Nile (L. Nasser), Aswan, Egypt	Dec-10	23.9703	32.8962	152	Apr-11	23.9702	32.8963	152
	48	Lake Qarun, Faiyum (SE), Egypt	Nov-10	29.4694	30.7696	-51	Apr-11	29.4683	30.7789	-44
	49	Lake Qarun, Faiyum (SW), Egypt	Nov-10	29.4694	30.7696	-51	-	-	-	-
	50	Lake Qarun, Faiyum (W), Egypt	-	-	-	-	Apr-11	29.4541	30.4003	-46

Due to the extent of the study area it was impossible to sample all major stretches of the River Nile during the peak of the rainy season and at minimum flow. It should also be noted that due to logistical and financial constraints, dry-season samples from the Upper and Lower Niles were collected two years apart and therefore do not reflect continuous sampling down the length of the river during a single dry season. Unfortunately, political instability prevented travel through South Sudan, thereby ruling out sampling of the Sudd and Bahr el Ghazal swamps, which are believed to play important roles in both the hydrological (Sutcliffe, 1974), and Si cycles (McCarthy et al., 1989). Logistical and safety considerations also prevented sampling of the Blue Nile between the Blue Nile Gorge, west of Lake Tana, and just above its confluence with the White Nile in Khartoum.

5.3.2 Sample collection and storage

Samples were collected in pre-cleaned HDPE bottles from freely flowing water. In each case, the collection bottle and lid were rinsed three times in the water of interest before collecting the final sample 30cm below the surface. Immediately after collection, electrical conductivity, water temperature and pH were measured using a handheld meter (Hanna Instrument: HI9835). In the field, samples were filtered through 0.45µm Millipore™ cellulose nitrate filters (47mm diameter) to remove colloidal and particulate Si (including biogenic silica), as well as suspended organic matter, and acidified with 1-2ml of ultra-pure HCl to a pH of between 2 and 3 to prevent any further biological activity or polymerization (Georg et al., 2006b). They were stored in clean 250ml HDPE bottles, and where possible, in dark and cool conditions whilst in the field. Air was evacuated by squeezing each bottle and allowing the contents to overflow before sealing it with a screw cap. These actions minimise biological activity and gas exchange prior to analysis. Filter papers were air-dried in order to retain the particulate matter for future analysis. On return to the UK, water samples were stored in the dark at 4℃ until they were analysed at the NIGL for H, O and Si isotopes and elemental concentrations.

5.3.3 Multi-elemental analysis of waters using ICP-MS

Careful selection of key rivers and lakes was required as only 46 of 79 waters collected were permitted for analysis by the NERC Isotope Geosciences Facility Steering Committee (NIGFSC) (Grant no. IP-1151-1109). Sub-samples from each of

the chosen water samples were taken to measure the major- and trace-element composition of individual waters. Of particular interest was the quantification of Si concentrations, firstly for the preparation of samples for Si isotope analysis and secondly for the understanding of processes operating within the Nile Basin. Quantification of Si was carried out using an Agilent 7500cx series quadrupole Inductively Coupled Plasma-Mass Spectrometer (ICP-MS), featuring an Octopole Reaction System (ORS), in combination with a CETAC auto-sampler at the BGS, Keyworth (analysis was carried out by Dr Simon Chenery and Thomas Barlow at BGS). The ORS removes matrix-based polyatomic interferences using a single set of cell conditions (helium mode) (Woods, 2007). Each sample was spiked with a mixed internal standard solution containing Sc, Ge, Rh, In, Te, Re and Ir at a ratio of 1:10 delivered continuously on-line via a T-piece. Accuracy was checked using certified reference water NIST 1643e. Typical uncertainty associated with ICP-MS is ±10% (3 S.D.). However, for, Na, Ca, Si, P, S, K, Fe, Zn, Sr and Ba, the overall uncertainty is of the order of ±15% For Li, B and Al the overall uncertainty is of the order of ±20%. I needed to screen individual sample compositions to identify high concentrations of individual elements which might saturate the column during purification of Si (e.g. Na, Mg, Al, Ba) or cause polyatomic interferences when analysing Si isotopes using the MC-ICP-MS (e.g. SO_4^{-2}, NO_3^-). Data were reported in ppb or µg/L except for the elements Na, Mg, P, S, K and Ca, which were reported as ppm or mg/L. Full compositional data can be found in Appendix I.

5.3.4 Si isotope analysis using MC-ICP-MS

5.3.4.1 Purification of Si for isotope analysis: column chemistry

Purification of Si was required to prevent potential matrix interferences from other components during isotope analysis by MC-ICP-MS and to prevent clogging of the sampler cone. Of the 46 water samples that were analysed for their chemical composition by ICP-MS, only 44 samples had Si concentrations high enough for Si-isotope analysis (Table 5.2). In a class 100 clean-room suite at the NIGL I used cation-exchange resin to chromatographically separate Si after adapting methods from Georg et al. (2006b) and van den Boorn et al. (2006) (see section 4.5 in Chapter 4). At a pH of between 2 and 8, Si species are either neutral ($Si(OH)_4$) or anionic ($H_3SiO_4^-$) and will therefore pass freely through cation-exchange resin whilst all major cations (Na, Ca, K, Mg, Al) are retained on the column.

Table 5.2: Water samples that were analysed for their chemical composition and underwent chromatographic separation of Si using cation-exchange resin. 46 samples plus 5 replicates had their chemical compositions determined. Two samples (Site numbers 18 and 19) had Si concentrations that were too low for Si-isotope analysis and were removed from any further analysis. Site numbers correspond to Figure 5.1.

Sampling date/season	Site no.	Site name and location	Initial Si conc. (ppm or mg/L)	Sample load (ml) on to cation-exchange column	Additional ml's of Milli-Q water to dilute to required final concentration	Total volume (ml) including 3ml elution with Milli-Q water	Final concentration of Si (ppm or mg/L)
Oct-10/Wet	3	River Mubuku, Rwenzori Mts., Uganda	5.7	4	0.6	7.6	3
Oct-10/Wet	4	River Ishasha, Uganda	5.6	4	0.47	7.47	3
Oct-10/Wet	5	River Ntungwe, Uganda	12.0	1	0	4	3
Oct-10/Wet	7	Lake Mahoma, Rwenzori Mts., Uganda	1.1	7	0.27	10.27	0.75
Oct-10/Wet	9	River Kagera, Uganda	7.1	3	1.1	7.1	3
Jun-09/Dry	11	River Semliki, Uganda-Congo	6.9	3	0.9	6.9	3
Oct-10/Wet	11	River Semliki, Uganda-Congo	8.9	2	0.93	5.93	3
Oct-10/Wet	11	River Semliki, Uganda-Congo	8.9	2	0.93	5.93	3
Oct-10/Wet	11	River Semliki, Uganda-Congo	8.9	2	0.93	5.93	3
Oct-10/Wet	11	River Semliki, Uganda-Congo	8.9	2	0.93	5.93	3
Oct-10/Wet	11	River Semliki, Uganda-Congo	8.9	2	0.93	5.93	3
Oct-10/Wet	11	River Semliki, Uganda-Congo	8.9	2	0.93	5.93	3
Jun-09/Dry	12	Kazinga Channel, Uganda	10.7	2	2.13	7.13	3
Oct-10/Wet	12	Kazinga Channel, Uganda	10.2	2	1.8	6.8	3
Dec-10/Wet	13	White Nile, Khartoum, Sudan	6.0	3	0	6	3
May-11/Dry	13	White Nile, Khartoum, Sudan	3.8	2	0.07	5.07	1.5
May-09/Dry	14	Albert Nile, Uganda	1.2	5	0	8	0.75
Nov-10/Wet	14	Albert Nile, Uganda	2.9	4	0.73	7.73	1.5
May-09/Dry	15	Victoria Nile Delta, Uganda	2.1	8	0.2	11.2	1.5
Nov-10/Wet	15	Victoria Nile Delta, Uganda	3.3	3	0.6	6.6	1.5
Jun-09/Dry	18	Victoria Nile, Bujagali Falls, Uganda	0.2	–	–	–	–
Nov-10/Wet	18	Victoria Nile, Bujagali Falls, Uganda	1.5	3	0	6	0.75
Jun-09/Dry	19	Outflow from Lake Victoria, Uganda	0.2	–	–	–	–
Nov-10/Wet	19	Outflow from Lake Victoria, Uganda	1.1	7	0.27	10.27	0.75
Jun-09/Dry	20	Lake Albert (south), Uganda-Congo	1.2	5	0	8	0.75
Oct-10/Wet	20	Lake Albert (south), Uganda-Congo	2.8	4	0.47	7.47	1.5
May-09/Dry	25	Ribb River, east Lake Tana, Ethiopia	3.3	3	0.6	6.6	1.5
Oct-10/Wet	25	Ribb River, east Lake Tana, Ethiopia	8.8	2	0.87	5.87	3
May-09/Dry	28	Chimba, Gilgel Abay, Ethiopia	10.9	2	2.27	7.27	3
Oct-10/Wet	28	Chimba, Gilgel Abay, Ethiopia	7.4	3	1.4	7.4	3
Oct-10/Wet	31	River Zerma, Ethiopia	18.9	1	2.3	6.3	3
Oct-10/Wet	32	River Tekezé, Ethiopia	9.9	2	1.6	6.6	3
Oct-10/Wet	33	River Megetch, N Lake Tana, Ethiopia	16.0	1	1.33	5.33	3
Dec-10/Wet	34	Blue Nile, Khartoum, Sudan	7.3	3	1.3	7.3	3
May-11/Dry	34	Blue Nile, Khartoum, Sudan	5.7	4	0.6	7.6	3
May-09/Dry	35	Tis Issat Falls, Blue Nile, Ethiopia	3.7	3	1.4	7.4	1.5
Oct-10/Wet	35	Tis Issat Falls, Blue Nile, Ethiopia	4.9	5	0.17	8.17	3
Dec-10/Wet	36	River Atbara, Atbara, Sudan	8.8	2	0.87	5.87	3
Apr-11/Dry	36	River Atbara, Atbara, Sudan	5.1	5	0.5	8.5	3
Dec-10/Wet	39	Main Nile, Dongola, Sudan	6.3	3	0.3	6.3	3
Apr-11/Dry	39	Main Nile, Dongola, Sudan	4.6	6	0.2	9.2	3
Dec-10/Wet	41	Main Nile, Atbara, Sudan	5.8	4	0.73	7.73	3
Apr-11/Dry	41	Main Nile, Atbara, Sudan	4.0	2	0.33	5.33	1.5
Nov-10/Wet	45	Main Nile, Cairo, Egypt	0.8	45	0	48	0.75
Apr-11/Dry	45	Main Nile, Cairo, Egypt	1.1	7	0.27	10.27	0.75
Dec-10/Wet	46	Main Nile, Luxor, Egypt	2.9	4	0.73	7.73	1.5
Apr-11/Dry	46	Main Nile, Luxor, Egypt	2.6	5	0.67	8.67	1.5
Dec-10/Wet	47	Main Nile (L. Nasser), Aswan, Egypt	3.4	3	0.8	6.8	1.5
Apr-11/Dry	47	Main Nile (L. Nasser), Aswan, Egypt	2.7	4	0.2	7.2	1.5
Nov-10/Wet	48	Lake Qarun, Faiyum (SE), Egypt	2.5	4.5	0	7.5	1.5
Apr-11/Dry	48	Lake Qarun, Faiyum (SE), Egypt	5.0	2	1.67	6.67	1.5

Prior to column chemistry, all consumables were cleaned with ultrapure (low Si; ppt) acids (e.g. Romil-UpA™, Aristar® Ultra or other quartz distilled brands) to remove any traces of inorganic constituents and Si (see Table 5.3). Unless otherwise stated, when referring to acids and reagents, Romil-UpA™ grade was used. The cation-exchange resin (Bio-Rad® AG 50W-X12) was pre-cleaned to remove fines that might clog the MC-ICP-MS during sample uptake (Table 5.3). Disposable Bio-Rad® Bio-Spin chromatography columns did not undergo a pre-cleaning stage as they would be cleaned during the wash stages of the resin. A full equipment list can be found in Appendix II.

Table 5.3: Procedure for cleaning consumables prior to chromatographic exchange.

Consumable	Acid/Reagent	Procedure
Savillex collection vials	4M HNO_3 (UpA) (only for new vials)	Thin layer to cover base of container to allow reflux for 24 hours on a hotplate at 120℃. Lid loosely tightened. Decant HNO_3 and rinse 3 times with Milli-Q water.
Storage bottles for acid solutions	2M HCl + HF (UpA)	Add enough HCl solution to cover base of container and add a few drops of HF. Reflux for 24 hours on a hotplate at 120℃. Decant HCl. Rinse with Milli-Q water 3 times and half fill with Milli-Q water to reflux overnight on the hotplate. Rinse with Milli-Q water and allow to dry.
Pipette tips and storage tubes	1.5M HCl + HF (SpA)	Put pipette tips and storage tubes and lids into a 1 litre Teflon® container and fill to top with HCl and a few drops of HF. Allow to reflux for 24 hours on a hotplate at 120℃. Lid loosely tightened. Decant HCl. Rinse with Milli-Q water 3 times and fill with Milli-Q water to reflux overnight on the hotplate. Rinse with Milli-Q water and allow to dry. Store in sealed bags.
Resin AG 50W-X12		Rinse resin over several days with Milli-Q water to remove fines. Shake resin in water and allow to settle, decant off supernatant (20-30 washes).
	1.5M HCl (UpA)	Add HCl solution to resin, enough to cover, until use. Store in Teflon® squeezy bottle.

Using 10ml disposable Bio-Rad® Bio-Spin chromatography columns mounted on a carousel/rack, 1.8ml of pre-cleaned resin was loaded into the resin reservoir, taking care to prevent the formation of air bubbles in the column. Prior to loading the sample on the column, a series of preconditioning washes with HCl, HNO_3 and Milli-Q water was carried out as detailed in Table 5.4. The pH of the last drop of Milli-Q water coming off the resin prior to loading the sample was tested to make sure that no acid solution remained. The sample was loaded 1ml at a time to prevent overloading on the column, and simply eluted with 3ml of Milli-Q water as the prevailing Si species do not bind to the resin (Georg et al., 2006b). A 3ml elution is required to ensure all Si is recovered (Georg et al., 2006b; van den Boorn et al., 2006).

The amount of sample loaded was based on the initial Si concentration and the final concentration required (i.e. 0.75, 1.5 or 3 ppm), but was generally between 1 and 8ml (Table 5.2). Where possible, final Si concentrations were diluted to 3ppm, however samples with initial Si concentrations of <4ppm and <1.5ppm were made to 1.5ppm and 0.75ppm final Si concentration respectively, as the 3ml elution meant that they were heavily diluted. Samples were diluted with Milli-Q water after column chemistry directly into the purified sample to obtain the required final concentration. Batches of samples (and reference materials) with matching final Si concentrations were required to stabilise the MC-ICP-MS. A minimum concentration of 0.75ppm was required to effectively obtain precise data. The full procedure for column chemistry and calculations can be found in Appendix III.

Table 5.4: Cleaning procedure for individual chromatographic columns with 1.8ml of resin. All acid solutions were made using Romil-UpA™ grade acid and Milli-Q water.

Volume	Concentration	Chemical
3 ml	3 M	HCl
3 ml	6 M	HCl
3 ml	7 M	HNO_3
3 ml	10 M	HCl
3 ml	6 M	HCl
3 ml	3 M	HCl
Fill		MQ-e
3 ml		MQ-e

5.3.4.2 Preparation of standards/reference material

Two silica (SiO_2) reference materials were used to check the accuracy and precision of Si isotope analysis: NBS-28 (NIST RM 8546) and Diatomite. NBS-28 is a quartz sand and is the international Si isotope standard reference material. Diatomite is a pure opal sample, whose values are widely reported in the literature (Reynolds et al., 2007), and is used here as a validation material. Since both NBS-28 and Diatomite are solids, they require dissolution prior to purification.

An alkaline fusion procedure, as set out by Georg et al. (2006b) and frequently used in the dissolution of rocks and minerals for determining Si content, was used to dissolved the solid reference materials into an aqueous solution. At NIGL, reference materials were ground to a powder in an alumina pestle and mortar. Following that, a known amount of powder (between 1 and 10mg) was transferred to a homemade Ag crucible (99.99% Ag sheet: Goodfellow) and mixed with 200mg of Merck Suprapur NaOH flux. The Ag crucible was placed into a pre-cleaned lidded, alumina crucible to prevent contamination. After 30 minutes at 720℃ in a muffle furnace, the resulting fusion-cake was dissolved in 20ml of Milli-Q water. A 0.1M NaOH 500ml stock solution of NBS-28 was made to 13ppm of Si with a pH of ~12. The reference solutions were processed through the same column chemistry procedure as the water samples, outlined in section 5.3.4.1. In addition, to process the samples and standards in the same way and to matrix-match the compositions, a sub-sample of the NBS-28 stock solution was acidified with UpA HCl to a pH of 2-3 prior to column chemistry.

5.3.4.3 Si isotope analysis using MC-ICP-MS

Si isotope analyses of aqueous solutions were made using a Thermo Fisher Neptune Plus Multi Collector-Inductively Coupled Plasma-Mass Spectrometer (MC-ICP-MS) at the NIGL, in wet plasma mode using a glass nebuliser coupled to a SSI quartz dual cyclonic spray chamber. Typical instrument operating conditions are summarised in Table 5.5. The instrument was operated in high resolution (HR) to overcome interferences from N-, O- and C-containing species that are not removed by ion-exchange purification. Isolation of these interferences from the isotopes of Si requires a resolution (R) of at least 4000 ($R=M/\Delta M$, where ΔM is the difference between the two masses of interest). The Neptune Plus at NIGL is capable of a

resolution of ~9000, more than sufficient for partial (or pseudo) resolution across the Si mass range. However, the interference free peak flat is typically very narrow (<15milli amu). At this resolution, any drift in magnet stability becomes significant; hence constant vigilance was required to ensure the magnet remained centred. Both samples and standard solutions were doped with the same level (matrix-match) of quartz distilled sulphuric acid (for sulphate), nitric acid (for nitrate) and hydrochloric acid (for chloride), in sufficient quantities to exceed the natural concentrations, to prevent isotopic bias, as recommended by Hughes et al. (2011) and van den Boorn et al. (2009) (see section 4.6 for further information).

Table 5.5: Summary of the analytical set-up used at the NIGL on the Neptune Plus MC-ICP-MS for Si isotope analysis.

Forward power	1200W
Reflected Power	<2W
Plasma Gas	16l/min
Auxiliary gas flow	0.8l/min
Nebuliser carrier gas flow	1.17l/min
Nebuliser	200ul/min glass (Glass Expansion)
Spray chamber	Stable Sample Introduction (SSI) quartz dual cyclonic
Type of detector	Faraday ($10^{11}\Omega$ resistors)
Torch	Demountable glass torch with Sapphire injector
Cones	Thermo Fisher nickel 'H' sample and skimmer
Sample uptake time	90 seconds
Wash time between samples	~ 5 minutes

Sensitivity of about 11V/ppm was obtained, which is comparable to, or better than values reported in the literature (Engström et al., 2006; Georg et al., 2006b; Zambardi and Poitrasson, 2011), with an instrument background contribution of ~0.4% (~45mV ^{28}Si measured on the blank acid). This was achieved by introducing samples to the system through a glass nebuliser coupled to a SSI quartz dual cyclonic spray chamber (wet plasma), optimising both the signal stability and intensity, while keeping background contributions to a minimum. Although experiments proved that the Cetac Aridus II introduction system (dry plasma) improved sensitivity, this was coupled with high and unstable background Si, making it unsuitable for the high precision analysis required for silicon isotope determinations. Background contributions were further reduced through the use of a sapphire injector (CPI International), rather than the conventional Si injector, and

through the avoidance of HF in the preparatory stages (section 5.3.4.1) which prevented erosion of the glass parts of the mass spectrometer (Georg et al., 2006b).

Mass bias and instrumental drift were corrected using a combined external Mg doping and standard-sample bracketing approach (Cardinal et al., 2003; Zambardi and Poitrasson, 2011). A typical sampling sequence was: blank – reference – blank – sample – blank, etc. Data are expressed in relative deviations of $^{30}Si/^{28}Si$ ratios from the NBS-28 standard (NIST RM 8546) using the common delta notation (δ) and expressed as parts per thousand (‰), using the following equation:

$$\delta^{30}Si = \left[\frac{\left({}^{30}Si/{}^{28}Si \right)_{sample}}{\left({}^{30}Si/{}^{28}Si \right)_{standard}} - 1 \right] \times 1000 \qquad \textbf{(Equation 1)}$$

Accuracy and reproducibility ($\delta^{30}Si$) were checked during analytical sessions using a secondary reference material (Diatomite).

5.3.5 Oxygen and hydrogen isotope analysis using IRMS

All 79 water samples collected from the Nile Basin were analysed for O and H isotopes by Isotope Ratio Mass Spectrometry (IRMS) at the NIGL by Carol Arrowsmith under the NIGFSC grant. For O-isotope analysis, the waters were equilibrated with CO_2 using an Isoprep 18 device. Mass spectrometry was performed on a VG SIRA. For H-isotope analysis, an on-line Cr reduction method was used with a EuroPyrOH-3110 system coupled to a Micromass Isoprime mass spectrometer. Isotopic ratios ($^{18}O/^{16}O$ and $^{2}H/^{1}H$) are expressed in standard delta notation, as $\delta^{18}O$ and $\delta^{2}H$ (‰, parts per mille), with respect to the international standard VSMOW (Vienna Standard Mean Ocean Water) using the following equation:

$$\delta^{18}O = \left[\frac{\left({}^{18}O/{}^{16}O \right)_{sample}}{\left({}^{18}O/{}^{16}O \right)_{standard}} - 1 \right] \times 1000 \qquad \textbf{(Equation 2)}$$

Analytical precision was typically ±0.05‰ for $\delta^{18}O$ and ±1.0‰ for $\delta^{2}H$.

5.4 Lake sediment cores

5.4.1 Sampling strategy

The main aim was to reconstruct changes in the intensity of biotic Si cycling since the Last Glacial Maximum (LGM) in the Nile Basin. Due to the novelty of the project and its technical constraints (restricted to the number of analyses determined by the grant in kind from the NIGFSC), the aim initially was for a broad (low-resolution) understanding of glacial / interglacial variations of the continental Si cycle, with the intention of focussing in at higher temporal resolution once significant results had been obtained. Sediments were generally sampled at 500-yr resolution back to the period of lowest lake levels at the end of the last glacial (~20ka), or as far back as individual cores allowed. This period spans the arid conditions at the end of the LGM, the onset of the enhanced summer monsoon (African Humid Period) at ~15 ka BP, and the shift to drier conditions from ~5.5 ka BP to present (Kutzbach and Street-Perrott, 1985). Beneficially, many of the cores had already had their biogenic silica (BSi) content and/or diatom concentrations measured, which aided the selection of samples for isotopic analysis.

To isolate enough diatoms for isotopic analysis (~5mg) (Leng and Sloane, 2008), the initial BSi concentrations needed to be relatively high (~10%). If the diatom concentration was lower, a correspondingly larger amount of sediment was processed. Prior work on the White Nile lakes (Victoria and Edward) provided confidence in their suitability for extracting pure diatom components; BSi concentrations in Lake Victoria and Lake Edward exceed 35% (Johnson et al., 2000; Russell et al., 2003a).

5.4.2 Sample material and selection

Sample material used in this research came from previous coring expeditions. One of the deciding factors for choosing the Nile Basin as suitable study region was the wealth of previously cored lakes and the availability of material with existing age models and useful proxy information. Sediment core material for Lake Victoria (White Nile, Uganda) and Lake Edward (White Nile, Uganda-D.R. Congo) was obtained from the US Limnological Research Centre at the National Lacustrine Core (LacCore) Facility at the University of Minnesota, USA, which was collected during

the International Decade for the East African Lakes (IDEAL) project (lake locations in Figure 5.1).

The benefit of using previously cored/studied material is that there are usually well established age-models and corresponding proxy data that complement the research and aid interpretation of new data. Specifically, for this research, data were available for most material on the biogenic silica (BSi) concentrations (%) and/or diatom valve concentrations, with corresponding age-depth models, which was extremely useful when selecting sediment samples for isotope analysis on diatom silica. It is a prerequisite that sediments are rich (≥10%) in BSi in order to obtain enough diatom material for isotope analysis (~5mg) (Leng and Sloane, 2008). If this is not the case, it is possible, to work with larger amounts of sediment, if available, in order to extract enough diatom material at the end. For example, it was common to begin with ~5-10g (dry weight) of sediment with ~8% BSi, achieved by sampling across a depth range of 5-10cm of core.

5.4.3 Age models

Existing age models for Lakes Victoria and Edward were available based on radiocarbon dating (Johnson et al., 2000; Russell et al., 2003a; Beuning and Russell, 2004). Existing age models were used rather than developing new models (see Chapters 7 and 8 for Lakes Victoria and Edward, respectively), in order to permit direct comparison with existing proxy data.

5.4.4 Determination of biogenic silica (BSi) concentrations

Biogenic silica (BSi) concentrations provide useful proxy information in their own right and serve as an indicator of past productivity, predominantly of diatoms. BSi concentration data were already available for Lakes Victoria and Edward, (Johnson et al., 1998; Russell et al., 2003a), and assisted with choosing suitable sample levels. The abundance of BSi was determined using a timed wet-alkaline chemical digestion that relies on biogenic silica components dissolving first before silicate minerals (DeMaster, 1981; Krausse et al., 1983; Conley, 1998; Conley and Schelske, 2001).

5.4.5 Purification of diatom silica for isotope analysis

Lake sediments are composed of a variety of components including silts, clays, fine sands, tephra shards, organic matter (e.g. pollen, charcoal, wood, algae), biogenic silica (e.g. diatoms, phytoliths, sponge spicules), and carbonates (e.g. shells) (Last and Smol, 2001; Schnurrenberger et al., 2003). In order to analyse diatom silica for O and Si isotopes, the diatom frustules must be free of any other components or "contaminants" that may be present in the sediments (Leng and Sloane, 2008). Contaminants in this sense refer to any remaining sediment components other than diatoms, as any contamination may significantly change the measured isotope values (Brewer et al., 2008). Several chemical and physical methodologies have been suggested for isolating and cleaning diatom frustules (Shemesh et al., 1988; Shemesh et al., 1995; Morley et al., 2004; Rings et al., 2004; Swann et al., 2006; Tyler et al., 2007). The methods used here to remove contaminants were tailored specifically for each individual sample, depending on its composition.

The first step was to remove carbonates and organics, following a similar methodology to that outlined by Morley et al. (2004) (Figure 5.2), whereby hydrochloric acid (HCl) and hydrogen peroxide (H_2O_2) were used, respectively. Removal of organics by H_2O_2 took up to several days (TOC often >10%). An additional treatment step with nitric acid (HNO_3) was employed to remove remaining organic matter and to etch the surface of the diatom frustules to release any clays trapped within the pores (personal communication with Professor Phil Barker at Lancaster University). Following that, samples were sieved at 63, 38 and 20 µm by gently washing through with deionised water. This step allowed samples to be divided and isolated into "groups" of contaminants, for example silts and clays, for ease of determining the next suitable methodological step and to isolate the diatoms further (Figure 5.2; Stage 2). Due to the large quantities of sediment used, sieving took up to several days per sample. All samples underwent this chemical (removal of organics and carbonates) and physical (sieving) procedure.

Subsequent additional steps were tailored to the individual samples depending on the remaining contaminant(s). Such additional steps included:

- **Differential settling**: to allow the settling out of heavier silts compared to the relatively buoyant diatoms which were decanted-off.
- **Heavy liquid separation**: using sodium polytungstate (SPT) at a specific gravity of ~2.2 g/ml to float-off diatoms (specific gravity of ~2.1 g/ml) whilst denser contaminants sank. Much lower densities allowed the separation of green algae (e.g. *Botryococcus* and *Pediastrum*) from diatoms.
- **Sonication**: using an ultrasonic bath mineral aggregates were broken-up and re-sieving/SPT often allowed them to be isolated from the diatoms
- **Additional treatments with HNO_3/H_2O_2**: sometimes it was necessary to treat samples again to remove stubborn organics or to remove organic matter that was exposed after sonication.
- **SPLITT**: gravitational split-flow thin fractionation uses laminar flow to separate samples into two components based on their density and hydrodynamic properties (Rings et al., 2004). This was carried out on some samples at the Environment Centre, Lancaster University.

Of the additional steps used, differential settling was most effective and extremely simple. A full step-by-step methodology can be found in Appendix IV. The most common size fractions used for isotope analysis, due to the final product being the cleanest, were 20-38 µm and 38-63 µm. It is very difficult to separate individual diatom species for isotope analysis due to their microscopic size (Swann et al., 2007), and so it is common to perform isotope analysis on bulk (mixed species) samples. A number of studies (Shemesh et al., 1995; Brandriss et al., 1998; Moschen et al., 2005; Schiff et al., 2009) have investigated whether individual species cause an offset in the isotope value; however their results showed either that species effects did not exist or that the offset was within analytical reducibility.

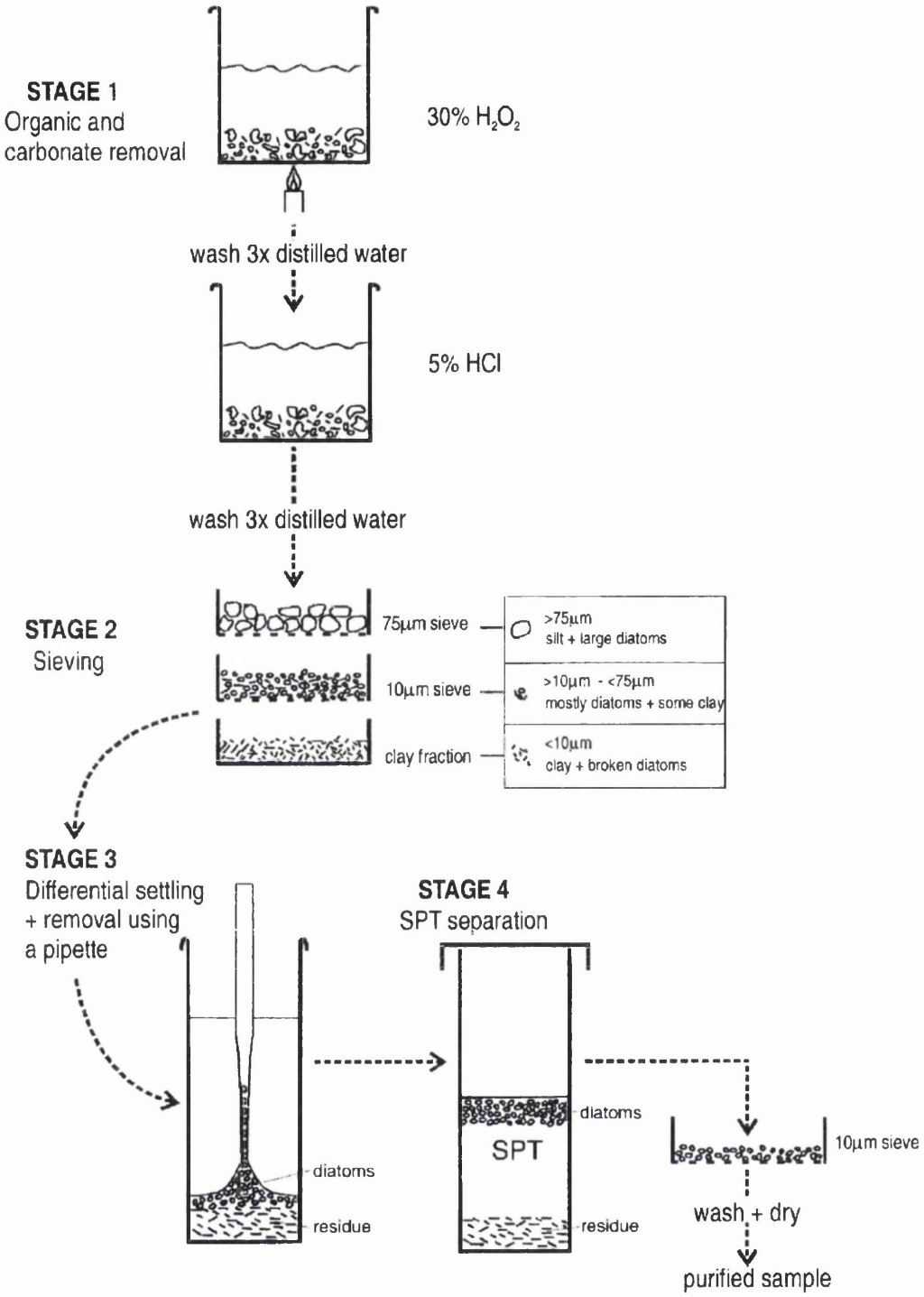

Figure 5.2: Methodology used by Morley et al. (2004) to extract diatoms from lake sediments for isotope analysis.

5.4.6 Assessment of contamination levels

At every stage of purification, each sample was visually assessed for remaining contaminants on temporary slides under a light microscope (Zeiss Axiophot) at x1000 magnification. After the final clean-up stage, to assess the level of purity of the samples, the ratio of diatoms versus remaining contaminant was measured by counting at least 300 particles (diatoms or contaminants) along transects across the full length of the slide to make sure that the whole coverslip was sampled (i.e. from the edges to the centre) (see methodology for making permanent slides in Appendix V). The diatom samples needed to be very pure (>97%) for isotope analysis in order to avoid significant contributions from other sedimentary components. Therefore, in addition to inspection by light microscopy, all samples were observed and imaged on a Hitachi S4800 Scanning Electron Microscope (SEM) to provide further evidence and records of sample purity. Once samples were deemed pure enough for isotope analysis, they were freeze-dried for 48 hours and analysed at the NIGL for coupled O and Si isotopes.

5.4.7 Coupled Si- and O-isotope measurements using GC-IRMS

Using the newly developed methodology at the NIGL for coupled O- and Si-isotope analysis of biogenic silica (Leng and Sloane, 2008), 43 sufficiently pure diatom samples extracted from sediments of Lakes Victoria and Edward were analysed by Hilary Sloane at the NIGL using a step-wise fluorination technique. 3-5mg of purified diatoms were loaded into nickel reaction tubes where they were outgassed for 2 hours at 250℃ to remove surficial water. Reaction with bromine pentafluoride at 250℃ for 6 minutes removed the outer layers of diatom silica (hydrous layer) containing exchangeable oxygen before a full reaction with an excess of reagent at 500℃ for 14 hours to dissociate the silica into oxygen, which was subsequently converted into CO_2 following the method described by Clayton and Mayeda (1963), and silicon as SiF_4. Following extraction, the collected gases were analysed for O and Si isotopes using a Finnigan MAT™ 253 Isotope Ratio Mass Spectrometer (IRMS). Full details of the fluorination line and methodology developed at NIGL are given by Leng and Sloane (2008). All $\delta^{18}O$ and $\delta^{30}Si$ data were reported relative to VSMOW and NBS-28, respectively. Using the NIGL within-run laboratory standard (BFC; diatomite from Shastra County, California) accuracy and reproducibility were tested. Accuracy (2σ) was checked on reference material BFC ($\delta^{18}O$: +28.88

±0.36‰, n = 13; $\delta^{30}Si$: +0.05 ±0.15‰, n = 7) (Figure 5.3), which yielded isotope compositions indistinguishable from previously published values (Leng and Sloane, 2008; Chapligin et al., 2011). Replicate analyses of sample material indicated a mean analytical reproducibility (1σ) of 0.19‰ (range: +0.08 to +0.30‰, n = 6) and 0.07‰ (range: +0.01 to +0.19‰, n =8) for oxygen-isotope ($\delta^{18}O_{diatom}$) and silicon-isotope ($\delta^{30}Si_{diatom}$) composition of diatom silica, respectively. Quality control of mass bias was checked by plotting $\delta^{29}Si$ by $\delta^{30}Si$ (Figure 5.4). Three diatom samples that plotted outside the expected mass-dependent fractionation relationship were identified as containing contamination, and were eliminated from further analysis (these samples are discussed in detail in Chapter 8, section 8.9.2).

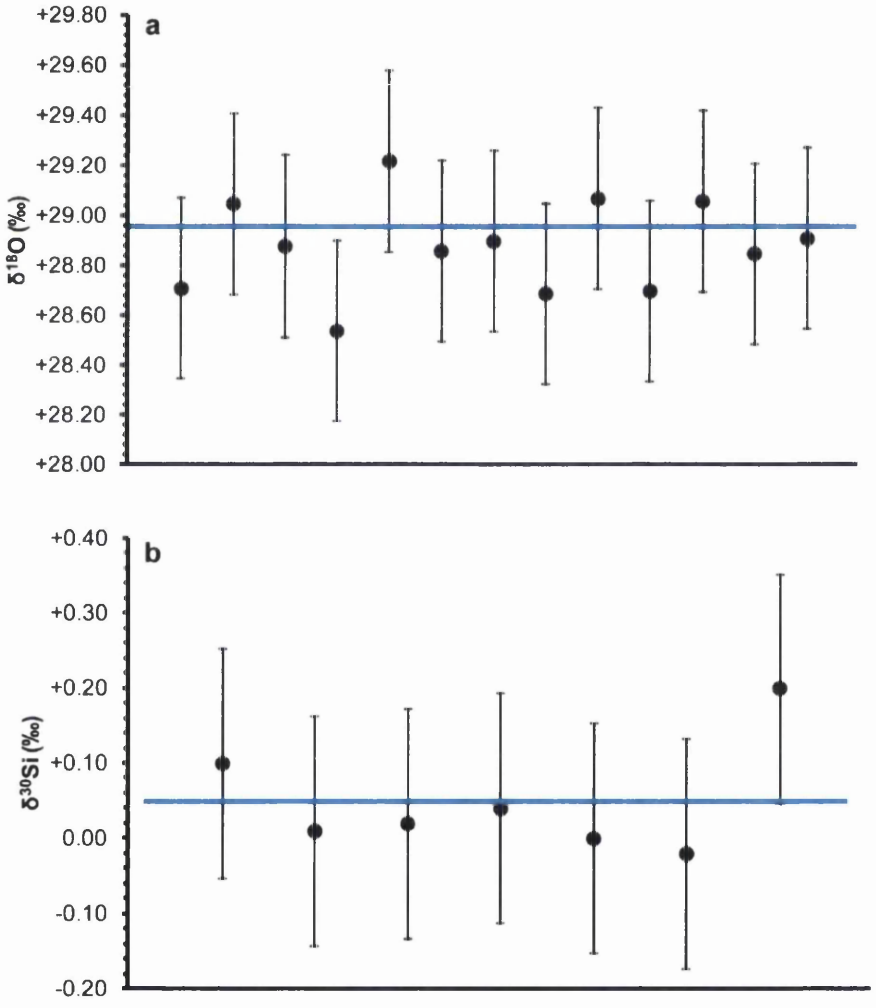

Figure 5.3: Reproducibility of reference material BFC (diatomite deposit from Shastra County, California, US) at NIGL for oxygen (a) and silicon (b) isotopes. Error bars are 2σ and the blue horizontal line represents the mean.

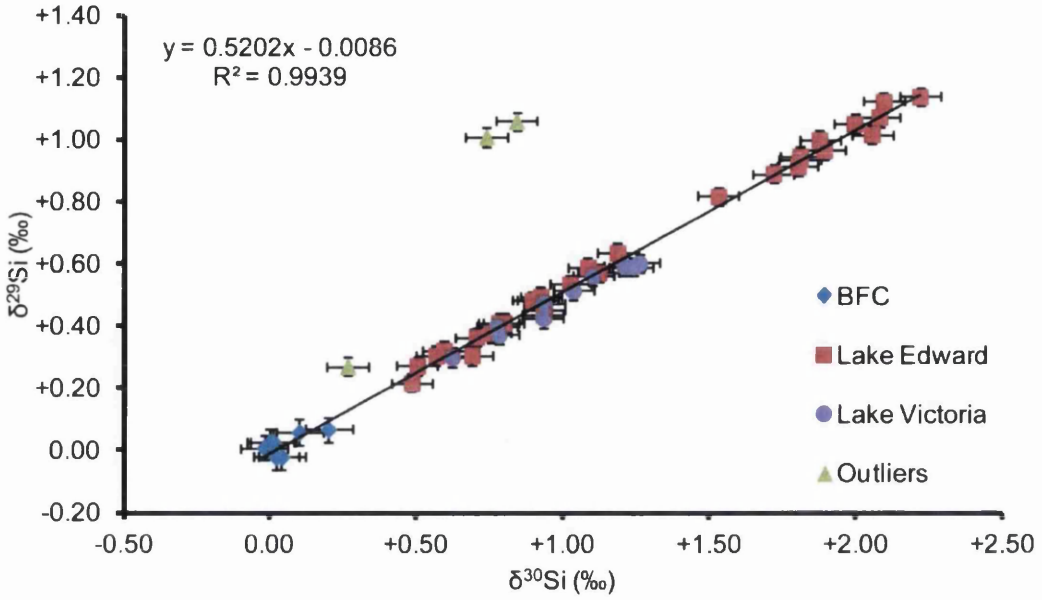

Figure 5.4: $\delta^{29}Si$ and $\delta^{30}Si$ values of all diatom samples and reference materials analysed. Error bars represent 1σ and are referred to in the text.

5.4.8 Lipid extraction

Sediments from Lakes Victoria and Edward were sampled at ~500-year resolution for total lipids (n = 59). A known amount of sediment (~1g) from each depth was freeze-dried and ground. Lipid class compounds were extracted from the dry sediment samples with dichloromethane (DCM)/methanol (9:1) using an accelerated solvent extractor (Dionex: ASE 200) at 100℃ and 15 00 psi for 25 minutes in 1 cycle. Following the methods of Ficken et al. (1998) and Huang et al. (1999), total extracts were split into acid and neutral fractions using solid phase extraction (Aminopropyl Bond Elut® cartridges). Samples were loaded on to pre-cleaned columns (DCM and DCM/isopropanol (2:1 v/v)) and the neutral fraction was eluted with DCM/isopropanol (2:1 v/v) and the acid fraction was recovered using 2% acetic acid in ether. The acid fraction was then methylated with methanolic HCl and set aside as the acid fraction was not used in this study. The neutral fraction was fractionated further into a hydrocarbon and a polar fraction by column chromatography using freshly activated alumina, eluting the hydrocarbons with hexane/DCM (9:1 v/v) and subsequently the polar fraction with methanol/DCM (1:1 v/v). The polar fraction was not investigated further in this thesis. The hydrocarbon fraction was de-sulphurized by the addition of activated copper turnings prior to the

separation of the branched hydrocarbons (non-adduct fraction) from the straight-chain hydrocarbons (adduct fraction) by urea adduction. A known amount of standard solution (*n*-C_{36} alkane) was added to each sample prior to analysis by gas chromatography-mass spectrometry (GC-MS). A detailed methodology for the lipid extraction and fractionation procedure can be found in Appendix VI.

5.4.9 Lipid analysis using GC-MS

Quantification and identification of straight chain hydrocarbons (adduct fraction: *n*-alkanes and *n*-alkenes) and branched hydrocarbons (non-adduct fraction) were carried out by GC–MS performed on an Agilent 6890 gas chromatograph (split/splitless injection, 70 eV, EI) interfaced directly with an Agilent 5975 mass spectrometer equipped with an automatic sampler and computer workstation. A HP5-MS fused silica capillary column (30 m × 0.25 mm; 0.25 μm film thickness) was used. The oven temperature was held at 60 ℃ for 1 min, ramped at 10 ℃ per minute to 180 ℃ and then ramped at 4 ℃ per minute to 300 ℃ where it was held for 15 minutes. Helium was used as the carrier gas. Compounds were identified by comparison with known mass spectra, with published data and with the NIST Mass Spectral Library spectra (version 2.0, 2005).

5.5 Chapter summary

The seasonal and strategic sampling strategy employed for understanding the modern isotope systematics of the Nile Basin is expected to provide, for the first time, knowledge of downstream processes of Si cycling under different climate conditions (dry and wet season sampling) and valuable information for interpreting the palaeo-record. Through the new methodology developed at the NIGL for analysing Si isotope of waters, accurate and precise measurements have been achieved, comparable or better than those in the literature. The utilisation of novel techniques, specifically coupled O- and Si-isotope measurements, for analysing sediments of Nile-fed lakes at important climate intervals are expected to capture an insight into how Si cycling has varied during the past under different climate regimes. Collectively, it was anticipated that these methodologies would provide complementary information and support further understanding of the continental Si cycle. Data resulting from these procedures will be presented in the following chapters.

Chapter 6 Modern surface water results

6.1 Introduction

A total of 79 water samples was collected from the River Nile in order to understand the modern isotope systematics in the Nile Basin to enable accurate interpretation of the palaeo-record. Measured parameters (pH, electrical conductance, major cation composition, δ^2H, $\delta^{18}O$, DSi and $\delta^{30}Si$) were plotted to identify relationships and trends, particularly with latitude and altitude. Due to the complicated hydrography of the River Nile (i.e. many tributaries), latitude is used here as a convenient proxy for downstream distance. As a result of contrasting geology in the headwater sub-basins (Figure 3.2), regression lines for physical and chemical characteristics have been plotted individually for each sub-basin for both wet and dry seasons. Trends for waters draining the Ethiopian Highlands (Blue Nile and Atbara) and from the Main Nile are plotted together due to the overriding impact of waters from the Ethiopian headwaters on physical and chemical composition of Main Nile waters. References to specific sampling sites are numbered in square brackets and correspond to those presented in Table 5.1 and Figure 5.1.

6.2 Physical characteristics: pH and electrical conductance

Almost all the water samples collected were tested for their pH and electrical conductance (EC) (Table 6.1). EC is a proxy for salinity as an increase in dissolved ions enhances both EC and salinity. On a few occasions it was not possible to obtain a reading as the instrument failed to calibrate or the apparatus did not function properly. pH values of White Nile waters ranged from slightly acidic to strongly alkaline (6.7 to 10.6) and varied very little between seasons (Figures 6.1 and 6.2). In contrast, waters from the Ethiopian Highlands (Blue Nile and Atbara catchments) displayed a greater range of values (5.9 to 11.7) and were less alkaline during wet-season conditions (Figures 6.1 and 6.2). In the Main Nile, less alkaline pH values (7.4 to 8.8) occurred during the dry season than during the wet season (9.2 to 10.6). Figures 6.1 and 6.2 show that pH values increased northwards and with decreasing altitude during the wet season but not in the dry season. No significant spatial trends were observed in pH during the dry season (Figures 6.1 and 6.2).

Table 6.1: Sample site locations and physical and chemical parameters.

			Wet season							
	Site No.	Sample site name	Date (month-year)	Latitude (decimal degrees)	Longitude (decimal degrees)	Altitude (m.a.s.l.)	Conductivity (µS/cm)	Water temperature (°C)	pH	Cation ratio $Na^+ + K^+ / Ca^{2+} + Mg^{2+}$
White Nile	1	Bujuku River, Rwenzori Mountains, Uganda	Oct-10	0.36	29.97	2552	43.5	11.4	-	-
	2	River Mubuku, Rwenzori Mountains, Uganda	Oct-10	0.36	29.97	2552	17.2	11.8	-	-
	3	River Mubuku, Rwenzori Mountains, Uganda	Oct-10	0.34	30.04	1608	52.3	16.5	-	0.3
	4	River Ishasha, Uganda	Oct-10	-0.62	29.66	934	55.1	22.2	7.8	0.6
	5	River Ntungwe, Uganda	Oct-10	-0.57	29.72	938	141.6	23.8	7.9	0.9
	6	Mpanga River, Uganda	Oct-10	0.08	30.32	1201	201.9	25.4	9.1	-
	7	Lake Mahoma, Rwenzori Mountains, Uganda	Oct-10	0.35	29.97	2880	23.9	15.2	-	0.5
	8	River Nkusi, Uganda	Nov-10	1.13	30.99	1029	107.8	23.0	7.8	-
	9	River Kagera, Uganda	Oct-10	-0.94	31.76	1139	141.2	25.2	7.3	0.7
	10	River Kafu, Uganda	Nov-10	1.55	32.04	1045	107.6	26.5	7.8	-
	11	River Semliki, Uganda-Congo	Oct-10	1.03	30.53	653	479.0	27.2	8.6	1.2
	12	Kazinga Channel, Uganda	Oct-10	-0.19	29.91	918	199.2	27.1	8.5	0.5
	13	White Nile, Khartoum, Sudan	Dec-10	15.61	32.49	391	183.3	22.6	10.2	0.8
	14	Albert Nile, Uganda	Nov-10	2.29	31.37	633	121.3	30.3	8.6	1.2
	15	Victoria Nile Delta, Uganda	Nov-10	2.25	31.38	628	133.3	27.6	8.5	1.0
	16	Lake Albert (north), Uganda-Congo	Nov-10	2.22	31.33	631	121.7	29.1	9.0	-
	17	Murchison Falls, Victoria Nile, Uganda	Nov-10	2.27	31.68	635	120.5	29.4	9.2	-
	18	Victoria Nile, Bujagali Falls, Uganda	Nov-10	0.48	33.16	1112	100.8	27.3	10.2	1.1
	19	Outflow from Lake Victoria (Jinja), Uganda	Nov-10	0.42	33.20	1135	104.8	26.6	10.6	1.3
	20	Lake Albert (south), Uganda-Congo	Oct-10	1.04	30.53	618	575.0	28.8	9.3	1.4
Blue Nile and Atbara River	25	Ribb River, east Lake Tana, Ethiopia	Oct-10	11.99	37.71	1799	175.3	25.1	6.9	0.3
	26	Gish Abbay, Ethiopia	Oct-10	10.97	37.20	2721	80.3	20.1	5.9	-
	27	Gilgel Abay, Ethiopia	Oct-10	11.36	37.03	1875	62.8	22.5	6.2	-
	28	Chimba, Gilgel Abay, Ethiopia	Oct-10	11.71	37.17	1809	106.4	20.9	6.3	0.3
	29	Alata River, Ethiopia	Oct-10	11.50	37.59	1617	129.2	23.2	7.5	-
	30	Gumara River, east Lake Tana, Ethiopia	Oct-10	11.84	37.64	1795	123.9	23.5	6.5	-
	31	River Zerma, Ethiopia	Oct-10	13.34	37.88	1220	186.0	23.2	6.8	0.2
	32	River Tekezé, Ethiopia	Oct-10	13.73	38.19	900	363.0	28.4	7.5	0.4
	33	River Megetch, north Lake Tana, Ethiopia	Oct-10	12.49	37.45	1882	435.0	26.6	8.3	0.2
	34	Blue Nile, Khartoum, Sudan	Dec-10	15.61	32.53	409	197.8	26.7	11.7	0.4
	35	Tis Issat Falls, Blue Nile, Ethiopia	Oct-10	11.49	37.59	1642	160.6	23.9	7.4	0.3
	36	River Atbara, Atbara, Sudan	Dec-10	17.68	33.98	353	342.0	21.7	10.4	0.3
	37	Blue Nile, Bahir Dar, Ethiopia	Oct-10	11.61	37.41	1804	141.9	25.2	6.7	-
Main Nile	38	Main Nile (Lake Nasser), Wadi Halfa, Sudan	Dec-10	21.81	31.32	170	236.9	19.3	10.6	-
	39	Main Nile, Dongola, Sudan	Dec-10	19.18	30.49	223	221.6	18.8	10.4	0.3
	40	Main Nile, Karima, Sudan	Dec-10	18.50	31.81	258	223.4	22.2	10.2	-
	41	Main Nile, Atbara, Sudan	Dec-10	17.66	33.97	357	196.6	21.9	10.0	0.6
	42	Main Nile, Khartoum, Sudan	Dec-10	15.65	32.51	409	184.5	24.0	10.1	-
	43	Main Nile, Aswan, Egypt	Dec-10	24.08	32.89	77	277.8	21.8	9.4	-
	44	Bahr Yusuf, Faiyum, Egypt	Nov-10	29.31	30.85	8	675.0	22.5	9.3	-
	45	Main Nile, Cairo, Egypt	Nov-10	30.04	31.23	4	1423.0	22.8	9.8	0.7
	46	Main Nile, Luxor, Egypt	Dec-10	25.70	32.38	82	342.0	23.1	10.1	0.6
	47	Main Nile (Lake Nasser), Aswan, Egypt	Dec-10	23.97	32.90	152	279.1	22.0	9.9	0.4
	48	Lake Qarun, Faiyum (south-east), Egypt	Nov-10	29.47	30.77	-51	35300.0	22.3	9.4	3.7
	49	Lake Qarun, Faiyum (south-west), Egypt	Nov-10	29.47	30.77	-51	46100.0	22.3	9.2	-

Table 6.1 (cont.)

			Dry season							
	Site No.	Sample site name	Date (month-year)	Latitude (decimal degrees)	Longitude (decimal degrees)	Altitude (m.a.s.l.)	Conductivity (µS/cm)	Water temperature (°C)	pH	Cation ratio $Na^{+}+K^{+}/Ca^{2+}+Mg^{2+}$
White Nile	11	River Semliki, Uganda-Congo	Jun-09	1.06	30.23	636	607.0	28.0	8.3	1.3
	12	Kazinga Channel, Uganda	Jun-09	-0.18	29.91	917	-	-	9.3	0.6
	13	White Nile, Khartoum, Sudan	May-11	15.61	32.49	391	283.0	-	8.3	1.3
	14	Albert Nile, Uganda	May-09	2.39	31.48	614	335.0	30.0	9.2	1.4
	15	Victoria Nile Delta, Uganda	May-09	2.24	31.39	618	144.2	28.8	6.7	1.3
	16	Lake Albert (north), Uganda-Congo	May-09	2.26	31.35	614	110.5	29.6	7.0	-
	17	Murchison Falls, Victoria Nile, Uganda	May-09	2.27	31.67	623	-	-	7.2	-
	18	Victoria Nile, Bujagali Falls, Uganda	Jun-09	0.46	33.18	1126	113.9	27.8	7.4	1.2
	19	Outflow from Lake Victoria (Jinja), Uganda	Jun-09	0.42	33.20	1137	118.0	26.8	7.4	1.1
	20	Lake Albert (south), Uganda-Congo	Jun-09	1.03	30.51	620	613.0	28.8	8.6	1.5
	21	Lake Edward, Uganda	Jun-09	-0.21	29.89	911	-	-	9.1	-
	22	Ssese Islands, Lake Victoria, Uganda	Jun-09	-0.26	32.04	1133	-	-	7.3	-
	23	Lake Victoria, Entebbe, Uganda	Jun-09	0.06	32.48	1134	113.6	27.9	7.5	-
	24	Paraa, Victoria Nile, Uganda	May-09	2.29	31.57	622	-	-	7.2	-
Blue Nile and Atbara River	25	Ribb River, east Lake Tana, Ethiopia	May-09	11.99	37.71	1794	475.0	25.7	8.8	0.4
	28	Chimba, Gilgel Abay, Ethiopia	May-09	11.71	37.17	1808	148.3	22.5	7.2	0.2
	29	Alata River, Ethiopia	May-09	11.49	37.59	1647	-	-	-	-
	30	Gumara River, east Lake Tana, Ethiopia	May-09	11.84	37.64	1795	283.0	26.8	9.0	-
	34	Blue Nile, Khartoum, Sudan	May-11	15.61	32.53	409	339.0	-	8.1	0.3
	35	Tis Issat Falls, Blue Nile, Ethiopia	May-09	11.49	37.59	1642	-	-	-	0.3
	36	River Atbara, Atbara, Sudan	Apr-11	17.68	33.98	353	325.0	-	8.3	0.4
	37	Blue Nile, Bahir Dar, Ethiopia	May-09	11.61	37.41	1788	157.7	25.7	7.9	-
Main Nile	38	Main Nile (Lake Nasser), Wadi Halfa, Sudan	Apr-11	22.02	31.34	178	228.0	-	8.4	-
	39	Main Nile, Dongola, Sudan	Apr-11	19.18	30.49	223	215.0	-	8.8	0.6
	40	Main Nile, Karima, Sudan	Apr-11	18.50	31.81	258	221.0	-	8.3	-
	41	Main Nile, Atbara, Sudan	Apr-11	17.66	33.97	357	287.0	-	8.1	1.2
	42	Main Nile, Khartoum, Sudan	May-11	15.66	32.51	377	291.0	-	8.2	-
	43	Main Nile, Aswan, Egypt	Apr-11	24.09	32.89	81	288.0	-	7.9	-
	44	Bahr Yusuf, Faiyum, Egypt	Apr-11	29.31	30.85	20	1000.0	-	8.1	-
	45	Main Nile, Cairo, Egypt	Apr-11	30.04	31.23	8	300.0	-	8.7	1.5
	46	Main Nile, Luxor, Egypt	Apr-11	25.70	32.64	67	291.0	-	7.7	0.6
	47	Main Nile (Lake Nasser), Aswan, Egypt	Apr-11	23.97	32.90	152	262.0	-	7.4	0.4
	48	Lake Qarun, Faiyum (south-east), Egypt	Apr-11	29.47	30.78	-44	44800.0	-	7.6	3.7
	50	Lake Qarun, Faiyum (west), Egypt	Apr-11	29.45	30.40	-46	50800.0	-	8.3	-

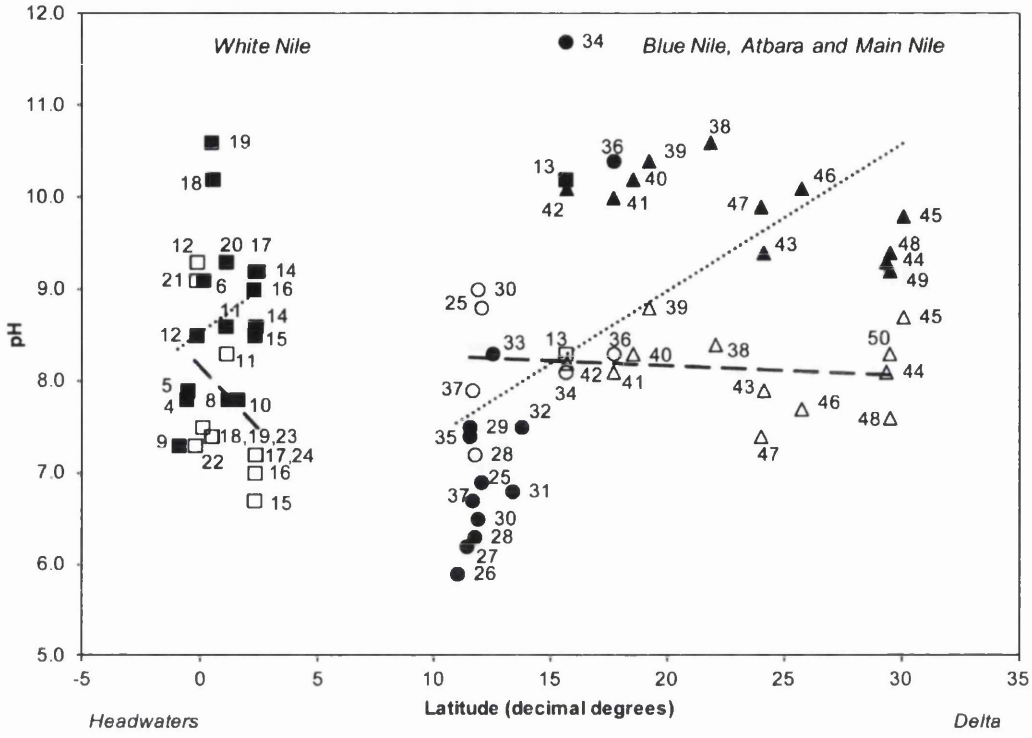

Figure 6.1: pH versus latitude. Wet season (closed symbols) and dry season (open symbols) samples are plotted for the White Nile (squares), Blue Nile (circles) and Main Nile (triangles). Seasonal trends are identified with individual regression lines for the White Nile (left-hand side) and the Blue Nile, Atbara and Main Nile (right-hand side) during the wet season (dotted line) and dry season (dashed line) to account for varying geology. White Nile wet season (dotted line; pH = 0.19·Latitude + 8.52, R^2 = 0.055, p = 0.423) and dry season (dashed line; pH = -0.28·Latitude + 8.16, R^2 = 0.110, p = 0.360). Blue Nile, Atbara and Main Nile wet season (dotted line; pH = 0.16·Latitude + 5.78, R^2 = 0.397, p = 0.025) and dry season (dashed line; pH = -0.01·Latitude + 8.37, R^2 = 0.021, p = 0.468). Sample site 13 (White Nile, Khartoum) has been omitted from the White Nile regression as its composition suggests that it may have been influenced by surface water, groundwater or sediments ultimately derived from the Blue Nile, although there are too few data to draw any firm conclusions at this point. For sample numbers, see Table 6.1.

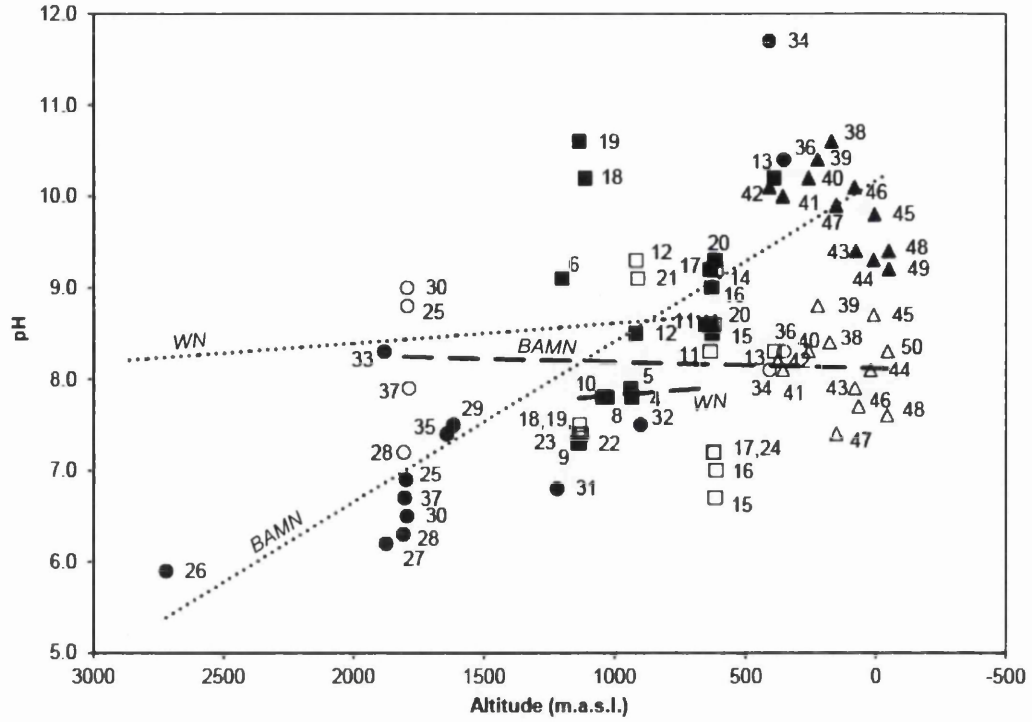

Figure 6.2: pH versus altitude. Wet season (closed symbols) and dry season (open symbols) samples are plotted for the White Nile (squares), Blue Nile (circles) and Main Nile (triangles). Seasonal trends are identified by individual regression lines for the White Nile (WN) and the Blue Nile, Atbara and Main Nile (BAMN) during the wet season (dotted line) and the dry season (dashed line) to account for varying geology. White Nile wet season (dotted line; $pH = 8.83 \cdot exp^{-3E-05 \cdot Altitude}$, $R^2 = 0.003$, $p = 0.496$) and dry season (dashed line; $pH = 7E-05 \cdot Altitude + 8.12$, $R^2 = 0.010$, $p = 0.487$). Blue Nile, Atbara and Main Nile wet season (dotted line; $pH = -1.8E-03 \cdot Altitude + 10.17$, $R^2 = 0.759$, $p < 0.001$) and dry season (dashed line; $pH = 2E-04 \cdot Altitude + 8.05$, $R^2 = 0.004$, $p = 0.495$). Sample site 13 (White Nile, Khartoum) has been omitted from the White Nile regression as its composition suggests that it may have been influenced by surface water, groundwater or sediments ultimately derived from the Blue Nile, although there are too few data to draw any firm conclusions at this point. For sample numbers, see Table 6.1.

6: Modern surface water results

The electrical conductance of the sampled waters ranged from 17.2 to 613 µS/cm in the White Nile, 62.8 to 475 µS/cm in the Blue Nile and Atbara, and 184.5 to 50,800 µS/cm along the Main Nile (Figures 6.3 and 6.4). Typically, rainwater has an EC of ~15 µS/cm and drinking water is lower than 700 µS/cm, whereas >45,000 µS/cm is considered seawater (Rhoades et al., 1992). Seasonal variations were small in all sub-basins, however, electrical conductivity was generally higher in dry-season samples (Figures 6.3 and 6.4).

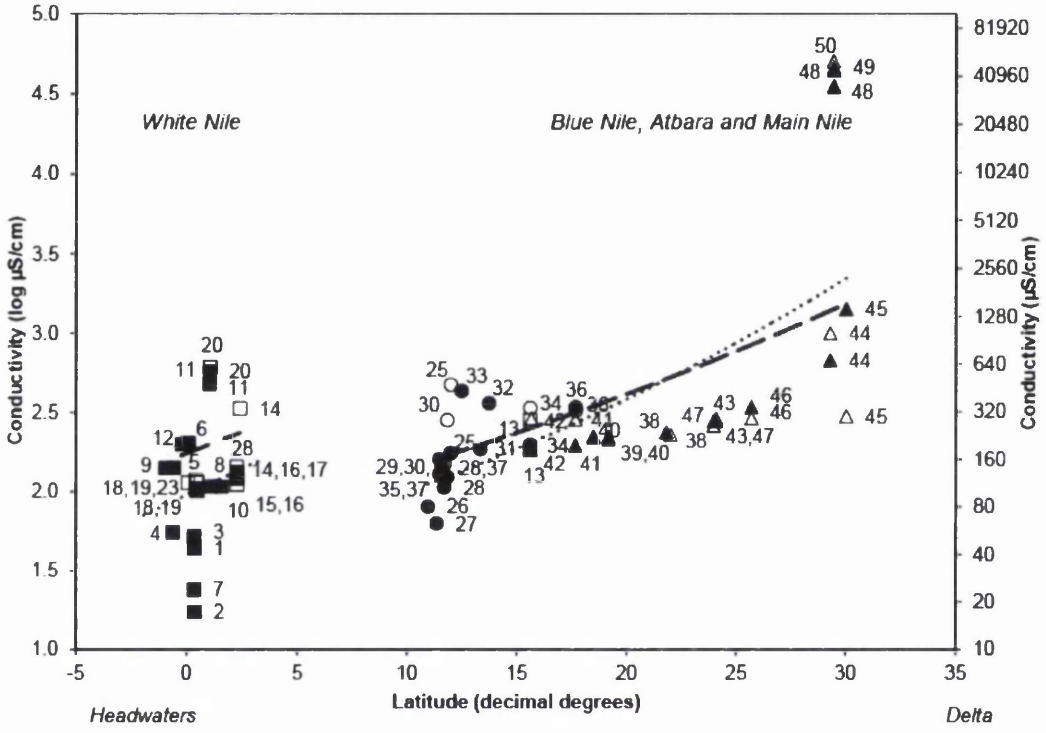

Figure 6.3: Conductivity versus latitude. Wet season (closed symbols) and dry season (open symbols) samples are plotted for the White Nile (squares), Blue Nile (circles) and Main Nile (triangles). Seasonal trends are identified with individual regression lines for the White Nile (left-hand side) and the Blue Nile, Atbara and Main Nile (right-hand side) during the wet season (dotted line) and dry season (dashed line) to account for varying geology. White Nile wet season (dotted line; Conductivity (log) = 0.07·Latitude + 1.98, R^2 = 0.033, p = 0.478) and dry season (dashed line; Conductivity (log) = 0.05·Latitude + 2.24, R^2 = 0.023, p = 0.447). Blue Nile, Atbara and Main Nile wet season (dotted line; Conductivity (log) = $1.54 \cdot \exp^{-0.03 \cdot Latitude}$, R^2 = 0.6104, p < 0.001) and dry season (dashed line; Conductivity (log) = $1.77 \cdot \exp^{-0.02 \cdot Latitude}$, R^2 = 0.352, p = 0.076). Sample site 13 (White Nile, Khartoum) has been omitted from the White Nile regression as its composition suggests that it may have been influenced by surface water, groundwater or sediments ultimately derived from the Blue Nile, although there are too few data to draw any firm conclusions at this point. For sample numbers, see Table 6.1.

Electrical conductivity was greatest towards the Delta in the Main Nile, particularly in the Nile-fed Lake Qarun in the Faiyum Depression [48-50] (Figures 6.3 and 6.4). All major sub-basins exhibited an increase in electrical conductivity northwards and with decreasing altitude (Figures 6.3 and 6.4).

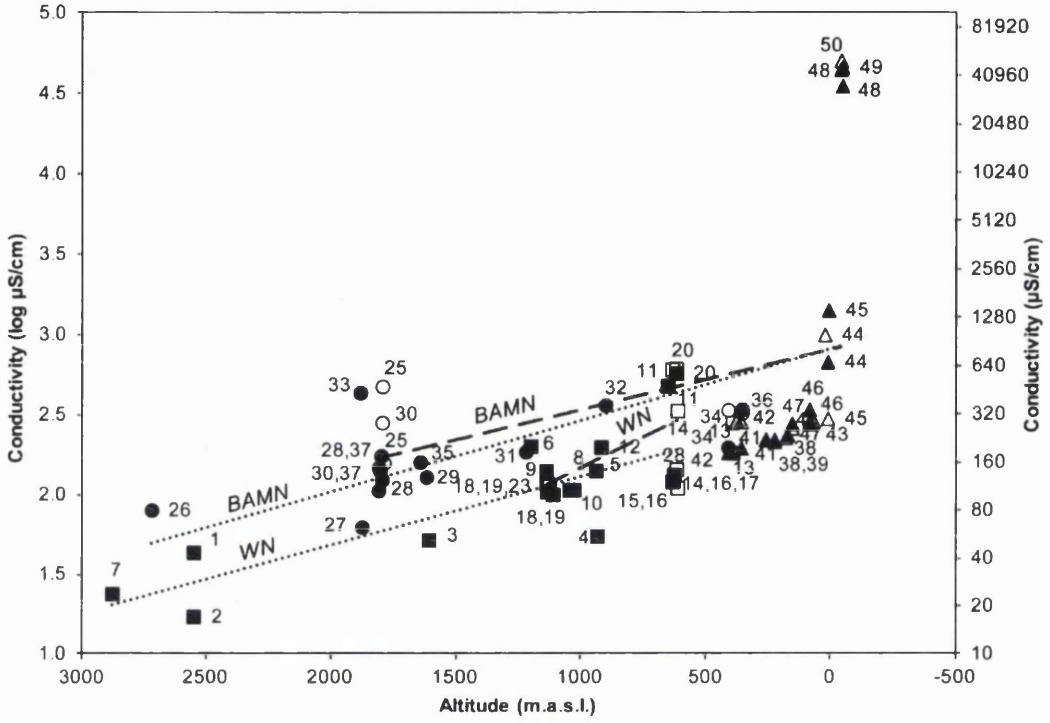

Figure 6.4: Conductivity versus altitude. Wet season (closed symbols) and dry season (open symbols) samples are plotted for the White Nile (squares), Blue Nile (circles) and Main Nile (triangles). Seasonal trends are identified with individual regression lines for the White Nile (WN) and the Blue Nile, Atbara and Main Nile (BAMN) during the wet season (dotted line) and dry season (dashed line) to account for varying geology. White Nile wet season (dotted line; Conductivity (log) = -4E-04·Altitude + 2.54, R^2 = 0.637, p = 0.002) and dry season (dashed line; Conductivity (log) = 8E-04·Altitude + 2.93, R^2 = 0.367, p = 0.186). Blue Nile, Atbara and Main Nile wet season (dotted line; Conductivity (log) = -4E-04·Altitude + 2.91, R^2 = 0.304, p = 0.070) and dry season (dashed line; Conductivity (log) = 4E-04·Altitude + 2.90, R^2 = 0.127, p = 0.308). Sample site 13 (White Nile, Khartoum) has been omitted from the White Nile regression as its composition suggests that it may have been influenced by surface water, groundwater or sediments ultimately derived from the Blue Nile, although there are too few data to draw any firm conclusions at this point. For sample numbers, see Table 6.1.

6.3 Chemical characteristics: major cations

A full list of the major ions measured in Nile waters can be found in Appendix I. Presented here is a cation ratio between alkaline and alkaline-earth metals (Na^+ + K^+ / Ca^{2+} + Mg^{2+}), which provides a measure of the degree of evaporative enrichment (Gasse et al., 1995; Gasse, 2002). Mg and Ca carbonate minerals are usually the first to precipitate. Hence, as evaporative concentration proceeds, the ratio of Na + K to Ca + Mg increases (Eugster and Hardie, 1978). Cation concentrations are expressed in meq l^{-1}.

The close relationship between the cation ratio and EC reflects an increase in dissolved ions with an increase in precipitation of Ca-Mg carbonates relative to Na carbonates (Figure 6.5). White Nile waters were relatively enriched in Na^+ and K^+, exhibiting cation-ratio values of 0.3 to 1.5 (Figures 6.6 and 6.7), whereas, the Blue Nile and Atbara values were much lower (0.2 to 0.4) (Figures 6.6 and 6.7). The Main Nile cation-ratio values are also high (0.3 to 3.7) relative to dilute waters draining basaltic terrain, particularly in the saline, closed Lake Qarun [48-50]. The trend lines for the major sub-basins show that the relative proportion of Na^+ + K^+ increases northwards and with decreasing altitude (Figures 6.6 and 6.7), indicating a downstream enrichment of alkali metals. Curvilinear regressions best describe waters originating from the Ethiopian Highlands and the Main Nile, emphasising the rapid enrichment of Na^+ + K^+ in the lower reaches of the Nile. Major cation concentrations were greatest during the dry season in all major sub-basins (Figures 6.5-6.7).

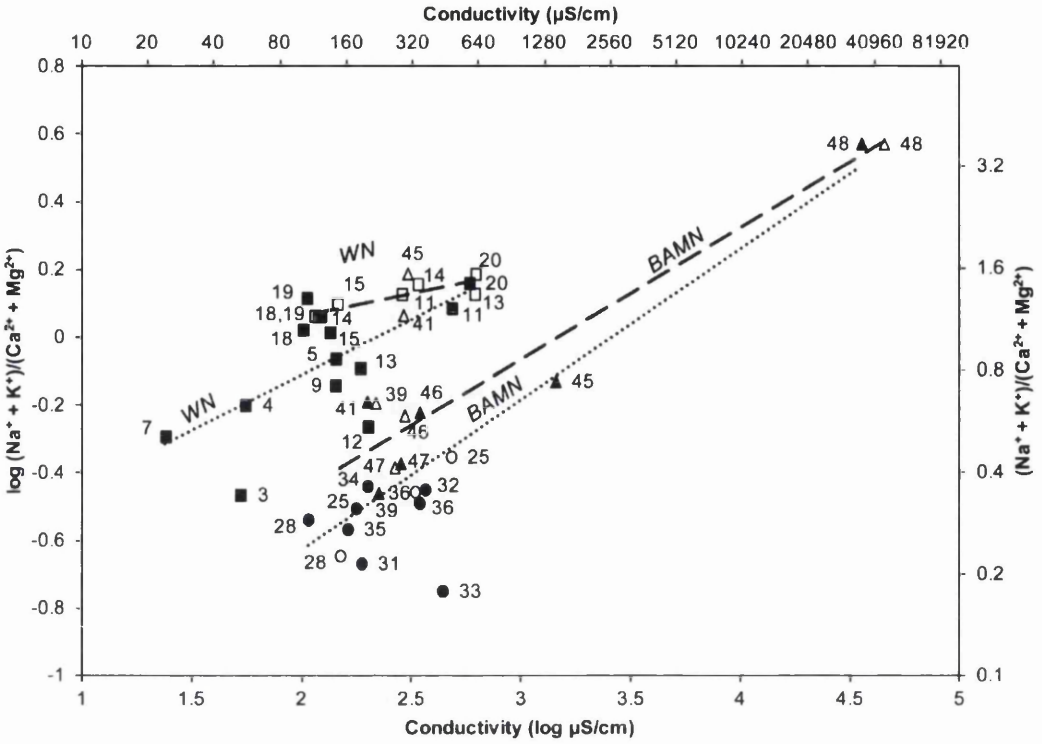

Figure 6.5: Cation ratio ($Na^+ + K^+ / Ca^{2+} + Mg^{2+}$) versus conductivity. Wet season (closed symbols) and dry season (open symbols) samples are plotted for the White Nile (squares), Blue Nile (circles) and Main Nile (triangles). Seasonal trends are identified with individual regression lines for the White Nile and the Blue Nile, Atbara and Main Nile during the wet season (dotted line) and dry season (dashed line) to account for varying geology. White Nile wet season (dotted line; Cation ratio (log) = 0.33·Conductivity - 0.76, R^2 = 0.428, p = 0.165) and dry season (dashed line; Cation ratio (log) = 0.13·Conductivity - 0.20, R^2 = 0.778, p = 0.070). Blue Nile, Atbara and Main Nile wet season (dotted line; Cation ratio (log) = 0.44·Conductivity - 1.52, R^2 = 0.743, p = 0.002) and dry season (dashed line; Cation ratio (log) = 0.39·Conductivity - 1.22, R^2 = 0.554, p = 0.096). Sample site 13 (White Nile, Khartoum) has been omitted from the White Nile regression as its composition suggests that it may have been influenced by surface water, groundwater or sediments ultimately derived from the Blue Nile, although there are too few data to draw any firm conclusions at this point. For sample numbers, see Table 6.1.

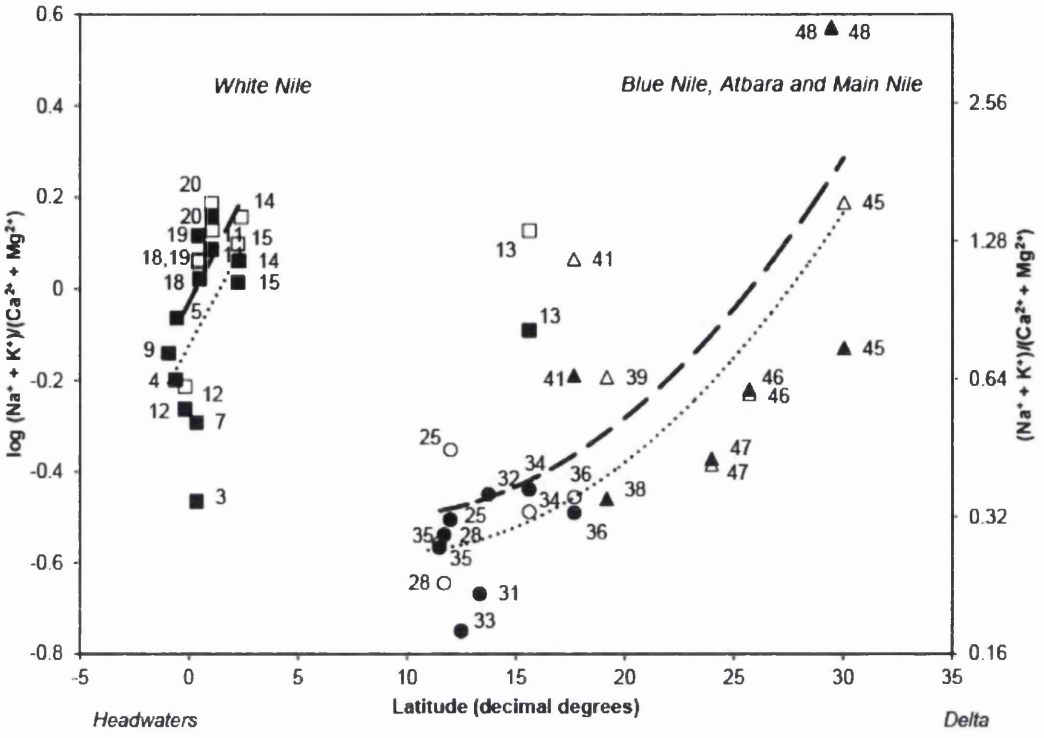

Figure 6.6: Cation ratio ($Na^+ + K^+ / Ca^{2+} + Mg^{2+}$) versus latitude. Wet season (closed symbols) and dry season (open symbols) samples are plotted for the White Nile (squares), Blue Nile (circles) and Main Nile (triangles). Seasonal trends are identified with individual regression lines for the White Nile (left-hand side) and the Blue Nile, Atbara and Main Nile (right-hand side) during the wet season (dotted line) and dry season (dashed line) to account for varying geology. White Nile wet season (dotted line; Cation ratio (log) = 0.09·Latitude - 0.12, R^2 = 0.225, p = 0.241) and dry season (dashed line; Cation ratio (log) = 0.09·Latitude - 0.03, R^2 = 0.447, p = 0.157). Blue Nile, Atbara and Main Nile wet season (dotted line; Cation ratio (log) = 1.7E-03·Latitude^2 - 0.03·Latitude - 0.43, R^2 = 0.653, p = 0.006) and dry season (dashed line; Cation ratio (log) = 1.8E-03·Latitude^2 - 0.03·Latitude - 0.35, R^2 = 0.622, p = 0.021). Sample site 13 (White Nile, Khartoum) has been omitted from the White Nile regression as its composition suggests that it may have been influenced by either surface water, groundwater or sediments ultimately derived from the Blue Nile, although there are too few data to draw any firm conclusions at this point. For sample numbers, see Table 6.1.

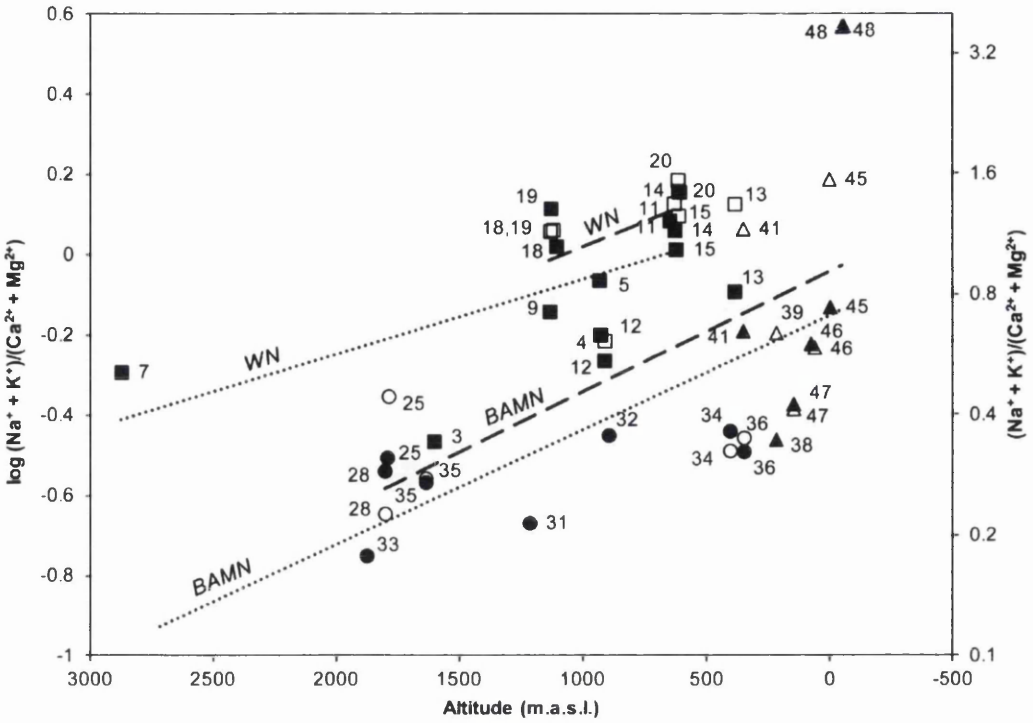

Figure 6.7: Cation ratio ($Na^+ + K^+ / Ca^{2+} + Mg^{2+}$) versus altitude. Wet season (closed symbols) and dry season (open symbols) samples are plotted for the White Nile (squares), Blue Nile (circles) and Main Nile (triangles). Seasonal trends are identified with individual regression lines for the White Nile (WN) and the Blue Nile, Atbara and Main Nile (BAMN) during the wet season (dotted line) and dry season (dashed line) to account for varying geology. White Nile wet season (dotted line; Cation ratio (log) = -2E-04·Altitude + 0.12, R^2 = 0.374, p = 0.116) and dry season (dashed line; Cation ratio (log) = -3E-04·Altitude + 0.27, R^2 = 0.216, p = 0.3201). Blue Nile, Atbara and Main Nile wet season (dotted line; Cation ratio (log) = -3E-04·Altitude - 0.04, R^2 = 0.375, p = 0.060) and dry season (dashed line; Cation ratio (log) = -3E-04·Altitude - 0.15, R^2 = 0.434, p = 0.128). Sample site 13 (White Nile, Khartoum) has been omitted from the White Nile regression as its composition suggests that it may have been influenced by surface water, groundwater or sediments ultimately derived from the Blue Nile, although there are too few data to draw any firm conclusions at this point. For sample numbers, see Table 6.1.

6.4 Isotope characteristics: $\delta^{18}O$ and $\delta^{2}H$

All $\delta^{2}H$ and $\delta^{18}O$ values for surface water samples (Table 6.2) are plotted for the Nile drainage as a whole (Figure 6.8a), and individually for the White (Figure 6.8b), Blue (Figure 6.8c) and Main (Figure 6.8d) Niles, with reference to the African Meteoric Water Line (AMWL) (solid line). The AMWL ($\delta^{2}H = 7.4 \cdot \delta^{18}O + 10.1$) represents the isotopic values of precipitation in the interior of East and Central Africa, and differs slightly from the GMWL (Cohen et al., 1997). The validity of using the AMWL is confirmed by the fact that small rivers draining into the main branches of the River Nile plot on or close to the AMWL. Sites deviating from the AMWL form local evaporative lines (LELs) which are shown for both wet- and dry-season conditions (Figure 6.8, Table 6.3).

$\delta^{18}O$ values in the Nile Basin ranged from -4.7 to +8.0‰ in the wet season and +0.6 to +8.8‰ in the dry season (Table 6.3). Dry-season samples (average $\delta^{18}O = +3.9 \pm 2.2$‰; $n = 34$) were significantly more enriched in ^{18}O than wet-season samples (average $\delta^{18}O = +0.8 \pm 2.9$‰; $n = 45$) (paired *t*-test, $p = 0.001$) (Figures 6.8a, 6.9-6.10). However, there was no significant difference between the slopes of the LELs in different seasons in any of the individual sub-basins (Figure 6.8b-d). Each major sub-basin exhibited distinct $\delta^{2}H$ and $\delta^{18}O$ values, especially during the wet season, with both $\delta^{2}H$ and $\delta^{18}O$ values increasing northwards and downstream (Figures 6.8 and 6.9; Table 6.3). The $\delta^{18}O$ values for the Main Nile were significantly higher than those of either the White Nile (separate variance *t*-test, $p < 0.01$) or the Blue Nile (separate variance *t*-test, $p < 0.0001$) during the wet season, but no statistically significant differences in $\delta^{18}O$ values between basins were found for the dry season (Figure 6.8; Table 6.3). Significant linear relationships were observed during the wet season between $\delta^{18}O$ and latitude (Figure 6.9; $r_s = 0.465$, $p < 0.001$), and $\delta^{18}O$ and altitude (Figure 6.10; $r_s = -0.724$, $p < 0.001$), although no significant trends were found in the dry season. Isotopically lower surface-water samples from high-altitude, headwater sites (Figures 6.9 and 6.10) in the White Nile (Figure 6.8b) and Blue Nile catchments (Figure 6.8c) displayed large d-excess values compared with the GMWL (+10‰) (Figure 6.11).

Table 6.2: Sample site locations and their corresponding isotope data.

							Wet season						
	Site No.	Sample site name	Date (month-year)	Latitude (decimal degrees)	Longitude (decimal degrees)	Altitude (m.a.s.l.)	$\delta^{18}O$ (‰) VSMOW	$\delta^{2}H$ (‰) VSMOW	d-excess (‰)	$\delta^{30}Si$(‰) NBS-28	$\delta^{29}Si$(‰) NBS-28	DSi conc. (mg/L)	(µM)
White Nile	1	Bujuku River, Rwenzori Mountains, Uganda	Oct-10	0.36	29.97	2552	-4.7	-18.4	+19.6	-	-	-	-
	2	River Mubuku, Rwenzori Mountains, Uganda	Oct-10	0.36	29.97	2552	-4.6	-17.0	+19.6	-	-	-	-
	3	River Mubuku, Rwenzori Mountains, Uganda	Oct-10	0.34	30.04	1608	-3.9	-11.4	+19.6	+0.99	+0.46	5.7	203
	4	River Ishasha, Uganda	Oct-10	-0.62	29.66	934	-2.4	-2.8	+16.3	+0.98	+0.60	5.6	199
	5	River Ntungwe, Uganda	Oct-10	-0.57	29.72	938	-1.8	-0.6	+13.8	+1.73	+0.87	12.0	427
	6	Mpanga River, Uganda	Oct-10	0.08	30.32	1201	-1.5	+1.3	+13.2	-	-	-	-
	7	Lake Mahoma, Rwenzori Mountains, Uganda	Oct-10	0.35	29.97	2880	-1.5	+0.5	+12.4	+0.48	+0.08	1.1	39
	8	River Nkusi, Uganda	Nov-10	1.13	30.99	1029	-1.3	+2.7	+12.8	-	-	-	-
	9	River Kagera, Uganda	Oct-10	-0.94	31.76	1139	-1.0	-0.1	+7.7	+2.14	+1.10	7.1	253
	10	River Kafu, Uganda	Nov-10	1.55	32.04	1045	-0.1	+7.7	+8.7	-	-	-	-
	11	River Semliki, Uganda-Congo	Oct-10	1.03	30.53	653	+0.2	+10.6	+9.2	+1.57	+0.85	8.9	317
	12	Kazinga Channel, Uganda	Oct-10	-0.19	29.91	918	+1.3	+15.5	+4.8	+1.74	+0.85	10.2	363
	13	White Nile, Khartoum, Sudan	Dec-10	15.61	32.49	391	+2.2	+22.1	+4.4	+2.36	+1.21	6.0	214
	14	Albert Nile, Uganda	Nov-10	2.29	31.37	633	+3.3	+25.3	-0.9	+2.28	+1.20	2.9	103
	15	Victoria Nile Delta, Uganda	Nov-10	2.25	31.38	628	+3.3	+24.6	-2.0	+1.88	+1.12	3.3	117
	16	Lake Albert (north), Uganda-Congo	Nov-10	2.22	31.33	631	+3.4	+25.3	-2.1	-	-	-	-
	17	Murchison Falls, Victoria Nile, Uganda	Nov-10	2.27	31.68	635	+3.5	+26.3	-1.6	-	-	-	-
	18	Victoria Nile, Bujagali Falls, Uganda	Nov-10	0.48	33.16	1112	+3.5	+26.1	-2.3	+2.02	+0.97	1.5	53
	19	Outflow from Lake Victoria (Jinja), Uganda	Nov-10	0.42	33.20	1135	+3.7	+25.9	-3.5	+2.36	+1.05	1.1	39
	20	Lake Albert (south), Uganda-Congo	Oct-10	1.04	30.53	618	+4.1	+31.7	-1.0	+2.13	+0.93	2.8	100
Blue Nile and Atbara River	25	Ribb River, east Lake Tana, Ethiopia	Oct-10	11.99	37.71	1799	-2.4	-4.9	+13.9	+1.82	+1.00	8.8	313
	26	Gish Abbay, Ethiopia	Oct-10	10.97	37.20	2721	-2.3	-0.6	+18.2	-	-	-	-
	27	Gilgel Abay, Ethiopia	Oct-10	11.36	37.03	1875	-2.2	+0.2	+17.5	-	-	-	-
	28	Chimba, Gilgel Abay, Ethiopia	Oct-10	11.71	37.17	1809	-1.9	+0.0	+14.9	+1.53	+0.81	7.4	263
	29	Alata River, Ethiopia	Oct-10	11.50	37.59	1617	-1.6	+0.1	+12.9	-	-	-	-
	30	Gumara River, east Lake Tana, Ethiopia	Oct-10	11.84	37.64	1795	-1.5	+2.3	+14.5	-	-	-	-
	31	River Zerma, Ethiopia	Oct-10	13.34	37.88	1220	-1.5	+4.3	+16.3	+1.22	+0.68	18.9	673
	32	River Tekezé, Ethiopia	Oct-10	13.73	38.19	900	-1.4	-0.0	+11.3	+1.89	+1.05	9.9	352
	33	River Megetch, north Lake Tana, Ethiopia	Oct-10	12.49	37.45	1882	-0.6	+5.9	+10.7	+1.66	+0.85	16.0	570
	34	Blue Nile, Khartoum, Sudan	Dec-10	15.61	32.53	409	+1.1	+16.3	+7.4	+2.50	+1.31	7.3	260
	35	Tis Issat Falls, Blue Nile, Ethiopia	Oct-10	11.49	37.59	1642	+1.1	+16.5	+7.4	+2.23	+1.06	4.9	174
	36	River Atbara, Atbara, Sudan	Dec-10	17.68	33.98	353	+2.5	+20.8	+1.0	+3.23	+1.78	8.8	313
	37	Blue Nile, Bahir Dar, Ethiopia	Oct-10	11.61	37.41	1804	+3.0	+26.7	+2.6	-	-	-	-
Main Nile	38	Main Nile (Lake Nasser), Wadi Halfa, Sudan	Dec-10	21.81	31.32	170	-0.0	+7.5	+7.8	-	-	-	-
	39	Main Nile, Dongola, Sudan	Dec-10	19.18	30.49	223	+0.2	+10.0	+8.6	+2.12	+1.06	6.3	224
	40	Main Nile, Karima, Sudan	Dec-10	18.50	31.81	258	+0.1	+10.0	+8.9	-	-	-	-
	41	Main Nile, Atbara, Sudan	Dec-10	17.66	33.97	357	+2.1	+20.7	+4.2	+2.62	+1.33	5.8	207
	42	Main Nile, Khartoum, Sudan	Dec-10	15.65	32.51	409	+2.1	+22.2	+5.3	-	-	-	-
	43	Main Nile, Aswan, Egypt	Dec-10	24.08	32.89	77	+3.4	+24.8	-2.1	-	-	-	-
	44	Bahr Yusuf, Faiyum, Egypt	Nov-10	29.31	30.85	8	+3.4	+25.6	-1.6	-	-	-	-
	45	Main Nile, Cairo, Egypt	Nov-10	30.04	31.23	4	+3.6	+26.2	-2.7	-	-	0.9	32
	46	Main Nile, Luxor, Egypt	Dec-10	25.70	32.38	82	+3.5	+26.7	-1.6	+3.45	+1.89	2.9	103
	47	Main Nile (Lake Nasser), Aswan, Egypt	Dec-10	23.97	32.90	152	+3.7	+27.0	-2.3	+3.45	+1.85	3.4	121
	48	Lake Qarun, Faiyum (south-east), Egypt	Nov-10	29.47	30.77	-51	+6.7	+41.7	-11.7	-	-	-	-
	49	Lake Qarun, Faiyum (south-west), Egypt	Nov-10	29.47	30.77	-51	+8.0	+47.7	-16.5	-	-	-	-

Table 6.2 (cont.)

							Dry season						
	Site No.	Sample site name	Date (month-year)	Latitude (decimal degrees)	Longitude (decimal degrees)	Altitude (m.a.s.l.)	$\delta^{18}O$ (‰) VSMOW	$\delta^{2}H$ (‰) VSMOW	d-excess (‰)	$\delta^{30}Si$(‰) NBS-28	$\delta^{29}Si$(‰) NBS-28	DSi conc. (mg/L)	DSi conc. (µM)
White Nile	11	River Semliki, Uganda-Congo	Jun-09	1.06	30.23	636	+1.4	+19.0	-150.3	+1.74	+0.91	6.9	246
	12	Kazinga Channel, Uganda	Jun-09	-0.18	29.91	917	+1.9	+19.2	-151.4	+1.54	+0.74	10.7	381
	13	White Nile, Khartoum, Sudan	May-11	15.61	32.49	391	+7.0	+47.5	-373.0	+1.70	+0.81	3.8	135
	14	Albert Nile, Uganda	May-09	2.39	31.48	614	+4.5	+33.9	-267.0	+2.51	+1.25	1.2	43
	15	Victoria Nile Delta, Uganda	May-09	2.24	31.39	618	+4.0	+29.2	-229.5	+2.16	+1.27	2.1	75
	16	Lake Albert (north), Uganda-Congo	May-09	2.26	31.35	614	+4.0	+29.6	-232.8	-	-	-	-
	17	Murchison Falls, Victoria Nile, Uganda	May-09	2.27	31.67	623	+4.0	+29.3	-230.7	-	-	-	-
	18	Victoria Nile, Bujagali Falls, Uganda	Jun-09	0.46	33.18	1126	+3.6	+29.0	-228.5	-	-	-	-
	19	Outflow from Lake Victoria (Jinja), Uganda	Jun-09	0.42	33.20	1137	+3.5	+29.1	-229.5	-	-	0.2	7
	20	Lake Albert (south), Uganda-Congo	Jun-09	1.03	30.51	620	+4.7	+34.8	-273.5	+2.66	+1.18	1.2	43
	21	Lake Edward, Uganda	Jun-09	-0.21	29.89	911	+1.9	+19.3	-152.8	-	-	-	-
	22	Ssese Islands, Lake Victoria, Uganda	Jun-09	-0.26	32.04	1133	+3.1	+26.0	-205.1	-	-	-	-
	23	Lake Victoria, Entebbe, Uganda	Jun-09	0.06	32.48	1134	+3.1	+26.8	-211.5	-	-	-	-
	24	Paraa, Victoria Nile, Uganda	May-09	2.29	31.57	622	+4.0	+29.0	-228.1	-	-	-	-
Blue Nile and Atbara River	25	Ribb River, east Lake Tana, Ethiopia	May-09	11.99	37.71	1794	+8.6	+47.3	-370.0	+3.51	+1.92	3.3	117
	28	Chimba, Gilgel Abay, Ethiopia	May-09	11.71	37.17	1808	+1.4	+15.5	-122.3	+1.74	+0.88	10.9	388
	29	Alata River, Ethiopia	May-09	11.49	37.59	1647	+0.6	+10.4	-82.9	-	-	-	-
	30	Gumara River, east Lake Tana, Ethiopia	May-09	11.84	37.64	1795	+5.6	+33.7	-263.8	-	-	-	-
	34	Blue Nile, Khartoum, Sudan	May-11	15.61	32.53	409	+4.2	+32.1	-252.4	+3.22	+1.70	5.7	203
	35	Tis Issat Falls, Blue Nile, Ethiopia	May-09	11.49	37.59	1642	+5.1	+37.9	-298.3	+3.31	+1.84	3.7	132
	36	River Atbara, Atbara, Sudan	Apr-11	17.68	33.98	353	+1.6	+15.3	-120.9	+3.41	+1.80	5.1	182
	37	Blue Nile, Bahir Dar, Ethiopia	May-09	11.61	37.41	1788	+5.1	+37.3	-293.3	-	-	-	-
Main Nile	38	Main Nile (Lake Nasser), Wadi Halfa, Sudan	Apr-11	22.02	31.34	178	+1.3	+16.8	-133.3	-	-	-	-
	39	Main Nile, Dongola, Sudan	Apr-11	19.18	30.49	223	+2.8	+26.3	-207.7	+2.83	+1.39	4.6	164
	40	Main Nile, Karima, Sudan	Apr-11	18.50	31.81	258	+2.9	+27.0	-213.4	-	-	-	-
	41	Main Nile, Atbara, Sudan	Apr-11	17.66	33.97	357	+6.6	+44.8	-351.8	+2.14	+1.29	4.0	142
	42	Main Nile, Khartoum, Sudan	May-11	15.66	32.51	377	+7.1	+48.0	-377.0	-	-	-	-
	43	Main Nile, Aswan, Egypt	Apr-11	24.09	32.89	81	+2.1	+21.1	-167.0	-	-	-	-
	44	Bahr Yusuf, Faiyum, Egypt	Apr-11	29.31	30.85	20	+2.8	+24.2	-190.8	-	-	-	-
	45	Main Nile, Cairo, Egypt	Apr-11	30.04	31.23	8	+2.8	+24.4	-192.1	+4.66	+2.26	1.1	39
	46	Main Nile, Luxor, Egypt	Apr-11	25.70	32.64	67	+2.3	+22.2	-175.2	+3.63	+1.96	2.6	93
	47	Main Nile (Lake Nasser), Aswan, Egypt	Apr-11	23.97	32.90	152	+2.1	+21.6	-170.5	+3.79	+2.01	2.7	96
	48	Lake Qarun, Faiyum (south-east), Egypt	Apr-11	29.47	30.78	-44	+7.6	+48.6	-381.1	-	-	-	-
	50	Lake Qarun, Faiyum (west), Egypt	Apr-11	29.45	30.40	-46	+8.8	+53.9	-422.2	-	-	-	-

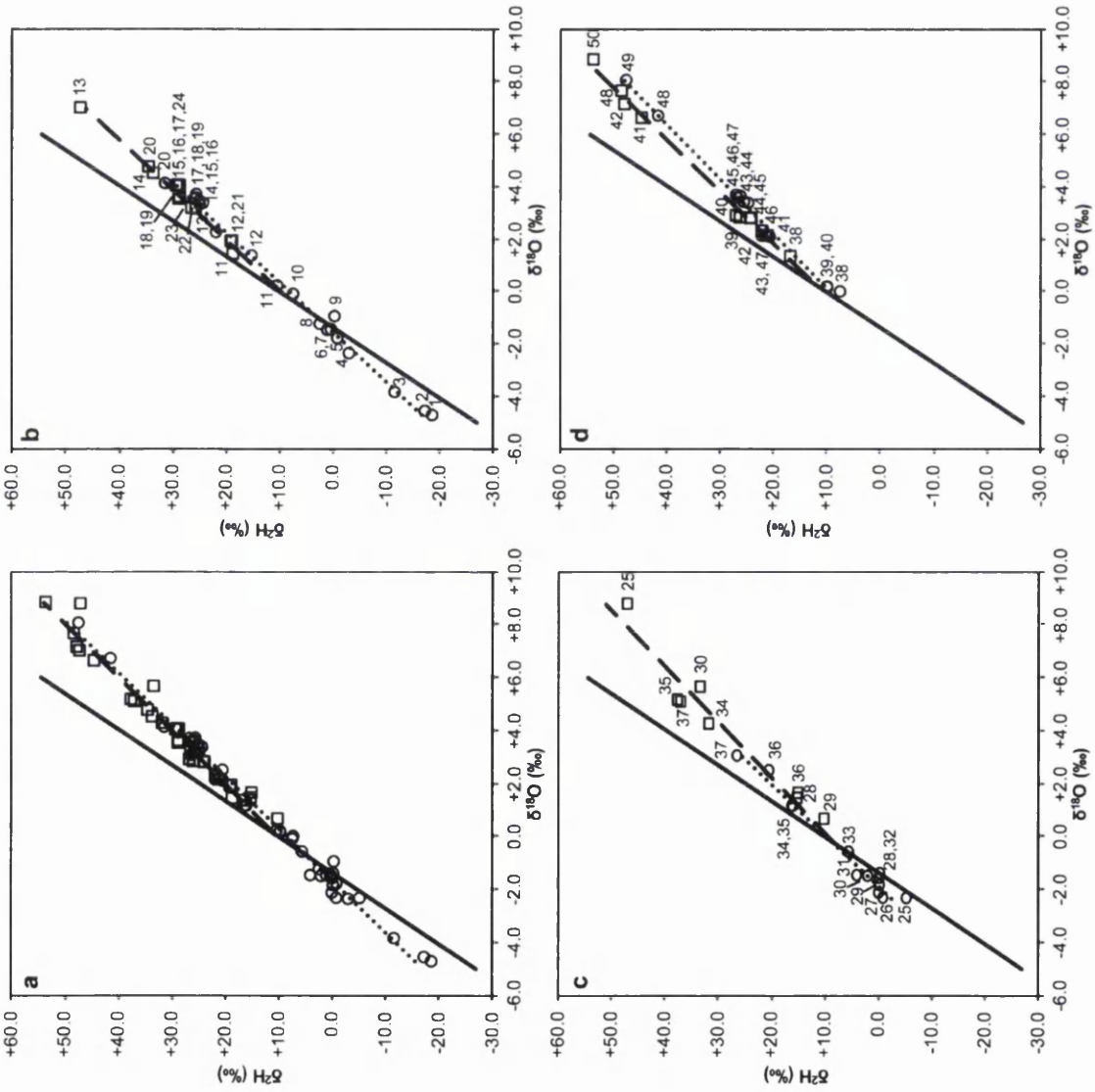

Figure 6.8: δ^2H and $\delta^{18}O$ of surface water samples for (a) the Nile basin, and for the major individual tributaries, (b) White Nile, (c) Blue Nile and (d) Main Nile. Samples collected during the wet season (circles) and dry season (squares) are plotted. The African Meteoric Water Line (AMWL) (solid line: $\delta^2H=7.4\delta^{18}O + 10.1$) (Cohen et al., 1997), wet- (dotted line) and dry-season (dashed line) local evaporative lines are plotted for reference. For sample numbers, see Table 6.2. Corresponding regression results can be found in Table 6.3.

Table 6.3: Regression results for δ^2H and $\delta^{18}O$ of surface water samples in Figure 6.8.

	Regression equation	R^2	Range of values		Mean				
Wet season			$\delta^{18}O$	δ^2H	$\delta^{18}O$	1 σ	δ^2H	1 σ	n
River Nile (all data)	$\delta^2H = 5.09 \cdot \delta^{18}O + 8.78$	0.989	-4.7 to +8.0	-18.4 to +47.7	+0.8	± 2.9	+12.7	± 14.8	45
White Nile	$\delta^2H = 5.27 \cdot \delta^{18}O + 8.22$	0.992	-4.7 to +4.0	-18.4 to +31.7	+0.3	± 3.0	+9.8	± 15.7	20
Blue Nile	$\delta^2H = 5.22 \cdot \delta^{18}O + 9.80$	0.973	-2.4 to +3.0	-4.9 to +26.8	-0.6	± 1.9	+6.7	± 9.9	13
Main Nile	$\delta^2H = 4.83 \cdot \delta^{18}O + 9.41$	0.992	-0.0 to + 8.0	+7.5 to +47.7	+3.1	± 2.5	+24.2	± 12.0	12
Dry season									
River Nile (all data)	$\delta^2H = 4.95 \cdot \delta^{18}O + 10.43$	0.966	+0.6 to +8.8	+10.5 to +53.9	+3.9	± 2.2	+29.7	± 10.9	34
White Nile	$\delta^2H = 5.23 \cdot \delta^{18}O + 9.75$	0.976	+1.4 to+ 7.0	+19.0 to +47.3	+3.6	± 1.4	+28.7	± 7.4	14
Blue Nile	$\delta^2H = 4.76 \cdot \delta^{18}O + 9.35$	0.947	+0.6 to +8.8	+10.5 to +47.3	+4.1	± 2.7	+28.7	± 13.3	8
Main Nile	$\delta^2H = 5.00 \cdot \delta^{18}O + 11.06$	0.994	+1.3 to +8.8	+16.8 to +53.9	+4.1	± 2.6	+31.6	± 13.1	12

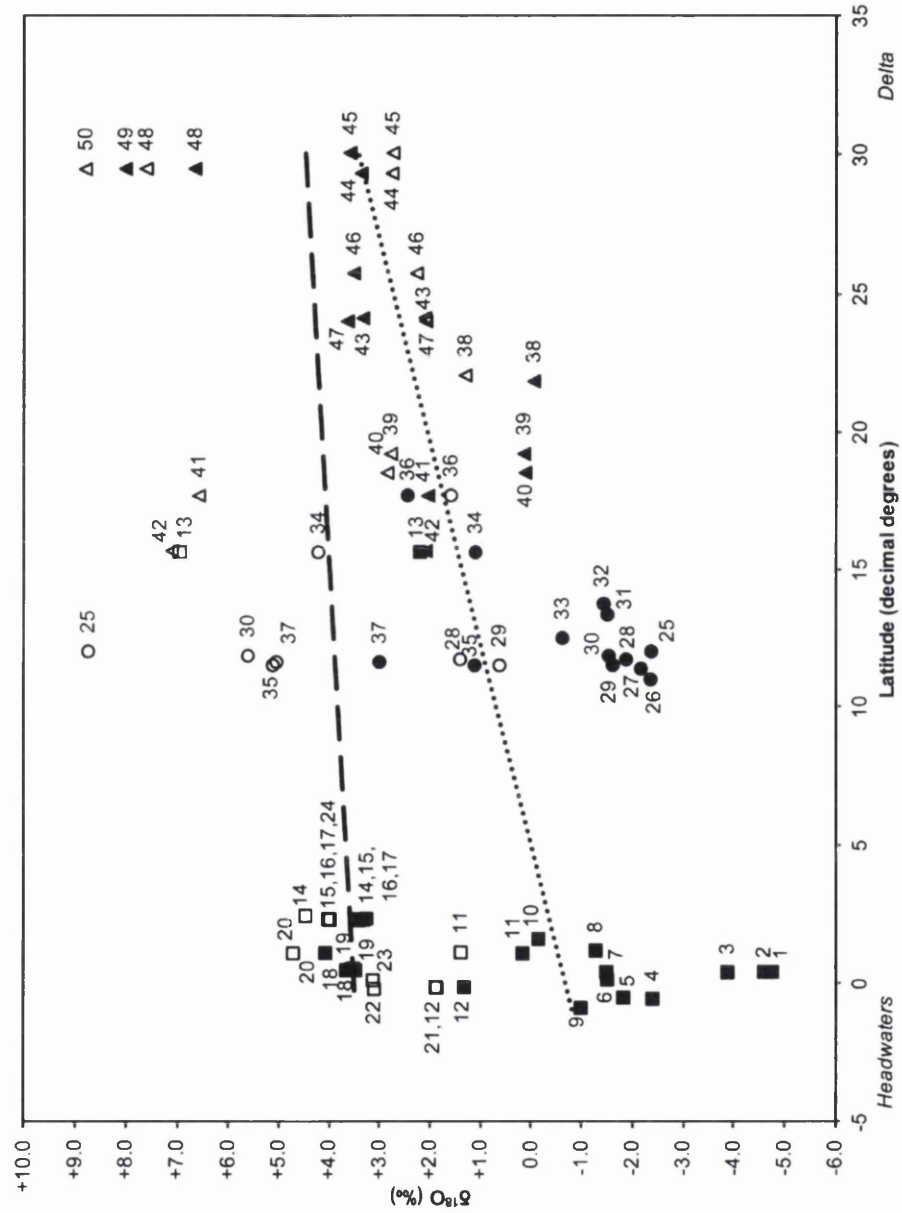

Figure 6.9: $\delta^{18}O$ versus latitude. Wet season (closed symbols) and dry season (open symbols) samples are plotted for the White Nile (squares), Blue Nile (circles) and Main Nile (triangles). Waters are more enriched during the dry season (dashed line; $\delta^{18}O$ = 0.03·Latitude + 3.49, r_s = 0.076, p = 0.338) than the wet season (dotted line; $\delta^{18}O$ = 0.14·Latitude - 0.68, r_s = 0.465, p < 0.001), and both seasons display progressive enrichment downstream. For sample numbers, see Table 6.2.

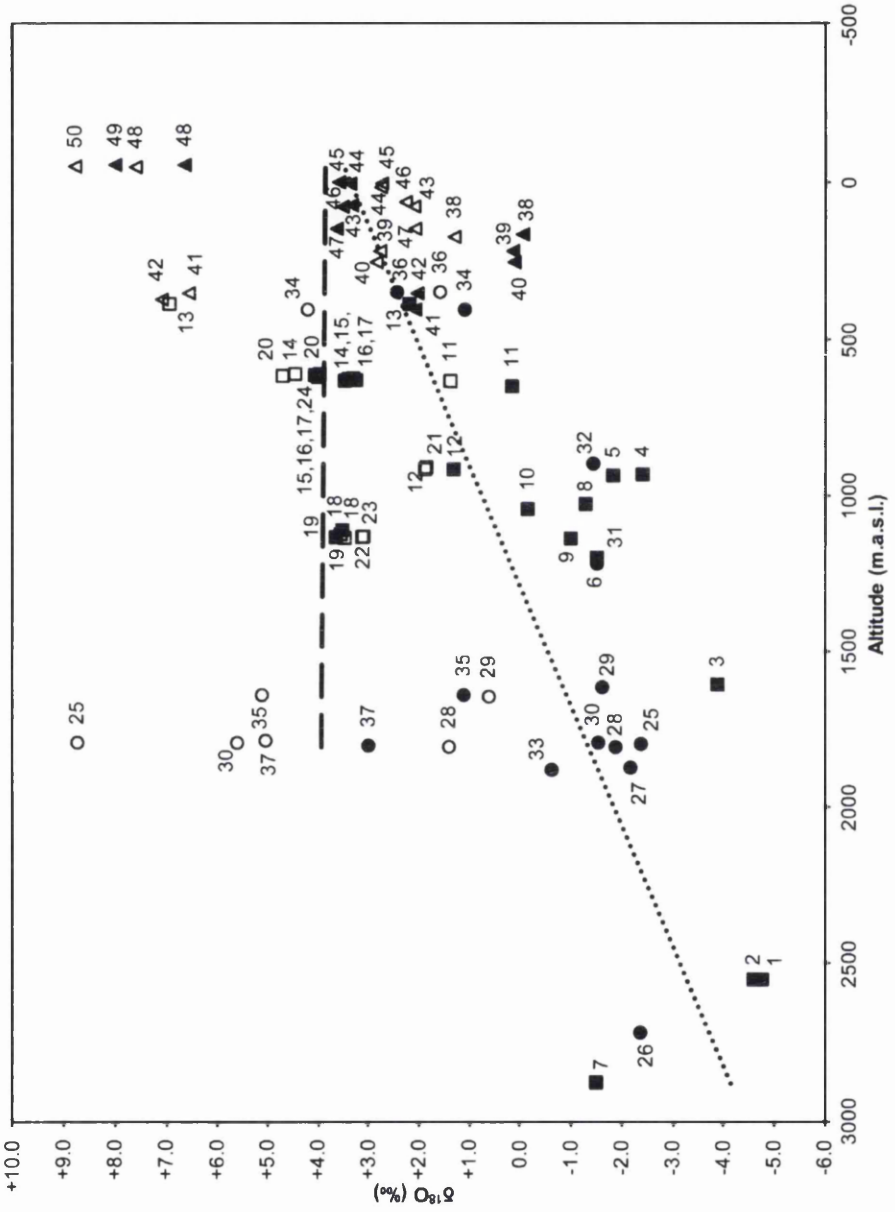

Figure 6.10: $\delta^{18}O$ versus altitude. Wet season (closed symbols) and dry season (open symbols) samples are plotted from the White Nile (squares), Blue Nile (circles) and Main Nile (triangles). Seasonal trends are identified with regression lines; wet season (dotted line; $\delta^{18}O$ = -0.003·Altitude + 3.36, r_s = –0.724, p < 0.001) and for the dry season (dashed line; $\delta^{18}O$ = 2E-05·Altitude + 3.88, r_s = 0.015, p = 0.468). For sample numbers, see Table 6.2.

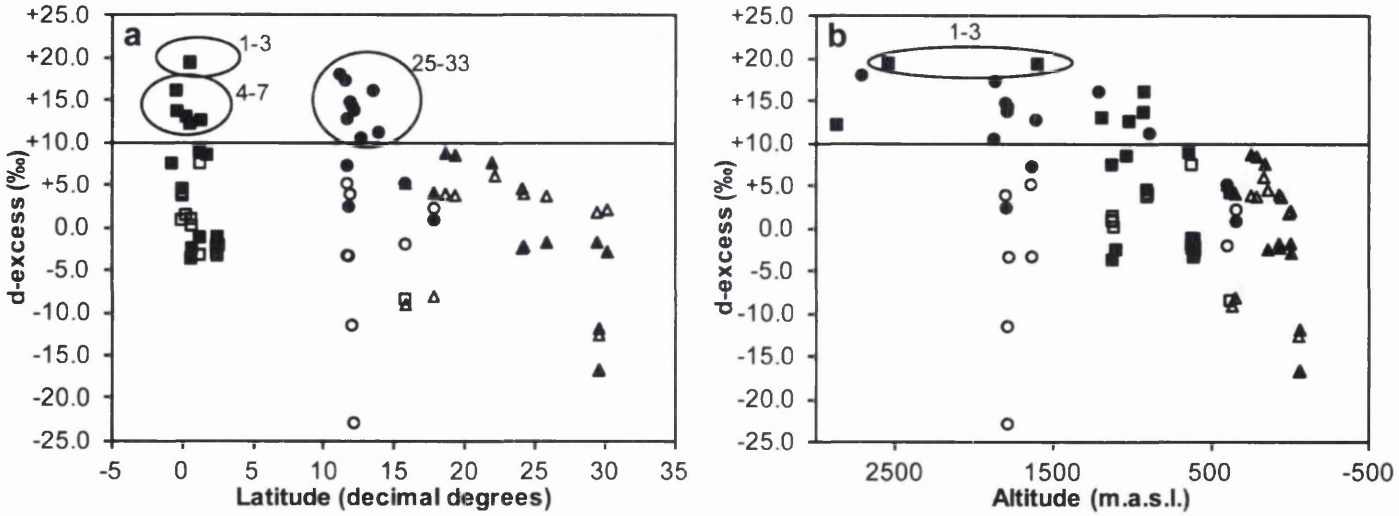

Figure 6.11: Seasonal variations of d-excess for the River Nile with latitude (a) and altitude (b). Wet-season (closed symbols) and dry-season (open symbols) samples are plotted from the White Nile (squares), Blue Nile (circles) and Main Nile (triangles). Horizontal line at +10‰ represents the GMWL. Circled samples are referred to in the text. For numbered samples see Table 6.2.

6.5 Isotope characteristics: DSi and $\delta^{30}Si$

Dissolved Si concentrations (DSi) are displayed in both milligrams per litre (mg/L) and micromolar (µM) units in order to facilitate comparisons with published literature (Figure 6.12; Table 6.2). µM values follow mg/L values in parentheses. Due to the contrasting geology in the individual sub-basins (Figure 3.2), regression lines for DSi have been plotted individually for both wet and dry seasons. Waters from the Ethiopian highlands (Blue Nile and Atbara catchments) had the highest DSi contents under both wet-season (average 10.3 ± 4.7 mg/L (365 ± 169 µM)) and dry-season conditions (average 5.7 ± 3.0 mg/L (204 ± 109 µM)), whereas White Nile waters contained roughly half as much Si (wet season: 5.2 ± 3.6 mg/L (187 ± 127 µM); dry season: 3.7 ± 3.8 mg/L (133 ± 135 µM)) (Figure 6.12). A northwards decrease in DSi was seen in all sub-basins during both seasons (Figure 6.12). DSi concentrations were highest during the wet season, particularly in rivers draining the Ethiopian Highlands (Figure 6.12).

Figure 6.12 (next page): Si concentration versus latitude. Si concentrations are presented in both mg/L (left y-axis) and µM (right y-axis) units. Wet season (closed symbols) and dry season (open symbols) samples are plotted for the White Nile (squares), Blue Nile (circles) and Main Nile (triangles). Seasonal trends are identified with individual regression lines for the White Nile (left-hand side) and the Blue Nile, Atbara and Main Nile (right-hand side) during the wet season (dotted line) and dry season (dashed line) to account for varying geology. White Nile wet season (dotted line; DSi = -1.67·Latitude + 6.00, r_s = –0.331, p = 0.133) and dry season (dashed line; DSi = -2.29·Latitude + 6.38, r_s = –0.054, p > 0.05). Blue Nile, Atbara and Main Nile wet season (dotted line; DSi = $41.57 \cdot \exp^{-0.11 \cdot Latitude}$, r_s = –0.576, p = 0.019) and dry season (dashed line; DSi = $14.33 \cdot \exp^{-0.07 \cdot Latitude}$, r_s = –0.612, p = 0.03). Sample site 13 (White Nile, Khartoum) has been omitted from the White Nile regression as its composition suggests that it may have been influenced by surface water, groundwater or sediments ultimately derived from the Blue Nile, although there are too few data to draw any firm conclusions at this point. For sample numbers, see Table 6.2.

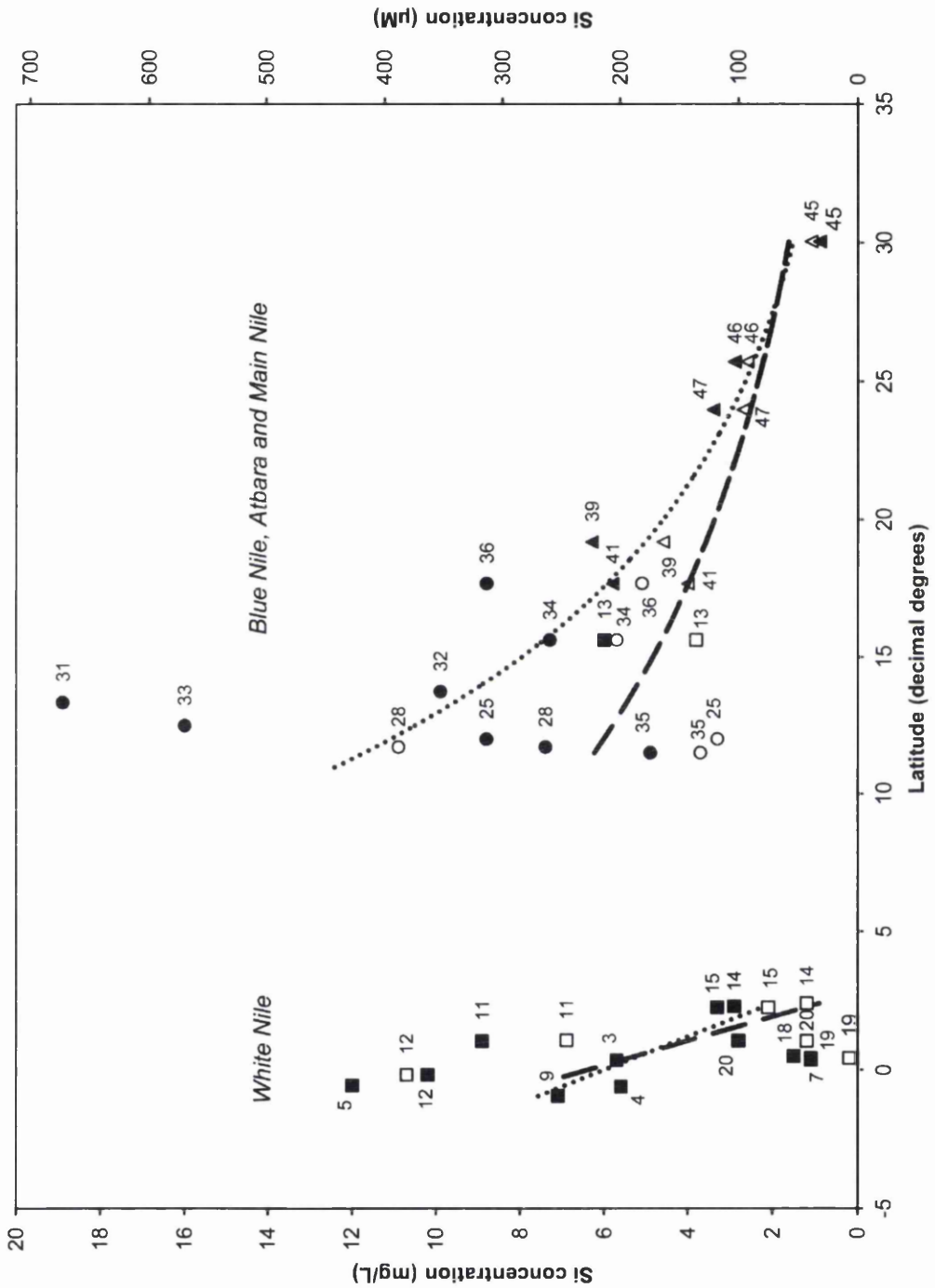
Si concentration (mg/L)
Si concentration (μM)
Latitude (decimal degrees)
White Nile
Blue Nile, Atbara and Main Nile

The $\delta^{30}Si$ values for both wet- and dry-season datasets are best described by curvilinear regressions (Figure 6.13). These curves reflect lower values in Nile headwaters, with progressive enrichment downstream, becoming more pronounced in the Main Nile (Figure 6.13). $\delta^{30}Si$ values ranged from +0.48 to +3.45‰ during the wet season and +1.54 to +4.66‰ during the dry season, raising the upper limit of reported global $\delta^{30}Si$ values for DSi in natural waters by more than 1‰. All samples had high $\delta^{30}Si$ compositions relative to the local geology and were higher in the dry season (av. +2.79 ± 0.91‰) than during the wet season (av. +2.02 ± 0.72‰), although there was less seasonal contrast in the Main Nile (Figure 6.13). $\delta^{30}Si$ and DSi were negatively correlated; low Si concentrations corresponded to high $\delta^{30}Si$ values, more so during the dry season (R^2 = 0.371; separate variance *t*-test, p = 0.012) than the wet season (R^2 = 0.058; separate variance *t*-test, p = 0.245) (Figure 6.14). Figure 6.15 shows a statistically strong, albeit non-causal, positive correlation between $\delta^{30}Si$ and $\delta^{18}O$ during the wet season (R^2 = 0.517; separate variance t-test, $p < 0.001$), when, as identified, both isotopic parameters became cumulatively enriched downstream (Figures 6.9 and 6.13). However, there was no statistically significant relationship between $\delta^{30}Si$ and $\delta^{18}O$ during the dry season.

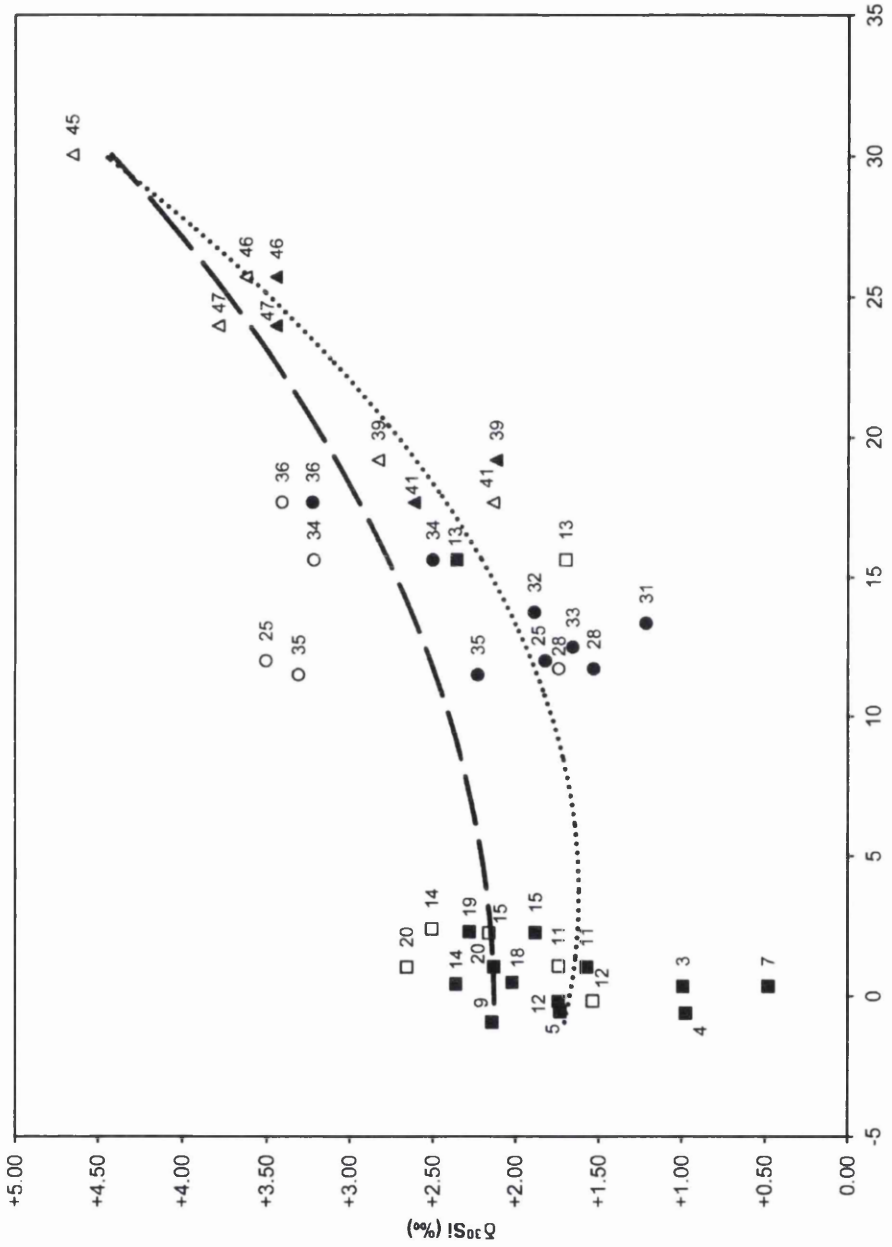

Figure 6.13: $\delta^{30}Si$ versus latitude. Wet season (closed symbols) and dry season (open symbols) samples are plotted from the White Nile (squares), Blue Nile (circles) and Main Nile (triangles). Seasonal trends are identified with curvilinear regression lines for the wet season (dotted line; $\delta^{30}Si = 0.004 \cdot (Latitude)^2 - 0.03 \cdot (Latitude) + 1.67$, $r_s = 0.596$, $p < 0.001$) and for the dry season (dashed line; $\delta^{30}Si = 0.002 \cdot (Latitude)^2 + 0.003 \cdot (Latitude) + 2.13$, $r_s = 0.668$, $p = 0.002$). For sample numbers, see Table 6.2.

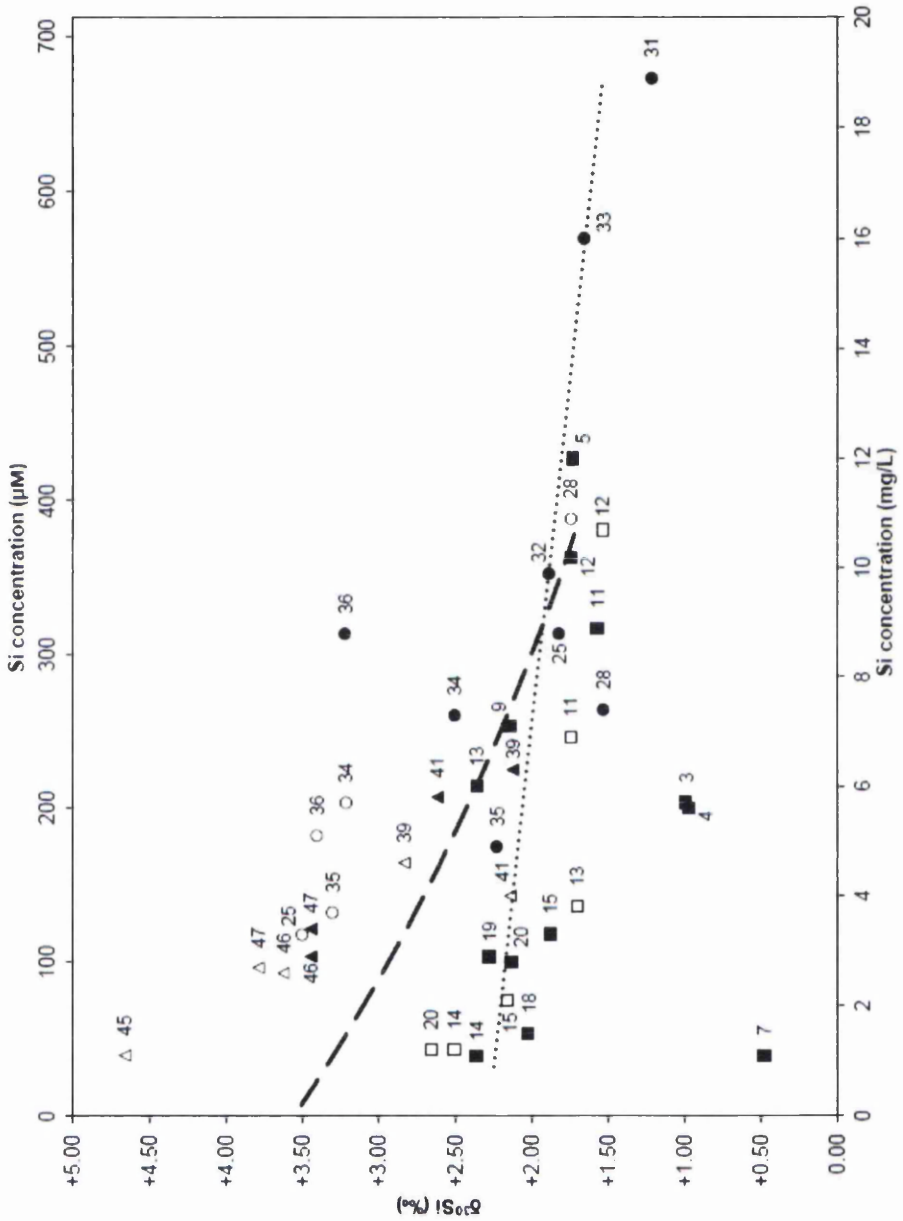

Figure 6.14: $\delta^{30}Si$ versus Si concentration. Si concentrations are presented in both mg/L (bottom x-axis) and µM (top x-axis) units. Wet-season (closed symbols) and dry-season (open symbols) samples are plotted from the White Nile (squares), Blue Nile (circles) and Main Nile (triangles). Seasonal trends are identified with regression lines for the wet season (dotted line; $\delta^{30}Si = -0.001 \cdot DSi + 2.28$, $R^2 = 0.058$, $p = 0.245$) and for the dry season (dashed line; $\delta^{30}Si = 3.56 \cdot exp^{-0.007 \cdot DSi}$, $R^2 = 0.371$, $p = 0.012$). For sample numbers, see Table 6.2.

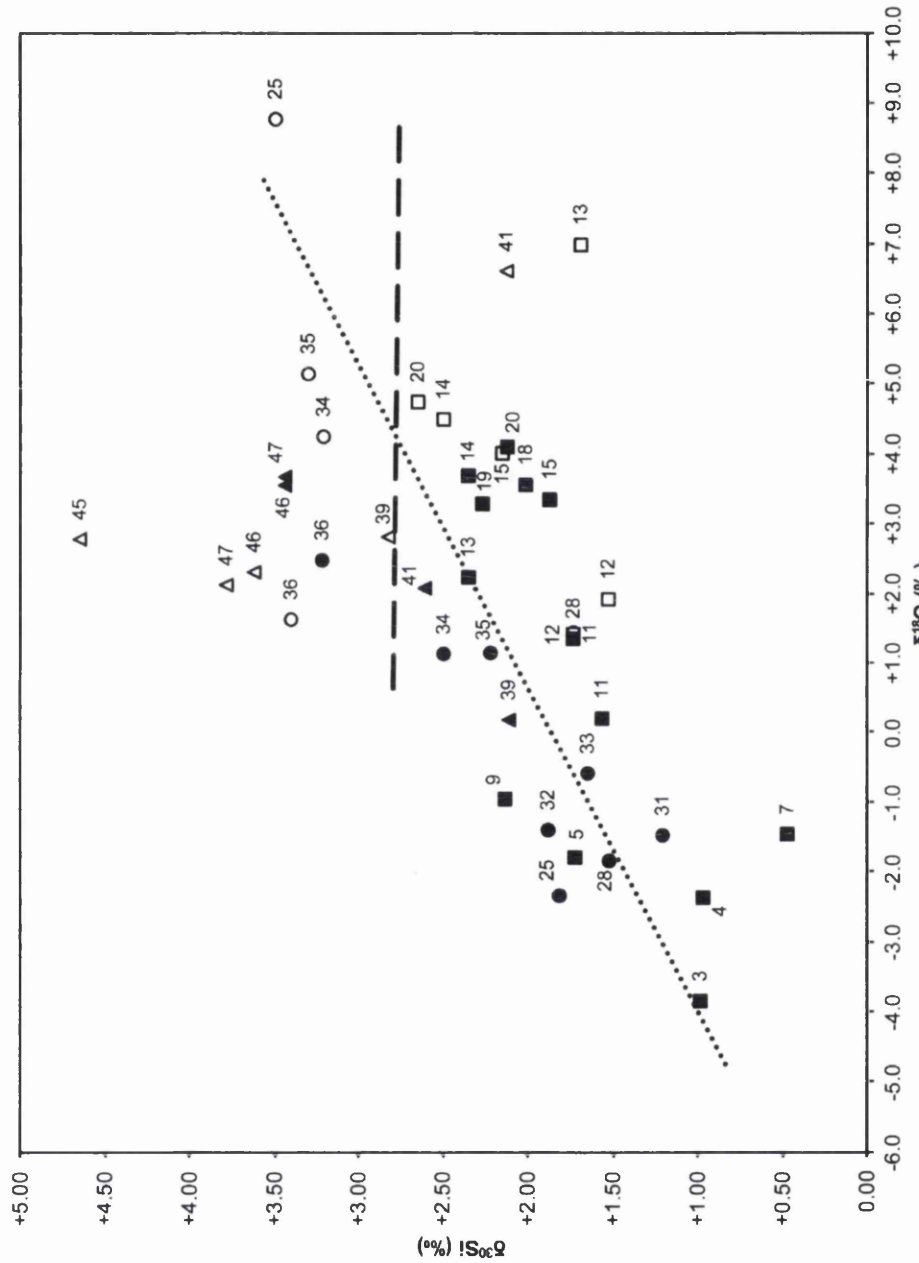

Figure 6.15: $\delta^{30}Si$ versus $\delta^{18}O$. Wet season (closed symbols) and dry season (open symbols) samples are plotted for the White Nile (squares), Blue Nile (circles) and Main Nile (triangles). Seasonal trends are identified with regression lines for the wet season (dotted line; $\delta^{30}Si = 0.22 \cdot \delta^{18}O + 1.86$, $R^2 = 0.517$, $p < 0.001$) and for the dry season (dashed line; $\delta^{30}Si = 0.003 \cdot \delta^{18}O + 2.80$, $R^2 = 5E\text{-}05$, $p = 0.980$). For sample numbers, see Table 1.

6.6 Chapter summary

To understand the modern isotope systematics in the Nile Basin, key physical, chemical and isotopic parameters were plotted to identify relationships and trends in the data. Physical characteristics included pH and electrical conductivity plotted against latitude and altitude to identify downstream trends of individual sub-basins. Downstream trends in pH were more defined during wet-season conditions and pH values indicated waters from the Ethiopian Highlands were more acidic than those of the White and Main Niles. Conductivity increased with distance downstream during both seasons although there was very little seasonal variation. The White Nile and the Blue Nile and Atbara differed in ionic composition, with the White Nile dominant in Na^+ and K^+ ions and the Blue Nile and Atbara waters comprised of predominantly Ca^+ and Mg^+ ions. Cation composition developed downstream into a Na-K carbonate-dominated system, particularly rapid in the Main Nile. Cation ratios were consistently higher during the dry-season in all sub-basins. The relationship between conductivity and cation ratio clearly indicates that conductivity increases with brine development.

The δ^2H and $\delta^{18}O$ values of all water samples plotted along local evaporative lines, deviating from the AMWL. Dry-season samples were significantly more enriched compared to the wet season. Sub-basin differences occurred, with generally lower δ^2H and $\delta^{18}O$ values in the headwaters and enrichment downstream. Some high altitude headwater sites had notably low δ^2H and $\delta^{18}O$ values and unusually high d-excess values. Similar downstream enrichment was observed in $\delta^{30}Si$, with higher values in dry-season samples. $\delta^{30}Si$ values obtained in this thesis extend the global upper limit of previously analysed waters by 1‰. DSi concentrations were greatest during wet-season conditions and in the Blue Nile and Atbara catchments, declining rapidly downstream. Negative trends between $\delta^{30}Si$ composition and DSi concentrations were identified, although the relationship in dry-season sampling was not so definitive. A significant positive relationship between $\delta^{18}O$ and $\delta^{30}Si$ was observed in wet-season samples. Downstream trends in δ^2H, $\delta^{18}O$, $\delta^{30}Si$ and DSi were often obscured in dry season sampling due to the composition of waters in the Main Nile. These trends and relationships that have been identified will be used to interpret the modern hydrological and Si cycles in the Nile Basin and assist with deciphering palaeo-record.

Chapter 7 Lake Victoria, East Africa

7.1 Introduction

The beginning of this chapter gives an account of the natural environment in which Lake Victoria is set, descriptions of the sediment core stratigraphy and an explanation for the age-model selection, followed by, a summary of the specific methodologies applied to Lake Victoria sediments to extract pure diatoms for stable O- and Si-isotope analysis. The final section of the chapter presents the results for Lake Victoria obtained from both diatom isotope analysis and from lipid biomarker analysis.

7.2 Study area

7.2.1 Geography

Lake Victoria is the third largest lake in the world (by surface area) at 68,800 km^2 (Kendall, 1969), after the Caspian Sea and Lake Superior. It straddles the equator in East Africa between the two branches of the Great Rift System, where its shores are shared by three countries: Uganda, Kenya and Tanzania (Figure 7.1). Lake Victoria is a relatively shallow lake with a mean depth of 40 m and maximum depth of 68m (Johnson et al., 2000), located at 1134 m.a.s.l at the headwaters of the White Nile. The basin is estimated to be only ~400,000 years old, forming as a result of uplift along the western branch of the Rift, causing westward flowing rivers to reverse and flow eastward into the sag between the rift valleys (Johnson et al., 2000). The watershed directly surrounding the lake is relatively flat, not exceeding ~25m above the lake surface (Kendall, 1969), whereas the outer basin to the east and west is enclosed by the shoulders of the rift valleys where elevations exceed 2000 meters (Figure 7.1). Due to its large surface area to volume ratio, and to its water balance being largely controlled by rainfall and evaporation, rather than inflows and outflows (Spigel and Coulter, 1996), it is particularly sensitive to climatic changes; drying out completely during the past as identified by seismic reflections and sediment core analysis (Kendall, 1969; Johnson et al., 1996; Johnson et al., 2000; Stager and Johnson, 2000; Talbot and Lærdal, 2000; Stager et al., 2002).

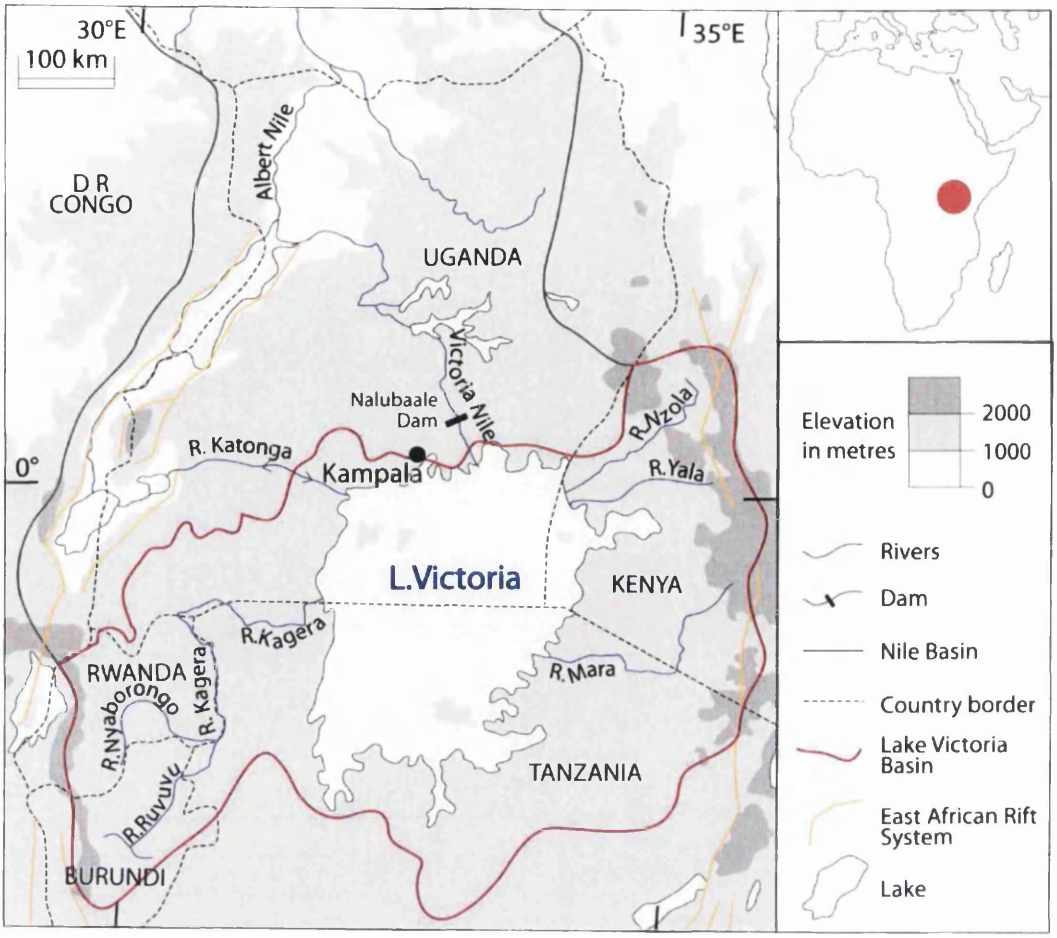

Figure 7.1: Location map of Lake Victoria including the main tributaries, topography and the rift system.

7.2.2 Geology

The Lake Victoria basin is largely comprised of Precambrian granitic and metamorphic rocks (e.g. gneisses, granulites and migmatites) (Figure 7.2). Small pockets of Cenozoic volcanic deposits, related to rift activities, are present on the eastern and western (Virunga Mountains) borders of the basin (Schlüter, 2008).

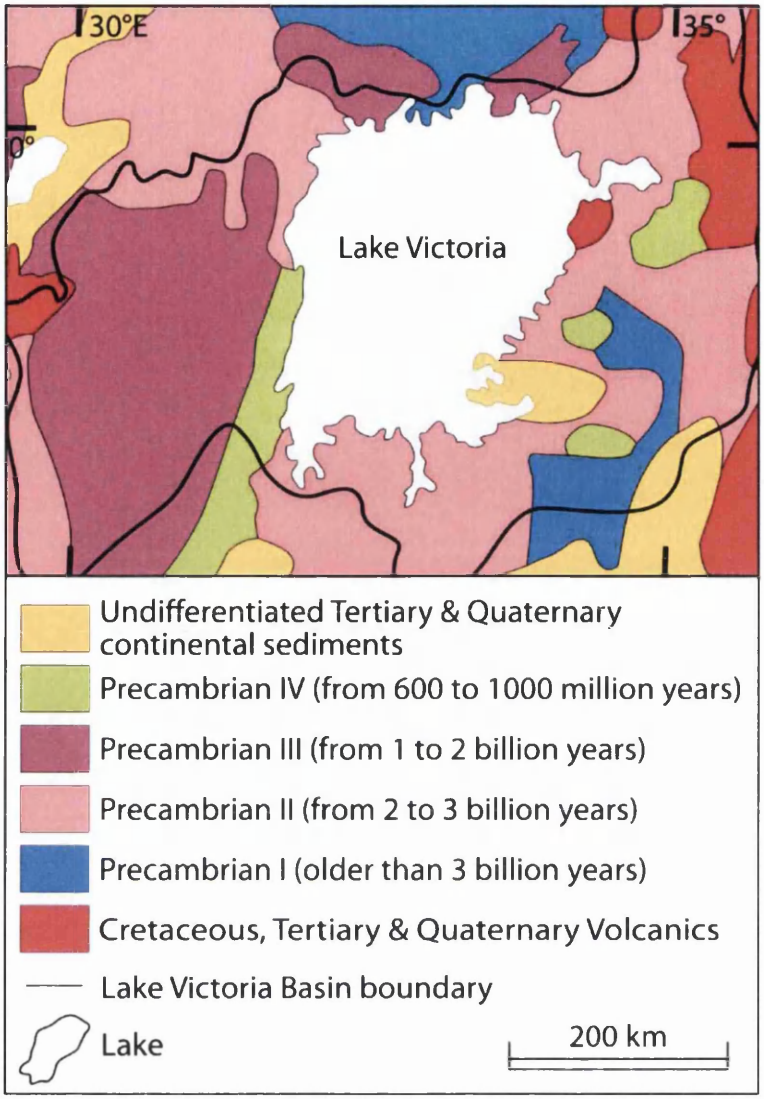

Figure 7.2: Simplified geology of the Lake Victoria basin (modified after Furon (1958)).

7.2.3 Climatology

The Lake Victoria Basin experiences a bimodal rainfall distribution with the "long rains" occurring between March and May and the "short rains" between October and December. Annual precipitation is ~1250-1500 mm/yr in the plains surrounding the lake and >2000 mm/yr in the highlands. The annual variation in rainfall is largely governed by the north-south migration of the Inter-tropical Convergence Zone (ITCZ) which is usually associated with intense, convective rainfall. The basin is sensitive to converging air flows (Johnson et al., 2000), where the northeasterly monsoon and southeasterly monsoon meet to form the ITCZ. In the west of the

basin the Congo Air Boundary separates the moist, humid Atlantic airflow from the easterly airflow sourced from the Indian Ocean (Nicholson, 1996; Tierney et al., 2011b) (see section 3.4. and Figure 3.3). Rainfall distribution is also influenced by the lake itself due to its circular geometry promoting the formation of a strong land-breeze circulation creating convective rainfall and thunder storms in the west during the night and in the east in the afternoon (Flohn and Fraedrich, 1966). Maximum rainfall occurs in the west where the prevailing south-easterly trade winds play an important role in displacing the centre of night-time convergence towards the west and northwest of the basin (Nicholson, 1996; Nicholson et al., 2000; Nicholson and Yin, 2002; Anyah et al., 2006). The mountains in the east (Aberdare Mountain range, Kenya) and the west (Virunga Mountains) of the basin experience enhanced rainfall due to orographic uplift. Estimates suggest that ~85% of water input into the lake orignates from rainfall directly over the lake itself (Crul, 1995; Sutcliffe and Parks, 1999; Sutcliffe, 2009). Mean annual air temperatures around Lake Victoria range from 16-17°C (min) to 27-30°C (max) and in the highlands from 22-24°C to <10°C (Hughes and Hughes, 1992). Evaporation rates are high, particularly over the lake itself where it is estimated that ~90% of water loss occurs through evaporation (Piper et al., 1986; Nicholson, 1998; Sutcliffe and Parks, 1999).

7.2.4 Hydrology

The lake catchment covers 194,000 km^2 and is drained by numerous rivers and streams (Piper et al., 1986) (Figure 7.1). The Kagera, with its tributaries (Ruvuvu and Nyabarongo) draining the highlands of Burundi and Rwanda, is the principal river inflow. The Katonga River in the west and several small tributaries in the north-east of the basin constituting the remainder of the major tributary inputs (Sutcliffe and Parks, 1999). Extensive swamp systems surround the lake and border along the lower reaches of the tributaries, in particular the Kagera River which supports a series of papyrus swamps (1600 km^2 below Rusumo Falls) and lakes (Sutcliffe and Parks, 1999). The tributary contribution to total water inputs to the lake is small at ~15%, with the remainder coming from direct precipitation over the lake (Nicholson, 1998; Sutcliffe, 2009). The only outflow is at Jinja in the north of the basin via the Victoria Nile which marks the beginning of the White Nile, providing a steady base flow to the Nile throughout the year. The water balance of the lake is primarily controlled by precipitation and evaporation over the lake itself rather than by inflows and outflows (Spigel and Coulter, 1996). Lake Victoria is monomictic; overturn of the

water column occurs during the cooler, windier season in May-August when strong southerly winds cause upwelling of nutrients (Talbot and Lærdal, 2000).

7.2.5 Vegetation

Terrestrial vegetation in the lowland areas (<2000m) of the Lake Victoria Basin is predominantly woodland and savanna (Langdale-Brown et al., 1964; White, 1983). Enhanced rainfall in the northern and western parts of the basin supports pockets of rainforest and in the highland peripheries of the basin forested slopes exist. Large areas of the basin are cultivated for subsidence farming (e.g. plantains, cassava, sweet potatoes and bananas) or used for domestic grazing, creating a mosaic pattern of natural vegetation and cultivated crops (Figure 7.3).

The fringes of Lake Victoria and the floodplains of the tributaries flowing into the lake are characterised by wetlands and swamps, supporting a variety of submerged and emergent macrophytes. In the lower reaches of Kagera River, a 150km stretch is flanked by a zone of lakes and swamps up to 15km wide and dominated by *Cyperus papyrus* (C_4 emergent sedge) and *Vossia cuspidate* (C_4 aquatic grass) (Figure 7.4) (Sutcliffe and Parks, 1999). Surrounding the lake itself are extensive areas of *Cyperus papyrus* and *Miscanthidium violaceum* (C_4 aquatic grass) swamps and in recent years many bays have been invaded by water hyacinth (*Echhornia crassipes*) (Kendall, 1969; Sutcliffe and Parks, 1999).

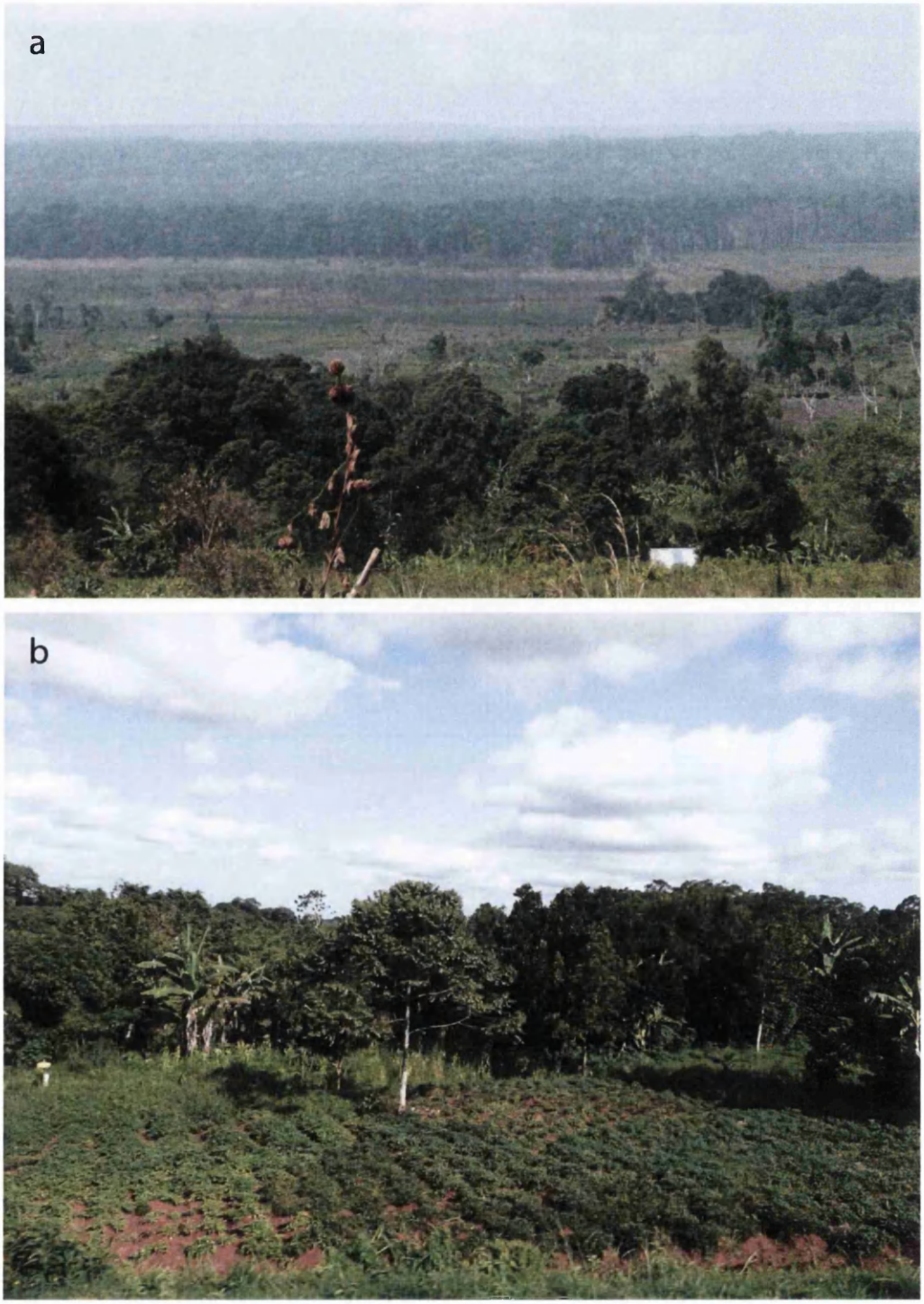

Figure 7.3: Forested area in the north-western region of the Lake Victoria basin being cleared for cultivation (a) and typical subsistence farming (cassava, plantain and maize in this example) in between natural evergreen forests (b).

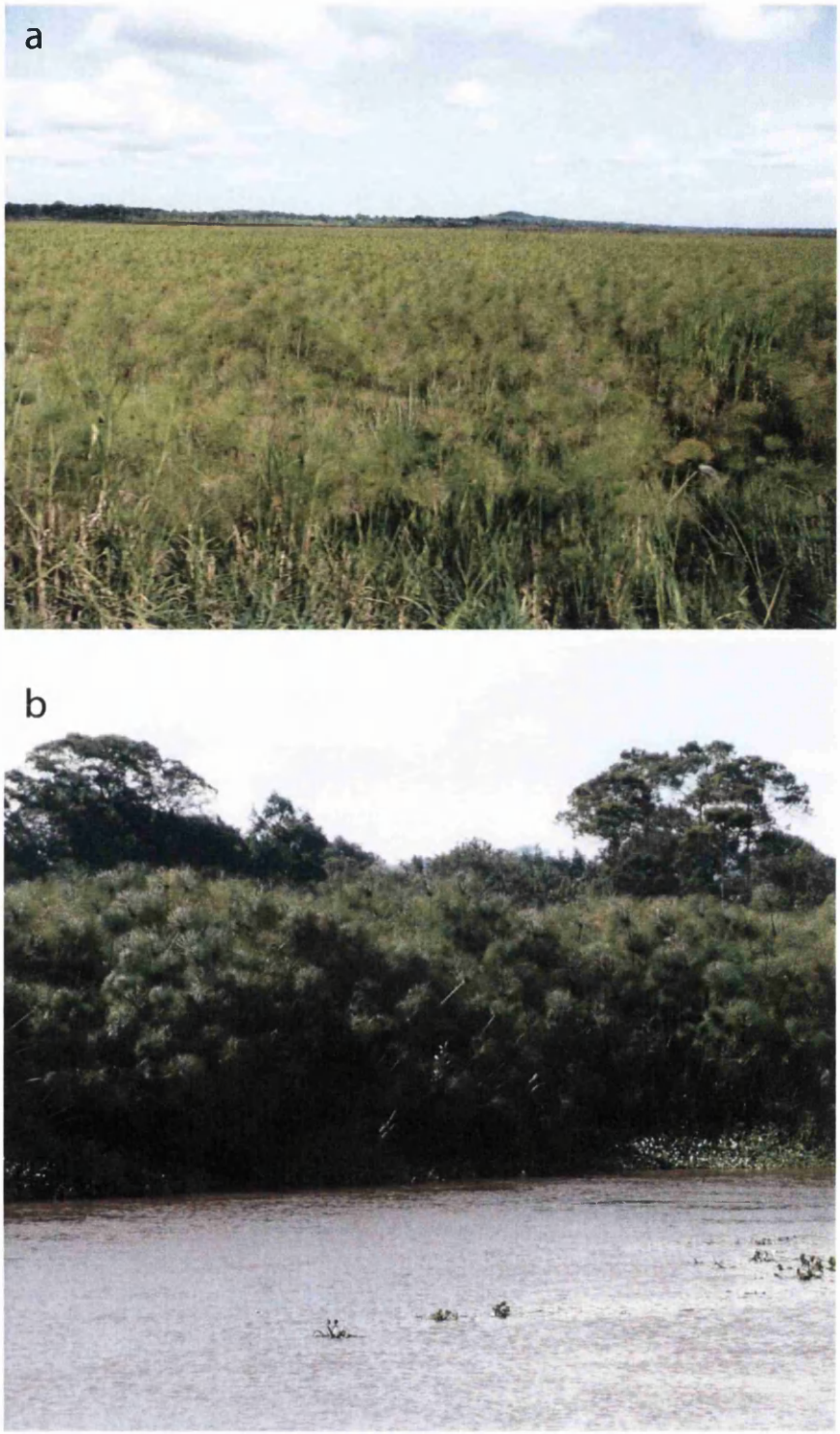

Figure 7.4: Photographs of (a) the extensive *Cyperus papyrus* swamp along the Katonga River (flowing into Lake Victoria from the west) and (b) of the *Cyperus papyrus* swamps dominating the lower stretch of the Kagera River just before it flows into Lake Victoria in the soutwest. *Vossia cuspidata* and *Eichhornia crassipes* (water hyacinth) are also present in front of the papyrus.

7.3 Lake Victoria, East Africa: previous palaeoenvironmental studies

Nine piston cores of varying length (and age) were recovered from Lake Victoria in 1995 and 1996 (Figure 7.5), as part of the International Decade for East Africa Lakes (IDEAL) multidisciplinary study of the lake. Coring sites were determined from seismic reflection profiles in order to obtain long, continuous records covering the Late Pleistocene. Cores were obtained using a modified Kullenberg corer (Kelts et al., 1986) on board the R/V Ibis vessel and subsequently stored at the Limnological Research Centre (LRC) at the University of Minnesota, USA. Material from these cores is available on request from LacCore, the US National Lacustrine Core Facility, based at the LRC.

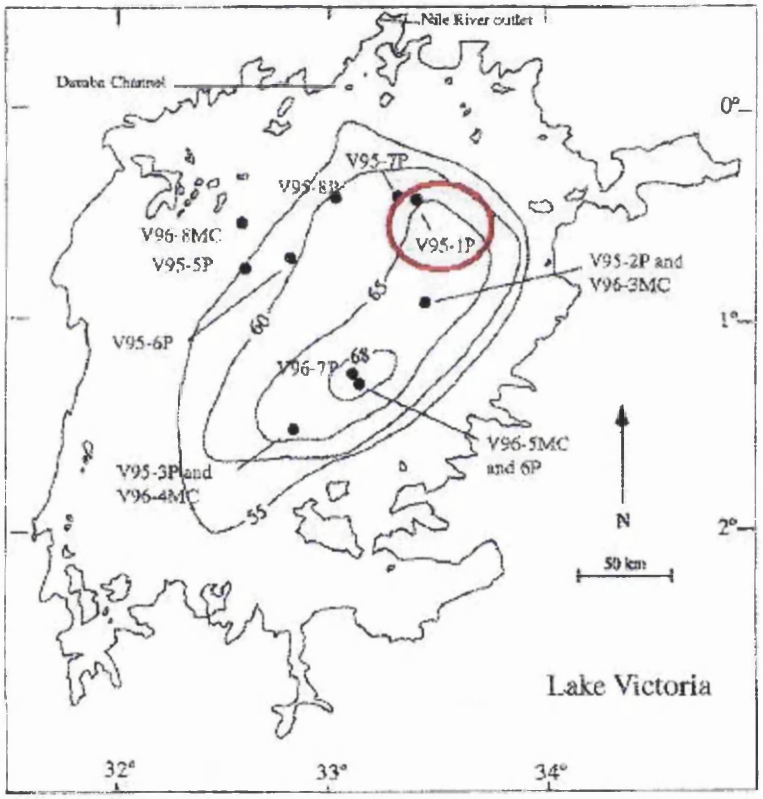

Figure 7.5: Bathymetric map of Lake Victoria, showing the core locations from the IDEAL study in 1995 and 1996. Depth contours are in meters (from: Johnson et al. (2000)). Core location of V95-1P is circled in red.

Prior to the IDEAL expedition in 1995, only five long sediment cores had been collected from Lake Victoria and analysed for past climatic and environmental changes (Figure 7.6) (Kendall, 1969; Stager, 1984; Stager et al., 1986; Talbot and

Livingstone, 1989). All of these cores were obtained from the northern part of the lake close to the current shoreline, and therefore may not have represented basin-wide conditions (Johnson, 1996). Hence, the core locations of the IDEAL expedition were spread across the basin in the offshore regions (Figure 7.5).

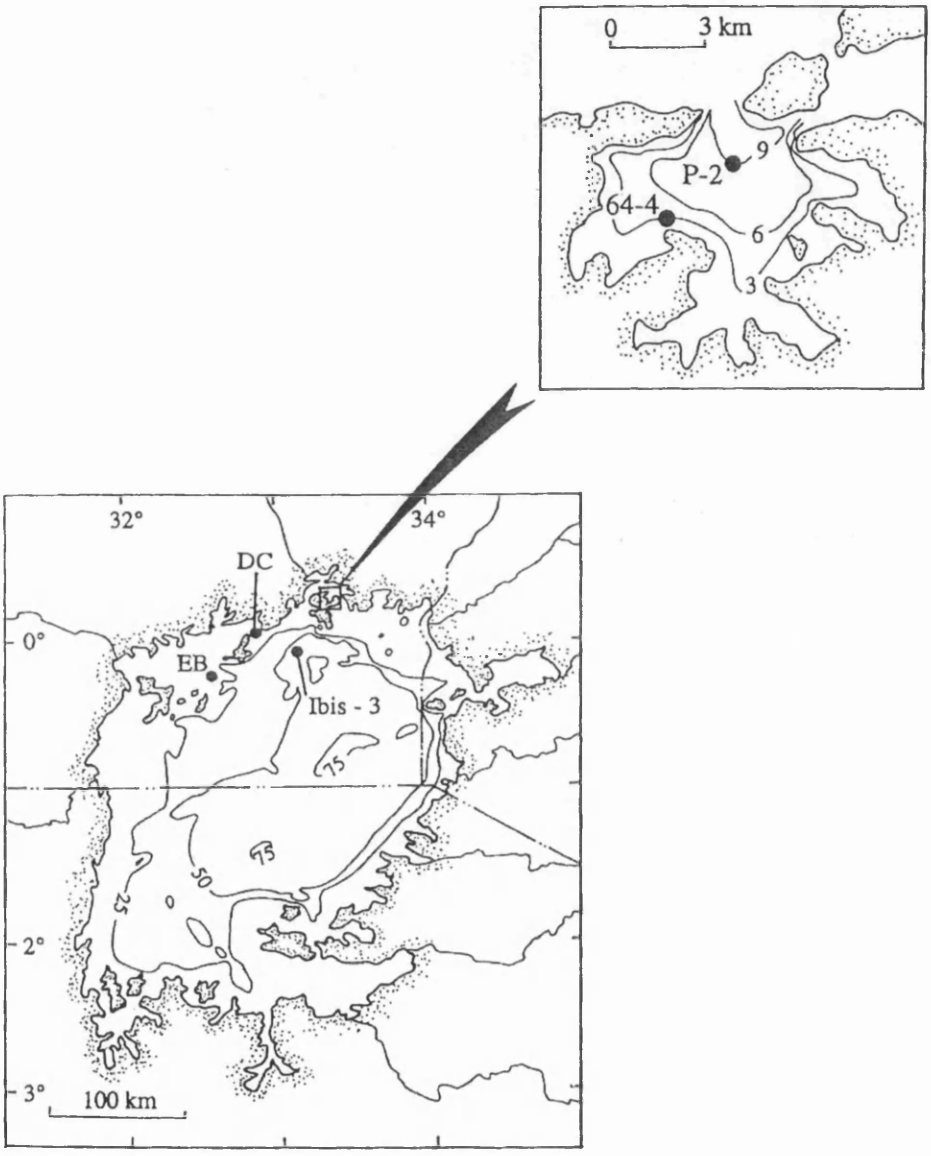

Figure 7.6: Cores obtained from Lake Victoria prior to the IDEAL expedition in 1995 (from Johnson (1996)). EB (Entebbe-B), P-2 and 64-4 (Pilkington Bay) (Kendall, 1969), DC (Damba Channel)/Ibis-1 (Stager, 1984; Stager et al., 1986; Talbot and Livingstone, 1989) and Ibis-3 (Stager et al., 1986; Talbot and Livingstone, 1989).

7: Lake Victoria

Core P-2 from Pilkington Bay, 18km southeast of the Nile outlet at Jinja in Uganda, is the best dated core based on 28 radiocarbon dates spanning the last ~15,000 ^{14}C yr BP (Kendall, 1969), and as a result the other pre-IDEAL cores were correlated with pollen (Kendall, 1969) and diatom (Stager, 1984; Stager et al., 1986) assemblages.

A palaeosol in the P-2 core provided the first indication that Lake Victoria may have dried out completely during the late Pleistocene (Kendall, 1969), which was later confirmed by seismic profiling and from other cores, including those of the IDEAL expedition (Johnson et al., 1996; Stager et al., 2002). Sedimentological evidence from seven cores registered lake-wide desiccation of Lake Victoria during the late Pleistocene, but only four have been dated above and below the discontinuity (Stager et al., 2002). The timing of this discontinuity indicates that the lake dried out at least once between 18 and 14 ka BP (Johnson et al., 1996; Stager et al., 2002; Stager and Johnson, 2008), possibly more than once given the existence of two palaeosols in offshore cores V95-1P and V95-2P (Johnson et al., 1996; Talbot and Lærdal, 2000) and three shell layers in coastal core Ibis-1 (Stager et al., 2002; Stager and Johnson, 2008). The lake began to refill from about 15 ka BP, synchronous with the onset of the Bølling-Allerød warm phase (Stager and Johnson, 2008), and overflowed into the Victoria Nile from about 14.2 to 14 ka BP (Talbot et al., 2000; Williams et al., 2006). A short period of reduced lake level occurred just prior to ~11.5 ka BP and possibly resulted in a brief return to closed-basin conditions associated with the dry European Younger Dryas period (Kendall, 1969; Johnson et al., 2000; Williams et al., 2000).

Orbital forcing is likely to have been the underlying cause of tropical aridity and weakening of the monsoons during the last glacial (Kutzbach and Street-Perrott, 1985; Prell and Kutzbach, 1987), although complex interactions between orbital forcing, atmosphere, ocean and land surface conditions probably resulted in the complete desiccation of Lake Victoria (Gasse, 2000; Stager et al., 2002; Kiage and Liu, 2006; Gasse et al., 2008). Increasing insolation contributed to the abrupt filling of Lake Victoria and overflow into the Victoria Nile, and the subsequent enhanced northern summer monsoon between ~15 to 5 ka BP, resulting in wetter and warmer conditions across northern Africa (see section 3.7 in Chapter 3). Superimposed on the long-term climatic trend from Lake Victoria were millennial-scale events, including the Younger Dryas and possibly Heinrich event (H-1) (Figure 7.7), thought

to be induced by marine circulation disruptions (Street-Perrott and Perrott, 1990; Bond et al., 1992; Bard et al., 2000), providing a link between major climatic events in the tropics and the high latitudes (Stager et al., 1997, 2003).

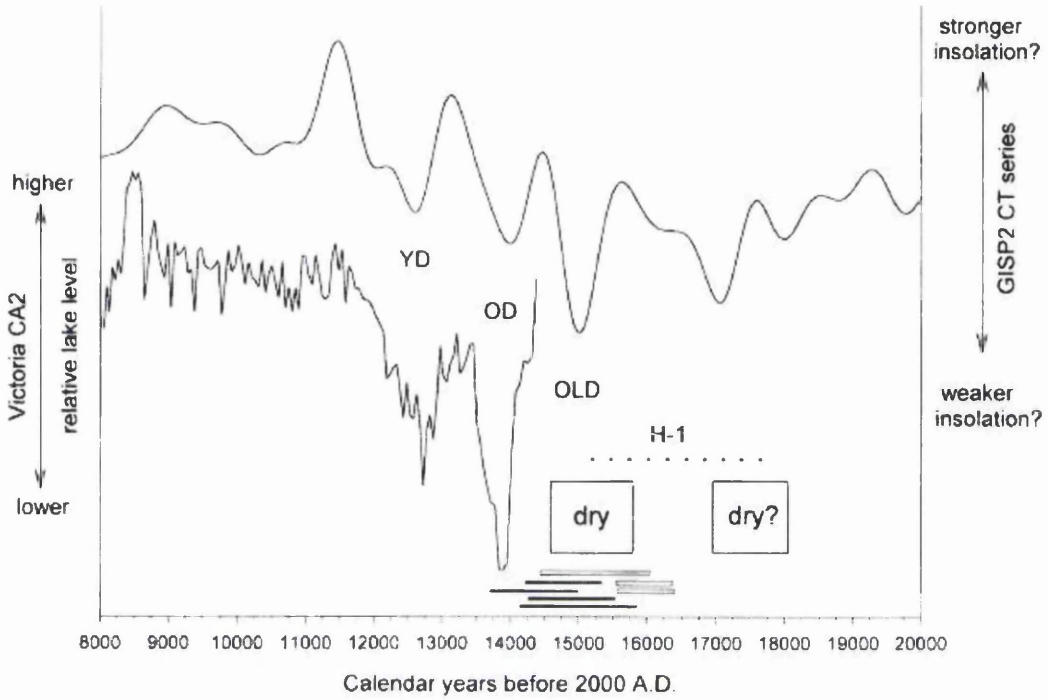

Figure 7.7: Palaeolake levels at Lake Victoria compared with the GISP2 atmospheric circulation index series (from Stager et al. 2002). Summed band pass components from the GISP2 record thought to be related to precession and solar variability, produce erratic pulses, or combination tones (CT), that reached extreme lows ca. 17.5-17.0 and 15-14.5 kyr BP (upper record). CA2=multi-species diatom records from Ibis-1 core combined through correspondence analysis into a single curve (axis 2; Stager et al. 1997); higher percentages of shallow-water taxa in the series lower the curve, thus indicating relatively lower lake levels. OLD, OD, YD=Europe's Oldest, Older, and Younger Dryas coolings. H-1 = Heinrich event. Open and solid lines= calendar age ranges from cores Ibis-1, Ibis-3, and V95-2P for the onset and end, respectively, of Victoria's final desiccation. 'Dry' box positions bracket proposed desiccation events.

Kendall (1969) carried out a detailed reconstruction of climatic and environmental changes in and around Lake Victoria during the last ~15,000 ^{14}C yr BP based on several proxies including sediment water content, carbonate content, pollen and diatom assemblages and green algae remains from three cores (P-2, 64-4 and Entebbe-B). The pollen evidence indicated a shift from predominantly C_4 savanna grasses associated with the LGM, to semi-deciduous forest shortly after the refilling of Lake Victoria (12,200 ^{14}C yr BP; ~14 ka BP) (Kendall, 1969). At the beginning of

the Holocene, the development of moist evergreen forest (e.g. Moraceae) indicated increased humidity and rainfall, after a decline in forest vegetation during the Younger Dryas period (Kendall, 1969). Between the early and mid-Holocene, a change to more seasonal rainfall caused a transition from evergreen to semi-deciduous forest beginning at ~6,000 ^{14}C yr BP (~6.8 ka BP) , and then forest decline started to occur by about ~3,000 ^{14}C yr BP (~3.2 ka BP), possibly associated with the penetration of agricultural activity in East Africa (Clark, 1962; Kendall, 1969).

Multiple studies of the diatom flora in both onshore and offshore cores (Kendall, 1969; Stager et al., 1997; Stager and Johnson, 2000; Stager et al., 2003) support the pollen evidence provided by core P-2 (Kendall, 1969), highlighting the nearly synchronous changes in lacustrine and terrestrial environments in the northern part of Lake Victoria (Figure 7.8) (Stager et al., 1997; Stager and Johnson, 2000). Diatom assemblages after the desiccation event (palaeosol) represented rising lake levels, although the presence of *Thalassiosira rudolfi* showed that the lake water was still chemically concentrated (Kendall, 1969; Stager and Johnson, 2000). High TOC and hydrogen index (HI) values in three cores (V95-2P, 3P and 7P) indicated an increasing contribution from phytoplankton, providing evidence for rising lake levels in a transgressive basin (Talbot and Lærdal, 2000). During the Younger Dryas interval (~13-11.5 ka BP) water level temporarily declined and the lake may have returned to closed conditions (Johnson et al., 2000), in response to severe aridity (Stager et al., 1997; Stager and Johnson, 2000).

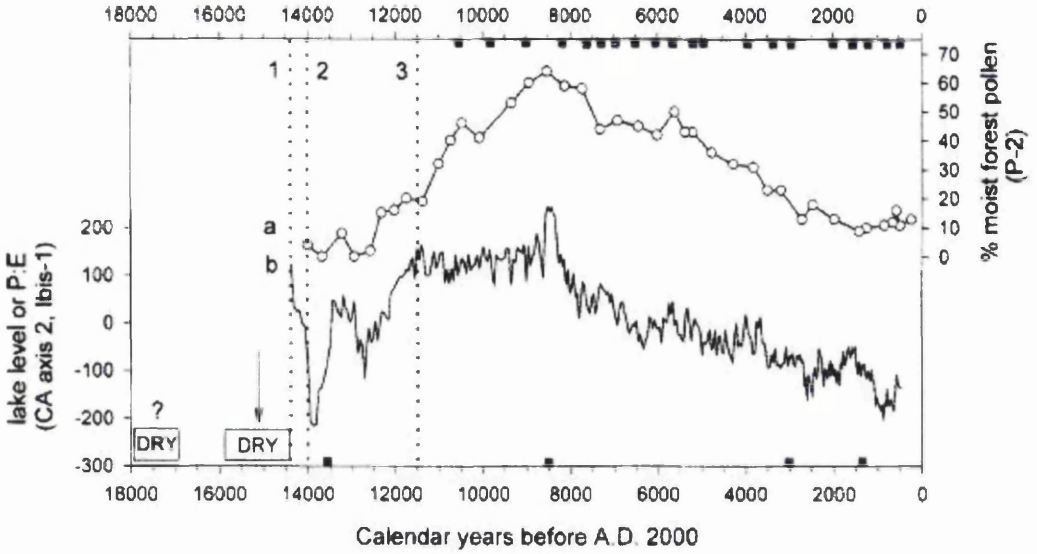

Figure 7.8: Two microfossil records from Lake Victoria (from Stager and Johnson (2008)). "Dry" boxes under the arrows indicate the periods during which desiccation would most probably occurred. (a) moist forest pollen in Pilkington Bay core P-2 (Moraceae, Urticaceae, *Alchornea*, *Macaranga* and *Trema*; after Kendall, 1969). (b) second correspondence analysis axis (CA axis 2) from the diatom record of Damba Channel core Ibis-1 (Stager et al. 2003), indicating relative lake level and/or precipitation:evaporation ratios (P:E). Black squares = ^{14}C dates. Dotted lines indicate likely dates for the progressive flooding of (1) Ibis-1 (2) P-2 and (3) 64-4 core sites.

High diatom productivity (elevated BSi concentrations) at the beginning of the Holocene (~11.5 to 8.3 ka BP) was associated with maximum P/E (precipitation:evaporation) ratios and thorough water column mixing under windy conditions (Stager et al., 1997; Stager and Johnson, 2000; Stager et al., 2003), during which time Late Victoria was at its largest (Kendall, 1969; Stager et al., 1986). These inferences are supported by an 8‰ lowering of $\delta^{18}O$ in aquatic cellulose at the beginning of the Holocene indicating a notable increase in precipitation (Beuning et al., 2002). Between 9.8 and 7.5 ka BP in several of the IDEAL cores, diatom productivity rapidly declined (as shown by low BSi concentrations) (Johnson et al., 2000). Johnson et al. (1998) used a mass balance model to estimate that internal silica cycling in Lake Victoria would only be able to sustain itself for ~40 years based on the reservoir of DSi already in the lake. Therefore, the long-term supply of DSi to the lake is controlled by the input from the catchment (Hecky et al., 1996; Johnson et al., 1998), as is the case for other large tropical African lakes (e.g. Lakes Malawi and Edward) (Johnson et al., 2001; Johnson et al., 2002; Bootsma, 2003; Russell and Johnson, 2005). Johnson et al.

(1998) found it hard to envisage a decline in DSi from river input during the wettest period in Lake Victoria's most recent history. In addition, a shift in the diatom assemblage from *Stephanodiscus astraea* to *Aulacoseira* species between ~10.7 and 8.2 ka BP indicated that silica was not limited (Kendall, 1969; Stager et al., 1997). Instead, Johnson et al. (2000) suggested that the period of minimum diatom productivity (9.8 and 7.5 ka BP) represented maximum stratification of the water column due to low wind strength or intense heating of the water column, which prevented diatoms from remaining in suspension (Stager and Johnson, 2000; Stager et al., 2003). Although not entirely synchronous, Johnson et al. (2000) suggested a shift in diatom species at ~8.3 ka BP from *Aulacoseira granulata* to *A. nyassensis*, identified in several cores (Stager et al., 1997, 2003), supported their argument of reduced wind activity and column mixing as the latter species can withstand prolonged sinking. Geochemical parameters (TOC, C/N, $\delta^{13}C$ and HI) in Lake Victoria were at their maximum during the interval of 10 to 4 ka BP, which Talbot and Lærdal (2000) also suggested indicated stratification of the water column. From the abundance of green algal remains, Johnson et al. (1998; 2000) hypothesised that diatoms were replaced by green algae during this period of low BSi accumulation in the lake sediments (~10 to 8 ka BP). In contrast, high productivity in inshore cores was interpreted as reflecting water mixing from land-lake breezes (Stager and Johnson, 2000; Stager et al., 2003). This episode of reduced biogenic silica accumulation coincided with the 8.2 ka cooling event documented in many archives in the North Atlantic region (Alley et al., 1997; Bond et al., 2001; Daley et al., 2011) and increasingly around the world, including Africa as a millennial-scale drying event (Johnson et al., 2000; Thompson et al., 2002; Stager et al., 2003; Rohling and Pälike, 2005).

A reduction in the duration and/or intensity of wind driven mixing continued into the mid-Holocene (Kendall, 1969; Stager et al., 1997; Johnson et al., 2000; Stager and Johnson, 2000; Talbot and Lærdal, 2000; Stager et al., 2003). A change in the diatom assemblages and a shift to semi-deciduous, seasonally dry forest taxa indicated the development of more marked dry seasons (Kendall, 1969; Stager et al., 1997, 2003). By ~5 ka BP, declining diatom abundance and a shift to pennate diatoms indicated more extensive shallows and hence lower lake level (Stager, 1984; Stager and Johnson, 2000), together with decreasing pollen deposition (Kendall, 1969), indicated reduced rainfall associated with a weakening summer monsoon (Street-Perrott and Kutzbach, 1985), as recorded in many archives across

tropical Africa (Gasse, 2000; Barker et al., 2004). Further reduction in water column mixing associated with decreased windiness at Lake Victoria was observed from the presence of *Nitzschia fonticola* (Stager et al., 1997; Stager and Johnson, 2000; Stager et al., 2003). The pollen evidence supported a reduced lake area responding to increased aridity by the rise in sedge and grass pollen suggesting encroachment of swamp vegetation at inshore sites, and expansion of regional grasslands during the late Holocene (Kendall, 1969).

7.4 Core V95-1P stratigraphy

Core V95-1P (00° 27.63'S, 33° 24.09'E) was selected for this research due to its long and continuous record dating back to ~20 ka BP (Johnson et al., 2000). Another obvious choice would have been the well dated, continuous sequence of V95-2P (basal age 13,240 ^{14}C years) (Beuning et al., 1997a; Ngobi et al., 1998; Johnson et al., 2000; Talbot and Lærdal, 2000; Beuning et al., 2002). However, due to its popularity in the early stages of the IDEAL project it has been heavily sampled and very little material remains (Tom Johnson and Jim Russell, pers. comm.).

Core V95-1P was collected from a depth of 65m in the north-eastern part of the lake and had a total length of 906.5cm (Figures 7.5 and 7.9). Between the base of the core and 714.5cm a fine silty-clay crumbly mud with a cottage cheese texture was present. This unit was fairly uniform throughout with little evidence of organic material. Above this unit was layer (~55cm-thick) of very fine grained mud containing large plant macrofossils including reed stem fragments. From 686-619.5cm a dark massive mud unit of a crumbly cottage cheese texture containing 'crumbs' of ~5mm were present. Scattered shells and wood fragments were found throughout the unit. A gradual transition into the overlying unit occurred, consisting of homogenous, massive, soft to firm mud for the remainder of the core. Between ~550-400cm sediments were described as diatomaceous muds. Based on the sediment texture two palaeosols have been identified in V95-1P (Tom Johnson and Jim Russell, pers. comm.), similar to V95-2P (Talbot and Lærdal, 2000), which indicates that the lake must have desiccated at these sites at least twice to enable soil formation. The upper palaeosol formed between 686 to 619.5cm and the lower palaeosol formed from the base of the core (906.5cm) to 741.5cm.

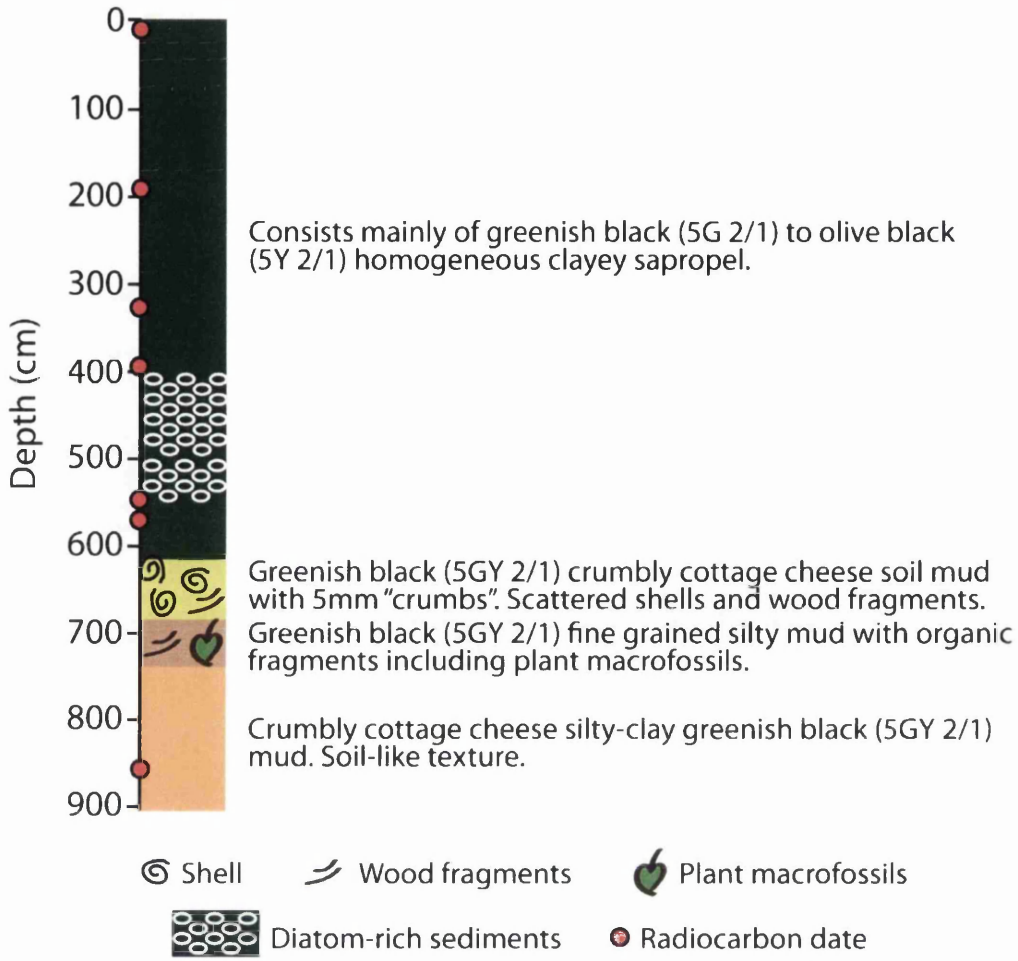

Figure 7.9: Core description of V95-1P and stratigraphic locations of radiocarbon dates. Stratigraphic unit descriptions were taken from the core log provided by Tom Johnson. Colours used to differentiate between units.

7.5 Age model

The age model for the Lake Victoria core V95-1P is based on seven radiocarbon dates (Table 7.1) (Johnson et al., 2000). It was deemed most appropriate to use the structure of the original, published age-depth model (linear interpolation) for V95-1P to enable direct comparison of data obtained in this thesis with other palaeoenvironmental data already derived from V95-1P, which may aid interpretation of the data presented in this thesis. Radiocarbon dates were re-calibrated with the most recent version of CALIB (version 6.0) (Stuiver et al., 2012) and the mid-point of the calibrated age range (1σ) was used (Table 7.1). The re-calibrated radiocarbon dates were inserted into the original age-depth model which was formed using linear interpolation between dates to allow for varying

sedimentation rates (Figure 7.10) (original age-model structure from Johnson et al. (2000)).

Table 7.1: Summary of ^{14}C age determinations for core V95-1P. Radiocarbon ages were re-calibrated to calendar years using CALIB 6.0 (Stuiver et al., 2012).

Depth (cm)	^{14}C date	Error (^{14}C years)	Calibrated age range (1σ) using CALIB 6.0		Calendar years BP (mid-point)	Calibrated dates after Johnson et al. 2000 (cal. yrs BP)	Material
5	1420	70	1285	1385	1335	1304	Pollen
199	4595	75	5373	5462	5418	5304	Pollen
318.5	6700	110	7485	7658	7572	7532	Pollen
398	8380	70	9395	9479	9437	9414	Pollen
548	11635	160	13332	13660	13496	13566	Pollen
568	12180	185	13796	14259	14028	14241	Pollen
859	16760	140	19810	20130	19970	19763	Pollen

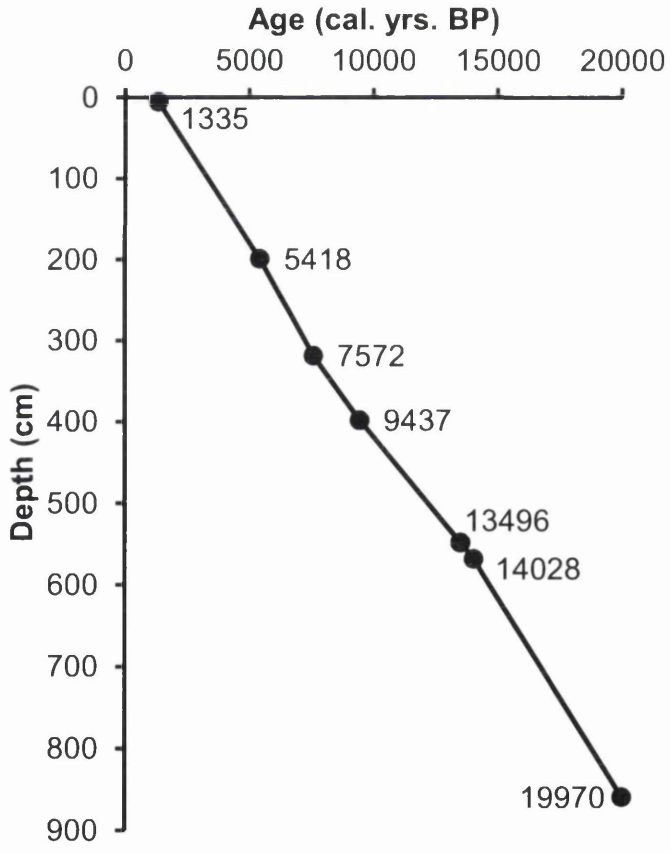

Figure 7.10: Age-depth model for V95-1P. Dates are expressed in calendar years BP (cal. yrs BP) (modified after Johnson et al. (2000)).

7.6 Existing data for core V95-1P

Existing data available for V95-1P, from Johnson et al. (1998), were plotted downcore (Figure 7.10a) using the age model formulated in section 7.5. Biogenic silica (BSi) concentrations reflect the accumulation of diatom frustules in Lake Victoria (Johnson et al., 1998). BSi below the upper palaeosol surface was low (4-5%). Shortly after the palaeosol at ~14.2 ka BP BSi rose to ~17% before temporarily decreasing to ~10% and then maximising at 36% at ~11.6 ka BP. Between ~10 and 8 ka BP, BSi declined to minima values of only 3-4%. After 8 ka BP, BSi rose to ~10% and remained stable for the remainder of the record. The availability of dissolved Si (DSi) for diatom uptake is controlled by the net supply from the catchment (inflows minus outflows) (Hecky et al., 1996; Johnson et al., 1998), rather than internal cycling in the lake which could only sustain itself for ~40 years based on the DSi reservoir in the lake (Johnson et al., 1998).

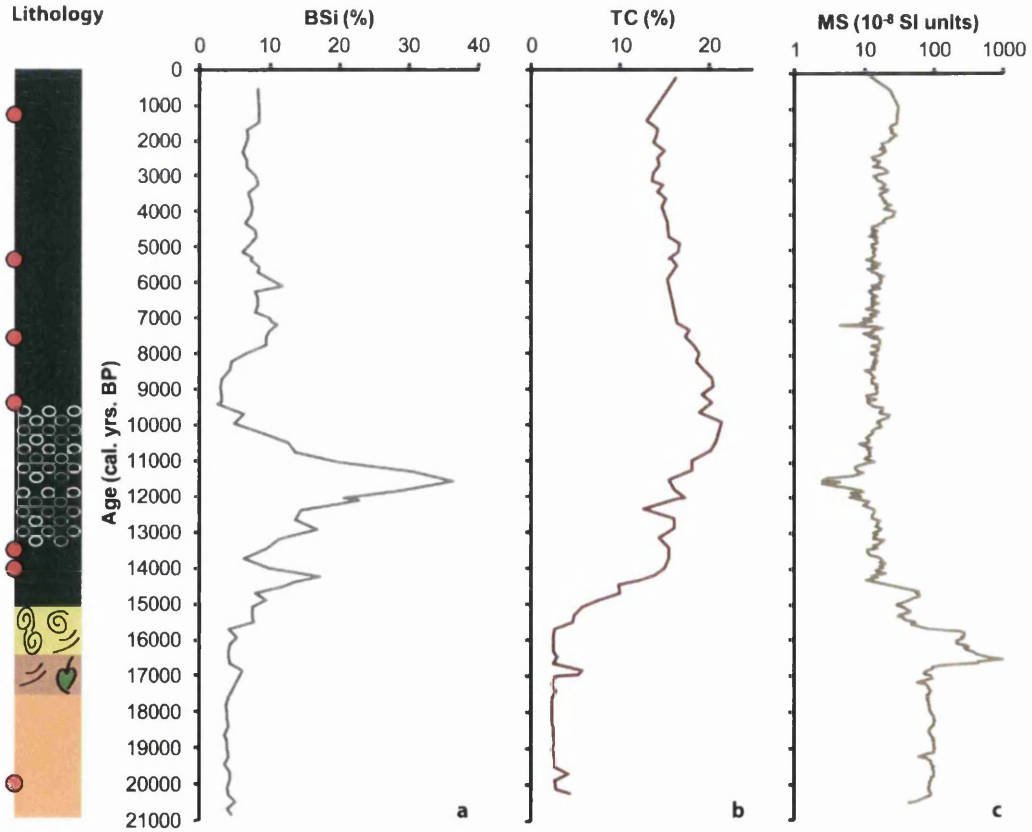

Figure 7.11: Biogenic silica (BSi) concentrations (a), total carbon (TC) (b) and magnetic susceptibility (MS) (c) data for core V95-1P. TC represents organic carbon as Lake Victoria sediments are carbonate free (from Johnson et al. (1998)).

The total carbon (TC) record for V95-1P represents total organic carbon as Lake Victoria sediments were carbonate free (Figure 7.11b) (Johnson et al., 1998). Organic carbon was very low (<3%) below the upper palaeosol surface, peaking slightly at ~17 ka BP. Above the upper palaeosol surface TC rose rapidly to between 10 and 20% for the remainder of the record. Maximum values (~22%) were reached at 10 ka BP. High hydrogen index (HI) in V95-2P indicated that organic matter in Lake Victoria was predominately from an algal origin (Talbot and Lærdal, 2000). The upper palaeosol was clearly marked by a peak in magnetic susceptibility (MS) between ~16.7 and 15.6 ka BP (Figure 7.11c). After ~14.3 ka, MS remained fairly stable between 15-25x10^{-8} SI units.

7.7 Preparation of Lake Victoria sediment samples for O- and Si-isotope analysis of diatom silica

Sediments below the upper palaeosol surface (~620cm; 15 ka BP) had very low BSi concentrations and were largely devoid of diatoms (Figure 7.11a). Therefore emphasis was placed on sediments above this surface which had BSi concentrations of between 3% and 36%. Sediment samples representing every ~500 years during the last 15 ka BP were treated chemically to remove organic matter and carbonates, and sieved at 63, 38 and 20μm (detailed methodologies can be found in section 5.4.5 of Chapter 5). All samples were inspected by light microscopy and assessed for their remaining sediment components. The main contaminants remaining within the Lake Victoria samples, together with the diatoms, were green algae (Chlorococcales), mineral grains (silts and clays) and charcoal fragments (Figure 7.12). For many of the samples (>50%), the ratio of diatoms to other sediment components was low, which made them unsuitable for further analysis as it was unlikely, even if it proved possible to separate the diatoms from the contaminants, that there would be enough diatom material for isotope analysis (3-5mg). It was only possible to purify samples from nine depths during the last ~15 ka BP. The following section outlines the sample-specific methods used to clean-up diatom silica from Lake Victoria, in addition to the standard techniques described in section 5.4.5 of Chapter 5.

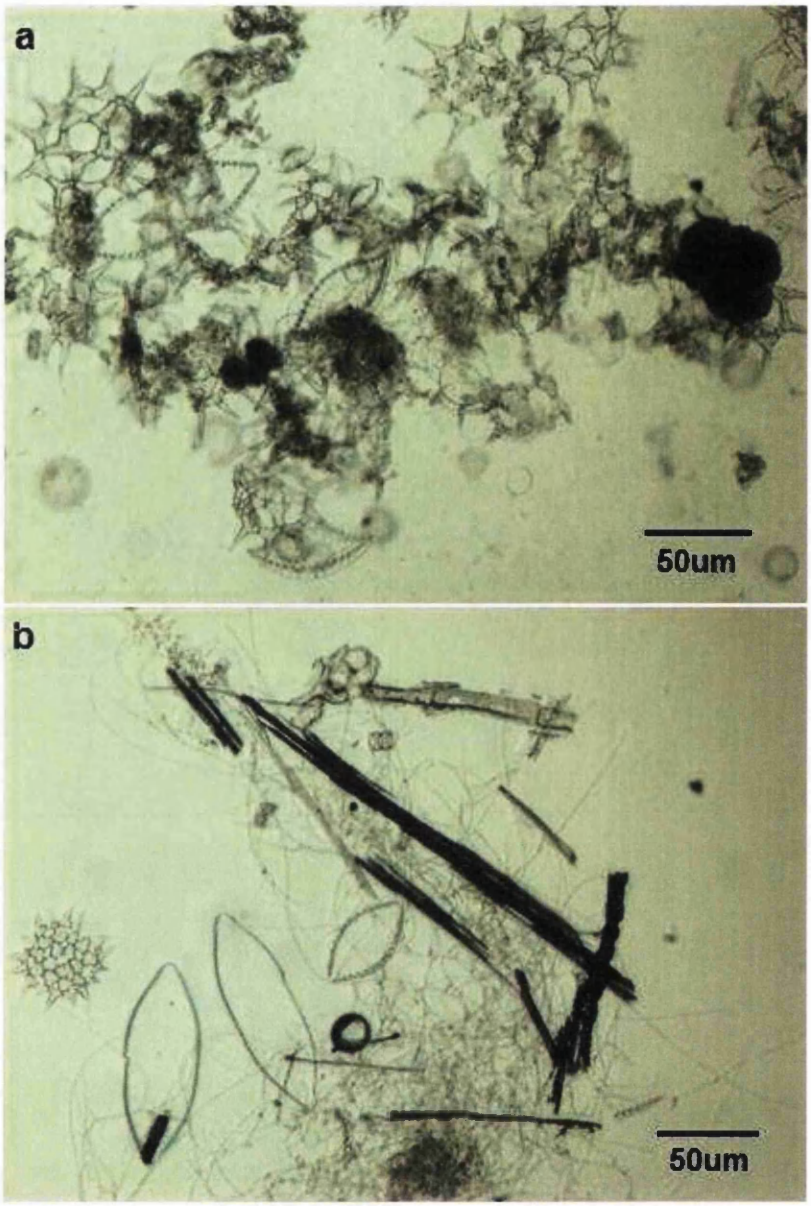

Figure 7.12: Typical composition of Lake Victoria sediment samples after chemical treatment to remove organic matter and carbonates: (a) large *Surirella* spp. and *Stephanodiscus* spp. with *Pediastrum simplex* var. *clathratum* and *Botryococcus braunii* (green algae); (b) large *Surirella* spp. with *Pediastrum simplex* var. *clathratum* and large flecks of charcoal.

7.7.1 Sample specific methodologies used to clean up diatom silica from Lake Victoria for stable-isotope analysis (O and Si)

Three genera of green algae, *Botryococcus, Pediastrum and Coelastrum* (Figure 7.13), survived the chemical treatment and were present throughout the core above the upper palaeosol. *Botryococcus braunii* and *Pediastrum simplex* var. *clathratum* were the most abundant species, with *Pediastrum boryanum*, *Pediastrum duplex* and *Coelastrum reticulatum* being less common. Sporopollenin in the cell walls of the green algae make them resistant to the chemical digestions used in this thesis (see section 5.4.5 in Chapter 5) (Jankovská and Komárek, 2000), and due to their similarity in size to the diatoms (20-80μm) they cannot be physically separated by sieving. Although rarely utilised, green algae can provide additional palaeoecological information for reconstructing past environments (van Geel, 2001).

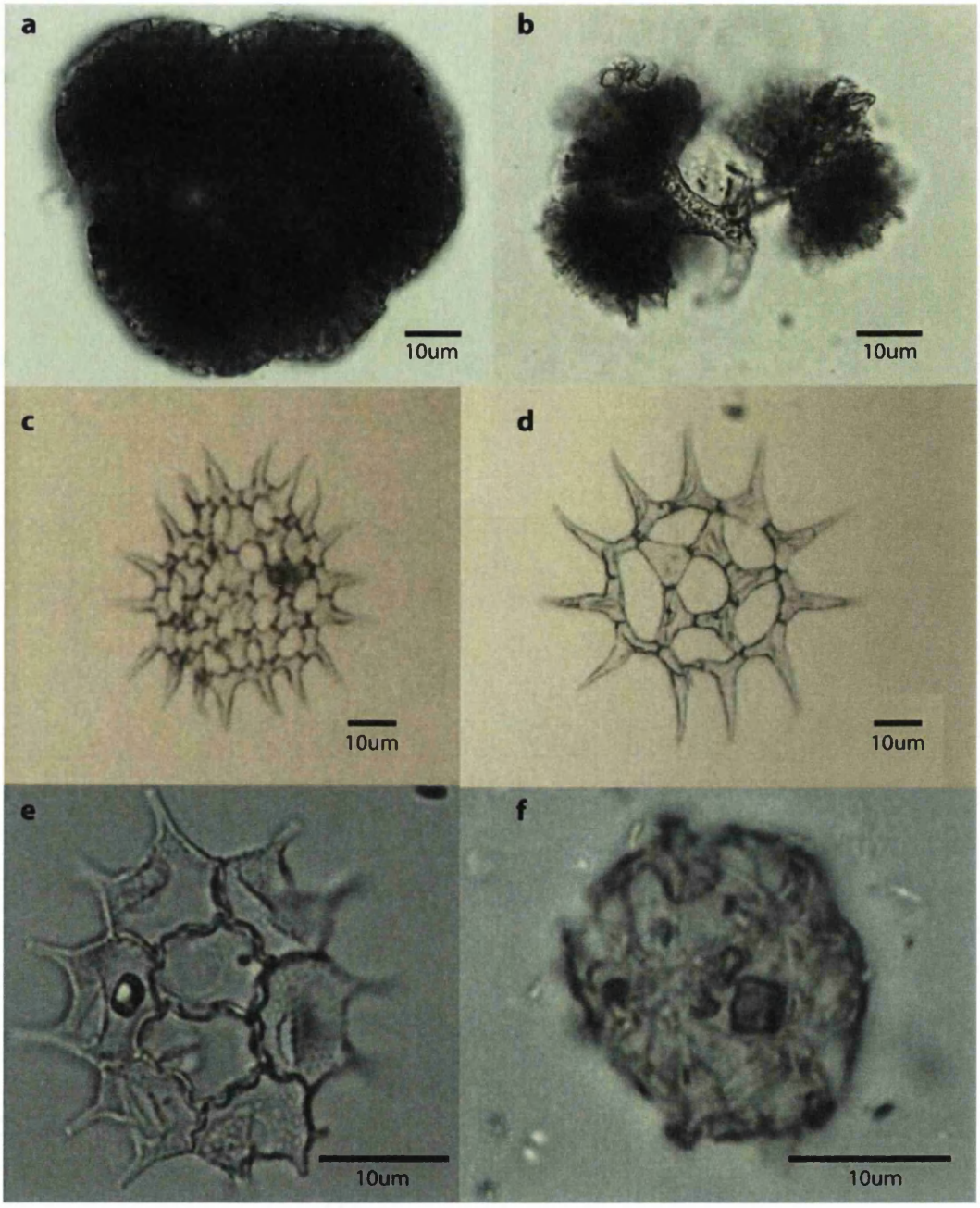

Figure 7.13: Light microscopy images of (a) *Botryococcus braunii* (8.4 ka BP), (b) *Botryococcus braunii* (5.8 ka BP), (c) *Pediastrum simplex* var. *clathratum* (14.9 ka BP), (d) *Pediastrum simplex* var. *clathratum* (11.6 ka BP), (e) *Pediastrum boryanum* (5.8 ka BP), (f) *Coelastrum reticulatum* (1.4 ka BP), found in Lake Victoria sediment samples throughout the last 15 ka BP.

Initially stronger acids (conc. nitric acid) were used to try and remove the remaining green algae but due to the sporopollenin in the cell walls this had little effect. Sonication was also used to see whether the green algae broke up into finer pieces so that they could be sieved out. Again, their resistant cell structure prevented them from disintegrating. As the densities of the green algae species were unknown, it was considered possible that if there was a density difference or a difference in the hydrodynamics properties between them and the diatoms then split-flow thin fractionation (SPLITT) could be used to separate the two components. However, using SPLITT, it soon became apparent that the spines of the *Pediastrum* spp. became interlocked, causing a blockage and preventing the remainder of the sample from flowing through the SPLITT. Eventually, differential settling was effective at separating *Pediastrum* and *Coelastrum* spp. from the diatoms. *Pediastrum* and *Coelastrum* appeared to be denser than the diatoms and *Brotryococcus braunii* as they sank first and allowed the later to be decanted off. This was also an efficient way to separate fine silt and clay mineral fragments and large sponge spicules from the diatoms (Figure 7.14). Subsequently, successful separation of the *Botryococcus braunii* from the diatoms came about when using SPT, to see whether the *Botryococcus braunii* could be separated by density. During the wash stages of the SPT procedure, *Botryococcus braunii* would float to the top of the centrifuge tube, allowing the green alga to be decanted off, indicating that the green alga were either significantly less dense than the diatoms of more hydrodynamic. To overcome the problem of contamination from charcoal, sub-samples in the >63μm range were avoided for isotope analysis. With the combination of methods and techniques available, purification of 10 individual samples from nine different depths from core V95-1P were suitably prepared for isotope analysis (full list of samples prepped in Appendix VII).

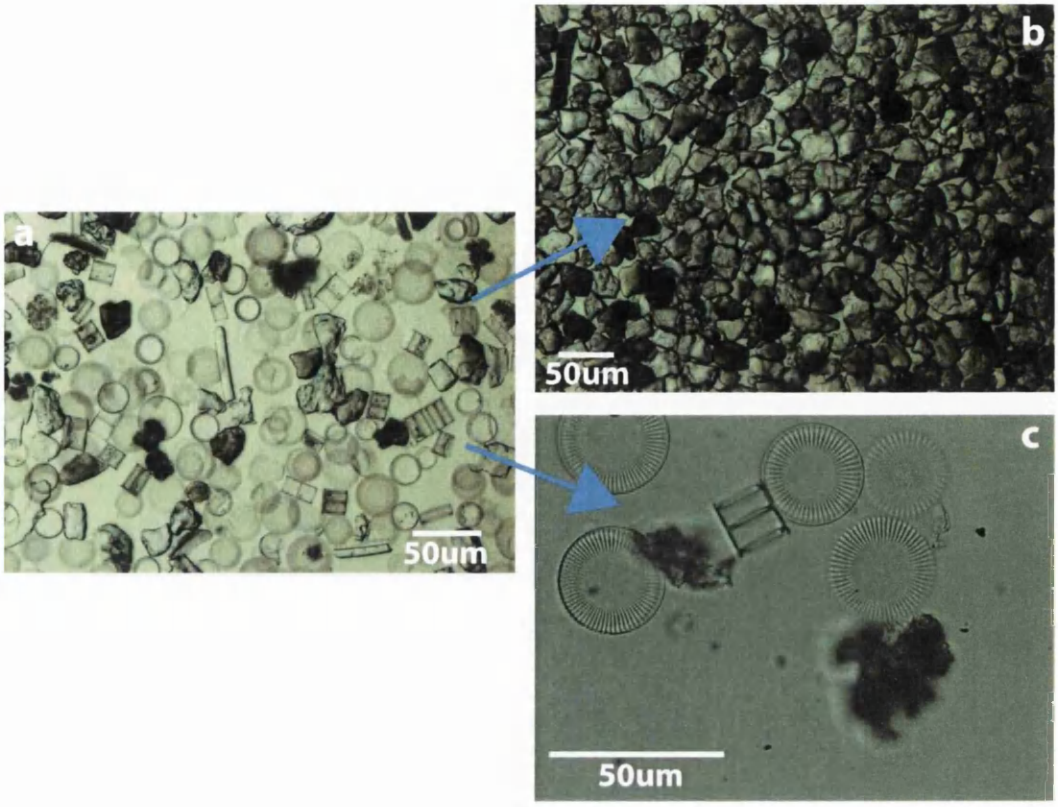

Figure 7.14: Using the differential settling approach to separate remaining sediment components (a) into mineral fraction (b); and diatom plus *Botryococcus braunii* fraction (c).

7.8 Lake Victoria sediment samples for lipid analysis

Samples were selected for lipid analysis at 500 yr resolution from the base of the core (~20 ka BP) to ~1 ka BP at the top (n = 38). The methods used to identify and quantify *n*-alkanes, *n*-alkenes and botryococcenes compounds from the total lipid fraction are fully described in Chapter 5, sections 5.4.8 to 5.4.9.

7.9 Results

7.9.1 Purified diatom silica

Diatoms represent the largest proportion of biogenic silica (>99%) in Lake Victoria sediments apart from the occasional sponge spicule or phytolith (Figure 7.15). Samples were comprised of a relatively small range of diatom species with the most abundant taxa being *Stephanodiscus*, *Aulacoseira* and *Surirella* spp. (Figure 7.16).

The most common size fraction of material used for isotope analysis was the 20-38µm fraction composed of predominantly *Stephanodiscus* and *Aulacoseira* spp. and occasional fragments of large *Surirella* spp. Breakage of the diatom frustules (e.g. Figure 7.16c & d) may have occurred during the cleaning of the diatoms for isotope analysis, as the remainder of the diatoms were well preserved throughout the core and there were no signs of dissolution or diagenesis (Figure 7.17). Only samples that were at least 97% free from contamination were chosen for isotope analysis (see section 5.4.7 in Chapter 5). These were examined and assessed by light microscopy and SEM. None of the analysed samples showed evidence of contamination based on replicated samples and from the observed relationship between $\delta^{29}Si$ and $\delta^{30}Si$ (Figure 7.18). All samples plot along the expected mass-dependent relationship of $\delta^{29}Si$ vs. $\delta^{30}Si$. This supports the analysis of contamination-free samples. Overall precision (2σ), based on replicate samples, was ±0.06‰ for $\delta^{29}Si$, ±0.14‰ for $\delta^{30}Si$ and ±0.38‰ for $\delta^{18}O$. All the samples analysed are presented in the following section (Figure 7.19).

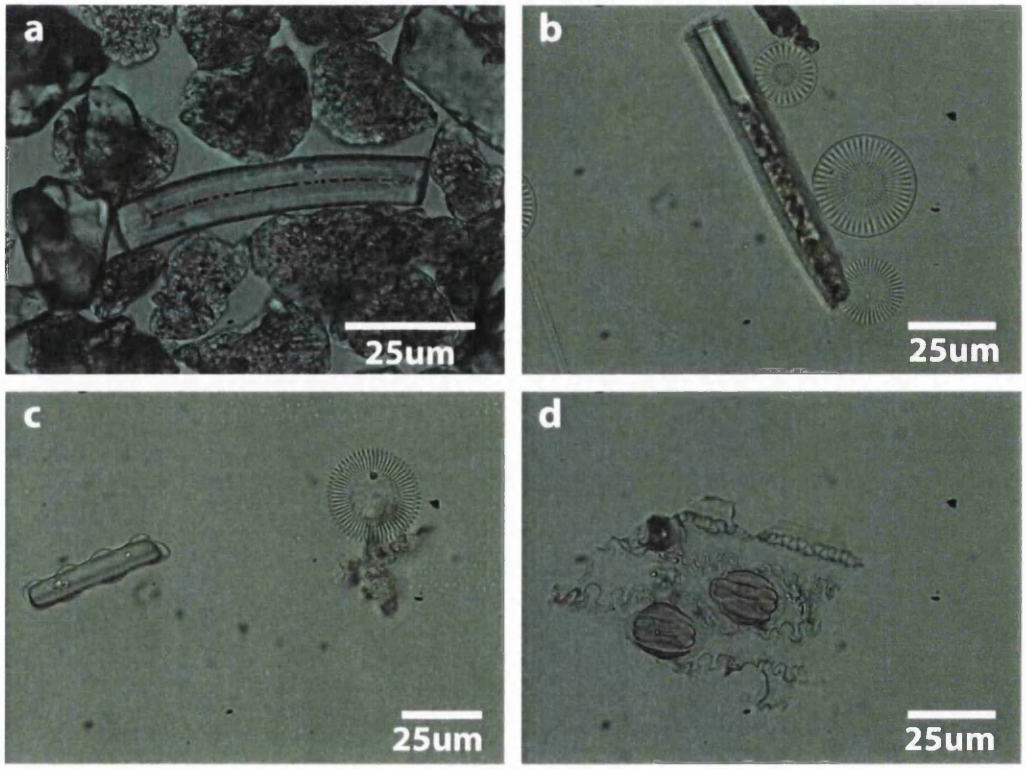

Figure 7.15: Light microscope images of sponge spicules (a & b), phytoliths (c) and grass cuticles with dumbbell-shaped phytoliths (d) which are occasionally present in Lake Victoria sediments.

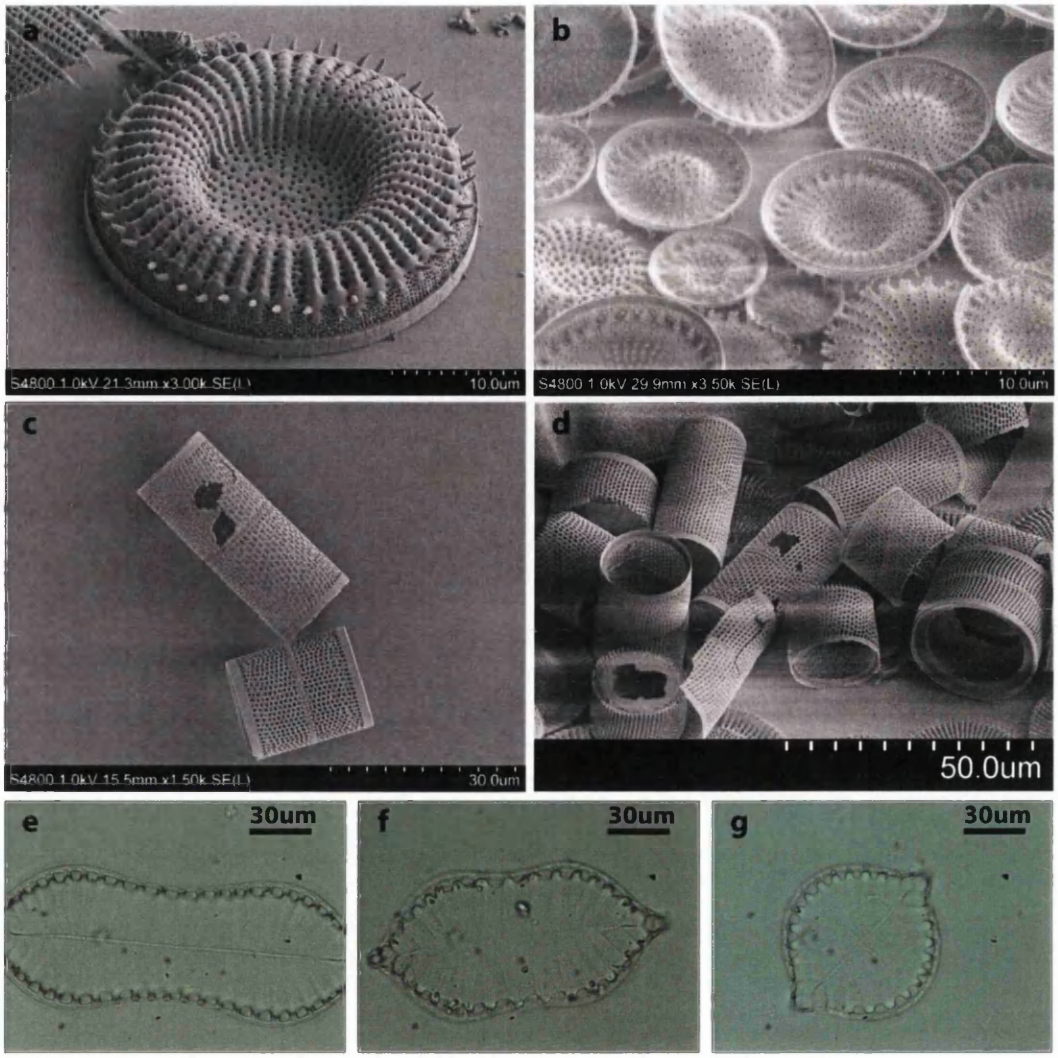

Figure 7.16: The most abundant diatom taxa in Lake Victoria. SEM photomicrographs of *Stephanodiscus* spp. (a & b) and *Aulacoseira* spp. (c & d) and light microscope images of *Surirella* spp. (e-g).

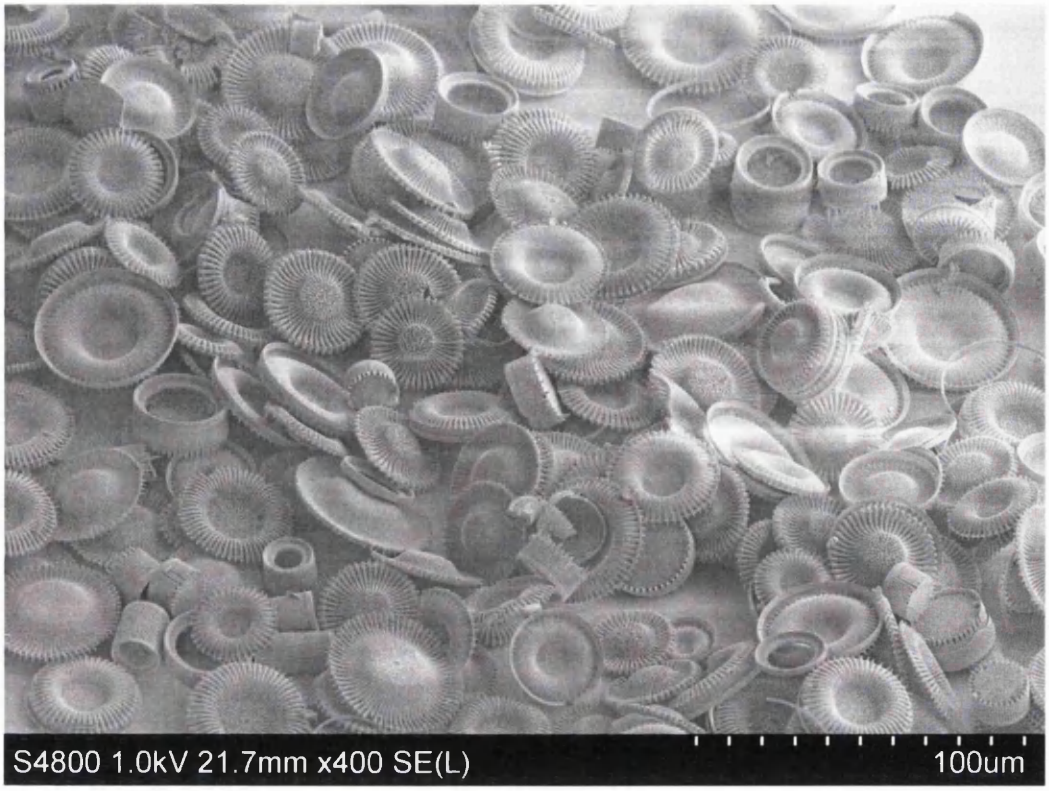

Figure 7.17: SEM image of cleaned diatoms from Lake Victoria (11.6 ka BP) showing the typical excellent preservation and purity of a diatom sample for isotope analysis.

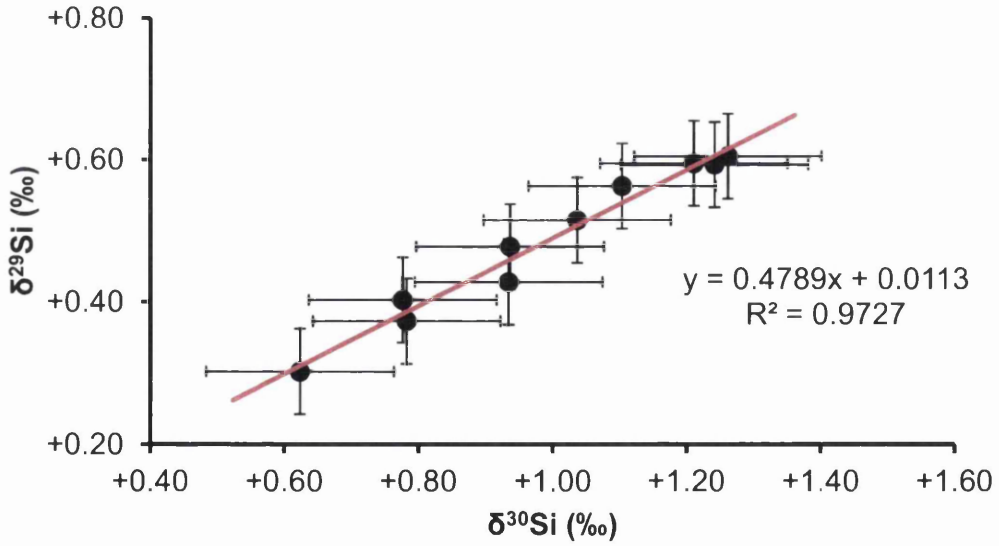

Figure 7.18: Silicon isotope measurements of all Lake Victoria samples. Error bars are ±0.06‰ for $\delta^{29}Si$ and ±0.14‰ for $\delta^{30}Si$ (2σ).

7.9.2 Oxygen and silicon isotope analysis of diatom silica

In the analysed sediments (dated 14.9 to 1.4 ka BP), $\delta^{18}O_{diatom}$ values varied from +39.4 to +44.0‰, corresponding to a range of 4.6‰ during the last 15 ka BP (Table 7.2; Figure 7.19a). During the late-glacial period, from 15 to 11.5 ka BP, $\delta^{18}O_{diatom}$ values were high and reached a maximum of +44.0‰ at 11.6 ka BP. At the beginning of the Holocene (~11.5 ka BP) a sudden shift to a minimum $\delta^{18}O_{diatom}$ value of +39.4‰ occurred at 10.7 ka BP. $\delta^{18}O_{diatom}$ values remained low throughout the early to mid-Holocene (11.5 to 5.5 ka BP). From the late Holocene onwards (from 5.5 ka BP) $\delta^{18}O_{diatom}$ values began to increase and then fell again to +40.6‰ at 1.4 ka BP.

$\delta^{30}Si_{diatom}$ values ranged from +0.62 to +1.26‰ during the last 15 ka BP, resulting in a total variation of 0.64‰ (Table 7.2; Figure 7.19b). During the late-glacial, $\delta^{30}Si_{diatom}$ values were high and displayed a gradual decrease of 0.30‰ from 15 to 11.6 ka BP. At the start of the Holocene, a decrease to +0.62‰ occurred, representing the lowest $\delta^{30}Si_{diatom}$ values recorded. $\delta^{30}Si_{diatom}$ values remained low and relatively stable during the early to mid-Holocene of between +0.62 to +0.94‰. From 5.5 ka BP onwards, $\delta^{30}Si_{diatom}$ values increased, reaching a maxima of +1.26‰ at 1.4 ka BP.

The relationship between $\delta^{30}Si_{diatom}$ and $\delta^{18}O_{diatom}$, although not directly causative and not statistically significant (R^2 = 0.25; p = 0.14), shows a trend of increasing $\delta^{30}Si_{diatom}$ with increasing $\delta^{18}O_{diatom}$ (Figure 7.20).

Table 7.2: Oxygen and Silicon isotope values from Lake Victoria with corresponding depths and calculated estimated ages.

Depth (cm)	Age (cal. yr. BP)	Size Fraction (µm)	$\delta^{18}O_{diatom}$ (‰)	$\delta^{29}Si_{diatom}$ (‰)	$\delta^{30}Si_{diatom}$ (‰)
7.50	1388	20-38	+40.6	+0.61	+1.26
86.75	3057	20-63	+42.4	+0.56	+1.10
200.75	5448	20-38	+41.7	+0.40	+0.78
337.50	8020	20-38	+40.7	+0.37	+0.78
352.00	8361	20-38	+40.1	+0.48	+0.94
443.50	10655	20-38	+39.4	+0.30	+0.62
480.25	11648	20-38	+44.0	+0.43	+0.93
520.25	12730	20-38	+40.5	+0.52	+1.04
612.25	14922	<20	+43.7	+0.59	+1.24
612.25	14922	<20	+43.3	+0.60	+1.21

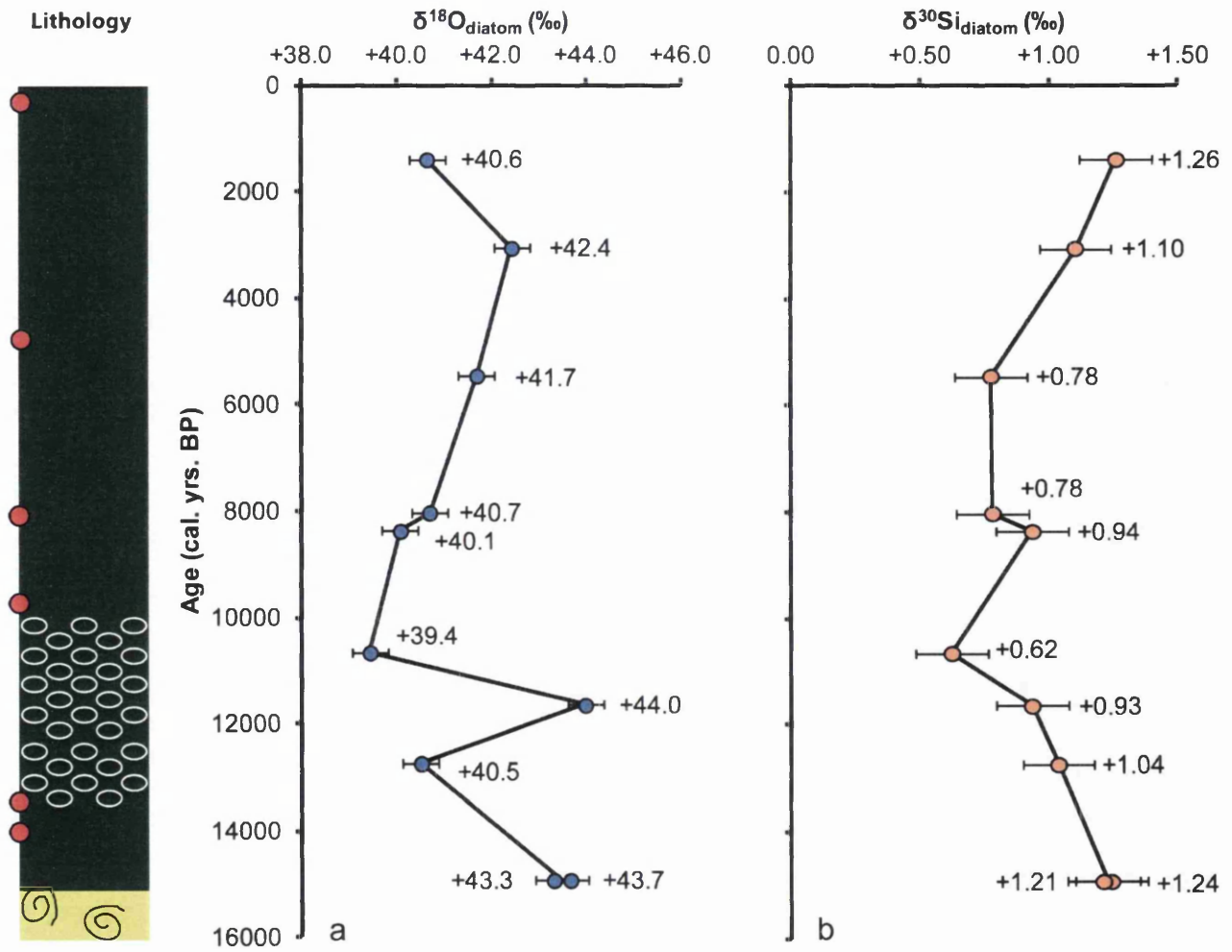

Figure 7.19: Variations in (a) $\delta^{18}O_{diatom}$ and (b) $\delta^{30}Si_{diatom}$ values in Lake Victoria during the last 15 ka BP. Labelled circles represent individual samples analysed with error bars (2σ). For replicated samples, the mean is used. For core description see Figure 7.9.

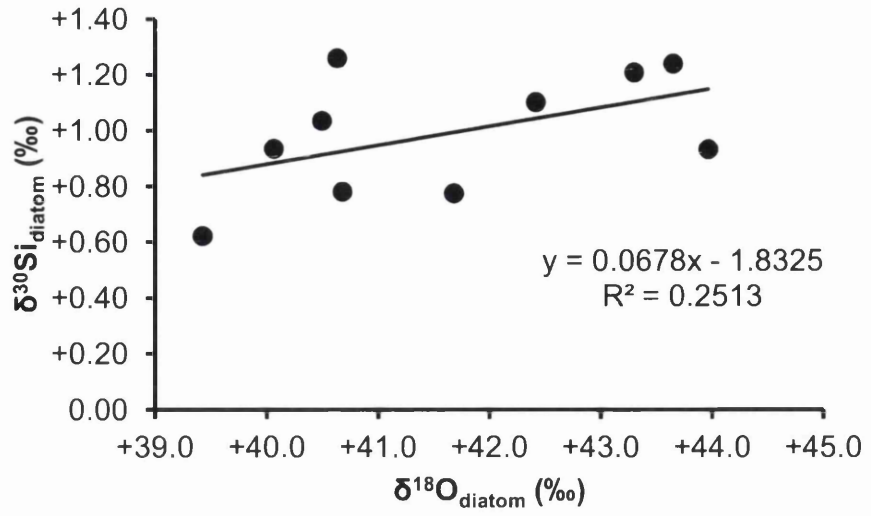

Figure 7.20: $\delta^{30}Si_{diatom}$ vs. $\delta^{18}O_{diatom}$ values from Lake Victoria sediments during the last 15 ka BP.

7.9.3 Lipids: abundance and distribution

The hydrocarbon fraction of total lipids was identified and quantified for the length of V95-1P core, representing the last ~21 ka BP (see Appendix VIII for full dataset). The Carbon Preference Index (CPI), a test for n-alkane maturity and preservation, showed that the n-alkane distributions in Lake Victoria had an odd-over-even predominance (Figure 7.21a; Table 7.3), as expected for hydrocarbon fractions (Meyers and Ishiwatari, 1993). The CPI was low (1.3-2.8) between ~20.7 to 11.5 ka BP (Figure 7.21a) which may reflect an in-wash of degraded plant material from the catchment. Abundances of *n*-alkanes were relatively low but consistently so throughout the record (Table 7.3), providing further support for good preservation of organic matter. The straight-chain hydrocarbons (*n*-alkanes and *n*-alkenes) were dominated by mid- and long-chain homologues (Figures 7.21 and 7.22; Table 7.1). C_{23}, C_{25}, C_{27}, C_{29}, C_{31} and C_{33} *n*-alkanes all had significant abundances. The C_{25} and C_{27} homologues were the dominant *n*-alkanes throughout the core, indicative of submerged/floating aquatic macrophytes origin (Ficken et al., 2000) and a higher plant origin (Eglinton and Hamilton, 1967) respectively, although the uppermost sample (LV1) also had an abundance of the short-chain *n*-alkanes (C_{17} and C_{19}) suggesting a significant contribution from aquatic algae (Cranwell et al., 1987).

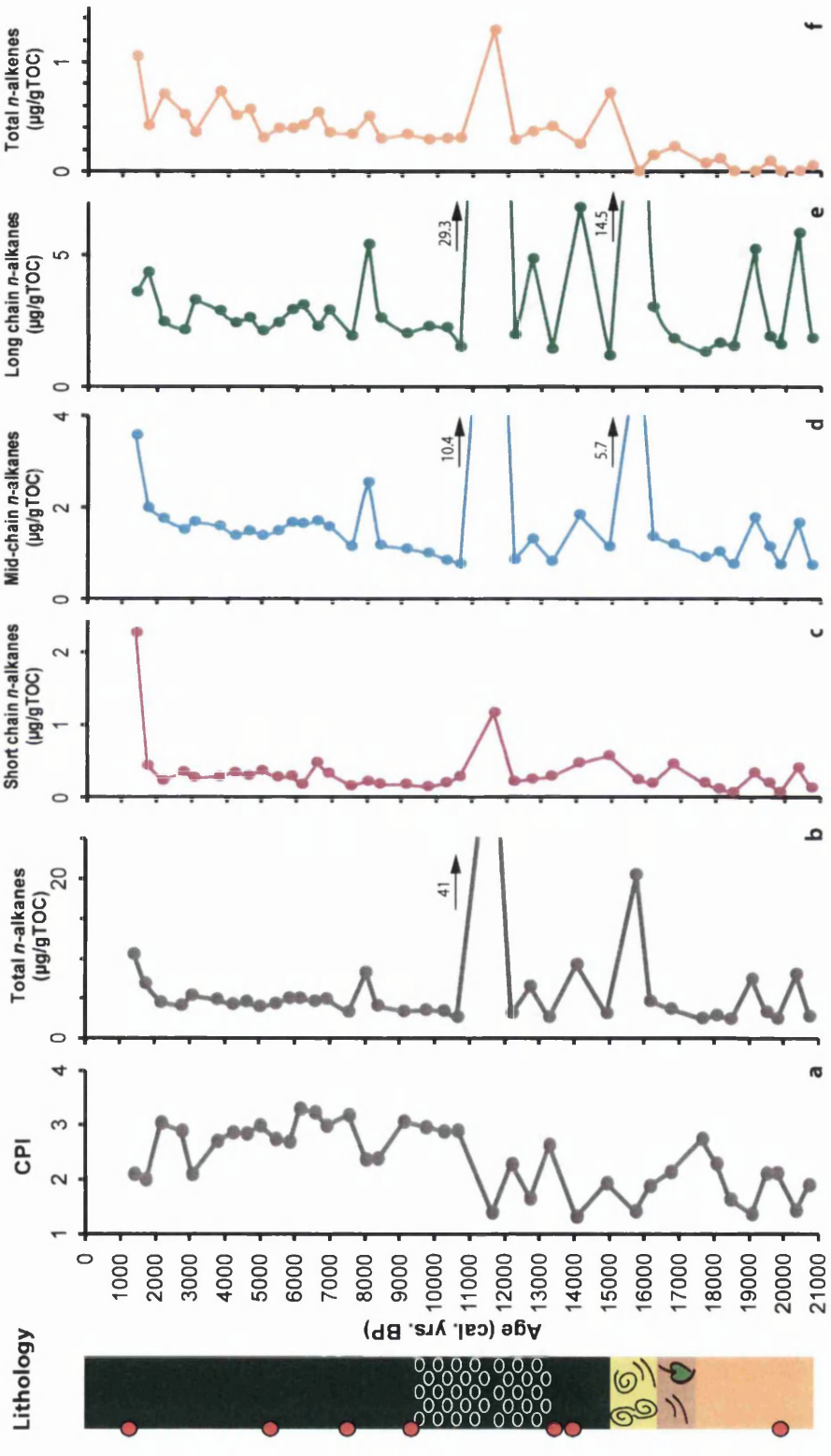

Figure 7.21: Carbon Preference Index (CPI) for *n*-alkanes from Lake Victoria (a) and their total abundance downcore (b). Short chain (C_{19}-C_{21} inclusive) (c), Mid-chain (C_{22}-C_{25} inclusive) (d) and Long chain (C_{26}-C_{35} inclusive) *n*-alkane abundance. Total *n*-alkene abundance (f). All abundances are expressed in µg/gTOC.

Table 7.3: Abundance and distribution parameters of *n*-alkanes, *n*-alkenes and botryococcenes in Lake Victoria during the last ~20.7 ka BP.

	n-alkanes										*n*-alkenes				Botryococcenes
Sample name	Age (cal. yr. BP)	Total abundance (µg/gTOC)	C no. Range	Most abundant C no.	CPI[1]	Short chain C_{19}-C_{21} inclusive (µg/gTOC)	Mid-chain C_{22}-C_{25} inclusive (µg/gTOC)	Long chain C_{26}-C_{35} inclusive (µg/gTOC)	P_{wax}[2]	P_{aq}[3]	Total abundance (µg/gTOC)	C no. Range	Most abundant C no.	P_{alg}[4]	Total abundance (µg/gTOC)
LV1	1388	10.5	17-35	25	2.1	2.3	3.6	3.6	0.50	0.69	1.05	18-29	27	0.32	9.5
LV2	1720	6.8	18-35	27	2.0	0.4	2.0	4.3	0.64	0.53	0.42	18-27	27	0.17	6.8
LV3	2162	4.5	18-35	27	3.0	0.2	1.8	2.5	0.56	0.68	0.71	20-29	27	0.36	6.7
LV4	2757	4.1	18-35	27	2.9	0.3	1.5	2.2	0.58	0.63	0.52	18-27	27	0.31	5.2
LV5	3057	5.3	18-35	27	2.1	0.3	1.7	3.3	0.62	0.57	0.36	20-27	27	0.19	6.9
LV6	3772	4.8	18-35	27	2.7	0.3	1.6	2.9	0.63	0.56	0.73	20-27	26	0.23	5.9
LV7	4220	4.2	18-35	27	2.9	0.3	1.4	2.4	0.62	0.58	0.51	18-29	27	0.23	7.5
LV8	4615	4.5	17-35	27	2.8	0.3	1.5	2.6	0.62	0.59	0.57	18-29	27	0.26	8.3
LV9	4993	3.9	18-35	27	3.0	0.4	1.4	2.1	0.60	0.61	0.31	19-27	27	0.23	4.9
LV10	5448	4.3	18-35	27	2.7	0.3	1.5	2.4	0.59	0.61	0.39	18-27	27	0.24	2.5
LV11	5843	4.9	18-35	27	2.7	0.3	1.7	2.9	0.61	0.60	0.39	18-27	27	0.22	4.3
LV12	6141	4.9	18-35	27	3.3	0.2	1.6	3.1	0.64	0.55	0.42	20-28	27	0.21	8.6
LV13	6564	4.6	18-35	27	3.2	0.5	1.7	2.3	0.57	0.64	0.54	18-28	27	0.29	7.5
LV14	6893	4.9	18-35	27	3.0	0.3	1.6	2.9	0.63	0.55	0.35	18-27	27	0.19	9.2
LV15	7537	3.2	18-35	27	3.2	0.2	1.1	1.9	0.60	0.59	0.34	18-28	27	0.26	7.2
LV16	8020	8.2	18-35	27	2.4	0.2	2.5	5.4	0.66	0.49	0.50	18-27	27	0.15	11.6
LV17	8361	4.0	18-35	27	2.4	0.2	1.2	2.6	0.65	0.52	0.30	18-27	27	0.19	15.2
LV18	9112	3.3	18-35	27	3.1	0.2	1.1	2.0	0.63	0.54	0.34	19-27	27	0.25	8.1
LV19	9743	3.5	18-35	27	3.0	0.1	1.0	2.3	0.68	0.47	0.29	18-27	27	0.19	6.0
LV20	10263	3.4	17-35	27	2.9	0.2	0.8	2.3	0.71	0.40	0.30	18-27	27	0.17	6.8
LV21	10655	2.6	18-35	27	2.9	0.3	0.8	1.5	0.67	0.47	0.30	18-27	27	0.21	2.6
LV22	11648	40.9	18-35	27	1.4	1.2	10.4	29.3	0.69	0.44	1.29	18-27	27	0.10	2.4
LV23	12209	3.1	18-35	27	2.3	0.2	0.9	2.0	0.66	0.48	0.29	18-27	27	0.22	0.3
LV24	12730	6.5	18-35	27	1.7	0.2	1.3	4.9	0.74	0.36	0.37	18-27	27	0.13	1.1

Table 7.3 (cont.)

	n-alkanes										*n*-alkenes				Botryococcenes
Sample name	Age (cal. yr. BP)	Total abundance (µg/gTOC)	C no. Range	Most abundant C no.	CPI[1]	Short chain C_{19}-C_{21} inclusive (µg/gTOC)	Mid-chain C_{22}-C_{25} inclusive (µg/gTOC)	Long chain C_{26}-C_{35} inclusive (µg/gTOC)	P_{wax}[2]	P_{aq}[3]	Total abundance (µg/gTOC)	C no. Range	Most abundant C no.	P_{alg}[4]	Total abundance (µg/gTOC)
LV25	13284	2.6	18-35	27	2.6	0.3	0.8	1.4	0.64	0.52	0.41	18-29	27	0.27	1.2
LV26	14068	9.2	18-35	27	1.3	0.5	1.8	6.8	0.74	0.38	0.25	22-27	27	0.09	0.5
LV27	14922	3.1	17-35	25	1.9	0.6	1.1	1.2	0.52	0.65	0.72	18-27	27	0.48	1.2
LV28	15748	20.4	18-35	27	1.4	0.2	5.7	14.5	0.66	0.49	0.00	–	–	–	0.2
LV29	16157	4.6	19-35	27	1.9	0.2	1.4	3.0	0.65	0.51	0.15	22-27	27	0.11	0.1
LV30	16753	3.6	17-35	27	2.1	0.5	1.2	1.8	0.59	0.58	0.22	18-27	27	0.17	1.0
LV31	17657	2.4	18-35	27	2.8	0.2	0.9	1.3	0.58	0.62	0.07	20-26	25	0.06	0.1
LV32	18070	2.8	18-35	27	2.3	0.1	1.0	1.7	0.59	0.59	0.12	20-26	26	0.03	0.1
LV33	18468	2.4	19-35	27	1.6	0.1	0.8	1.5	0.61	0.57	0.00	–	–	–	0.1
LV34	19080	7.4	18-35	27	1.4	0.3	1.8	5.2	0.69	0.45	0.00	–	–	–	0.1
LV35	19509	3.2	19-35	27	2.1	0.2	1.1	1.9	0.59	0.59	0.09	23-25	23	0.12	0.1
LV36	19815	2.4	19-35	27	2.1	0.1	0.7	1.6	0.65	0.51	0.00	–	–	–	0.1
LV37	20350	8.0	18-35	27	1.4	0.4	1.7	5.8	0.73	0.39	0.00	–	–	–	0.1
LV38	20728	2.7	19-35	27	1.9	0.1	0.7	1.8	0.68	0.47	0.05	23-27	27	0.07	0.0

[1]Carbon Preference Index (CPI): $2(C_{23-31}odd)/(C_{22-30}even + C_{24-32}even)$.
[2]P_{wax} (*n*-alkane land plant proxy) = $(C_{27} + C_{29} + C_{31})/(C_{23} + C_{25} + C_{27} + C_{29} + C_{31})$ (Zheng et al., 2007).
[3]P_{aq} (*n*-alkane non-emergent aquatic plant proxy) = $(C_{23} + C_{25})/(C_{23} + C_{25} + C_{29} + C_{31})$ (Ficken et al., 2000).
[4]P_{alg} (*n*-alkene algal proxy) = $(C_{23:1} + C_{25:1} + C_{27:1})/(C_{23:1} + C_{25:1} + C_{27:1} + C_{29} + C_{31} + C_{33})$ (modified after Zhang et al. (2004)).

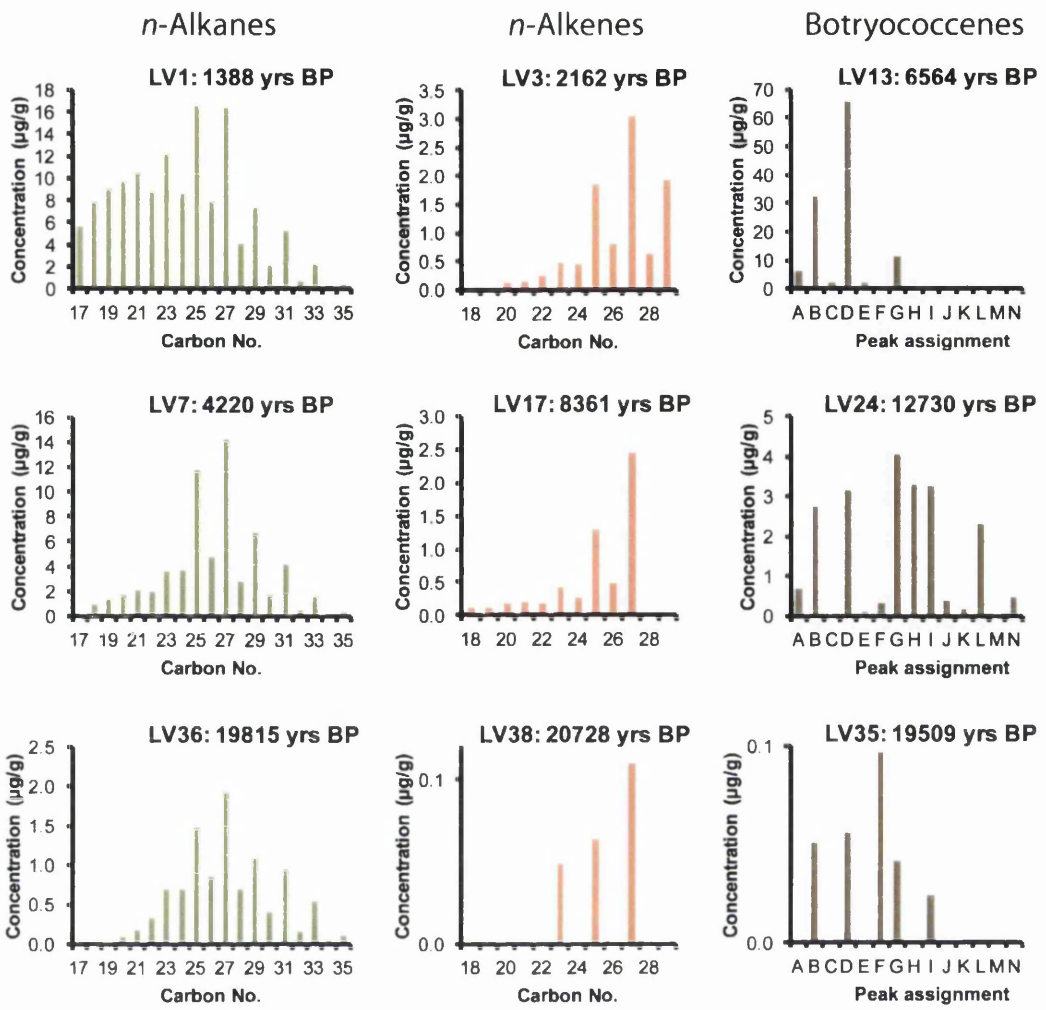

Figure 7.22: Homologue distribution and abundance of three typical samples from Lake Victoria representing the last ~20.7 ka BP, showing *n*-alkanes, *n*-alkenes and botryococcenes.

A *n*-alkane proxy, $P_{wax} = (C_{27} + C_{29} + C_{31})/(C_{23} + C_{25} + C_{27} + C_{29} + C_{31})$, was proposed by Zheng et al. (2007) to distinguish between contributions from emergent/terrestrial and submerged/floating plants, as the former have characteristic C_{27} and C_{29} *n*-alkane dominance and the latter maximise at C_{23} and C_{25} (Ficken et al., 2000). During the last ~20.7 ka BP at Lake Victoria, P_{wax} varied from 0.50 to 0.74, signifying variations in relative contribution of organic matter (Figure 7.23a; Table 7.3). During the early part of the record (~20.7 to 19.0 ka BP), P_{wax} values were relatively high (0.59 to 0.73) signifying a dominance of emergent/terrestrial plants. From ~18.5 to 16.7 ka BP, lower P_{wax} values (0.58-0.61) suggest a period of increasing contributions from submerged/floating macrophytes, followed by a return to higher values between ~16.2 and 15.7 ka BP. An abrupt shift to a near-minimal

P_{wax} value (0.52) occurred from ~15.7 to 14.9 ka BP, followed by an even bigger increase to maximum P_{wax} values (0.74) at ~14.1 ka BP. P_{wax} values remained high for several millennia (~14.1 to 9.7 ka BP) indicating a large contribution from emergent/terrestrial plants, before progressively declining through the early to late Holocene, suggesting decreasing contributions from emergent/terrestrial plants. Although P_{wax} values continued to decline during the late Holocene, they remained fairly stable (0.59-0.63), particularly between ~5.8 and 3 ka BP. An abrupt decrease to minimum P_{wax} values at the top of the record (~1.4 ka) signifies a move towards submerged and floating macrophyte dominance as highlighted by a large increase in the C_{23} *n*-alkane (Figure 7.22).

Another useful *n*-alkane based proxy proposed by Ficken et al. (2000) to reflect non-emergent aquatic plant input to lake sediments is the $P_{aq} = (C_{23} + C_{25})/(C_{23} + C_{25} + C_{29} + C_{31})$. A P_{aq} value of greater than 0.4 signifies a important fraction of sedimentary *n*-alkanes from submerged/floating plants (Ficken et al., 2000). In Lake Victoria sediments, P_{aq} varied from 0.36 to 0.69 during the last ~20.7 ka BP (Figure 7.23b; Table 7.3). As deglaciation proceeded (~20.7 and 19.0 ka BP), P_{aq} values were relatively low (0.39-0.59). Shortly afterwards, P_{aq} values gradually rose and then declined (between ~19-15.7 ka BP) indicating a brief increase in non-emergent aquatic plants. An abrupt increase to a value of 0.65 at 15.0 ka BP was followed by just an abrupt decrease to minimal P_{aq} values (0.36-0.54) during the late glacial and into the early Holocene (~14.1-8.0 ka BP), suggesting increased input from emergent and terrestrial plants. From 7.5 ka BP onwards, P_{aq} values were high and remained fairly stable, between 0.53 to 0.69, indicating that inputs from submerged/floating plants were important. P_{wax} and P_{aq} values varied closely together (Figure 7.23), responding in opposite directions, which reflects the similar components (i.e. homologues) used to distinguish relative inputs from emergent/terrestrial plants (P_{wax}) and submerged/floating macrophytes (P_{aq}).

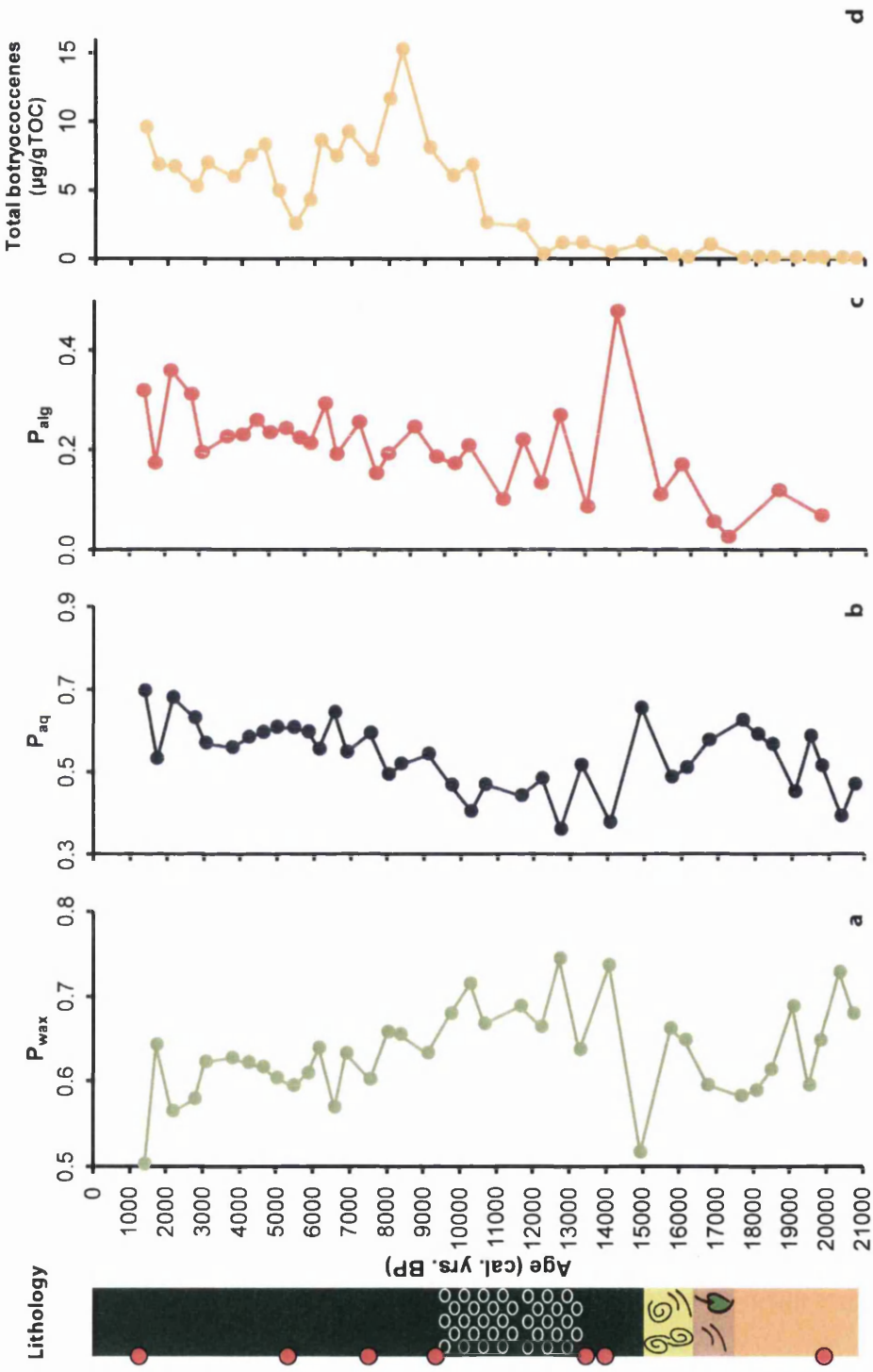

Figure 7.23: Contributions from (a) higher plants (P_{wax}), (b) non-emergent aquatic plants (P_{aq}), (c) algae (P_{alg}) and (d) the abundance of botryococcenes during the last ~20.7 ka BP in Lake Victoria sediments. $P_{wax} = (C_{27} + C_{29} + C_{31})/(C_{23} + C_{25} + C_{27} + C_{29} + C_{31})$ (Zheng et al., 2007), $P_{aq} = (C_{23} + C_{25})/(C_{23} + C_{25} + C_{29} + C_{31})$ (Ficken et al., 2000) and $P_{alg} = (C_{23:1} + C_{25:1} + C_{27:1})/(C_{23:1} + C_{25:1} + C_{27:1} + C_{29} + C_{31} + C_{33})$ (modified after Zhang et al. (2004)). For core descriptions see Figure 7.9.

Fourteen individual botryococcene compounds have been identified in the hydrocarbon fraction of Lake Victoria sediments (Figure 7.22). Although I have not been able to identify their structures at present, from their mass spectra and molecular weight, the compounds (A-N; Figure 7.22) have been provisionally identified as C_{32}, C_{33} and C_{34} botryococcenes (Figure 7.24; Table 7.4). Homologues B ($C_{32}H_{54}$), D ($C_{33}H_{60}$) and G ($C_{34}H_{66}$) are consistently the dominant botryococcenes throughout the record. Botryococcenes are present in Lake Victoria sediments above the upper palaeosol (~15 ka BP) and abundant during the Holocene period, peaking at 15.2µg/gTOC at ~8.4 ka BP (Figure 7.23d; Table 7.3). These botryococcenes are likely to be related to the green alga, *Botryococcus braunii*, which was identified by light microscopy in high abundance in Lake Victoria sediments during diatom purification (section 7.7).

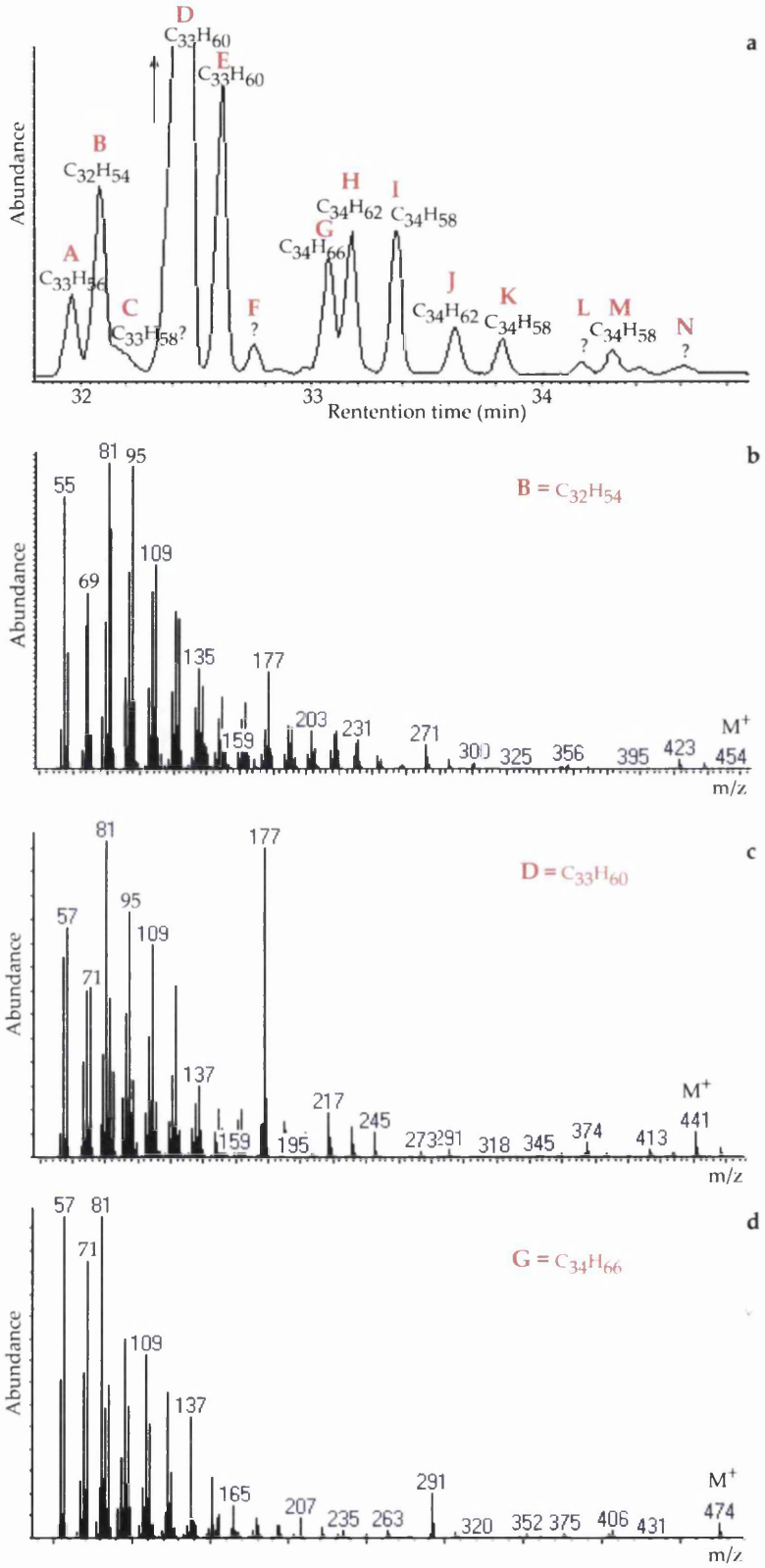

Figure 7.24: Total ion current showing typical distribution of botryococcenes found in Lake Victoria (a). Mass spectra of botryococcene compounds B ($C_{32}H_{54}$) (b), D ($C_{33}H_{60}$) (c), and G ($C_{34}H_{66}$) (d) identified in Lake Victoria.

Table 7.4: Characteristics of botryococcenes detected in Lake Victoria

Compound letter	Molecular weight (M^+)	Formula
A	452	$C_{33}H_{56}$
B	438	$C_{32}H_{54}$
C	454	$C_{33}H_{58}$?
D	456	$C_{33}H_{60}$
E	456	$C_{33}H_{60}$
F	Unknown	?
G	474	$C_{34}H_{66}$
H	470	$C_{34}H_{62}$
I	466	$C_{34}H_{58}$
J	470	$C_{34}H_{62}$
K	466	$C_{34}H_{58}$
L	Unknown	?
M	466	$C_{34}H_{58}$
N	Unknown	?

In addition to the *n*-alkanes and botryococcenes, *n*-alkenes were also present in the hydrocarbon fraction in high abundance with C numbers ranging from 18 to 29 (Figure 7.22; Table 7.3), and with a high odd over even predominance. $C_{27:1}$ was the most dominant *n*-alkene with significant contributions of $C_{23:1}$ and $C_{25:1}$ *n*-alkenes. Based on Zhang et al.'s (2004) P_{alg} proxy (P_{alg} = ($C_{23:1}$ + $C_{25:1}$ + $C_{27:1}$ + Cyclobotryococcatriene)/($C_{23:1}$ + $C_{25:1}$ + $C_{27:1}$ + Cyclobotryococcatriene + C_{29} + C_{31} + C_{33})), which determines the relative contributions of aquatic algae to terrestrial and emergent plant input, a modified version was created here based on the *n*-alkene component as no cyclobotryococcatriene compounds were identified in Lake Victoria sediments. The revised P_{alg} formula is as follows: P_{alg} = ($C_{23:1}$ + $C_{25:1}$ + $C_{27:1}$)/($C_{23:1}$ + $C_{25:1}$ + $C_{27:1}$ + C_{29} + C_{31} + C_{33}).

The P_{alg} values in Lake Victoria ranged from 0.03 to 0.48 during the last ~20.7 ka BP (Figure 7.23c; Table 7.3), signifying variable contributions from algae and emergent/terrestrial plants during the past. During the earliest part of the record (~20.7 to 16.2 ka BP), P_{alg} values were very low, close to zero, signifying limited algal contributions to Lake Victoria sediments during this period. A sudden increase in P_{alg} to maximum values (0.48) occurred between ~16.2 to 14.9 ka BP, followed by a rapid shift to lower values (0.09) at 14.1 ka BP. From ~14.1 to 6.6 ka BP P_{alg} increased gradually from 0.09 to 0.29. Between ~6.1 to 3.1 ka BP P_{alg} remained fairly stable at around 0.23. From ~3 ka BP onwards P_{alg} values were higher and fluctuating.

P_{alg} and P_{aq} exhibit a significant positive correlation (R^2 = 0.31; p = 0.0007) (Figure 7.25), indicating a trend of increasing P_{alg} values with increasing P_{aq} values (Figure 7.23). A relationship between algae and floating/submerged macrophytes is plausible considering increased abundance of macrophytes can cause water stagnation and encourage algal blooms.

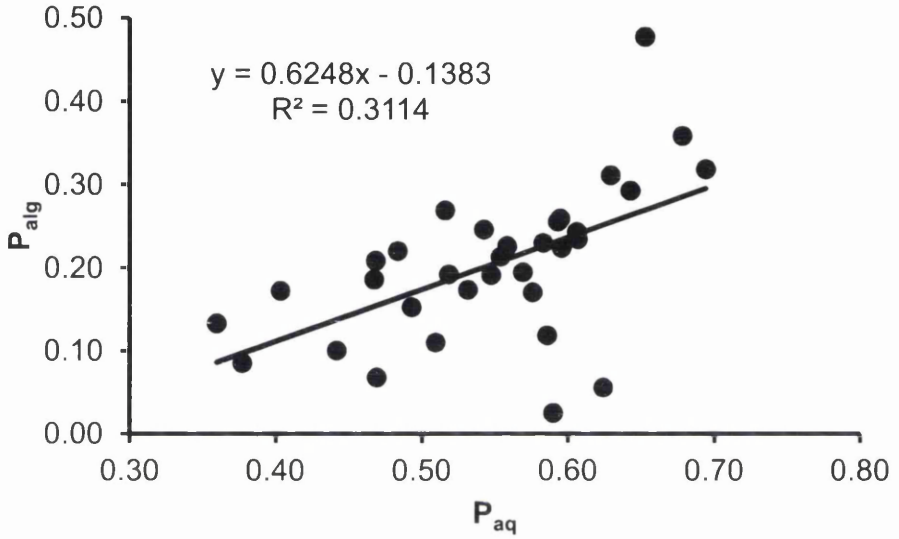

Figure 7.25: P_{alg} and P_{aq} proxies are significantly correlated (R^2 = 0.31; p = 0.0007) in Lake Victoria sediments indicating a strong relationship between algae and floating/submerged aquatic plants.

7.10 Chapter summary

Lake Victoria is the third largest lake in the world and marks the lacustrine headwaters of the White Nile. Its large surface area and relatively shallow depth, combined with precipitation and evaporation being the main controls on its water balance, cause it to be very sensitive to climatic changes. Multi-proxy studies have shown that it did dry out completely during the Late Pleistocene, at least once. Marked variations in the climate over East Africa during the last 20 ka BP have certainly had a major impact on vegetation and hydrology in the Lake Victoria Basin, and therefore it is likely that Si cycling has varied in response.

Advantageously, material from pre-existing cores obtained from the IDEAL expedition were available, together with well developed age models and existing data (BSi, TC and MS) to assist sampling and interpretation of the data obtained in

this thesis. V95-1P was a long, continuous core without hiatuses, although the sediment lithology suggests periods of complete desiccation when soil formation commenced (i.e. palaeosols). Unfortunately, diatom concentrations were low in large parts of the core, combined with difficulties associated with separating the diatoms from other sediment components (i.e. charcoal fragments, green algae and clay minerals), making it impossible to achieve 500-year resolution throughout, although analytical precision was good on the data that were obtained. It was possible to achieve 500-year resolution for lipid biomarkers for the length (21 ka BP) of the V95-1P core due to high organic carbon content in the majority of the sediments.

8 Lake Edward, East Africa

8.1 Introduction

At the beginning of this chapter, key aspects of the environmental and geographical setting of Lake Edward are presented, followed by detailed information on the selection of sediment cores used in this study, of their composition and corresponding age models. A brief explanation of the sampling interval used is followed by details of the specific methods used to extract pure diatom silica from Lake Edward sediments and the problems that arose. Finally, the results of O- and Si-isotope analysis of diatom silica and lipid biomarker analyses are presented.

8.2 Study area

8.2.1 Geography

Lake Edward is located on the borders of Uganda and the Democratic Republic of Congo (DR Congo) in the western arm of the East African Rift System at an altitude of 912m a.s.l. (Figure 8.1). The lake has a surface area of 2,325km^2 and a maximum depth of 117m, with the deepest point located towards the western edge (Lærdal and Talbot, 2002; Russell et al., 2003a). Lake Edward is bounded to the north by the Rwenzori Mountains (>5000m), to the west by the Albertine Rift Mountains (2500-3000m a.s.l. within 15km of the lake shoreline), to the south by the Virunga Volcanoes (>4500m a.s.l.) and to the east by the more gently rising Kigezi Highlands (1500-2700m a.s.l.).

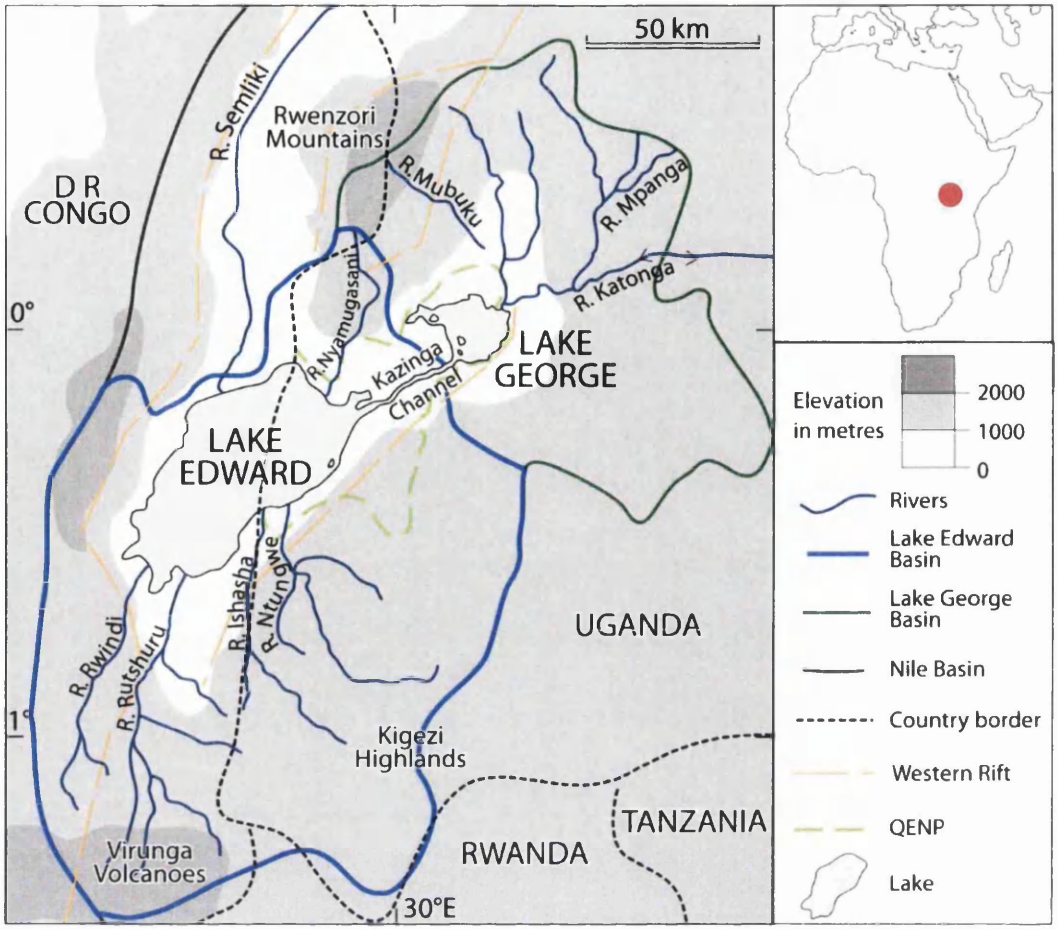

Figure 8.1: Location map of Lake Edward including major rivers and drainage regions, topography, Queen Elizabeth National Park (QENP) and boundaries of the West Rift.

8.2.2 Geology

The northern part of the Western Rift system is largely underlain by Precambrian basement rocks (e.g. gneisses and granites) with areas around the great Rift Lakes and associated river valleys containing Quaternary alluvial deposits (Figure 8.2). Neogene volcanics (e.g. alkaline basalts) can be found in the southwest of the basin in the Virunga volcanic area and in small pockets close to Lakes George and Edward, where young (~50ka) volcanic craters and vents exist (Schlüter, 2008).

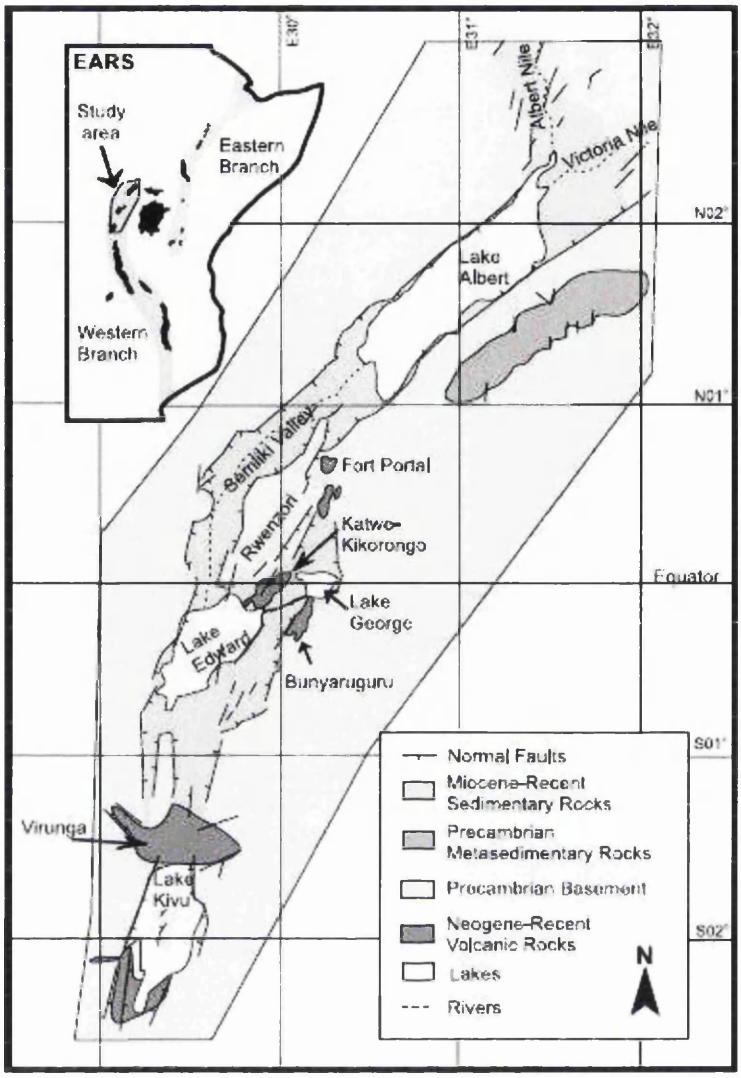

Figure 8.2: The geology of the northern section of the Western Rift (from Lærdal and Talbot (2002)).

In addition to the faults surrounding Lake Edward associated with the East African Rift System, a fault scarp with a north-south orientation, the Kasindi Fault Zone (KFZ) (Lærdal and Talbot, 2002), is located in the centre of Lake Edward (Figure 8.9). To the west of this fault zone lies the deepest part of the lake (117m). The lake has effectively been split into two sub-basins, with the eastern (shallow) basin being subject to small scale faulting and that has effected sedimentary patterns in the sub-basins (Lærdal and Talbot, 2002; Lærdal et al., 2002; Russell et al., 2003a).

8.2.3 Climatology

Like Lake Victoria, the Lake Edward Basin exhibits a bimodal rainfall pattern with rainy seasons occurring between October and December and again between March and May, associated with the twice-yearly passage of the ITCZ across the equator (Figure 3.3) (Nicholson, 1996). Lake Edward receives moisture from the prevailing easterly Indian Ocean Monsoons whilst its close proximity to the Congo Air Boundary (CAB) (Figure 3.3), suggests that it may also receive contributions from Atlantic Ocean via the Congo Airstream (Russell and Johnson, 2006). Annual rainfall is about 900mm/yr over the lake with substantially more being received in the elevated regions surrounding Lake Edward (Viner and Smith, 1973), accordingly, tributaries rising in these regions provide the largest sources of water input to the lake (Russell and Johnson, 2005). Russell and Johnson (2006) estimate that 54% of water losses from Lake Edward occurs through evaporation and the remainder through the outflow, the Semliki River.

8.2.4 Hydrology

The catchment area of Lake Edward covers 15,840km^2. The major inflows into the lake are the Ishasha and Ntungwe Rivers in the southwest, draining the Kigezi Highlands, the Rutshuru and the Rwindi Rivers from the Virunga Volcanoes and several smaller rivers from the steep mountains in the DRC to the west of the lake (Figure 8.1) (Lehman, 2002; Russell et al., 2003a; Beuning and Russell, 2004; Russell and Johnson, 2006). Several rivers drain the Rwenzori Mountains to the north of the basin, in particular, the Nyamugasani River. In addition, the Kazinga Channel, a 30km-long 1km-wide drowned river valley which flows sluggishly from Lake George (914m a.s.l.) in the east, is another primary inflow. Lake George also receives a significant amount of runoff from the Rwenzori Mountains from its eastern side (Russell and Johnson, 2006). The current outflow is through the Semliki River at the northwest of the lake which flows northwards into Lake Albert and subsequently into the White Nile. Unfortunately, there are few gauging station data available for the Lake Edward catchment, and therefore exact inputs are unknown, although river runoff is believed to be the most important source of water (Lehman, 2002).

8.2.5 Vegetation

Vegetation in the Rift Valley floor surrounding Lake Edward consists of a mosaic of East African evergreen bushland and thicket, secondary *Acacia* wooded grassland, and farmland (Figures 8.3 and 8.4) (White, 1983). Surrounding the Kazinga Channel, in the Queen Elizabeth National Park, areas of dense *Euphorbia dawei* and thicket spread down the steep slopes to the river (Figure 8.5) (Beuning and Russell, 2004). In the highlands to the east of Lake Edward and northeast of Lake George, forest reserves (e.g. Maramagambo, Kashoya-Kitomi and Kibale Forest) protect large remnants of moist semi-deciduous rainforests (Figures 8.6 and 8.7). In the mountainous regions to the north (Rwenzori Mountains), south (Virunga Volcanoes) and west, the vegetation grades from Afromontane rainforest to Ericaceous shrubland to afro alpine vegetation with altitude (Langdale-Brown et al., 1964; Livingstone, 1967; White, 1983; Jolly et al., 1997; Beuning and Russell, 2004). The contrast in vegetation between the plains and the higher ground is a reflection of the more arid climate around the lake itself compared to the highlands.

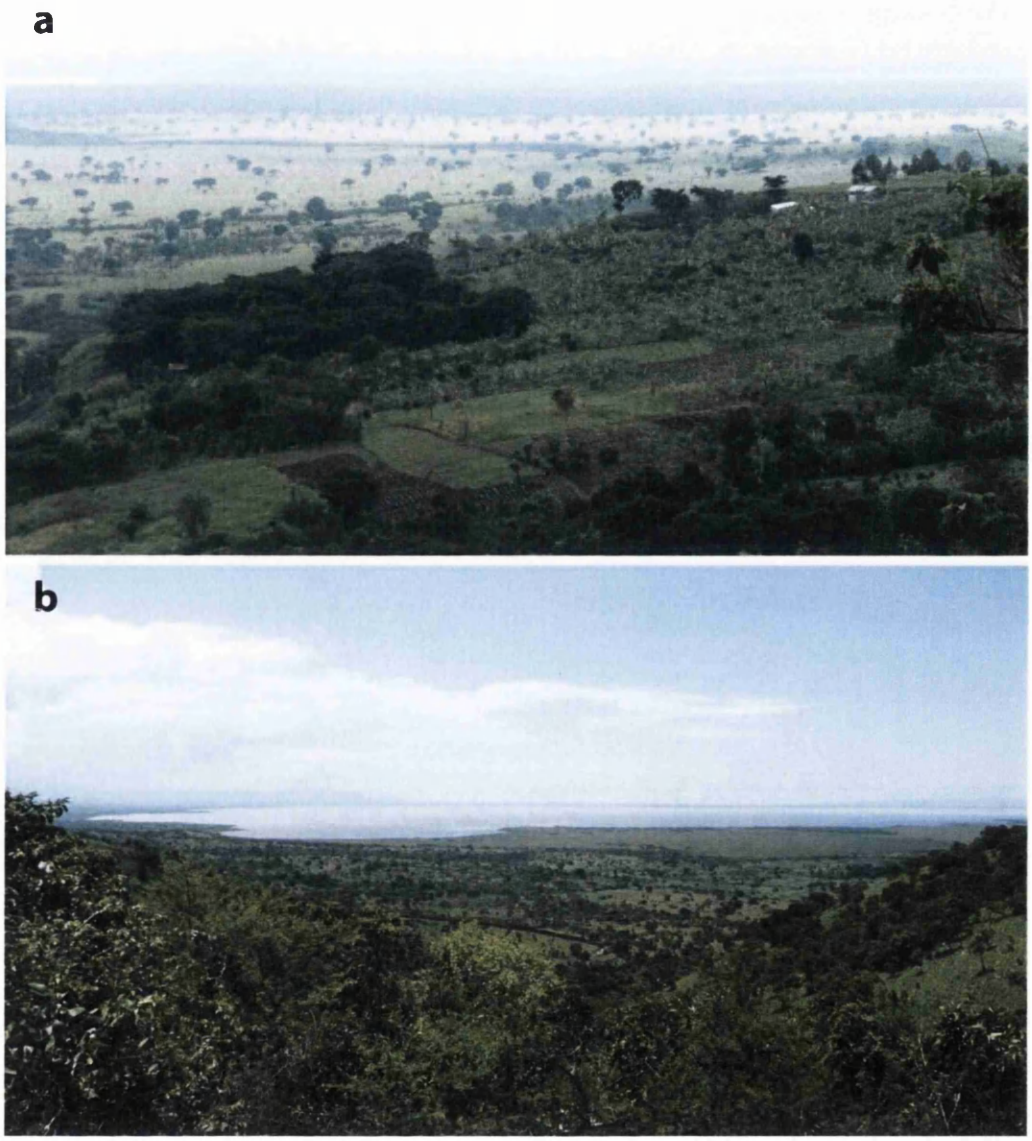

Figure 8.3: Photograph (a) taken from the Kichwamba Escarpment looking down onto Lake Edward across cultivated slopes and into the wooded savanna of the Rift Valley. (b) a view over Lake George and the surrounding plains from the steep terrain near the Mpanga River in the northeast of the basin.

Figure 8.4: Rift valley floor vegetation surrounding Lake Edward. Abundant *Acacia* wooded grassland and thicket.

Figure 8.5: Vegetation found along the Kazinga Channel between Lakes George and Edward, particularly thickets of *Euphorbia dawei*.

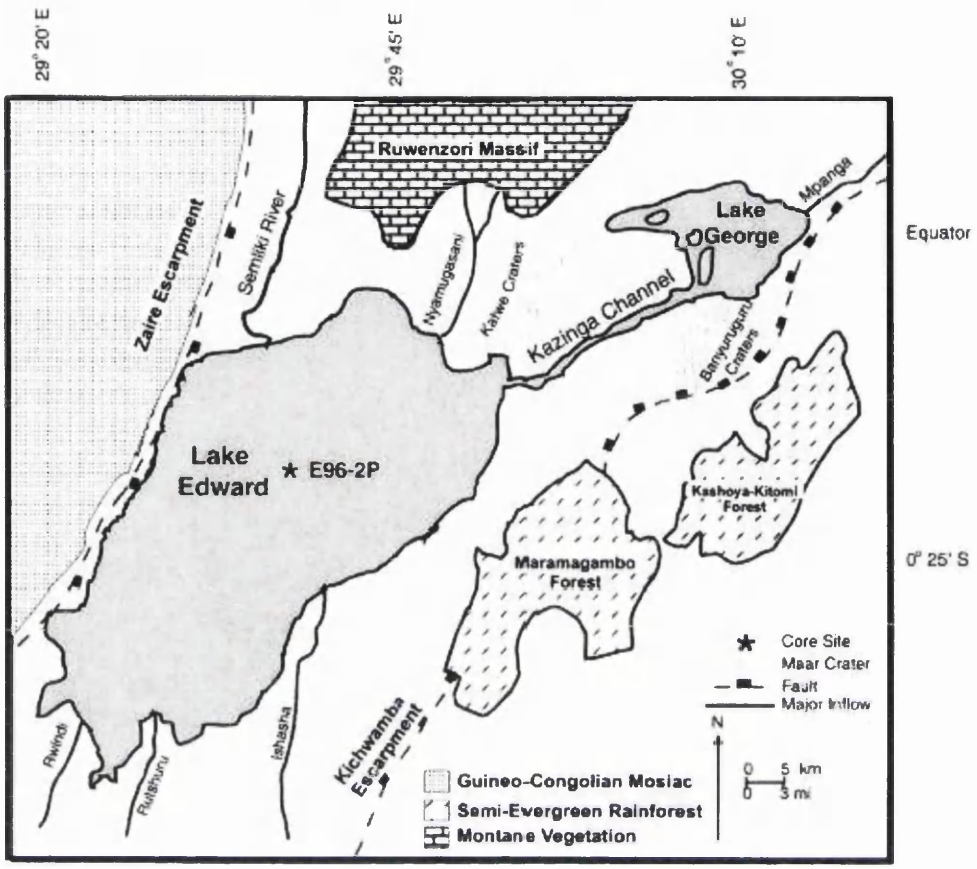

Figure 8.6: General vegetation map of the Lake Edward Basin. Between the two escarpments, in the Rift Valley, the vegetation is a mosaic of wooded grassland, bushland and *Acacia* savanna (from Beuning and Russell (2004)).

Figure 8.7: Photograph of the semi-evergreen rainforest in the Maramagambo Forest Reserve to the east of Lake Edward.

Figure 8.8: Photograph of the Afromontane rainforest vegetation present in the Rwenzori Mountains at between ~1,700-2,300m to 3,000-3,300m.

At the mouths of tributaries entering Lake Edward, large areas of graminoid swamp vegetation exist, including *Cyperus papyrus* (C_4 sedge) and *Phragmites mauritianus* (C_3 grass) (e.g. Rivers Ishasha and Ntungwe in the east and Rivers Rutshuru and Rwindi in the south) (Hughes and Hughes, 1992). Extensive areas of swamp also exist in the headwaters of some of the tributaries, in particular in the Kigezi Highlands, where lakes such as Lake Bunyonyi drain (Green, 2009). In addition, the shores of Lake George are surrounded by wetlands consisting of predominately *Cyperus papyrus*, and a massive swamp (100km^2) of papyrus and *Ficus* (fig) extends for 20km north (14km wide) of Lake George, fed by rivers from the Rwenzori Mountains (Hughes and Hughes, 1992; Green, 2009). *Potamogeton pectinatus* is the dominant submerged macrophyte, together with *Najas marina* and *Vallisneria aethiopica* (Hughes and Hughes, 1992).

8.3 Lake Edward, East Africa: previous palaeoenvironmental studies

Apart from initial investigations by the Woods Hole Oceanographic Institute (WHOI) in the 1970's (Hecky and Degans, 1973), very little work had been carried out on the palaeolimnology of Lake Edward until the IDEAL expedition in 1996 began. A total of four cores (E96-1P, E96-2P, E96-5M and E96-1P) of varying length and age was collected from Lake Edward (Figure 8.9), which between them span the Holocene epoch. From the sediment stratigraphy and from radiocarbon dating there was some evidence of reworked sediments and hiatuses, particularly in the shallower cores (Lærdal et al., 2002; Russell et al., 2003a; Beuning and Russell, 2004). Not only has climate affected the Lake Edward basin but also tectonics have modified the sedimentary record through tectonically induced lake level changes and also introducing reworked deposits through seismic activity, making it difficult to separate the two (Lærdal et al., 2002). An insight into glacial climate conditions from a slump deposit situated within early Holocene muds, thought to be tectonically activated and dated to 20.6 ka ^{14}C BP (Figure 8.10) (Lærdal et al., 2002; Russell et al., 2003a). The lithological properties, geochemical composition and the presence of iron oxides and authigenic calcite suggested that the deposit was initially formed by sub-aerial exposure and subsequent precipitation of high-Mg authigenic calcite in highly evaporated lake waters (Lærdal et al., 2002; Russell et al., 2003a; Beuning and Russell, 2004). Drier conditions at Lake Edward during the LGM are consistent with other palaeoclimate records in tropical Africa (Barker et al., 2004 and Gasse et al., 2008 and references therein). Tectonic influences on the Holocene lake basin seem to be minimal (Russell et al., 2003a).

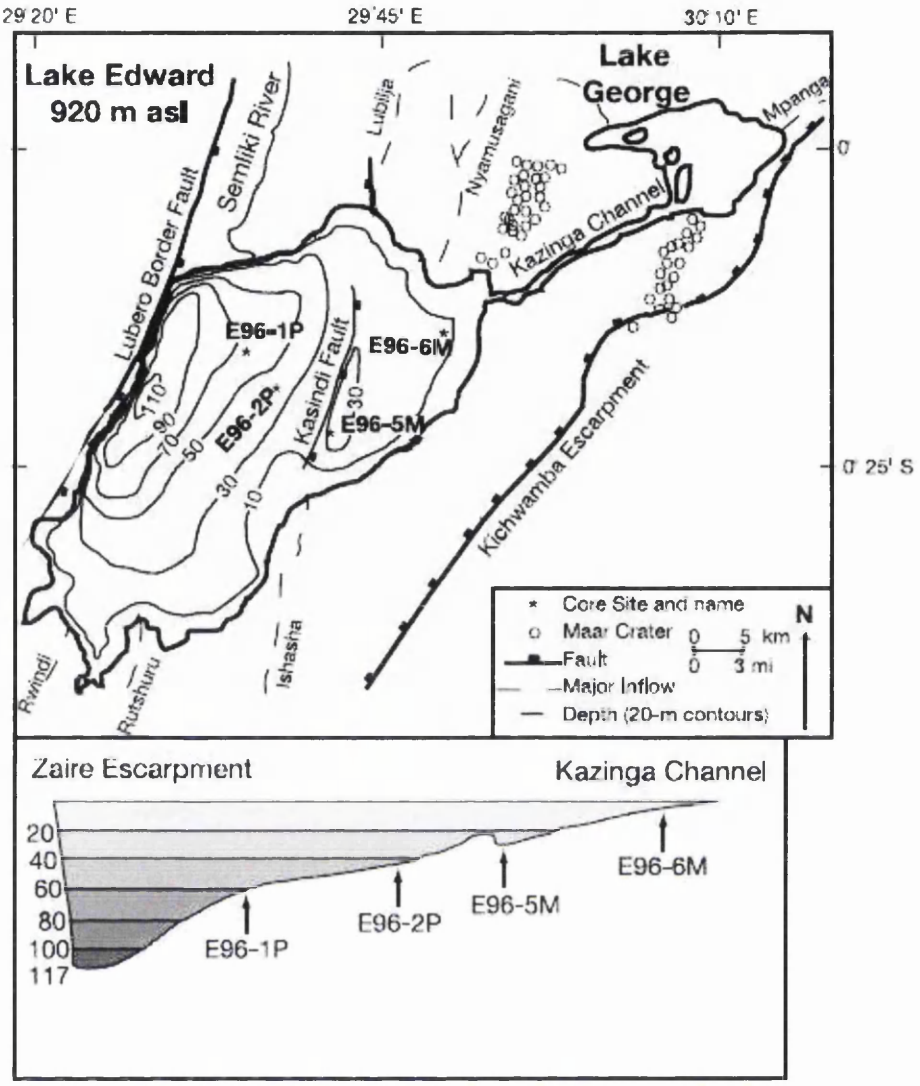

Figure 8.9: Bathymetric map of Lake Edward showing the core locations and a cross-sectional sketch of the Lake Edward Basin illustrating the water depth and position of the core sites (from Russell et al. (2003a)).

The long-term climate trend identified at Lake Edward, as seen in many East African records (Gasse, 2000; Barker et al., 2004; Kiage and Liu, 2006; Gasse et al., 2008), of an early- to mid-Holocene interval of high lake levels brought about by orbitally forced increase in monsoon rainfall, followed by increasing aridity from ~5.2 ka BP, as the monsoon intensity declined (Russell et al., 2003a; Russell et al., 2003b; Russell and Johnson, 2005). In addition to this long term trend several centennial- to millennial-scale events have been identified, particularly at ~4 and 2 ka BP (Russell et al., 2003a; Russell et al., 2003b; Russell and Johnson, 2005). Several high-resolution studies during the late Holocene have identified climatic events of

multi-decadal duration at Lake Edward (Russell et al., 2003b; Russell and Johnson, 2005, 2007), but are not discussed here in detail due to the main focus of this research being on orbital-scale changes.

Evidence for wet conditions in the Lake Edward basin during the early- to mid-Holocene (from ~11.2 to 6.7 ka BP) comes largely from pollen evidence which shows that moist semi-deciduous, lowland forest taxa (e.g. *Celtis* spp., *Alchornea* spp., *Olea* spp. and Moraceae) were prominent (Figure 8.11). Higher lake levels were inferred, as much as 12.5m based on beach shorelines between 11.2 and 9 ka BP (Beuning and Russell, 2004). A subsequent early Holocene decline in lake level was thought to be due to tectonic lowering of the Semliki outlet and not climatically induced (Lærdal et al., 2002; Russell et al., 2003a). Beuning and Russell (2004) estimated that an increase of 25-60% in annual precipitation compared to present (1500-2000 vs. 1200mm/yr today) would be required to sustain the extensive moist semi-deciduous lowland tropical forest on the Rift Valley floor. It was possibly even wetter between ~9 and 6.7 ka BP, based on slight changes of the pollen taxa, relatively high sedimentary sulphur concentrations (tracer for iron delivery from the catchment) and clastic sedimentation, indicating greater runoff (Figure 8.10). BSi concentrations also declined gradually during this period suggesting lake levels had risen and an increase in flow at the outlet due to enhanced rainfall, resulted in decreased residence time of DSi in the lake (Beuning and Russell, 2004). However, Russell and Johnson (2005) emphasised that increased wetness would actually mobilise more DSi resulting in an increase of BSi accumulation, assuming that diatoms were the main phytoplankton. As with Lake Victoria, and some of the other large Africa lakes (e.g. Lake Malawi (Bootsma, 2003)) the hypolimnion of Lake Edward is too small to sustain the long-term changes seen in the BSi record. Russell and Johnson (2005) calculated the residence time of DSi in Lake Edward to be only 4 years and concluded, therefore, that river inputs to the lake controlled the supply of DSi.

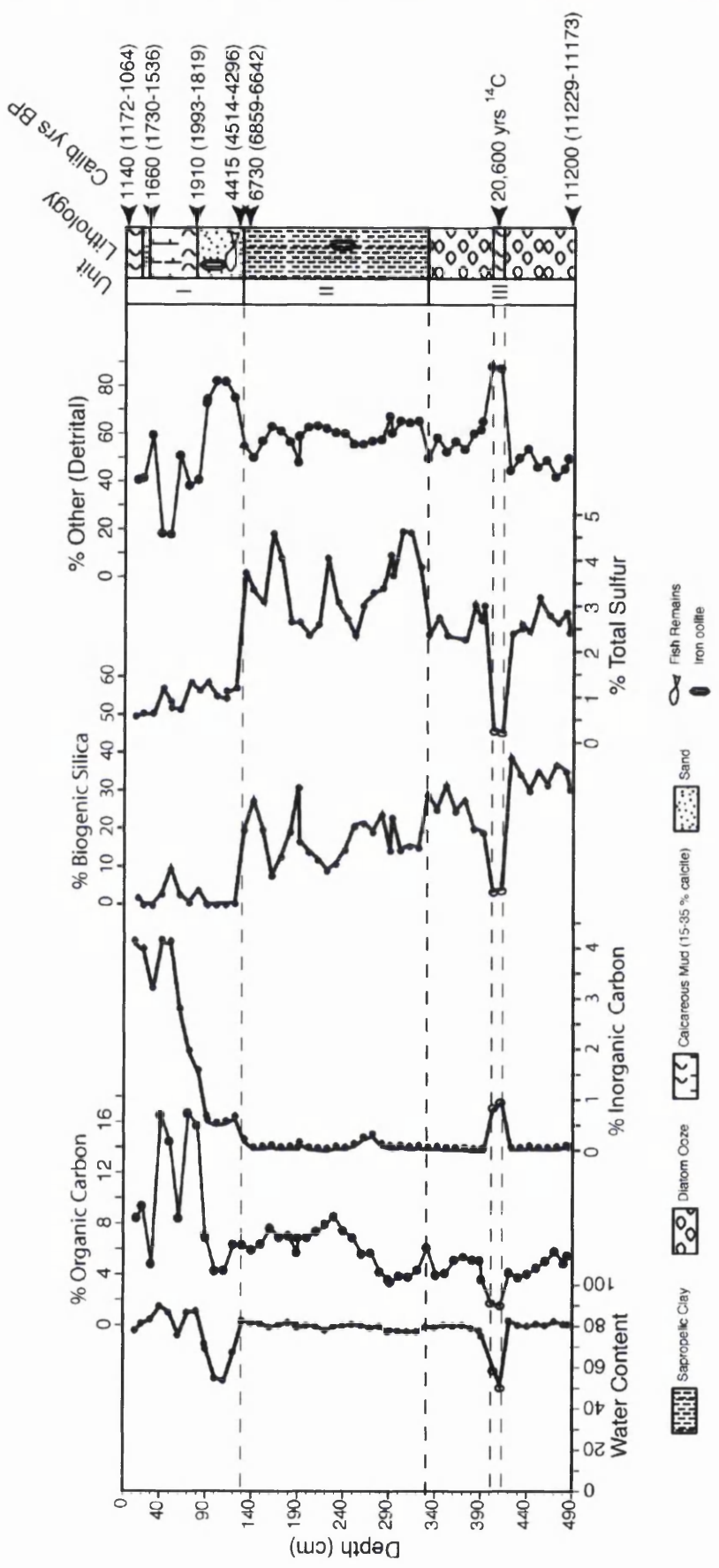

Figure 8.10: Lithological and geochemical profiles for core E96-2P, Lake Edward. Open circles represent data points from a massive slump of Pleistocene material deposited within unit III (from Beuning and Russell (2004)).

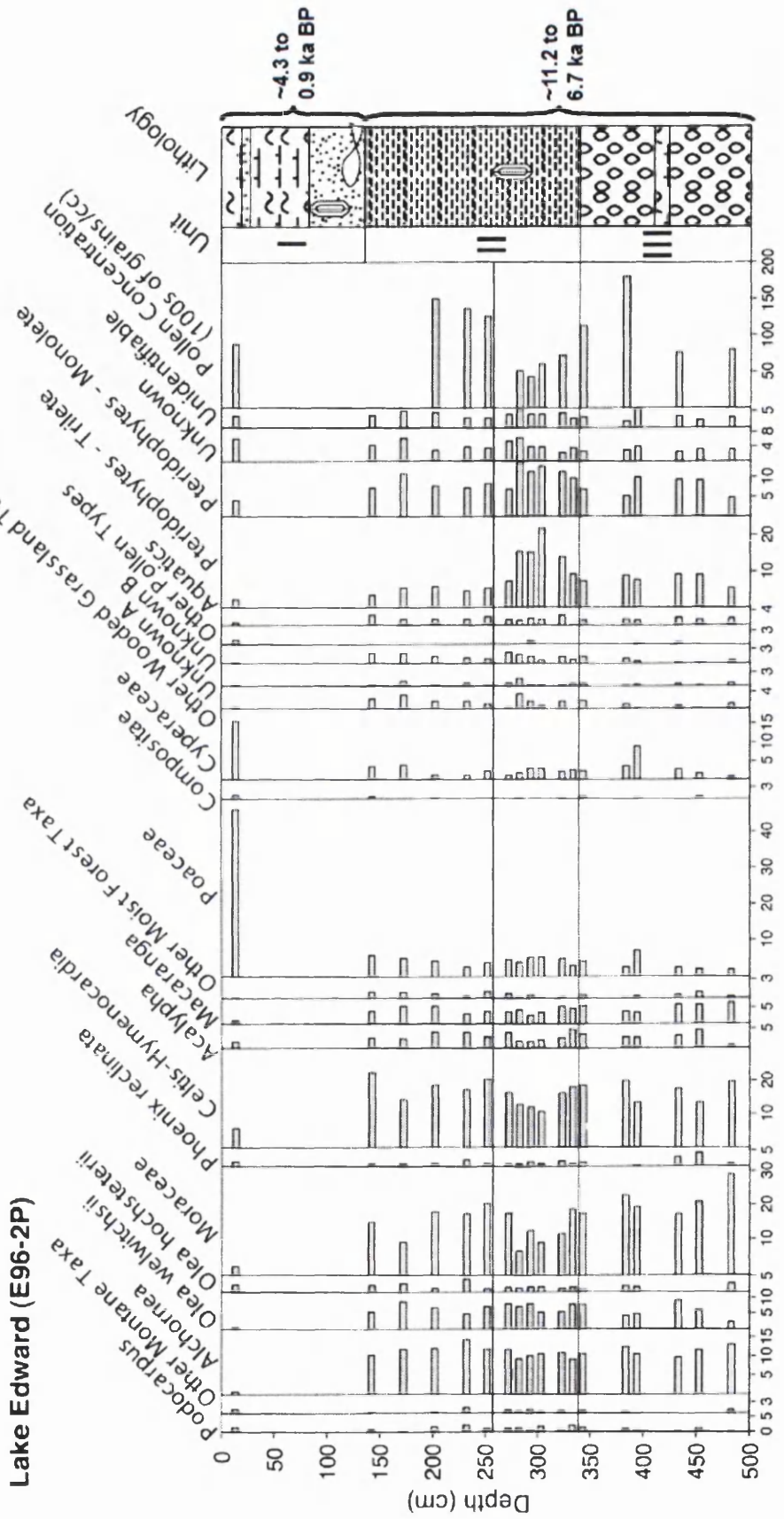

Figure 8.11: Pollen percentage diagram from core E96-2P, Lake Edward. Percentages are based on percent total of all identified, non-aquatic pollen grains and spores (from Beuning and Russell (2004)).

The onset of drier conditions was apparent at ~5.4 ka BP at Lake Edward due to the presence of authigenic calcite and a change in lithology from dark gray clays to reddish carbonate mud reflecting a transition to more arid conditions (Russell et al., 2003a; Russell and Johnson, 2005). The long-term positive trend in %Mg in calcite was used a as proxy to identify progressively more arid conditions and a gradual reduction in monsoon intensity (Figure 8.12) (Russell et al., 2003a; Russell and Johnson, 2005). The Mg content of calcite rises as evaporative concentration of a lake increases (Kelts and Hsü, 1978; Russell et al., 2003a). From 5.2 to 2 ka BP Mg% rose gradually indicating increasing aridity, and then from ~2 ka BP a slight decrease in Mg% suggested a return to wetter conditions. The $\delta^{18}O$ composition of calcite also shows this long-term trend (Figure 8.12) (Russell et al., 2003b; Russell and Johnson, 2005).

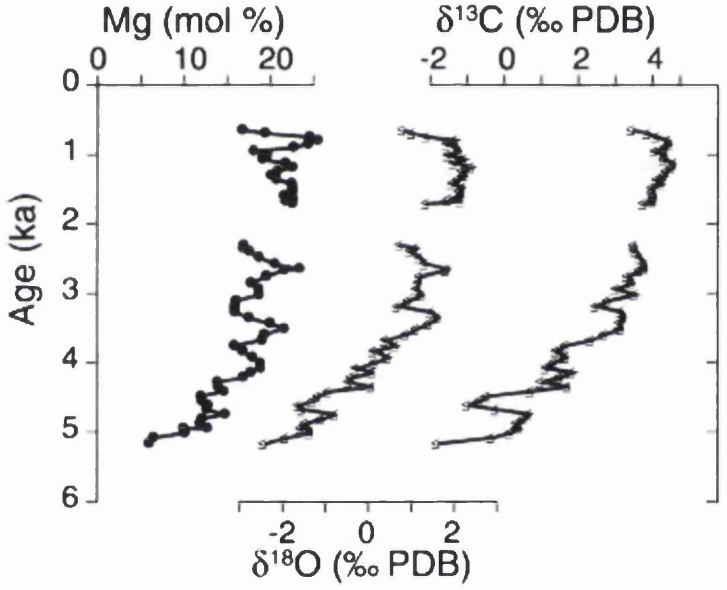

Figure 8.12: Mg% and $\delta^{18}O$and $\delta^{13}C$ in calcite for core E96-5M, Lake Edward (from Russell et al. (2003b). The long-term trend of increasing Mg% and $\delta^{18}O$ and $\delta^{13}C$ in calcite indicated that the lake water became progressive enriched during the late Holocene due to evaporative concentration under drier conditions (reduced P/E).

Ferruginous sands in core E96-2P provided clear evidence of lake low stands between ~4.0 and 2.0 ka BP, but the precise timing of these events were difficult to establish (Russell et al., 2003a). Through high-resolution analysis of Mg% and BSi%, a series of decadal- to centennial-scale droughts was identified during the last 4.9 ka BP (Russell et al., 2003b; Russell and Johnson, 2005). The covariance

of high-resolution Mg% and BSi% records in core E96-1P indicated that low BSi% represented reduced lake levels, as increased alkalinity through the evaporative concentration of dissolved carbonate would encourage the dissolution of diatom frustules in surface sediments and the formation of inorganic Si nodules, suggesting that BSi during at least the last ~5000 years was a water balance or drought indicator rather than a diatom productivity measure (Russell and Johnson, 2005). A drought event was identified at ~4.2 ka BP, which coincided with a severe drying episode recognised in many other East African palaeoclimate records (cf. Gasse 2000). Immediately prior to 3.6 ka ^{14}C BP, Lake George to the east desiccated and to the north Lake Albert exhibited lake low stands (Viner, 1977; Beuning et al., 1997c), indicating regional aridity in western Uganda. Although a more significant low stand was identified at Lake Edward at ~2 ka BP from a 7% shift in Mg% in clacite (Russell et al., 2003b; Russell and Johnson, 2005). Desiccation of Lake George would have resulted in an abrupt termination of nutrient-rich, warm waters flowing into Lake Edward through the Kazinga Channel (Russell et al., 2003a). Between ~5.4 to 2 ka BP lake levels in Lake Edward were lower than present until the water level rose shortly after ~2ka BP, possibly indicating re-establishment of the connection between Lake Edward and Lake George through the Kazinga Channel (Russell et al., 2003a).

In summary, the environment during the early- to mid-Holocene surrounding Lake Edward was one of moist, tropical forest with high P/E and lake levels, in response to enhanced monsoon rainfall driven by orbital forcing and combined with changes in surface boundary conditions, increased soil moisture and higher sea-surface temperatures (Kutzbach and Street-Perrott, 1985). From the mid-Holocene, drier conditions associated with a decline in monsoon strength, resulted in declining lake levels. Superimposed on the long-term drying trend were short, abrupt drought events, including one at ~4 ka BP which was thought to be related to regional aridity changes across tropical Africa (Street-Perrott and Perrot, 1993). From ~ 2 ka BP, the climate improved, allowing lake levels to rise and the re-establishment of a connection between Lakes George and Edward.

8.4 Sediment cores and stratigraphy

Three of the cores obtained during the IDEAL expedition (E96-1P, E96-5M and E96-2P) are used here to form a Holocene sequence (hereafter referred to as 1P, 5M and 2P) (Figure 8.9). Details of the collection and storage conditions of the core material can be found in Lærdal et al. (2002). Material from these cores is available on request from LacCore, the US National Lacustrine Core Facility, based at the Limnological Research Centre (LRC) at the University of Minnesota, USA. Core descriptions taken from Russell et al. (2003a) and Beuning and Russell (2004) are presented in the following sections.

Due to varying lengths and therefore varying ages of all three cores, a selection of material from each core has been used to formulate a record for the whole of the Holocene period. Suitable core sections have been chosen for analysis based on their sedimentary patterns in order to avoid erosion surfaces and sedimentary hiatuses found in some of the cores (Russell and Kelts, 1999; Lærdal et al., 2002; Russell et al., 2003a; Beuning and Russell, 2004).

8.4.1 E96-1P

Core 1P (0°15.5'S, 29°35.0'E), with a length of 706 cm was collected from 63m water depth (Figure 8.9), the deepest part of the basin to be cored. It is composed of alternating beds of dark calcareous sapropel and diatom ooze (Figure 8.13a). Below 240cm the diatom ooze is well-laminated, typically on mm-scale, and amorphous opaline silica nodules of 0.3 to 3cm diameter occasionally occur (Russell et al., 2003a). Biogenic silica and TOC are high throughout the core, up to ~60% and ~30% respectively (Lærdal et al., 2002; Russell et al., 2003a). Fine charcoal fragments are present throughout the core. 1P appears not to contain any erosion surfaces or hiatuses (Lærdal et al., 2002).

8.4.2 E96-5M

Core 5M (0°21.4'S, 29°42.1'E) was the longest to be extracted from Lake Edward (768.5cm) (Figure 8.13b), from a water depth of 30m to the east of the Kasindi Fault (Figure 8.9). The base of the core to 564cm, consists of a sapropel clay with no structure and relatively rich in diatoms (BSi: ~3-12%) (Lærdal et al., 2002; Russell et

al., 2003a). This unit terminates at 564cm with a wavy, unconformable contact with the overlying unit. Radiocarbon dates from either side of this contact indicate that there is only a brief hiatus, if any (Russell et al., 2003a). From 564 to 190cm a darker, organic-rich and diatom-depleted sapropel clay continues, containing fragments of ostracods, fish and molluscs. This unit terminates with an upper erosional surface and with a 6cm-thick calcareous mud containing sand-sized mineral aggregates and cemented clay particles. Radiocarbon dates confirm that this is a hiatus in the sediment record (Russell et al., 2003a). The upper unit from ~184cm to the top is a organic-rich and diatom-depleted clayey carbonate mud containing fragments of ostracods and fish bones.

8.4.3 E96-2P

Core 2P (0°18.9'S, 29°37.1'E) is 489cm long and was collected from a water depth of 46cm (Figure 8.9). The base to 330cm, comprises a organic-rich (TOC: ~10-20%), finely laminated diatom ooze (BSi: ~30-42%) (alternating sub-mm laminations with sapropelic clays) (Figure 8.13c). In the middle of this unit is a 13cm-thick calcareous silty clay unit which has an erosional upper and lower contact and has subsequently been interpreted as a slump deposit (Russell et al., 2003a; Beuning and Russell, 2004). From 330 to 125cm a sapropelic clay with lenticularly laminated diatomaceous intervals is present. This is abruptly terminated by a ferruginous sand unit containing ostracod and plant debris (36cm-thick). Dating either side of this erosion surface indicates a sedimentary hiatus of approx. 2000 years (Russell et al., 2003a). Above this unit is a organic-rich calcareous mud deposit with occasional thick black sand lenses.

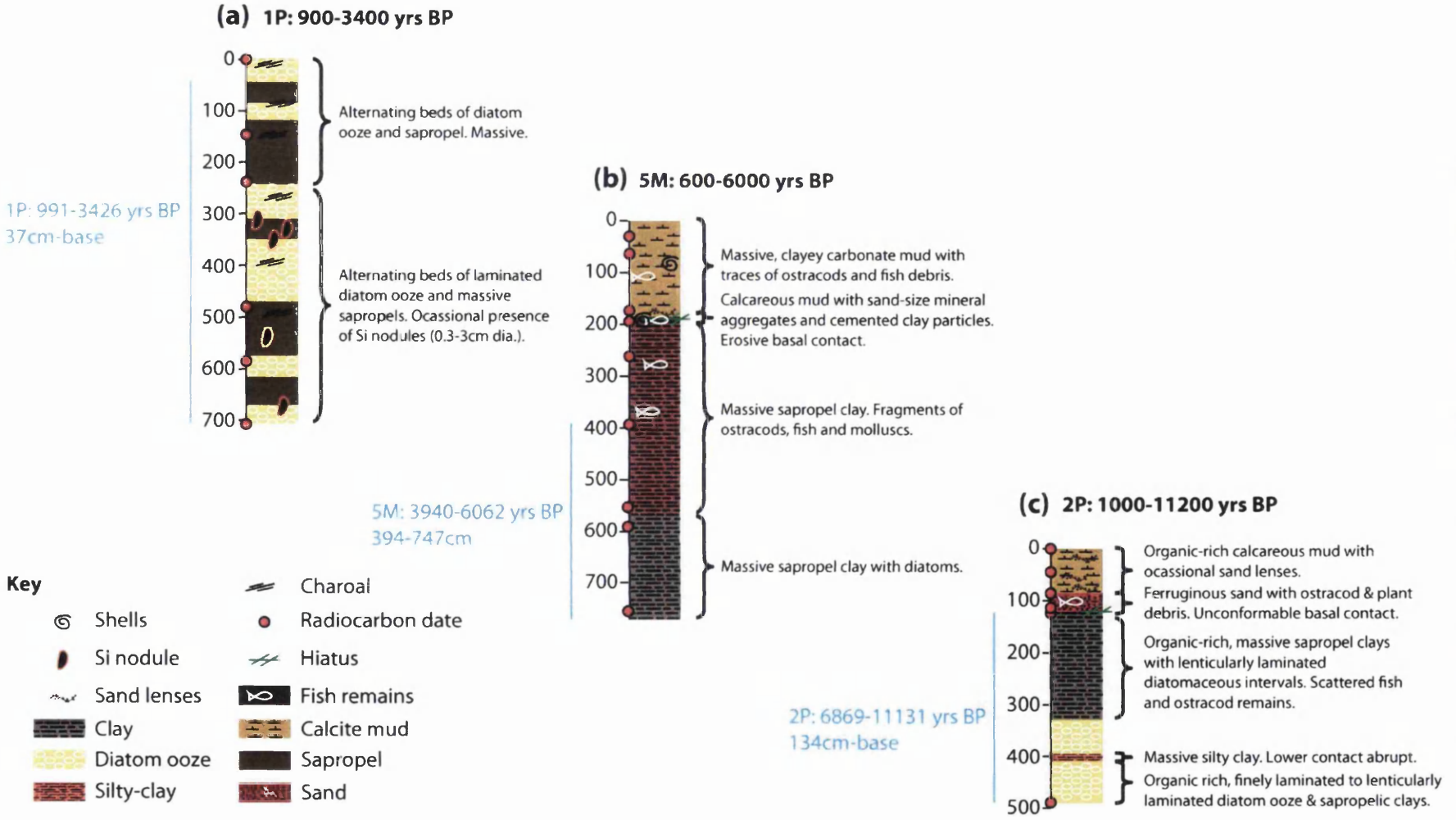

Figure 8.13: Sediment core stratigraphy for Lake Edward for 1P, 5M and 2P. Age ranges for each core are from Russell et al. (2003a). Turquoise solid vertical lines marks sections of cores used in this research to form a combined Holocene record.

8.5 Age models

As already highlighted in the previous section, three sediment cores from Lake Edward were used to form a complete Holocene record. An age model for each individual core was already available (Russell et al., 2003a) (1P and 5M) and Beuning and Russell (2004) (2P). Based on radiocarbon dates from charcoal, plant material and wood, age-depth models were formed through linear interpolation between individual dates, to account for varying sedimentation rates (Russell et al., 2003a). Core chronologies were based on terrestrial material only due to a old carbon reservoir effect resulting in large errors of ~3000-4000 ^{14}C years on aquatic material (Lærdal et al., 2002). Age models were constructed in the same way as those previously published but with re-calibrated radiocarbon dates with the latest CALIB program (version 6.0) (Stuiver et al., 2012).

8.5.1 E96-1P

The core chronology for 1P was based on 6 radiocarbon dates and the age model was constructed using linear interpolation between dates (Table 8.1; Figure 8.14). No obvious hiatuses or erosion surfaces were present. The sediments in 1P span from ~3400 yrs BP at the base to ~900 years BP at the top of the sequence.

Table 8.1: Summary of ^{14}C age determinations for core E96-1P. All radiocarbon ages were calibrated to calendar years using CALIB 6.0 (Stuiver et al., 2012).

Depth (cm)	^{14}C date	Error (^{14}C years)	Calibrated age range (1σ) using CALIB 6		Calendar years BP	Calibrated dates after Russell et al. 2003a) (cal. yrs BP)	Material
2	1020	40	910	976	943	932	Charcoal
146	1225	85	1065	1188	1127	1171	Charcoal
238.5	1530	70	1352	1424	1388	1410	Charcoal
486	2560	110	2486	2763	2625	2738	Charcoal
593.5	3090	60	3243	3378	3311	3279	Charcoal
704.1	3220	45	3385	3472	3429	3449	Gramineae Fragment

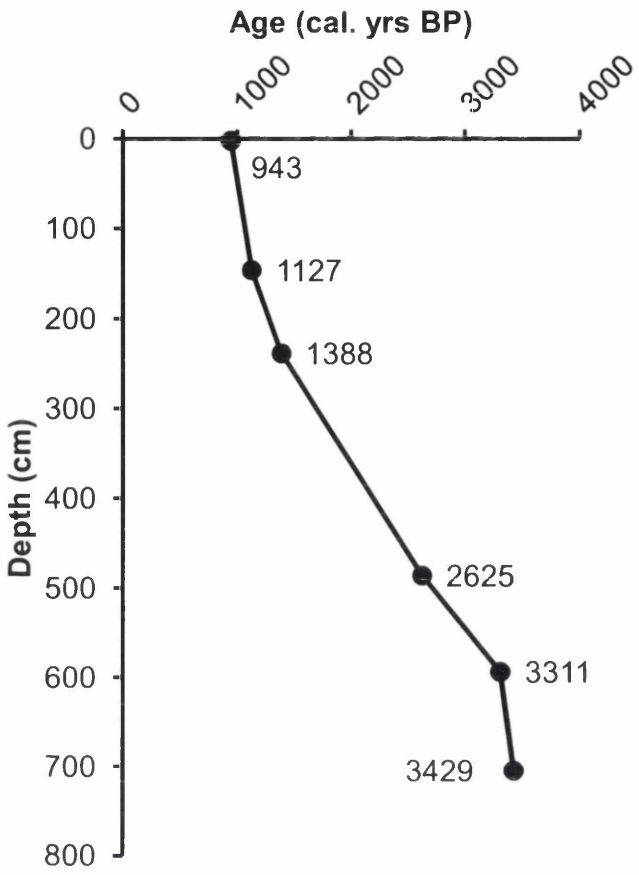

Figure 8.14: Age-depth model for E96-1P. Dates are expressed in calendar years BP (cal. yrs. BP) (modified after Russell et al. (2003a)).

8.5.2 E96-5M

The age model for 5M is based on nine radiocarbon dates (Table 8.2), and was constructed using linear interpolation between calibrated dates (Figure 8.15). As identified in the sediment sequence, a hiatus occurs at ~190cm. The sediments of 5M cover the last 6100 yrs.

Table 8.2: Summary of ^{14}C age determinations for core E96-5M. All radiocarbon ages were calibrated to calendar years using CALIB 6.0 (Stuiver et al., 2012).

Depth (cm)	^{14}C date	Error (^{14}C years)	Calibrated age range (1σ) using CALIB 6		Calendar years BP	Calibrated dates after Russell et al. 2003a) (cal. yrs BP)	Material
30	895	40	742	800	771	789	Charcoal
60	1030	35	924	967	946	942	Charcoal
184.2	1770	35	1616	1676	1646	1640	Charcoal
195.7	2313	47	2306	2359	2333	2343	Charcoal
261.7	2771	48	2837	2895	2866	2854	Charcoal
395.4	3610	50	3852	3979	3916	3899	Wood
554.2	4500	55	5051	5144	5098	5108	Wood
595.8	4800	160	5431	5663	5547	5497	Charcoal
755	5310	110	5988	6208	6098	6073	Charcoal

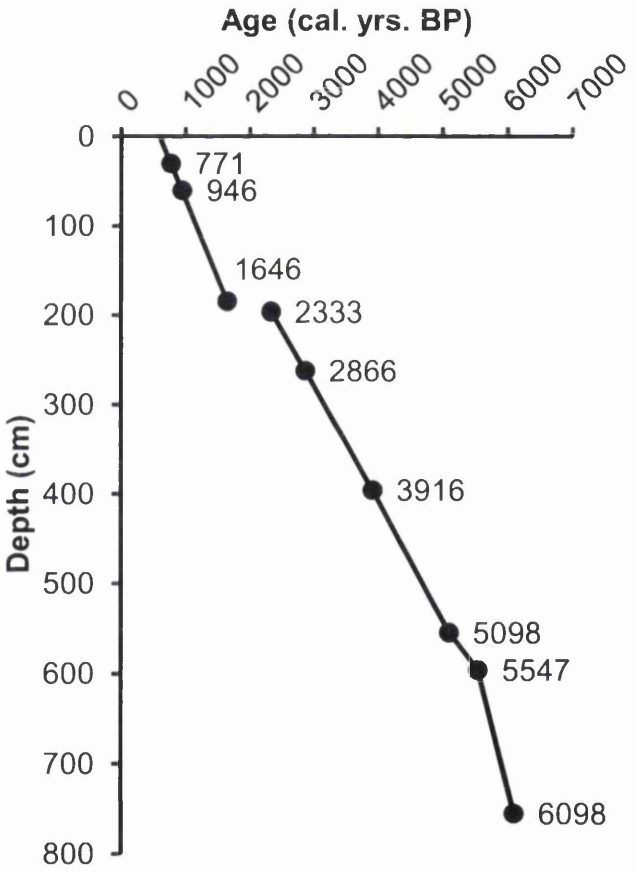

Figure 8.15: Age-depth model for E96-5M. Dates are expressed in calendar years BP (cal. yrs. BP) (modified after Russell et al. (2003a)).

8.5.3 E96-2P

The age-model for core 2P was based on six radiocarbon dates (Table 8.3), and similarly constructed using linear interpolation (Figure 8.16). A hiatus was identified at ~125cm (Figure 8.13c) (Russell et al., 2003a). Radiocarbon dating of charcoal fragments from either side of the erosional surface indicates an interruption in the sediment record of ~2000 years (Russell et al., 2003a). Also, identified in 2P was a reworked deposit towards the base of the core at ~396-409cm which was compositionally very different from the surrounding sediments and was dated to 20,600 ^{14}C years (Lærdal et al., 2002; Russell et al., 2003a; Beuning and Russell, 2004). It was identified as a slump deposit from the surrounding steep terrain and may have been seismically activated (Russell et al., 2003a; Beuning and Russell, 2004). This deposit was removed from further analysis and the age model accounts for this (Figure 8.16).

Table 8.3: Summary of ^{14}C age determinations for core E96-2P. All radiocarbon ages were calibrated to calendar years using CALIB 6.0 (Stuiver et al., 2012).

Depth (cm)	^{14}C date	Error (^{14}C years)	Calibrated age range (1σ) using CALIB 6		Calendar years BP	Calibrated dates after Beuning and Russell 2004) (cal. yrs BP)	Material
12	1203	42	1065	1176	1121	1139	Charcoal
36	1737	85	1539	1736	1638	1658	Charcoal
86	1950	90	1811	2002	1907	1914	Charcoal
124.7	3950	70	4293	4448	4371	4415	Charcoal
128.7	5920	100	6639	6885	6762	6731	Charcoal
472.5	9800	60	11182	11253	11218	11198	Gramineae Fragment

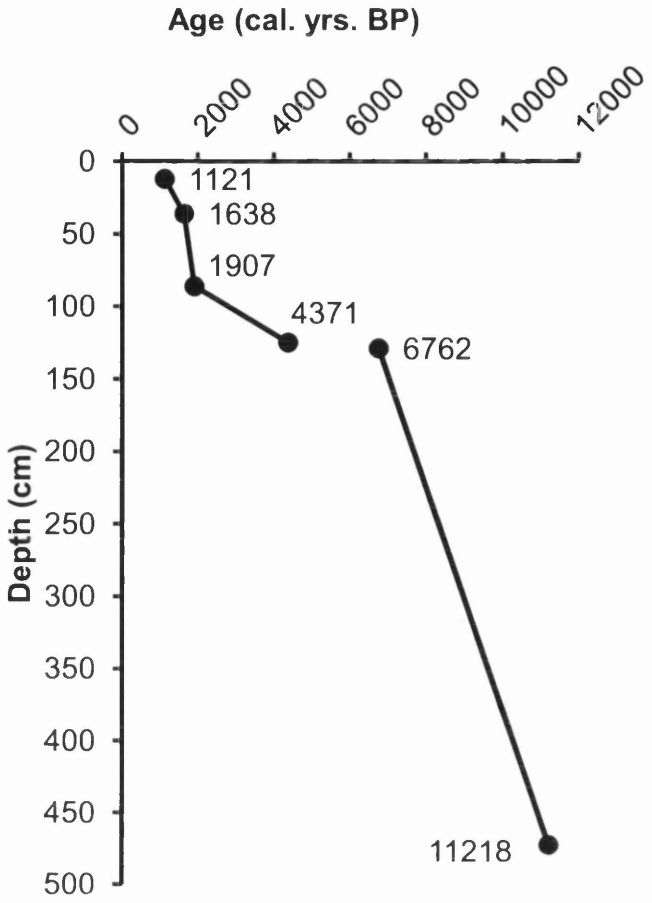

Figure 8.16: Age-depth model for E96-2P. Dates are expressed in calendar years BP (cal. yrs. BP) (modified after Russell et al. (2003a)).

8.6 Existing data for Lake Edward cores

Additional data was published for the Lake Edward cores collected during the IDEAL expedition in Lærdal et al. (2002) and Russell et al. (2003a). However, in the initial publication of the data by Lærdal et al. (2002), age models were tentative and were subsequently revised in succeeding publications (e.g. Russell et al. (2003a; Russell et al., 2003b; Beuning and Russell, 2004; Russell and Johnson, 2005, 2007)). Russell et al. (2003a) did not publish all of the original data using the new age models, so the inclusion here of the work by Lærdal et al. (2002) is described for each core, rather than graphically displayed due to differences in age models used (Lærdal et al., 2002). Data for biogenic silica concentrations (BSi) was obtained from Jim Russell at Brown University, Rhode Island, USA for all three cores. Therefore it was possible to plot them downcore by age using the age

models derived for this thesis (Figure 8.17). The original downcore plots (Lærdal et al., 2002) of total organic carbon (TOC), total organic nitrogen (TON), carbon/nitrogen ratios (C/N), hydrogen index (HI), carbon isotope composition of organic matter ($\delta^{13}C$) and BSi are presented in Appendix IX.

8.6.1 E96-1P

TOC and TON values fluctuated between 10 and 30% and 0.4 and 2%, respectively, throughout the core (~3.4 to 0.9 ka BP). C/N values were high, averaging 27 between 3.4 and 1.7 ka BP (706-300cm), and then they gradually declined to between 16 and 8 during the later part of the record (~1.7 to 0.9 ka BP / 300-0cm). HI values were high (700-850) throughout the whole core and $\delta^{13}C$ values were low (-27‰) at the base and then rose to -23‰ towards the top. BSi was highly fluctuating between 2 and 60% (Figure 8.17).

8.6.2 E96-5M

TOC and TON varied little between 8 and 12% and 0.5 to 1%, respectively, in the section of the core used in this thesis (6.1 to 3.9 ka BP / 390-750cm). C/N values were also stable at 14-16. HI was high and averaged ~500. $\delta^{13}C$ values were steady at -24‰. BSi was relatively low but stable, between 4 and 11% (Figure 8.17).

8.6.3 E96-2P

TOC and TON were relatively low between 5 and 8% and 0.2 to 0.4%, respectively, throughout the core section used in this thesis (~11.2 to 6.9 ka BP / 489-134cm). C/N ratios were fairly constant at ~15 but with occasional fluctuations to 30. HI values were high at ~400 to 600 and $\delta^{13}C$ values were very stable at ~-25‰. BSi values were initially high between 30 and 40% and then gradually decreased to 10% by ~7 ka BP (Figure 8.17).

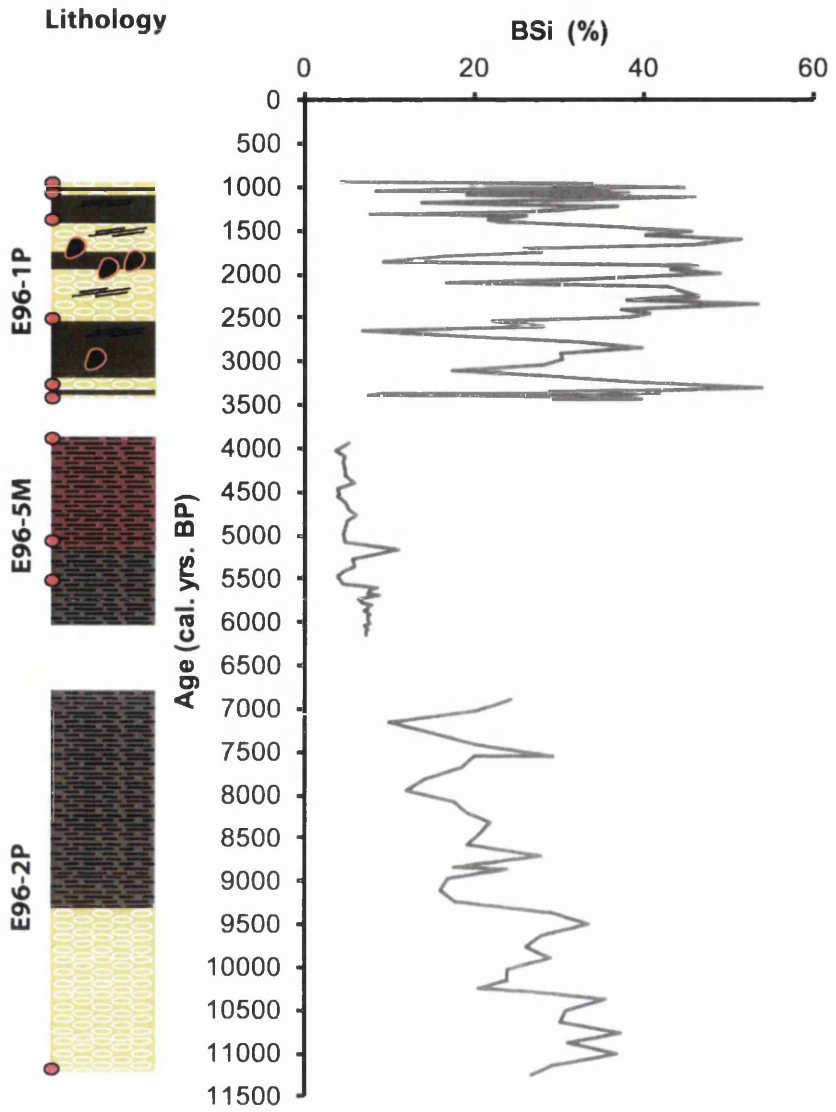

Figure 8.17: BSi concentration data for Lake Edward cores, E96-1P, E96-5M and E96-2P (after Russell et al. (2003a)), plotted against age (cal. yr BP) using the age models from section 8.5.

8.7 Selection of Lake Edward sediment samples for stable-isotope analysis of diatom silica (O and Si), and for lipid analysis

Sediment samples from Lake Edward were carefully selected from a combination of cores retrieved from the lake during the IDEAL expedition in 1996, to form a Holocene record that avoided problems associated with discontinuous sedimentation (e.g. hiatuses, desiccation and erosion surfaces). As already

displayed in the previous sections, several of the sediment archives exhibited discontinuous sedimentation or reworked deposits in sections of the cores. Through strategic sampling from all three cores (1P, 5M and 2P) a suite of samples for diatom isotope analysis and lipid analysis to document the Holocene period have been chosen.

Samples from 704-137cm (~3,400-900 yrs BP) of 1P have been selected to cover the most recent period of the Holocene (Figure 8.13a). 1P is the only core that shows continuous, uninterrupted sedimentation, probably due to its location in the deepest part of the basin, furthest from river inputs and the Kasindi fault (Figure 8.9). Sediments between 474 to 394 cm (~6,000-3,900 yrs BP) from core 5M were chosen to cover the mid-Holocene period, avoiding the hiatus at 190cm. Material from core 2P were selected from 489 to 134cm, avoiding the hiatus of 2000 years at 125cm and to span the period from ~11,100 to 6,900 yrs BP.

From microscopic observation I observed that the most significant contribution of biogenic silica to Lake Edward sediments was from diatoms. The majority of sediments in the selected core sections have very high biogenic silica concentrations, up to 68% in 1P (Lærdal et al., 2002; Russell et al., 2003a), making them particularly suitable for extracting diatoms for stable-isotope analysis. In addition, high TOC throughout the cores (Lærdal et al., 2002) make them good for lipid analysis. Similarly to the sampling strategy used for Lake Victoria, sediment samples from Lake Edward were selected at intervals of approximately every 500 years (n = 21) in order to observe millennial-scale changes through the Holocene. This sampling resolution was applied due to the analytical costs involved for isotope analysis and the scientific priority to obtain records of long-term changes.

8.7.1 Sample specific methods used to clean-up diatom silica from Lake Edward for stable-isotope analysis (O and Si)

Amorphous inorganic silica nodules and concretions were identified in sections with low BSi in the sediment record of core 1P (Figure 8.13a) by Russell et al. (2003a) and Russell and Johnson (2005), and therefore may impact on isotope signatures if present in diatom samples used for O- and Si-isotope analysis. Through careful sampling of core 1P, these horizons have been avoided and no evidence for inorganic silica nodules were found in 1P samples. However, on one occasion,

evidence for silica nodules were found in a sample from core 2P via SEM (Figure 8.18); this was the only occasion that these structures were observed and they have not been identified in 2P before. I consider this to be a small, isolated example and therefore it can be assumed that it will not have had a significant impact on the isotope composition of the respective sample.

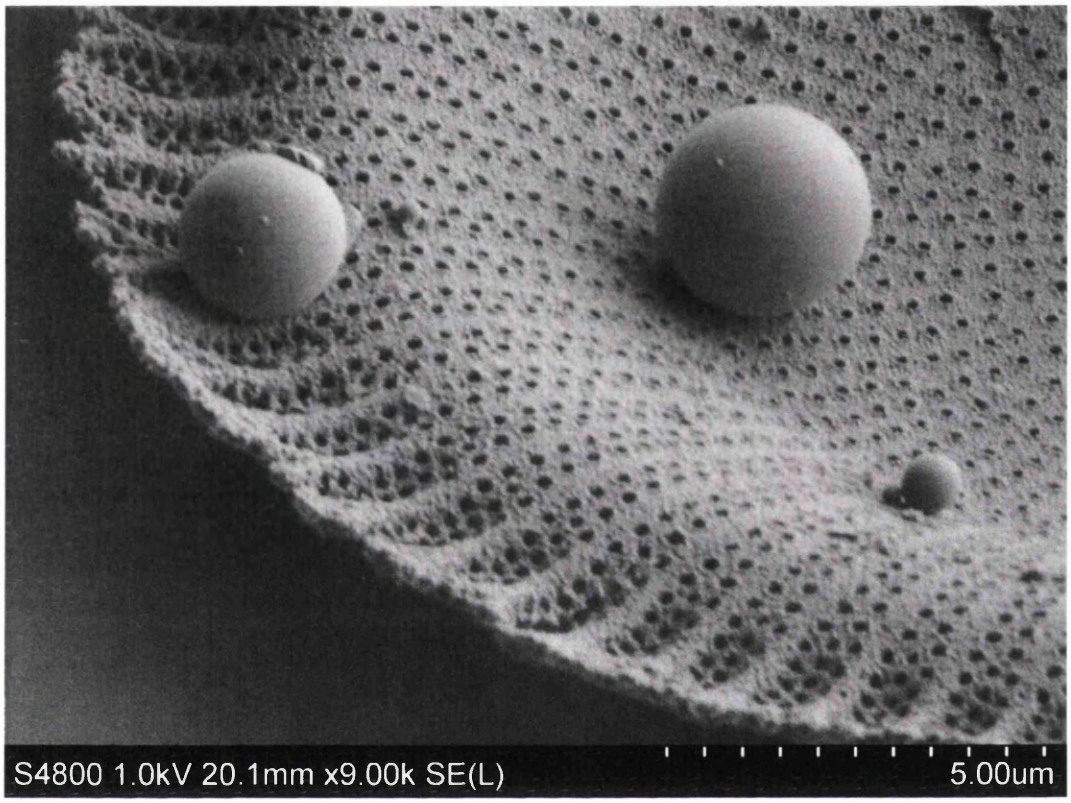

Figure 8.18: Amorphous silica lepispheres (0.5-3µm-diameter) identified in a single sample from core 2P at 7,900 yrs BP (215-219cm). Thought to be associated with silica nodules as identified by Russell et al. (2003a) and Russell and Johnson (2005) in core 1P.

Due to their high diatom concentrations, most of the Lake Edward samples were, in the first instance, good to work with. The main contaminant remaining after organics and carbonates had been removed (for methodology see section 5.4.5 in Chapter 5) was clusters of silt- and clay-sized mineral grains together with diatom fragments, forming aggregates of 30-50 µm diameter (Figure 8.19). This problem was overcome by sonifying the samples for short bursts of 10 seconds at a time (to avoid unnecessary breakages of diatom frustules), repeated 10-20 times to break down the mineral aggregates into individual components. The samples were then sieved at the usual 20, 38 and 63µm sieve sizes, and the resulting sub-samples

were chosen for further clean-up procedures (e.g. differential settling and SPT) based on the remaining contaminants. Two samples, one from 1P (~2,900 yrs BP; 531-537cm) and one from 5M (3,900 yrs BP; 394-402cm) contained mineral aggregates that could not be broken up and therefore removed by sieving. Under cross-polarised light, the aggregates appeared to be composed of feldspar and quartz grains cemented together by an opaque mineral cement (possibly calcite or amorphous silica), very dissimilar in composition to the other aggregates that were easily broken-up. It is likely that these cemented aggregates are associated with inorganic precipitation, possibly with the formation of Si nodules and concretions, although this cannot be determined for certain. The cemented mineral aggregates in these two samples formed a large proportion of the sample (50:50 diatoms to mineral aggregates) and were therefore discounted for further analysis.

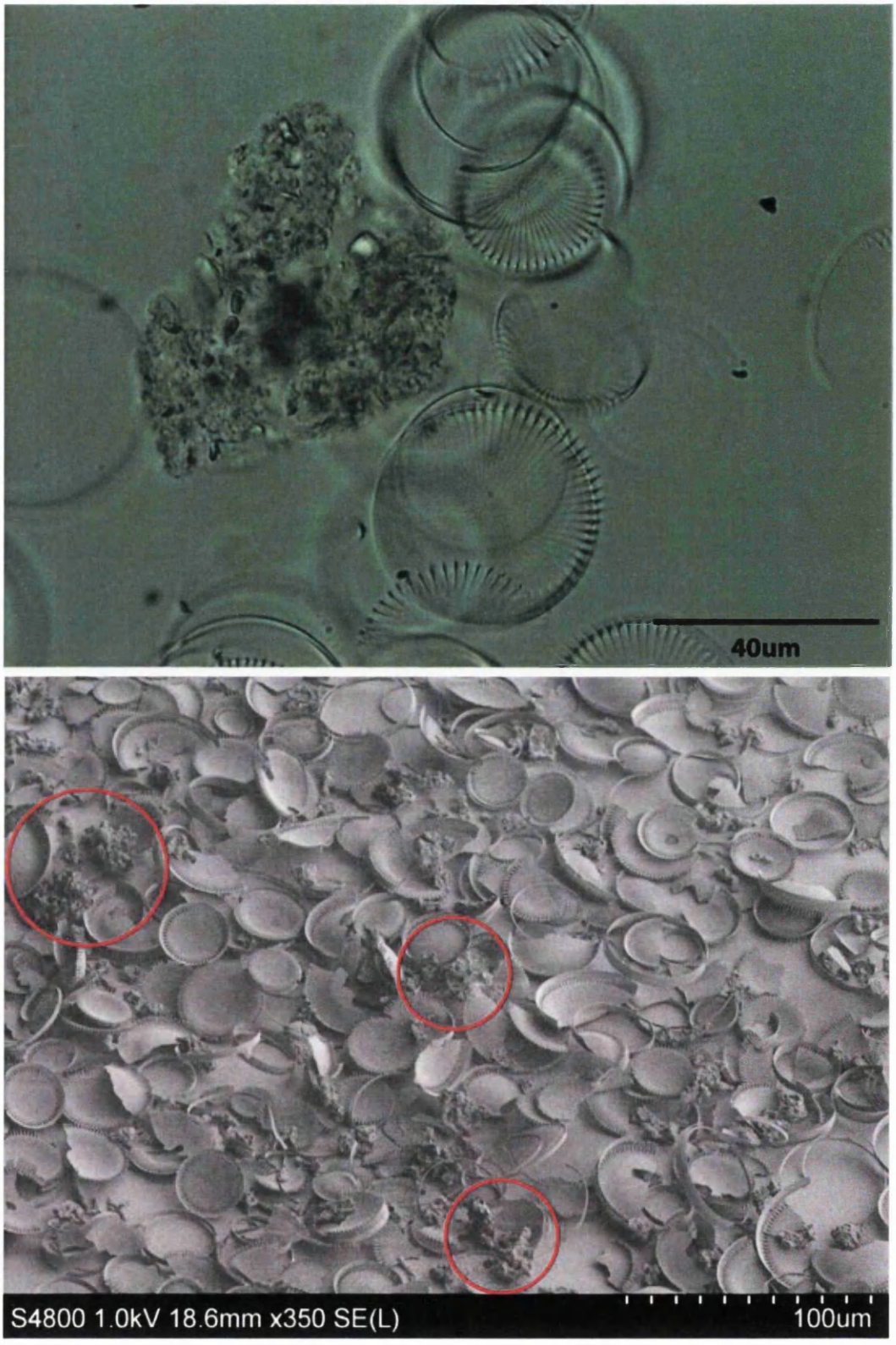

Figure 8.19: Examples of mineral aggregates found in samples throughout the Lake Edward cores by (a) light microscopy and (b) SEM.

In addition to mineral aggregates, some of the Lake Edward samples also contained a significant green algae component. In particular, in the Late Holocene record (1P), *Pediastrum boryanum* (Figure 8.20) and to a lesser extent an unidentified *Botryococcus* spp. (different from that found in Lake Victoria) were present. Interestingly, the majority of *Pediastrum* floated to the top of the conical flask during the organic matter removal stages and could be decanted off. Any remaining *Pediastrum* in the sample were removed from the diatoms through differential settling. *Botryococcus* was removed during the wash-stages of SPT, as described for Lake Victoria in section 7.7.1.

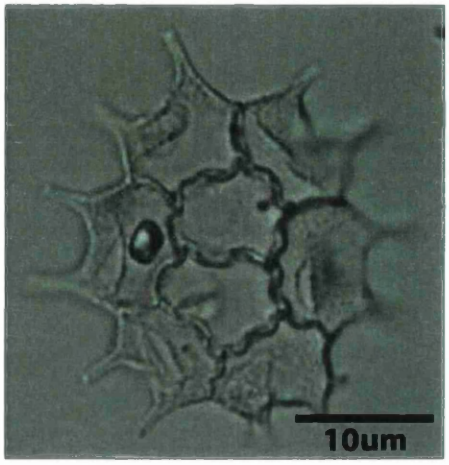

Figure 8.20: Light microscopic image of *Pediastrum boryanum,* commonly found in abundance in the late Holocene record of Lake Edward.

Another problem encountered in Lake Edward sediments, particularly those that were very diatomaceous, was that mats of interlocking diatom girdle bands trapped contaminants (e.g. mineral grains, green algae) (Figure 8.21). However, this was overcome by repeated sonication and re-sieving. And finally, due to large charcoal fragments found in some samples, the >63µm fraction was avoided for isotope analysis when necessary.

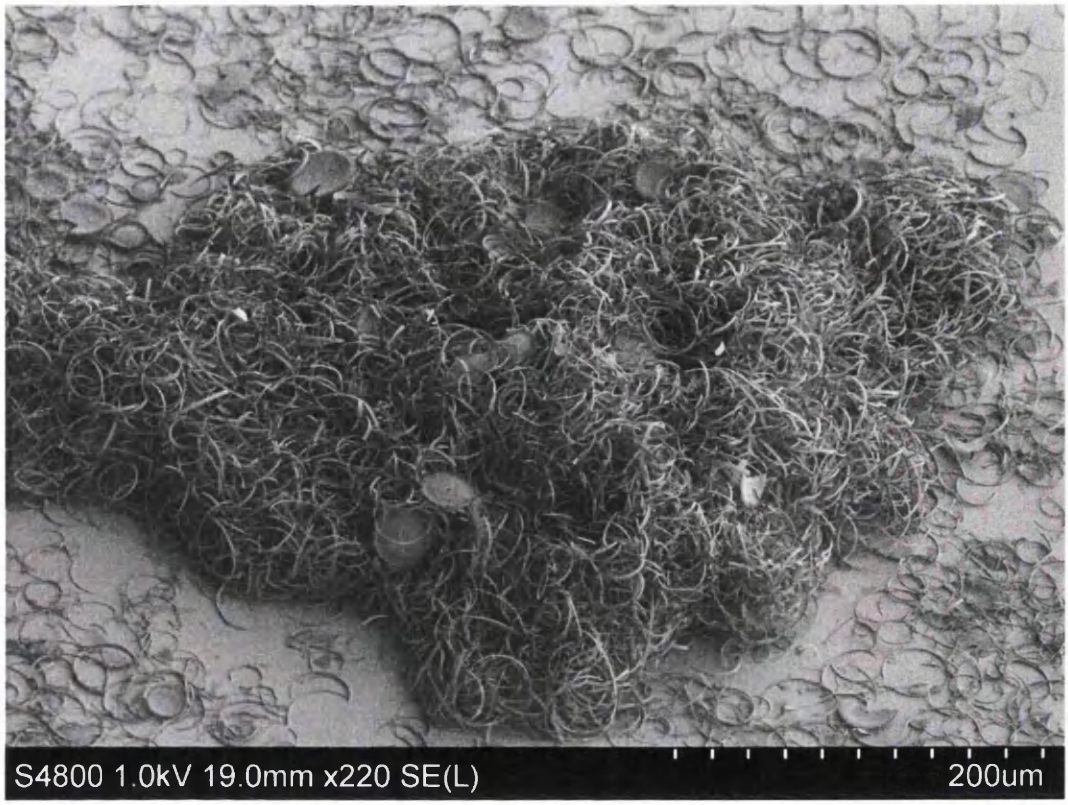

Figure 8.21: SEM image of "mats" of interlocking girdle bands that occurred in Lake Edward sediments and require sonication and re-sieving to disentangle them in order to remove any contamination trapped in-between.

8.8 Lake Edward sediment samples for lipid analysis

Samples were selected for lipid analysis at a resolution of ~500 years from the length of the Holocene (n = 21). The methods used to identify and quantify *n*-alkanes, *n*-alkenes and botryococcene compounds from the total lipid fraction are fully described in Chapter 5, sections 5.4.8 to 5.4.9.

8.9 Results

8.9.1 Purified diatom silica

Diatoms form the largest biogenic silica component in Lake Edward sediments (>99%) with the addition of an occasional sponge spicule or phytolith. The diatom assemblages were dominated by a few main genera; *Stephanodiscus*, *Surirella* and *Nitzschia* (Figure 8.22). *Stephanodiscus* spp. were dominant throughout the whole

Holocene record. A notable shift in the diatom species composition during the mid-Holocene, between 5.2 to 4.3 ka BP (core 5M between 565 and 455 cm) was observed when purifying diatoms for isotope analysis. A change from a mixed assemblage of diatom species comprised of *Stephanodiscus*, *Aulacoseira*, *Suriella*, *Nitzschia*, *Synedra* and *Cymbella* to a composition of purely one taxon, *Stephanodiscus*, occurred. Of the 21 sediment sample depths selected (500-year resolution), 19 of the samples were successfully purified for O- and Si-isotope analysis. Apart from some diatoms that showed signs of breakage (especially the large *Suriella* spp.), thought to have incurred during the clean-up stages, the remainder were well preserved throughout the sediments and there were no signs of dissolution or diagenesis (Figure 8.23). The most common size fraction of material used for isotope analysis was 20-38µm but when charcoal was not present in the larger fractions, the >63µm fraction was frequently analysed. Whenever possible, for many of the sediment sample depths, several size fractions were analysed to check for diatom species/size effects and for contamination by problem components (e.g. charcoal fragments). In total, including replicates and multiple size fractions for some samples, 33 cleaned diatom samples were analysed for $\delta^{18}O$ and $\delta^{30}Si$ (full list of samples analysed in Appendix X).

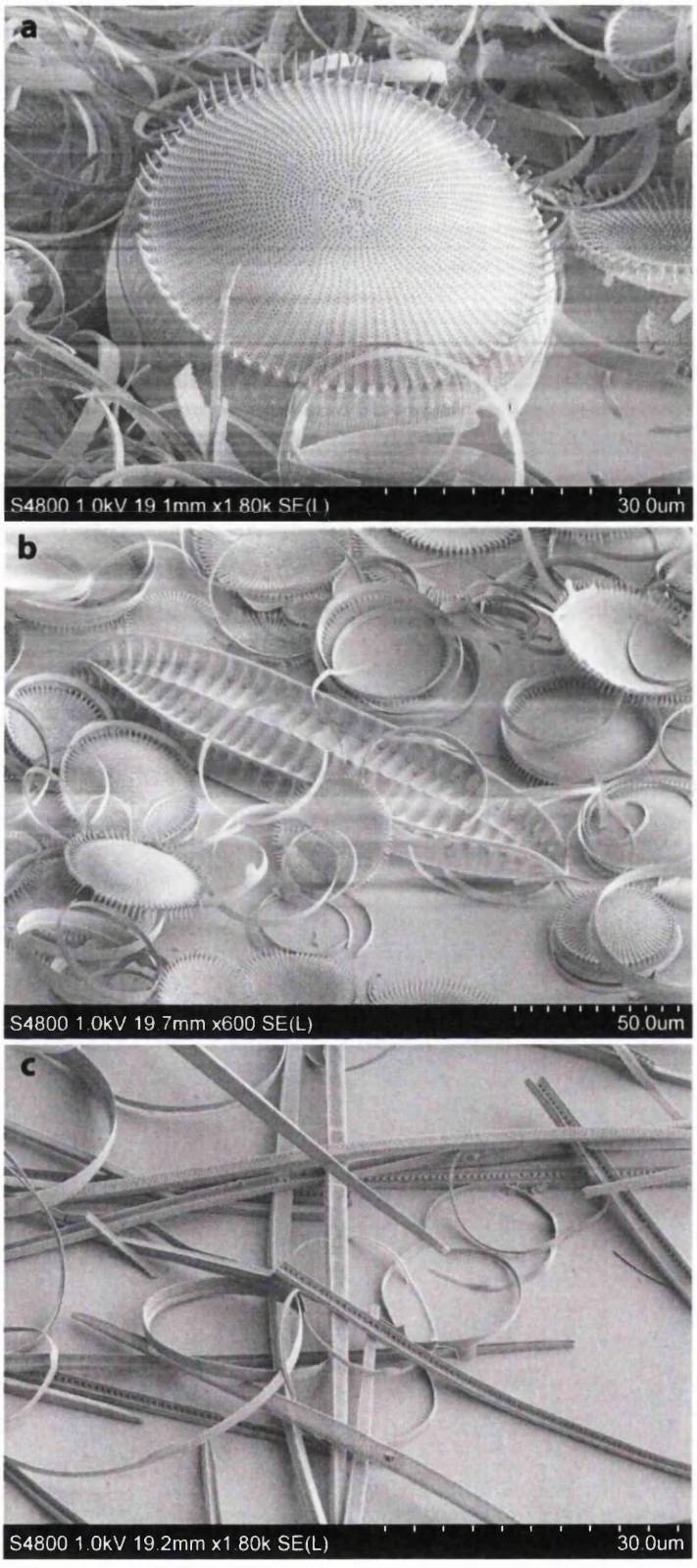

Figure 8.22: SEM images of the most abundant diatom taxa in Lake Edward: (a) *Stephanodiscus* spp, (b) *Surirella* spp. (centre) and (c) *Nitzschia* spp.

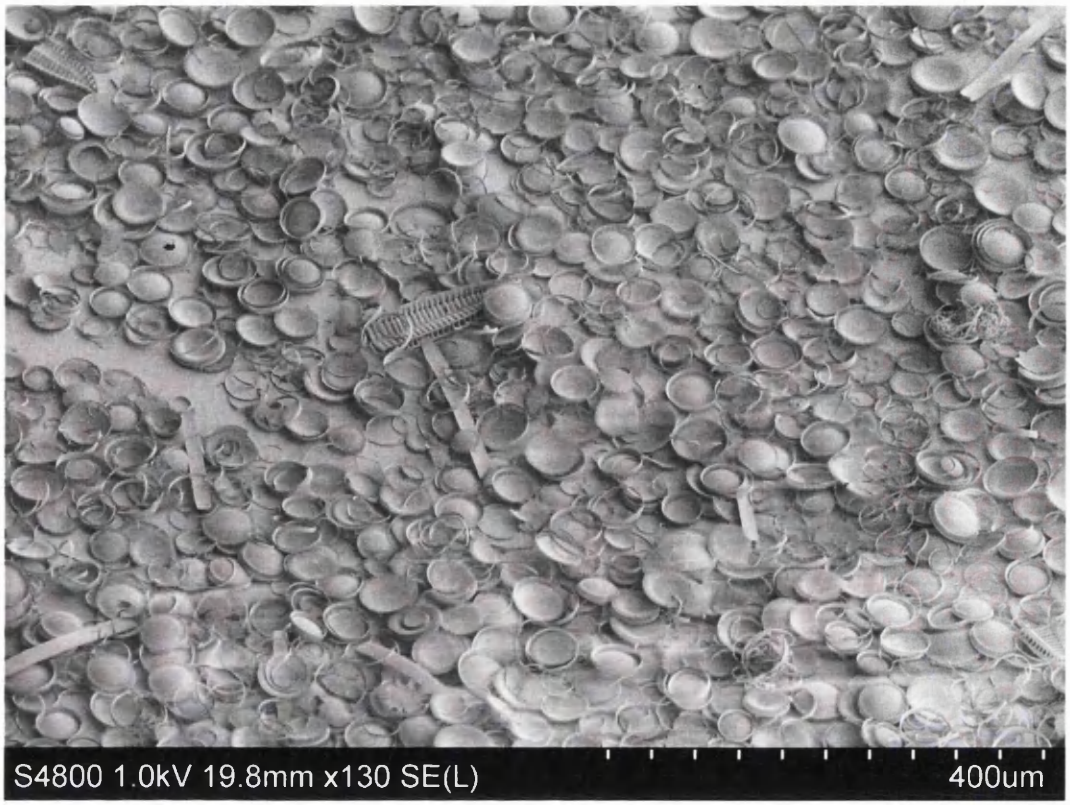

Figure 8.23: SEM image of purified diatoms from Lake Edward (1.9 ka BP) used for isotope analysis and showing the excellent preservation and purity of a diatom sample typically found in Lake Edward.

Analytical precision (2σ), based on replicate samples, was ±0.06‰ for $\delta^{29}Si$, ±0.14‰ for $\delta^{30}Si$ and ±0.38‰ for $\delta^{18}O$. From replicated samples and from the observed relationship of $\delta^{29}Si$ to $\delta^{30}Si$ (Figure 8.24), some samples were removed due to erroneous results caused by potential contamination in the purified samples (e.g. charcoal and silicate minerals) (Appendix IX for samples that were removed). Samples (n = 3) that did not plot along the expected mass-dependent relationship between $\delta^{29}Si$ and $\delta^{30}Si$ (Figure 8.24), were suspected to be contaminated, possibly by small silicate minerals remaining with the diatoms. Therefore, the final dataset (see Appendix IX) includes 26 $\delta^{18}O$ values and 30 $\delta^{30}Si$ values obtained for the Holocene. There was no evidence for significant variations in isotope values between size fractions; consequently, the mean value is employed for depths with multiple sub-samples.

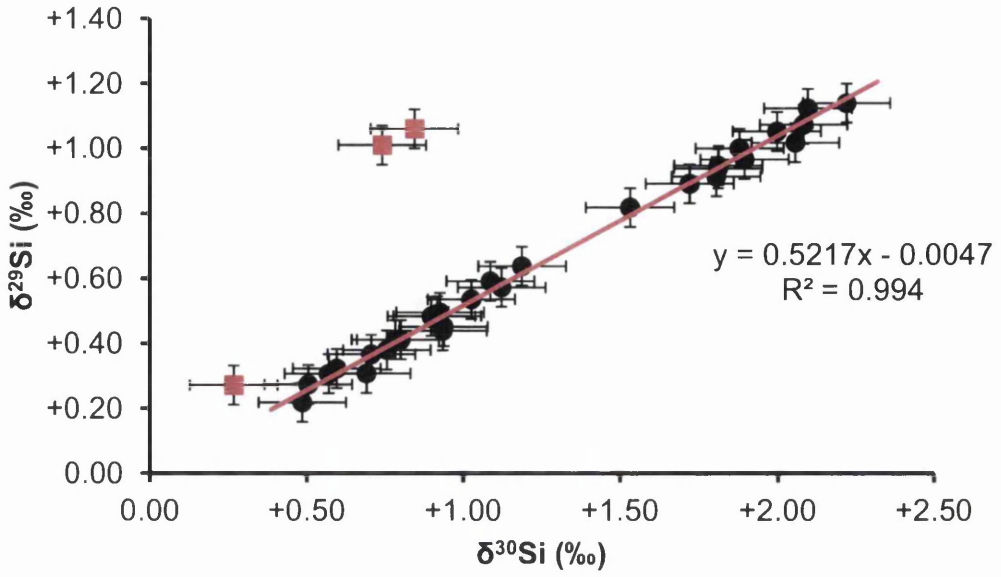

Figure 8.24: Silicon isotope measurements of all Lake Edward diatom samples. Three samples (red squares) do not plot along the expected mass-dependent relationship between $\delta^{29}Si$ and $\delta^{30}Si$, and therefore are suspected to be contaminated, probably by small silicate minerals remaining with the diatoms. These three samples have been removed from further analysis. Error bars are ±0.06‰ for $\delta^{29}Si$ and ±0.14‰ for $\delta^{30}Si$ (2σ).

8.9.2 Oxygen and silicon isotope analysis of diatom silica

During the Holocene, $\delta^{18}O_{diatom}$ values varied by 7.2‰ in the sediments of Lake Edward (Table 8.4; Figure 8.25a). Early Holocene (~11.1-7.3 ka BP) $\delta^{18}O_{diatom}$ values were relatively low and stable, although fluctuating between +36.8 and +38.5‰. Between ~6.9 and 5.6 ka BP $\delta^{18}O_{diatom}$ values increased abruptly by 4.6‰, from +35.4 to +40.0‰. A sudden decrease of 3.2‰ between ~5.6 and 5.2 ka BP was followed by an abrupt increase of 3.5‰ at 4.4 ka BP to +40.3‰. From ~4.4 ka BP onwards, $\delta^{18}O_{diatom}$ values gradually began to increase, reaching a maximum for the whole Holocene (+42.6‰) at ~1.9 ka BP and then decreasing slightly (to +41.6 at ~1.4 ka BP) before reaching +42.2‰ at ~1 ka BP.

$\delta^{30}Si_{diatom}$ values varied by 1.67‰ during the Holocene, from +0.49 to +2.16‰ (Table 8.4; Figure 8.25b). During the early Holocene (~10.7 to 9.8 ka BP), they were relatively low (+0.49 to +0.60‰) after declining from +1.07‰ at 11.1 ka BP. Between ~9.8 and 9.5 ka BP, a positive shift of 0.51‰ occurred leading to stable values (+0.69 – +1.00‰) lasting until ~4.4 ka BP. From ~4.4 to 3.4 ka BP $\delta^{30}Si_{diatom}$

values increased by +1.23‰ to the highest value of the entire Holocene (+2.16‰), shortly followed by an abrupt decrease to +1.06‰ at ~2.9 ka BP. During the Late Holocene (~2.9 to 1.0 ka BP) they rose again to relatively high values, peaking at +1.99‰ at 1.4 ka BP, followed by a small downturn to 1.92‰ by ~1 ka BP.

The relationship between $\delta^{30}Si_{diatom}$ and $\delta^{18}O_{diatom}$, although not directly causative, is statistically significant ($R^2 = 0.63$; $p < 0.0001$). Showing a trend of increasing $\delta^{30}Si_{diatom}$ with increasing $\delta^{18}O_{diatom}$ (Figure 8.26).

Table 8.4: Oxygen and Silicon isotope values from diatoms in Lake Edward cores, with corresponding depths and estimated ages.

Depth (cm)	Age (cal. yr. BP)	Size fraction (µm)	$\delta^{18}O_{diatom}$ (‰)	$\delta^{29}Si_{diatom}$ (‰)	$\delta^{30}Si_{diatom}$ (‰)
40.0	991	>63	–	+0.97	+1.89
40.0	991	38-63	+41.83	+1.02	+2.06
40.0	991	20-38	+42.54	+0.91	+1.80
248.3	1436	>63	+41.56	+1.07	+2.08
248.3	1436	38-63	+41.82	+1.05	+2.00
248.3	1436	20-38	+41.30	+1.00	+1.88
350.0	1945	20-38	+42.88	+0.94	+1.81
350.0	1945	20-38	+42.70	+0.89	+1.72
350.0	1945	>63	–	+0.82	+1.53
350.0	1945	38-63	+42.11	+0.95	+1.81
534.0	2931	>63	+41.41	+0.64	+1.19
534.0	2931	>63	+41.31	+0.50	+0.93
702.3	3426	>63	+40.35	+1.14	+2.22
702.3	3426	>63	–	+1.12	+2.10
458.4	4386	20-38	+40.31	+0.44	+0.93
562.5	5189	20-38	+36.77	+0.31	+0.69
608.8	5593	20-38	+39.98	+0.41	+0.78
137.2	6869	>63	+35.38	+0.41	+0.80
167.2	7258	20-38	+37.78	+0.48	+0.90
217.5	7908	20-38	+36.81	+0.38	+0.76
256.7	8417	>63	+38.53	+0.37	+0.71
297.0	8939	20-38	+36.94	+0.45	+0.94
338.0	9470	>63	–	+0.59	+1.09
338.0	9470	20-38	+38.52	+0.49	+0.92
364.3	9810	>63	+36.56	+0.22	+0.49
364.3	9810	>63	+36.97	+0.27	+0.50
410.5	10409	>63	+38.40	+0.31	+0.57
431.5	10681	>63	+38.14	+0.32	+0.60
466.3	11131	20-38	+38.30	+0.57	+1.12
466.3	11131	20-38	+37.95	+0.54	+1.03

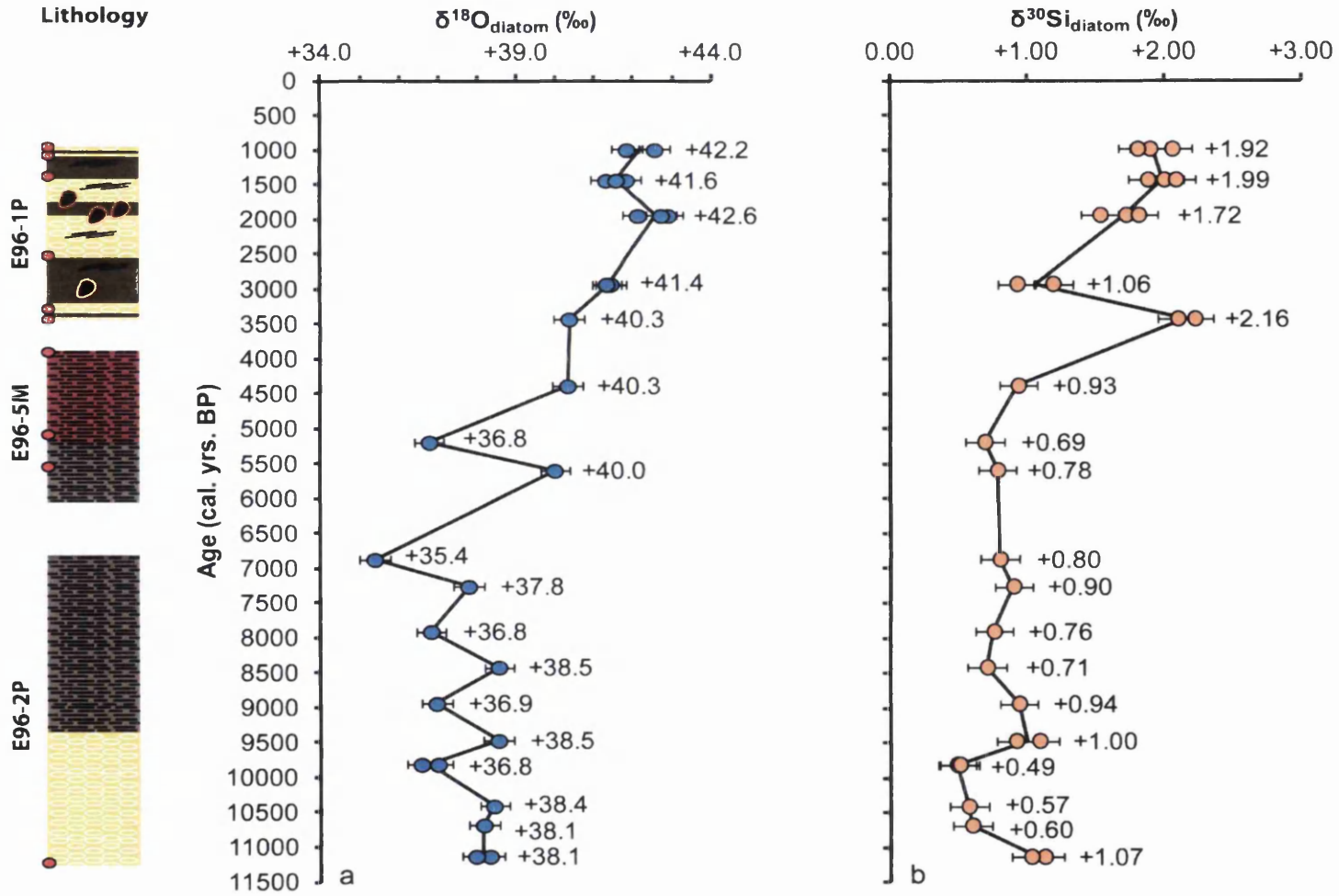

Figure 8.25: Variations in (a) $\delta^{18}O_{diatom}$ and (b) $\delta^{30}Si_{diatom}$ values of Lake Edward cores during the Holocene. Data points are labelled, and mean values for different size fractions are shown. Error bars represent 2σ. For core descriptions see Figure 8.13.

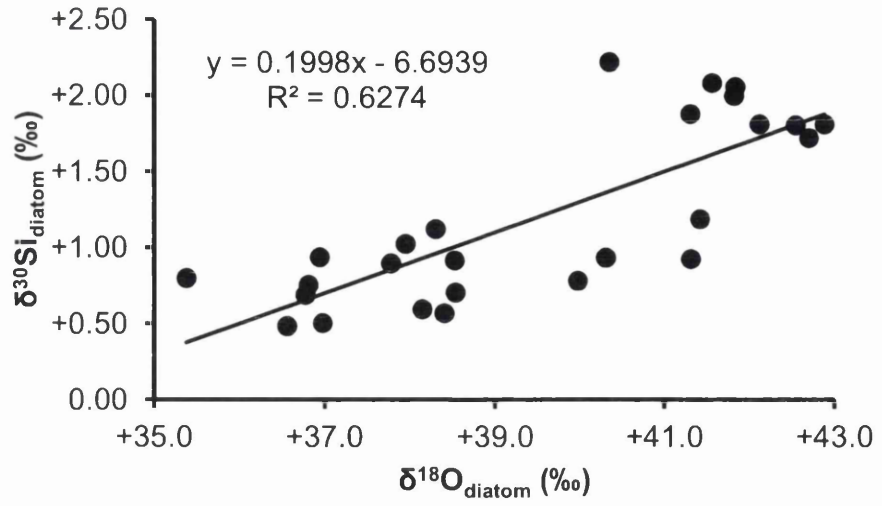

Figure 8.26: $\delta^{30}Si_{diatom}$ vs. $\delta^{18}O_{diatom}$ values from Lake Edward Holocene sediments.

8.9.3 Lipids: abundance and distribution

The hydrocarbon fraction of total lipids has been identified and quantified for the Lake Edward Holocene record (Appendix XI for the full dataset). The Carbon Preference Index (CPI), which ranged from 1.1 to 10.2, is often used as measure of odd- over even-numbered carbon molecules in *n*-alkanes, where odd-numbered chains dominate primary hydrocarbon compositions (Meyers and Ishiwatari, 1993). Low CPI values (≈1) may indicate diagenesis, although in this case, a decrease in the abundance of *n*-alkanes does not parallel changes in the CPI (Figure 8.27). Instead, the CPI responds to a sudden shift to dominance of the C_{23} *n*-alkane, suggesting a significant input from aquatic macrophytes, which can be an important contributor of organic matter to lake sediments (Brenner et al., 2006). In addition, the presence and high abundance of *n*-alkenes, which are hydrocarbons with a single bond and are less refractory than *n*-alkanes, in Lake Edward sediments supports the notion that diagenesis has been limited in the majority of the record.

The dominant components of the hydrocarbon fraction were the mid- to long-chain *n*-alkanes and *n*-alkenes (Figures 8.27 and 8.28; Table 8.5). C_{23}, C_{25}, C_{27}, C_{29} and C_{31} *n*-alkanes all have significant abundances. The long-chain, C_{27} and C_{29} homologues were the dominant *n*-alkanes in the early- to mid-Holocene period with

a shift between ~3.9 to 3.4ka BP to mid-chain *n*-alkanes, with a C_{23} homologue predominance for the late Holocene (Figures 8.27 and 8.28; Table 8.5). A dominance of long-chain *n*-alkanes are indicative of terrestrial higher plant origin (Eglinton and Hamilton, 1967), whereas mid-chain *n*-alkanes have been identified as being characteristic of aquatic plant macrophytes (submerged and floating) (Cranwell, 1984; Viso et al., 1993; Ficken et al., 2000).

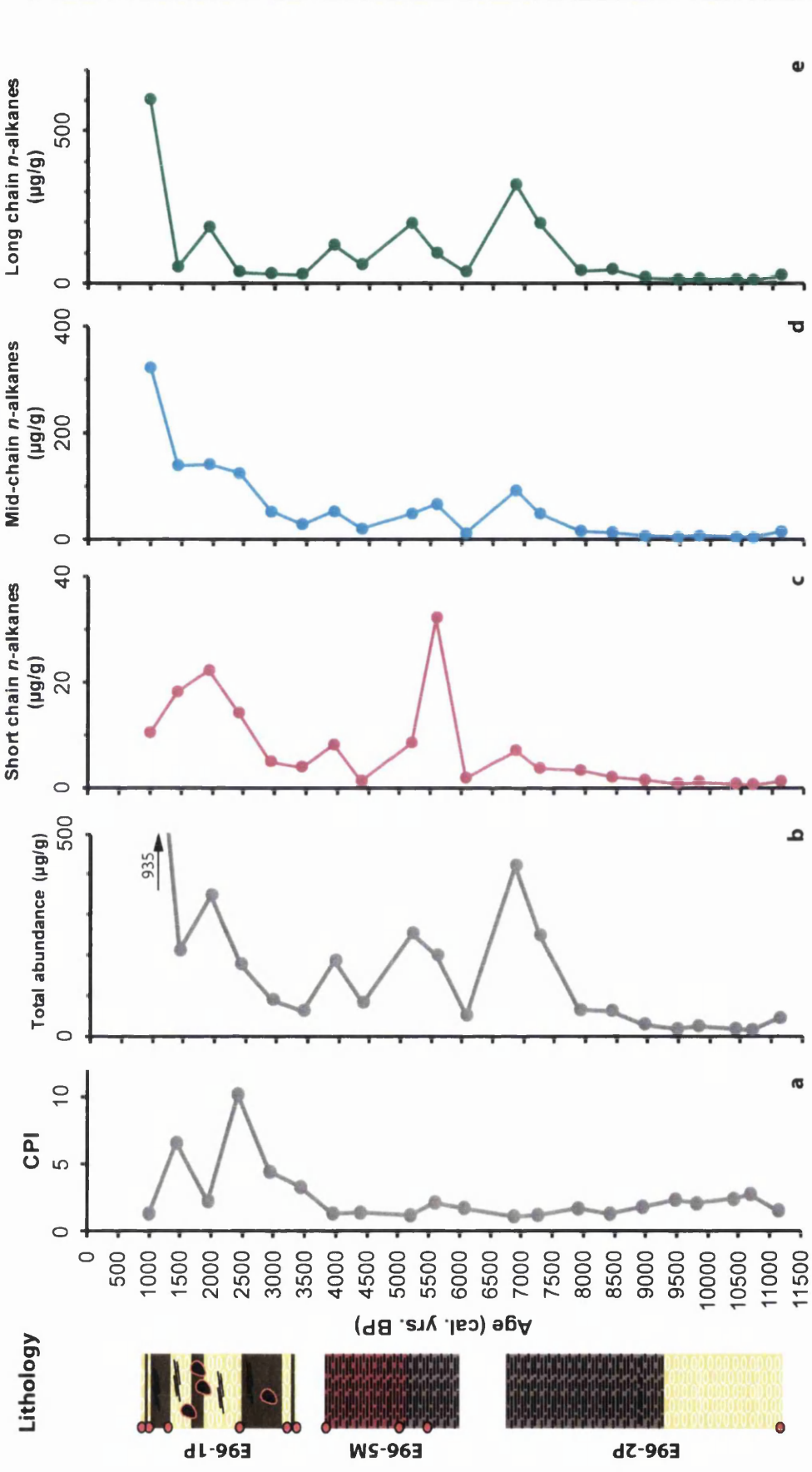

Figure 8.27: Carbon Preference Index (CPI) for *n*-alkanes from Lake Edward (a) and their total abundance downcore (b). Short chain (C_{19}-C_{21} inclusive) (c), Mid-chain (C_{22}-C_{25} inclusive) (d) and Long chain (C_{26}-C_{35} inclusive) *n*-alkane abundance expressed in µg/g.

Table 8.5: Abundance and distribution parameters of *n*-alkanes and *n*-alkenes in Holocene sediments of Lake Edward.

		n-alkanes									*n*-alkenes			
Sample name	Age (cal. yrs. BP)	Total abundance (µg/g)	C no. Range	Most abundant C no.	CPI[1]	Short chain C_{19}-C_{21} inclusive (µg/g)	Mid-chain C_{22}-C_{25} inclusive (µg/g)	Long chain C_{26}-C_{35} inclusive (µg/g)	P_{wax}[2]	P_{aq}[3]	Total abundance (µg/g)	C no. Range	Most abundant C no.	P_{alg}[4]
ED1	991	935	19-35	27	1.3	10.3	323.4	601.7	0.56	0.60	31	25-27	27	0.16
ED2	1436	211	19-35	23	6.6	18.1	140.0	52.8	0.21	0.89	118	23-27	27	0.87
ED3	1945	348	19-35	23	2.2	22.1	141.9	183.8	0.44	0.73	85	23-27	27	0.62
ED4	2420	177	19-35	23	10.2	14.1	125.1	37.6	0.18	0.93	73	23-27	27	0.87
ED5	2931	90	19-35	23	4.4	4.9	52.9	31.8	0.31	0.87	25	23-27	27	0.77
ED6	3426	62	19-35	23	3.3	3.8	29.3	29.3	0.40	0.73	15	23-27	27	0.58
ED17	3940	186	18-35	27	1.3	8.0	53.2	124.7	0.61	0.55	12	23-27	27	0.26
ED18	4386	83	19-35	27	1.4	1.2	20.5	60.8	0.68	0.44	10	23-30	30	0.19
ED19	5189	254	18-35	29	1.2	8.4	49.1	195.8	0.74	0.36	4	23-27	27	0.07
ED20	5593	199	18-35	25	2.1	32.1	66.9	98.3	0.50	0.66	40	23-27	27	0.58
ED21	6062	51	18-35	27	1.7	1.7	12.0	37.4	0.69	0.43	16	21-29	28	0.36
ED7	6869	422	19-35	27	1.1	6.9	92.2	322.5	0.72	0.41	0	–	–	–
ED8	7258	249	19-35	27	1.2	3.5	49.0	196.0	0.75	0.36	7	23-27	27	0.10
ED9	7908	64	17-35	27	1.7	3.1	16.8	41.2	0.65	0.49	6	23-27	27	0.28
ED10	8417	62	17-35	27	1.3	1.9	14.3	45.1	0.70	0.42	2	23-27	27	0.14
ED11	8939	29	17-35	29	1.8	1.4	7.1	19.6	0.71	0.39	1	23-27	27	0.15
ED12	9470	17	18-35	27	2.4	0.7	4.9	11.6	0.68	0.45	4	23-29	27	0.39
ED13	9810	24	18-35	29	2.1	1.1	7.4	15.5	0.66	0.45	2	23-27	27	0.23
ED14	10409	18	18-35	29	2.4	0.6	5.2	12.0	0.67	0.43	1	23-27	27	0.17
ED15	10681	15	18-35	29	2.8	0.5	4.3	10.1	0.67	0.43	1	23-27	27	0.20
ED16	11131	44	19-35	27	1.5	1.1	15.8	27.0	0.56	0.57	1	23-27	27	0.11

[1]Carbon Preference Index (CPI): $2(C_{23-31}odd)/(C_{22-30}even + C_{24-32}even)$.
[2]P_{wax} (*n*-alkane land plant proxy) = $(C_{27} + C_{29} + C_{31})/(C_{23} + C_{25} + C_{27} + C_{29} + C_{31})$ (Zheng et al., 2007).
[3]P_{aq} (*n*-alkane non-emergent aquatic plant proxy) = $(C_{23} + C_{25})/(C_{23} + C_{25} + C_{29} + C_{31})$ (Ficken et al., 2000).
[4]P_{alg} (*n*-alkene algae proxy) = $(C_{23:1} + C_{25:1} + C_{27:1} +)/(C_{23:1} + C_{25:1} + C_{27:1} + C_{29} + C_{31} + C_{33})$ (modified after Zhang et al. (2004)).

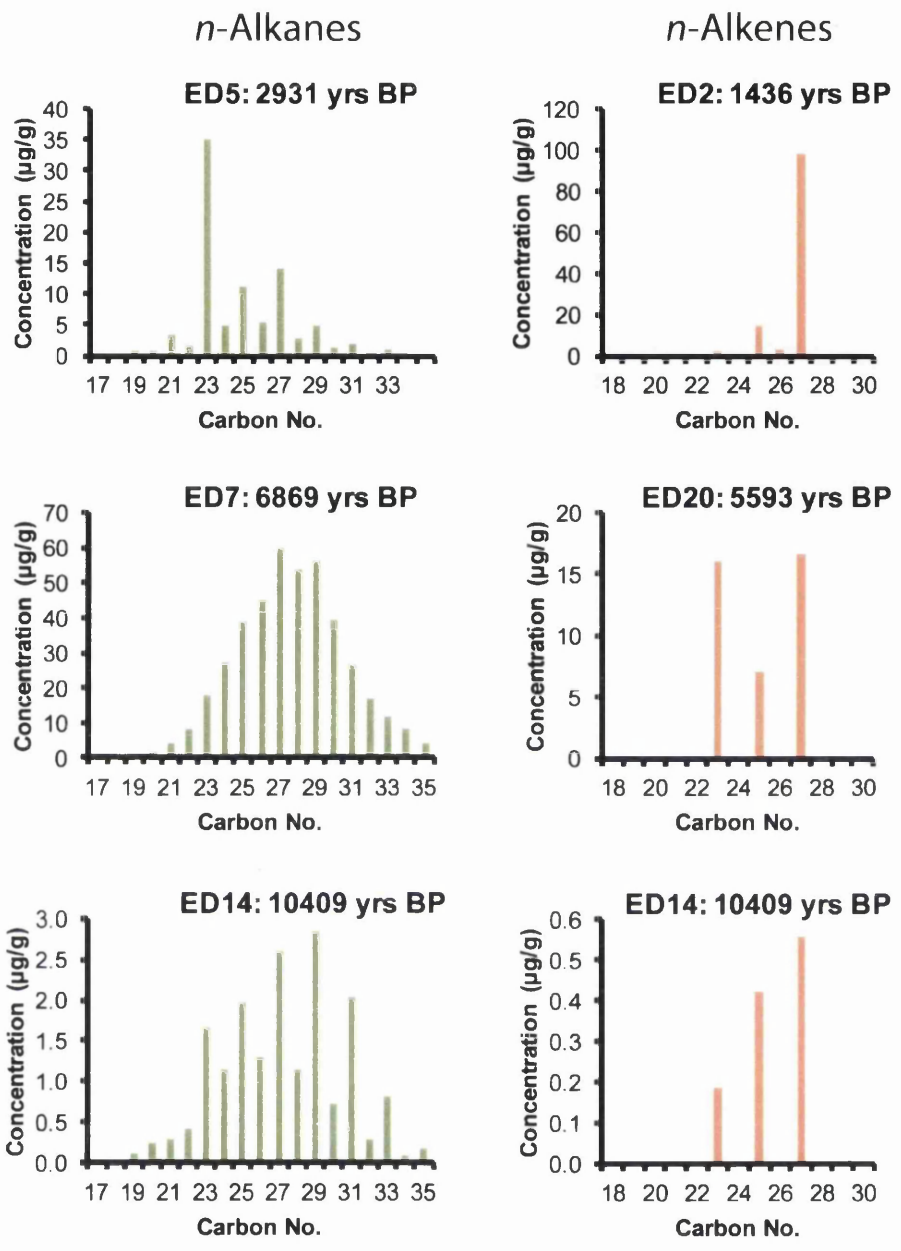

Figure 8.28: Typical homologue distribution and abundance of *n*-alkanes and *n*-alkenes for three selected samples from Lake Edward during the Holocene.

A *n*-alkane proxy, $P_{wax} = (C_{27} + C_{29} + C_{31})/(C_{23} + C_{25} + C_{27} + C_{29} + C_{31})$, was proposed (Zheng et al., 2007) to distinguish between contributions from emergent/terrestrial and submerged/floating plants, as the former exhibit characteristic C_{27} and C_{29} *n*-alkanes dominance and the latter maximise at C_{23} and C_{25} *n*-alkanes (Ficken et al., 2000). In the Holocene at Lake Edward, P_{wax} varied from 0.18 to 0.75, signifying changes in the origin of the organic matter (Figure 8.29a; Table 8.5). At the

beginning of the Holocene P_{wax} values increased from 0.56 to 0.67 and remained high and relatively stable (between 0.65 to 0.75) during the early Holocene (~11-6ka BP) suggesting contributions largely from emergent aquatic macrophytes and vascular land plants. At 5.6 ka BP, an abrupt shift to lower values (0.50) occurred, suggesting a significant input from submerged/floating vegetation at that time. Just as abrupt, P_{wax} values were briefly restored to early Holocene values before beginning to decrease persistently at ~4 ka BP. P_{wax} values begin to decrease rapidly to a minimum at 2.4 ka BP, suggesting a decline in contributions from emergent/terrestrial vegetation and a shift towards significant input from submerged and floating macrophytes. During the late Holocene (~2.4-0.9 ka BP), P_{wax} values fluctuated greatly but remained very low, indicating the predominance of submerged/floating vegetation.

Another useful *n*-alkane based proxy proposed by Ficken et al. (2000) to reflect non-emergent aquatic plant input to lake sediments is the $P_{aq} = (C_{23} + C_{25})/(C_{23} + C_{25} + C_{29} + C_{31})$. A P_{aq} value of greater than 0.4 signifies a important fraction of sedimentary *n*-alkanes from submerged/floating plants (Ficken et al., 2000). In Lake Edward sediments during the Holocene, P_{aq} varied from 0.36 to 0.93 (Figure 8.29b; Table 8.5). At the beginning of the Holocene (~11.1 ka BP) P_{aq} values were relatively high (0.57). Between ~10.7 to 6.1 ka BP, P_{aq} values were low and stable (0.36-0.49), indicating a prolonged period of reduced input from non-emergent aquatic plants. Between 6.1 ka and 5.6 ka BP, a sharp rise in P_{aq} values to 0.66 was followed by an abrupt decline to minima values (0.36) at 5.2 ka BP. From ~5.2 ka BP to 2.4 ka BP P_{aq} values steadily increased to maximum values of 0.93, signifying increasing contributions from submerged/floating macrophytes. From ~2.4 ka BP onwards, P_{aq} values remained high but fluctuating. P_{wax} and P_{aq} values co-vary in the opposite direction, which reflects the similar n-alkane components used to distinguish relative inputs from emergent/terrestrial plants (P_{wax}) and submerged/floating macrophytes (P_{aq}).

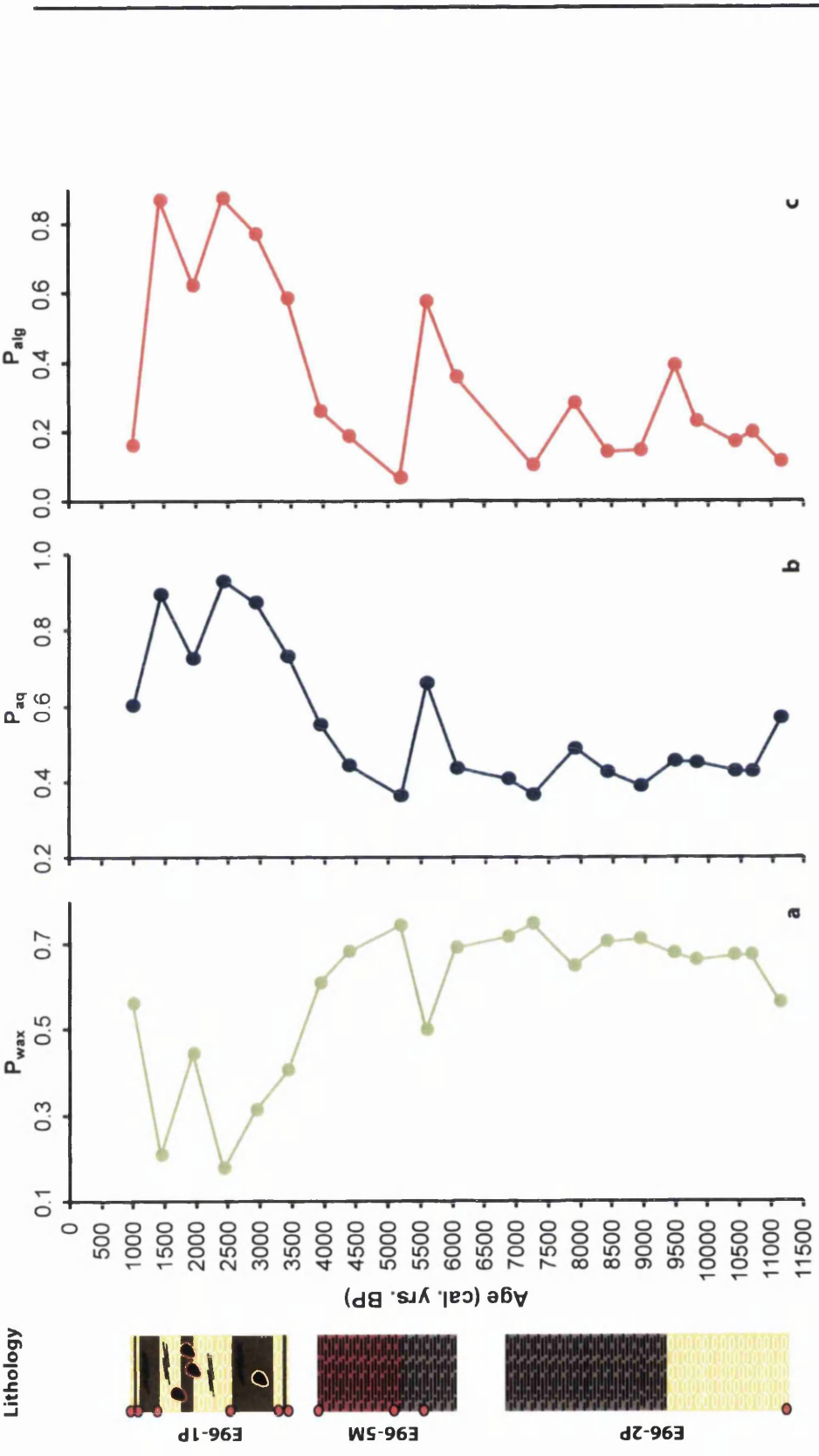

Figure 8.29: Holocene variations in (a) higher plant (P_{wax}), (b) non-emergent aquatic plants (P_{aq}) and (c) algal (P_{alg}) contributions in Lake Edward. $P_{wax} = (C_{27} + C_{29} + C_{31})/(C_{23} + C_{25} + C_{27} + C_{29} + C_{31})$ (Zheng et al., 2007), $P_{aq} = (C_{23} + C_{25})/(C_{23} + C_{25} + C_{29} + C_{31})$ (Ficken et al., 2000) and $P_{alg} = (C_{23:1} + C_{25:1} + C_{27:1})/(C_{23:1} + C_{25:1} + C_{27:1} + C_{29} + C_{31} + C_{33})$ (modified after (Zhang et al., 2004).

n-Alkenes were also present in the hydrocarbon fraction and occurred in high abundance (1-118µg/g) throughout the Lake Edward sediments (apart from ED7; ~6.9 ka BP), with C numbers ranging from 21 to 29 and odd-over-even predominance, with $C_{27:1}$ being the dominant homologue (Figure 8.28; Table 8.5), similar to Lake Victoria (section 7.9.3 in Chapter 7). Many studies have reported high abundances of mid- to long-chain *n*-alkenes in river and lacustrine sediments and suggest that they are algal indicators (Matsumoto et al., 1990; Zhang et al., 2004; Theissen et al., 2005; de Mesmay et al., 2007; Xu and Jaffé, 2009). Zhang et al. (2004) formulated the P_{alg} proxy (P_{alg} = ($C_{23:1}$ + $C_{25:1}$ + $C_{27:1}$ + Cyclobotryococcatriene)/($C_{23:1}$ + $C_{25:1}$ + $C_{27:1}$ + Cyclobotryococcatriene + C_{29} + C_{31} + C_{33})) to incorporate these *n*-alkenes and determine their relative abundance to terrestrial and emergent plants to determine the algal contribution. As no botryococcene compounds were found in Lake Edward, Zhang et al.'s (2004) formula has been modified to incorporate just *n*-alkene compounds: P_{alg} = ($C_{23:1}$ + $C_{25:1}$ + $C_{27:1}$)/($C_{23:1}$ + $C_{25:1}$ + $C_{27:1}$ + C_{29} + C_{31} + C_{33}).

The P_{alg} values of Lake Edward sediments range from 0.10 to 0.87, signifying variable contributions from algae during the Holocene (Figure 8.29c). During the early Holocene P_{alg} values were relatively low, suggesting minimal inputs from algae and dominance by terrestrial sources. Between ~7.3 and 5.6 ka BP a shift to much higher values (0.36-0.58) occurred, signifying increased contributions from algal components. An abrupt transition from high (0.58) to minimal (0.07) P_{alg} values occurred between 5.6 and 5.2 ka BP, indicating a significant decline in contributions from algae. From 5.2 ka BP, a progressive increase in the P_{alg} value, to a maximum of 0.87 at ~2.4 ka BP occurred, indicating a period of increasing importance of algal sources relative to terrestrial plants. From ~1.4 to 1ka BP, P_{alg} values shifted from maximum to almost minimal values for the whole Holocene, signifying a sudden change from algal to terrestrial plant dominance.

The P_{alg} and P_{aq} records are remarkably synchronous in Lake Edward (Figure 8.29). As was highlighted in section 7.9.3 at Lake Victoria, a relationship between algae and floating/submerged macrophytes is highly likely as floating macrophytes are known for their epiphytic communities (Komárek and Jankovská, 2001; Brenner et al., 2006). Figure 8.30 shows this strong positive relationship (R^2 = 0.84; $p < 0.0001$) between P_{alg} and P_{aq}.

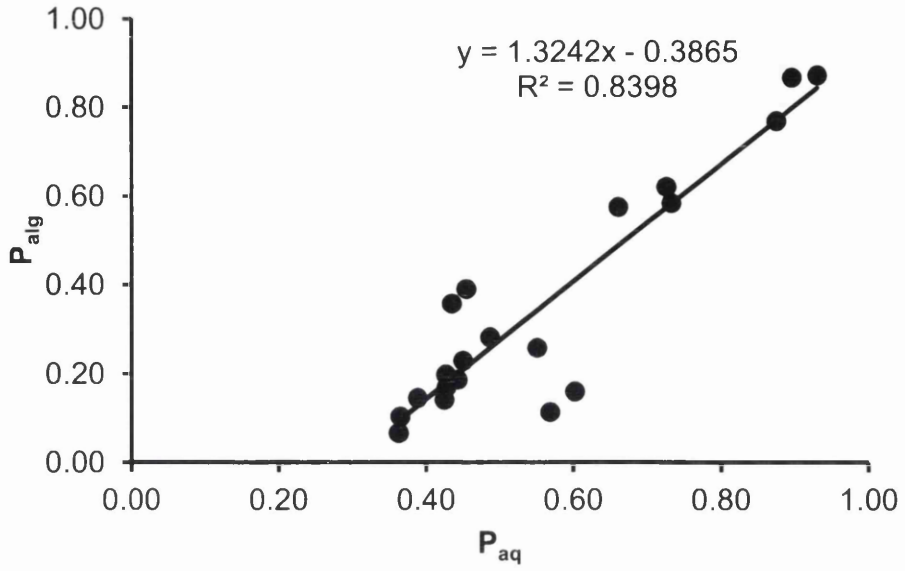

Figure 8.30: P_{alg} and P_{aq} proxies are significantly correlated (R^2 = 0.84; p < 0.0001) in Lake Edward sediments.

8.10 Chapter summary

Like Lake Victoria, Lake Edward, a rift-valley lake on the Uganda-DR Congo border, is a headwater lake of the White Nile fed by rivers that drain the mountains of Burundi, DR Congo and Uganda. Again, similar to Lake Victoria, pre-existing material was available for Lake Edward, obtained during the IDEAL expedition in 1996. Unfortunately, no single core spanned the entire Holocene period, rather a combination of three cores was used and together with careful sampling, discontinuous sedimentation intervals (i.e. hiatuses) were avoided, providing a record for the whole of the Holocene. The sediments of Lake Edward are highly diatomaceous and organic rich making them ideal for both diatom isotope analysis and lipid-biomarker analysis. Although there were problematic sediment components mixed in with the diatoms, these were eventually eliminated by a variety of methods. Apart from a few diatom samples that could not be purified to an acceptable level for isotope analysis, a ~500-year resolution record for both lipid biomarkers and diatom isotope composition (O and Si) was obtained for the Holocene at Lake Edward.

Chapter 9 Discussion

9.1 Introduction

The first part of this chapter provides interpretations of the physical, chemical and isotope data of the modern waters from the Nile Basin. The modern waters are then used to help explain the palaeo-records of Lakes Victoria and Edward. Subsequently, Si cycling dynamics in the White Nile headwaters was assessed during the last 15 ka BP and compared to a proposed model of forest ecosystem development, followed by comparison with other lake sediment records. In sections 9.2 and 9.3 reference to specific sampling sites are numbered in square brackets and correspond to those presented in Table 6.1 and Figure 6.1 in Chapter 6.

9.2 Modern waters: $\delta^{18}O$ and $\delta^{2}H$

Remarkably, all surface-water samples from the Nile drainage plotted along effectively the same evaporative line with a slope of about 5 (Figure 6.8a), implying similar isotope systematics, including kinetic effects imparted during evaporation. Individual sampling sites migrated seasonally up and down the LELs representing their respective sub-basins (Figure 6.8), yielding dry-season samples that were significantly higher in $\delta^{2}H$ and $\delta^{18}O$ than wet-season samples, as the combined result of increased evapotranspiration and evaporation losses under conditions of lower humidity.

The isotopically lowest values were obtained in the headwaters [samples 1-7, 25-33] and the isotopically highest towards the Delta in Lake Qarun [48-50] (Figures 6.8 and 6.9). Progressive downstream increases in both isotope ratios along the Nile are attributable mainly to cumulative evaporation losses from swamps and open water bodies, such as the Sudd, the equatorial great lakes and slow moving branches of the River Nile. This inference of evaporative enrichment is supported by the increase in electrical conductance and precipitation of alkali metals (Na^{+} and K^{+}) in downstream waters (Figures 6.3-6.7). However, the composition of the waters also reflect the strong northwards decline in total rainfall and total number of wet months (Figure 3.4). The downstream increase in $\delta^{18}O$ was only significant during the wet season (Figure 6.10). In contrast, the latitudinal trend was not well defined during the dry season when water-management practices such as irrigation and use

of dams to control seasonal flow were more prevalent, most notably along the Main Nile (Figure 6.9). For example, waters collected from east of Lake Tana [25, 30] in the Ethiopian Highlands had greatly enriched $\delta^{18}O$ values during the dry season (Figures 6.8c and 6.9), reflecting the use of irrigation in the intensively cultivated Fogera Plain (~500,000 ha) (World Bank, 2008), which is bounded by the Rivers Ribb [25] and Gumara [30]. Waters sampled from the Main Nile, close to Khartoum [41-42], were extremely enriched in ^{18}O compared to downstream sites (except for Lake Qarun which is hydrologically closed) [38-40, 43-47] but had a similar composition to the White Nile [13] upstream (Figure 6.8), indicating a possible release of isotopically enriched waters from the Jebel Aulia Dam (~50 km south of Khartoum) on the White Nile (Figure 3.1), shortly prior to sampling at Khartoum.

The corresponding lack of a significant altitudinal gradient in $\delta^{18}O$ during the dry season (Figure 6.10) can be explained by several factors: greater evaporative enrichment as a result of decreased humidity (see elevated EC and high cation-ratios downstream (Figures 6.3-6.7); active water management in the Tana headwaters and along the Main Nile; and sampling during more than one dry season. The altitudinal isotope gradient observed in River Nile waters during the wet season (–2.6‰ km^{-1}) was similar to the slope of rainfall samples from other tropical regions, which varied between -2.7 ± 0.3‰ km^{-1} and -1.6 ± 0.05‰ km^{-1} (Gonfiantini et al., 2001), as a result of progressive rainout of ^{18}O following a Rayleigh adiabatic condensation process. However, deviations from the average altitudinal gradient were seen at sub-basin scale in the Nile drainage (not shown).

The most negative values of $\delta^{2}H$ and $\delta^{18}O$ were found at high-altitude sites in the headwaters of the White [1-7] and Blue [25-33] Niles during the wet season (Figures 6.9 and 6.10). This is attributed to the combined effects of orographic enhancement and the very continental location with respect to oceanic moisture sources (Indian and Atlantic Oceans) (Figure 3.3); both these effects are associated with progressive rainout of the heavier isotopes of hydrogen and oxygen, resulting in isotopically depleted rainfall. Evaporative enrichment at these sites is limited by the steep gradients of the rivers and high humidity during the wet season. In addition, these samples displayed large d-excess values (>10‰) (Figure 6.11), indicating that they originated from rainfall that formed in part from recycled moisture (Gat and Matsui, 1991; Gat et al., 1994).

9: Discussion

It has been recently shown that precipitation during the summer rainy season in western Ethiopia carries the isotopic imprint of recycled continental moisture transported by south-westerly and westerly flow from the Congo rainforest and the swamps of the Sudd (Levin et al., 2009; Kebede and Travi, 2012), supporting earlier work by Rozanski et al. (1996) and Sonntag et al. (1979). Kebede and Travi (2012) found that water samples from the Blue Nile Plateau had the highest d-excess values in their Ethiopian dataset, which they attributed to recycling of moisture through evapotranspiration and evaporation from open water, at both local and continental scales. While vegetation-controlled vapour loss (transpiration) is generally non-fractionating (Salati et al., 1979; Gat and Matsui, 1991; Gat et al., 1994), evaporation from soils and surface waters produces vapour with high d-excess values, resulting in subsequent rainfall with these characteristics.

In the northern Ethiopian Highlands during the rainy season, convective clouds tend to form at the end of the morning as a result of daytime heating of the land, creating rain in the afternoon (Nyssen et al., 2005). Hence, evaporation from large surface water bodies (Gat et al., 1994), for example Lake Tana and its surrounding wetlands, are likely to be a significant source of recycled water vapour, resulting in precipitation and initial surface runoff with large d-excess values. Similarly, over Lake Victoria (68,000 km^2), the largest lake in Africa, rainfall is enhanced by a strong nocturnal land-lake breeze (Flohn and Fraedrich, 1966); the prevailing south-easterly trade winds play an important role by displacing the centre of night-time convergence towards the Rwenzori Mountains in the northwest of the basin (Nicholson et al., 2000; Yin et al., 2000; Nicholson and Yin, 2002; Okonga et al., 2006), helping to explain the occurrence of surface waters in western Uganda with large d-excess values. Isotope data from the IAEA-WMO station at Entebbe, on the northern shores of the lake, confirm the occurrence of significant rainfall originating from evaporated waters of Lake Victoria (Rozanski et al., 1996).

With the above evidence in mind, it is suggested that surface water samples from western Uganda [1-7] and the Blue Nile [25-33] with high d-excess values represent moisture recycled from continental source(s), including the large water bodies found in their respective headwaters (notably Lakes Victoria and Tana), together with contributions from large swamps such as the Sudd and the Bahr el Ghazal in South Sudan. It is also feasible that in addition to recycled moisture evaporated from Lake Victoria, the largest d-excess (and most depleted isotope values), found in rivers

flowing from the glacierized peaks of the Rwenzori Mountains [1-3] reflect elevated d-excess values developed during snow formation (Jouzel and Merlivat, 1984). The remainder of the River Nile samples have low d-excess values (<10‰) which are consistent with evaporative losses from surface waters (Figure 6.11).

9.3 Modern waters: DSi and $\delta^{30}Si$

Dissolved Si (DSi) is ultimately derived from weathering of silicate rocks. Globally, weathering rates are high in tropical headwaters where high relief, high annual-mean temperatures and monsoonal rainfall facilitate rapid physical weathering and erosion, creating freshly weathered surfaces and thereby enhancing the rate of chemical weathering (Brady and Carroll, 1994; White and Blum, 1995; Cochran and Berner, 1996; Gaillardet et al., 1999). In addition to the effects of bedrock composition, topography and climate, it has been shown that higher plants accelerate the rate of silicate weathering by improving the moisture and organic-matter status of soils (Hinsinger et al., 2001). Interactions between plant roots and soil microbes in the rhizosphere also expedite chemical weathering (Kelly et al., 1998; Lucas, 2001).

The most important control on dissolved silicon concentrations in the major Nile sub-basins is bedrock geology (Figures 3.2 and 6.12). Average DSi values were greatest in the Blue Nile drainage, which is predominantly underlain by trap basalts, rich in ferromagnesian minerals that are highly susceptible to chemical weathering (Cochran and Berner, 1996; Dessert et al., 2003; Dupré et al., 2003). This is highlighted in the physical and chemical compositions of the waters where low pH values (Figures 6.1-6.2) and low concentration of alkali metals (Na^+ and K^+) (Figures 6.6-6.7) reflects the dissolution of ferromagnesian minerals such as Mg^{2+} during chemical weathering. The seasonal contrast in DSi concentrations was also greatest in the Blue Nile Basin, which has only one rainy season per year, in contrast to the bimodal but more evenly distributed rainfall regime of the White Nile headwaters. Given the steep, exposed topography of the Ethiopian Highlands, flushing of DSi from soils and desorption of Si from suspended-sediment particles can be inferred to reach a maximum during the flood season (Hall et al., 1977; Sinada and Abdel Karim, 1984). In contrast, DSi concentrations in the White Nile headwaters were lower and declined much more rapidly downstream, which can be explained by a combination of: 1) quartz-rich, granitoid bedrocks that are more

resistant to weathering; and 2) rapid silica uptake by Si-accumulating plants in the densely vegetated equatorial catchments, and by diatom blooms and stands of aquatic macrophytes in the chain of large lakes and swamps (Talling, 1963, 1966; McCarthy et al., 1989). Figure 6.12 shows that the Ethiopian Highlands are the predominant source of DSi for the Main Nile, along which DSi concentrations decline exponentially with latitude, due to the lack of major tributary inputs after the River Atbara.

All our water samples from the River Nile were enriched in ^{30}Si relative to expected values for local bedrock, indicating that the light isotope ^{28}Si had been preferentially removed through formation of pedogenic minerals, phytoliths or diatom frustules. Based on our current dataset alone, we cannot rule out fractionation of Si isotopes by neoformation of amorphous silica and clays as an important process in the Si cycle in the Nile Basin (Basile-Doelsch, 2006; Opfergelt et al., 2008). However, the large range of $\delta^{30}Si$ values in surface waters and their progressive downstream enrichment (Figure 6.13) are consistent with intense Si cycling by aquatic ecosystems. Seasonal contrasts observed in both DSi concentrations and $\delta^{30}Si$ values are most readily explained by strong coupling between DSi supply and biological demand. In general, DSi concentrations were lowest during the dry season, when soil moisture and runoff in the catchments were reduced, inhibiting the mobilisation of Si from soils and sediments, and limiting the available DSi for biological uptake. The reduction in DSi concentrations during the dry season corresponded to a rise in $\delta^{30}Si$ values (Figure 6.14), indicating that biological demand for DSi exceeded supply. This was particularly apparent in the headwater lakes, and will be discussed in detail later. In contrast, wet-season DSi concentrations were higher and the corresponding $\delta^{30}Si$ values were less enriched. This suggests that increased mobilization of Si from the catchments occurred during the rains, when an influx of turbid floodwaters would also tend to inhibit diatom productivity (Talling et al., 2009), thereby decreasing biological uptake of the light isotope ^{28}Si compared with the dry season. Engström et al. (2010) observed similar isotope variations in DSi in a river in northern Sweden, where a combination of seasonal discharge from snowmelt, vegetation changes and lacustrine diatom productivity significantly affected the DSi transport in the basin.

The lowest DSi concentrations were found in the headwater lakes or their outflows (e.g. Lakes Victoria, Albert and Tana) and in the lower reaches of the Nile [45-47], in

association with elevated $\delta^{30}Si$ values (Figures 6.12 and 6.14). Once again, this inverse relationship (low DSi, high $\delta^{30}Si$) can be attributed to the balance between DSi supply and demand. Immediately surrounding the headwater lakes are extensive wetland areas containing known Si-accumulator plants such as *Cyperus papyrus*, *Phragmites* and other emergent macrophytes that are likely to take up significant amounts of Si (Gaudet, 1977; McCarthy et al., 1989; Hodson et al., 2005; Struyf et al., 2007; Struyf and Conley, 2009; Schoelynck et al., 2010). Si extraction by accumulator plants and diatom blooms during the dry season would significantly reduce the amount of DSi in the lake waters, driving up $\delta^{30}Si$ values. In the lower reaches of the Nile, low DSi concentrations and strongly enriched $\delta^{30}Si$ values also reflect an excess of demand over supply. The Main Nile lacks major tributary inputs for the last ~2700 km of its course through the Eastern Sahara. Terrestrial vegetation is greatly reduced by the hyperarid climate, which also limits the supply of DSi along this stretch, resulting in a rapidly diminishing stock as Si is taken up by Si-accumulating organisms such as diatoms. Storage of floodwaters in reservoirs behind large dams sited along the Main Nile (e.g. Jebel Aulia, Merowe and Aswan) had a similar effect to that of the headwater lakes, since they hold back the flux of Si downstream and enhance uptake of soluble Si by aquatic organisms.

Several anomalous sites in the White Nile headwaters [3 & 4, 7] displayed low DSi concentrations (Figure 6.14). Their corresponding $\delta^{30}Si$ values were also very low, although still greatly enriched relative to the expected $\delta^{30}Si$ signature of the local bedrock (–0.10 to –0.07‰: André et al. (2006)) (Figure 6.14). These rivers drain the Rwenzori and Virunga Mountains, respectively. It is suggested that bare rock surfaces, thin soils and sparse vegetation cover on the upper slopes of these mountains retard chemical weathering (Moulton et al., 2000) and Si biocycling (Georg et al., 2006a), resulting in a combination of low DSi concentrations and depleted $\delta^{30}Si$ values.

Si biocycling appears to be most intense in the Blue Nile Basin, particularly during the dry season, as the difference between the expected $\delta^{30}Si$ composition of the local rock (basalt: –0.29‰ ± 0.08‰ (Savage et al., 2011)) and the river waters is greater than in the White Nile Basin (Figure 6.12). Several factors may account for this large fractionation. Sampling was undertaken at the end of the dry season, immediately before the rains began, when it is likely that the supply of DSi was at its lowest whilst biological demand was at its peak. The $\delta^{30}Si$ value of the outflow from

Lake Tana [35] was already significantly enriched relative to the expected range of values for basalt and to the Blue Nile further downstream [34], indicating that a large proportion of this enrichment occurred in the headwaters. It seems likely that towards the end of the dry season, availability of DSi within the Tana catchment was very limited, causing the $\delta^{30}Si$ values of river waters to rise as biological demand persists.

Although the positive correlation observed between $\delta^{18}O$ and $\delta^{30}Si$ during the wet season (Figure 6.15) is not directly causal, both isotope ratios evolved in parallel due to cumulative downstream losses of the light isotopes ^{16}O through evaporation and ^{28}Si through biological uptake, respectively. In contrast, during the dry season, anthropogenic impacts on the hydrological cycle and intense local biocycling of Si obscured any general trend. When outliers clearly affected by water-management practices (i.e. irrigation and major reservoirs) were removed [sites: 25, 13 & 41], a similar positive trend to the wet season was observed, although with higher values of both $\delta^{30}Si$ and $\delta^{18}O$ (updated regression not shown: $R^2 = 0.023$, $p = 0.622$). However, the trendline is still not significant after the removal of these three outliers; it is likely that the isotope values of other samples from the Main Nile were affected by human activity to a less obvious degree. Based on the wet-season dataset alone, Si supply from the Nile headwaters (represented by $\delta^{30}Si$) appears to be strongly linked to catchment hydrology (represented by $\delta^{18}O$), which is not surprising given that mobilisation of DSi from soils and sediments is primarily dependent on rainfall and runoff.

9.4 Modern waters: summary

Stable isotopes of H, O and Si in surface waters from the Nile Basin were used as tracers for the hydrological and Si cycles, respectively. Physical and chemical characteristics of surface waters supported the inferences made from the isotopic data. Large seasonal shifts in H- and O-isotope compositions reflected changes in water balance. During the dry season, lower humidity favoured evaporative enrichment of surface waters and cumulative downstream losses from swamps and open water bodies. The Main Nile showed the greatest evaporative enrichment, due to the year-round arid climate and lack of rainfall or tributary input for 2700 km downstream from its confluence with the Atbara. Seasonal changes in DSi concentrations and Si isotopes provide useful information on Si cycling under

different climate regimes in the Nile Basin. This study has increased the global upper limit of $\delta^{30}Si$ for dissolved Si in natural waters by more than 1‰. Contrasting geology in the headwaters of the White and Blue Nile is clearly reflected in pH values, cationic composition and DSi concentrations. The highest levels of DSi (and low pH and relatively high Mg^{2+} concentration) in the Blue Nile headwaters were due to the basaltic bedrock and steep, easily erodible, sparsely vegetated slopes of the Ethiopian Highlands. Low DSi concentrations and correspondingly enriched Si-isotope values are found in the headwater lakes and in the Main Nile where depletion of Si by aquatic organisms (notably diatoms and macrophytes) is thought to be important. Extensive downstream enrichment of Si isotopes and depletion of DSi during both wet and dry seasons in the River Nile imply active Si biocycling. The heavy isotope ^{30}Si is enriched in surface waters during the dry season due to a reduction in mobilisation of DSi from the catchment relative to aquatic demand. Localized anthropogenic impacts on the isotope composition of surface waters are identifiable with respect to both the hydrological and Si cycles, especially during the dry season and along the Main Nile where irrigation and retention of stored floodwaters behind large dams are most prevalent. Nevertheless, modern seasonal variations of DSi and $\delta^{30}Si$ in the River Nile indicate that the Si flux from large tropical rivers to the oceans is not constant and is likely to be highly variable on Quaternary time scales.

9.5 Modern waters: Implications for interpreting the Quaternary palaeorecord

The modern seasonal water isotope data suggest that changes in rainfall induced by orbital forcing would have had synergistic impacts on the water and Si cycles in the Nile Basin. The isotopic composition of diatom silica reflects the aqueous environment in which the frustules formed (Leng and Barker, 2006; Leng and Swann, 2010). Therefore, diatoms can be used as tracers for the hydrological ($\delta^{18}O_{diatom}$) and Si ($\delta^{30}Si_{diatom}$) cycles. In the tropics, $\delta^{18}O_{diatom}$ primarily reflects changes in moisture balance (P/E ratio) (Barker et al., 2001; Polissar et al., 2006; Barker et al., 2007; Hernández et al., 2010; Barker et al., 2011; Hernández et al., 2011), and as shown in the modern data (section 9.2), $\delta^{18}O_{water}$ responds to seasonal variations in P/E. $\delta^{30}Si_{diatom}$, although a relatively new isotopic proxy, applied hitherto mainly to marine diatoms, has shown great promise for tracking changes in continental Si cycling (Street-Perrott et al., 2008; Swann et al., 2010).

Modern seasonal variations of DSi and $\delta^{30}Si$ in the River Nile indicate that the Si flux from large tropical rivers to the oceans is not constant and is likely to be highly variable on Quaternary time scales. Coupled measurements of the O- and Si-isotope compositions of freshwater diatom frustules preserved in sediment records have the potential to clarify the relationship between water balance and Si cycling under different climate regimes. In the following sections, based on the modern isotope systematics of the Nile Basin, depleted $\delta^{18}O_{diatom}$ values are interpreted as indicating reduced evaporative enrichment resulting from a more humid climate (increased P/E). Low $\delta^{30}Si_{diatom}$ values are used to infer an enhanced supply of DSi relative to the demand from siliceous aquatic organisms.

9.6 Palaeoenvironmental interpretation of Si cycling in the Lake Victoria basin

During the LGM, tropical Africa was much drier and cooler than today (Gasse, 2000; Barker et al., 2004; Schefuβ et al., 2005; Weijers et al., 2007; Tierney et al., 2008; Gasse et al., 2008 and references therein) in response to orbitally-induced changes in monsoon strength (Kutzbach and Street-Perrott, 1985), enabling the major lowering of lake levels and even complete desiccation of several of the large lakes (Johnson et al., 1996; Beuning et al., 1997b; Talbot and Lærdal, 2000; Stager et al., 2002), and reduced flow of the River Nile (Adamson et al., 1980; Talbot et al., 2000; Williams et al., 2006). At Lake Victoria, in cores V95-1P and V95-2P, two palaeosols and a peak in magnetic susceptibility (Figure 9.1i) testify the desiccation as the lake must have completely dried out to enable soil formation, estimated to have occurred between ~18 and 17 ka BP and again sometime between 15.9 and 14.2 ka BP (Talbot and Livingstone, 1989; Talbot and Lærdal, 2000; Stager et al., 2002). The pollen assemblage, including the presence of Afromontane coniferous tree *Podocarpus*, and open vegetation of regional grasslands, indicated cooler and reduced moisture conditions during the deglaciation (Kendall, 1969; Livingstone, 1975). Limited terrestrial vascular plant input observed in the lipid data between ~21 and 15 ka BP supported an open/sparse landscape (Figure 9.1e-g).

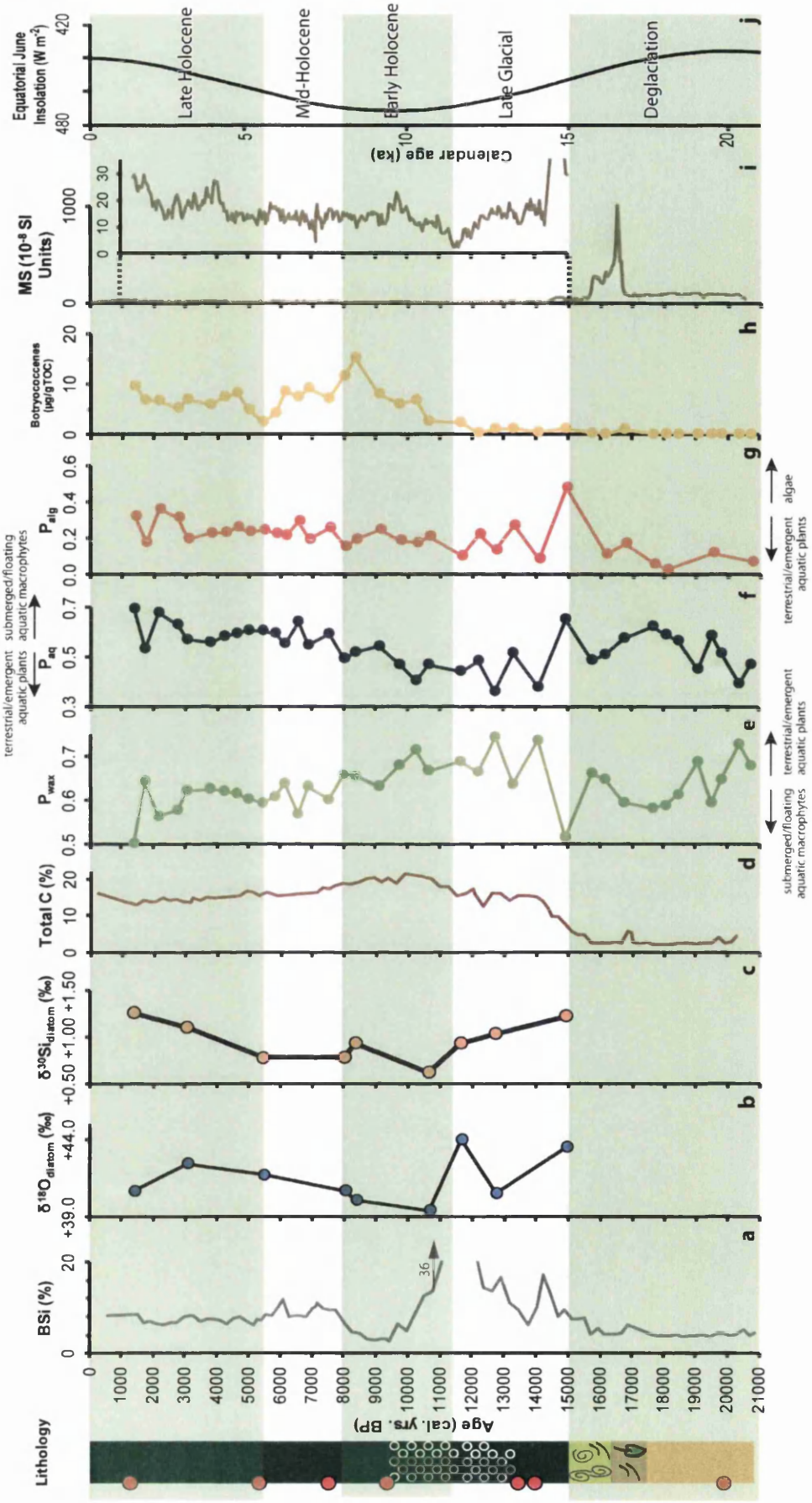
Lithology
Age (cal. yrs. BP)
BSi (%)
$\delta^{18}O_{diatom}$ (‰)
$\delta^{30}Si_{diatom}$ (‰)
Total C (%)
P_{wax}
P_{aq}
P_{alg}
Botryococcenes (µg/gTOC)
MS (10^{-6} SI Units)
Calendar age (ka)
Equatorial June Insolation (W m^{-2})
Late Holocene
Mid-Holocene
Early Holocene
Late Glacial
Deglaciation
terrestrial/emergent aquatic plants
submerged/floating aquatic macrophytes
algae

Figure 9.1 (previous page): Temporal variations in Lake Victoria sediments of biogenic silica concentrations (BSi%) (Johnson et al., 1998) (a), oxygen isotope values of diatom silica ($\delta^{18}O_{diatom}$) (b), silicon isotope values of diatom silica ($\delta^{30}Si_{diatom}$) (c), total carbon concentration (Total C%) (Johnson et al., 1998) (d), biomarker proxies to distinguish contributions from; terrestrial and emergent aquatic plants (P_{wax}) (e), non-emergent aquatic macrophytes (submerged/floating) (P_{aq}) (f), algae (P_{alg}) (g). Total abundance of botryococcene compounds (h), magnetic susceptibility (Ngobi et al., 1998) (i), with equatorial insolation (scale reversed) for June (boreal summer) (Berger and Loutre, 1991) (j).

Insolation changes alone could not account for the abrupt events observed at Lake Victoria or elsewhere in tropical Africa during the deglaciation (Kutzbach and Street-Perrott, 1985). Instead, it has been suggested that the "drying events" recorded at Lake Victoria were entirely synchronous with the North Atlantic ice-rafting Heinrich event 1 between ~18 and 15 ka BP (Stager et al., 2002), when maxima ice-rafting occurred at the onset and end of the interval (Elliot et al., 1998; Bard et al., 2000), corresponding to the two palaeosols observed at Lake Victoria; creating a link between high latitude and tropical climates (Stager et al., 2002). An increase in submerged/floating aquatic macrophytes (Figure 9.1e&f), combined with a peak in organic carbon (Figure 9.1d) and the presence of lacustrine-type sediments in the intervening period (~17 to 16 ka BP) support a temporary climate amelioration for ~2000 years, enabling at least a shallow water body to exist (Talbot and Livingstone, 1989; Talbot and Lærdal, 2000).

Between 15.7 and 14.2 ka BP, a considerable shift in all the measured proxies occurred suggesting a major change in the climate and environment of the Lake Victoria basin at that time (Figure 9.1). The transformation coincided with the abrupt onset of the East African Humid Period (EAHP) at ~15 ka BP when insolation reached a threshold coupled with feedback mechanisms associated with surface boundary conditions, increased soil moisture and sea-surface temperature changes, resulted in enhanced monsoon conditions until ~6 and 5 ka BP (Street-Perrott et al., 1990; Kutzbach et al., 1996; Kutzbach and Liu, 1997). Rapid filling of Lake Victoria occurred, and shortly after 14.2 ka BP overflow into the White Nile began (Talbot et al., 2000; Williams et al., 2006). Climate amelioration resulted in the gradual development of semi-deciduous open forest vegetation around Lake Victoria during the late-glacial (Kendall, 1969), corresponding to an increasing dominance of terrestrial vascular plant input (Figure 9.1e-g). As the lake filled, inputs from aquatic non-emergent vegetation (Figure 9.1f) became less important, presumably due to

rising lake levels and the resulting increase in water column depth. Productivity from plankton must have been high in the lake to allow the accumulation of large quantities of BSi and TC (organic carbon) (Figure 9.1a&d), in stark contrast to the earlier deglaciation period.

As the climate improved at ~15 ka BP, $\delta^{30}Si_{diatom}$ was high (Figure 9.1c) signifying that DSi was in demand by aquatic biota, corresponding to high productivity of BSi (Figure 9.1a). Initially, after the dry climatic conditions associated with the North Atlantic H1 event, and as the lake began to fill, mobilisation and availability of silica would have been low relative to the biological demand. As the climate improved, due to orbital forcing, the basin rapidly filled (Johnson et al., 2000; Talbot and Lærdal, 2000; Stager and Johnson, 2008), dissolving soil phytoliths from a transgressed basin which was previously vegetated by grasslands (Kendall, 1969; Stager et al., 1997; Johnson et al., 1998; Johnson et al., 2000), and are known Si accumulators (Blecker et al., 2006), resulting in a short-lived influx of TSi (ASi and DSi). In parallel, forest development in the catchment would have provided an increasing supply of DSi through increased silicate-rock weathering and dissolution of stored soil phytoliths, resulting in the progressive decline in $\delta^{30}Si_{diatom}$ values through the late-glacial (Figure 9.1c). The fact that BSi concentrations increased (Figure 9.1a) as $\delta^{30}Si_{diatom}$ decreased (Figure 9.1c) during the late glacial signifies a significant supply of DSi to the lake, as was observed in the modern data (Figure 6.14). $\delta^{18}O_{diatom}$ also declined rapidly after the basin was transgressed (Figure 9.1b), responding to the enhanced rainfall and the overflow of the lake at the White Nile outlet, causing a freshening of the lake water and lowering evaporative enrichment. An abrupt rise in $\delta^{18}O_{diatom}$ at ~11.6 ka BP (Figure 9.1b) marked the termination of the brief dry, cold European Younger Dryas period which resulted in a sudden drop in tree pollen taxa and a shift in diatom assemblages responding to reduced humidity and lake level decline at Lake Victoria (Kendall, 1969; Stager et al., 1997; Stager et al., 2002).

During the early Holocene, the Lake Victoria basin was at its wettest (Kendall, 1969; Stager et al., 1986; Beuning et al., 2002; Stager et al., 2003) and most productive (maxima BSi and TC accumulation; Figure 9.1a&d), in response to enhanced monsoon rainfall particularly in boreal summer and autumn (Tierney et al., 2011a). Lake levels were at their maximum and catchment vegetation, for the first time, consisted of moist evergreen tropical rainforest (Kendall, 1969). Both $\delta^{18}O_{diatom}$ and

$\delta^{30}Si_{diatom}$ were at their lowest values for the whole record, signifying humid conditions (high P/E) and a profusion of DSi in the basin, respectively (Figure 9.1b&c).

Through the early to mid-Holocene, $\delta^{18}O_{diatom}$ and $\delta^{30}Si_{diatom}$ remained low indicating the persistence of wet and humid conditions (high P/E), together with large amounts of TSi from the catchment preventing the enrichment of $\delta^{30}Si_{diatom}$. Interestingly, BSi accumulation was at its lowest between ~10 and 8 ka BP (Figure 9.1a), signifying that diatom productivity had declined (Johnson et al., 1998; Stager and Johnson, 2000). However, the cause of this decline is of interest with regards to the silicon and other nutrient cycles, as $\delta^{30}Si_{diatom}$ is also low indicating that DSi was not limiting (Figure 9.1c). Kendall (1969) also postulated that DSi concentrations were greatest in the early Holocene due to a change in the dominant diatom species from *Stephanodiscus astraea*, which requires only low Si:P concentrations (Kilham et al., 1986; Kilham and Kilham, 1990), to *Melosira* (*Aulacoseira*) species which need elevated levels of DSi but have low P requirements (Kilham et al., 1986; Stager et al., 2003). In addition, Johnson et al. (1998) proposed that DSi would have been plentiful during the early Holocene due to increased runoff from the catchment. As DSi was clearly not limited, I am led to believe that there must have been some other limiting nutrient which prevented the accumulation of BSi between ~10 and 8 ka BP.

With the catchment at its most vegetated and hosting a closed evergreen forest (Kendall, 1969), the landscape would have been very stable and erosion limited. The magnetic susceptibility data imply that soil erosion rates were very low and stable throughout the more vegetated conditions of the last 14 ka BP (Figure 9.1i). Phosphate, which is tightly bound to soil particles would not have been easily mobilised from the catchment (Goldman and Horne, 1983; Smil, 2000; Kochian, 2012). It is therefore hypothesised that the supply of P from the catchment became limited due to a densely vegetated and stable catchment which prevented the erosion of soil bound P (Haberyan and Hecky, 1987). In addition, stratification of the water column, as suggested by Stager and Johnson (2000) and Johnson et al. (2000), would have prevented replenishment of P from bottom sediments, resulting in a reduced supply of P from in and around the lake causing diatoms to be outcompeted by other phytoplankton, such as green algae or cyanobacteria (Johnson et al., 1998; Johnson et al., 2000). Coincidentally, the lowest diatom

productivity occurs with a peak in the total abundance of botryococcene biomarkers (Figure 9.1h), suggesting that the green algal species *Botryococcus braunii* may have outcompeted diatoms between 10 and 8 ka BP due to its ability to survive in oligotrophic systems (Jankovská and Komárek, 2000; Smittenberg et al., 2005). This episode of reduced biogenic silica accumulation coincided with the 8.2 ka cooling event documented in many archives in the North Atlantic region (Alley et al., 1997; Bond et al., 2001; Daley et al., 2011) and increasingly in African archives (Gasse, 2000; Thompson et al., 2002; Stager et al., 2003; Barker et al., 2004; Kiage and Liu, 2006). Although there is limited evidence from other proxies that it affected the Lake Victoria basin (Figure 9.1).

After ~8 ka BP, diatom production resumed again, but at lower levels compared to those of the early Holocene (Figure 9.1a). A major shift in diatom species from *Aulacoseira granulata* to *A. nyassensis* in several of the Lake Victoria cores (Stager et al., 1997; Stager and Johnson, 2000), combined with a steady progression to a semi-deciduous, seasonally dry forest suggested a change in wind regime and increasing seasonality (Kendall, 1969; Stager et al., 1997). An increase in P input from the catchment, indicated by the rapid change to *A. nyassensis* which have the highest P requirements of the *Aulacoseira* species (Kilham et al., 1986), may have encouraged diatom productivity to increase again. The lipid data indicate a gradual decline in the relative importance of emergent/terrestrial higher plants during the mid-Holocene supporting a change in vegetation to a more open forest (Figure 9.1e-f). The change in forest composition does not appear to have altered the intensity of Si cycling immediately, as $\delta^{30}Si_{diatom}$ remained low until the last 5 ka BP.

During the late Holocene, $\delta^{18}O_{diatom}$ gradually increased, signifying evaporative enrichment of lake waters in response to a reduction of rainfall associated with the decline of the EAHP (Tierney et al., 2011a). Pollen evidence also suggested drier conditions indicated by a decline in forest taxa from ~3.5-3.0 ka ^{14}C BP (~3.7 ka BP) and related to an increase in grassland expanse (Kendall, 1969). However, it is difficult to differentiate between climatic and human-induced vegetation changes, and it is likely that from ~ 3 ka BP iron-age settlers had an impact on modifying the vegetation through deforestation and cultivation in East Africa (Clark, 1962; Kendall, 1969; Kiage and Liu, 2006). The stability of lipid biomarkers during the late Holocene until ~3.5 ka BP (Figure 9.1e-g) suggests only subtle changes in the plant composition in and around Lake Victoria up until that time.

After 3.5 ka BP, biomarker proxies (Figure 9.1e-g) indicate a shift in vegetation types towards submerged/floating aquatic vegetation (Figure 9.1f) corresponding to a decline in lake level associated with increased aridity (Stager et al., 2003). At the same time $\delta^{30}Si_{diatom}$ increased whilst BSi accumulation remained steady (Figure 9.1a&c), suggesting that the DSi supply was declining. This was likely for several reasons: a reduction in the mobilisation of DSi from the catchment as a result of decreased rainfall, a decline in bedrock weathering by deep rooted plants in response to changes in vegetation composition, a gradual depletion of stored soil phytoliths, and an increased uptake of Si by emergent (e.g. papyrus and *Typha*) and submerged/floating (e.g. *Nymphaea*) aquatic macrophyte species (Kendall, 1969). An increase in P_{aq} and P_{alg} (Figure 9.1f&g) and a small increasing trend in botryococcene concentrations (Figure 9.1h) suggest that aquatic macrophytes and non-diatom algae or cyanobacteria, such as *B. Braunii* and *Pediastrum simplex* as identified Kendall (1969), may have been more important, benefitting from lower lake levels and a modest increase in P supply with eroded topsoil.

9.7 Palaeoenvironmental interpretation of Si cycling in the Lake Edward basin

After the arid conditions of the LGM as identified by a slump deposit dated to 20.6 ka ^{14}C BP with high-Mg content in calcite indicating formation in evaporated waters (Lærdal et al., 2002; Russell et al., 2003a; Beuning and Russell, 2004), the early Holocene climate in the Lake Edward basin was much wetter (Russell et al., 2003a). All of the measured parameters during the early Holocene were relatively constant (Figure 9.2b-f), indicating that the climate and environmental conditions were stable and unchanging at Lake Edward (Lærdal et al., 2002; Russell et al., 2003a). $\delta^{18}O_{diatom}$ was low throughout the early to mid-Holocene suggesting P/E was high (Figure 9.2b), and that it was much wetter than today (Beuning and Russell, 2004). This is supported by the pollen data which portrays a moist semi-deciduous, lowland rainforest surrounding Lake Edward during at least 11.2 and 6.7 ka BP (Beuning and Russell, 2004). It was hypothesised by Beuning and Russell (2004) that it was wettest between ~9 and 6.7 ka BP. However, the $\delta^{18}O_{diatom}$ values obtained here are not significantly different from those obtained at the start of the Holocene (Figure 9.2b), and therefore do not necessarily support wetter conditions between 9 and 6.7 ka BP. Tropical rainforest vegetation would have enhanced silicate-rock weathering (Lucas et al., 1993; Drever, 1994; Alexandre et al., 1997; Kelly et al., 1998; Lucas,

2001), promoting the availability of DSi, and elevated runoff from the catchment would have enabled the mobilisation of DSi into the lake, resulting in low $\delta^{30}Si_{diatom}$ (Figure 9.2c). Diatom production was high during the early Holocene as identified by high BSi accumulation (Figure 9.2a), although it gradually declines tracking the decrease in boreal summer insolation (Figure 9.2g). The lipid biomarker profiles support an environment dominated by terrestrial/emergent vascular plants relative to submerged/floating aquatic plants (Figure 9.2d-f), perhaps reflecting higher lake levels during the early Holocene (Beuning and Russell, 2004).

Towards the end of the mid-Holocene at ~5.6ka BP, a distinct shift in almost all of the measured proxies (apart from $\delta^{30}Si_{diatom}$) (Figure 9.2) indicated an abrupt, short-lived drying event which likely caused a decline in lake level resulting in shallower and more concentrated lake waters (i.e. increased $\delta^{18}O_{diatom}$ and submerged/floating aquatic vegetation (Figure 9.2b&e) and a temporary decline in terrestrial/emergent plants (Figure 9.2d). Although this event had been identified by a peak in TOC, TON and high HI (Lærdal et al., 2002; Russell et al., 2003a), it has not been identified as a specific climate event. Similarly, an abrupt decrease in precipitation at ~5.7 ka BP was identified in a high resolution diatom study from Lake Victoria (Stager et al., 2003) and an abrupt cooling event at ~5.2 ka BP in the Kilimanjaro ice cores (Thompson et al., 2002). These events corresponded with many of the tropical African lakes completely drying up or experiencing significant lake level decline at the end of the Mid-Holocene due to a combination of decreasing insolation and other types of forcing (solar, volcanic), reinforced by feedbacks within the climate system (e.g. changes in soil moisture availability, surface albedo and atmospheric circulation) (Gasse, 2000).

Figure 9.2 (next page): Temporal variations in Lake Edward of biogenic silica concentrations (BSi%) (Russell et al., 2003a) (a), oxygen isotope values of diatom silica ($\delta^{18}O_{diatom}$) (b), silicon isotope values of diatom silica ($\delta^{30}Si_{diatom}$) (c), biomarker proxies to distinguish contributions from; terrestrial and emergent aquatic plants (P_{wax}) (d), non-emergent aquatic macrophytes (submerged/floating) (P_{aq}) (e), algae (P_{alg}) (f). Equatorial insolation (scale reversed) for June (boreal summer) (Berger and Loutre, 1991) (g).

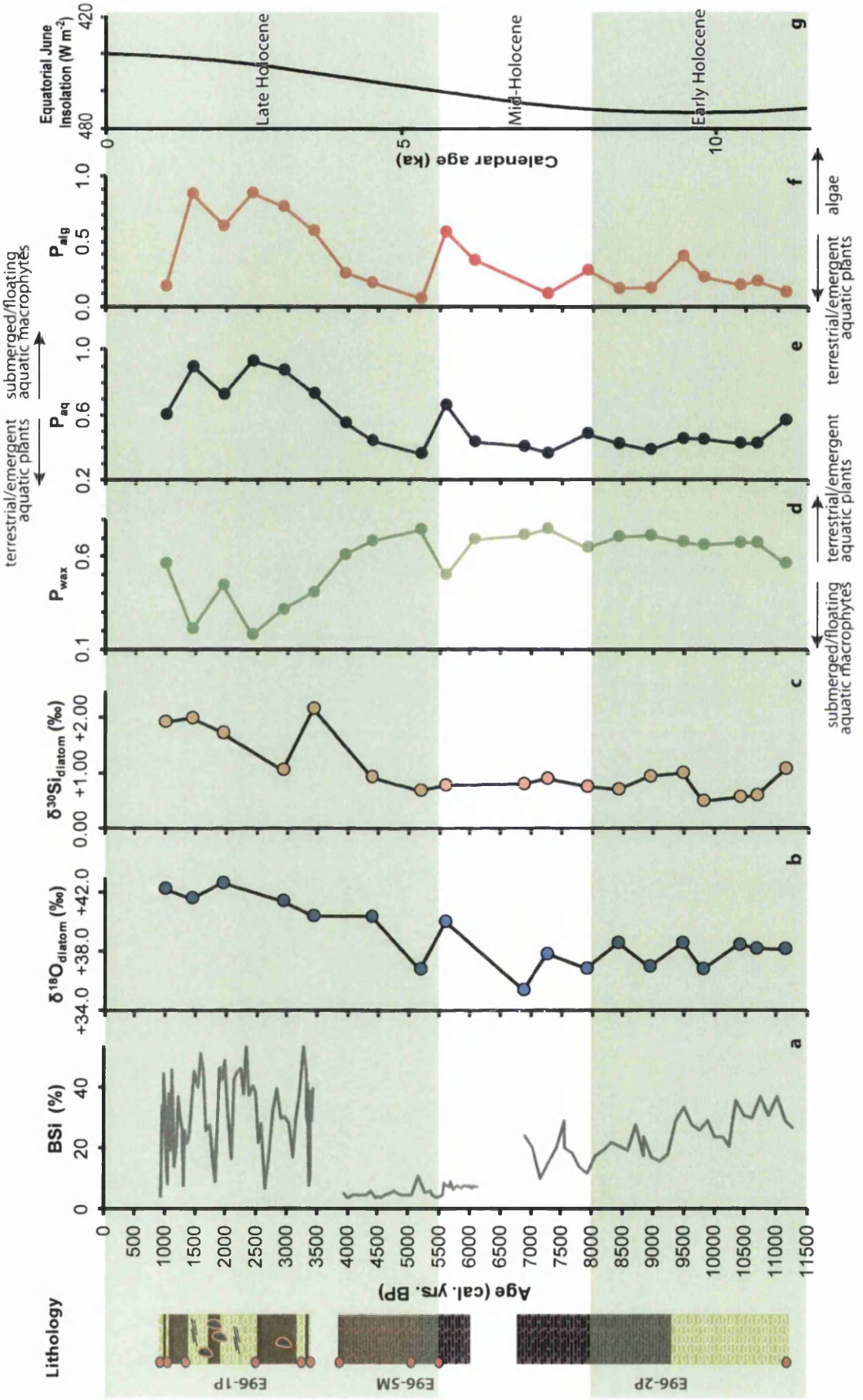
Lithology
E96-1P
E96-5M
E96-2P
Age (cal. yrs. BP)
BSi (%)
δ18Odiatom (‰)
δ30Sidiatom (‰)
Pwax
Paq
Palg
terrestrial/emergent aquatic plants
submerged/floating aquatic macrophytes
algae
Calendar age (ka)
Equatorial June Insolation (W m-2)
Late Holocene
Mid-Holocene
Early Holocene

During the late Holocene, all measured proxies (Figure 9.2b-f) progressively changed, associated with a transformation in lithology at ~5.2 ka BP from dark grey clays to reddish carbonate mud. Inception of precipitation of authigenic calcite implies increasing evaporative concentration of the lake water (Kelts and Hsü, 1978; Russell et al., 2003a; Russell and Johnson, 2005), consistent with the gradual increase in $\delta^{18}O_{diatom}$ values, signifying a progressive reduction of monsoon rainfall as a result of declining insolation forcing (Figure 9.2b). Similarly, an increase in the ratio of biomarkers derived from submerged/floating aquatic macrophytes and algae and a corresponding decline in those representing terrestrial/emergent vegetation (Figure 9.2d-f), supporting reduced lake levels and moisture availability in response to a decrease in P/E (Russell et al., 2003a; Russell et al., 2003b; Russell and Johnson, 2005). Unfortunately, there are limited pollen data for Lake Edward during the late Holocene (Beuning and Russell, 2004). However, evidence from the Rwanda/Burundi Highlands to the south, and Lake Albert and the Rwenzori Mountains to the north suggested a shift towards grassland pollen types (e.g. Poaceae and Cyperaceae), (Livingstone, 1967; Beuning et al., 1997c; Marchant and Taylor, 1997), probably similar to the wooded savanna found in the Queen Elizabeth National Park today, in response to drier conditions across equatorial Africa during the Late Holocene (Gasse, 2000; Barker et al., 2004; Kiage and Liu, 2006).

Reduced lake levels would have encouraged large areas of submerged/floating aquatic macrophytes to form in marginal shallows around Lake Edward, as seen by an increase in P_{aq} proxy during the late Holocene (Figure 9.2e). Synchronous with this increase in submerged and floating macrophytes was an increase in the algal contribution to organic matter (Figure 9.2f). A strong correlation between P_{aq} and P_{alg} proxies (R^2 = 0.84 (Figure 8.30) suggests that they are related. Aquatic macrophytes are often associated with epiphytic communities (Brenner et al., 2006), particularly diatoms and green alga *Pediastrum* (Komárek and Jankovská, 2001), as for example in Lake Nkunga, Mt Kenya, where *Pediastrum* is found living in stands of water lilies (*Nymphaea*) (Street-Perrott et al., 2007). It was noted during the preparation of diatoms for isotope analysis, that green algae, in particular *Pediastrum*, made an appearance in Lake Edward sediments from ~4 ka BP onwards, coinciding with an increase in algae as identified by an increase in the P_{alg} proxy (Figure 9.2f). Although not conclusive, it appears that the increase in algal signature in organic matter during the late Holocene is indicative of increasing predominance of green algae in response to aquatic macrophyte expansion. High

HI and C/N ratios may indicate that organic matter formed in waters with severe nitrogen deficiency due to lake stratification (Lærdal et al., 2002), which would have favoured the dominance of cyanobacteria or green algae over diatoms (Hecky and Kling, 1987). It has already been suggested that on short time scales BSi% represents water balance changes rather than diatom productivity (Russell et al., 2003b; Russell and Johnson, 2005), and therefore may not be representative of diatom production over the long-term. Undoubtedly though, diatom productivity was high during the late Holocene with BSi concentrations reaching ~60% dry weight at times during the last 3.5 ka BP (Figure 9.2a).

Brenner et al. (2006) suggested that the proliferation of submerged macrophytes in Florida lakes was due to increased P loading due to human settlement and forest clearance. With a decrease in catchment biomass, from either human activity (evidence lacking for this at Lake Edward), or from climate-driven changes during the late Holocene, one would expect increased erosion resulting in the mobilisation of P from soils. Further evidence for P loading in Lake Edward during the late Holocene is from a change in the diatom assemblage to a single genus of *Stephanodiscus* from the mid- to late Holocene transition (section 8.9.1, Chapter 8). *Stephanodiscus* spp. dominate when Si:P ratios are low (Kilham et al., 1986; Kilham and Kilham, 1990), and outcompete other diatom species during low light conditions (Kilham et al., 1986), which may have occurred when aquatic macrophytes developed in marginal shallows around the edge of Lake Edward as it shrank. Lake Albert to the north, which relies heavily on inflow from Lake Edward via the Semliki River (Beuning et al., 1997c), also had low DSi (and possibly relatively high P) between ~5 ka BP and present reflected by a diatom assemblage consisting of *Stephanodiscus rotula* and *Nitzschia bacala* (Hecky and Degans, 1973; Harvey, 1976; Richardson et al., 1978). Reduced DSi in Lake Edward would explain the enrichment of $\delta^{30}Si_{diatom}$ during the late Holocene (Figure 9.2c). The change from tropical rain forest to wooded grasslands, as inferred for the late Holocene pollen assemblages at Lake Edward, would have drastically changed Si cycling dynamics in the catchment. A reduction in terrestrial biomass and Si accumulator plants associated with the disappearance of tropical rainforest would have reduced silicate-rock weathering and the stock of available Si (Struyf et al., 2010). In addition, decreased precipitation would have reduced annual runoff and mobilisation of DSi from the catchment, as seen during the LGM in Lakes Kivu and Tanganyika (Haberyan and Hecky, 1987). Furthermore, the expansion of aquatic macrophytes

(Figure 9.2e), many of which take up significant quantities of Si (Schoelynck et al., 2010), would have further depleted the supply of DSi available in the lake water, resulting in elevated $\delta^{30}Si_{diatom}$ during the late Holocene (Figure 9.2c).

A peak in $\delta^{30}Si_{diatom}$ to maximum values occurred during the late Holocene at ~3.4 ka BP (Figure 9.2c), indicating that DSi was limited. This may represent a cessation in the flow of nutrient-rich waters from Lake George, which desiccated prior to ~4.0 ka BP (Viner, 1977). Refilling of its basin was estimated to have begun from 3.6 ka ^{14}C BP (~3.9 ka BP) (Viner, 1977), but re-establishment of its outflow to Lake Edward via the Kazinga Channel may not have occurred until after 2 ka BP (Russell et al., 2003a). $\delta^{18}O_{diatom}$ does not seem to register this event at 3.4 ka BP (Figure 9.2b), which may indicate that the inflow from Lake George does not have a freshening effect on Lake Edward waters. In fact, $\delta^{18}O_{diatom}$ decreases slightly supporting a decline in the inflow of concentrated warm waters from Lake George. The modern water data support this inference as the Kazinga Channel waters were enriched in ^{18}O and electrical conductance was higher than other river inputs (e.g. Rivers Ishasha and Ntungwe) (Tables 6.1 and 6.2). From ~ 2 ka BP, amelioration of the climate as identified by a slight decline in $\delta^{18}O_{calcite}$ (Russell and Johnson, 2005) and $\delta^{18}O_{diatom}$ (Figure 9.2b), resulted in a lake level rise at Lake Edward (Russell et al., 2003a; Russell and Johnson, 2005), and reconnection with Lake George through the Kazinga Channel. Simultaneously, biomarkers representing terrestrial/emergent vegetation increased (Figure 9.2d) and submerged/floating aquatic macrophytes and algae declined (Figure 9.2e&f), also supporting a lake level rise and climate recovery in the basin, but not nearly reaching early Holocene conditions.

9.8 Long-term trends of Si cycling in the headwaters of the White Nile since the LGM

Figures 9.1 and 9.2 strongly suggest that on multi-millennial time scales orbital forcing controlled the hydrological balance ($\delta^{18}O_{diatom}$) and Si cycling ($\delta^{30}Si_{diatom}$) in both the basins of Lakes Victoria and Edward. As originally hypothesised, variation in the climate, driven by insolation changes, influenced hydrology and vegetation which in turn affected the dynamics of biogeochemical Si cycling. Although not directly causal, the strong positive relationship between $\delta^{18}O_{diatom}$ and $\delta^{30}Si_{diatom}$

(Figures 7.20 and 8.26) provides further support that hydrology and Si cycling are responding to the same controlling mechanism of orbital forcing.

During periods of minimum seasonality of insolation (i.e. the LGM and the late Holocene), the climate in the headwaters of the White Nile was dry and P/E ratios were low, as shown by enriched $\delta^{18}O_{diatom}$ values (Figures 9.1b and 9.2b). In contrast, during the early to mid-Holocene, enhanced monsoons, due to an increase in boreal-summer insolation resulted in high P/E ratios, and therefore low $\delta^{18}O_{diatom}$ values. Similarly, at Lake Challa, at the foot of Mount Kilimanjaro, Barker et al. (2011) found that $\delta^{18}O_{diatom}$ values during the last 25 ka BP exhibited a smooth evolution coinciding with the precessional-driven monsoons.

These long-term variations in P/E ratios since the LGM at Lakes Victoria and Edward have produced major changes in the vegetation as identified from the lipid biomarker proxies (Figures 9.1e-g and 9.2d-f) and from pollen data (Kendall, 1969; Beuning and Russell, 2004), for the respective lakes. During deglaciation (~21 to 15 ka BP), plant biomass was diminished and consisted of dry regional grasslands (Kendall, 1969). Commencement of the EAHP at ~15 ka BP, as insolation reached a critical threshold (Kutzbach and Street-Perrott, 1985; Prell and Kutzbach, 1987, enabled the development of moist semi-deciduous forests during the late glacial (Kendall, 1969). By the start of the Holocene, insolation and precipitation were at a peak, sustaining evergreen tropical rainforest both at Lake Victoria and Lake Edward (Kendall, 1969; Beuning and Russell, 2004). Towards the end of the mid-Holocene seasonality of insolation over the Northern Hemisphere declined, and a gradual change in vegetation to drier species occurred (e.g. wooded savanna). Reduced P/E resulted in lower lake levels which encouraged the expansion of submerged/floating aquatic macrophytes (Figures 9.1f and 9.2e) and associated algal epiphytic communities (Figures 9.1g and 9.2f).

The evolution of Si cycling, as traced by $\delta^{30}Si_{diatom}$ and driven by orbital forcing during the last 20 ka BP in the basins of Lakes Victoria and Edward (Figures 9.1 and 9.2), is analogous to the conceptual model proposed by Struyf et al. (2010) for temperate forest development (Figure 9.3). According to this model the "developing forest" state is similar to that of the late glacial at Lake Victoria when semi-deciduous forests began to colonise the basin in response to increased moisture from the enhanced summer monsoon (Kutzbach and Street-Perrott, 1985). Gradually, as the forest developed, a soil stock of ASi would have formed and the

export of biologically reactive TSi into the lakes would have increased with time, as is identified in the progressive decline in $\delta^{30}Si_{diatom}$ values through the late glacial. By the start of the Holocene vegetation was well established and both basins hosted evergreen lowland rainforests which stimulated silicate-rock weathering through their deep roots creating a high turn-over of Si and a large stock of soil ASi (Cochran and Berner, 1996; Kelly et al., 1998; Hinsinger et al., 2001; Lucas, 2001; Brantley et al., 2011). Dissolution and mobilisation of ASi through runoff would have been high and eventually reached an equilibrium as exhibited by the low and stable $\delta^{30}Si_{diatom}$ values during the early to mid-Holocene (comparable to the "climax forest" state in Figure 9.3). In the late Holocene, as P/E declined in response to decreased insolation (high $\delta^{18}O_{diatom}$) (Figures 9.1b and 9.2b), rainforest gradually gave way to open savanna grasslands (Kendall, 1969) with a shallower rooting depth, causing a decline in terrestrial biomass (Figures 9.1e and 9.2d) and deep rooted vegetation, resulting in greatly reduced Si cycling in the catchment (equivalent to "early deforestation" and "climax cultivated" scenarios in Figure 9.3). Combined with reduced runoff and a declining ASi soil stock, decreased export of TSi into the lakes would have caused a decrease in DSi supply relative to demand from diatoms, causing a progressive increase in $\delta^{30}Si_{diatom}$ values (Figures 9.1c and 9.2c). The expansion of aquatic macrophytes (Figures 9.1f and 9.2e) in response to lower lakes levels would have further depleted DSi availability as many aquatic macrophytes and wetland species are known to be Si accumulators (Gaudet, 1977; Struyf et al., 2005; Schoelynck et al., 2010).

The temporary increase of TSi export exhibited during the "early deforestation" scenario (Figure 9.3) is similar to what would be expected when Lake Victoria began to refill shortly after 15ka BP (Johnson et al., 2000; Talbot and Lærdal, 2000; Stager and Johnson, 2008). As surrounding land was flooded by the rising waters of the lake and new shorelines were created, mobilisation of a large pool of grass phytoliths in the surrounding soils resulted in a large influx of DSi (McLachlan, 1970).

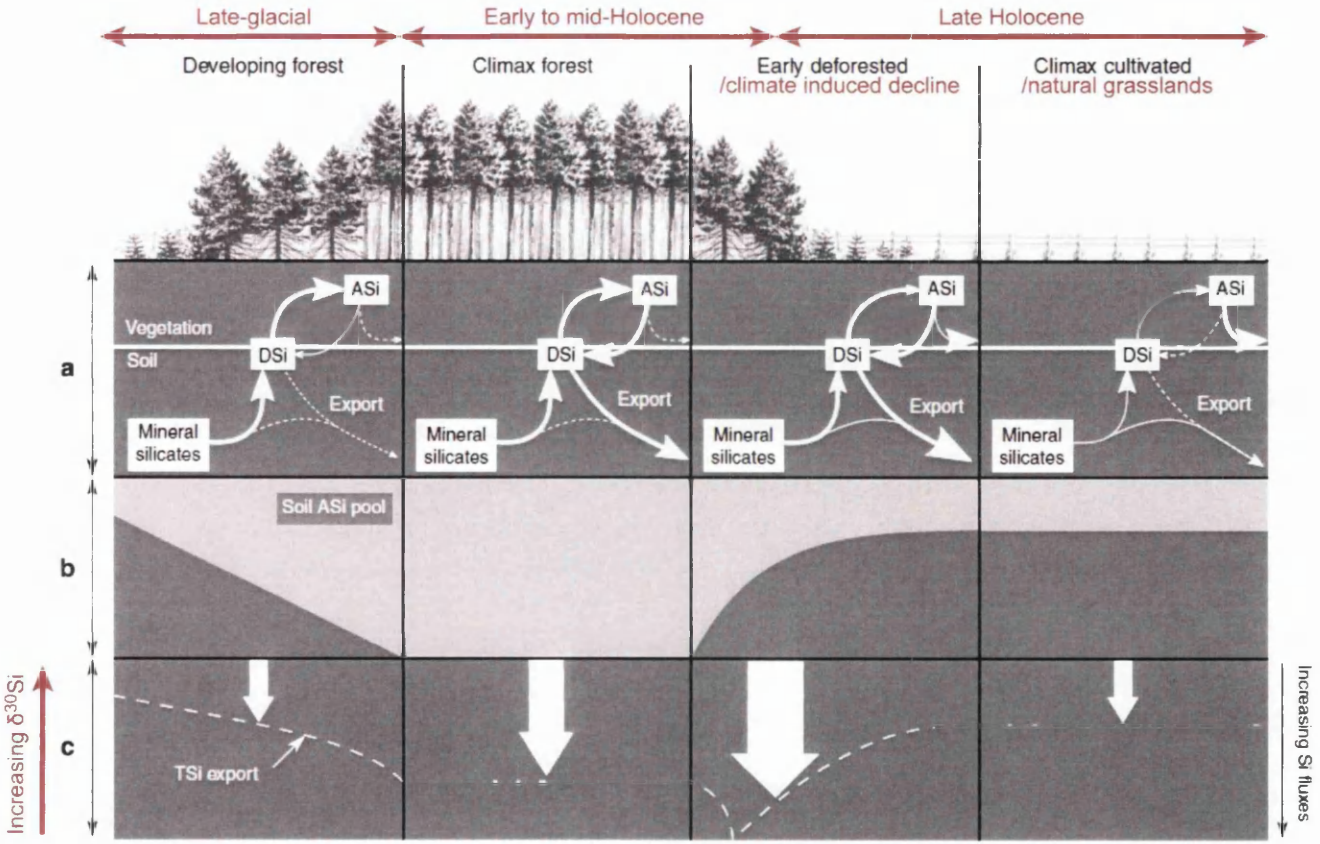

Figure 9.3: A conceptual model of Si cycling as vegetation ecosystems develop and change in a European drainage basin. (a) Hypothesized Si cycling in developing forest, climax forest, early deforested areas and equilibrium cultured areas, the associated soil ASi stock (b) and the resultant magnitude of TSi export (c). In *a*, boxes represent stocks of Si. Arrows represent fluxes: the thickness of arrows is representative for flux size. Dashed arrows represent irrelevant fluxes. In *b*, the light grey area represents the size of the soil ASi pool. In *c*, the sizes of the arrows represent relative TSi fluxes. The dashed line represents the hypothesized evolution of the magnitude of the TSi fluxes: the closer the dashed line is to the figure bottom, the higher the TSi export (as also indicated by the arrow to the right below). ASi: amorphous Si; DSi: dissolved Si; TSi: ASi+DSi. Modified after Struyf et al. (2010).

9.9 Summary: Si cycling at Lakes Victoria and Edward

On glacial / interglacial time scales, variation in the riverine Si flux from the White Nile, as observed from $\delta^{30}Si_{diatom}$, will have had a significant impact on the Si supply to the Mediterranean Sea. The similarity of the two lake records (Figures 9.1 and 9.2) during the Holocene epoch (the only timeframe for which they overlap), clearly indicates that they were responding to the same external forcing mechanism, identified as orbital forcing. It is likely therefore, that other lakes will have undergone the same forcing and consequently similar biogeochemical Si cycling dynamics, ultimately impacting on the export of Si to the oceans and affecting the regulation of CO_2 in the atmosphere. The evidence obtained in this thesis indicates that the riverine flux of Si to the oceans would have been lower during glacial periods, in contradiction to Froelich et al. (1992) who suggested the dissolved Si flux to the oceans during glacial periods increased.

Compared to other $\delta^{18}O_{diatom}$ records in East Africa, $\delta^{18}O_{diatom}$ values at Lakes Victoria and Edward are enriched compared to Lake Rutundu on Mount Kenya (Street-Perrott et al., 2008) but similar to those obtained at Lake Challa at the foot of Kilimanjaro (Barker et al., 2011) for the same time interval. These $\delta^{18}O_{diatom}$ records reflect changes in moisture balance as well, and therefore, it is likely that the lower values exhibited at Lake Rutundu (~3085m asl) reflect progressive rain-out of ^{18}O due to the altitude-effect (Dansgaard, 1964). Lake Victoria had slightly higher $\delta^{18}O_{diatom}$ values than Lake Edward (Figures 9.1 and 9.2), reflecting the dominant control of precipitation and evaporation on water balance at Lake Victoria as an atmosphere-dominated lake (Street-Perrott and Harrison, 1985; Piper et al., 1986; Spigel and Coulter, 1996; Nicholson, 1998).

Based on the current knowledge of biological fractionation between the uptake of DSi to produce diatom silica (fractionation factor: -1.1‰; (De La Rocha et al., 1997; Varela et al., 2004)), the range of $\delta^{30}Si_{diatom}$ values obtained at Lake Victoria during the last 15 ka BP (+0.62 to +1.26‰) (Figure 9.1) are consistent with a Rayleigh model (closed system). This is not surprising given its vast size (>68,000 km^2) and dominance of precipitation and evaporation in controlling the water balance relative to inflows and outflows (Spigel and Coulter, 1996). Lake Edward on the other hand, had a larger range of $\delta^{30}Si_{diatom}$ values, +0.49 to +2.16‰ (Figure 9.2), implying that Lake Edward represented a steady state model (open system). Although there are

only two other records that have determined $\delta^{30}Si_{diatom}$ from lake sediments on glacial / interglacial time scales, in Lake Rutundu, Mount Kenya (Street-Perrott et al., 2008) and Lake El'gygytgyn, northeast Siberia (Swann et al., 2010), $\delta^{30}Si_{diatom}$ values are higher in equatorial Lakes Victoria and Edward. This is not surprising as it is likely that Si cycling was enhanced in these large lowland tropical lakes, resulting in more of a demand for Si by diatoms relative to the supply, which resulted in higher $\delta^{30}Si_{diatom}$ values.

From results obtained in this thesis and from the $\delta^{30}Si_{diatom}$ record obtained in Siberia (Swann et al., 2010), I hypothesise that the underlying control on *global* Si cycling (and therefore the riverine flux of Si) on glacial / interglacial time scales was from northern hemisphere changes in insolation, which modified climate (temperature and hydrology) and vegetation, and consequently continental Si cycling dynamics. As seen in this thesis, in both modern waters and from diatom silica, Si cycling was greatest during drier intervals as a result of 1) decreased silicate-rock weathering within the catchment, 2) reduced mobilisation of Si from the catchment by surface runoff, and 3) more efficient utilisation of Si by aquatic biota.

Chapter 10 Conclusions

This final chapter presents the major findings of the thesis. Firstly, a summary of the main results from the modern waters sampled along the River Nile, followed by the main findings of the palaeo-record from Lakes Victoria and Edward in the headwaters of the White Nile. Finally, from the outcomes of this thesis, future work and research directions are suggested to help develop the field of continental biogeochemical Si cycling further.

10.1 Main findings: Modern waters

Seasonal variations in hydrology and Si cycling in the Nile Basin were investigated using stable isotope (H, O and Si) compositions and dissolved Si (DSi) concentrations in surface waters. Physical and chemical characteristics of surface waters supported the findings made from the isotope data.

Main findings from physical and chemical compositions:

- Progressive increase in the precipitation of Na and K carbonate minerals and electrical conductance northwards and downstream signified progressive evaporative enrichment of waters which was enhanced during the dry season under conditions of lower humidity.
- Contrasting geology of the headwater sub-basins was apparent in pH values and cation composition, where waters from the Ethiopian Highlands were less alkaline and had highly concentrated Mg waters as a result of easily erodible ferromagnesian minerals in the basaltic terrain.

Main findings about the hydrological cycle from H- and O-isotopes:

- Large seasonal shifts in δ^2H and $\delta^{18}O$ compositions reflected changes in water balance.
- During the dry season, lower humidity favoured evaporative enrichment of surface waters and was reflected in higher δ^2H and $\delta^{18}O$ values.
- Cumulative downstream losses from swamps and open water bodies, were identified by progressive downstream enrichment of δ^2H and $\delta^{18}O$ values.
- The Main Nile showed the greatest evaporative enrichment, due to the year-round arid climate and lack of rainfall or tributary input for 2700 km downstream from its confluence with the Atbara River.

10: Conclusions

This was the first (sub)continental study to investigate seasonal changes in Si cycling along the length of a river using Si isotopes. Seasonal changes in DSi concentrations and Si isotopes provided useful information on Si cycling under different climate regimes in the Nile Basin.

Main findings from Si-isotopes and DSi concentrations:

- This study has increased the global upper limit of $\delta^{30}Si$ for dissolved Si in natural waters by more than 1‰, extending the range from between -0.17 and +3.40‰ to -0.17 and +4.66‰.
- Contrasting geology in the headwaters of the White and Blue Nile were clearly reflected in DSi concentrations. The highest levels of DSi in the Blue Nile headwaters were due to the basaltic bedrock and steep, easily erodible, sparsely vegetated slopes of the Ethiopian Highlands.
- Low DSi concentrations and correspondingly enriched Si-isotope values are found in the headwater lakes and in the Main Nile, where depletion of Si by aquatic organisms (notably diatoms and macrophytes) are thought to be important.
- Extensive downstream enrichment of Si isotopes and depletion of DSi during both wet and dry seasons in the River Nile imply active Si biocycling. The heavy isotope ^{30}Si was enriched in surface waters during the dry season due to a reduction in mobilisation of DSi from the catchment relative to aquatic demand.
- Localized anthropogenic impacts on the isotope composition of surface waters were identifiable with respect to both the hydrological and Si cycles, especially during the dry season and along the Main Nile where irrigation and retention of stored floodwaters behind large dams are most prevalent.

Overall conclusion:

Modern seasonal variations of DSi and $\delta^{30}Si$ in the River Nile indicated that the Si flux from the River Nile to the Mediterranean Sea is not constant and is likely to be highly variable on Quaternary time scales.

10.2 Main findings: palaeo-records of Lakes Victoria and Edward

The results of the modern water sampling in the Nile Basin were used to help interpret the palaeo-record of lacustrine sequences from Lakes Victoria and Edward in the White Nile headwaters. Using O- and Si-isotope analysis of diatom silica as tracers of the hydrological and Si cycles, respectively, and lipid-biomarker analysis to track changes in aquatic and terrestrial ecosystems, Si cycling in the White Nile headwaters was reconstructed for the last 15 ka BP.

Main findings:

- Si cycling was greatest during the early to mid-Holocene (~11.5 to 5.5 ka BP) at both Lakes Victoria and Edward when the enhanced summer monsoon (low $\delta^{18}O_{diatom}$ values), driven by orbital forcing, enabled the proliferation of water-bodies and vegetation in the catchment, which in turn accelerated silicate-rock weathering and the mobilisation of TSi in surface runoff, providing a plentiful supply of DSi for diatom productivity (low $\delta^{30}Si_{diatom}$ values).
- In contrast, during drier conditions (e.g. the last glacial and late Holocene) (high $\delta^{18}O_{diatom}$ values), Si cycling was reduced in response to decreased boreal summer insolation. Reduced biomass and a decline in deep-rooted vegetation to stimulate silicate-rock weathering, combined with a declining soil stock of ASi and reduced run-off in the catchment resulted in biological demand for Si exceeding the supply which caused high $\delta^{30}Si_{diatom}$ values.

The above findings overturn the original research hypothesis. At the beginning of this thesis it was proposed that the flux of Si from the River Nile to the Mediterranean Sea would have been greatest during drier intervals when a sparsely vegetated environment would have allowed erosion of soils and the transfer of TSi into rivers and lakes. However, it appears that DSi was actually reduced during drier intervals as a result of reduced continental Si cycling, quite the opposite to what was originally hypothesised in this thesis and presented by Froelich et al. (1992). The simultaneous smooth response of all the measured proxies ($\delta^{18}O_{diatom}$, $\delta^{30}Si_{diatom}$, P_{wax}, P_{aq}, P_{alg}) to insolation changes during the last ~15 ka BP at both lakes clearly identifies orbital forcing as the controlling factor of long-term changes in hydrology and Si cycling in the White Nile headwaters.

10.3 Future work

Due to the novelty of Si-isotope analysis on solutions at NIGL, financial and time constraints meant that it was only possible to analyse half of the water samples for Si isotopes. Analysis of the remaining waters would enhance the understanding of continental Si cycling further by providing a more in-depth view of individual catchments and sub-basins within the Nile system. Furthermore, it is essential to obtain samples from the Sudd and the Bahr el Ghazal swamps in South Sudan which likely play an important role in both the hydrological and Si cycles. It was not possible to sample these regions during the time of fieldwork due to political instability. In addition to Si-isotopes, measurement of Ge/Si ratios on waters would provide further useful information on Si cycling dynamics in the catchment by determining whether the DSi had been cycled through the soil-plant system or come straight from silicate-rock weathering before being exported into rivers and lakes.

In terms of the palaeoenvironmental research carried out in this thesis, work is ongoing to identify the structures of the botryococcene compounds found in Lake Victoria with the possibility of linking them to a specific species of *Botryococcus.* Further analysis of O- and Si-isotope composition of diatoms in other Nile-fed sediments along the length of the River Nile would enhance this research further, enabling a transect of downstream sites in order to track Si cycling at specific time-slices during important climate intervals (e.g. LGM, EAHP and late Holocene). On a global scale, further catchment and large, downstream studies are required to test the hypothesis that global continental Si cycling is controlled by northern hemisphere insolation changes, as identified here in the Nile Basin and in northeast Siberia by Swann et al. (2010). It would also be beneficial to extend the time scale over several glacial \ interglacial cycles. If it was found that all fluvial systems were responding to the same long-term forcing, such that global riverine fluxes of Si were reduced during drier periods, this would have significant implications for the marine Si budget and therefore the global C cycle. Important regions for future work would be in volcanic regions, particularly in the tropics where silicate rock weathering is high. Other regions which may be important are the Siberian Traps, the volcanic regions of Alaska and the Pacific Northwest of the USA.

10.4 Summary

Overall, this research has been a success. The findings suggest that continental biota do have an important role in the global biogeochemical cycle of Si and have a significant impact on controlling the flux of Si to the oceans on glacial \ interglacial time scales. Although fieldwork was logistically challenging on occasion, it was still possible to obtain a respectable collection of water samples from the Nile Basin. There were times during the preparation of sediment samples when it was difficult to isolate diatoms from other sediment components for isotope analysis, to the point where it became impossible to purify diatoms in large parts of the Lake Victoria core. Careful selection of sediment samples with high initial diatom concentration and an assessment of the other sediment components in future will aid this. The combination of proxies used in this thesis combined with previously published data has resulted in achieving the main aim of reconstructing Si cycling in the Nile Basin during the last 15 ka BP.

Appendix

Appendix I.

Major ion concentrations of surface waters analysed by ICP-MS: wet-season water samples

Sample site number	Detection limit	Li µg/l ppb <1	Be µg/l ppb <0.01	B µg/l ppb <10	Na mg/l ppm <0.2	Mg mg/l ppm <0.01	Al µg/l ppb <1	Si µg/l ppb <50	P mg/l ppm <0.01	S mg/l ppm <1	K mg/l ppm <0.02	Ca mg/l ppm <0.3	Ti µg/l ppb <0.05	V µg/l ppb <0.4	Cr µg/l ppb <0.05	Mn µg/l ppb <0.2	Fe µg/l ppb <1	Co µg/l ppb <0.01
3	River Mubuku, Rwenzori Mountains, Uganda	1	0.01	-7	2.3	1.18	63	6760	0.02	1	0.98	5.3	0.83	0.7	0.21	4.5	80	0.07
4	River Ishasha, Uganda	3	0.02	0	3.1	1.80	63	6564	0.01	3	2.59	3.4	1.45	0.8	0.29	59.5	194	0.46
5	River Ntungwe, Uganda	2	0.04	1	12.5	3.76	129	14060	0.01	9	3.01	8.2	4.35	1.9	0.36	137.6	254	0.50
7	Lake Mahoma, Rwenzori Mountains, Uganda	0	0.01	-7	0.5	0.22	31	1249	0.00	0	0.49	1.0	0.24	0.1	0.08	12.1	28	0.08
9	River Kagera, Uganda	1	0.01	-4	9.7	5.39	31	8359	0.00	3	6.55	7.5	1.21	0.5	0.13	8.0	170	0.07
11	River Semliki, Uganda-Congo	6	0.01	18	40.6	17.89	25	10424	0.11	6	30.26	12.3	3.28	4.2	0.17	2.7	40	0.12
12	Kazinga Channel, Uganda	1	0.00	-2	14.7	7.86	8	12031	0.00	2	4.10	14.4	0.17	2.9	0.13	1.8	4	0.15
13	White Nile, Khartoum, Sudan	0	0.01	6	15.1	5.99	43	7103	0.03	1	6.53	10.4	1.14	3.5	0.16	10.4	65	0.13
14	Albert Nile, Uganda	0	0.00	1	12.3	2.97	89	3430	0.00	0	3.32	5.9	3.24	0.8	0.25	6.6	77	0.08
15	Victoria Nile Delta, Uganda	1	0.00	1	11.4	3.06	29	3830	0.00	1	3.69	6.4	1.19	0.8	0.19	2.6	49	0.07
18	Victoria Nile, Bujagali Falls, Uganda	1	0.00	1	9.4	2.46	5	1719	0.01	1	3.47	5.4	0.04	0.4	0.03	0.5	3	0.02
19	Outflow from Lake Victoria (Jinja), Uganda	0	0.00	1	10.4	2.36	5	1240	0.00	0	3.90	4.6	0.02	0.3	0.04	1.2	4	0.04
20	Lake Albert (south), Uganda-Congo	7	0.00	31	53.6	22.00	27	3253	0.02	5	37.91	9.6	1.81	3.3	0.11	0.7	76	0.17
25	Ribb River, east Lake Tana, Ethiopia	0	0.00	-2	8.3	5.22	34	10321	0.09	2	2.05	17.8	0.70	4.6	0.15	0.4	21	0.07
28	Chimba, Gilgel Abay, Ethiopia	0	0.00	-4	3.9	3.56	116	8762	0.00	1	1.16	8.0	0.61	1.1	0.21	2.3	76	0.10
31	River Zerma, Ethiopia	0	0.00	-5	6.3	6.74	3	22290	0.02	1	1.78	18.8	0.08	10.3	1.09	1.1	1	0.04
32	River Tekezé, Ethiopia	0	0.00	22	19.8	12.19	13	11659	0.04	12	2.71	32.4	0.16	9.2	0.19	0.6	2	0.06
33	River Megetch, north Lake Tana, Ethiopia	0	0.00	-2	12.5	16.93	4	18770	0.13	3	2.91	41.6	0.06	9.3	0.33	10.1	1	0.21
34	Blue Nile, Khartoum, Sudan	0	0.00	1	8.9	6.18	16	8612	0.00	5	2.51	14.5	0.28	12.9	0.16	0.5	10	0.19
35	Tis Issat Falls, Blue Nile, Ethiopia	0	0.00	-1	5.0	4.58	92	5778	0.02	1	1.74	11.6	1.46	3.2	0.20	3.6	77	0.12
36	River Atbara, Atbara, Sudan	0	0.00	4	18.1	12.21	3	10298	0.02	3	2.56	32.6	0.06	23.7	0.22	0.5	1	0.08
39	Main Nile, Dongola, Sudan	0	0.00	2	11.2	5.76	7	7431	0.03	3	2.85	22.9	0.07	8.3	0.29	0.3	1	0.04
41	Main Nile, Atbara, Sudan	0	0.00	6	14.3	5.49	18	6823	0.03	1	5.55	14.7	0.61	5.6	0.13	0.8	30	0.08
45	Main Nile, Cairo, Egypt	0	0.00	22	41.5	12.86	32	912	0.00	16	7.37	32.7	0.04	4.6	0.09	8.2	6	0.06
46	Main Nile, Luxor, Egypt	0	0.00	10	24.6	8.96	2	3430	0.00	6	5.00	25.1	0.04	5.4	0.15	0.7	2	0.03
47	Main Nile (Lake Nasser), Aswan, Egypt	0	0.00	10	15.8	8.46	2	4041	0.00	5	5.34	24.9	0.03	5.4	0.04	0.6	1	0.03
48	Lake Qarun, Faiyum (south-east), Egypt	20	0.00	1289	7566.3	826.13	59	2972	0.03	3015	202.84	432.9	4.15	8.2	0.29	6.6	68	0.39

Cont.

Sample site number	Ni µg/l ppb <0.1	Cu µg/l ppb <0.4	Zn µg/l ppb <0.5	Ga µg/l ppb <0.03	As µg/l ppb <0.04	Se µg/l ppb <0.1	Rb µg/l ppb <0.01	Sr µg/l ppb <0.1	Y µg/l ppb <0.005	Zr µg/l ppb <0.05	Nb µg/l ppb <0.02	Mo µg/l ppb <0.08	Ag µg/l ppb <0.05	Cd µg/l ppb <0.01	Sn µg/l ppb <0.04	Sb µg/l ppb <0.005	Cs µg/l ppb <0.005	Ba µg/l ppb <0.1	La µg/l ppb <0.002	Ce µg/l ppb <0.002	Pr µg/l ppb <0.002	Nd µg/l ppb <0.04
3	0.5	1.7	3.3	-0.02	0.03	0.1	1.21	29.2	0.104	0.08	0.01	0.27	0.00	0.01	-0.01	0.027	0.007	10.3	0.209	0.303	0.042	0.16
4	1.5	2.1	4.1	-0.01	0.64	0.1	3.48	34.8	0.261	0.46	0.02	0.08	0.01	0.01	0.02	0.029	0.033	16.7	0.387	0.908	0.111	0.46
5	1.6	1.6	2.1	0.01	0.35	0.2	4.32	84.1	0.324	0.34	0.05	0.31	0.01	0.01	0.02	0.033	0.026	36.5	0.572	1.287	0.134	0.51
7	0.2	2.0	8.0	-0.03	0.01	0.0	0.87	9.1	0.061	0.06	0.00	0.00	0.00	0.01	-0.01	0.072	0.001	5.9	0.078	0.140	0.017	0.07
9	0.3	1.2	3.1	-0.02	0.42	0.1	7.16	78.0	0.077	0.15	0.01	0.17	0.22	0.01	0.02	0.013	0.028	18.4	0.109	0.220	0.024	0.09
11	0.9	3.9	1.2	-0.01	0.40	0.1	11.25	289.5	0.142	0.27	0.06	1.96	0.05	0.03	0.00	0.047	0.043	61.4	0.202	0.345	0.042	0.16
12	0.4	0.9	1.9	-0.01	0.10	0.0	4.49	244.6	0.022	0.02	0.00	0.16	0.21	0.01	0.09	0.048	0.005	50.3	0.018	0.027	0.004	0.02
13	1.0	1.7	0.8	-0.01	0.33	0.0	2.75	129.4	0.086	0.07	0.01	0.29	0.00	0.04	0.00	0.029	0.005	43.4	0.089	0.189	0.024	0.10
14	0.5	0.7	0.8	0.00	0.17	0.0	4.18	88.6	0.072	0.06	0.01	0.21	0.00	0.01	-0.01	0.018	0.004	43.1	0.121	0.194	0.024	0.06
15	0.4	0.8	1.6	-0.02	0.16	0.0	4.46	91.8	0.044	0.03	0.00	0.18	0.00	0.00	-0.01	0.017	0.009	38.0	0.068	0.114	0.015	0.06
18	0.2	0.5	1.4	-0.02	0.16	0.0	4.26	86.9	0.003	0.00	0.00	0.16	0.01	0.01	-0.01	0.034	0.029	28.3	0.003	0.003	0.001	0.01
19	0.2	1.3	1.9	-0.03	0.16	0.0	4.14	82.7	0.005	-0.01	0.00	0.20	0.02	0.03	0.01	0.020	0.013	28.8	0.003	0.005	0.000	-0.02
20	0.4	1.2	2.1	-0.01	0.45	0.0	18.02	305.7	0.081	0.14	0.02	2.36	0.00	0.31	-0.01	0.071	0.049	76.5	0.086	0.175	0.019	0.07
25	0.4	1.1	2.3	-0.01	0.23	0.1	0.92	159.5	0.056	0.06	0.00	0.60	0.00	0.00	0.10	0.034	0.001	29.3	0.030	0.047	0.008	0.04
28	0.5	2.2	5.6	-0.01	0.09	0.0	0.89	47.4	0.106	0.07	0.00	0.02	0.00	0.01	0.04	0.018	0.004	18.7	0.066	0.167	0.020	0.09
31	0.1	1.9	2.9	-0.02	0.07	0.1	0.43	69.1	0.028	0.01	0.00	0.08	0.04	0.00	0.02	0.022	0.000	3.4	0.008	0.008	0.002	0.02
32	0.5	1.8	1.5	0.01	0.96	0.7	0.41	253.1	0.036	0.01	0.00	1.88	0.01	0.17	0.05	0.059	0.001	21.2	0.011	0.014	0.002	0.00
33	0.8	1.3	1.4	-0.02	0.16	0.1	0.94	231.0	0.143	0.01	0.00	0.29	0.01	0.19	0.06	0.034	0.002	22.0	0.017	0.018	0.005	0.02
34	0.4	2.0	1.2	0.03	0.41	0.1	0.88	108.3	0.013	0.04	0.00	0.76	0.02	0.02	0.02	0.046	0.006	12.4	0.010	0.020	0.002	0.01
35	0.8	4.2	5.8	0.00	0.15	0.1	0.72	72.4	0.074	0.05	0.00	0.28	0.05	0.03	0.04	0.025	0.001	14.8	0.038	0.074	0.011	0.05
36	0.5	3.2	0.3	-0.01	0.99	0.2	0.54	189.0	0.055	0.00	0.00	1.00	0.01	0.03	0.03	0.069	0.011	19.4	0.006	0.006	0.001	-0.02
39	0.5	1.5	0.4	0.00	0.36	0.4	0.83	129.7	0.023	0.01	0.00	0.89	0.00	0.01	0.00	0.048	0.005	18.8	0.005	0.005	0.000	-0.03
41	0.8	2.1	0.2	-0.01	0.39	0.1	1.77	109.9	0.061	0.04	0.00	0.40	0.00	0.02	0.00	0.027	0.002	21.6	0.058	0.114	0.015	0.06
45	0.6	1.0	0.6	-0.01	0.44	0.1	1.98	328.6	0.023	0.01	0.00	1.16	0.03	0.05	0.03	0.051	0.007	33.2	0.004	0.007	0.001	0.01
46	0.4	1.3	0.8	-0.02	0.48	0.7	1.46	200.6	0.018	0.00	0.00	1.20	0.00	0.02	-0.01	0.058	0.012	29.2	0.005	0.005	0.000	-0.03
47	0.4	0.6	1.1	-0.02	0.49	0.1	1.54	175.4	0.007	0.00	0.00	1.10	0.00	0.01	0.01	0.050	0.008	28.0	0.002	0.001	0.000	0.01
48	1.7	2.7	1.8	0.00	5.72	4.5	16.11	11114.0	0.135	0.40	0.02	15.43	0.04	0.10	0.02	0.397	0.026	74.2	0.058	0.122	0.016	0.02

Cont.

Sample site number	Sm µg/l ppb <0.002	Eu µg/l ppb <0.002	Tb µg/l ppb <0.002	Gd µg/l ppb <0.002	Dy µg/l ppb <0.002	Ho µg/l ppb <0.002	Er µg/l ppb <0.002	Tm µg/l ppb <0.002	Yb µg/l ppb <0.002	Lu µg/l ppb <0.002	Hf µg/l ppb <0.01	Ta µg/l ppb <0.02	W µg/l ppb <0.05	Tl µg/l ppb <0.01	Pb µg/l ppb <0.02	Th µg/l ppb <0.005	U µg/l ppb <0.002
3	0.025	0.005	0.003	0.028	0.016	0.003	0.008	0.001	0.007	0.001	0.00	0.0	-0.01	0.00	0.24	0.010	0.261
4	0.081	0.015	0.009	0.081	0.043	0.008	0.024	0.003	0.020	0.003	0.01	0.0	0.00	0.01	0.11	0.029	0.071
5	0.084	0.017	0.011	0.094	0.056	0.011	0.031	0.004	0.022	0.004	0.01	0.0	0.01	0.01	0.14	0.038	0.138
7	0.011	0.002	0.001	0.011	0.006	0.001	0.005	0.001	0.005	0.001	0.00	0.0	-0.02	0.00	0.10	0.002	0.009
9	0.015	0.004	0.002	0.019	0.012	0.002	0.006	0.001	0.006	0.001	0.00	0.0	-0.01	0.01	0.11	0.009	0.052
11	0.026	0.007	0.004	0.027	0.022	0.005	0.015	0.002	0.012	0.002	0.01	0.0	0.06	0.01	0.11	0.025	0.920
12	0.002	0.000	0.000	0.003	0.002	0.000	0.002	0.000	0.001	0.000	0.00	0.0	-0.01	0.00	0.07	0.000	0.207
13	0.018	0.004	0.003	0.020	0.012	0.003	0.008	0.001	0.006	0.001	0.00	0.0	-0.01	0.00	0.07	0.004	0.085
14	0.017	0.003	0.002	0.016	0.012	0.002	0.007	0.001	0.006	0.001	0.00	0.0	-0.01	0.00	0.08	0.011	0.029
15	0.008	0.003	0.001	0.010	0.006	0.001	0.003	0.001	0.003	0.000	0.00	0.0	-0.01	0.00	0.05	0.002	0.067
18	0.000	0.000	0.000	0.001	0.000	0.000	0.000	0.000	0.000	0.000	0.00	0.0	0.00	0.01	0.05	0.000	0.007
19	0.000	0.000	0.000	0.001	0.000	0.000	0.000	0.000	0.000	0.000	0.00	0.0	-0.01	0.00	0.03	0.000	0.008
20	0.015	0.002	0.002	0.014	0.011	0.003	0.008	0.001	0.007	0.001	0.00	0.0	0.09	0.00	0.18	0.013	0.912
25	0.007	0.002	0.001	0.009	0.007	0.002	0.004	0.001	0.004	0.001	0.00	0.0	-0.01	0.00	0.05	0.000	0.109
28	0.019	0.005	0.003	0.024	0.017	0.003	0.009	0.001	0.008	0.002	0.00	0.0	-0.01	0.00	0.15	0.000	0.006
31	0.003	0.001	0.001	0.004	0.004	0.001	0.002	0.000	0.002	0.000	0.00	0.0	-0.01	0.00	0.05	-0.001	0.013
32	0.002	0.001	0.001	0.004	0.003	0.001	0.003	0.000	0.002	0.000	0.00	0.0	0.01	0.01	0.08	0.000	0.436
33	0.007	0.002	0.002	0.011	0.013	0.003	0.013	0.002	0.013	0.002	0.00	0.0	-0.01	0.00	0.15	-0.001	0.110
34	0.001	0.001	0.000	0.003	0.002	0.000	0.001	0.000	0.000	0.000	0.00	0.0	0.00	0.00	0.04	0.000	0.521
35	0.011	0.003	0.002	0.014	0.012	0.002	0.006	0.001	0.006	0.001	0.00	0.0	-0.01	0.00	0.12	0.000	0.045
36	0.001	0.001	0.001	0.004	0.003	0.001	0.004	0.000	0.003	0.000	0.00	0.0	0.01	0.00	0.03	0.000	0.445
39	0.000	0.000	0.000	0.002	0.001	0.000	0.002	0.000	0.002	0.000	0.00	0.0	0.00	0.00	0.04	0.000	0.273
41	0.011	0.003	0.002	0.013	0.009	0.002	0.006	0.001	0.004	0.001	0.00	0.0	-0.01	0.01	0.03	0.002	0.195
45	0.000	0.001	0.000	0.002	0.001	0.000	0.002	0.000	0.002	0.000	0.00	0.0	-0.01	0.00	0.06	-0.001	0.437
46	0.000	0.000	0.000	0.002	0.001	0.000	0.001	0.000	0.001	0.000	0.00	0.0	0.00	0.00	0.04	0.000	0.407
47	0.000	0.000	0.000	0.000	0.000	0.000	0.000	0.000	0.000	0.000	0.00	0.0	-0.01	0.00	0.07	0.000	0.304
48	0.016	0.004	0.005	0.028	0.018	0.004	0.011	0.002	0.010	0.002	0.01	0.0	0.00	0.01	0.37	0.010	9.413

Major ion concentrations of surface waters analysed by ICP-MS: dry-season water samples

Sample site number		Li µg/l ppb	Be µg/l ppb	B µg/l ppb	Na mg/l ppm	Mg mg/l ppm	Al µg/l ppb	Si µg/l ppb	P mg/l ppm	S mg/l ppm	K mg/l ppm	Ca mg/l ppm	Ti µg/l ppb	V µg/l ppb	Cr µg/l ppb	Mn µg/l ppb	Fe µg/l ppb	Co µg/l ppb
	Detection limit	**<1**	**<0.01**	**<10**	**<0.2**	**<0.01**	**<1**	**<50**	**<0.01**	**<1**	**<0.02**	**<0.3**	**<0.05**	**<0.4**	**<0.05**	**<0.2**	**<1**	**<0.01**
11	River Semliki, Uganda-Congo	9	0.01	27	56.7	24.76	33	8103	0.10	9	42.06	12.1	0.89	5.5	0.27	1.3	20	0.13
12	Kazinga Channel, Uganda	2	0.00	-2	16.9	7.54	13	12614	0.01	2	3.43	14.5	0.91	3.1	0.24	2.3	11	0.13
13	White Nile, Khartoum, Sudan	1	0.00	6	32.6	8.89	52	4441	0.03	1	10.90	10.7	1.76	4.2	0.19	2.6	37	0.10
14	Albert Nile, Uganda	3	0.00	17	34.4	12.77	26	1353	0.04	3	20.98	7.3	0.48	2.6	0.09	0.5	10	0.07
15	Victoria Nile Delta, Uganda	1	0.00	3	11.9	2.68	82	2428	0.01	1	3.75	5.4	3.10	1.0	0.22	1.2	43	0.06
18	Victoria Nile, Bujagali Falls, Uganda	1	0.00	1	9.6	2.48	4	237	0.02	0	3.86	4.9	0.09	0.3	0.04	0.3	6	0.02
19	Outflow from Lake Victoria (Jinja), Uganda	1	0.00	1	9.5	2.46	4	228	0.01	0	4.00	5.0	0.06	0.4	0.05	0.3	5	0.02
20	Lake Albert (south), Uganda-Congo	6	0.00	35	63.2	24.80	13	1353	0.00	6	43.92	9.6	0.34	5.7	0.15	1.1	11	0.18
25	Ribb River, east Lake Tana, Ethiopia	0	0.00	7	33.8	17.36	6	3901	0.05	6	6.99	45.7	0.10	11.1	0.10	187.8	3	0.70
28	Chimba, Gilgel Abay, Ethiopia	0	0.00	-3	6.5	8.36	40	12795	0.00	0	2.47	16.9	0.57	2.9	0.19	1.4	22	0.13
34	Blue Nile, Khartoum, Sudan	0	0.01	9	16.9	10.32	91	6738	0.01	12	2.92	32.8	2.74	8.4	0.16	40.4	79	0.34
35	Tis Issat Falls, Blue Nile, Ethiopia	0	0.00	2	6.5	6.12	108	4409	0.00	2	2.97	15.7	1.19	2.7	0.34	3.3	72	0.10
36	River Atbara, Atbara, Sudan	0	0.00	14	19.2	11.65	10	6024	0.04	6	2.23	31.9	0.11	19.5	0.23	14.2	2	0.12
39	Main Nile, Dongola, Sudan	0	0.00	7	17.9	5.68	15	5413	0.01	1	4.54	18.6	0.42	8.4	0.19	0.4	8	0.06
41	Main Nile, Atbara, Sudan	0	0.00	6	32.3	8.44	32	4750	0.04	2	9.58	14.5	1.30	6.8	0.17	1.0	19	0.07
45	Main Nile, Cairo, Egypt	0	0.00	34	106.3	18.59	16	1314	0.00	34	7.16	31.8	0.10	6.5	0.14	5.1	4	0.06
46	Main Nile, Luxor, Egypt	0	0.00	11	24.5	8.98	10	3041	0.00	7	4.80	25.6	0.05	6.4	0.16	1.4	1	0.03
47	Main Nile (Lake Nasser), Aswan, Egypt	0	0.00	6	15.0	8.03	4	3164	0.00	4	4.55	24.0	0.02	6.6	0.11	0.7	2	0.03
48	Lake Qarun, Faiyum (south-east), Egypt	31	0.00	1964	10068.5	1135.77	1	5838	0.03	3918	264.34	523.1	0.53	3.2	0.16	481.3	3	0.37

Cont.

Sample site number	Ni µg/l ppb <0.1	Cu µg/l ppb <0.4	Zn µg/l ppb <0.5	Ga µg/l ppb <0.03	As µg/l ppb <0.04	Se µg/l ppb <0.1	Rb µg/l ppb <0.01	Sr µg/l ppb <0.1	Y µg/l ppb <0.005	Zr µg/l ppb <0.05	Nb µg/l ppb <0.02	Mo µg/l ppb <0.08	Ag µg/l ppb <0.05	Cd µg/l ppb <0.01	Sn µg/l ppb <0.04	Sb µg/l ppb <0.005	Cs µg/l ppb <0.005	Ba µg/l ppb <0.1	La µg/l ppb <0.002	Ce µg/l ppb <0.002	Pr µg/l ppb <0.002	Nd µg/l ppb <0.04
11	0.9	1.8	2.3	0.00	0.53	0.1	19.62	384.6	0.080	0.27	0.01	2.70	0.01	0.08	0.01	0.046	0.115	61.5	0.079	0.156	0.019	0.07
12	0.9	0.8	2.3	-0.02	0.09	0.0	4.15	254.9	0.017	0.02	0.01	0.18	0.07	0.02	0.02	0.020	0.003	49.7	0.019	0.035	0.004	0.01
13	0.7	1.6	0.6	-0.01	0.34	0.0	5.29	165.8	0.057	0.07	0.01	0.68	0.00	0.00	0.00	0.024	0.006	57.6	0.055	0.106	0.012	0.03
14	0.5	0.4	1.6	-0.01	0.28	0.0	10.94	192.6	0.036	0.01	0.00	1.22	0.05	0.04	0.04	0.039	0.007	54.3	0.027	0.044	0.006	0.03
15	0.8	0.8	4.2	0.00	0.13	0.0	4.21	84.8	0.075	0.05	0.02	0.20	0.01	0.09	0.09	0.038	0.002	38.5	0.119	0.198	0.026	0.10
18	0.3	0.1	1.1	-0.03	0.16	0.0	4.18	81.2	0.003	0.00	0.00	0.21	0.13	0.04	0.01	0.020	0.005	28.6	0.003	0.004	0.001	0.01
19	0.1	0.2	2.6	-0.03	0.15	0.0	4.13	82.7	0.004	0.00	0.00	0.19	0.26	0.02	0.01	0.014	0.005	28.1	0.003	0.005	0.001	0.00
20	1.4	1.5	3.0	-0.01	0.53	0.0	18.78	331.7	0.077	0.08	0.00	2.74	0.01	0.08	0.06	0.059	0.013	92.9	0.068	0.141	0.015	0.06
25	1.7	1.4	1.4	0.01	0.82	0.2	2.19	468.6	0.096	0.04	0.00	4.73	0.00	0.05	0.02	0.135	0.001	106.3	0.017	0.027	0.004	0.01
28	0.9	1.7	2.5	-0.01	0.21	0.1	2.64	99.3	0.042	0.01	0.00	0.31	0.01	0.28	0.02	0.023	0.004	30.3	0.029	0.058	0.007	0.03
34	0.8	1.9	1.1	0.00	0.53	0.1	1.47	200.2	0.120	0.16	0.01	1.08	0.00	0.01	0.00	0.049	0.007	39.4	0.098	0.229	0.025	0.08
35	0.7	1.5	4.8	-0.01	0.20	0.1	1.20	109.2	0.083	0.04	0.00	0.31	0.01	0.21	0.04	0.036	0.002	24.3	0.063	0.133	0.017	0.06
36	0.6	2.1	0.4	0.00	0.95	0.5	0.62	189.5	0.041	0.00	0.00	1.44	0.02	0.01	0.03	0.086	0.001	21.6	0.005	0.009	0.001	-0.02
39	0.7	2.1	1.1	0.00	0.44	0.6	1.44	117.8	0.033	0.02	0.00	0.56	0.02	0.01	0.05	0.044	0.003	19.5	0.018	0.031	0.003	-0.01
41	0.7	2.0	0.7	0.00	0.41	0.0	3.35	157.1	0.046	0.03	0.01	0.70	0.00	0.00	0.01	0.029	0.005	31.2	0.028	0.057	0.007	0.00
45	0.7	1.7	1.8	-0.02	0.51	0.2	2.13	380.2	0.018	0.01	0.00	1.49	0.03	0.01	0.03	0.060	0.001	31.3	0.003	0.004	0.000	-0.02
46	0.4	1.0	0.7	0.02	0.47	0.9	1.40	191.7	0.013	0.00	0.00	1.30	0.00	0.00	0.02	0.074	0.001	29.1	0.002	0.001	-0.001	-0.03
47	0.6	0.8	1.7	-0.02	0.42	0.1	1.35	166.7	0.003	0.00	0.00	1.21	0.01	0.00	0.03	0.047	0.000	28.6	0.001	0.000	0.000	-0.03
48	1.3	1.4	5.9	0.00	7.01	2.7	18.91	15884.4	0.098	0.14	0.01	16.04	0.04	0.11	0.09	0.350	0.014	78.8	0.009	0.007	0.002	-0.04

Cont.

Sample site number	Sm µg/l ppb <0.002	Eu µg/l ppb <0.002	Tb µg/l ppb <0.002	Gd µg/l ppb <0.002	Dy µg/l ppb <0.002	Ho µg/l ppb <0.002	Er µg/l ppb <0.002	Tm µg/l ppb <0.002	Yb µg/l ppb <0.002	Lu µg/l ppb <0.002	Hf µg/l ppb <0.01	Ta µg/l ppb <0.02	W µg/l ppb <0.05	Tl µg/l ppb <0.01	Pb µg/l ppb <0.02	Th µg/l ppb <0.005	U µg/l ppb <0.002
11	0.011	0.003	0.002	0.013	0.009	0.002	0.007	0.001	0.007	0.001	0.01	0.0	0.16	0.01	0.11	0.007	1.073
12	0.002	0.001	0.000	0.003	0.002	0.000	0.001	0.000	0.001	0.000	0.00	0.0	-0.01	0.00	0.09	0.001	0.116
13	0.009	0.002	0.001	0.011	0.008	0.002	0.005	0.001	0.005	0.001	0.00	0.0	0.00	0.00	0.04	0.005	0.279
14	0.004	0.000	0.001	0.005	0.003	0.001	0.003	0.000	0.002	0.000	0.00	0.0	0.03	0.00	0.15	0.001	0.267
15	0.016	0.004	0.002	0.018	0.010	0.002	0.006	0.001	0.004	0.001	0.00	0.0	-0.01	0.01	0.24	0.006	0.009
18	0.001	0.000	0.000	0.001	0.000	0.000	0.000	0.000	0.000	0.000	0.00	0.0	-0.01	0.00	0.07	0.000	0.004
19	0.000	0.000	0.000	0.000	0.000	0.000	0.000	0.000	0.000	0.000	0.00	0.0	-0.01	0.00	0.04	0.000	0.003
20	0.009	0.003	0.002	0.011	0.008	0.002	0.006	0.001	0.007	0.001	0.00	0.0	0.12	0.00	0.15	0.004	0.821
25	0.004	0.001	0.001	0.007	0.007	0.002	0.007	0.001	0.006	0.001	0.00	0.0	0.02	0.01	0.07	0.000	2.761
28	0.006	0.002	0.001	0.008	0.006	0.001	0.004	0.000	0.002	0.001	0.00	0.0	-0.01	0.01	0.11	0.000	0.103
34	0.020	0.005	0.004	0.026	0.020	0.004	0.012	0.002	0.009	0.001	0.01	0.0	-0.01	0.01	0.13	0.003	0.882
35	0.013	0.005	0.002	0.017	0.014	0.003	0.007	0.001	0.005	0.001	0.00	0.0	-0.01	0.01	0.22	0.000	0.083
36	0.002	0.000	0.001	0.003	0.004	0.001	0.002	0.000	0.002	0.000	0.00	0.0	0.03	0.00	0.02	0.000	0.586
39	0.004	0.001	0.001	0.006	0.004	0.001	0.003	0.000	0.002	0.000	0.00	0.0	0.00	0.00	0.04	0.001	0.294
41	0.005	0.001	0.001	0.006	0.005	0.001	0.004	0.001	0.003	0.000	0.00	0.0	0.00	0.01	0.02	0.002	0.364
45	0.000	0.000	0.000	0.002	0.001	0.000	0.002	0.000	0.001	0.000	0.00	0.0	0.00	0.00	0.12	0.000	0.614
46	0.000	0.000	0.000	0.004	0.001	0.000	0.001	0.000	0.000	0.000	0.00	0.0	0.00	0.00	0.06	0.000	0.424
47	0.000	0.000	0.000	0.000	0.000	0.000	0.000	0.000	0.001	0.000	0.00	0.0	0.00	0.00	0.14	0.000	0.398
48	0.010	0.001	0.002	0.011	0.009	0.002	0.007	0.002	0.008	0.002	0.01	0.0	-0.01	0.01	1.29	0.003	10.767

Appendix II.

Full equipment list and laboratory consumables for chromatographic separation of Si.

Stand/carousel to hold 10ml disposable Bio-Rad® Bio-Spin chromatography columns
10ml disposable Bio-Rad® Bio-Spin chromatography columns
Bio-Rad® cation-exchange resin 50W-X12 (200–400 mesh) in H+ form
Savillex® collection vials and lids
Teflon® waste collection beakers
Pipette tips
Pipettors (various; 1-5ml, 100-1000µL, 40-200µL)
pH papers
250ml squeezy HDPE bottles with caps for acid/reagent solutions
30ml squeezy HDPE bottle with cap
2-3 1L HDPE containers for cleaning pipettes
Hotplate
Millipore Milli-Q® Integral water purification system
Person protection equipment
Class 100 clean lab and fume hoods

Acids/Reagents
Romil-UpA™ HCl, HNO3, HF
Romil-SpA™ HCl

Appendix III.

Full procedure for chromatographic separation of Si

Column chemistry for Si isotopes

Use ultra-pure acids (i.e. double-distilled, UpA).

Cleaning 1.8ml of Bio-rad AG 50W-X12 resin in 10ml Bio-rad columns (individual columns)

Rinse resin over several days with MQ-e to remove fines. Shake resin in water and allow to settle, decant off supernatant (20-30 washes). Transfer resin into 1.5 M HCl solution to squeeze into columns. Shake resin in HCl solution before use to make sure that resin is in liquid form in order to squirt directly into resin reservoir without air bubbles forming in the column.

Volume	Concentration	Chemical
3 ml	3 M	HCl
3 ml	6 M	HCl
3 ml	7 M	HNO_3
3 ml	10 M	HCl
3 ml	6 M	HCl
3 ml	3 M	HCl
Fill		MQ-e
3 ml		MQ-e

Check pH of column with the last drop of MQ-e coming off the resin. pH should be neutral (4-7).

Chemicals required for cleaning a batch of 16 columns:

~100 ml 3 M HCl (UpA)

~100 ml 6 M HCl (UpA)

~50 ml conc. HCl (UpA)

~ 50 ml 7 M HNO_3 (UpA)

Appendix III

Column Chemistry

Do not allow the column to dry-out at anytime; channels may form in the resin and allow cations to move through the column into the collection beaker.
Final concentration of 0.75, 1.5 or 3 ppm

	Volume (ml)	Molarity	Chemical	Collect	Notes
Load					
	X	-	Sample	Yes	
Wash in					
	1	-	MQ-e	Yes	
Elute	1	-	MQ-e	Yes	
	1	-	MQ-e	Yes	

Samples

Final concentration of 0.75, 1.5 or 3 ppm

Column #	Sample	Si Conc. (ppm)	Load (ml)	Steps (ml)	Additional ml's required (directly into beaker)	Final total volume (ml)
1	Blank (1)	-	0	1 + 1 + 1	0	3
2	Blank (2)	-	0	1 + 1 + 1	0	3
3	NBS-28 (1)	13	1	**1** + 1 + 1 + 1	0.33	4.33
4	NBS-28 (2)	13	1	**1** + 1 + 1 + 1	0.33	4.33
5						
6						
7						
8						
9						
10						
11						
12						
13						
14						
15						
16						

Include two standards (NBS-28) and two blanks ((MQ-e) in a batch of 16.

Appendix III

Dilution calculations for sample load onto chromatography columns

The known initial Si concentration is inputted into the spreadsheet in column B with the final required Si concentration selected in column D (preferably 3ppm). The elution amount is fixed at 3ml (column C). The sample load (column A) depends on columns B and D and is determined using the formulas in columns E-H. Dilution factor (column F) cannot be <1 and the addition of Milli-Q water cannot be negative (column G). Once these criteria are met, the green text (in this case row 5 (sample load = 3ml)) highlight the minimum sample load required to obtain a final solution of 3ppm Si, and the corresponding final dilution required (column G).

	A	B	C	D	E	F	G	H
1	Sample load (ml)	Initial Si conc. (ppm)	Elution with Milli-Q water (ml)	Final required Si conc. (3, 1.5 or 0.75ppm)	Conc. after column chemistry (ppm)	Dilution factor	Additional mls required of Milli-Q water	Final volume (ml)
2								
3	1	6	3	3	=(B3*A3)/(C3+A3)	=(E3/D3)	=((C3+A3)*F3)-(C3+A3)	=G3+C3+A3
4	2	6	3	3	=(B4*A4)/(C4+A4)	=(E4/D4)	=((C4+A4)*F4)-(C4+A4)	=G4+C4+A4
5	3	6	3	3	=(B5*A5)/(C5+A5)	=(E5/D5)	=((C5+A5)*F5)-(C5+A5)	=G5+C5+A5
6	4	6	3	3	=(B6*A6)/(C6+A6)	=(E6/D6)	=((C6+A6)*F6)-(C6+A6)	=G6+C6+A6
7	5	6	3	3	=(B7*A7)/(C7+A7)	=(E7/D7)	=((C7+A7)*F7)-(C7+A7)	=G7+C7+A7
8	6	6	3	3	=(B8*A8)/(C8+A8)	=(E8/D8)	=((C8+A8)*F8)-(C8+A8)	=G8+C8+A8
9	7	6	3	3	=(B9*A9)/(C9+A9)	=(E9/D9)	=((C9+A9)*F9)-(C9+A9)	=G9+C9+A9
10	8	6	3	3	=(B10*A10)/(C10+A10)	=(E10/D10)	=((C10+A10)*F10)-(C10+A10)	=G10+C10+A10
11	9	6	3	3	=(B11*A11)/(C11+A11)	=(E11/D11)	=((C11+A11)*F11)-(C11+A11)	=G11+C11+A11
12	10	6	3	3	=(B12*A12)/(C12+A12)	=(E12/D12)	=((C12+A12)*F12)-(C12+A12)	=G12+C12+A12
13	11	6	3	3	=(B13*A13)/(C13+A13)	=(E13/D13)	=((C13+A13)*F13)-(C13+A13)	=G13+C13+A13
14	12	6	3	3	=(B14*A14)/(C14+A14)	=(E14/D14)	=((C14+A14)*F14)-(C14+A14)	=G14+C14+A14
15	20	6	3	3	=(B15*A15)/(C15+A15)	=(E15/D15)	=((C15+A15)*F15)-(C15+A15)	=G15+C15+A15

Appendix IV.

Detailed method for purifying diatoms from lake sediments

Add samples to conical flasks for the first two steps. In this case, 500ml flasks were used to accommodate the large amounts of initial material (5-10g). Some samples were split over two flasks.

Wear personal protective equipment at all times (lab coat, goggles, gloves etc).

Essential steps towards diatom purification:

Removal of carbonates

1. Gradually add 10% HCl to the wetted sample. On average samples required about 150ml of solution per flask. Carbonate-rich samples may need more reagent/time to react. Once reaction has subsided add flasks to 75℃ water bath for 2 hours until reaction is complete.
2. Keep swirling and washing sides down with 10% HCl every 30-45 minutes whilst in the water bath to expose sample surface area to acid.
3. Once reaction is finished, top up conical flask with ~500ml deionised H_2O and allow to settle overnight.
4. Decant supernatant and top up with ~500ml deionised H_2O and allow to settle overnight.
5. Decant supernatant and top up with ~500ml deionised H_2O and allow to settle overnight.
6. Decant supernatant to a minimum.

1000ml 10% HCl solution: add 100ml of analytical grade HCl to 900ml deionised H_2O.

Removal of organics

1. Slowly add ~100ml conc. H_2O_2 to each flask to cover sediment, leave for ~45 minutes to allow initial reaction to subside before putting into a water bath at 80℃.
2. Swirl flasks every 45 minutes to agitate sediment.
3. Once reaction has slowed (2-3 hours), add a further 100ml conc. H_2O_2.
4. If after a day in the water bath (~ 8 hours), the reaction is still going, top samples up with deionised H_2O and leave overnight.
5. Decant supernatant and begin again with conc. H_2O_2 (repeat steps 1-4).
6. Decant supernatant and top up with ~500ml deionised H_2O and allow to settle overnight.
7. Decant supernatant and top up with ~500ml deionised H_2O and allow to settle overnight.
8. Decant supernatant to a minimum.

N.B. Some samples had cloudy supernatant even after settling overnight. Supernatants were checked under the microscope before decanting to make sure there were no diatoms.

9. Add ~100ml conc. HNO_3 to each flask. Most organic matter will have been removed by H_2O_2 so only a small reaction should occur.
10. Place flasks in a water bath at 75℃ for 2 hour s until reaction has ended. Swirling flasks every ~45 minutes and washing sides down with HNO_3.
11. Top up flask with ~500ml deionised H_2O and allow to settle overnight.
12. Decant supernatant and top up with ~500ml deionised H_2O and allow to settle overnight.
13. Decant supernatant and top up with ~500ml deionised H_2O and allow to settle overnight.
14. Decant supernatant to a minimum.

Sieving at 63, 38 and 20 µm

1. Sit a 100mm diameter stainless steel/brass 63 µm sieve on top of a 1 litre Pyrex beaker and sieve sample with deionised H_2O from a wash bottle. Depending on remaining sample size after removal of organics and carbonates, several litre beakers may be required and will need to settle overnight. Set aside >63 µm fraction.
2. Similarly, sit a 100mm diatom stainless steel/brass 38 µm sieve on top of a 1 litre Pyrex beaker and sieve <63 µm fraction with deionised H_2O from a wash bottle. Allow <38 µm fraction to settle overnight and set aside >38 µm fraction.
3. Again, sit 100mm diameter stainless steel/brass 20 µm sieve on top of a 1 litre Pyrex beaker and sieve <38 µm fraction with deionised H_2O from a wash bottle. Allow <20 µm fraction to settle overnight and set aside >20 µm fraction.
4. After sieving, there should be a >63, 38-63, 20-38 and <20 µm fraction for each sample. Keep samples wet at all times.

Occasionally 125 µm stainless steel/brass sieves and 10 µm mesh fabric were used for certain samples to enable further separation from contaminants.

Optional additional purification steps:
If removal of organics and carbonates, followed by sieving does not successfully purify diatoms, further steps may be required to achieve this.

Differential settling
Suitable for separating silt/clay minerals from diatoms.

1. Using a small (~50ml) plastic container with screw lid, add chosen size fraction to container and add deionised H_2O. Screw lid tightly and gentle shake/tilt container back and forth to mixed sample. Allow to stand for 10-20 seconds and decant diatoms (supernatant). Repeat several more times until most diatoms have been decanted. The residue that sinks to the bottom is the contaminant.

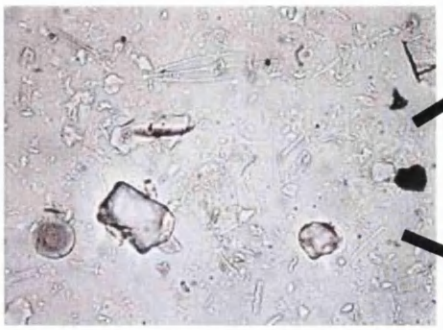

Remaining composition of a sample after removal of organics and carbonates.

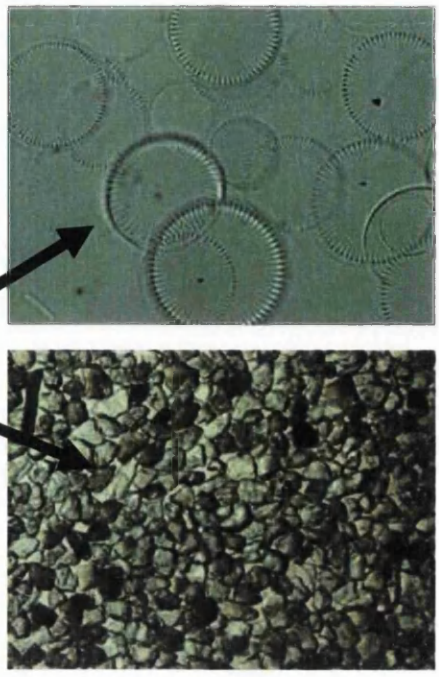

After sieving and using differential settling, diatoms (top) and mineral grain components (bottom) were

Heavy liquid separation (SPT)

Suitable for separating components which have distinct specific gravities (e.g. diatoms and mineral grains). A series of steps which gradually lower the specific gravity of a solution in very small increments allows various components to sink whilst diatoms float.

Methodology adapted from Snelling and Swann (2009) *Sample preparation of Antarctic Marine diatoms for isotope analysis.* NIGL, BGS, Keyworth.

Equipment

Test-tubes (10-15 ml) made of polystyrene **not** polypropylene
Pipette Pasteur (3 ml)
Pipette (1 ml)
Variable volume pipettors 1-5ml and 100-1000µL
Sodium polytungstate (SPT) (available from Sometu-Europa http://www.sometu.de/)
Cellulose nitrate membrane filters (1 µm and 0.45 µm sized filters are necessary for SPT recycling)

Sample preparation

1. Place sample in test tubes and label as "A".
2. Syphon off solution, leaving sediment only.

SPT: 1st separation

3. Make up heavy liquid solution using Sodium Polytungstate (SPT) powder to achieve a specific gravity of 2.25-2.3 (Diatom s.g. is approx. 2.1).
4. Ensure SPT powder is fully dissolved, solution should be transparent.
5. Add 4 ml of SPT to samples and shake to combine.
6. Centrifuge samples at 2500 rpm for 20 minutes.

7. Label a second set of tubes with the sample number followed by 'B'.
8. The diatoms should be concentrated at the top of the liquid.
9. Add a small amount of water and use a 3 ml pipette to mix the diatom float to break up any lumps.
10. Pipette off the float taking some of the SPT and water and add to tube 'B'.
11. Add a little more water and pipette off the remaining liquid to the top of the residue.
12. Add a further 4 ml of SPT to the residue tube, shake and centrifuge for 20 mins at 2500 rpm.
13. Remove any evident diatoms following stages 9-11 and add to 'B'.

Stages 12-13 may not be necessary.

Check to see if any diatoms are "floated". If none, this stage is not necessary.

Making new SPT: Dissolve SPT granules in deionised H_2O according to packet instructions. Using a magnetic stirrer make sure all SPT is dissolved. Density can be increased by putting on a hotplate (<105℃) and all ow to evaporate, stirring continuously. Allow to stabilise at room temperature and use a hydrometer to measure the density (a measuring cylinder is suitable for the height required to accommodate hydrometer). Once desired specific gravity is achieve, it is ready for use. Long term storage should not be in glassware.

SPT: 1st clean-up

14. Add 5 mls of water to residue test tube "A", shake and centrifuge for 5 mins at 1500 rpm.
15. Syphon liquid into the SPT waste beaker.
16. Add 10 mls water to residue ("A"), shake, centrifuge for 5 mins at 1500 rpm.
17. Syphon liquid down sink and archive "A".
18. Top the test tube "B" up with water to c. 12 ml and shake.
19. Centrifuge for 5 mins at 1500 rpm.
20. Diatoms should sink to bottom. Syphon liquid into SPT waste beaker.

SPT: 2nd separation

21. Add 4 ml of SPT to "B" and 0.15 ml of water. Shake until sample mixed.
22. Centrifuge for 20 mins at 2500 rpm.
23. Label a set of tubes as "C".
24. Collect diatoms as directed at 8-11 but into tube 'C'.
25. Repeat steps 14-17 for residue "B".
26. Repeat steps 18-20 for "C".

SPT: 3rd separation

27. Repeat steps 21-25 but add 0.3 ml of water to SPT, Residue will be in test tube "C" and diatoms in test tube "D".
28. After 3rd SPT, add water to "D" to c. 10 ml. Centrifuge for 5 mins at 1500 rpm.
29. Syphon solution water into SPT waste beaker.
30. Repeat step 28-29.

31. Repeat step 28 with solution going into sink.

Several more SPT clean-up stages with SPT may be required by adding increasing increments of water to slowly decrease the specific gravity.

SPT recycling

1. Sieve SPT from waste beaker through 1 µm cellulose nitrate membrane filter paper into a clean beaker.
2. Repeat Step 1 using 0.45 µm filter.
3. Place SPT solution on a hotplate (max temperature should be 105℃), continuously stirring. Once volume has been reduced to at least 2.3 g/ml, SPT can be reused.

Sonication

In some samples, mineral aggregates existed, preventing them from being sieved through the appropriate sieve fraction. To break up the mineral aggregates but not damaging the diatoms, it was found that short repeated exposures in a sonication bath broke up the aggregates and through re-sieving, mineral grains could be isolated from the diatoms.

1. Put sample in a ~50 ml plastic container with a sealed lid and add ~30ml deionised H_2O.
2. Put sample container in ultrasonic bath with container lid above waterline (to avoid any infiltration or sample loss). Switch on for 10 seconds. Repeat this 10-20 times. Depending on diatom fragility this may need to be reduced.
3. After sonication, sieve sample again at the appropriate size fractions.

Additional treatments of HNO_3/H_2O_2

Samples with resistant organic matter may require additional treatments of HNO_3 or H_2O_2. Return sample to conical flask and repeat treatment with the above removal of organics procedure.

SPLITT

Some samples underwent split-flow thin fractionation (SPLITT) which uses gravity to separate two components based on their specific gravity and hydrodynamic properties through laminar flow (Rings et al., 2004). Simply, samples are transported in deionised water through a narrow channel under a constant flow rate and particles are split towards two outlets. A detailed methodology can be found in Rings et al. (2004). Analysis was carried out at the Environment Centre at Lancaster University. For samples in the 20-38 µm and 38-63 µm range inlet flows of 8-10 ml/min were used for samples and 12-15 ml/min for deionised water.

Appendix V.

Diatom slide preparation

Permanent slides were made of the final purified diatom samples sent for isotope analysis. The following method is adapted from: http://www.geog.ucl.ac.uk/about-the-department/support-services/laboratory/laboratory-methods/lake-sediment-analysis/diatom-slide-preparation

Diatom slides are usually made up by allowing the diatom suspension to settle out on a cover slip overnight, as described below. This produces an even spread of diatoms over the cover slip but it can take up to two days.

Equipment
Hotplate
Round glass coverslips 19mm diameter
Glass slides
3 ml pipettes for each sample
Naphrax diatom mountant
Rigid metal tray
Deionised water

Procedure

1. Dilute the cleaned diatom suspension to a suitable concentration. The suspension should nearly be totally clear. Fine particles in suspension should be just visible when the suspension is held up to the light.
2. Place coverslips on a metal tray in a position where they will not be disturbed, away from dust sources and air currents.
3. Using a 3 ml pipette, place up to 0.5ml of well mixed diatom suspension on each coverslip, cover the tray to keep off dust and leave to dry. This may take up to two days.
4. Once coverslips are dry, heat a hotplate in a fume cupboard to 130°C.
5. Place 1 drop of Naphrax on a glass slide and invert the cover slip with the dried diatoms over the drop.
6. Heat the slide on the hotplate for 15-20 minutes to drive off the toluene in the Naphrax.
7. Allow the slide to cool and then check that the cover slip does not move when pushed with a fingernail. If it does move then the slide will need to be heated a little longer.

Appendix VI.

Lipid extraction from lake sediments

Sample preparation

Weigh a known amount (~1g) of freeze-dried sediment and mix with general purpose grade sand and sandwich within the ASE cell by filters (cellulose filters, 19.8 mm) at each end.

Lipid extraction

The total lipid fraction was extracted using a Dionex accelerated solvent extractor (ASE 200) using the following methodology:

Pressure	1500 psi
Heat	5 minutes
Temperature	100
Static	20 minutes
Flush	60%
Purge	60 seconds
Cycle	1
Solvent A (dichloromethane)	90%
Solvent B (methanol)	10%

Extract clean-up

1. Label a round-bottom glass flask (rbf) with sample number and decant total lipid extract, extracted by the ASE, into the rbf.
2. Reduce the volume of dichloromethane (DCM)/MeOH extract using a rotary evaporator (~170-200 mBar, water bath ~40°C).
3. Transfer the reduced extract to a pre-weighed 3.5ml glass vial with DCM and rinse rbf repeatedly with DCM until all extract has been transferred to the vial.
4. Take to dryness at ~60℃ under a gentle stream o f nitrogen gas, and re-weigh vial to determine amount of residue (total extract).

Separation of Neutral and Acid fractions (Ficken et al., 1998)

1. Re-dissolve residue in 1ml (DCM)/isopropanol (2:1 v/v).
2. Label and weigh two 7ml vials with "Neutrals" and "Acids".
3. Wash a 3ml aminopropyl (HN_2) Bond Elut® 500mg column with DCM twice and discard solvent. Do not allow the column to dry-out.
4. Wash column with DCM/isopropanol (2:1 v/v) once and discard solvent, again do not allow to dry-out.
5. Place empty neutral vial under column once wash stage has completed.
6. Add total extract onto column, washing out 3.5ml vial with additional DCM / isopropanol (2:1 v/v) and allow to penetrate column, but ensuring column does not dry-out.
7. Elute neutral fraction with ~6ml of DCM/isopropanol (2:1 v/v).

8. After last drop of neutral fraction, set aside neutral vial and replace with acid vial.
9. Elute the acid fraction with ~6ml of freshly made 2% acetic acid in ether, once again ensuring column does not dry out. Squeeze last drop of acid fraction using pipettor.
10. Dry both neutral and acid fractions at ~60℃ un der a gentle stream of nitrogen gas, and re-weigh vials to determine amount of neutral versus acid fraction.

Acid methylation

1. Add 50ml methanol (CH_3OH) to a large (>150ml) rbf and slowly pipette a couple of drops of Acetyl Chloride (CH_3COCl) into the flask, swirling after every few drops. Add a total of 2.5ml CH_3COCl to make 5% CH_3COCl.
2. Add ~100µL Toluene to the acid fraction in the 7ml vial.
3. Add 1.5ml 5% CH_3COCl to the acid fraction and leave at 60°C overnight with the cap loosely fitted.
4. Remove from the hotplate and add ~1-2ml hexane/ether (5:1 v/v) to the 7ml vial.
5. Add ~1ml 0.1N KCl/CH_2Cl_2 to vial.
6. Srew lid to vial and shake vigorously and leave to seperate
7. Transfer top part (organic fraction) into a 3.5ml vial.
8. Add ~1-2ml hexane/ether (5:1 v/v) to the 7ml vial again and repeat steps 7-8.
9. Repeat steps 7-9.
10. Repeat steps 7-8.
11. Dry sample at ~60℃ under a gentle stream of ni trogen gas.

Neutral fraction separation (hydrocarbons and polars)

1. Weigh two 7ml vials and label one "alkanes" (hydrocarbons) and one "polar".
2. Clamp glass columns (~15ml) and create a pad at the base of the column were extracted cotton wool about 2cm thick.
3. On top of the cotton wool add a 3cm-thick layer of freshly activated alumina (aluminium oxide). Alumina kept dry in a drying oven.
4. Add a few drops of DCM to the neutral fraction residue in the 3.5ml vial to re-dissolve and add a small amount of alumina to absorb the DCM and neutral fraction.
5. Place "alkanes" 7ml vial beneath the column.
6. Pour the neutral fraction onto the column and add hexane/DCM (9:1 v/v) solution to column until 7ml vial is filled.
7. Once the alkanes vial is filled, replace with the "polar" vial and add methanol/DCM (1:1 v/v) to the column until all solution has drained through column and the vial filled.
8. Dry sample vials at ~60℃ under a gentle stream of nitrogen gas.
9. Weigh both alkanes and polar vials.

Appendix VI

De-sulphurisation

1. In a beaker, add HCl to copper turnings to clean.
2. Rinse well with deionised H_2O, twice.
3. Rinse with methanol 2-3 times and decant.
4. Rinse with DCM 2-3 times and decant and allow to dry by shaking turnings. Copper should be bright and shiny and stored in an air tight jar until use.
5. Add a small amount of DCM to "alkanes" vials and add a small amount of the activated copper to absorb sulphur. Continue adding more copper until it no longer turns dull/black.
6. Leave overnight.

Urea adduction of the n-alkane fraction

1. In a solution bottle, make a saturated solution of urea in methanol by adding urea crystals to methanol until no more dissolves and a layer of urea remains at the bottom, and set aside.
2. Add 1-2ml DCM to the copper turnings in the alkanes vial to pipette-off sample and put into a 15ml glass centrifuge tube, repeat twice.
3. Add 50% of the volume of DCM of acetone to the tube and shake.
4. Add 1ml of saturated solution of urea in methanol and continue to shake.
5. Evaporate solvent under a stream of nitrogen gas without heating.
6. Extract the non-adducted hydrocarbons by adding 10ml hexane to the mixture.
7. Sonicate for 30 seconds and centrifuge for 10 minutes at 1500 rpm.
8. Once centrifuged, pipette off the solvent without disturbing the urea crystals into a rbf.
9. Add another 10ml hexane to the centrifuge tube and repeat steps 7-8 a further two times.
10. Reduce solvent (~30ml) by rotary evaporation.
11. Transfer the non-adduct fraction in hexane (4 x 2ml) to a glass centrifuge tube.
12. Repeat the adduction procedure again on the non-adduct fraction.
13. Filter the hexane washings through a small plug of cotton wool in a pipette and collect in vial labelled "N-A".
14. To remove the adducted hydrocarbons (*n*-alkanes) from the urea crystals, dissolve both urea plugs (from initial adduction process and that from the repeat) in deionised water (10ml) and combine.
15. Extract the solution with hexane (2 x 10ml).
16. Evaporate the combined hexane extracts and take to dryness under a stream of nitrogen in "AD" labelled vials.

Standard solution (n-C_{36} alkane)

1. Add 25mg of hexatriacontane to 100ml hexane to form a standard solution.
2. Add a known amount of standard solution (typically 100 µL) to each fraction prior to analysis by GC-MS by syringing into vials and transferring to mass spectrometer vials.

Appendix VII.

Purified diatom samples from Lake Victoria analysed for O- and Si-isotope analysis (n = 10)

Depth range (cm)	Average depth (cm)	Age range (cal. yr. BP)	Average age (cal. yr. BP)	Size fraction (µm)	$\delta^{18}O_{diatom}$ (‰)	Average $\delta^{18}O_{diatom}$ (‰)	$\delta^{29}Si_{diatom}$ (‰)	Average $\delta^{29}Si_{diatom}$ (‰)	$\delta^{30}Si_{diatom}$ (‰)	Average $\delta^{30}Si_{diatom}$ (‰)
5.0-10.0	7.5	1336-1441	1388	20-38	+40.6	+40.6	+0.61	+0.61	+1.26	+1.26
84.0-89.5	86.8	2999-3115	3057	20-63	+42.4	+42.4	+0.56	+0.56	+1.10	+1.10
198.5-203.0	200.8	5409-5487	5448	20-38	+41.7	+41.7	+0.40	+0.40	+0.78	+0.78
335.5-339.5	337.5	7973-8067	8020	20-38	+40.7	+40.7	+0.37	+0.37	+0.78	+0.78
350.0-354.0	352.0	8314-8408	8361	20-38	+40.1	+40.1	+0.48	+0.48	+0.94	+0.94
441.5-445.5	443.5	10601-10709	10655	20-38	+39.4	+39.4	+0.30	+0.30	+0.62	+0.62
478.5-482.0	480.3	11601-11696	11648	20-38	+44.0	+44.0	+0.43	+0.43	+0.93	+0.93
517.5-523.0	520.3	12655-12804	12730	20-38	+40.5	+40.5	+0.52	+0.52	+1.04	+1.04
610.0-614.5	612.3	14876-14968	14922	<20	+43.7	+43.5	+0.59	+0.59	+1.24	+1.23
610.0-614.6	612.3	14876-14969	14922	<20	+43.3		+0.60		+1.21	

Appendix VIII.

Lipid data: raw *n*-alkane data for Lake Victoria

					Peak area of n-alkane compounds							
Sample ID	Age (cal. yr. BP)	Weight of sediment extracted (g)	Amount of standard added (µg)	Area of standard	C16	C17	C18	C19	C20	C21	C22	C23
LV1	1388	0.8216	24.8	164033735	17288830	30610336	43209606	49002067	53149936	56772798	48175043	66227580
LV2	1720	1.237	24.8	160344413	0	0	5351232	10921621	15994022	22426312	21853670	50255111
LV3	2162	1.003	24.8	113039847	0	0	321925	1827035	4369454	8293952	8494818	22497282
LV4	2757	0.904	24.8	128975801	0	0	3320767	4843197	7990775	10683295	10618822	19025902
LV5	3057	0.4513	24.8	138981508	0	0	2180785	1847424	3052603	4488523	4715105	10387283
LV6	3772	0.6983	24.8	157854334	0	0	3171769	3963001	6586144	7672259	7993938	17909013
LV7	4220	0.8438	24.8	172140984	0	0	5418858	7925664	10092170	12175717	11397402	21141418
LV8	4615	0.9377	24.8	132206537	0	3072491	5842253	6615698	7416482	8871623	8474180	19277508
LV9	4993	1.0763	24.8	125940155	0	0	3966141	7337775	11681264	14543630	13783167	23623228
LV10	5448	0.4577	24.8	119980040	0	0	2792912	2121284	3449462	4403718	4112696	9568484
LV11	5843	0.9397	24.8	143965555	0	0	4485925	6052140	7707571	10439567	10698556	24156397
LV12	6141	0.9223	24.8	149547499	0	0	890376	2415046	4795958	7725143	8674215	22762095
LV13	6564	1.0961	24.8	115614619	0	0	8348623	9428530	14153060	16459954	15914950	27348992
LV14	6893	0.9868	24.8	168046383	0	0	5798956	9460627	11731691	14824409	14500401	30284214
LV15	7537	1.4181	24.8	142558337	0	0	3272306	5202624	6312768	10217854	9950909	26852032
LV16	8020	0.4273	24.8	70977013	0	0	682626	1166891	1458574	2396966	3247705	9347461
LV17	8361	0.8692	24.8	141383164	0	0	4601706	4402226	5550052	7338982	7678383	18242931
LV18	9112	0.8737	24.8	143298366	0	0	1064590	2786906	5716073	8671567	9037162	17539942
LV19	9743	1.0008	24.8	129014395	0	0	2302684	3245178	4379839	6608805	6694286	16172224
LV20	10263	1.0609	24.8	152291801	0	3538965	6271343	7673711	8991244	10648470	10795014	19644023
LV21	10655	1.0297	24.8	133331423	0	0	4754199	7297034	11449126	12661937	12376564	16361032
LV22	11648	0.6299	24.8	11009937	0	0	309439	824980	1290924	2928493	3492423	8155814
LV23	12209	1.1274	24.8	159951390	0	0	3948585	6195118	7824771	11604512	10133036	20050530
LV24	12730	1.0651	24.8	133011104	0	0	4057632	4911836	7211857	10792369	10713173	21770173
LV25	13284	1.3284	24.8	131527664	0	0	5493273	7734360	9898357	11497013	10326970	17605054
LV26	14068	0.8402	24.8	134366313	0	0	4725252	4578397	8794525	18881791	12080198	26014373
LV27	14922	1.1417	24.8	148041163	0	4399678	5222978	6443818	10492455	12860385	12002125	15402867
LV28	15748	4.4842	24.8	46250854	0	0	156319	518228	1465231	3336266	7615993	23201973
LV29	16157	4.8677	24.8	112670386	0	0	0	1200680	3669985	5474716	7950512	16619776
LV30	16753	3.2153	24.8	128587922	0	4200378	9076401	10524876	15361271	18298034	18253982	27519894
LV31	17657	4.0557	24.8	135230069	0	0	684186	4477350	2457899	3234029	5466507	11576635
LV32	18070	4.1436	24.8	151917333	0	0	438812	543047	2439885	3746783	6789586	13589818
LV33	18468	4.5549	24.8	88666909	0	0	0	214210	963828	1491230	3080921	6942768
LV34	19080	3.9111	24.8	145173957	0	0	2075528	1893709	6442809	10436846	10428514	21086022
LV35	19509	4.32	24.8	146177337	0	0	0	1801058	4721540	6319352	10753504	18409389
LV36	19815	1.8461	24.8	133645012	0	0	0	237753	941212	1722489	3301911	6855152
LV37	20350	2.166	24.8	136012345	0	0	3872360	1900838	9475409	9990678	10208462	18554600
LV38	20728	2.6767	24.8	124254986	0	0	0	1272773	3329407	3012815	4680424	9505852

Cont.

Sample ID	Age (cal. yr. BP)	Peak area of n-alkane compounds											
		C24	C25	C26	C27	C28	C29	C30	C31	C32	C33	C34	C35
LV1	1388	47183065	90051342	42689013	88815792	22061682	40269545	11235407	28601156	3625997	12066238	1298027	2555152
LV2	1720	43103677	110889997	64338125	147336012	62188171	95856301	37206134	46224674	13823016	18255097	4642116	4255104
LV3	2162	18173430	61571295	22631328	69009643	11754503	26567944	5890695	13334168	1361484	4136352	257223	605934
LV4	2757	17000642	55279804	20456632	58254179	12558870	31556466	5138143	12233764	904796	3859260	331629	584891
LV5	3057	11448232	31525801	16400466	37228591	13401334	21838588	7892766	9904435	2581278	3028200	924452	498574
LV6	3772	19969269	58251724	25098905	67457424	15711903	41685983	9216461	18599015	2606971	6615891	774494	1478356
LV7	4220	21863675	69044959	27683462	83388888	16437123	39798558	9996971	24715844	2702968	9463818	631211	2129782
LV8	4615	20335151	66739285	26633209	79387899	16333343	36798047	9880347	21833088	2678817	7876781	658338	1520360
LV9	4993	21169707	68093239	25885086	79854943	16001857	43085731	6520389	16402743	1387595	4924905	316277	666175
LV10	5448	9123066	31019573	12104549	33033418	8693058	18955945	3931747	7421141	1141585	2307355	262533	409023
LV11	5843	23305875	81399548	31748608	92493492	25447341	51904418	12583092	19758956	3295170	5685417	900450	1139842
LV12	6141	23797983	85147912	31225436	103568717	18473159	60252579	11304124	26701761	2569833	9018069	545030	1572029
LV13	6564	21329426	78845680	25800524	81113080	13758884	42780374	6661081	16249673	1295451	4601415	283695	674061
LV14	6893	30237540	98499139	36796528	114768916	27459146	71113526	13483153	35423909	3797396	13578920	1069510	2893449
LV15	7537	24924006	99440833	34430500	104060915	21308120	61428494	12460356	25269099	2999854	7825650	789201	1412821
LV16	8020	13704148	32686343	15989973	37284711	12629108	27307345	6627780	15950963	2275087	5423787	671395	1075828
LV17	8361	20813473	65618444	30751774	80809754	27562671	52406881	16100119	25552203	5179736	8730981	1673633	1957982
LV18	9112	17028776	62202824	23243708	69918023	16539842	44520710	8374891	22771907	2157428	7687172	466170	1233239
LV19	9743	18500242	57098311	24779136	71325190	19660357	52967941	9336753	30579101	2804177	11639635	685812	1804393
LV20	10263	21357250	64223395	27219098	85043826	30289844	72880194	15035837	51291625	4572325	19667227	977714	3402054
LV21	10655	14798978	41846086	17063498	50377208	13519959	38955860	7505031	27131482	2337082	9800883	628385	1462709
LV22	11648	12075871	21334657	19525094	27623584	19790402	23214629	12044756	14077861	4382510	4441011	1511727	687805
LV23	12209	17802905	53276168	27656907	66145103	25875089	49640957	16102779	28722550	5677094	9767481	1837288	1813674
LV24	12730	27227634	60821979	50485606	92167555	59524078	87635690	42163933	59554395	18815543	23845412	6610747	6062133
LV25	13284	17238828	37714532	18455510	44874635	9581485	26249610	6102642	25679362	2297789	9284022	662838	1554013
LV26	14068	32507656	55364092	61672506	92255980	71014792	81865868	49527587	52628115	22472195	20637699	7852826	5262589
LV27	14922	12128546	20028841	8839430	18964325	6670616	10910550	3344523	7950721	1549351	2960087	329863	500196
LV28	15748	35263246	59201776	49072682	73874938	46928302	52971987	29523085	34019484	11925696	15278006	4192919	3622821
LV29	16157	15398111	33248400	20806536	43627062	19761975	27262896	12645325	20795713	4897330	9421789	1646028	2099641
LV30	16753	23793911	46428815	24920762	54012083	16111993	32222989	9096024	22270059	4164177	10580595	1496775	2406656
LV31	17657	9147022	20558675	9001060	25361687	4555902	9286345	2069405	10071151	871137	5374421	338789	1118135
LV32	18070	12132094	26877595	12934439	29706954	8580345	14401998	4876107	13733568	1819866	7642529	673247	1731614
LV33	18468	6650657	13866532	9524353	16929899	8893683	9745185	5118945	6253639	2005760	2448815	627944	544894
LV34	19080	23975886	43682936	41238454	63508216	43570227	48214417	30686181	30730451	12392305	13197759	4431520	3528465
LV35	19509	14638025	30623859	16064904	37208824	12194891	18256169	7258864	16426954	3307220	9697057	1061924	2276021
LV36	19815	6820376	14714068	8594475	19173504	6930243	10914164	3982857	9486479	1562230	5349955	612177	1083717
LV37	20350	19945490	38678132	38696104	63973266	44969745	53080910	31424304	35794513	12742572	17079956	4511947	4451753
LV38	20728	9987376	19733536	12965681	28688530	12933064	17919161	7971585	15180627	3279997	7684390	1038459	1441861

Cont.

Sample ID	Age (cal. yr. BP)	Weight of sediment extracted (g)	Amount of standard added (µg)	Area of standard	Concentration of n-alkane compounds (µg/g)												
					C17	C18	C19	C20	C21	C22	C23	C24	C25	C26	C27	C28	C29
LV1	1388	0.8216	24.8	164033735	5.63	7.95	9.02	9.78	10.45	8.87	12.19	8.68	16.57	7.86	16.34	4.06	7.41
LV2	1720	1.237	24.8	160344413	0.00	0.67	1.37	2.00	2.80	2.73	6.28	5.39	13.87	8.04	18.42	7.78	11.99
LV3	2162	1.003	24.8	113039847	0.00	0.07	0.40	0.96	1.81	1.86	4.92	3.98	13.47	4.95	15.09	2.57	5.81
LV4	2757	0.904	24.8	128975801	0.00	0.71	1.03	1.70	2.27	2.26	4.05	3.62	11.76	4.35	12.39	2.67	6.71
LV5	3057	0.4513	24.8	138981508	0.00	0.86	0.73	1.21	1.77	1.86	4.11	4.53	12.47	6.48	14.72	5.30	8.63
LV6	3772	0.6983	24.8	157854334	0.00	0.71	0.89	1.48	1.73	1.80	4.03	4.49	13.11	5.65	15.18	3.53	9.38
LV7	4220	0.8438	24.8	172140984	0.00	0.93	1.35	1.72	2.08	1.95	3.61	3.73	11.79	4.73	14.24	2.81	6.80
LV8	4615	0.9377	24.8	132206537	0.61	1.17	1.32	1.48	1.77	1.70	3.86	4.07	13.35	5.33	15.88	3.27	7.36
LV9	4993	1.0763	24.8	125940155	0.00	0.73	1.34	2.14	2.66	2.52	4.32	3.87	12.46	4.74	14.61	2.93	7.88
LV10	5448	0.4577	24.8	119980040	0.00	1.26	0.96	1.56	1.99	1.86	4.32	4.12	14.01	5.47	14.92	3.93	8.56
LV11	5843	0.9397	24.8	143965555	0.00	0.82	1.11	1.41	1.91	1.96	4.43	4.27	14.92	5.82	16.96	4.66	9.51
LV12	6141	0.9223	24.8	149547499	0.00	0.16	0.43	0.86	1.39	1.56	4.09	4.28	15.31	5.61	18.62	3.32	10.83
LV13	6564	1.0961	24.8	115614619	0.00	1.63	1.85	2.77	3.22	3.11	5.35	4.17	15.43	5.05	15.87	2.69	8.37
LV14	6893	0.9868	24.8	168046383	0.00	0.87	1.41	1.75	2.22	2.17	4.53	4.52	14.73	5.50	17.16	4.11	10.64
LV15	7537	1.4181	24.8	142558337	0.00	0.40	0.64	0.77	1.25	1.22	3.29	3.06	12.20	4.22	12.77	2.61	7.54
LV16	8020	0.4273	24.8	70977013	0.00	0.56	0.95	1.19	1.96	2.66	7.64	11.21	26.73	13.08	30.49	10.33	22.33
LV17	8361	0.8692	24.8	141383164	0.00	0.93	0.89	1.12	1.48	1.55	3.68	4.20	13.24	6.21	16.31	5.56	10.58
LV18	9112	0.8737	24.8	143298366	0.00	0.21	0.55	1.13	1.72	1.79	3.47	3.37	12.32	4.60	13.85	3.28	8.82
LV19	9743	1.0008	24.8	129014395	0.00	0.44	0.62	0.84	1.27	1.29	3.11	3.55	10.97	4.76	13.70	3.78	10.17
LV20	10263	1.0609	24.8	152291801	0.54	0.96	1.18	1.38	1.63	1.66	3.02	3.28	9.86	4.18	13.05	4.65	11.19
LV21	10655	1.0297	24.8	133331423	0.00	0.86	1.32	2.07	2.29	2.24	2.96	2.67	7.56	3.08	9.10	2.44	7.04
LV22	11648	0.6299	24.8	11009937	0.00	1.11	2.95	4.62	10.47	12.49	29.17	43.18	76.29	69.82	98.78	70.77	83.02
LV23	12209	1.1274	24.8	159951390	0.00	0.54	0.85	1.08	1.60	1.39	2.76	2.45	7.33	3.80	9.10	3.56	6.83
LV24	12730	1.0651	24.8	133011104	0.00	0.71	0.86	1.26	1.89	1.88	3.81	4.77	10.65	8.84	16.13	10.42	15.34
LV25	13284	1.3284	24.8	131527664	0.00	0.78	1.10	1.40	1.63	1.47	2.50	2.45	5.35	2.62	6.37	1.36	3.73
LV26	14068	0.8402	24.8	134366313	0.00	1.04	1.01	1.93	4.15	2.65	5.71	7.14	12.16	13.55	20.27	15.60	17.98
LV27	14922	1.1417	24.8	148041163	0.65	0.77	0.95	1.54	1.89	1.76	2.26	1.78	2.94	1.30	2.78	0.98	1.60
LV28	15748	4.4842	24.8	46250854	0.00	0.02	0.06	0.18	0.40	0.91	2.77	4.22	7.08	5.87	8.83	5.61	6.33
LV29	16157	4.8677	24.8	112670386	0.00	0.00	0.05	0.17	0.25	0.36	0.75	0.70	1.50	0.94	1.97	0.89	1.23
LV30	16753	3.2153	24.8	128587922	0.25	0.54	0.63	0.92	1.10	1.09	1.65	1.43	2.78	1.49	3.24	0.97	1.93
LV31	17657	4.0557	24.8	135230069	0.00	0.03	0.20	0.11	0.15	0.25	0.52	0.41	0.93	0.41	1.15	0.21	0.42
LV32	18070	4.1436	24.8	151917333	0.00	0.02	0.02	0.10	0.15	0.27	0.54	0.48	1.06	0.51	1.17	0.34	0.57
LV33	18468	4.5549	24.8	88666909	0.00	0.00	0.01	0.06	0.09	0.19	0.43	0.41	0.85	0.58	1.04	0.55	0.60
LV34	19080	3.9111	24.8	145173957	0.00	0.09	0.08	0.28	0.46	0.46	0.92	1.05	1.91	1.80	2.77	1.90	2.11
LV35	19509	4.32	24.8	146177337	0.00	0.00	0.07	0.19	0.25	0.42	0.72	0.57	1.20	0.63	1.46	0.48	0.72
LV36	19815	1.8461	24.8	133645012	0.00	0.00	0.02	0.09	0.17	0.33	0.69	0.69	1.48	0.86	1.93	0.70	1.10
LV37	20350	2.166	24.8	136012345	0.00	0.33	0.16	0.80	0.84	0.86	1.56	1.68	3.26	3.26	5.39	3.79	4.47
LV38	20728	2.6767	24.8	124254986	0.00	0.00	0.09	0.25	0.22	0.35	0.71	0.74	1.47	0.97	2.14	0.96	1.34

Cont.

		Concentration of n-alkane compounds (µg/g)						*n*-alkane parameters					
Sample ID	Age (cal. yr. BP)	C30	C31	C32	C33	C34	C35	Total abundance (µg/gTOC)	C no. range	Most abundant C no.	CPI	Pwax	Paq
LV1	1388	2.07	5.26	0.67	2.22	0.24	0.47	10.5	17-35	25	2.1	0.50	0.69
LV2	1720	4.65	5.78	1.73	2.28	0.58	0.53	6.8	18-35	27	2.0	0.64	0.53
LV3	2162	1.29	2.92	0.30	0.90	0.06	0.13	4.5	18-35	27	3.0	0.56	0.68
LV4	2757	1.09	2.60	0.19	0.82	0.07	0.12	4.1	18-35	27	2.9	0.58	0.63
LV5	3057	3.12	3.92	1.02	1.20	0.37	0.20	5.3	18-35	27	2.1	0.62	0.57
LV6	3772	2.07	4.18	0.59	1.49	0.17	0.33	4.8	18-35	27	2.7	0.63	0.56
LV7	4220	1.71	4.22	0.46	1.62	0.11	0.36	4.2	18-35	27	2.9	0.62	0.58
LV8	4615	1.98	4.37	0.54	1.58	0.13	0.30	4.5	17-35	27	2.8	0.62	0.59
LV9	4993	1.19	3.00	0.25	0.90	0.06	0.12	3.9	18-35	27	3.0	0.60	0.61
LV10	5448	1.78	3.35	0.52	1.04	0.12	0.18	4.3	18-35	27	2.7	0.59	0.61
LV11	5843	2.31	3.62	0.60	1.04	0.17	0.21	4.9	18-35	27	2.7	0.61	0.60
LV12	6141	2.03	4.80	0.46	1.62	0.10	0.28	4.9	18-35	27	3.3	0.64	0.55
LV13	6564	1.30	3.18	0.25	0.90	0.06	0.13	4.6	18-35	27	3.2	0.57	0.64
LV14	6893	2.02	5.30	0.57	2.03	0.16	0.43	4.9	18-35	27	3.0	0.63	0.55
LV15	7537	1.53	3.10	0.37	0.96	0.10	0.17	3.2	18-35	27	3.2	0.60	0.59
LV16	8020	5.42	13.04	1.86	4.44	0.55	0.88	8.2	18-35	27	2.4	0.66	0.49
LV17	8361	3.25	5.16	1.05	1.76	0.34	0.40	4.0	18-35	27	2.4	0.65	0.52
LV18	9112	1.66	4.51	0.43	1.52	0.09	0.24	3.3	18-35	27	3.1	0.63	0.54
LV19	9743	1.79	5.87	0.54	2.24	0.13	0.35	3.5	18-35	27	3.0	0.68	0.47
LV20	10263	2.31	7.87	0.70	3.02	0.15	0.52	3.4	17-35	27	2.9	0.71	0.40
LV21	10655	1.36	4.90	0.42	1.77	0.11	0.26	2.6	18-35	27	2.9	0.67	0.47
LV22	11648	43.07	50.34	15.67	15.88	5.41	2.46	40.9	18-35	27	1.4	0.69	0.44
LV23	12209	2.21	3.95	0.78	1.34	0.25	0.25	3.1	18-35	27	2.3	0.66	0.48
LV24	12730	7.38	10.43	3.29	4.17	1.16	1.06	6.5	18-35	27	1.7	0.74	0.36
LV25	13284	0.87	3.64	0.33	1.32	0.09	0.22	2.6	18-35	27	2.6	0.64	0.52
LV26	14068	10.88	11.56	4.94	4.53	1.73	1.16	9.2	18-35	27	1.3	0.74	0.38
LV27	14922	0.49	1.17	0.23	0.43	0.05	0.07	3.1	17-35	25	1.9	0.52	0.65
LV28	15748	3.53	4.07	1.43	1.83	0.50	0.43	20.4	18-35	27	1.4	0.66	0.49
LV29	16157	0.57	0.94	0.22	0.43	0.07	0.09	4.6	19-35	27	1.9	0.65	0.51
LV30	16753	0.55	1.34	0.25	0.63	0.09	0.14	3.6	17-35	27	2.1	0.59	0.58
LV31	17657	0.09	0.46	0.04	0.24	0.02	0.05	2.4	18-35	27	2.8	0.58	0.62
LV32	18070	0.19	0.54	0.07	0.30	0.03	0.07	2.8	18-35	27	2.3	0.59	0.59
LV33	18468	0.31	0.38	0.12	0.15	0.04	0.03	2.4	19-35	27	1.6	0.61	0.57
LV34	19080	1.34	1.34	0.54	0.58	0.19	0.15	7.4	18-35	27	1.4	0.69	0.45
LV35	19509	0.29	0.65	0.13	0.38	0.04	0.09	3.2	19-35	27	2.1	0.59	0.59
LV36	19815	0.40	0.95	0.16	0.54	0.06	0.11	2.4	19-35	27	2.1	0.65	0.51
LV37	20350	2.65	3.01	1.07	1.44	0.38	0.37	8.0	18-35	27	1.4	0.73	0.39
LV38	20728	0.59	1.13	0.24	0.57	0.08	0.11	2.7	19-35	27	1.9	0.68	0.47

Concentration = ((area of compound/area of standard) x amount of standard added)/weight of sediment extracted.

CPI (Carbon Preference Index) = $2(C_{23\text{-}31}\text{odd})/(C_{22\text{-}30}\text{even} + C_{24\text{-}32}\text{even})$.

P_{wax} (*n*-alkane land plant proxy) = $(C_{27} + C_{29} + C_{31})/(C_{23} + C_{25} + C_{27} + C_{29} + C_{31})$ (Zheng et al., 2007).

P_{alg} (*n*-alkane non-emergent aquatic plant proxy) = $(C_{23} + C_{25})/(C_{23} + C_{25} + C_{29} + C_{31})$ (Ficken et al., 2000).

Raw *n*-alkene data for Lake Victoria

Sample ID	Age (cal. yr. BP)	Weight of sediment extracted (g)	Amount of standard added (µg)	Area of standard	Peak area of n-alkene compounds									
					C18	C19	C20	C21	C22	C23	C24	C25	C26	C27
LV1	1388	0.8216	24.8	164033735	2016425	2894732	2686016	2290953	3011313	4651932	5014946	12776486	812202	20394957
LV2	1720	1.237	24.8	160344413	330745	496364	995954	997096	1039447	3413750	3629965	12235756	6142481	18019163
LV3	2162	1.003	24.8	113039847	0	0	561332	646567	1117326	2190831	2031917	8448932	3725865	13966316
LV4	2757	0.904	24.8	128975801	286626	4843197	1282601	902484	1374062	1712270	1794363	6349598	2867761	13471309
LV5	3057	0.4513	24.8	138981508	0	0	806002	308363	728338	729692	798273	2736482	1222677	4940787
LV6	3772	0.6983	24.8	157854334	0	0	581436	446481	699704	1368463	1351143	5804029	25098905	12374545
LV7	4220	0.8438	24.8	172140984	537346	528897	866522	772757	1170515	2038886	1565420	6945195	3545493	13099779
LV8	4615	0.9377	24.8	132206537	532464	630333	697673	649797	772970	1591384	1425138	6110892	3066437	15569870
LV9	4993	1.0763	24.8	125940155	0	477970	1300752	909214	1291884	1834605	1574791	5815925	2870158	12085404
LV10	5448	0.4577	24.8	119980040	745008	291421	961702	481094	728119	806188	735799	2469920	1056766	5937522
LV11	5843	0.9397	24.8	143965555	558771	770145	1599965	1194546	1705192	2178368	1725036	6953436	2750547	13198402
LV12	6141	0.9223	24.8	149547499	0	0	473349	586845	807622	1732632	1464638	7190794	2868439	17098994
LV13	6564	1.0961	24.8	115614619	947356	1229907	3348908	1730714	4405651	3867997	1751978	7118386	3116373	15354248
LV14	6893	0.9868	24.8	168046383	583753	716621	890658	1022170	1031491	2505650	1812919	7720423	4246527	18197646
LV15	7537	1.4181	24.8	142558337	732500	711483	1477573	1384964	1536152	2820236	2097497	9047788	3642677	20590552
LV16	8020	0.4273	24.8	70977013	252444	0	321788	350018	262448	692386	376173	2076199	1316336	6010062
LV17	8361	0.8692	24.8	141383164	613127	570299	907938	989386	948812	2136334	1345418	6389322	2371368	12110681
LV18	9112	0.8737	24.8	143298366	0	240903	978438	1057931	1545653	2284384	1615798	6465320	2779886	15729048
LV19	9743	1.0008	24.8	129014395	413915	311656	705030	789848	769373	1602551	1168030	6133317	2483287	14035896
LV20	10263	1.0609	24.8	152291801	1185170	829037	1273555	1255368	1889095	2614219	1663392	8696560	3306470	18667664
LV21	10655	1.0297	24.8	133331423	820114	1427930	3059035	2065770	2483007	2429117	1711847	6342135	2348249	11239960
LV22	11648	0.6299	24.8	11009937	107262	115679	230608	249930	238927	536906	0	1119738	0	3007277
LV23	12209	1.1274	24.8	159951390	501321	603255	1404276	1318214	1420313	2882701	1286603	8118755	2495739	13898909
LV24	12730	1.0651	24.8	133011104	493855	639831	1392810	1264000	1193538	2904825	1073887	6980461	1119738	16429452
LV25	13284	1.3284	24.8	131527664	347262	745169	1140702	1188872	1146648	3820371	1522307	7681569	2656497	11047324
LV26	14068	0.8402	24.8	134366313	0	0	0	0	2628064	4159079	0	3741629	0	6594195
LV27	14922	1.1417	24.8	148041163	1604667	3340066	4529884	1819169	3770011	2448355	857094	7465151	1674757	10018455
LV28	15748	4.4842	24.8	46250854	0	0	0	0	0	0	0	0	0	0
LV29	16157	4.8677	24.8	112670386	0	0	0	0	800678	575825	0	1676623	0	4870415
LV30	16753	3.2153	24.8	128587922	1131505	594745	1477110	731454	1648509	1774783	1337120	3511302	1482232	8081716
LV31	17657	4.0557	24.8	135230069	0	0	564702	336249	494553	375787	495331	1089342	463159	0
LV32	18070	4.1436	24.8	151917333	0	0	504660	666080	368920	529299	1115558	394376	3061025	0
LV33	18468	4.5549	24.8	88666909	0	0	0	0	0	0	0	0	0	0
LV34	19080	3.9111	24.8	145173957	0	0	0	0	0	0	0	0	0	0
LV35	19509	4.32	24.8	146177337	0	0	0	0	0	3184228	0	2789308	0	0
LV36	19815	1.8461	24.8	133645012	0	0	0	0	0	0	0	0	0	0
LV37	20350	2.166	24.8	136012345	0	0	0	0	0	0	0	0	0	0
LV38	20728	2.6767	24.8	124254986	0	0	0	0	0	652131	0	854931	0	1473621

Cont.

		Peak area of n-alkene compounds		Concentration of n-alkene compounds (µg/g)												*n*-alkene parameters			
Sample ID	Age (cal. yr. BP)	C28	C29	C18	C19	C20	C21	C22	C23	C24	C25	C26	C27	C28	C29	Total abundance (µg/gTOC)	C no. range	Most abundant C no.	P_{alg}
LV1	1388	11387381	6104012	0.37	0.53	0.49	0.42	0.55	0.86	0.92	2.35	0.15	3.75	2.10	1.12	1.05	18-29	27	0.32
LV2	1720	0	0	0.04	0.06	0.12	0.12	0.13	0.43	0.45	1.53	0.77	2.25	0.00	0.00	0.42	18-27	27	0.17
LV3	2162	2923510	8870354	0.00	0.00	0.12	0.14	0.24	0.48	0.44	1.85	0.81	3.05	0.64	1.94	0.71	20-29	27	0.36
LV4	2757	0	0	0.06	1.03	0.27	0.19	0.29	0.36	0.38	1.35	0.61	2.87	0.00	0.00	0.52	18-27	27	0.31
LV5	3057	0	0	0.00	0.00	0.32	0.12	0.29	0.29	0.32	1.08	0.48	1.95	0.00	0.00	0.36	20-27	27	0.19
LV6	3772	0	0	0.00	0.00	0.13	0.10	0.16	0.31	0.30	1.31	5.65	2.78	0.00	0.00	0.73	20-27	26	0.23
LV7	4220	2574757	11865574	0.09	0.09	0.15	0.13	0.20	0.35	0.27	1.19	0.61	2.24	0.44	2.03	0.51	18-29	27	0.23
LV8	4615	3051229	9714263	0.11	0.13	0.14	0.13	0.15	0.32	0.29	1.22	0.61	3.11	0.61	1.94	0.57	18-29	27	0.26
LV9	4993	0	0	0.00	0.09	0.24	0.17	0.24	0.34	0.29	1.06	0.53	2.21	0.00	0.00	0.31	19-27	27	0.23
LV10	5448	0	0	0.34	0.13	0.43	0.22	0.33	0.36	0.33	1.12	0.48	2.68	0.00	0.00	0.39	18-27	27	0.24
LV11	5843	0	0	0.10	0.14	0.29	0.22	0.31	0.40	0.32	1.27	0.50	2.42	0.00	0.00	0.39	18-27	27	0.22
LV12	6141	3634597	0	0.00	0.00	0.09	0.11	0.15	0.31	0.26	1.29	0.52	3.07	0.65	0.00	0.42	20-28	27	0.21
LV13	6564	2365844	0	0.19	0.24	0.66	0.34	0.86	0.76	0.34	1.39	0.61	3.00	0.46	0.00	0.54	18-28	27	0.29
LV14	6893	0	0	0.09	0.11	0.13	0.15	0.15	0.37	0.27	1.15	0.64	2.72	0.00	0.00	0.35	18-27	27	0.19
LV15	7537	3699343	0	0.09	0.09	0.18	0.17	0.19	0.35	0.26	1.11	0.45	2.53	0.45	0.00	0.34	18-28	27	0.26
LV16	8020	0	0	0.21	0.00	0.26	0.29	0.21	0.57	0.31	1.70	1.08	4.91	0.00	0.00	0.50	18-27	27	0.15
LV17	8361	0	0	0.12	0.12	0.18	0.20	0.19	0.43	0.27	1.29	0.48	2.44	0.00	0.00	0.30	18-27	27	0.19
LV18	9112	0	0	0.00	0.05	0.19	0.21	0.31	0.45	0.32	1.28	0.55	3.12	0.00	0.00	0.34	19-27	27	0.25
LV19	9743	0	0	0.08	0.06	0.14	0.15	0.15	0.31	0.22	1.18	0.48	2.70	0.00	0.00	0.29	18-27	27	0.19
LV20	10263	0	0	0.18	0.13	0.20	0.19	0.29	0.40	0.26	1.33	0.51	2.87	0.00	0.00	0.30	18-27	27	0.17
LV21	10655	0	0	0.15	0.26	0.55	0.37	0.45	0.44	0.31	1.15	0.42	2.03	0.00	0.00	0.30	18-27	27	0.21
LV22	11648	0	0	0.38	0.41	0.82	0.89	0.85	1.92	0.00	4.00	0.00	10.75	0.00	0.00	1.29	18-27	27	0.10
LV23	12209	0	0	0.07	0.08	0.19	0.18	0.20	0.40	0.18	1.12	0.34	1.91	0.00	0.00	0.29	18-27	27	0.22
LV24	12730	0	0	0.09	0.11	0.24	0.22	0.21	0.51	0.19	1.22	0.20	2.88	0.00	0.00	0.37	18-27	27	0.13
LV25	13284	2274468	7770545	0.05	0.11	0.16	0.17	0.16	0.54	0.22	1.09	0.38	1.57	0.32	1.10	0.41	18-29	27	0.27
LV26	14068	0	0	0.00	0.00	0.00	0.00	0.58	0.91	0.00	0.82	0.00	1.45	0.00	0.00	0.25	22-27	27	0.09
LV27	14922	0	0	0.24	0.49	0.66	0.27	0.55	0.36	0.13	1.10	0.25	1.47	0.00	0.00	0.72	18-27	27	0.48
LV28	15748	0	0	0.00	0.00	0.00	0.00	0.00	0.00	0.00	0.00	0.00	0.00	0.00	0.00	0.00	–	–	–
LV29	16157	0	0	0.00	0.00	0.00	0.00	0.04	0.03	0.00	0.08	0.00	0.22	0.00	0.00	0.15	22-27	27	0.11
LV30	16753	0	0	0.07	0.04	0.09	0.04	0.10	0.11	0.08	0.21	0.09	0.48	0.00	0.00	0.22	18-27	27	0.17
LV31	17657	0	0	0.00	0.00	0.03	0.02	0.02	0.02	0.02	0.05	0.02	0.00	0.00	0.00	0.07	20-26	25	0.06
LV32	18070	0	0	0.00	0.00	0.02	0.03	0.01	0.02	0.04	0.02	0.12	0.00	0.00	0.00	0.12	20-26	26	0.03
LV33	18468	0	0	0.00	0.00	0.00	0.00	0.00	0.00	0.00	0.00	0.00	0.00	0.00	0.00	0.00	–	–	–
LV34	19080	0	0	0.00	0.00	0.00	0.00	0.00	0.00	0.00	0.00	0.00	0.00	0.00	0.00	0.00	–	–	–
LV35	19509	0	0	0.00	0.00	0.00	0.00	0.00	0.13	0.00	0.11	0.00	0.00	0.00	0.00	0.09	23-25	23	0.12
LV36	19815	0	0	0.00	0.00	0.00	0.00	0.00	0.00	0.00	0.00	0.00	0.00	0.00	0.00	0.00	–	–	–
LV37	20350	0	0	0.00	0.00	0.00	0.00	0.00	0.00	0.00	0.00	0.00	0.00	0.00	0.00	0.00	–	–	–
LV38	20728	0	0	0.00	0.00	0.00	0.00	0.00	0.05	0.00	0.06	0.00	0.11	0.00	0.00	0.05	23-27	27	0.07

Concentration = ((area of compound/area of standard) x amount of standard added)/weight of sediment extracted.

P_{alg} (*n*-alkene algal proxy) = $(C_{23:1} + C_{25:1} + C_{27:1})/(C_{23:1} + C_{25:1} + C_{27:1} + C_{29} + C_{31} + C_{33})$ (modified after Zhang et al. (2004)).

Raw botryococcenes data for Lake Victoria

Sample ID	Age (cal. yr. BP)	Weight of sediment extracted (g)	Amount of standard added (µg)	Area of standard	Peak area of botryococcene compounds					
					A	B	C	D	E	F
LV1	1388	0.8216	24.8	128787642	33889212	119643229	14603750	239879207	13874995	10664143
LV2	1720	1.237	24.8	166237255	49673954	195529412	10789931	402959816	20449622	9332099
LV3	2162	1.003	24.8	147287114	8880869	179747649	3280657	276967387	3522568	2404378
LV4	2757	0.904	24.8	133024394	10144710	103801291	3170985	194254029	2032297	0
LV5	3057	0.4513	24.8	145864613	4413903	61502455	1922140	135718942	560303	1315465
LV6	3772	0.6983	24.8	152722846	21316369	91686778	4977378	172518369	7408846	2948701
LV7	4220	0.8438	24.8	132931610	26091049	140877785	6379594	261062974	7350321	3111914
LV8	4615	0.9377	24.8	148688336	38343178	167578937	8385041	332313981	18612801	7214424
LV9	4993	1.0763	24.8	128320611	15289938	47053977	4735255	295590690	2670759	1906825
LV10	5448	0.4577	24.8	147617061	1385719	21800058	0	54616697	0	550604
LV11	5843	0.9397	24.8	154778415	10514433	85820008	3855657	210475608	4982706	0
LV12	6141	0.9223	24.8	131584000	41290436	133111205	13709039	290378918	33391037	8753172
LV13	6564	1.0961	24.8	145610267	39823531	210343869	14938416	425239089	15334915	0
LV14	6893	0.9868	24.8	154603141	53527279	271989996	0	416212859	42483141	10192782
LV15	7537	1.4181	24.8	168324300	209022045	230193029	0	627807169	12239185	6153799
LV16	8020	0.4273	24.8	152309168	26299303	177119847	7864651	311735807	8672535	3711309
LV17	8361	0.8692	24.8	136710980	86122506	449077612	0	748454671	21431734	9034817
LV18	9112	0.8737	24.8	139363775	0	316355596	0	399785450	4127637	0
LV19	9743	1.0008	24.8	162798950	28568978	226791530	0	350473246	32224714	8012519
LV20	10263	1.0609	24.8	130495732	29754811	70382546	14995990	399516386	93490188	12323144
LV21	10655	1.0297	24.8	149101270	8911376	50630904	3398178	224518593	1329553	0
LV22	11648	0.6299	24.8	153626226	3212123	10312574	0	53391407	8111007	3971915
LV23	12209	1.1274	24.8	151722234	0	5103750	0	7394187	251534	856680
LV24	12730	1.0651	24.8	145642367	4322657	17247783	0	19828077	539144	1876062
LV25	13284	1.3284	24.8	151923369	5053654	33151643	2096735	51544059	3043998	2095388
LV26	14068	0.8402	24.8	81861084	0	5221020	0	7230298	0	457895
LV27	14922	1.1417	24.8	124021661	39866422	4497919	0	4236431	0	0
LV28	15748	4.4842	24.8	148033001	813270	3565884	0	4955772	0	1732004
LV29	16157	4.8677	24.8	99885797	0	1499874	0	2048949	317382	705144
LV30	16753	3.2153	24.8	98184062	651044	24742179	855283	42524420	0	0
LV31	17657	4.0557	24.8	136716861	253061	872336	0	814968	158262	589561
LV32	18070	4.1436	24.8	139844742	201681	1717557	0	2086284	229049	1255848
LV33	18468	4.5549	24.8	155346072	0	1936365	0	1709879	344211	1587615
LV34	19080	3.9111	24.8	119817270	0	1781172	0	940453	0	862868
LV35	19509	4.32	24.8	109022186	0	969790	0	1065676	0	1839151
LV36	19815	1.8461	24.8	137344811	188345	1267276	0	718605	0	1109472
LV37	20350	2.166	24.8	137138355	0	1478642	0	1345476	0	534339
LV38	20728	2.6767	24.8	115183566	0	626825	0	317771	0	338601

Cont.

		Peak area of botryococcene compounds							
Sample ID	Age (cal. yr. BP)	G	H	I	J	K	L	M	N
LV1	1388	85122709	0	0	0	9373750	21668299	0	13387756
LV2	1720	82606969	11215799	12568997	5293418	4655946	10816948	0	11006515
LV3	2162	71380736	0	0	1633360	1543578	2342961	0	3075936
LV4	2757	49325368	0	1231492	0	1129515	1436929	0	2060447
LV5	3057	36082535	0	1893513	0	8018517	922943	0	907954
LV6	3772	61747709	5924210	5038372	1751412	1285293	4257610	0	3154533
LV7	4220	60189452	4991760	3504920	1903198	1389549	4451286	1888795	4742458
LV8	4615	108339690	17560350	12517019	4397654	2779731	6074119	0	5011077
LV9	4993	89744134	0	0	0	2424470	2887942	0	1852897
LV10	5448	32704466	0	0	0	1385440	964625	0	500365
LV11	5843	59479363	0	2697746	0	5919312	2068310	0	1419433
LV12	6141	70059459	22695690	19426602	5989422	4299627	4067662	2306573	4022529
LV13	6564	73061875	0	0	6249274	5815787	6382816	0	3798505
LV14	6893	74659683	25368986	24579746	7778345	6192957	7051615	4104553	7985833
LV15	7537	94635337	7387970	4842094	3777113	3488438	5393034	0	8653257
LV16	8020	22936371	9595249	6660591	1686491	1780371	1606715	0	3465945
LV17	8361	57697913	13240590	10152793	6272110	5542337	11610150	6401275	12624693
LV18	9112	32110817	0	0	0	9727336	1676004	0	3916626
LV19	9743	32031715	30038869	22215063	9561448	7139929	5978814	4341960	7816933
LV20	10263	43804396	52560415	49935751	21903516	15275598	7118609	12202583	8933167
LV21	10655	32975644	0	0	0	5433034	2328873	0	3120403
LV22	11648	14527641	28210985	10133604	8189927	5456027	2829348	2833357	3790715
LV23	12209	19654527	2761852	840188	806572	671620	2300100	0	1073698
LV24	12730	25376290	20597560	20517469	2321910	1175140	14587338	0	2918691
LV25	13284	24903460	8255356	1717474	1398153	663318	10707968	0	1964509
LV26	14068	6807454	0	0	0	0	1192158	0	465252
LV27	14922	2396351	0	0	0	0	13811890	0	0
LV28	15748	1744463	0	964282	614746	2525857	1028420	0	0
LV29	16157	684313	0	0	0	340465	524254	0	268620
LV30	16753	6622652	0	0	0	635855	657343	0	697192
LV31	17657	215410	197776	0	0	0	267005	0	0
LV32	18070	118360	593706	0	0	317802	380921	0	0
LV33	18468	369856	549260	0	0	456585	728520	0	352741
LV34	19080	1045319	0	0	0	260028	466323	0	0
LV35	19509	796233	0	462835	0	0	0	0	0
LV36	19815	767952	0	0	0	378756	347943	0	465489
LV37	20350	1049555	0	0	0	0	420606	0	0
LV38	20728	365341	0	0	0	147552	165882	0	0

Cont.

Sample ID	Age (cal. yr. BP)	Weight of sediment extracted (g)	Amount of standard added (µg)	Area of standard	Concentration of botryococcene compounds (µg/g)					
					A	B	C	D	E	F
LV1	1388	0.8216	24.8	128787642	7.9428897	28.041755	3.4227994	56.222437	3.2519952	2.4994417
LV2	1720	1.237	24.8	166237255	5.990766	23.58119	1.3012846	48.59766	2.4662603	1.1254675
LV3	2162	1.003	24.8	147287114	1.4908758	30.175134	0.5507403	46.495897	0.5913511	0.4036349
LV4	2757	0.904	24.8	133024394	2.0921441	21.406946	0.6539524	40.061019	0.4191207	0
LV5	3057	0.4513	24.8	145864613	1.6628734	23.170151	0.7241381	51.130127	0.211086	0.4955822
LV6	3772	0.6983	24.8	152722846	4.9569993	21.321234	1.1574607	40.118157	1.7228846	0.6857035
LV7	4220	0.8438	24.8	132931610	5.7686665	31.147731	1.4105125	57.720379	1.6251378	0.6880365
LV8	4615	0.9377	24.8	148688336	6.8202292	29.807825	1.4914753	59.109798	3.3107211	1.2832537
LV9	4993	1.0763	24.8	128320611	2.7455392	8.4492519	0.8502865	53.077771	0.4795751	0.3423992
LV10	5448	0.4577	24.8	147617061	0.5086387	8.0018768	0	20.047473	0	0.2021034
LV11	5843	0.9397	24.8	154778415	1.7928251	14.633244	0.6574314	35.888378	0.8496055	0
LV12	6141	0.9223	24.8	131584000	8.4377345	27.201384	2.8014534	59.33917	6.8234858	1.7887179
LV13	6564	1.0961	24.8	145610267	6.1879852	32.684313	2.321208	66.075839	2.382818	0
LV14	6893	0.9868	24.8	154603141	8.7012049	44.21373	0	67.658088	6.9059089	1.6569025
LV15	7537	1.4181	24.8	168324300	21.716513	23.91609	0	65.22653	1.2716	0.6393539
LV16	8020	0.4273	24.8	152309168	10.021598	67.493192	2.9968996	118.78988	3.3047515	1.4142294
LV17	8361	0.8692	24.8	136710980	17.97402	93.723818	0	156.20469	4.4728659	1.8855929
LV18	9112	0.8737	24.8	139363775	0	64.433981	0	81.426624	0.8406998	0
LV19	9743	1.0008	24.8	162798950	4.3485803	34.520702	0	53.346712	4.9050321	1.2196125
LV20	10263	1.0609	24.8	130495732	5.3301339	12.607991	2.6863096	71.567446	16.747383	2.2075088
LV21	10655	1.0297	24.8	149101270	1.4394759	8.1785311	0.5489158	36.267025	0.2147659	0
LV22	11648	0.6299	24.8	153626226	0.8232029	2.6429064	0	13.68315	2.0786889	1.0179224
LV23	12209	1.1274	24.8	151722234	0	0.7399695	0	1.0720495	0.0364688	0.1242061
LV24	12730	1.0651	24.8	145642367	0.6910737	2.7574449	0	3.1699628	0.0861943	0.2999306
LV25	13284	1.3284	24.8	151923369	0.6210174	4.0738336	0.2576569	6.3339823	0.3740611	0.2574914
LV26	14068	0.8402	24.8	81861084	0	1.8825515	0	2.6070401	0	0.1651039
LV27	14922	1.1417	24.8	124021661	6.9824751	0.787796	0	0.7419972	0	0
LV28	15748	4.4842	24.8	148033001	0.0303839	0.1332218	0	0.1851482	0	0.0647079
LV29	16157	4.8677	24.8	99885797	0	0.0765031	0	0.1045094	0.0161885	0.0359668
LV30	16753	3.2153	24.8	98184062	0.0511446	1.9436906	0.0671891	3.3406239	0	0
LV31	17657	4.0557	24.8	136716861	0.0113185	0.0390164	0	0.0364506	0.0070785	0.0263689
LV32	18070	4.1436	24.8	139844742	0.0086316	0.0735087	0	0.0892897	0.0098029	0.0537483
LV33	18468	4.5549	24.8	155346072	0	0.0678672	0	0.0599291	0.0120642	0.0556439
LV34	19080	3.9111	24.8	119817270	0	0.0942626	0	0.0497703	0	0.0456644
LV35	19509	4.32	24.8	109022186	0	0.0510659	0	0.0561149	0	0.0968435
LV36	19815	1.8461	24.8	137344811	0.0184221	0.1239525	0	0.0702869	0	0.1085177
LV37	20350	2.166	24.8	137138355	0	0.1234518	0	0.1123337	0	0.0446119
LV38	20728	2.6767	24.8	115183566	0	0.0504206	0	0.0255609	0	0.0272364

Cont.

Sample ID	Age (cal. yr. BP)	Concentration of botryococcene compounds (µg/g) G	H	I	J	K	L	M	N	Botryococcene parameters Total abundance (µg/gTOC)
LV1	1388	19.9509	0	0	0	2.1970019	5.0785751	0	3.137797	9.5
LV2	1720	9.9625453	1.352645	1.5158431	0.6383955	0.5615153	1.3045429	0	1.327405	6.8
LV3	2162	11.98304	0	0	0.2742003	0.2591281	0.3933246	0	0.5163727	6.7
LV4	2757	10.172373	0	0.2539707	0	0.2329399	0.2963379	0	0.4249261	5.2
LV5	3057	13.593567	0	0.7133533	0	3.020859	0.3477053	0	0.3420584	6.9
LV6	3772	14.359075	1.377641	1.1716445	0.4072808	0.2988875	0.9900828	0	0.7335686	5.9
LV7	4220	13.307739	1.1036658	0.7749292	0.4207924	0.3072259	0.9841683	0.4176079	1.0485458	7.5
LV8	4615	19.270743	3.1235181	2.226444	0.7822254	0.49444	1.0804238	0	0.891337	8.3
LV9	4993	16.114914	0	0	0	0.4353502	0.5185736	0	0.3327156	4.9
LV10	5448	12.004423	0	0	0	0.5085363	0.3540729	0	0.1836628	2.5
LV11	5843	10.141878	0	0.459995	0	1.009307	0.3526693	0	0.2420287	4.3
LV12	6141	14.316708	4.6378829	3.9698421	1.2239433	0.8786323	0.8312301	0.4713501	0.8220071	8.6
LV13	6564	11.35273	0	0	0.9710444	0.9036869	0.9917948	0	0.5902313	7.5
LV14	6893	12.136414	4.1238925	3.9955964	1.2644202	1.0067052	1.1462856	0.6672216	1.2981487	9.2
LV15	7537	9.8322144	0.7675791	0.5030732	0.3924262	0.3624341	0.5603136	0	0.8990371	7.2
LV16	8020	8.740121	3.6563604	2.5380812	0.6426533	0.6784272	0.6122539	0	1.3207311	11.6
LV17	8361	12.041724	2.7633501	2.1189177	1.3090078	1.156702	2.4230724	1.3359649	2.6348105	15.2
LV18	9112	6.5401965	0	0	0	1.981223	0.3413615	0	0.797722	8.1
LV19	9743	4.8756551	4.5723173	3.3814295	1.4553802	1.0867926	0.9100554	0.6609043	1.1898417	6.0
LV20	10263	7.8469091	9.4154202	8.9452505	3.9236906	2.7363972	1.2751934	2.1859121	1.6002446	6.8
LV21	10655	5.3266347	0	0	0	0.877611	0.3761884	0	0.5040462	2.6
LV22	11648	3.7231438	7.2299112	2.59704	2.0989145	1.3982706	0.7251053	0.7261327	0.9714844	2.4
LV23	12209	2.8496204	0.4004284	0.121815	0.1169412	0.0973751	0.333481	0	0.1556706	0.3
LV24	12730	4.0569691	3.2929819	3.2801776	0.3712094	0.1878725	2.3321131	0	0.4666182	1.1
LV25	13284	3.0602572	1.0144579	0.2110515	0.1718118	0.0815117	1.3158467	0	0.2414083	1.2
LV26	14068	2.4545746	0	0	0	0	0.4298583	0	0.1677567	0.5
LV27	14922	0.4197131	0	0	0	0	2.4191079	0	0	1.2
LV28	15748	0.0651733	0	0.0360257	0.022967	0.0943663	0.0384219	0	0	0.2
LV29	16157	0.0349043	0	0	0	0.0173659	0.0267403	0	0.0137013	0.1
LV30	16753	0.5202608	0	0	0	0.0499514	0.0516394	0	0.0547699	1.0
LV31	17657	0.0096345	0.0088458	0	0	0	0.0119422	0	0	0.1
LV32	18070	0.0050656	0.0254097	0	0	0.0136014	0.0163028	0	0	0.1
LV33	18468	0.012963	0.0192509	0	0	0.0160027	0.0255337	0	0.0123631	0.1
LV34	19080	0.05532	0	0	0	0.0137611	0.0246786	0	0	0.1
LV35	19509	0.0419269	0	0.0243713	0	0	0	0	0	0.1
LV36	19815	0.0751135	0	0	0	0.0370462	0.0340324	0	0.0455296	0.1
LV37	20350	0.0876273	0	0	0	0	0.0351164	0	0	0.1
LV38	20728	0.0293873	0	0	0	0.0118688	0.0133432	0	0	0.0

Appendix IX.

Geochemical characteristics of Lake Edward cores.

Published in Lærdal et al. (2002) but age-depth relationships have been subsequently changed so attention should be drawn to core depths rather than core chronology. N.B. Labelled ages to the left are in radiocarbon years. Vertical turquoise line represents core sections that were used in this thesis.

E96-1P

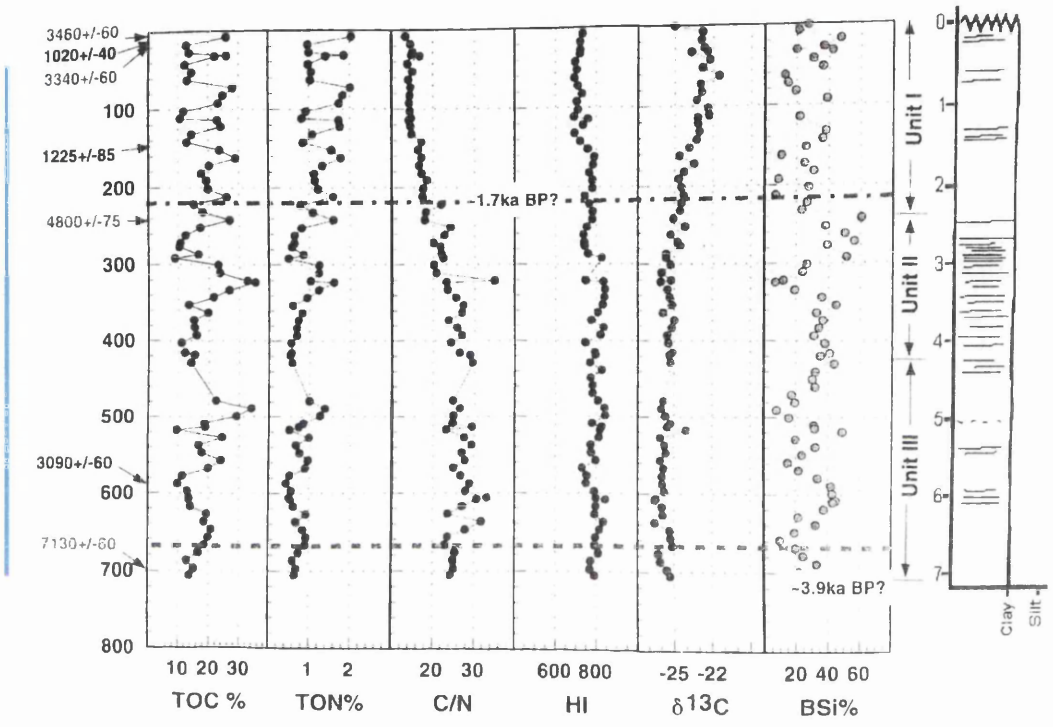

Appendix IX

E96-5M

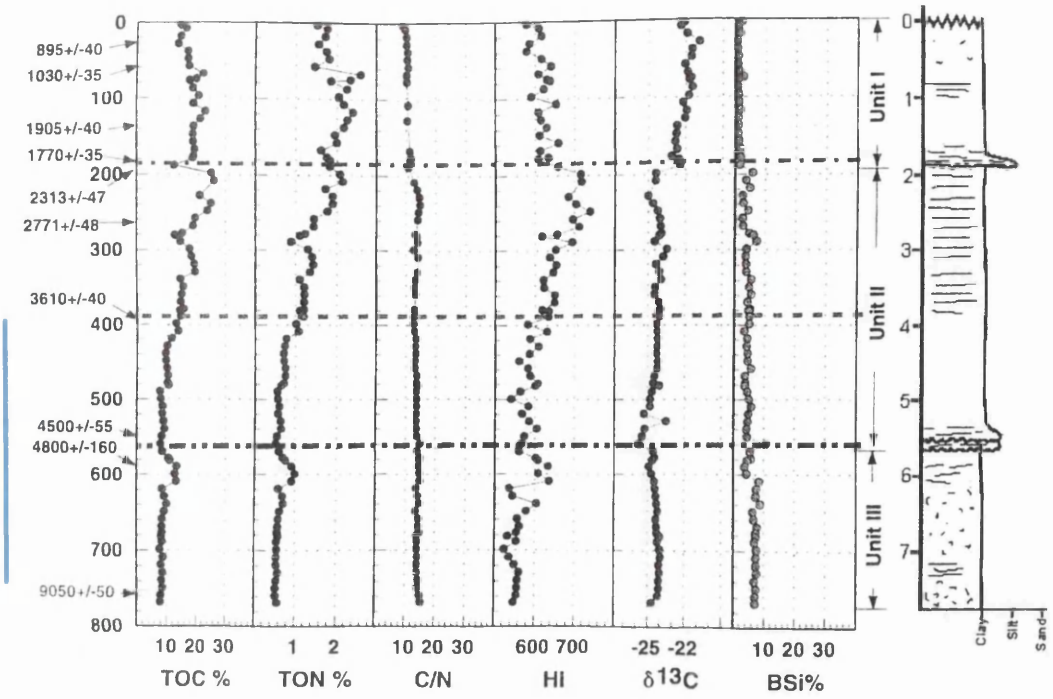

E96-1P

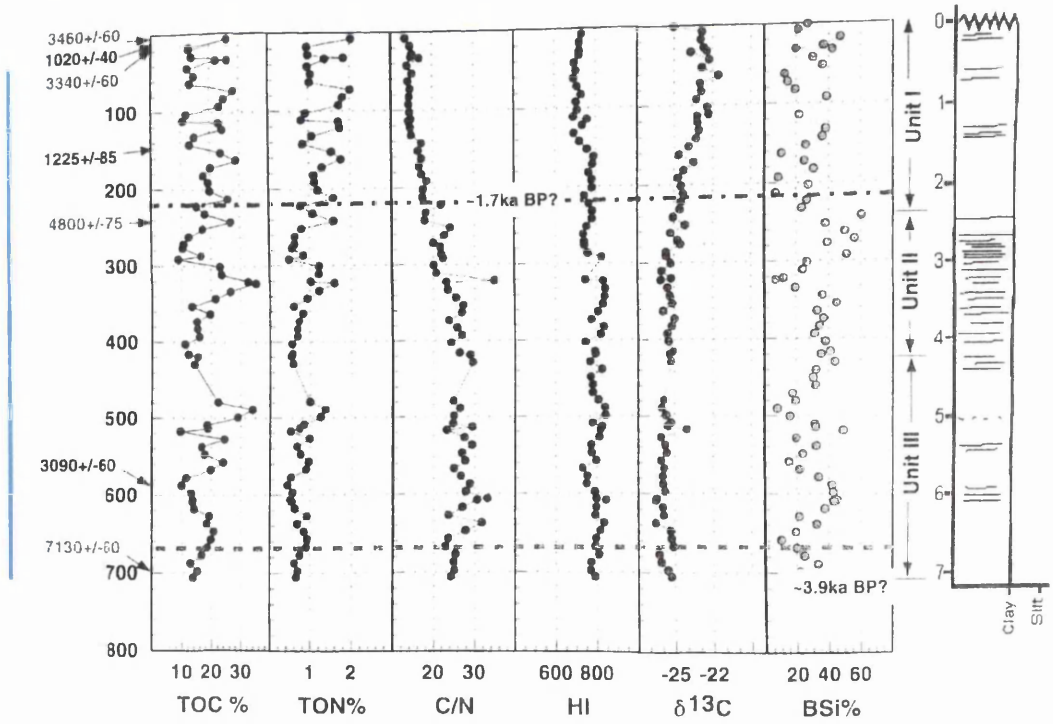

Appendix X.

Purified diatom samples from Lake Edward analysed for O- and Si-isotope analysis (n = 33), including outliers

Core	Depth range (cm)	Av. depth (cm)	Age range (Cal. yrs. BP)	Av. age (Cal. yrs. BP)	Size fraction (µm)	$\delta^{18}O_{diatom}$ (‰)	Average $\delta^{18}O_{diatom}$ (‰)	$\delta^{29}Si_{diatom}$ (‰)	Average $\delta^{29}Si_{diatom}$ (‰)	$\delta^{30}Si_{diatom}$ (‰)	Average $\delta^{30}Si_{diatom}$ (‰)
1P	37-43	40.0	988-995	991	>63	+44.49		+0.97		+1.89	
1P	37-43	40.0	988-995	991	38-63	+41.83	+42.19	+1.02	+0.97	+2.06	+1.92
1P	37-43	40.0	988-995	991	20-38	+42.54		+0.91		+1.80	
1P	246-250.5	248.3	1425-1448	1436	>63	+41.56		+1.07		+2.08	
1P	246-250.5	248.3	1425-1448	1436	38-63	+41.82	+41.56	+1.05	+1.04	+2.00	+1.99
1P	246-250.5	248.3	1425-1448	1436	20-38	+41.30		+1.00		+1.88	
1P	347.5-352.5	350.0	1932-1957	1945	20-38	+42.88		+0.94		+1.81	
1P	347.5-352.5	350.0	1932-1957	1945	20-38	+42.70	+42.57	+0.89	+0.90	+1.72	+1.72
1P	347.5-352.5	350.0	1932-1957	1945	>63	+40.95		+0.82		+1.53	
1P	347.5-352.5	350.0	1932-1957	1945	38-63	+42.11		+0.95		+1.81	
1P	531-537	534.0	2912-2950	2931	>63	+41.41	+41.36	+0.64	+0.57	+1.19	+1.06
1P	531-537	534.0	2912-2950	2931	>63	+41.31		+0.50		+0.93	
1P	700-704.5	702.3	3424-3429	3426	>63	+40.35	+40.35	+1.14	+1.13	+2.22	+2.16
1P	700-704.5	702.3	3424-3429	3426	>63	–	–	+1.12		+2.10	
5M	455.1-461.6	458.4	4361-4410	4386	20-38	+40.31	+40.31	+0.44	+0.44	+0.93	+0.93
5M	559.7-565.2	562.5	5160-5219	5189	20-38	+36.77	+36.77	+0.31	+0.31	+0.69	+0.69
5M	605.8-611.8	608.8	5582-5603	5593	20-38	+39.98	+39.98	+0.41	+0.41	+0.78	+0.78
5M	741.5-747.5	744.5	6052-6073	6062	20-38	+35.56	–	+1.01	–	+0.74	–
5M	741.5-747.5	744.5	6052-6073	6062	20-38	+37.46	–	+1.06	–	+0.84	–
2P	134.7-139.7	137.2	6837-6901	6869	>63	+35.38	+35.38	+0.41	+0.41	+0.80	+0.80
2P	165.2-169.2	167.2	7232-7283	7258	20-38	+37.78	+37.78	+0.48	+0.48	+0.90	+0.90

Core	Depth range (cm)	Av. depth (cm)	Age range (Cal. yrs. BP)	Av. age (Cal. yrs. BP)	Size fraction (µm)	$\delta^{18}O_{diatom}$ (‰)	Average $\delta^{18}O_{diatom}$ (‰)	$\delta^{29}Si_{diatom}$ (‰)	Average $\delta^{29}Si_{diatom}$ (‰)	$\delta^{30}Si_{diatom}$ (‰)	Average $\delta^{30}Si_{diatom}$ (‰)
2P	215.7-219.2	217.5	7886-7931	7908	20-38	+36.81	+36.81	+0.38	+0.38	+0.76	+0.76
2P	254.7-258.7	256.7	8391-8443	8417	>63	+38.53	+38.53	+0.37	+0.37	+0.71	+0.71
2P	254.7-258.7	256.7	8391-8443	8417	38-63	+34.25		+0.27	–	+0.27	–
2P	293.5-300.5	297.0	8894-8984	8939	20-38	+36.94	+36.94	+0.45	+0.45	+0.94	+0.94
2P	335.5-340.5	338.0	9438-9502	9470	>63	+34.22	+38.52	+0.59	+0.54	+1.09	+1.00
2P	335.5-340.5	338.0	9438-9502	9470	20-38	+38.52		+0.49		+0.92	
2P	361.5-367.0	364.3	9774-9846	9810	>63	+36.56	+36.77	+0.22	+0.25	+0.49	+0.49
2P	361.5-367.0	364.3	9774-9846	9810	>63	+36.97		+0.27		+0.50	
2P	408.5-412.5	410.5	10383-10435	10409	>63	+38.40	+38.40	+0.31	+0.31	+0.57	+0.57
2P	429.5-433.5	431.5	10655-10707	10681	>63	+38.14	+38.14	+0.32	+0.32	+0.60	+0.60
2P	464.5-468.0	466.3	11109-11154	11131	20-38	+38.30	+38.12	+0.57	+0.55	+1.12	+1.07
2P	464.5-468.1	466.3	11109-11154	11131	20-38	+37.95		+0.54		+1.03	

Highlighted data points were deemed to be outliers due to poor reproducibility or not conforming to the expected mass-dependent relationship of $\delta^{29}Si$ vs. $\delta^{30}Si$. Probably due to contamination by charcoal (affecting O-isotopes) or silicate minerals (affecting both O- and Si-isotopes).

Appendix XI.

Lipid data: raw *n*-alkanes data for Lake Edward

					Peak area of *n*-alkane compounds								
Sample ID	Age (cal. yrs. BP)	Weight of sediment extracted (g)	Amount of standard added (µg)	Area of standard	C17	C18	C19	C20	C21	C22	C23	C24	C25
ED1	991	0.2741	24.8	9631002	0	0	45551	198100	855382	1847339	10622950	9066645	12883553
ED2	1436	0.6613	24.8	68807456	0	0	4403000	4276817	24461673	6212506	196936627	13824290	39805232
ED3	1945	0.8216	24.8	31458443	0	0	1651351	4184378	17245754	5986290	85644159	16990497	39315262
ED4	2420	0.5592	24.8	111494574	0	0	2542292	2789172	30110767	5506783	259740394	9657840	39589385
ED5	2931	1.0667	24.8	6684089	0	0	178793	218375	1003992	494961	10071937	1387548	3260348
ED6	3426	1.41	24.8	70532673	0	0	2194864	2282575	10847241	3567611	74653938	11258322	27985924
ED17	3940	0.406	24.8	112739926	0	485663	1497736	3012391	10298532	6177565	31161571	23110618	37692943
ED18	4386	0.51	24.8	73202696	0	0	166865	482779	1084888	1833566	7573201	8540364	12979437
ED19	5189	0.4524	24.8	90574025	0	830534	1476062	3073815	9329184	6876713	16537849	22967004	34671370
ED20	5593	0.3884	24.8	57727248	0	1816317	3059897	16498244	9460049	11117966	22530259	1650989	25176009
ED21	6062	0.8683	24.8	133398264	0	394323	1161278	2233612	4598902	3851651	17345197	12746487	21886221
ED7	6869	0.9301	24.8	2162231	0	0	63795	151864	345520	661177	1469716	2200988	3141155
ED8	7258	1.9971	24.8	5276172	0	0	213095	372492	916263	1547962	4281440	5932682	9058256
ED9	7908	1.7058	24.8	78369557	10321577	2504036	5400507	3592980	7971492	5294972	28809762	20166116	36390828
ED10	8417	1.6243	24.8	73053021	1600257	1103619	1615981	2136659	5387053	4937766	15002540	18702880	29540121
ED11	8939	1.7821	24.8	104269898	2724470	2455443	2272190	3029035	4943896	4313098	12566532	14540471	21911670
ED12	9470	1.6205	24.8	101196642	0	322173	870072	1350894	2665796	2029898	9731539	7392214	13304021
ED13	9810	1.4982	24.8	91534252	0	723914	1325100	1774331	2914219	3495462	10501905	10672997	16328262
ED14	10409	1.8561	24.8	106665609	0	378526	898778	1879840	2324186	3318805	13359970	9048541	15673052
ED15	10681	1.9775	24.8	139104679	0	553876	1070416	1550904	3357907	3413383	16591659	9355617	18644800
ED16	11131	0.5791	24.8	95182197	0	0	397595	827908	1309706	2294495	11282030	9249430	12380470

Cont.

Sample ID	Age (cal. yrs. BP)	Peak area of *n*-alkane compounds									
		C26	C27	C28	C29	C30	C31	C32	C33	C34	C35
ED1	991	11758954	14396538	10808400	10514880	6419826	5030911	2276278	1600928	844576	393019
ED2	1436	13631348	33995484	9474220	17589988	4435719	10229995	2041848	4260764	609408	547722
ED3	1945	29305388	52122840	29199681	31973222	18623790	15313628	6662995	5315900	1999720	988377
ED4	2420	11753318	41290925	7781994	15244886	3070752	7479738	1408422	3388826	633571	2430454
ED5	2931	1530512	4100275	784845	1347978	370190	578988	114547	257873	46159	2716
ED6	3426	15999839	32145489	14228908	25393246	7721426	12167006	2808280	5143620	881226	907480
ED17	3940	34620830	50339116	37593246	37022867	27041617	19139476	11025126	7318257	4088145	1930232
ED18	4386	12017955	18056729	12508944	16655257	8413267	9221669	7576948	3458380	2864515	828303
ED19	5189	42057802	57249782	51282362	58532948	37263201	31595993	19042301	13843352	7771474	4916388
ED20	5593	19828642	22848222	10467379	18046428	5806899	6435198	2148802	2072152	836728	381022
ED21	6062	15165333	36447332	10700150	33208316	21449363	17791873	21867398	6263115	9893656	1860192
ED7	6869	3654401	4852328	4364584	4561828	3203102	2164121	1366615	975981	671007	337243
ED8	7258	10915048	16047299	13781432	14952919	9609407	8305533	4097872	3097003	1613794	843766
ED9	7908	31632641	50856154	30863971	44623003	19635489	24138876	7860591	8121459	2722714	1888775
ED10	8417	33063011	45742749	35466892	39714840	20993867	20615312	8328069	6877035	2970278	2152811
ED11	8939	18890050	30217769	17581187	33497454	10499806	20879315	3975635	8378266	1310637	1923300
ED12	9470	9372077	20763059	7387963	18127250	4362958	9515032	1673488	3207301	866690	1208173
ED13	9810	10192785	19634416	8755961	20308395	5352058	12468731	2894086	4134340	961705	1216586
ED14	10409	10235461	20736104	9149903	22640200	5738412	16216718	2229965	6451456	656995	1447235
ED15	10681	10218606	25164636	9988947	27412780	6491624	19933808	2438197	8202053	917999	1739472
ED16	11131	9764487	12350912	8173601	11175773	5327187	6790529	2344854	2603626	893130	610684

Cont.

Sample ID	Age (cal. yrs. BP)	Weight of sediment extracted (g)	Amount of standard added (µg)	Area of standard	Concentration of *n*-alkane compounds (µg/g)												
					C17	C18	C19	C20	C21	C22	C23	C24	C25	C26	C27	C28	C29
ED1	991	0.2741	24.8	9631002	0.00	0.00	0.43	1.86	8.04	17.35	99.80	85.18	121.03	110.47	135.25	101.54	98.78
ED2	1436	0.6613	24.8	68807456	0.00	0.00	2.40	2.33	13.33	3.39	107.34	7.53	21.69	7.43	18.53	5.16	9.59
ED3	1945	0.8216	24.8	31458443	0.00	0.00	1.58	4.01	16.55	5.74	82.18	16.30	37.72	28.12	50.01	28.02	30.68
ED4	2420	0.5592	24.8	111494574	0.00	0.00	1.01	1.11	11.98	2.19	103.32	3.84	15.75	4.68	16.42	3.10	6.06
ED5	2931	1.0667	24.8	6684089	0.00	0.00	0.62	0.76	3.49	1.72	35.03	4.83	11.34	5.32	14.26	2.73	4.69
ED6	3426	1.41	24.8	70532673	0.00	0.00	0.55	0.57	2.70	0.89	18.62	2.81	6.98	3.99	8.02	3.55	6.33
ED17	3940	0.406	24.8	112739926	0.00	0.26	0.81	1.63	5.58	3.35	16.88	12.52	20.42	18.76	27.27	20.37	20.06
ED18	4386	0.51	24.8	73202696	0.00	0.00	0.11	0.32	0.72	1.22	5.03	5.67	8.62	7.98	11.99	8.31	11.06
ED19	5189	0.4524	24.8	90574025	0.00	0.50	0.89	1.86	5.65	4.16	10.01	13.90	20.98	25.45	34.65	31.04	35.43
ED20	5593	0.3884	24.8	57727248	0.00	2.01	3.38	18.25	10.46	12.30	24.92	1.83	27.85	21.93	25.27	11.58	19.96
ED21	6062	0.8683	24.8	133398264	0.00	0.08	0.25	0.48	0.98	0.82	3.71	2.73	4.69	3.25	7.80	2.29	7.11
ED7	6869	0.9301	24.8	2162231	0.00	0.00	0.79	1.87	4.26	8.15	18.12	27.14	38.74	45.06	59.84	53.82	56.25
ED8	7258	1.9971	24.8	5276172	0.00	0.00	0.50	0.88	2.16	3.64	10.08	13.96	21.32	25.69	37.77	32.44	35.19
ED9	7908	1.7058	24.8	78369557	1.91	0.46	1.00	0.67	1.48	0.98	5.34	3.74	6.75	5.87	9.43	5.73	8.28
ED10	8417	1.6243	24.8	73053021	0.33	0.23	0.34	0.45	1.13	1.03	3.14	3.91	6.17	6.91	9.56	7.41	8.30
ED11	8939	1.7821	24.8	104269898	0.36	0.33	0.30	0.40	0.66	0.58	1.68	1.94	2.92	2.52	4.03	2.35	4.47
ED12	9470	1.6205	24.8	101196642	0.00	0.05	0.13	0.20	0.40	0.31	1.47	1.12	2.01	1.42	3.14	1.12	2.74
ED13	9810	1.4982	24.8	91534252	0.00	0.13	0.24	0.32	0.53	0.63	1.90	1.93	2.95	1.84	3.55	1.58	3.67
ED14	10409	1.8561	24.8	106665609	0.00	0.05	0.11	0.24	0.29	0.42	1.67	1.13	1.96	1.28	2.60	1.15	2.84
ED15	10681	1.9775	24.8	139104679	0.00	0.05	0.10	0.14	0.30	0.31	1.50	0.84	1.68	0.92	2.27	0.90	2.47
ED16	11131	0.5791	24.8	95182197	0.00	0.00	0.18	0.37	0.59	1.03	5.08	4.16	5.57	4.39	5.56	3.68	5.03

Cont.

Sample ID	Age (cal. yrs. BP)	Concentration of *n*-alkane compounds (µg/g) C30	C31	C32	C33	C34	C35	*n*-alkane parameters Total abundance (µg/g)	C no. range	Most abundant C no.	CPI	Pwax	Paq
ED1	991	60.31	47.26	21.38	15.04	7.93	3.69	935	19-35	27	1.3	0.56	0.60
ED2	1436	2.42	5.58	1.11	2.32	0.33	0.30	211	19-35	23	6.6	0.21	0.89
ED3	1945	17.87	14.69	6.39	5.10	1.92	0.95	348	19-35	23	2.2	0.44	0.73
ED4	2420	1.22	2.98	0.56	1.35	0.25	0.97	177	19-35	23	10.2	0.18	0.93
ED5	2931	1.29	2.01	0.40	0.90	0.16	0.01	90	19-35	23	4.4	0.31	0.87
ED6	3426	1.93	3.03	0.70	1.28	0.22	0.23	62	19-35	23	3.3	0.40	0.73
ED17	3940	14.65	10.37	5.97	3.97	2.22	1.05	186	18-35	27	1.3	0.61	0.55
ED18	4386	5.59	6.13	5.03	2.30	1.90	0.55	83	19-35	27	1.4	0.68	0.44
ED19	5189	22.55	19.12	11.53	8.38	4.70	2.98	254	18-35	29	1.2	0.74	0.36
ED20	5593	6.42	7.12	2.38	2.29	0.93	0.42	199	18-36	25	2.1	0.50	0.66
ED21	6062	4.59	3.81	4.68	1.34	2.12	0.40	51	18-37	27	1.7	0.69	0.43
ED7	6869	39.50	26.69	16.85	12.04	8.27	4.16	422	19-35	27	1.1	0.72	0.41
ED8	7258	22.62	19.55	9.64	7.29	3.80	1.99	249	19-35	27	1.2	0.75	0.36
ED9	7908	3.64	4.48	1.46	1.51	0.51	0.35	64	17-35	27	1.7	0.65	0.49
ED10	8417	4.39	4.31	1.74	1.44	0.62	0.45	62	17-35	27	1.3	0.70	0.42
ED11	8939	1.40	2.79	0.53	1.12	0.17	0.26	29	17-35	29	1.8	0.71	0.39
ED12	9470	0.66	1.44	0.25	0.49	0.13	0.18	17	18-35	27	2.4	0.68	0.45
ED13	9810	0.97	2.25	0.52	0.75	0.17	0.22	24	18-35	29	2.1	0.66	0.45
ED14	10409	0.72	2.03	0.28	0.81	0.08	0.18	18	18-35	29	2.4	0.67	0.43
ED15	10681	0.59	1.80	0.22	0.74	0.08	0.16	15	18-35	29	2.8	0.67	0.43
ED16	11131	2.40	3.06	1.06	1.17	0.40	0.27	44	19-35	27	1.5	0.56	0.57

Concentration = ((area of compound/area of standard) x amount of standard added)/weight of sediment extracted.

CPI (Carbon Preference Index) = $2(C_{23-31}odd)/(C_{22-30}even + C_{24-32}even)$.

P_{wax} (*n*-alkane land plant proxy) = $(C_{27} + C_{29} + C_{31})/(C_{23} + C_{25} + C_{27} + C_{29} + C_{31})$ (Zheng et al., 2007).

P_{alg} (*n*-alkane non-emergent aquatic plant proxy) = $(C_{23} + C_{25})/(C_{23} + C_{25} + C_{29} + C_{31})$ (Ficken et al., 2000).

Raw *n*-alkene data for Lake Edward

Sample ID	Age (cal. yrs. BP)	Weight of sediment extracted (g)	Amount of standard added (µg)	Area of standard	Peak area of *n*-alkene compounds									
					C21	C22	C23	C24	C25	C26	C27	C28	C29	C30
ED1	991	0.2741	24.8	9631002	0	0	0	0	382048	0	2888630	0	0	0
ED2	1436	0.6613	24.8	68807456	0	0	4603464	0	26067324	5816358	179909692	0	0	0
ED3	1945	0.8216	24.8	31458443	0	0	1820082	0	10448893	1755337	74067181	0	0	0
ED4	2420	0.5592	24.8	111494574	0	0	5788749	0	22441630	3468454	151064502	0	0	0
ED5	2931	1.0667	24.8	6684089	0	0	264631	0	658567	0	6382209	0	0	0
ED6	3426	1.41	24.8	70532673	0	0	2189713	0	6753192	1294645	51157127	0	0	0
ED17	3940	0.406	24.8	112739926	0	0	728729	0	2286136	0	19167850	0	0	0
ED18	4386	0.51	24.8	73202696	0	0	281693	0	675066	0	5786600	0	0	8290019
ED19	5189	0.4524	24.8	90574025	0	0	801912	0	905669	0	5719245	0	0	0
ED20	5593	0.3884	24.8	57727248	0	0	14577859	0	6348348	0	15104839	0	0	0
ED21	6062	0.8683	24.8	133398264	1016764	467937	2583262	639038	3481013	1809434	25906720	28612057	11783214	0
ED7	6869	0.9301	24.8	2162231	0	0	0	0	0	0	0	0	0	0
ED8	7258	1.9971	24.8	5276172	0	0	452833	0	646420	0	1958411	0	0	0
ED9	7908	1.7058	24.8	78369557	0	0	2558237	456464	4559243	1350302	23198996	0	0	0
ED10	8417	1.6243	24.8	73053021	0	0	2056729	0	2171415	0	6869434	0	0	0
ED11	8939	1.7821	24.8	104269898	0	0	2860170	0	2789124	0	5066862	0	0	0
ED12	9470	1.6205	24.8	101196642	0	0	1138243	0	2352626	0	16360776	0	7303716	0
ED13	9810	1.4982	24.8	91534252	0	0	1931719	0	4012295	0	5071524	0	0	0
ED14	10409	1.8561	24.8	106665609	0	0	1485789	0	3390327	0	4461736	0	0	0
ED15	10681	1.9775	24.8	139104679	0	0	2277137	0	5200883	0	6271640	0	0	0
ED16	11131	0.5791	24.8	95182197	0	0	520092	0	1004893	0	1122019	0	0	0

Cont.

Sample	Age (cal. yrs. BP)	Concentration of *n*-alkene compounds (µg/g)										*n*-alkenes parameters			
		C21	C22	C23	C24	C25	C26	C27	C28	C29	C30	Total abundance (µg/g)	C no. range	Most abundant C no.	P_{alg}
ED1	991	0.00	0.00	0.00	0.00	3.59	0.00	27.14	0.00	0.00	0.00	30.73	25-27	27	0.16
ED2	1436	0.00	0.00	2.51	0.00	14.21	3.17	98.06	0.00	0.00	0.00	117.94	23-27	27	0.87
ED3	1945	0.00	0.00	1.75	0.00	10.03	1.68	71.07	0.00	0.00	0.00	84.53	23-27	27	0.62
ED4	2420	0.00	0.00	2.30	0.00	8.93	1.38	60.09	0.00	0.00	0.00	72.70	23-27	27	0.87
ED5	2931	0.00	0.00	0.92	0.00	2.29	0.00	22.20	0.00	0.00	0.00	25.41	23-27	27	0.77
ED6	3426	0.00	0.00	0.55	0.00	1.68	0.32	12.76	0.00	0.00	0.00	15.31	23-27	27	0.58
ED17	3940	0.00	0.00	0.39	0.00	1.24	0.00	10.39	0.00	0.00	0.00	12.02	23-27	27	0.26
ED18	4386	0.00	0.00	0.19	0.00	0.45	0.00	3.84	0.00	0.00	5.51	9.99	23-30	30	0.19
ED19	5189	0.00	0.00	0.49	0.00	0.55	0.00	3.46	0.00	0.00	0.00	4.49	23-27	27	0.07
ED20	5593	0.00	0.00	16.12	0.00	7.02	0.00	16.71	0.00	0.00	0.00	39.85	23-27	27	0.58
ED21	6062	0.22	0.10	0.55	0.14	0.75	0.39	5.55	6.13	2.52	0.00	16.34	21-29	28	0.36
ED7	6869	0.00	0.00	0.00	0.00	0.00	0.00	0.00	0.00	0.00	0.00	0.00	–	–	–
ED8	7258	0.00	0.00	1.07	0.00	1.52	0.00	4.61	0.00	0.00	0.00	7.20	23-27	27	0.10
ED9	7908	0.00	0.00	0.47	0.08	0.85	0.25	4.30	0.00	0.00	0.00	5.96	23-27	27	0.28
ED10	8417	0.00	0.00	0.43	0.00	0.45	0.00	1.44	0.00	0.00	0.00	2.32	23-27	27	0.14
ED11	8939	0.00	0.00	0.38	0.00	0.37	0.00	0.68	0.00	0.00	0.00	1.43	23-27	27	0.15
ED12	9470	0.00	0.00	0.17	0.00	0.36	0.00	2.47	0.00	1.10	0.00	4.11	23-29	27	0.39
ED13	9810	0.00	0.00	0.35	0.00	0.73	0.00	0.92	0.00	0.00	0.00	1.99	23-27	27	0.23
ED14	10409	0.00	0.00	0.19	0.00	0.42	0.00	0.56	0.00	0.00	0.00	1.17	23-27	27	0.17
ED15	10681	0.00	0.00	0.21	0.00	0.47	0.00	0.57	0.00	0.00	0.00	1.24	23-27	27	0.20
ED16	11131	0.00	0.00	0.23	0.00	0.45	0.00	0.50	0.00	0.00	0.00	1.19	23-27	27	0.11

Concentration = ((area of compound/area of standard) x amount of standard added)/weight of sediment extracted.

P_{alg} (*n*-alkene algae proxy) = $(C_{23:1} + C_{25:1} + C_{27:1} +)/(C_{23:1} + C_{25:1} + C_{27:1} + C_{29} + C_{31} + C_{33})$ (modified after Zhang et al. (2004)).

Bibliography

Abraham, K., Opfergelt, S., Fripiat, F., Cavagna, A.-J., De Jong, J.T.M., Foley, S.F., André, L., Cardinal, D., 2008. δ^{30}Si and δ^{29}Si Determinations on USGS BHVO-1 and BHVO-2 Reference Materials with a New Configuration on a Nu Plasma Multi-Collector ICP-MS. Geostandards and Geoanalytical Research 32, 193-202.

Abu-Zied, M.A., El-Shibini, F.Z., 1997. Egypt's High Aswan Dam. Water Resources Development 13, 209-217.

Adamson, D.A., Gasse, F., Street, F.A., Williams, M.A.J., 1980. Late Quaternary history of the Nile. Nature 288, 50-55.

Alexandre, A., Bouvet, M., Abbadie, L., 2011. The role of savannas in the terrestrial Si cycle: a case-study from Lamto, Ivory Coast. Global and Planetary Change 78, 162-169.

Alexandre, A., Meunier, J.D., Colin, F., Koud, J.M., 1997. Plant impact on the biogeochemical cycle of silicon and related weathering processes. Geochimica et Cosmochimica Acta 61, 677-682.

Alleman, L.Y., Cardinal, D., Cocquyt, C., Plisnier, P.-D., Descy, J.-P., Kimirei, I., Sinyinza, D., André, L., 2005. Silicon isotopic fractionation in Lake Tanganyika and its main tributaries. Journal of Great Lakes Research 31, 509-519.

Alley, R.B., Mayewski, P.A., Sowers, T., Stuvier, M., Taylor, K.C., Clark, P.U., 1997. Holocene climatic instability: a prominent, widespread event 8200 years ago. Geology 25, 483-486.

Alverson, K.D., Bradley, R.S., Pederson, T.F., 2003. Paleoclimate, Global Change and the Future. Springer-Verlag, New York, p. 220.

André, L., Cardinal, D., Alleman, L.Y., Moorbath, S., 2006. Silicon isotopes in ~3.8 Ga West Greenland rocks as a clue to the Eoarchaean supracrustal Si cycle. Earth and Planetary Science Letters 245, 162-173.

Anyah, R.O., Semazzi, F.H.M., Xie, L., 2006. Simulated physical mechanisms associated with climate variability over Lake Victoria Basin in East Africa. Monthly Weather Review 137, 3588-3609.

Araguás-Araguás, L., Fröhlich, K., Rozanski, K., 2000. Deuterium and oxygen-18 isotope composition of precipitation and atmospheric moisture. Hydrological Processes 14, 1341-1355.

Archer, D., Winguth, A., Lea, D., Mahowald, N., 2000. What caused the glacial/interglacial atmospheric pCO_2 cycles? Reviews of Geophysics 38, 159-189.

Barber, D.C., Dyke, A., Hillaire-Marcel, C., Jennings, A.E., Andrews, J.T., Kerwin, M.W., Bilodeau, G., McNeely, R., Southon, J., Morehead, M.D., Gagnon, J.-M., 1999. Forcing of the cold event of 8,200 years ago by catastrophic drainage of Laurentide lakes. Nature 400, 344-348.

Bard, E., 2002. Climate shock: abrupt climate changes over millennial timescales. Physics Today 55, 32-38.

Bibliography

Bard, E., Rostek, F., Turon, J.-L., Gendreau, S., 2000. Hydrological impact of Heinrich events in the subtropical northeast Atlantic. Science 289, 1321-1324.

Barker, P.A., Hurrell, E.R., Leng, M.J., Wolff, C., Cocquyt, C., Sloane, H.J., Verschuren, D., 2011. Seasonality in equatorial climate over the past 25 k.y. revealed by oxygen isotope records from Mount Kilimanjaro. Geology 39, 1111-1114.

Barker, P.A., Leng, M.J., Gasse, F., Huang, Y., 2007. Century-to-millennial scale climatic variability in Lake Malawi revealed by isotope records. Earth and Planetary Science Letters 261, 93-103.

Barker, P.A., Street-Perrott, F.A., Leng, M.J., Greenwood, P.B., Swain, D.L., Perrott, R.A., Telford, R.J., Ficken, K.J., 2001. A 14,000-year oxygen isotope record from diatom silica in two alpine lakes on Mt. Kenya. Science 292, 2307-2310.

Barker, P.A., Talbot, M.R., Street-Perrott, F.A., Marret, F., Scourse, J., Odada, E.O., 2004. Late Quaternary climatic variability in intertropical Africa, In: Battarbee, R.W., Gasse, F., Stickley, C.E. (Eds.), Past climate variability through Europe and Africa. Springer, Dordrecht, The Netherlands, pp. 117-138.

Barnes, M.A., Barnes, W.C., 1978. Organic compounds in lake sediments, In: Lerman, A. (Ed.), Lakes: Chemistry, Geology, Physics. Springer-Verlag, Berlin, pp. 127-152.

Bartoli, F., 1983. The biogeochemical cycle of silicon in two temperate forest ecosystems. Ecological Bulletin 35, 469-476.

Basile-Doelsch, I., 2006. Si stable isotopes in the Earth's surface: a review. Journal of Geochemical Exploration 88, 252-256.

Berger, A., Loutre, M.F., 1991. Insolation values for the climate of the last 10 million years. Quaternary Science Reviews 10, 297-317.

Berner, E.K., Berner, R.A., 2012. Global Environment: Water, Air, and Geochemical Cycles. Princeton University Press, USA.

Berner, R.A., 1992. Weathering, plants, and the long-term carbon cycle. Geochimica et Cosmochimica Acta 56, 3225-3231.

Berner, R.A., 1994. GEOCARB II: a revised model of atmospheric CO_2 over Phanerozoic time. American Journal of Science 294, 56-91.

Berner, R.A., 1995. Chemical weathering and its effect on atmospheric CO_2 and climate. Reviews in Mineralogy 31, 565-583.

Berner, R.A., 1997. The rise of plants and their effect on weathering and atmospheric CO_2. Science 276, 544-546.

Berner, R.A., Caldeira, K., 2002. The geological carbon cycle and the evolution of atmospheric carbon dioxide, AGU Fall Meeting Abstracts.

Bibliography

Berner, R.A., Lasaga, A.C., Garrels, R.M., 1983. The carbonate-silicate geochemical cycle and its effect on atmospheric carbon dioxide over the past 100 million years. American Journal of Science 283, 641-683.

Beuning, K.R.M., Kelts, K., Ito, E., Johnson, T.C., 1997a. Paleohydrology of Lake Victoria, East Africa, inferred from 18O/16O ratios in sediment cellulose. Geology 25, 1083-1086.

Beuning, K.R.M., Kelts, K., Russell, J., Wolfe, B.B., 2002. Reassessment of Lake Victoria-Upper Nile River paleohydrology from oxygen isotope records of lake-sediment cellulose. Geology 30, 559-562.

Beuning, K.R.M., Russell, J.M., 2004. Vegetation and sedimentation in the Lake Edward Basin, Uganda-Congo during the late Pleistocene and early Holocene. Journal of Paleolimnology 32, 1-18.

Beuning, K.R.M., Talbot, M.R., Kelts, K., 1997b. A revised 30,000-year palaeoclimatic and palaeohydrologic history of Lake Albert, East Africa. Palaeogeography, Palaeoclimatology, Palaeoecology 136, 259–279.

Beuning, K.R.M., Talbot, M.R., Kelts, K., 1997c. A revised 30,000-year paleoclimatic and paleohydrologic history of Lake Albert, East Africa. Palaeogeography, Palaeoclimatology, Palaeoecology 136, 259-279.

Blecker, S.W., McCulley, R.L., Chadwick, O.A., Kelly, E.F., 2006. Biologic cycling of silica across a grassland bioclimosequence. Global Biogeochemical Cycles 20, GB3023.

Bluth, G.J.S., Kump, L.R., 1994. Lithologic and climatologic controls of river chemistry. Geochimica et Cosmochimica Acta 58, 2341-2359.

Bond, G., Heinrich, H., Broecker, W., Labeyrie, L., McManus, J., Andrews, J., Huon, S., Jantschik, R., Clasen, S., Simet, C., Tedesco, K., Kias, M., Bonani, G., Ivy, S., 1992. Evidence for massive discharges of icebergs into the North Atlantic ocean during the last glacial period. Nature 360, 245-249.

Bond, G., Kromer, B., Beer, J., Muscheler, R., Evans, M.N., Showers, W., Hoffmann, S., Lotti-Bond, R., Hajdas, I., Bonani, G., 2001. Persistent solar influence on North Atlantic climate during the Holocene. Nature 294, 2130-2136.

Bootsma, H.A., 2003. Inputs, outputs, and internal cycling of silica in a large, tropical lake. Journal of Great Lakes Research 29, 121-138.

Bradley, R.S., 1999. Paleoclimatology: Reconstructing Climates of the Quaternary. Academic Press, San Diego, USA.

Brady, P.V., Carroll, S.A., 1994. Direct effects of CO_2 and temperature on silicate weathering: possible implications for climate control. Geochimica et Cosmochimica Acta 58, 1853-1856.

Brandriss, M.E., O'Neil, J.R., Edlund, M.B., Stoermer, E.F., 1998. Oxygen isotope fractionation between diatomaceous silica and water. Geochimica et Cosmochimica Acta 62, 1119-1125.

Bibliography

Brantley, S.L., Megonigal, J.P., Scatena, F.N., Balogh-Brunstad, Z., Barnes, R.T., Bruns, M.A., Van Cappellen, P., Dontsova, K., Hartnett, H.E., Hartshorn, A.S., Heimsath, A., Herndon, E., Jin, L., Keller, C.K., Leake, J.R., McDowell, W.H., Meinzer, F.C., Mozdzer, T.J., Petsch, S., Pett-Ridge, J., Pregitzer, K.S., Raymond, P.A., Riebe, C.S., Shumaker, K., Sutton-Grier, A., Walter, R., Yoo, K., 2011. Twelve testable hypotheses on the geobiology of weathering. Geobiology 9, 140-165.

Bray, E.E., Evans, E.D., 1961. Distribution of *n*-paraffins as a clue to recognition of source beds. Geochimica et Cosmochimica Acta 22, 2-15.

Brenner, M., Hodell, D.A., Leyden, B.W., Curtis, J.H., Kenney, W.F., Gu, B., Newman, J.M., 2006. Mechanisms for organic matter and phosphorus burial in sediments of a shallow, subtropical, macrophyte-dominated lake. Journal of Paleolimnology 35, 129-148.

Brewer, T.S., Leng, M.J., Mackay, A.W., Lamb, A.L., Tyler, J.J., Marsh, N.G., 2008. Unravelling contamination signals in biogenic silica oxygen isotope composition: the role of major and trace element geochemistry. Journal of Quaternary Science 23, 321-330.

Camberlin, P., 2009. Nile basin climates, In: Dumont, H.J. (Ed.), The Nile: Origin, Environments, Limnology and Human Use. Springer-Verlag, New York, pp. 307-333.

Cardinal, D., Alleman, L.Y., de Jong, J., Ziegler, K., André, L., 2003. Isotopic composition of silicon measured by multicollector plasma source mass spectrometry in dry plasma mode. Journal of Analytical Atomic Spectrometry 18, 213-218.

Cardinal, D., Gaillardet, J., Hughes, H.J., Opfergelt, S., André, L., 2010. Contrasting silicon isotope signatures in rivers from the Congo Basin and the specific behaviour of organic-rich waters. Geophysical Research Letters 37, L12403.

Castañeda, I.S., Schouten, S., 2011. A review of molecular organic proxies for examining modern and ancient lacustrine environments. Quaternary Science Reviews 30, 2851-2891.

Chapligin, B., Leng, M.J., Webb, E., Alexandre, A., Dodd, J.P., Ijiri, A., LÃ¼cke, A., Shemesh, A., Abelmann, A., Herzschuh, U., Longstaffe, F.J., Meyer, H., Moschen, R., Okazaki, Y., Rees, N.H., Sharp, Z.D., Sloane, H.J., Sonzogni, C., Swann, G.E.A., Sylvestre, F., Tyler, J.J., Yam, R., 2011. Inter-laboratory comparison of oxygen isotope compositions from biogenic silica. Geochimica et Cosmochimica Acta 75, 7242-7256.

Chen, J., Li, J., Tian, S., Kalugin, I., Darin, A., Xu, S., 2012. Silicon isotope composition of diatoms as a paleoenvironmental proxy in Lake Huguangyan, South China. Journal of Asian Earth Sciences 45, 268-274.

Church, M., Burt, T.P., Galay, V.J., Kondolf, G.M., 2011. Rivers, In: Slaymaker, O., Spencer, T., Embleton-Hamann, C. (Eds.), Geomorphology and global environmental change. Cambridge University Press, Cambridge, UK, pp. 98-129.

Clark, D., 1962. The spread of food production in sub-Saharan Africa. The Journal of African History 3, 211-228.

Bibliography

Clark, I.D., Fritz, P., 1997. Environmental isotopes in hydrogeology. CRC Press, Florida.

Clarke, G.K.C., Leverington, D.W., Teller, J.T., Dyke, A.S., 2004. Paleohydraulics of the last outburst flood from glacial Lake Agassiz and the 8200 BP cold event. Quaternary Science Reviews 23, 389-407.

Clayton, R.N., Mayeda, T.K., 1963. The use of bromine pentafluoride in the extraction of oxygen from oxides and silicates from isotopic analysis. Geochimica et Cosmochimica Acta 27, 43-52.

Cochran, M.F., Berner, R.A., 1996. Promotion of chemical weathering by higher plants: field observations on Hawaiian basalts. Chemical Geology 132, 71-77.

Cohen, A.S., Talbot, M.R., Awramik, S.M., Dettman, D.L., Abell, P., 1997. Lake level and palaeoenvironmental history of Lake Tanganyika, Africa, as inferred from late Holocene and modern stromatolites. Geological Society of America Bulletin 109, 444-460.

COHMAP, 1988. Climatic changes of the last 18,000 years: observations and model simulations. Science 241, 1043-1052.

Conley, D.J., 1997. Riverine contribution of biogenic silica to the oceanic silica budget. Limnology and Oceanography 42, 774-777.

Conley, D.J., 1998. An interlaboratory comparison for the measurement of biogenic silica in sediments. Marine Chemistry 63, 39-48.

Conley, D.J., 2002. Terrestrial ecosystems and the global biogeochemical silica cycle. Global Biogeochemical Cycles 16, 68.61-68.68.

Conley, D.J., Schelske, C.L., 2001. Biogenic Silica, In: Smol, J.P., Birks, H.J.B., Last, W.M. (Eds.), Tracking Environmental Change Using Lake Sediments. Kluwer Academic Publishers, Dordrecht, The Netherlands, pp. 281-293.

Conway, D., 1997. A water balance model of the Upper Blue Nile in Ethiopia. Hydrological Sciences-Journal des Sciences Hydrologiques 42, 265-286.

Conway, D., 2000. The climate and hydrology of the upper Blue Nile River. The Geographical Journal 166, 49-62.

Cornelis, J.-T., Delvaux, B., Georg, R.B., Lucas, Y., Ranger, J., Opfergelt, S., 2011. Tracing the origin of dissolved silicon transferred from various soil-plant systems towards rivers: a review. Biogeosciences 8, 89-112.

Cornelis, J.-T., Ranger, J., Iserentant, A., Delvauz, B., 2010a. Tree species impact the terrestrial cycle of silicon through various uptakes. Biogeochemistry 97, 231-245.

Cornelis, J.T., Delvaux, B., Cardinal, D., André, L., Ranger, J., Opfergelt, S., 2010b. Tracing mechanisms controlling the release of dissolved silicon in forest soil solutions using Si isotopes and Ge/Si ratios. Geochimica et Cosmochimica Acta 74, 3913-3924.

Bibliography

Craig, H., 1961. Isotopic variations in meteoric waters. Science 133, 1702-1703.

Craig, H., Gordon, L.I., 1965. Deuterium and oxygen-18 variations in the ocean and marine atmosphere, In: Tongiorgi, E. (Ed.), Stable isotopes in oceanographic studies and paleotemperatures, V. Lischi, Spoleto, Italy, pp. 9-130.

Cranwell, P.A., 1973. Chain-length distribution of *n*-alkanes from lake sediments in relaion to post-glacial environmental change. Freshwater Biology 3, 259-265.

Cranwell, P.A., 1984. Lipid geochemistry of sediments from Upton Broad, a small productive lake. Organic Geochemistry 7, 25-37.

Cranwell, P.A., Eglinton, G., Robinson, N., 1987. Lipids of aquatic organisms as potential contributors to lacustrine sediments. Organic Geochemistry 11, 513-527.

Crul, R.C.M., 1995. Management and Conservation of the African Great Lakes: Lakes Victoria, Tanganyika and Malawi, IHP-IV project M-5-1. UNESCO, p. 107.

Daley, T.J., Thomas, E.R., Holmes, J.A., Street-Perrott, F.A., Chapman, M.R., Tindall, J.C., Valdes, P.J., Loader, N.J., Marshall, J.D., Wolff, E.W., Hopley, P.J., Atkinson, T., Barber, K.E., Fisher, E.H., Robertson, I., Hughes, P.D.M., Roberts, C.N., 2011. The 8200 yr BP cold event in stable isotope records from the North Atlantic region. Global and Planetary Change 79, 288-302.

Dansgaard, W., 1964. Stable isotopes in precipitation. Tellus 16, 436-468.

De La Rocha, C.L., 2002. Measurement of silicon stable isotope natural abundances via multicollector inductively coupled plasma mass spectrometry (MC-ICP-MS). Geochemistry Geophysics Geosystems 3, 1045.

De La Rocha, C.L., Bickle, M.J., 2005. Sensitivity of silicon isotopes to whole-ocean changes in the silica cycle. Marine Geology 217, 267-282.

De La Rocha, C.L., Brzezinski, M.A., DeNiro, M.J., 1996. Purification, recovery, and laser-driven fluorination of silicon from dissolved and particulate silica for the measurement of natural stable isotope abundances. Analytical Chemistry 68, 3746-3750.

De La Rocha, C.L., Brzezinski, M.A., DeNiro, M.J., 1997. Fractionation of silicon isotopes by marine diatoms during biogenic silica formation. Geochimica et Cosmochimica Acta 61, 5051-5056.

De La Rocha, C.L., Brzezinski, M.A., DeNiro, M.J., 2000. A first look at the distribution of the stable isotopes of silicon in natural waters. Geochimica et Cosmochimica Acta 64, 2467-2477.

De La Rocha, C.L., Brzezinski, M.A., DeNiro, M.J., Shemesh, A., 1998. Silicon-isotope composition of diatoms as an indicator of past oceanic change. Nature 395, 680-683.

de Mesmay, R., Grossi, V., Williamson, D., Kajula, S., Derenne, S., 2007. Novel mono-, di- and tri-unsaturated very long chain (C_{37}–C_{43}) *n*-alkenes in alkenone-free lacustrine sediments (Lake Masoko, Tanzania). Organic Geochemistry 38, 323-333.

Bibliography

DeFreitas, A.S.W., McCulloch, A.W., McInnes, A.G., 1991. Recovery of silica from aqueous silicate solutions via trialkyl or tetraalkylammonium silicomolybdate. Canadian Journal of Chemistry 69, 611-614.

Delvigne, C., Opfergelt, S., Cardinal, D., Delvaux, B., André, L., 2009. Distinct silicon and germanium pathways in the soil-plant system: evidence from banana and horsetail. Journal of Geophysical Research 114, G02013.

DeMaster, D.J., 1981. The supply and accumulation of silica in the marine environment. Geochimica et Cosmochimica Acta 45, 1715-1732.

deMenocal, P., Ortiz, J., Guilderson, T., Adkins, J., Sarnthein, M., Baker, L., Yarusinsky, M., 2000a. Abrupt onset and termination of the African Humid Period: rapid climate responses to gradual insolation forcing. Quaternary Science Reviews 19, 347-361.

deMenocal, P., Ortiz, J., Guilderson, T., Sarnthein, M., 2000b. Coherent high- and low-latitude climate variability during the Holocene warm period. Science 288, 2198-2202.

Derry, L.A., Kurtz, A.C., Ziegler, K., Chadwick, O.A., 2005. Biological control of terrestrial silica cycling and export fluxes to watersheds. Nature 433, 728-731.

Derry, L.A., Pett-Ridge, J.C., Kurtz, A.C., Troester, J.W., 2006. Ge/Si and $^{87}Sr/^{86}Sr$ tracers of weathering reactions and hydrologic pathways in a tropical granitoid system. Journal of Geochemical Exploration 88, 271-274.

Dessert, C., Dupré, B., Gaillardet, J., François, L.M., Allègre, C.J., 2003. Basalt weathering laws and the impact of basalt weathering on the global carbon cycle. Chemical Geology 202, 257-273.

Ding, T., Wan, D., Wang, C., Zhang, F., 2004. Silicon isotope compositions of dissolved silicon and suspended matter in the Yangtze River, China. Geochimica et Cosmochimica Acta 68, 205-216.

Ding, T.P., Gao, J.F., Tian, S.H., Wang, H.B., Li, M., 2011. Silicon isotopic composition of dissolves silicon and suspended particulate matter in the Yellow River, China, with implications for the global silicon cycle. Geochimica et Cosmochimica Acta 75, 6672-6689.

Ding, T.P., Jiang, S.Y., Wan, D.F., Li, Y.H., Li, J.C., Song, H.B., Liu, Z.J., Yao, X.M., 1996. Silicon Isotope Geochemistry. Geological Publishing House, Beijing.

Ding, T.P., Tian, S.H., Sun, L., Wu, L.H., Zhou, J.X., Chen, Z.Y., 2008a. Silicon isotope fractionation between rice plants and nutrient solution and its significance to the study of the silicon cycle. Geochimica et Cosmochimica Acta 72, 5600-5615.

Ding, T.P., Zhou, J.X., Wan, D.F., Chen, Z.Y., Wang, C.Y., Zhang, F., 2008b. Silicon isotope fractionation in bamboo and its significance to the biogeochemical cycle of silicon. Geochimica et Cosmochimica Acta 72, 1381-1395.

Douthitt, C.B., 1982. The geochemistry of the stable isotopes of silicon. Geochimica et Cosmochimica Acta 46, 1449-1458.

Bibliography

Drake, N., Bristow, C., 2006. Shorelines in the Sahara: geomorphological evidence for an enhanced monsoon from palaeolake Megachad. The Holocene 16, 901-911.

Drever, J.I., 1994. The effect of land plants on weathering rates of silicate minerals. Geochimica et Cosmochimica Acta 58, 2325-2332.

Dugdale, R.C., Wilkerson, F.P., 2001. Sources and fates of silicon in the ocean: the role of diatoms in the climate and glacial cycles. Scientia Marina 65, 141-152.

Dupré, B., Dessert, C., Oliva, P., Goddéris, Y., Viers, J., François, L., Millot, R., Gaillardet, J., 2003. Rivers, chemical weathering and Earth's climate. Comptes Rendus Geoscience 335, 1141-1160.

Egan, K.E., Rickaby, R.E.M., Leng, M.J., Hendry, K.R., Hermoso, M., Sloane, H.J., Bostock, H., Halliday, A.N., 2012. Diatom silicon isotopes as a proxy for silicic acid utilisation: a Southern Ocean core top calibration. Geochimica et Cosmochimica Acta in press.

Eglinton, G., Hamilton, R.J., 1967. Leaf epicuticular waxes. Science 156, 1322-1335.

El-Shabrawy, G.M., Dumont, H.J., 2009. The Fayum Depression and its lakes, In: Dumont, H.J. (Ed.), The Nile: Origin, Environments, Limnology and Human Use. Springer-Verlag, New York, pp. 95-124.

Elliot, M., Labeyrie, L., Bond, G., Cortijo, E., Turon, J.-L., Tisnerat, N., Duplessy, J.-C., 1998. Millennial-scale iceberg discharges in the Irminger Basin during the last glacial period: relationship with the Heinrich events and environmental settings. Paleoceanography 13, 433-446.

Engström, E., Rodushkin, I., Baxter, D.C., Öhlander, B., 2006. Chromatographic Purification for the Determination of Dissolved Silicon Isotopic Compositions in Natural Waters by High-Resolution Multicollector Inductively Coupled Plasma Mass Spectrometry. Analytical Chemistry 78, 250-257.

Engström, E., Rodushkin, I., Ingri, J., Baxter, D.C., Ecke, F., Österlund, H., Öhlander, B., 2010. Temporal isotopic variations of dissolved silicon in a pristine boreal river. Chemical Geology 271, 142-152.

Epstein, E., 1994. The anomaly of silicon in plant biology. Proceedings of the National Academy of Sciences of the USA 91, 11-17.

Epstein, E., 1999. Silicon. Annual Review of Plant Physiology and Plant Molecular Biology 50, 641-664.

Eugster, H.P., Hardie, L.A., 1978. Chapter 8: Saline Lakes, In: Lerman, A. (Ed.), Lakes: Chemistry, Geology, Physics. Springer-Verlag, New York, pp. 237-293.

Exley, C., 1998. Silicon in life: a bioinorganic solution to bioorganic essentiality. Journal of Inorganic Biochemistry 69, 139-144.

Ficken, K.J., Li, B., Swain, D.L., Eglinton, G., 2000. An *n*-alkane proxy for the sedimentary input of submerged/floating freshwater aquatic macrophytes. Organic Geochemistry 31, 745-749.

Bibliography

Ficken, K.J., Street-Perrott, F.A., Perrott, R.A., Swain, D.L., Olago, D.O., Eglinton, G., 1998. Glacial/interglacial variations in carbon cycling revealed by molecular and isotope stratigraphy of Lake Nkunga, Mt. Kenya, East Africa. Organic Geochemistry 29, 1701-1719.

Filippelli, G.M., Carnahan, J.W., Derry, L.A., Kurtz, A.C., 2000. Terrestrial records of Ge/Si cycling derived from lake diatoms. Chemical Geology 168, 9-26.

Flohn, H., Fraedrich, K., 1966. Tagesperiodische Zirkulation und Niederschlagsverteilung am Viktoria-See (Ostafrika). Meteorologische Rundschau 19, 157-165.

Flower, R.J., Stickley, C., Rose, N.L., Peglar, S., Fathi, A.A., Appleby, P.G., 2006. Environmental changes at the desert margin: an assessment of recent paleolimnological records in Lake Qarun, Middle Egypt Journal of Paleolimnology 35, 1-24.

Foucault, A., Stanley, D.J., 1989. Late quaternary palaeoclimatic oscillations in East Africa recorded by heavy minerals in the nile delta. Nature 339, 44-46.

Fritz, P., 1981. River waters, In: Gat, J.R., Gonfiantini, R. (Eds.), Stable Isotope Hydrology: Deuterium and Oxygen-18 in the Water Cycle. IAEA Technical Report Series 210, pp. 177-201.

Froelich, P.N., Blanc, V., Mortlock, R.A., Chillrud, S.N., Dunstan, W., Udomkit, A., Peng, T.-H., 1992. River fluxes of dissolved silica to the ocean were higher during glacials: Ge/Si in diatoms, rivers and oceans. Paleoceanography 7, 739-767.

Fröhlich, K., Gibson, J.J., Aggarwal, P.K., 2002. Deuterium excess in precipitation and its climatological significance, Study of Environmental Change using Isotope Techniques. International Atomic Energy Agency, International Conference in Vienna, Austria, 23–27 April 2001, pp. 54-65.

Fulweiler, R.W., Nixon, S.W., 2005. Terrestrial vegetation and the seasonal cycle of dissolved silica in a southern New England coastal river. Biogeochemistry 74, 115-130.

Furon, R., 1958. Esquisse Structurale Provisoire de l'Afrique, 1 : 10,000,000. Association des Services Geologiques Africains (ASGA) Congrès Géologique International.

Gaillardet, J., Dupré, B., Louvat, P., Allègre, C.J., 1999. Global silicate weathering and CO_2 consumption rates deduced from the chemistry of large rivers. Chemical Geology 159, 3-30.

Gao, J., Ding, T., Tian, S., 2006. Silicon isotope composition of dissolved silicon and suspended matter in the yellow river, China. Geochimica et Cosmochimica Acta 70, A192.

Garcin, Y., Vincens, A., Williamson, D., Buchet, G., Guiot, J., 2007. Abrupt resumption of the African Monsoon at the Younger Dryas-Holocene climatic transition. Quaternary Science Reviews 26, 690-704.

Bibliography

Gasse, F., 2000. Hydrological changes in the African tropics since the Last Glacial Maximum. Quaternary Science Reviews 19, 189-211.

Gasse, F., 2002. Diatom-inferred salinity and carbonate oxygen isotopes in Holocene waterbodies of the western Sahara and Sahel (Africa). Quaternary Science Reviews 21, 737-767.

Gasse, F., Chalié, F., Vincens, A., Williams, M.A.J., Williamson, D., 2008. Climatic patterns in equatorial and southern Africa from 30,000 to 10,000 years ago reconstructed from terrestrial and near-shore proxy data. Quaternary Science Reviews 27, 2316-2340.

Gasse, F., Juggins, S., Khelifa, L.B., 1995. Diatom-based transfer functions for inferring past hydrochemical chacteristics of African lakes. Palaeogeography, Palaeoclimatology, Palaeoecology 117, 31-54.

Gat, J.R., 1996. Oxygen and hydrogen isotopes in the hydrological cycle. Annual Review of Earth and Planetary Science 24, 225-262.

Gat, J.R., 2000. Atmospheric water balance-the isotopic perspective. Hydrological Processes 14, 1357-1369.

Gat, J.R., Bowser, C.J., Kendall, C., 1994. The contribution of evaporation from the Great Lakes to the continental atmosphere: estimate based on stable isotope data. Geophysical Research Letters 21, 557-560.

Gat, J.R., Matsui, E., 1991. Atmospheric water balance in the Amazon Basin: an isotopic evapotranspiration model. Journal of Geophysical Research 96, 13,179-113,188.

Gaudet, J.J., 1977. Uptake, accumulation, and loss of nutrients by papyrus in tropical swamps. Ecology 58, 415-422.

Georg, R.B., Reynolds, B.C., Frank, M., Halliday, A.N., 2006a. Mechanisms controlling the silicon isotopic compositions of river waters. Earth and Planetary Science Letters 249, 290-306.

Georg, R.B., Reynolds, B.C., Frank, M., Halliday, A.N., 2006b. New sample preparation techniques for the determination of Si isotopic compositions using MC-ICPMS. Chemical Geology 235, 95-104.

Georg, R.B., Reynolds, B.C., West, A.J., Burton, K.W., Halliday, A.N., 2007. Silicon isotope variations accompanying basalt weathering in Iceland. Earth and Planetary Science Letters 261, 476–490.

Georg, R.B., West, A.J., Basu, A.R., Halliday, A.N., 2009. Silicon fluxes and isotope composition of direct groundwater discharge into the Bay of Bengal and the effect on the global ocean silicon isotope budget. Earth and Planetary Science Letters 283, 67–74.

Gérard, F., Mayer, K.U., Hodson, M.J., Ranger, J., 2008. Modelling the biogeochemical cycle of silicon in soils: Application to a temperate forest ecosystem. Geochimica et Cosmochimica Acta 72, 741-758.

Bibliography

Gibson, J.J., Fekete, B.M., Bowen, G.J., 2010. Stable isotopes in large scale hydrological applications, In: West, J.B., Bowen, G.J., Dawson, T.E., Tu, K.P. (Eds.), Isoscapes: Understanding movement, pattern, and process on Earth through isotope mapping. Springer, pp. 389-405.

Goldman, C.R., Horne, A.J., 1983. Limnology. McGraw-Hill, Japan.

Gonfiantini, R., Roche, M.-A., Olivry, J.-C., Fontes, J.-C., Zuppi, G.M., 2001. The altitude effect on the isotopic composition of tropical rains. Chemical Geology 181, 147-167.

Goudie, A.S., 2004. Encyclopedia of Geomorphology,1. Routledge, London.

Green, J., 2009. Nilotic Lakes of the Western Rift, In: Dumont, H.J. (Ed.), The Nile: Origin, Environments, Limnology and Human Use. Springer Science + Business Media B.V., pp. 263-286.

Green, J., El-Moghraby, A.I., 2009. Swamps of the upper White Nile, In: Dumont, H.J. (Ed.), The Nile: Origin, Environments, Limnology and Human Use. Springer Science + Business Media B.V., pp. 193-204.

Griffiths, J.F., 1972. Climates of Africa. Elsevier, Amsterdam.

Haberyan, K.A., Hecky, R.E., 1987. The Late Pleistocene and Holocene stratigraphy and palaeolimnology of lakes Kivu and Tanganyika. Palaeogeography, Palaeoclimatology, Palaeoecology 61, 169-197.

Hall, A., Valente, I.M.C.B.S., Davies, B.R., 1977. The Zambezi river in Moçambique: the physico- chemical status of the middle and lower Zambezi prior to the closure of the Cabora Bassa Dam. Freshwater Biology 7, 187-206.

Harrison, K.G., 2000. Role of increased marine silica input on paleo-pCO_2 levels. Paleoceanography 15, 292-298.

Harvey, T.J., 1976. The paleolimnology of Lake Mobutu Sese Seko, Uganda-Zaire: the last 28,000 years. Ph.D Thesis: Duke University, Durham, USA.

Hassan, F., 1986. Holocene lakes and prehsitoric settlements of the Western Faiyum, Egypt. Journal of Archaeological Science 13, 483-501.

Hassan, F.A., 1997. The dynamics of a riverine civilization: a geoarchaeological perspective on the Nile Valley, Egypt. World Archaeology 29, 51-74.

Hays, J.D., Imbrie, J., Shackleton, N.J., 1976. Variations in the Earth's Orbit: Pacemaker of the Ice Ages. Science 194, 1121-1132.

Hecky, R.E., Bootsma, H.A., Mugidde, R.M., Bugenyi, F.W.B., 1996. Phosphorous pumps, nitrogen sinks and silicon drains: plumbing nutrients in the African Great Lakes, In: Johnson, T.C., Odada, E.O. (Eds.), Limnology, climatology and paleoclimatology of the East African lakes. Gordon and Breach Publishers, Amsterdam, pp. 205-224.

Hecky, R.E., Degans, E.T., 1973. Late Pleistocene-Holocene Chemical Stratigraphy and Paleolimnology of the Rift Valley Lakes of Central Africa, Woods Hole

Oceanographic Institution Technical Report, WHOI-73-28. Woods Hole Oceanographic Institution, Woods Hole, Massachusetts, p. 133.

Hecky, R.E., Kling, H.J., 1987. Phytoplankton ecology of the great lakes in the rift valleys of Central Africa. Archive für Hydrobiologie Beihefte Ergebnisse der Limnologie 25, 197-228.

Hemming, S.R., 2004. Heinrich events: massive late Pleistocene detritus layer of the North Atlantic and their global climate imprint. Review of Geophysics 42, 1-43.

Hernández, A., Bao, R., Giralt, S., Barker, P.A., Leng, M.J., Sloane, H.J., Sáez, A., 2011. Biogeochemical processes controlling oxygen and carbon isotopes of diatom silica in Late Glacial to Holocene lacustrine rhythmites. Palaeogeography, Palaeoclimatology, Palaeoecology 299, 413-425.

Hernández, A., Giralt, S., Bao, R., Sáez, A., Leng, M.J., Barker, P.A., 2010. ENSO and solar activity signals from oxygen isotopes in diatom silica during late glacial-Holocene transition in Central Andes (18°S). Journa l of Paleolimnology 44, 413-429.

Hilley, G., Porder, S., 2008. A framework for predicting global silicate weathering and CO_2 drawdown rates over geologic time-scales. Proceedings of the National Academy of Sciences of the United States of America 105, 16855-16859.

Hinsinger, P., Barros, O.N.F., Benedetti, M.F., Noack, Y., Callot, G., 2001. Plant-induced weathering of a basaltic rock: experimental evidence. Geochimica et Cosmochimica Acta 65, 137-152.

Hodson, M.J., White, P.J., Mead, A., Broadley, M.R., 2005. Phylogenetic variation in the silicon composition of plants. Annals of Botany 96, 1027-1046.

Huang, Y., Street-Perrott, F.A., Perrott, R.A., Metzger, P., Eglington, G., 1999. Glacial–interglacial environmental changes inferred from molecular and compound-specific δ13C analyses of sediments from Sacred Lake, Mt. Kenya. Geochimica et Cosmochimica Acta 63, 1383-1404.

Hughes, H.J., Bouillon, S., André, L., Cardinal, D., 2012. The effects of weathering variability and anthropogenic pressures upon silicon cycling in an intertropical watershed (Tana River, Kenya). Chemical Geology 308-309, 18-25.

Hughes, H.J., Delvigne, C., Korntheuer, M., de Jong, J., Andre, L., Cardinal, D., 2011. Controlling the mass bias introduced by anionic and organic matrices in silicon isotopic measurements by MC-ICP-MS. Journal of Analytical Atomic Spectrometry 26, 1892-1896.

Hughes, R.H., Hughes, J.S., 1992. A Directory of African wetlands. IUCN, Gland, Switzerland and Cambridge, UK / UNEP, Nairobi, Kenya / WCMC, Cambridge, UK.

Hurst, H.E., 1952. The Nile: a general account of the river and utilization of its waters. Constable, London.

Imbrie, J., Imbrie, K.P., 1979. Ice Ages: Solving the Mystery. Macmillan, London.

Jankovská, V., Komárek, J., 2000. Indicative value of pediastrum and other coccal green algae in palaeoecology. Folia Geobotanica 35, 59-82.

Bibliography

Johnson, T.C., 1996. Sedimentary processes and signals of past climatic changes in the large lakes of the East African Rift Valley, In: Johnson, T.C., Odada, E.O. (Eds.), The Limnology, Climatology and Paleoclimatology of the East African Lakes. Gordon and Breach Publishers, Amsterdam, The Netherlands, pp. 367-412.

Johnson, T.C., Barry, S.L., Chan, Y., Wilkinson, P., 2001. Decadal record of climate variability spanning the past 700 yr in the Southern Tropics of East Africa. Geology 29, 83-86.

Johnson, T.C., Brown, E.T., McManus, J., Barry, S., Barker, P., Gasse, F., 2002. A high-resolution paleoclimate record spanning the past 25,000 years in southern East Africa. Science 296, 113-132.

Johnson, T.C., Brown, E.T., Shi, J., 2011. Biogenic silica deposition in Lake Malawi, East Africa over the past 150,000 years. Palaeogeography, Palaeoclimatology, Palaeoecology 303, 103-109.

Johnson, T.C., Chan, Y., Beuning, K., Kelts, K., Ngobi, G., Verschuren, D., 1998. Biogenic silica profiles in Holocene cores from Lake Victoria: implications for lake level history and initiation of the Victoria Nile, In: Lehman, J.T. (Ed.), Environmental Change and Response in East African Lakes. Kluwer Press, Amsterdam, pp. 75-88.

Johnson, T.C., Kelts, K., Odada, E., 2000. The Holocene history of Lake Victoria. Ambio 29, 2-11.

Johnson, T.C., Scholz, C.A., Talbot, M., Kelts, K., Ricketts, R.D., Ngobi, G., Beuning, K., Ssemmanda, I., McGill, J.W., 1996. Late Pleistocene desiccation of Lake Victoria and rapid evolution of cichlid fishes. Science 273, 1091-1093.

Jolly, D., Harrison, S.P., Damnati, B., Bonnefille, R., 1998. Simulated climate and biomes of Africa during the late quaternary: comparison with pollen and lake status data. Quaternary Science Reviews 17, 629-657.

Jolly, D., Taylor, D., Marchant, R., Hamilton, A., Bonnefille, R., Buchet, G., Riollet, G., 1997. Vegetation dynamics in central Africa since 18,000 yr BP: pollen records from the interlacustrine of Burundi, Rwanda and western Uganda. Journal of Biogeography 24, 495-512.

Jones, L.H.P., Handreck, K.A., 1967. Silica in soils, plants and animals. Advances in Agronomy 19, 107-149.

Joussaume, S., Taylor, K.E., Braconnot, P., Mitchell, J.F.B., Kutzbach, J.E., Harrison, S.P., Prentice, I.C., Broccoli, A.J., Abe, O.-A., Bartlein, P.J., Bonfils, C., Dong, B., Guiot, J., Herterich, K., Hewitt, C.D., Jolly, D., Kim, J.W., Kislov, A., Kitoh, A., Loutre, M.F., Masson, V., McAvaney, B., McFarlane, N., De, N.-N., Peitier, W.R., Peterschmitt, J.Y., Pollard, D., Rind, D., Royer, J.F., Schlesinger, M.E., Syktus, J., Thompson, S., Valdes, P., Vettoretti, G., Webb, R.S., Wyputta, U., 1999. Monsoon changes for 6000 years ago: results of 18 simulations from the Paleoclimate Modeling Intercomparison Project (PMIP). Geophysical Research Letters 26, 859-862.

Jouzel, J., Merlivat, L., 1984. Deuterium and oxygen 18 in precipitation: modeling of the isotopic effects during snow formation. Journal of Geophysical Research 89, 11749-11757.

Kebede, S., Travi, Y., 2012. Origin of the $\delta^{18}O$ and $\delta^{2}H$ composition of meteoric waters in Ethiopia. Quaternary International 257, 4-12.

Kebede, S., Travi, Y., Alemayehu, T., Ayenew, T., 2005. Groundwater recharge, circulation and geochemical evolution in the source region of the Blue Nile River, Ethiopia. Applied Geochemistry 20, 1658-1676.

Kebede, S., Travi, Y., Alemayehu, T., Marc, V., 2006. Water balance of Lake Tana and its sensitivity to fluctuations in rainfall, Blue Nile basin, Ethiopia. Journal of Hydrology 316, 233-247.

Kelly, E.F., Chadwick, O.A., Hilinski, T.E., 1998. The effect of plants on mineral weathering. Biogeochemistry 42, 21-53.

Kelts, K., Briegel, U., Ghilardi, K., Hsu, K., 1986. The limnogeology-ETH coring system. Schweizerische Zeitschrift für Hydrologie 48, 104-115.

Kelts, K., Hsü, K.J., 1978. Freshwater carbonate sedimentation, In: Lerman, A. (Ed.), Lakes: Chemistry, Geology, Physics. Springer-Verlag, New York, pp. 295-323.

Kendall, R.L., 1969. An ecological history of the Lake Victoria basin. Ecological Monographs 39, 121-176.

Kiage, L.M., Liu, K.-B., 2006. Late Quaternary paleoenvironmental changes in East Africa: a review of multiproxy evidence from palynology, lake sediments, and associated records. Progress in Physical Geography 30, 633-658.

Kilham, P., Kilham, S.S., 1990. Endless summer: internal loading processes dominate nutrient cycling in tropical lakes. Freshwater Biology 23, 379-389.

Kilham, P., Kilham, S.S., Hecky, R.E., 1986. Hypothesized resource relationships amoung African planktonic diatoms. Limnology and Oceanography 31, 1169-1181.

Killops, A., Killops, V., 2005. Introduction to Organic Geochemistry. Blackwell Publishing, UK.

Knoll, M.A., James, W.C., 1987. Effect of the advent and diversification of vascular land plants on mineral weathering through geologic time. Geology 15, 1099-1102.

Kochian, L.V., 2012. Plant nutrition: rooting for more phosphorus. Nature 488, 466-467.

Komárek, J., Jankovská, V., 2001. Review of the green algal genus *Pediastrum*: implication for pollen-analytical research. Bibliotheca Phycologica 108, 1-127.

Krausse, G.L., Schelske, C.L., Davis, C.O., 1983. Comparision of three wet-alkaline methods of digestion of biogenic silica in water. Freshwater Biology 13, 73-81.

Kump, L.R., Brantley, S.L., Arthur, M.A., 2000. Chemical weathering, atmospheric CO_2 and climate. Annual Review of Earth and Planetary Sciences 28, 611-667.

Kurtz, A.C., Derry, L.A., 2004. Tracing silicate weathering and terrestrial silica cycling with Ge/Si ratios, In: Wanty, R.B., Seal, R.R. (Eds.), Proceedings of the 11th

International Symposium on Water Rock Interaction. A.A. Balkema Publishers, Rotterdam, pp. 833-836.

Kurtz, A.C., Derry, L.A., Chadwick, O.A., 2002. Germanium-silicon fractionation in the weathering environment. Geochimica et Cosmochimica Acta 66, 1525-1537.

Kutzbach, J.E., Bonan, G., Foley, J., Harrison, S.P., 1996. Vegetation and soil feedbacks on the response of the African monsoon to orbital forcing in the early to middle Holocene. Nature 384, 623-626.

Kutzbach, J.E., Guetter, P.J., 1986. The influence of changing orbital parameters and surface boundary conditions on climate stimulations for the past 18000 years. Journal of Atmospheric Sciences 43, 1726-1759.

Kutzbach, J.E., Liu, Z., 1997. Response of the African monsoon to orbital forcing and ocean feedbacks in the middle Holocene. Science 278, 440-443.

Kutzbach, J.E., Street-Perrott, F.A., 1985. Milankovitch forcing of fluctuations in the level of tropical lakes from 18 to 0 kyr BP. Nature 317, 130-134.

Lærdal, T., Talbot, M.R., 2002. Basin neotectonics of Lakes Edward and George, East African Rift. 187, 213-232.

Lærdal, T., Talbot, M.R., Russell, J.M., 2002. Late Quaternary sedimentation and climate in the Lakes Edward and George area, Uganda-Congo, In: Odada, E.O., Olago, D.O. (Eds.), The East African Great Lakes: Limnology, Palaeolimnology and Biodiversity. Springer, Netherlands, pp. 429-470.

Lamb, H.F., Bates, C.R., Coombes, P.V., Marshall, M.H., Umer, M., Davies, S.J., Dejen, E., 2007. Late Pleistocene desiccation of Lake Tana, source of the Blue Nile. Quaternary Science Reviews 26, 287-299.

Langdale-Brown, I., Osmaston, H.A., J.G., W., 1964. The Vegetation of Uganda and its Bearing on Land Use. Government of Uganda, Entebbe.

Laruelle, G.G., Roubeix, V., Sferratore, A., Brodherr, B., Ciuffa, D., Conley, D.J., Dürr, H.H., Garnier, J., Lancelot, C., Le Thi Phuong, Q., Meunier, J.-D., Meybeck, M., Michalopoulos, P., Moriceau, B., Ní Longphuirt, S., Loucaides, S., Papush, L., Presti, M., Ragueneau, O., Regnier, P., Saccone, L., Slomp, C.P., Spiteri, C., Van Cappellen, P., 2009. Anthropogenic perturbations of the silicon cycle at the global scale: key role of the land-ocean transition. Global Biogeochemical Cycles 23, GB4031.

Last, W.M., Smol, J.P., 2001. Tracking Environmental Change Using Lake Sediments,Volume 1: Basin Analysis, Coring, and Chronological Techniques. Kluwer Academic Publishers, Dordrecht, The Netherlands, p. 548.

Lehman, J.T., 2002. Application of satellite AVHRR to water balance, mixing dynamics, and the chemistry of Lake Edward, East Africa, In: Odada, E.O., Olago, D. (Eds.), The East African Great Lakes: Limnology, palaeolimnology and biodiversity. Kluwer Academic Publishers, The Netherlands, pp. 235-260.

Bibliography

Leng, M.J., Barker, P.A., 2006. A review of the oxygen isotope composition of lacustrine diatom silica for palaeoclimate reconstruction. Earth Science Reviews 75, 5-27.

Leng, M.J., Marshall, J.D., 2004. Palaeoclimate interpretation of stable isotope data from lake sediment archives. Quaternary Science Reviews 23, 811-831.

Leng, M.J., Sloane, H.J., 2008. Combined oxygen and silicon isotope analysis of biogenic silica. Journal of Quaternary Science 23, 313-319.

Leng, M.J., Swann, G.E.A., 2010. Stable isotopes in diatom silica, In: Smol, J.P., Stoermer, E.F. (Eds.), The Diatoms: Applications for the Environmental and Earth Sciences. Cambridge University Press, Cambridge, UK, pp. 127-143.

Leng, M.J., Swann, G.E.A., Hodson, M.J., Tyler, J.J., Patwardhan, S.V., Sloane, H.J., 2009. The potential use of silicon isotope composition of biogenic silica as a proxy for environmental change. Silicon 1, 65-77.

Levin, N.E., Zipser, E.J., Cerling, T.E., 2009. Isotopic composition of waters from Ethiopia and Kenya: Insights into moisture sources for eastern Africa. Journal of Geophysical Research 114, D23306.

Livingstone, D., 1967. Postglacial vegetation of the Ruwenzori Mountains in equatorial Africa. Ecological Monographs 37, 25-52.

Livingstone, D.A., 1975. Late Quaternary climatic change in Africa. Annual Review of Ecology and Systematics 6, 249-280.

Loughnan, F.C., 1969. Chemical Weathering of the Silicate Minerals. American Elsevier Publishing Company, New York.

Lovering, T.S., 1959. Significance of accumulator plants in rock weathering. Bulletin of the Geological Society of America 70, 781-800.

Lucas, Y., 2001. The role of plants in controlling rates and products of weathering: importance of biological pumping. Annual Review of Earth and Planetary Sciences 29, 135-163.

Lucas, Y., Luizão, F.J., Chauvel, A., Rouiller, J., Nahon, D., 1993. The relation between biological activity of the rain forest and mineral composition of soils. Science 260, 521-523.

Lugolobi, F., Kurtz, A.C., Derry, L.A., 2010. Germanium–silicon fractionation in a tropical, granitic weathering environment. Geochimica et Cosmochimica Acta 74, 1294-1308.

Ma, J.F., Miyake, Y., Takahashi, E., 2001. Silicon as a beneficial element for crop plants, In: Datnoff, L.E., Snyder, G.H., Korndörfer, G.H. (Eds.), Silicon in Agriculture. Elsevier, Amsterdam, pp. 17-39.

Ma, J.F., Yamaji, N., 2006. Silicon uptake and accumulation in higher plants. Trends in Plant Science 11, 392-397.

Bibliography

Marchant, R., Taylor, D., 1997. Late Pleistocene and Holocene history at Mubwindi Swamp, southwest Uganda. Quaternary Research 47, 316–328.

Markewitz, D., Richter, D.D., 1998. The *bio* in aluminium and silicon geochemistry. Biogeochemistry 42, 235-252.

Marschner, H., 1995. Mineral Nutrition of Higher Plants, 2nd ed. Academic Press, London.

Matsumoto, G.I., Akiyama, M., Watanuki, K., Torii, T., 1990. Unusual distributions of long-chain *n*-alkanes and *n*-alkenes in Antarctic soil. Organic Geochemistry 15, 403-412.

Mayaux, P., Bartholomé, E., Cabral, A., Cherlet, M., Defourny, P., Di Gregorio, A., Diallo, O., Massart, M., Nonguierma, A., Pekel, J.-F., Pretorius, C., Vancutsem, C., Vasconcelos, M., 2003. The land cover map for Africa in the year 2000. http://www-gem.jrc.it/glc2000, accessed on

McCarthy, T.S., McIver, J.R., Cairncross, B., Ellery, W.N., Ellery, K., 1989. The inorganic geochemistry of peat from the Maunachira channel swamp system, Okavango Delta, Botswana. Geochimica et Cosmochimica Acta 53, 1077-1089.

McLachlan, A.J., 1970. Submerged trees as a substrate for benthic fauna in the recently created Lake Kariba (Central Africa). Journal of Applied Ecology 7, 253-266.

McManus, J.F., Francois, R., Gherardi, J.-M., Keigwin, L.D., Brown-Leger, S., 2004. Collapse and rapid resumption of Atlantic meridional circulation linked to deglacial climate changes. Nature 428, 834-837.

Merlivat, L., Jouzel, J., 1979. Global climatic interpretation of the deuterium-oxygen 18 relationship for precipitation. Journal of Geophysical Research 84, 5029-5033.

Meyers, P.A., 1997. Organic geochemical proxies of paleoceanographic, paleolimnologic and paleoclimatic processes. Organic Geochemistry 27, 213-250.

Meyers, P.A., Ishiwatari, R., 1993. Lacustrine organic geochemistry: an overview of indicators of organic matter sources and diagenesis in lake sediments. Organic Geochemistry 20, 867-900.

Milligan, A.J., Varela, D.E., Brzezinski, M.A., Morel, F.M.M., 2004. Dynamics of silicon metabolism and silicon isotopic discrimination in a marine diatom as a function of pCO_2. Limnology and Oceanography 49, 322–329.

Mohamed, Y.A., van den Hurk, B.J.J.M., Savenije, H.H.G., Bastiaanssen, W.G.M., 2005. Impact of the Sudd wetland on the Nile hydroclimatology. Water Resources Research 41, W08420.

Morley, D.W., Leng, M.J., Mackay, A.W., Sloane, H.J., Rioual, P., Battarbee, R.W., 2004. Cleaning lake sediment samples for diatom oxygen isotope analysis. Journal of Paleolimnology 31, 391-401.

Bibliography

Moschen, R., Lücke, A., Schleser, G.H., 2005. Sensitivity of biogenic silica oxygen isotopes to changes in surface water temperature and palaeoclimatology. Geophysical Research Letters 32, L07708.

Moulton, K.L., West, J., Berner, R.A., 2000. Solute flux and mineral mass balance approaches to the quantification of plant effects on silicate weathering. American Journal of Science 300, 539-570.

Murnane, R.J., Stallard, R.F., 1990. Germanium and silicon in rivers of the Orinoco drainage basin. Nature 344, 749-752.

Nelson, D.M., Tréguer, P., Brzezinski, M.A., Leynaert, A., Quéguiner, B., 1995. Production and dissolution of biogenic silica in the ocean: Revised global estimates, comparison with regional data and relationship to biogenic sedimentation. Global Biogeochemical Cycles 9, 359-372.

Ngobi, G.N., Kelts, K., Johnson, T.C., Solheid, P.A., 1998. Environmental magnetism of Late Pleistocene/Holocene sequences from Lake Victoria, East Africa, In: Lehman, J.T. (Ed.), Environmental Change and Response in East African Lakes. Kluwer Press, Amsterdam, pp. 59-73.

Nicholson, S.E., 1996. A review of climate dynamics and climate variability in Eastern Africa, In: Johnson, T.C., Odada, E.O. (Eds.), The Limnology, Climatology and Paleoclimatology of the East African Lakes. Gordon and Breach Publishers, Amsterdam, The Netherlands, pp. 25-56.

Nicholson, S.E., 1998. Historical fluctuations of Lake Victoria and other lakes in the northern rift valley of East Africa, In: Lehman, J.T. (Ed.), Environmental change and response in East African lakes. Kluwer Academic Publishers, The Netherlands, pp. 7-35.

Nicholson, S.E., Yin, X., 2002. Mesoscale patterns of rainfall, cloudiness and evaporation over the Great Lakes of East Africa, In: Odada, E.O., Olago, D.O. (Eds.), The East African Great Lakes: Limnology, Palaeolimnology and Biodiversity. Kluwer, Dordrecht, pp. 93–119.

Nicholson, S.E., Yin, X., Ba, M.B., 2000. On the feasibility of using a lake water balance model to infer rainfall: an example from Lake Victoria. Hydrological Sciences-Journal des Sciences Hydrologiques 45, 75-95.

Nyssen, J., Vandenreyken, H., Poesen, J., Moeyersons, J., Deckers, J., Haile, M., Salles, C., Govers, G., 2005. Rainfall erosivity and variability in the Northern Ethiopian Highlands. Journal of Hydrology 311, 172-187.

Ogallo, L.J., 1988. Relationships between seasonal rainfall in east Africa and the Southern Oscillation. Journal of Climatology 8, 31-43.

Okonga, J.R., Sewagudde, S.M., Mngodo, R.J., Sangale, F.D., Mwanuzi, F.L., Hecky, R.E., 2006. Water balance of Lake Victoria, In: Odada, E.O., Olago, D.O. (Eds.), Proceedings of the 11th World Lakes Conference, Nairobi, Kenya, pp. 47-56.

Opfergelt, S., Delvaux, B., André, L., Cardinal, D., 2008. Plant silicon isotopic signature might reflect soil weathering degree. Biogeochemistry 91, 163-175.

Opfergelt, S., Eiriksdottir, E.S., Burton, K.W., Einarsson, A., Siebert, C., Gislason, S.R., Halliday, A.N., 2011. Quantifying the impact of freshwater diatom productivity on silicon isotopes and silicon fluxes: Lake Myvatn, Iceland. Earth and Planetary Science Letters 305, 73–82.

Pachur, H.-J., Kröpelin, S., 1987. Wadi Howar: paleoclimatic evidence from an extinct river system in the southeastern Sahara. Science 237, 298-300.

Peters, K.E., Walters, C.C., Moldowan, J.M., 2007. The Biomarker Guide, Volume 1: Biomarkers and Isotopes in the Environment and Human History. Cambridge University Press, UK.

Petit, J.R., Jouzel, J., Raynaud, D., Barkov, N.I., Barnola, J.M., Basile, I., Bender, M., Chappellaz, J., Davis, M., Delaygue, G., Delmotte, M., Kotlyakov, V.M., Legrand, M., Lipenkov, V.Y., Lorius, C., Pepin, L., Ritz, C., Saltzman, E., Stievenard, M., 1999. Climate and atmospheric history of the past 420,000 years from the Vostok ice core, Antarctica. Nature 399, 429-436.

Pichevin, L.E., Reynolds, B.C., Ganeshram, R.S., Cacho, I., Pena, L., Keefe, K., Ellam, R.M., 2009. Enhanced carbon pump inferred from relaxation of nutrient limitation in the glacial ocean. Nature 459, 1114-1117.

Piper, B.S., Plinston, D.T., Sutcliffe, J.V., 1986. The water balance of Lake Victoria. Hydrological Sciences - Journal 31, 25-37.

Polissar, P.J., Abbott, M.B., Shemesh, A., Wolfe, A.P., Bradley, R.S., 2006. Holocene hydrologic balance of tropical South America from oxygen isotopes of lake sediment opal, Venezuelan Andes. Earth and Planetary Science Letters 242, 375-389.

Prell, W.L., Kutzbach, J.E., 1987. Monsoon variability over the past 150,000 years. Journal of Geophysical Research, [Atmospheres] 92, 8411-8425.

Prentice, I.C., Jolly, D., BIOME 6000 participants, 2000. Mid-Holocene and glacial-maximum vegetation geography of the northern continents and Africa. Journal of Biogeography 27, 507-519.

Ragueneau, O., Schultes, S., Bidle, K., Claquin, P., Moriceau, B., 2006. Si and C interactions in the world ocean: Importance of ecological processes and implications for the role of diatoms in the biological pump. Global Biogeochemical Cycles 20, GB4S02.

Raven, J.A., 1983. The transport and function of silicon in plants. Biological Reviews 58, 179-207.

Revel, M., Ducassou, E., Grousset, F.E., Bernasconi, S.M., Migeon, S., Revillon, S., Mascle, J., Murat, A., Zaragosi, S., Bosch, D., 2010. 100,000 years of African monsoon variability recorded in sediments of the Nile margin. Quaternary Science Reviews 29, 1342-1362.

Reynolds, B.C., Aggarwal, J., Andre, L., Baxter, D., Beucher, C., Brzezinski, M.A., Engstrom, E., Georg, R.B., Land, M., Leng, M.J., Opfergelt, S., Rodushkin, I., Sloane, H.J., van den Boorn, S.H.J.M., Vroon, P.Z., Cardinal, D., 2007. An inter-

laboratory comparison of Si isotope reference materials. Journal of Analytical Atomic Spectrometry 22, 561-568.

Reynolds, B.C., Georg, R.B., Burton, K.W., James, R.H., Halliday, A.N., 2006a. Silicon isotope variations in river waters: a weathering proxy? Geochimica et Cosmochimica Acta 70, A530.

Reynolds, B.C., Georg, R.B., Oberli, F., Wiechert, U., Halliday, A.N., 2006b. Re-assessment of silicon isotope reference materials using high-resolution multi-collector ICP-MS. Journal of Analytical Atomic Spectrometry 21, 266-269.

Reynolds, J.H., Verhoogen, J., 1953. Natural variations in the isotopic constitution of silicon. Geochimica et Cosmochimica Acta 3, 224-234.

Rhoades, J.D., Kandiah, A., Mashali, A.M., 1992. The use of saline waters for crop production, FAO irrigation and drainage paper 48. FAO, Rome.

Richardson, J.L., Harvey, T.J., Holdship, S.A., 1978. Diatom in the history of shallow East African lakes. Polskie Archiwum Hydrobiologii 25, 341-353.

Rings, A., Lücke, A., Schleser, G.H., 2004. A new method for the quantitative separation of diatom frustules from lake sediments. Limnology and Oceanography Methods 2, 25-34.

Roberts, N., Taieb, M., Barker, P., Damnati, B., Icole, M., Williamson, D., 1993. Timing of the Younger Dryas event in East Africa from lake-level changes. Nature 366, 146-148.

Rohling, E.J., Pälike, H., 2005. Centennial-scale climate cooling with a sudden cold event around 8,200 years ago. Nature 434, 975-979.

Rossignol-Strick, M., Nesteroff, W., Olive, P., Vergnaud-Grazzini, C., 1982. After the deluge: Mediterranean stagnation and sapropel formation. Nature 295, 105-110.

Round, F.E., Crawford, R.M., Mann, D.G., 1990. The Diatoms: biology and morphology of the genera. Cambridge University Press, Cambridge, UK.

Rozanski, K., Araguas-Araguas, L., Gonfiantini, R., 1996. Isotope patterns of precipitation in the East African region, In: Johnson, T.C., Odada, E.O. (Eds.), The Limnology, Climatology and Paleoclimatology of the East African Lakes. Gordon and Breach Publishers, Amsterdam, The Netherlands, pp. 79-93.

Rozanski, K., Araguás-Araguás, L., Gonfiantini, R., 1993. Isotopic patterns in modern global precipitation, In: Swart, P.K., Lohmann, K.C., McKenzie, J., Savin, S. (Eds.), Climate change in continental isotopic records. AGU, Washington, D.C., pp. 1-36.

Russell, J.M., Johnson, T.C., 2005. A high resolution geochemical record from Lake Edward, Uganda Congo and the timing and causes of tropical African drought during the late Holocene. Quaternary Science Reviews 24, 1375-1389.

Russell, J.M., Johnson, T.C., 2006. The water balance and stable isotope hydrology of Lake Edward, Uganda-Congo. Journal of Great Lakes Research 32, 77-90.

Bibliography

Russell, J.M., Johnson, T.C., 2007. Little Ice Age drought in equatorial Africa: Intertropical Convergence Zone migrations and El Niño-Southern Oscillation variability. Geology 35, 21-24.

Russell, J.M., Johnson, T.C., Kelts, K.R., Lærdal, T., Talbot, M.R., 2003a. An 11000-yr lithostratigraphic and paleohydrologic record from Equatorial Africa: Lake Edward, Uganda-Congo. Palaeogeography, Palaeoclimatology, Palaeoecology 193, 25-49.

Russell, J.M., Johnson, T.C., Talbot, M.R., 2003b. A 725 yr cycle in the climate of central Africa during the late Holocene. Geology 31, 677-680.

Russell, J.M., Kelts, K.R., 1999. The sedimentologic history of Lake Edward, Uganda, IDEAL Bulletin (Summer), pp. 1-3.

Sachse, D., Radke, J., Gleixner, G., 2006. δD values of individual *n*-alkanes from terrestrial plants along a climatic gradient - implications for the sedimentary biomarker record. Organic Geochemistry 37, 469-483.

SAHRA, 2005. Fractionation during precipitation. http://web.sahra.arizona.edu/programs/isotopes/oxygen.html#4, accessed on 21.09.2012.

Said, R., 1993. The River Nile: geology, hydrology and utilization. Pergamon Press, Oxford.

Salati, E., A., D.O., Matsui, E., Gat, J.R., 1979. Recycling of water in the Amazon Basin: an isotopic study. Water Resources Research 15, 1250-1258.

Savage, P.S., Georg, R.B., Williams, H.M., Burton, K.W., Halliday, A.N., 2011. Silicon isotope fractionation during magmatic differentiation. Geochimica et Cosmochimica Acta 75, 6124-6139.

Schiff, C.J., Kaufman, D.S., Wolfe, A.P., Dodd, J., Sharp, Z., 2009. Late Holocene storm-trajectory changes inferred from the oxygen isotope composition of lake diatoms, south Alaska. Journal of Paleolimnology 41, 189-208.

Schlüter, T., 2008. Geological Atlas of Africa: with Notes on Stratigraphy, Tectonics, Economic Geology, Geohazards, Geosites and Geoscientific Education of Each Country, 2nd ed. Springer-Verlag, Berlin.

Schnurrenberger, D., Russell, J., Kelts, K., 2003. Classification of lacustrine sediments based on sedimentary components. Journal of Paleolimnology 29, 141-154.

Schoelynck, J., Bal, K., Backx, H., Okruszko, T., Meire, P., Struyf, E., 2010. Silica uptake in aquatic and wetland macrophytes: a strategic choice between silica, lignin and cellulose? New Phytologist 186, 385-391.

Sepulchre, P., Ramstein, G., Fluteau, F., Schuster, M., Tiercelin, J.-J., Brunet, M., 2006. Tectonic uplift and eastern Africa aridification. Science 313, 1419-1423.

Shahin, M., 1985. Hydrology of the Nile Basin. Elsevier, Amsterdam.

Bibliography

Shemesh, A., Burckle, L.H., Hays, J.D., 1995. Late Pleistocene oxygen isotope records of biogenic silica from the Atlantic sector of the Southern Ocean. Paleoceanography 10, 179-196.

Shemesh, A., Mortlock, R.A., Smith, R.J., Froelich, P.N., 1988. Determination of Ge/Si in marine siliceous microfossils: Separation, cleaning and dissolution of diatoms and radiolaria. Marine Chemistry 25, 305-323.

Sigman, D.M., Boyle, E.A., 2000. Glacial/interglacial variations in atmospheric carbon dioxide. Nature 407, 859-869.

Sinada, F., Abdel Karim, A.G., 1984. Physical and chemcial characteristics of the Blue Nile and the White Nile at Khartoum. Hydrobiologia 110, 21-32.

Smetacek, V., 1998. Diatoms and the silicate factor. Nature 391, 224-225.

Smil, V., 2000. Phosphorus in the environment: natural flows and human interferences. Annual Review of Energy and the Environment 25, 53-88.

Smittenberg, R.H., Baas, M., Schouten, S., Sinninghe Damste, J.S., 2005. The demise of the alga *Botryococcus braunii* from a Norwegian fjord was due to early eutrophication. The Holocene 15, 133-140.

Smol, J., Stoermer, E., 2010. The diatoms: applications for the environmental and earth sciences. Cambridge University Press, UK, p. 686.

Sonntag, E., Klitzsch, E., Lohnert, E.P., El-Shazly, E.M., Munnich, K.O., Junghans, C., Thorweihe, U., Weistroffer, K., Swailem, F.M., 1979. Palaeoclimatic information from deuterium and oxygen-18 in carbon-14 dated north Saharian groundwaters, Isotope Hydrology 1978, vol. II. International Atomic Energy Agency, Vienna.

Spigel, R.H., Coulter, G.W., 1996. Comparison of hydrology and physical limnology of the East African Great Lakes: Tanganyika, Malawi, Victoria, Kivu and Turkana (with references to some North American Great Lakes), In: Johnson, T.C., Odada, E.O. (Eds.), The limnology, climatology, and paleoclimatology of the East African lakes. Gordon and Breach Publishers, Amsterdam, The Netherlands, pp. 103-135.

Stager, J.C., 1984. The diatom record of Lake Victoria (East Africa): the last 17,000 years, In: Mann, D.G. (Ed.), Proceedings of the Seventh Diatom Symposium, August 1982, Philadelphia, pp. 455-476.

Stager, J.C., Cumming, B.F., Meeker, L.D., 1997. A high-resolution 11,400-yr diatom record from Lake Victoria, East Africa. Quaternary Research 47, 81-89.

Stager, J.C., Cumming, B.F., Meeker, L.D., 2003. A 10,000-year high-resolution diatom record from Pilkington Bay, Lake Victoria, East Africa. Quaternary Research 59, 172-181.

Stager, J.C., Johnson, T.C., 2000. A 12,400 ^{14}C yr offshore diatom record from east central Lake Victoria, East Africa. Journal of Paleolimnology 23, 373-383.

Stager, J.C., Johnson, T.C., 2008. The late Pleistocene desiccation of Lake Victoria and the origin of its endemic biota Hydrobiologia 596, 5-16.

Bibliography

Stager, J.C., Mayewski, P.A., Meeker, L.D., 2002. Cooling cycles, Heinrich event 1, and the desiccation of Lake Victoria. Palaeogeography, Palaeoclimatology, Palaeoecology 183, 169-178.

Stager, J.C., Reinthal, P.N., Livingstone, D.A., 1986. A 25,000-year history for Lake Victoria, East Africa, and some comments on its significance for the evolution of cichlid fishes. Freshwater Biology 16, 15-19.

Stager, J.C., Ryves, D.B., Chase, B.M., Pausata, F.S.R., 2011. Catastrophic drought in the Afro-Asian monsoon region during Heinrich Event 1. Science 331, 1299-1302.

Stanley, J.-D., Krom, M.D., Cliff, R.A., Woodward, J.C., 2003. Short contribution: Nile flow failure at the end of the Old Kingdom, Egypt: Strontium isotopic and petrologic evidence. Geoarchaeology 18, 395-402.

Stern, L.A., Blisniuk, P.M., 2002. Stable isotope composition of precipitation across the southern Patagonian Andes. Journal of Geophysical Research 107, 4667.

Stewart, M.K., 1975. Stable isotope fractionation due to evaporation and isotopic exchange of falling waterdrops: applications to atmospheric processes and evaporation of lakes. Journal of Geophysical Research 80, 1133-1146.

Street-Perrott, F.A., Barker, P.A., 2008. Biogenic silica: a neglected component of the coupled global continental biogeochemical cycles of carbon and silicon. Earth Surface Processes and Landforms 33, 1436-1457.

Street-Perrott, F.A., Barker, P.A., Leng, M., J., Sloane, H.J., Wooller, M.J., Ficken, K.J., Swain, D.L., 2008. Towards an understanding of late Quaternary variations in the continental biogeochemical cycle of silicon: multi-isotope and sediment-flux data for Lake Rutundu, Mt Kenya, East Africa, since 38 ka BP. Journal of Quaternary Science 23, 375-387.

Street-Perrott, F.A., Barker, P.A., Swain, D.L., Ficken, K.J., Wooller, M.J., Olago, D.O., Huang, Y., 2007. Late Quaternary changes in ecosystems and carbon cycling on Mt. Kenya, East Africa: a landscape-ecological perspective based on multi-proxy lake-sediment influxes. Quaternary Science Reviews 26, 1838-1860.

Street-Perrott, F.A., Harrison, S.P., 1985. Lake levels and climate reconstruction, In: Hecht, A.D. (Ed.), Paleoclimate analysis and modeling. John Wiley and Sons, Canada, pp. 291-340.

Street-Perrott, F.A., Kutzbach, J.E., 1985. Milankovitch forcing of fluctuations in the level of tropical lakes from 18 to 0 kyr BP. Nature 317, 130-134.

Street-Perrott, F.A., Mitchell, J.F.B., Marchand, D.S., Brunner, J.S., 1990. Milankovitch and albedo forcing of the tropical monsoons: a comparision of geological evidence and numerical simulations for 9000 yBP. Transactions of the Royal Society of Edinburgh: Earth Sciences 81, 407-427.

Street-Perrott, F.A., Perrot, R.A., 1993. Holocene vegetation, lake levels, and climate of Africa, In: Wright, H.E.J., Kutzbach, J.E., Webb, T.I., Ruddiman, W.F., Street-Perrott, F.A., Bartlein, P.J. (Eds.), Global Climates since the Last Glacial Maximum. University of Minnesota Press, Minneapolis, pp. 318-356.

Bibliography

Street-Perrott, F.A., Perrott, R.A., 1990. Abrupt climate fluctuations in the tropics: the influence of Atlantic Ocean circulation. Nature 343, 607-612.

Struyf, E., Conley, D.J., 2009. Silica: an essential nutrient in wetland biogeochemistry. Frontiers in Ecology and the Environment 7, 88-94.

Struyf, E., Conley, D.J., 2012. Emerging understanding of the ecosystem silica filter. Biogeochemistry 107, 9-18.

Struyf, E., Damme, S.V., Gribsholt, B., Meire, P., 2005. Freshwater marshes as dissolved silica recyclers in an estuarine environment (Schelde estuary, Belgium). Hydrobiologia 540, 69-77.

Struyf, E., Smis, A., Van Damme, S., Garnier, J., Govers, G., Van Wesemael, B., Conley, D.J., Batelaan, O., Frot, E., Clymans, W., Vandevenne, F., Lancelot, C., Goos, P., Meire, P., 2010. Historical land use change has lowered terrestrial silica mobilization. Nature Communications 1, 129.

Struyf, E., Smis, A., Van Damme, S., Meire, P., Conley, D.J., 2009. The global biogeochemical silicon cycle. Silicon 1, 207-213.

Struyf, E., Van Damme, S., Gribsholt, B., Bal, K., Beauchard, O., Middelburg, J., Meire, P., 2007. Phragmites australis and silica cycling in tidal wetlands. Aquatic botany 87, 134-140.

Stuiver, M., Reimer, P.J., Reimer, R.W., 2012. CALIB 6.0. http://calib.qub.ac.uk/calib/, accessed on 16/07/2012.

Sutcliffe, J.V., 2009. The hydrology of the Nile Basin, In: Dumont, H.J. (Ed.), The Nile: Origin, Environments, Limnology and Human Use. Springer Science + Business Media B.V., pp. 335-364.

Sutcliffe, J.V., Parks, Y.P., 1999. The Hydrology of the Nile, IAHS Special Publications,5. International Association of Hydrological Sciences Press, Wallingford, UK.

Swann, G.E.A., Leng, M.J., 2009. A review of diatom $\delta^{18}O$ in palaeoceanography. Quaternary Science Reviews 28, 384-398.

Swann, G.E.A., Leng, M.J., Juschus, O., Melles, M., Brigham-Grette, J., Sloane, H.J., 2010. A combine oxygen and silicon diatom isotope record of Late Quaternary change in Lake El'gygytgyn, North East Siberia. Quaternary Science Reviews 29, 774-786.

Swann, G.E.A., Leng, M.J., Sloane, H.J., Maslin, M.A., Onodera, J., 2007. Diatom oxygen isotopes: Evidence of a species effect in the sediment record. Geochem. Geophys. Geosyst. 8, Q06012.

Swann, G.E.A., Maslin, M.A., Leng, M.J., Sloane, H.J., Haug, G.H., 2006. Diatom $\delta^{18}O$ evidence for the development of the modern halocline system in the subarctic northwest Pacific at the onset of major Northern Hemisphere glaciation. Paleoceanography 21, PA1009.

Talbot, M.R., Lærdal, T., 2000. The Late Pleistocene-Holocene palaeolimnology of Lake Victoria, East Africa, based upon elemental and isotopic analyses of sedimentary organic matter. Journal of Paleolimnology 23, 141-164.

Talbot, M.R., Livingstone, D.A., 1989. Hydrogen index and carbon isotopes of lacustrine organic matter as lake level indicators. Palaeogeography, Palaeoclimatology, Palaeoecology 70, 121–137.

Talbot, M.R., Williams, M.A.J., Adamson, D.A., 2000. Strontium isotope evidence for late Pleistocene reestablishment of an integrated Nile drainage network. Geology 28, 343-346.

Talling, J.F., 1963. Origin of stratification in an African Rift lake. Limnology and Oceanography 8, 68–78.

Talling, J.F., 1966. The annual cycle of stratification and phytoplankton growth in Lake Victoria (East Africa). Internationale Revue der gesamten Hydrobiologie 51, 545–621.

Talling, J.F., Sinada, F., Taha, O.E., Sobhy, E.M.H., 2009. Phytoplankton: composition, development and productivity, In: Dumont, H.J. (Ed.), The Nile: Origin, Environments, Limnology and Human Use. Springer Science + Business Media B.V., pp. 431-462.

Teller, J.T., Boyd, M., Yanga, Z., Korc, P.S.G., Fard, A.M., 2005. Alternative routing of Lake Agassiz overflow during the Younger Dryas: new dates, paleotopography, and a re-evaluation. Quaternary Science Reviews 24, 1890-1905.

Teller, J.T., Leverington, D.W., Mann, J.D., 2002. Freshwater outbursts to the oceans from glacial Lake Agassiz and their role in climate change during the last deglaciation. Quaternary Science Reviews 21, 879-887.

Theissen, K.M., Zinniker, D.A., Moldowan, J.M., Dunbar, R.B., Rowe, H.D., 2005. Pronounced occurrence of long-chain alkenones and dinosterol in a 25,000-year lipid molecular fossil record from Lake Titicaca, South America. Geochimica et Cosmochimica Acta 69, 623-636.

Thompson, L.G., Mosley-Thompson, E., Davis, M.E., Henderson, K.A., Brecher, H.H., Zagorodnov, V.S., Mashiotta, T.A., Lin, P.-N., Mikhalenko, V.N., Hardy, D.R., Beer, J., 2002. Kilimanjaro ice core records: evidence of Holocene climate change in tropical Africa. Science 298, 589-593.

Tierney, J.E., Lewis, S.C., Cook, B.I., LeGrande, A.N., Schmidt, G.A., 2011a. Model, proxy and isotopic perspectives on the East African Humid Period. Earth and Planetary Science Letters 307, 103-112.

Tierney, J.E., Russell, J.M., Sinninghe Damsté, J.S., Huang, Y., Verschuren, D., 2011b. Late Quaternary behavior of the East African monsoon and the importance of the Congo Air Boundary. Quaternary Science Reviews 30, 798-807.

Tjallingii, R., Claussen, M., Stuut, J.-B.W., Fohlmeister, J., Jahn, A., Bickert, T., Lamy, F., Röhl, U., 2008. Coherent high- and low-latitude control of the northwest African hydrological balance. Nature Geoscience 1, 670-675.

Bibliography

Tréguer, P., Nelson, D.M., Van Bennekom, A.J., DeMaster, D.J., Leynaert, A., Quéguiner, B., 1995. The silica balance in the world ocean: a reestimate. Science 268, 375-379.

Tréguer, P., Pondaven, P., 2000. Silica control of carbon dioxide. Nature 406, 358-359.

Tyler, J.J., Leng, M.J., Sloane, H.J., 2007. The effects of organic removal treatment on the integrity of $\delta^{18}O$ measurements from biogenic silica. Journal of Paleolimnology 37, 491-497.

van den Boorn, S.H.J.M., Vroon, P.Z., van Belle, C.C., van der Wagt, B., Schwieters, J., van Bergen, M.J., 2006. Determination of silicon isotope ratios in silicate materials by high-resolution MC-ICP-MS using a sodium hydroxide sample digestion method. Journal of Analytical Atomic Spectrometry 21, 734-742.

van den Boorn, S.H.J.M., Vroon, P.Z., van Bergen, M.J., 2009. Sulfur-induced offsets in MC-ICP-MS silicon-isotope measurements. Journal of Analytical Atomic Spectrometry 24, 1111-1114.

van Geel, B., 2001. Non-pollen palynomorphs, In: Smol, J.P., Birks, H.J.B., Last, W.M. (Eds.), Tracking Environmental Change Using Lake Sediments. Volume 3: Terrestrial, Algal, and Siliceous Indicators. Kluwer Academic Publishers, Dordrecht, The Netherlands, pp. 99-119.

Varela, D.E., Pride, C.J., Brzezinski, M.A., 2004. Biological fractionation of silicon isotopes in Southern Ocean surface waters. Global Biogeochemical Cycles 18, GB1047.

Viner, A.B., 1977. The sediments of Lake George (Uganda). IV: Vertical distribution of chemical features in relation to ecological history and nutrient recycling. Archiv für Hydrobiologie 80, 40-69.

Viner, A.B., Smith, I.B., 1973. Geographical, historical, and physical aspects of Lake George Proceedings of the Royal Society of London, Series B: Biological Sciences 184, 235-270.

Viso, A.-C., Pesando, D., Bernard, P., Marty, J.-C., 1993. Lipid components of the Mediterranean seagrass *Posidonia Oceanica*. Phytochemistry 34, 381-387.

Wedepohl, K.H., 1995. The composition of the continental crust. Geochimica et Cosmochimica Acta 59, 1217-1232.

White, A.F., Blum, A.E., 1995. Effects of climate on chemical weathering in watersheds. Geochimica et Cosmochimica Acta 59, 1729-1747.

White, F., 1983. The Vegetation of Africa. A Descriptive Memoir to Accompany the UNESCO/AETFAT/UNSO Vegetation Map of Africa. UNESCO, Paris.

Wickbold, R., 1959. Die anreicherung sehr kleiner mengen kieselsäure durch Ionenaustausch. Fresenius Zeitschrift für Analytische Chemie 171, 81-87.

Williams, M., Talbot, M., Aharon, P., Salaam, Y.A., Williams, F., Brendeland, K.I., 2006. Abrupt return of the summer monsoon 15,000 years ago: new supporting

evidence from the lower White Nile valley and Lake Albert. Quaternary Science Reviews 25, 2651-2665.

Williams, M.A.J., Adamson, D., Cock, B., McEvedy, R., 2000. Late Quaternary environments in the White Nile region, Sudan. Global and Planetary Change 26, 305-316.

Williams, M.A.J., Williams, F.M., Duller, G.A.T., Munro, R.N., El Tom, O.A.M., Barrows, T.T., Macklin, M., Woodward, J., Talbot, M.R., Haberlah, D., Fluin, J., 2010. Late Quaternary floods and droughts in the Nile valley, Sudan: new evidence from optically stimulated luminescence and AMS radiocarbon dating. Quaternary Sciences Reviews 29, 1116-1137.

Woods, G., 2007. Measurement of trace elements in malt spirit beverages (Whisky) by 7500cx ICP-MS. Agilent Technologies, USA.

Woodward, J.C., Macklin, M.G., Krom, M.D., Williams, M.A.J., 2007. The Nile: evolution, Quaternary river environments and material fluxes, In: Gupta, A. (Ed.), Large rivers: geomorphology and management. John Wiley and Sons Ltd, Chichester, UK, pp. 261-291.

World Bank, 2008. Project appraisal document on a proposed credit in the amount of SDR 27.4 million (US$45 million equivalent) to the federal Democratic Republic of Ethiopia for a Tana and Beles integrated water resources development project. World Bank, Washington DC, USA.

Xu, Y., Jaffé, R., 2009. Geochemical record of anthropogenic impacts on Lake Valencia, Venezuela. Applied Geochemistry 24, 411-418.

Yin, X., Nicholson, S.E., Ba, M.B., 2000. On the diurnal cycle of cloudiness over Lake Victoria and its influence on evaporation from the lake. Hydrological Sciences-Journal des Sciences Hydrologiques 45, 407-424.

Yool, A., Tyrrell, T., 2003. Role of diatoms in regulating the ocean's silicon cycle. Global Biogeochemical Cycles 17, 1103.

Zambardi, T., Poitrasson, F., 2011. Precise Determination of Silicon Isotopes in Silicate Rock Reference Materials by MC-ICP-MS. Geostandards and Geoanalytical Research 35, 89-99.

Zhang, Z., Zhao, M., Yang, X., Wang, S., Jiang, X., Oldfield, F., Eglinton, G., 2004. A hydrocarbon biomarker record for the last 40 kyr of plant input to Lake Heqing, southwestern China. Organic Geochemistry 35, 595-613.

Zheng, Y., Zhou, W., Meyers, P.A., Xie, S., 2007. Lipid biomarkers in the Zoigê-Hongyuan peat deposit: indicators of Holocene climate changes in West China. Organic Geochemistry 38, 1927-1940.